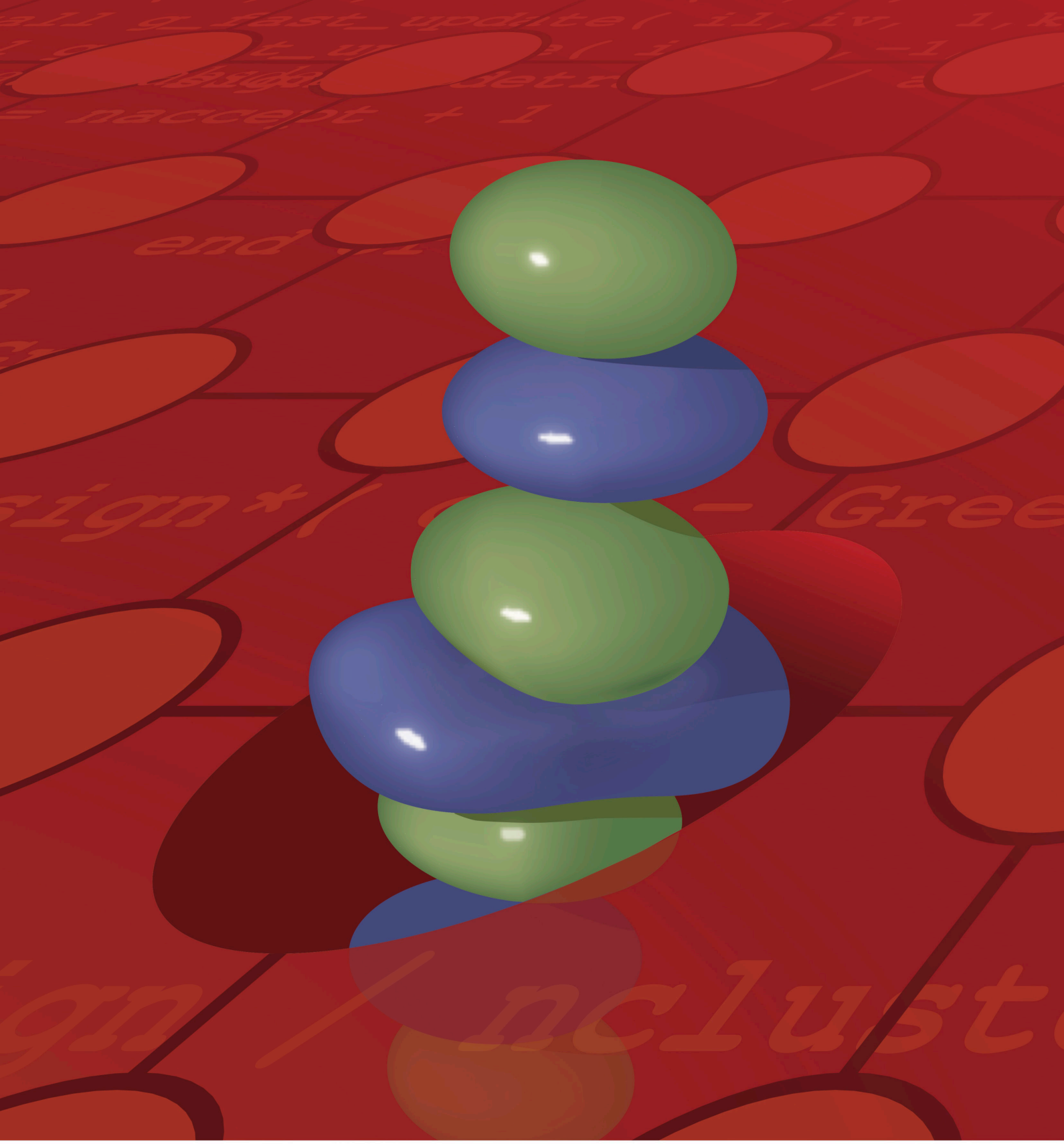


Understanding Correlated Materials with DMFT

Eva Pavarini, Erik Koch, Alexander Lichtenstein, and Dieter Vollhardt (Eds.)

JÜLICH
Forschungszentrum

Schriften des Forschungszentrums Jülich
Reihe Modeling and Simulation Band / Volume 15

Forschungszentrum Jülich GmbH
Peter Grünberg Institute
Jülich Supercomputing Centre

Lecture Notes of the Autumn School on Correlated Electrons 2025

Eva Pavarini, Erik Koch, Alexander Lichtenstein, and Dieter Vollhardt (Eds.)

Understanding Correlated Materials with DMFT

Autumn School organized by
the Peter Grünberg Institute
at Forschungszentrum Jülich
22 – 26 September 2025

Schriften des Forschungszentrums Jülich
Modeling and Simulation Band / Volume 15

ISSN 2192-8525 ISBN 978-3-95806-813-1

Bibliographic information published by the Deutsche Nationalbibliothek.
Die Deutsche Nationalbibliothek lists this publication in the Deutsche Nationalbibliografie; detailed bibliographic data are available in the Internet at http://dnb.d-nb.de.

Publisher:	Forschungszentrum Jülich GmbH Jülich Supercomputing Centre
Cover Design:	Grafische Medien, Forschungszentrum Jülich GmbH
Printer:	Schloemer & Partner GmbH, Düren
Copyright:	Forschungszentrum Jülich 2025
Distributor:	Forschungszentrum Jülich Zentralbibliothek, Verlag 52425 Jülich Phone +49 (0)2461 61-5368 · Fax +49 (0)2461 61-6103 e-mail: zb-publikation@fz-juelich.de www.fz-juelich.de/zb

Schriften des Forschungszentrums Jülich
Reihe Modeling and Simulation, Band / Volume 15

ISSN 2192-8525
ISBN 978-3-95806-813-1

Vollständig frei verfügbar über das Publikationsportal des Forschungszentrums Jülich (JuSER) unter www.fz-juelich.de/zb/openaccess

This is an Open Access publication distributed under the terms of the Creative Commons Attribution License 4.0, which permits unrestricted use, distribution, and reproduction in any medium, provided the original work is properly cited.

Contents

Preface

1. Understanding Correlated Materials with Lattice Fermions in Infinite Dimensions
   Dieter Vollhardt
2. Density Functional Theory for the Sceptical
   Robert Jones
3. Dynamical Mean-Field Theory for Materials
   Eva Pavarini
4. Hund's Metal Physics in the Iron-Based Superconductors
   Luca de' Medici
5. DMFT for Moiré Systems
   Tim Wehling
6. Effect of Charge Self-Consistency in Calculations for Transition-Metal Oxides
   Claude Ederer
7. A Perspective on Screened Coulomb Interactions from the constrained Random Phase Approximation
   Jan Tomczak
8. Dynamical Mean-Field Theory for Correlated Electrons with Disorder
   Krzysztof Byczuk
9. Learning Feynman Diagrams with Tensor Trains
   Xavier Waintal
10. QMC for Nonequilibrium Systems
    Philipp Werner
11. Analytic Continuation of Quantum Monte Carlo Data
    Erik Koch
12. Functional Renormalization of Strongly Correlated Electrons: DMFT as a Booster Rocket
    Walter Metzner
13. Path Integrals and Reference Systems
    Alexander Lichtenstein
14. Unconventional Superconductivity in the Dynamical Vertex Approximation
    Karsten Held
15. Dynamical Mean-Field Theory with Quantum Computing
    Thomas Ayral

Index

Preface

Dynamical mean-field theory (DMFT) has established itself as the method of choice for understanding emergent phases in correlated materials. In fact, its combination with density-functional theory (DFT) via the construction of materials-specific many-body Hamiltonians has opened the path to the description of correlation effects beyond the level of generic models. This, together with the development of powerful quantum-impurity solvers, and the help of modern massively-parallel supercomputers, provides powerful tools for unraveling correlation effects and has revolutionized the field of correlated materials science. The goal of this year's school is to provide students with an overview of the method and its application to materials, with a view towards the future of many-body simulations. The program will start with fundamental models and concepts, introducing the Hubbard model, density-functional theory and the principles of DMFT. More advanced lectures will focus on the DFT+DMFT technique and its extensions. Specialized lectures will then demonstrate how the approach can be used to identify the mechanism of paradigmatic emergent phenomena in materials: non-conventional superconductivity, orbital ordering, Mott phases, disorder, Hund's metal behavior, and pseudogap phases. The topics will be treated with a focus on explaining key experiments in a realistic setting and with an outlook on materials design.

A school of this size and scope requires backing from many sources. We are very grateful for all the practical and financial support we have received. The Peter Grünberg Institute at the Forschungszentrum Jülich and the Jülich Supercomputing Centre provided the major part of the funding and were vital for the organization of the school as well as for the production of this book. The Institute for Complex Adaptive Matter (ICAM) continued also this year to support the school and supplied additional funds.

The nature of a school makes it desirable to have the lecture notes available when the lectures are given. This way students get the chance to work through the lectures thoroughly while their memory is still fresh. We are therefore extremely grateful to the lecturers that, despite tight deadlines, provided their manuscripts in time for the production of this book. We are confident that the lecture notes collected here will not only serve the participants of the school but will also be useful for other students entering the exciting field of strongly-correlated materials.

We are grateful to Mrs. J. Timmer of the Verlag des Forschungszentrum Jülich and to Mrs. D. Mans of the Grafische Betriebe for providing their expert support in producing the present volume on a tight schedule. We heartily thank our students and postdocs who helped with proofreading the manuscripts, often on quite short notice: Elaheh Adibi, Amit Chauhan, Qiwei Li, and Xue-Jing Zhang.

Finally, our special thanks go to Dipl.-Ing. R. Hölzle for his invaluable advice on the innumerable questions concerning the organization of such an endeavor, and to Mrs. L. Snyders for expertly handling all practical issues.

Eva Pavarini, Erik Koch, Alexander Lichtenstein, and Dieter Vollhardt

August 2025

1 Understanding Correlated Materials with Lattice Fermions in Infinite Dimensions

Dieter Vollhardt
Center for Electronic Correlations and Magnetism
University of Augsburg

Contents

1 Electronic correlations **2**
1.1 Correlated materials . . . 2
1.2 The many-electron problem . . . 2

2 The minimal model for interacting lattice electrons **3**
2.1 Unique features of the Hubbard model . . . 3

3 Mean-field theories for the many-electron problem **6**
3.1 Hartree-Fock theory . . . 6
3.2 Infinite dimensions and mean-field behavior . . . 7

4 Static approximations for the Hubbard model **10**
4.1 Factorization approach: Hartree mean-field theory . . . 10
4.2 Variational approach: Gutzwiller wave function . . . 11

5 Lattice fermions in infinite dimensions **14**
5.1 Simplifications of diagrammatic quantum many-body theory . . . 15
5.2 The Hubbard model in $d = \infty$ . . . 16

6 Dynamical mean-field theory for correlated electrons **20**
6.1 The self-consistent equations . . . 20
6.2 Application of DMFT to the Hubbard model . . . 22
6.3 Beyond DMFT . . . 25

7 Understanding correlated materials with DMFT **27**
7.1 DFT+DMFT and GW+DMFT . . . 27
7.2 Applications . . . 28

8 Conclusions **30**

E. Pavarini, E. Koch, A. Lichtenstein, and D. Vollhardt (eds.)
Understanding Correlated Materials with DMFT
Modeling and Simulation Vol. 15
Forschungszentrum Jülich, 2025, ISBN 978-3-95806-813-1
http://www.cond-mat.de/events/correl25

1 Electronic correlations

1.1 Correlated materials

The effective interaction between electrons in solids differs significantly from the bare classical Coulomb interaction, since it depends not only on material-specific properties such as the electronic band structure and screening but, more generally, on exchange and correlation effects. Materials whose properties are strongly influenced by electronic correlations are referred to as "correlated electron materials", or simply "correlated materials".

It has long been known that correlation effects are strong in materials with partially filled d and f electron shells and narrow energy bands as in the $3d$ transition metals [1] or the rare–earths [2] and their compounds. But more recently it was found that strong electronic correlations can occur even in materials without transition metal or rare-earth elements, such as "Moiré" (or, more generally, twisted) van der Waals heterostructures [3].

Electronic correlations in solids often result in complex physics such as heavy fermion behavior and unconventional superconductivity [4], especially high temperature superconductivity [5], colossal magnetoresistance [6], Mott metal-insulator transitions [7], the fractional quantum Hall effect [8], and Fermi liquid instabilities [9]. The recent discovery of correlation phenomena and rich phase diagrams in Moiré heterostructures [3] has further increased the interest in correlation physics.

The exceptional properties of correlated materials are not only of interest for fundamental research but may also be relevant for technological applications. Namely, the unusual sensitivity of correlated electron materials upon changes of external parameters such as temperature, pressure, electromagnetic fields, and doping can be employed to develop materials with useful functionalities [10]. For example, Moiré heterostructures may enable "twistronics", a new approach to device engineering [11]. Consequently there is a great need for the development of appropriate models and theoretical investigation techniques which allow for a comprehensive and at the same time reliable exploration of correlated materials [12].

1.2 The many-electron problem

The investigation of electronic correlation effects in solids requires the application of quantum many-body theory for electrons ("many-electron theory"). This is faced by two closely connected problems: the need for a sufficiently simple model of correlated electrons and its solution. Progress in this direction was remarkably slow.[1] A microscopic model of corre-

[1] Given the fact that the Heisenberg model [13], which explains ferromagnetic order of localized spins in solids as the result of quantum-mechanical exchange processes, had been introduced already in 1928, and Bloch's [14] subsequent observation that a model for ferromagnetism in $3d$ transition metals had to include the mobile nature of the electrons, one might naively expect that this set the stage for the rapid formulation of a correlated electron model and its approximate investigation. But this was not the case (for a historical review of the evolution of the quantum-mechanical theory of metals from 1928 to 1933, which describes the conceptual problems of that time, see ref. [15]). One reason for the slow development of a many-electron theory was that in the 1930s and 40s nuclear physics attracted more attention than solid-state physics, with a very specific focus of research during the 2nd World War. But apart from that, the sheer complexity of the many-body problem itself did not allow for

lated electrons did not emerge until 1963, when a lattice model was proposed independently by Gutzwiller [17], Hubbard [18], and Kanamori [19] to explain ferromagnetism in $3d$ transition metals. Today this model is referred to as "Hubbard model".

2 The minimal model for interacting lattice electrons

Fermionic particles that move and interact on a lattice rather than in the continuum are referred to as "lattice fermions". The minimal microscopic model of interacting lattice fermions is the single-band Hubbard model. The Hamiltonian consists of the kinetic energy $\hat{H}_0$ and the interaction energy $\hat{H}_{\rm int}$ (in the following operators are denoted by a hat)

$$\hat{H} = \hat{H}_0 + \hat{H}_{\rm int}, \tag{1a}$$

$$\hat{H}_0 = \sum_{\boldsymbol{R}_i,\boldsymbol{R}_j,\sigma} t_{ij}\, \hat{c}^\dagger_{i\sigma}\hat{c}_{j\sigma} = \sum_{\boldsymbol{k},\sigma} \varepsilon_{\boldsymbol{k}}\hat{n}_{\boldsymbol{k}\sigma}, \tag{1b}$$

$$\hat{H}_{\rm int} = U\sum_{\boldsymbol{R}_i} \hat{n}_{i\uparrow}\hat{n}_{i\downarrow} \equiv U\hat{D}. \tag{1c}$$

Here $\hat{c}^\dagger_{i\sigma}(\hat{c}_{i\sigma})$ are creation (annihilation) operators of fermions with spin σ at site $\boldsymbol{R}_i$ (for simplicity denoted by i), $\hat{n}_{i\sigma} = \hat{c}^\dagger_{i\sigma}\hat{c}_{i\sigma}$, and $\hat{D} = \sum_{\boldsymbol{R}_i}\hat{D}_i$ is the operator of total double occupation of the system with $\hat{D}_i = \hat{n}_{i\uparrow}\hat{n}_{i\downarrow}$ as the operator of double occupation of a lattice site i. The Fourier transform of the kinetic energy in (1b), where t_{ij} is the amplitude for hopping between sites i and j, defines the dispersion $\varepsilon_{\boldsymbol{k}}$ and the momentum distribution operator $\hat{n}_{\boldsymbol{k}\sigma}$ with $\boldsymbol{k}$ as the wave vector. In the following the hopping is restricted to nearest-neighbor sites i and j, such that $-t \equiv t_{ij}$. A schematic picture of the Hubbard model is shown in Fig. 1.

2.1 Unique features of the Hubbard model

In the Hubbard model the Coulomb interaction between two electrons is assumed to be so strongly screened that it can be described by a local interaction U which occurs only *on* a lattice site.[2] Due to the Pauli exclusion principle such an on-site interaction is only possible if the two electrons have opposite spin. Thus it seems as if the interaction between the electrons was spin-dependent. But the Coulomb interaction is, of course, a spin-independent two-body interaction; the fact that the operators in (1c) contain spin indices is merely a consequence of the quantum mechanical treatment of electrons in a localized basis. A special feature of a purely

quick successes. High hurdles had to be overcome, both regarding the development of appropriate mathematical techniques (field-theoretic and diagrammatic methods, Green functions, etc.) and physical concepts (multiple scattering, screening of the long-range Coulomb interaction, quasiparticles and Fermi liquid theory, electron-phonon coupling, superconductivity, metal-insulator transitions, disorder, superexchange, localized magnetic states in metals, etc.). A discussion of the many-body problem and of some of the important developments up to 1961 can be found in the lecture notes and reprint volume by Pines [16].

[2] For that reason the Hubbard model applies particularly well to cold fermionic atoms in optical lattices where the bare interaction is indeed extremely short-ranged [20].

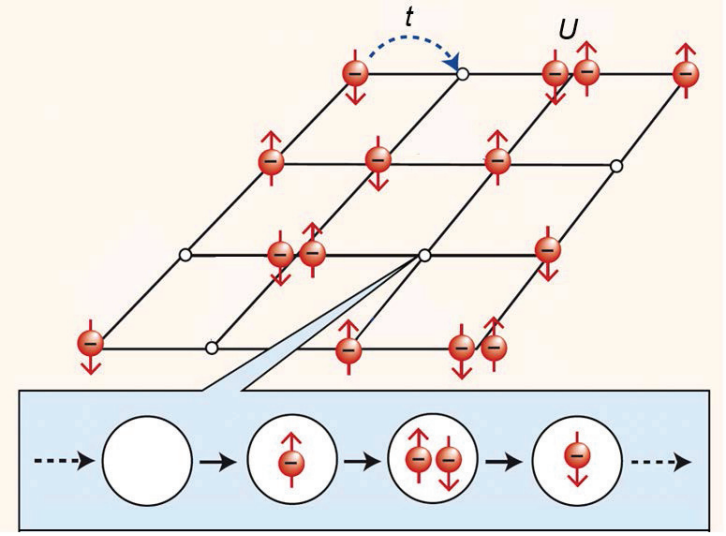


Fig. 1: *Schematic illustration of interacting electrons in a solid described by the Hubbard model. The ions enter only as a rigid lattice, here represented by a square lattice. The electrons, which have mass, negative charge, and spin (↑ or ↓), are quantum particles which tunnel ("hop") from one lattice site to the next with a hopping amplitude t. Together with the lattice structure this determines the band structure of the non-interacting electrons. The quantum dynamics leads to fluctuations in the occupation of lattice sites as indicated by the sequence at the bottom: a lattice site can either be unoccupied, singly occupied (↑ or ↓), or doubly occupied. When two electrons meet on a lattice site, which is only possible if they have opposite spins because of the Pauli exclusion principle, they encounter a local interaction U.*

local interaction is its complete independence of the lattice structure and spatial dimension of the system.

The physics described by the Hubbard model is clearly very different from that of electrons with a long-range Coulomb interaction in the continuum. Therefore the Hubbard model is far from obvious. Its formulation required fundamentally new insights into the nature of the many-body problem of interacting fermions (see footnote 1). In particular, screening is a basic ingredient of the many-body problem of metals.[3]

While the kinetic energy $\hat{H}_0$ is diagonal in momentum space and reflects the wave nature of the electrons, the interaction energy $\hat{H}_{\rm int}$ is diagonal in position space and characterizes their particle properties. In view of the uncertainty principle the two parts of the Hamiltonian are therefore maximally "quantum incompatible".

[3]It should be noted that Anderson had introduced the main ingredient of the Hubbard model, namely a local interaction between spin-up and spin-down d electrons with strength U, already in his 1959 paper on the theory of superexchange interactions [21] and, even more explicitly in his 1961 paper on localized magnetic states in metals, where he formulated a model of s and d electrons referred to today as "single impurity Anderson Model" (SIAM) or "Anderson impurity model" (AIM) [22]. The latter paper inspired Wolff [23] to study the formation of localized magnetic moments in dilute alloys in terms of a model with a single-band of noninteracting d electrons which can interact only on a single site. In this sense the Hubbard model could be called "periodic Wolff model" in analogy to the standard terminology "periodic Anderson model", which generalizes the AIM by extending the interaction to all sites of the lattice. Apparently Gutzwiller, Hubbard and Kanamori did not know the earlier work of Anderson and Wolff; at least they did not refer to their papers.

The Coulomb interaction between electrons with equal spin direction, e.g., on neighboring sites, is not described by the Hubbard model, but can be easily included. Similarly, the model can be generalized to more than one band. Indeed, in a Wannier basis the Hubbard model can be derived systematically from a general Hamiltonian of interacting electrons which consists of a kinetic energy, the ionic potential $U_{\text{ion}}(\boldsymbol{r})$, and the two-body Coulomb interaction $V_{\text{ee}}(\boldsymbol{r}-\boldsymbol{r}')$ [18]; for a discussion see ref. [24].

As mentioned above, the Hubbard model was originally introduced to provide a microscopic explanation of ferromagnetism in $3d$ transition metals [17–19]. Indeed, taken by itself the Hubbard interaction favors a ferromagnetic ground state, since this corresponds to the state with the lowest (zero) energy due to the absence of doubly occupied sites. However, this argument ignores the other term in the Hamiltonian, the kinetic energy. While the lattice structure and spatial dimension do not influence the Hubbard interaction, they play a very important role in the kinetic energy, where they determine, for example, the density of states of the electronic band at the Fermi energy (see section 5).

The single-band Hubbard model is the fundamental lattice model of interacting fermions.[4] As a consequence, many well-known models can be derived from it in special limits of the model parameters. For example, at half filling and in the limit $U \gg t$ the Hubbard model corresponds to the Heisenberg model with antiferromagnetic exchange coupling $J = 4t^2/U$.

2.1.1 How can the Hubbard model be solved?

In spite of the extreme simplifications of the Hubbard model compared with interacting electrons in a real solid, the model still cannot be solved analytically, except in dimension $d=1$ for nearest-neighbor hopping [25]. For dimensions $d=2,\ 3$ comprehensive analytic solutions of the Hubbard and related models are not available. This is due to the complicated quantum dynamics and, in the case of fermions, the non-trivial algebra introduced by the Pauli exclusion principle.

In view of the fundamental limitations of exact analytical approaches one might hope that, at least, modern supercomputers can provide detailed numerical insights into the thermodynamic and spectral properties of correlated fermionic systems. However, classical computers are fundamentally limited by the exponential growth of the Hilbert space with system size. Therefore they can solve the Hubbard model and related correlation models only on finite, often rather small lattices and in certain parameter regimes (here "solving" means calculating the ground state energy and correlation functions, simulating dynamics and mapping out phase diagrams).[5] In principle, quantum computers will be able solve many-electron models much more efficiently than classical computers. However, there are still significant challenges. In particular, improve-

[4] More generally, the Hubbard model is the fundamental lattice model of quantum particles, since it may also be used for interacting bosons [20].

[5] Recently significant progress was made in the case of the three-dimensional Hubbard model at half-filling, where numerically exact auxiliary-field Quantum Monte Carlo computations of magnetic, thermodynamic, and dynamical properties have become possible for lattices up to 20^3 sites [26]. However, more complicated fermionic lattice models in $d=3$, especially models for realistic materials with many orbitals and energy bands, can be solved only on much smaller lattices.

ments in error correction, hardware scaling, and algorithm design will be necessary before it is possible to study large, realistic systems. Therefore quantum computers are not yet capable of accurately computing physical properties of large, realistic correlated electron systems beyond what classical methods can handle [27].
This shows very clearly that there is still a great need for analytically tractable, non-perturbative approximation schemes, which are applicable for all input parameters. Moreover, to understand the characteristic physical properties of a many-body problem "good" approximations are required.[6] Here mean-field theories play an important role.

3 Mean-field theories for the many-electron problem

In the theory of classical and quantum many-body systems an overall description of the properties of a model is often obtained within a *mean-field theory*. A mean-field theory is an approximation, where each particle (electron, spin, etc.) is assumed to experience an average ("mean") field created by all other particles, rather than the explicit particle-particle interaction. Although the term is frequently used it is not well defined, since there exist numerous ways to derive such theories. One construction scheme is based on the factorization of the interaction, as in the case of the mean-field theory for the Ising model for classical spins, or the Hartree-Fock theory for electronic models (see below). The factorization ("decoupling") implies a neglect of fluctuations (or of the correlation of fluctuations), which reduces the original many-body problem to a solvable "independent-particle" problem, where a single particle now interacts with a mean field provided by the other particles. Mean-field theories are a powerful first step for analyzing many-body systems; they provide qualitative insights and make calculations tractable.

3.1 Hartree-Fock theory

Hartree-Fock theory is an independent-electron approximation which, mathematically, may be interpreted in two different ways. Starting from the Hamiltonian level, it can be viewed as a factorization of the electron-electron interaction, whereby the actual many-electron problem is reduced to one where each electron now moves in a mean field (or mean potential) generated by all other electrons. This simplified problem is then solvable, the solution being given by the Hartree-Fock wave function, i.e., a single Slater determinant of one-electron spin-orbitals which ensures that the wave function remains antisymmetric under electron exchange, satisfying the Pauli exclusion principle. Alternatively, starting from the wave function, Hartree-Fock theory may be viewed as an approximation of the total N-electron wave function as a single Slater determinant of one-electron spin-orbitals. Applying this wave function to the electron-electron interaction corresponds to a decoupling of the interaction. Both views lead to the same results.

[6] Approximations are useful not only per se, but also because they allow us to better understand the key features of a complicated physics problem. As Peierls wrote: "*... the art of choosing a suitable approximation, of checking its consistency and finding at least intuitive reasons for expecting the approximation to be satisfactory, is much more subtle than that of solving an equation exactly*" [28].

While Hartree-Fock theory respects the Pauli principle, it neglects interaction-induced correlations between the electrons due to the decoupling/factorization procedure on which the approximation is based. Hence Hartree-Fock theory is a static mean-field approximation.[7]
To account for electronic correlation effects one must go beyond Hartree-Fock theory. Wigner [29] was apparently the first who tried to calculate the contribution of the mutual electronic interaction to the ground state energy beyond the Hartree-Fock result, which he referred to as "correlation energy". The correlation energy is defined as $E_{\text{corr}} = E_{\text{exact}} - E_{\text{HF}}$ where E_{exact} is the exact non-relativistic electronic energy and E_{HF} is the Hartree-Fock energy. Since Hartree-Fock theory does not include electron correlations, one always has $E_{\text{corr}} < 0$.

3.2 Infinite dimensions and mean-field behavior

Another, in general unrelated, mean-field construction scheme makes use of the simplifications that occur when some parameter is assumed to be large (in fact, infinite), whereby fluctuations are suppressed. In this case a particle no longer experiences the actual, fluctuating interaction with the other particles, but feels the interaction only as a "mean field". Depending on the model this parameter can be the length of the spins S, the spin degeneracy N, the spatial dimension d, or the coordination number Z, i.e., the number of nearest neighbors of a lattice site.[8], Mean-field theories obtained in such a limit, supplemented if possible by an expansion in the inverse of the large parameter, can provide valuable insights into the fundamental properties of a model. Perhaps the best-known mean-field theory in many-body physics is the "Weiss molecular-field theory" for the Ising model (see below). It is a prototypical "single-site mean-field theory" which becomes exact in the limit of infinite coordination number Z or infinite dimension d. It should be noted that the coordination number of a three-dimensional lattice can already be quite large, e.g., $Z = 6$ for a simple cubic lattice, $Z = 8$ for a bcc lattice and $Z = 12$ for an fcc-lattice.
Investigations of many-particle models in the limit $d, Z \to \infty$ do not go far back in time. In fact, Z was originally regarded as a measure of the *range* of the interaction between spins in the Ising

[7]The conclusion that Hartree-Fock theory does not include correlations calls for further discussion. The antisymmetry of the Hartree-Fock wave function required by the Pauli principle keeps electrons with equal spin apart, and thereby leads to a reduced probability of finding two electrons with the same spin close together in position space ("Pauli hole"). This corresponds to a spatial correlation, implying that Hartree-Fock theory *does* include a specific form of (static) correlation – at least for electrons with the same spin. However, this correlation is a result of the Fermi-Dirac statistics, i.e., is due to the effective quantum mechanical exchange interaction between indistinguishable electrons and is not caused by a classical force such as the Coulomb repulsion, which makes *all* electrons avoid each other ("Coulomb hole") regardless of spin to reduce the energy. The approximation of the many-electron wave function as a single Slater determinant means that each electron experiences an averaged potential rather than explicit electron-electron interactions. This neglects the instantaneous Coulomb interaction between electrons (i.e., the Hartree-Fock wave function does not adjust to the instantaneous repulsion), leading to an overestimation of the total energy. In particular, correlations among electrons with opposite spin are then completely missing. Therefore Hartree-Fock theory is a static mean-field approximation which does not describe (dynamic) electronic correlations between the electrons.

[8]For regular lattices both a dimension d and a coordination number Z can be defined. The coordination number Z is then determined by the dimension d and the lattice structure. But there exist other lattice-like structures, such as the Bethe lattice, which cannot be associated with a physical dimension d, although a coordination number Z is well-defined.

model, and thus of the number of spins in the range of the interaction [30]. In this case the limit $Z \to \infty$ describes an infinitely long-ranged interaction. Since a particle or spin then interacts with infinitely many other particles or spins (which are all "neighbors", i.e., the system has "infinite connectivity"), this limit was originally referred to as "limit of high density" [30] and only later as "limit of infinite dimensions" [31]. Thereafter the Ising model and other classical models were investigated on general d-dimensional hypercubic lattices. Today Z denotes the coordination number, i.e., the number of nearest neighbors.
Mean-field theories derived in the limit of infinite coordination number Z or dimension d provide an approximate solution of the many-body problem which retains characteristic features of the problem in $d < \infty$ and provides insights into the (unknown) solution in $d = 3$. This will now be illustrated by the Ising model in infinite dimensions.

3.2.1 Ising model

To explain ferromagnetism in three-dimensional solids from a microscopic point of view, Ising investigated a minimal model of interacting classical spins with a *non-magnetic* interaction between neighboring elementary magnets [32]. The Hamiltonian function for the Ising model with coupling J between two nearest-neighbor spins at lattice sites $\boldsymbol{R}_i$, $\boldsymbol{R}_j$ is given by

$$H = -\frac{1}{2} J \sum_{\langle \boldsymbol{R}_i, \boldsymbol{R}_j \rangle} S_i S_j, \tag{2}$$

where we assume ferromagnetic coupling ($J > 0$) and $\langle \boldsymbol{R}_i, \boldsymbol{R}_j \rangle$ indicates summation over all nearest-neighbor sites (the factor $1/2$ prevents double counting of sites). This can also be written as

$$H = -\sum_{\boldsymbol{R}_i} h_i S_i, \tag{3}$$

where now every spin S_i interacts with a site-dependent, i.e., locally fluctuating, field

$$h_i = J \sum_{\boldsymbol{R}_j}^{(i)} S_j \tag{4}$$

generated by the coupling of the spin S_i to its neighboring sites; here the superscript (i) on the summation symbol indicates summation over the Z nearest-neighbor sites of $\boldsymbol{R}_i$.

Mean field theory of the Ising model In mean-field theory the interaction of a spin with its local field in (3) is decoupled (factorized), i.e., h_i is replaced by a mean field h_{MF}, which leads to the mean-field Hamiltonian

$$H^{\mathrm{MF}} = -h_{\mathrm{MF}} \sum_{\boldsymbol{R}_i} S_i + E_{\mathrm{shift}} \,. \tag{5}$$

Now a spin S_i interacts only with a global field $h_{\mathrm{MF}} = JZS$ (the "molecular" or "Weiss" field), where $S \equiv \langle S_i \rangle = (1/L) \sum_{i=0}^{L} S_i$ is the average value of S_i, $E_{\mathrm{shift}} = LJZS^2/2$ is a constant energy shift, and L is the number of lattice sites of the system.

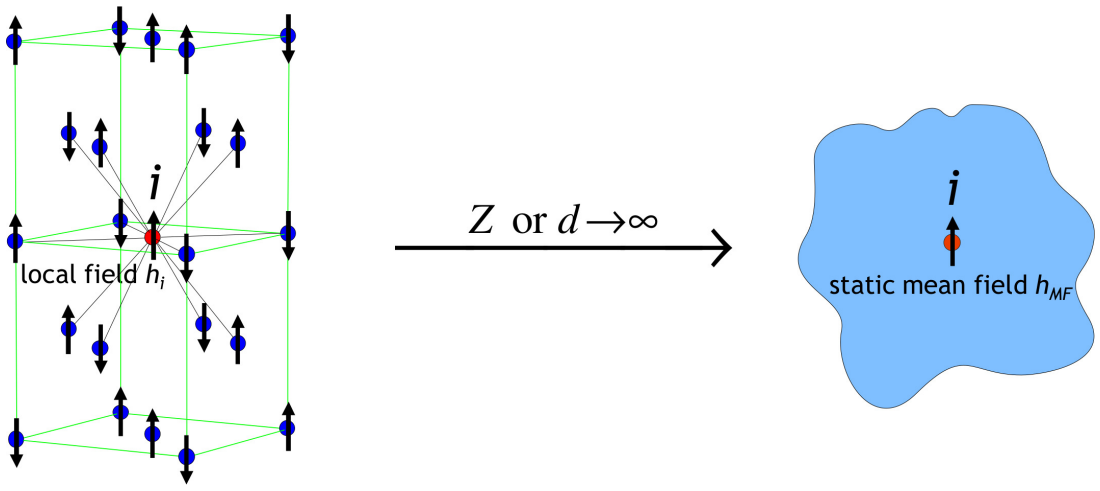


Fig. 2: *Already in three dimensions ($d = 3$) can the coordination number Z of a lattice be quite large, as in the face-centered cubic lattice shown on the left, where $Z = 12$. In the limit $Z \to \infty$, or equivalently $d \to \infty$, the Ising model effectively reduces to a single-site problem where the fluctuating local field h_i is replaced by a static global ("molecular") mean field $h_{\rm MF}$.*

Next we show that in infinite dimensions or for infinite coordination number Z this decoupling arises naturally. First we have to rescale the coupling constant J as

$$J = \frac{J^*}{Z} \ , \ J^* = \text{const.} \tag{6}$$

With this "classical scaling" $h_{\rm MF}$ and the energy (or the energy density in the thermodynamic limit) remain finite in the limit $Z \to \infty$. Writing $S_i = S + \delta S_i$, where δS_i is the deviation of S_i from its average S, (4) becomes $h_i = J^*\big(S + \Delta S_i\big)$, where

$$\Delta S_i = \frac{1}{Z} \sum_{\boldsymbol{R}_j}^{(i)} \delta S_j \tag{7}$$

is the sum of the fluctuations δS_j of the Z nearest-neighbor spins of S_i per nearest neighbor. These fluctuations are assumed to be uncorrelated, i.e., random. The law of large numbers then implies that the sum increases only as $\sqrt{Z}$ for $Z \to \infty$, such that ΔS_i altogether *decreases* as $1/\sqrt{Z}$ in this limit. As a consequence the local field h_i can indeed be replaced by its mean $h_{\rm MF}$ (central limit theorem). Hence the Hamiltonian function (5) becomes purely local

$$H^{\rm MF} = \sum_{\boldsymbol{R}_i} H_i + E_{\rm shift} \ , \tag{8}$$

where $H_i = -h_{\rm MF}\, S_i$. Thereby the problem reduces to an effective single-site problem (see Fig. 2). We note that S corresponds to the magnetization m of the system ($S \equiv m$). In the paramagnetic phase, where $m = 0$, the mean field $h_{\rm MF}$ vanishes; hence (5) and (8) are only non-trivial in the presence of ferromagnetic order.

The self-consistent equation of the mean-field theory The magnetization m is obtained from the partition function of the mean-field Hamiltonian (5) as $m = \tanh(\beta h_{\rm MF})$ where $\beta =$

$1/(k_BT)$. The condition $h_{\rm MF} = JZS \equiv J^*m$ then yields the well-known self-consistent equation for the magnetization m as

$$m = \tanh\big(\beta J^* m\big). \tag{9}$$

The mean-field theory is seen to become exact in the limit of infinite coordination number Z or dimension d.[9]
In this case $1/Z$ or $1/d$ serve as a small parameter which can be used, in principle, to improve the mean-field theory systematically (see section 7.1 of ref. [33]). This mean-field theory contains no unphysical singularities, is applicable for all values of the input parameters (temperature and/or external magnetic field) and is often viewed as the prototypical mean-field theory in statistical mechanics.

4 Static approximations for the Hubbard model

4.1 Factorization approach: Hartree mean-field theory

Lattice fermion models such as the Hubbard model are much more complicated than models with localized spins. Therefore the construction of a mean-field theory with the comprehensive properties of the mean-field theory of the Ising model will be more complicated, too. The simplest static mean-field theory of the Hubbard model is the Hartree approximation (an exchange (Fock) term does not arise in this case since the Hubbard interaction acts only for electrons with opposite spin on the same lattice site) [34]. To clarify the characteristic features of this mean-field theory we proceed as in the derivation of the mean-field theory of the Ising model and factorize the interaction term. To this end we rewrite the Hubbard interaction in the form of (3), i.e., we let an electron with spin σ at site $\boldsymbol{R}_i$ interact with a local field $\hat{h}_{i\sigma}$ ($\hat{h}_{i\sigma}$ is an operator and therefore a dynamic variable) produced by an electron with opposite spin on that site

$$\hat{H}_{\rm int} = \sum_{\boldsymbol{R}_i,\sigma} \hat{h}_{i\sigma}\hat{n}_{i\sigma}, \tag{10}$$

where $\hat{h}_{i\sigma} = \frac{1}{2}U\hat{n}_{i,-\sigma}$ (the factor $1/2$ is due to the summation over both spin directions). Next we replace the operator $\hat{h}_{i\sigma}$ by its expectation value $\langle\hat{h}_{i\sigma}\rangle$, now a real number, and obtain the single-particle ("mean-field") Hamiltonian

$$\hat{H}^{\rm MF} = \hat{H}_{\rm kin} + \sum_{\boldsymbol{R}_i,\sigma} \langle\hat{h}_{i\sigma}\rangle\hat{n}_{i\sigma} + E_{\rm shift}\,, \tag{11}$$

where $E_{\rm shift}$ is a constant energy shift. Now a σ-electron at site $\boldsymbol{R}_i$ interacts only with a local *static* field $\langle\hat{h}_{i\sigma}\rangle = \frac{1}{2}U\langle\hat{n}_{i-\sigma}\rangle$, which can be determined self-consistently using the single-particle Hamiltonian (11). The above decoupling of the operators corresponds to the Hartree approximation whereby correlated fluctuations *on* the site $\boldsymbol{R}_i$ are neglected.

[9] Due to the simplicity of the Ising model, the limits of infinite dimensions d and of infinitely long-ranged spin coupling J both yield the same mean-field theory. However, for more complicated models, in particular quantum models with itinerant degrees of freedom, this will generally not be the case.

It should be noted that although (11) is now an effective single-particle problem it can generally not be solved exactly since the mean field $\langle \hat{h}_{i\sigma} \rangle$ may vary from site to site, leading to solutions without long-range order. This is a new feature originating from the quantum-mechanical kinetic energy in the Hamiltonian.

The Hartree approximation is valid in the weak-coupling limit ($U \to 0$) and/or low-density limit ($n \to 0$), but clearly does not become exact in the limit $d \to \infty$, since the Hubbard interaction between two electrons is purely local and hence does not dependent on the spatial dimension. Therefore the physics behind the factorizations (8) and (11) is very different. Namely, (8) describes the decoupling of a spin from a bath of infinitely many neighboring spins whose fluctuations become unimportant in the limit $d \to \infty$, while (11) corresponds to the decoupling of an electron from *one* other electron (with opposite spin) on the same site.

While the Hartree approximation is useful for investigations at weak coupling, it will lead to fundamentally incorrect results at strong coupling when the double occupation of a lattice site becomes energetically very unfavorable and is therefore suppressed. Indeed, a factorization of the local correlation function $\langle \hat{n}_{i\uparrow} \hat{n}_{i\downarrow} \rangle \to \langle \hat{n}_{i\uparrow} \rangle \langle \hat{n}_{i\downarrow} \rangle$ eliminates correlation effects generated by the local quantum dynamics (see footnote 7). Hence the nature of the Hartree mean-field theory of spin-$\frac{1}{2}$ electrons with a local interaction is very different from the Weiss mean-field theory of spins with nearest-neighbor coupling.

4.2 Variational approach: Gutzwiller wave function

Another useful approximation scheme for quantum many-body systems makes use of variational wave functions [35]. Starting from a physically motivated many-body trial wave function the energy expectation value is calculated and is then minimized with respect to the variational parameters. Although variational wave functions usually yield only approximate results, they have several advantages: they are physically intuitive, can be custom tailored to a particular problem, can be used even when standard perturbation methods fail or are inapplicable, and provide a rigorous upper bound for the exact ground state energy by Ritz's variational principle.

To investigate the properties of the electronic correlation model (1) (which, actually, Gutzwiller was the first to introduce [17], but which was later named after Hubbard), Gutzwiller also proposed a simple variational wave function [17]. This "Gutzwiller wave function" introduces correlations into the ground-state wave function for non-interacting electrons through a correlation factor—a local operator in real space—which is constructed from the double occupation operator $\hat{D}$, (1c), as

$$|\Psi_G\rangle = g^{\hat{D}} |\mathrm{FG}\rangle = \prod_{\boldsymbol{R}_i} \left[1 - (1-g)\hat{D}_i\right] |\mathrm{FG}\rangle. \tag{12}$$

Here $|\mathrm{FG}\rangle$ is the wave function of the non-interacting Fermi gas and g is a variational parameter with $0 \leq g \leq 1$. The projector $g^{\hat{D}}$ globally reduces the amplitude of those spin configurations in $|\mathrm{FG}\rangle$ with too many doubly occupied sites for given repulsion U. The limit $g = 1$ describes the non-interacting case, while $g \to 0$ corresponds to $U \to \infty$.

The Gutzwiller wave function can be used to calculate the expectation value of an operator, e.g., the ground state energy of the Hubbard model, (1), as

$$E_{\rm G}(g,U) \equiv \frac{\langle \Psi_G|\hat{H}|\Psi_G\rangle}{\langle \Psi_G|\Psi_G\rangle}. \tag{13}$$

By computing the minimum of $E_{\rm G}(g,U)$ with respect to the variational parameter g, the latter is determined as a function of the interaction parameter U.

4.2.1 Gutzwiller approximation

In general the evaluation of expectation values in terms of $|\Psi_G\rangle$ cannot be performed exactly. Therefore Gutzwiller additionally introduced a non-perturbative approximation scheme whereby he obtained an explicit expression for the ground state energy of the Hubbard model [17, 36, 37]. The results of Gutzwiller's rather complicated approach were later re-derived by counting classical spin configurations [38] as described below; for details see ref. [39]. The idea behind the Gutzwiller approximation can be easily understood by calculating the norm $\langle \Psi_G|\Psi_G\rangle$. Namely, by working in configuration space the ground state of the Fermi gas can be written as

$$\big|{\rm FG}\big\rangle = \sum_D \sum_{\{i_D\}} A_{i_D} \big|\Psi_{i_D}\big\rangle, \tag{14}$$

where $|\Psi_{i_D}\rangle$ is a spin configuration with D doubly occupied sites, with A_{i_D} as the corresponding probability amplitude. The sum extends over the whole set $\{i_D\}$ of different configurations with the same D, and over all D. For a system with L lattice sites and N_σ electrons with spin σ ("σ-electrons") the number N_D of different configurations in $\{i_D\}$ is given by the combinatorial expression

$$N_D = \frac{L!}{L_\uparrow!\, L_\downarrow!\, D!\, E!}, \tag{15}$$

where $L_\sigma = N_\sigma - D$ and $E = L - N_\uparrow - N_\downarrow + D$ are the numbers of singly occupied and empty sites, respectively. Since $|\Psi_{i_D}\rangle$ is an eigenstate of $\hat{D}$, the norm of $|\Psi_G\rangle$ reads

$$\langle \Psi_G|\Psi_G\rangle = \sum_D g^{2D} \sum_{\{i_D\}} \big|A_{i_D}\big|^2. \tag{16}$$

The Gutzwiller approximation effectively amounts to neglecting spatial correlations between the spins of the electrons. The probability $|A_{i_D}|^2$ for a specific spin configuration with D doubly occupied sites is then the same for all configurations of electrons on the lattice, i.e., is given by the classical combinatorial result for uncorrelated particles

$$\big|A_{i_D}\big|^2 = P_\uparrow P_\downarrow\,. \tag{17}$$

Here $P_\sigma = 1/\binom{L}{N_\sigma} \simeq n_\sigma^{N_\sigma}(1-n_\sigma)^{L-N_\sigma}$, with $n_\sigma = N_\sigma/L$, is the probability for an arbitrary configuration of σ-electrons to occur. In this case (16) reduces to

$$\langle \Psi_G|\Psi_G\rangle = P_\uparrow P_\downarrow \sum_D g^{2D} N_D. \tag{18}$$

In the thermodynamic limit the sum in (18) is dominated by its largest term corresponding to a value $D = \bar{D}$, where $\bar{D}$ is determined by [36]

$$g^2 = \frac{\bar{d}\big(1 - n_\uparrow - n_\downarrow + \bar{d}\big)}{\big(n_\downarrow - \bar{d}\big)\big(n_\uparrow - \bar{d}\big)}, \tag{19}$$

with $\bar{d} = \bar{D}/L$. Equation (19) has the form of the law of mass action where, however, the correlation parameter g^2 rather than the Boltzmann factor regulates the dynamical equilibrium between the concentrations of singly occupied sites on one side of this "chemical reaction" and that of doubly occupied sites and holes on the other.[10] Eq. (19) uniquely relates $\bar{d}$ and g, such that g may be replaced by the quantity $\bar{d}$.

The expectation value of the interaction term, which is local in real space and thereby dimension independent, can be evaluated in the same way as $\langle \Psi_G | \Psi_G \rangle$. By contrast, the expectation value of the kinetic energy, which is non-local since it involves hopping between two sites, is approximated by neglecting the surrounding of these two sites, i.e., the two sites are thought to be decoupled from the rest of the system [39].

The non-magnetic ground state energy per lattice site of the Hubbard model at half filling ($n_\uparrow = n_\downarrow = 1/2$) is then found as

$$E_G[\bar{d}(g)]/L = q(\bar{d})\,\varepsilon_0 + U\,\bar{d}, \tag{20}$$

which has to be minimized with respect to the variational parameter $\bar{d}$. Here ε_0 is the internal energy of non-interacting electrons and $q = 8(1{-}2\bar{d})\bar{d} \leq 1$ may be viewed as a reduction factor of the kinetic energy (or the band width) due to correlations. In the Gutzwiller approximation, electronic correlations are therefore found to lead only to a simple renormalization of the kinetic energy of the electrons.

4.2.2 Brinkman-Rice metal-insulator transition

The results of the Gutzwiller approximation may be interpreted as follows [17, 36]: they describe a correlated, normal-state fermionic system at zero temperature whose momentum distribution has a discontinuity q at the Fermi level, where $q{=}1$ in the non-interacting case, which is reduced to $q < 1$ by the interaction as in a Landau Fermi liquid. In 1970 Brinkman and Rice [41] showed that for a half-filled band the minimization of (20) yields $q = 1{-}\bar{U}^2$, $\bar{d} = \frac{1}{4}\big(1{-}\bar{U}\big)$, and $E/L = -|\varepsilon_0|\big(1{-}\bar{U}\big)^2$, where $\bar{U} = U/\big(8|\varepsilon_0|\big)$. They noticed that in this case the Gutzwiller approximation describes a transition at a finite critical interaction strength $U_c = 8|\varepsilon_0|$ from an itinerant to a localized state, where lattice sites are singly occupied and the discontinuity q vanishes. This "Brinkman-Rice transition" therefore corresponds to a correlation induced ("Mott") metal-insulator transition. They argued [41] that the inverse of q can be identified with the effective mass of Landau quasiparticles, $q^{-1} = m^*/m \geq 1$, which diverges at U_c.

The results obtained with the Gutzwiller approximation are intuitively understandable (they are very "physical"). In the 1970s and 80s it was the only approximation scheme which was

[10] In fact, (19), with g^2 replaced by the Boltzmann factor $e^{-\beta U}$, is the exact result for the Hubbard model with infinite-range hopping [40].

able to describe a Mott metal-insulator transition at a finite value of the interaction *and* was in accord with basic properties of Landau Fermi liquid theory.[11] This was confirmed by a detailed investigation of the assumptions and implications of the Gutzwiller approximation that showed that the Gutzwiller-Brinkman-Rice theory was not only in qualitative [44], but even in good quantitative agreement with properties of normal-liquid ^{3}He [39]; for a discussion see section 3 of ref. [45].

4.2.3 Can the Gutzwiller approximation be derived by quantum many-body methods?

In the Gutzwiller approximation the quantum mechanical expectation value of the ground state energy of the Hubbard model is evaluated by counting classical spin configurations – hence it is a quasiclassical approximation [38, 39]. It was later shown that these results are reproduced by a two-site cluster factorization when intersite correlations are neglected [46]. Since intersite correlations decrease with increasing spatial dimension [46], it was to be expected that the Gutzwiller approximation is equivalent to a cluster expansion in position space in the limit $d \to \infty$ [39]. The question was then, whether the results of the Gutzwiller approximation – a real-space approximation for lattice fermions – can be derived also by quantum many-body theory in a systematic way.[12] A few years later Walter Metzner and I [49] provided an answer, by employing a new diagrammatic quantum many-body approach. Namely, we showed that the Gutzwiller approximation corresponds to the calculation of the expectation values of operators with the Gutzwiller wave function in the limit $d \to \infty$, as will be explained next; for a more detailed discussion see section 4 of ref. [45].

5 Lattice fermions in infinite dimensions

Using quantum many-body theory the expectation values of the kinetic and the interaction energy of the Hubbard model (1) in terms of the Gutzwiller wave function can be expressed diagrammatically for arbitrary dimensions d [49]. In $d = 1$ it is even possible to calculate and sum the diagrams analytically to all orders [49].[13] But this no longer works in dimensions $d = 2, 3$. By numerical calculations we found that in high dimensions the values of individual diagrams

[11] Other well-known approximation schemes, in particular those proposed by Hubbard, do not have these important properties: in the Hubbard-I approximation [18], which interpolates between the atomic limit and the non-interacting band, a band gap opens for any $U > 0$, while in the Hubbard-III approximation [42], which corresponds to the coherent potential approximation [43] for disordered systems, the Fermi surface volume is not conserved.

[12] I discussed this question in 1983-84 with several colleagues, in particular with Andrei Ruckenstein during my stay at the Bell Laboratories in Murray Hill in 1983. At that time Andrei tried to understand how to think about the Brinkman-Rice transition in correlated electronic systems in the presence of disorder. This eventually led him and Gabi Kotliar to formulate a functional integral representation of the Hubbard and Anderson models in terms of auxiliary bosons, whose simplest saddle-point approximation ("slave-boson mean-field theory") reproduces exactly the results of the Gutzwiller approximation [47,48]. Thus they had shown that the results of the Gutzwiller approximation could also be obtained without the use of the Gutzwiller variational wave function.

[13] The diagrams have the same form as the usual Feynman diagrams in quantum many-body theory, but a line corresponds to the time-independent single-particle density matrix $g^0_{ij,\sigma} = \langle \hat{c}^\dagger_{i\sigma} \hat{c}_{j\sigma} \rangle_0$ of the non-interacting system rather than to the single-particle propagator $G^0_{ij,\sigma}(t)$ since the variational approach involves only static quantities.

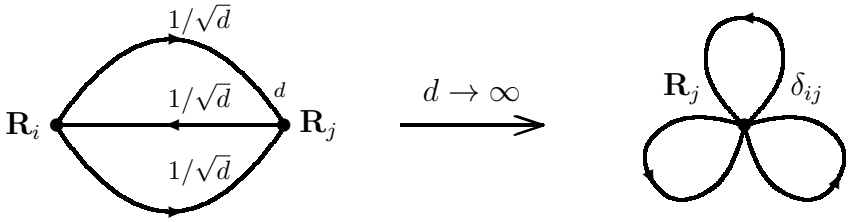


Fig. 3: *Collapse of the irreducible self-energy diagram for the Hubbard model in second-order perturbation theory in U in the limit $d \to \infty$. Left hand side: For nearest-neighbor sites $\boldsymbol{R}_i$, $\boldsymbol{R}_j$ the diagram is of the order $1/d^{3/2}$. Right hand side: Only for $i = j$ does the diagram give a finite contribution in the limit $d \to \infty$.*

approach a constant, which could be calculated analytically if the momentum conservation at a vertex was neglected. The sum over all diagrams gave exactly the results of the Gutzwiller approximation [49]. In view of the random generation of momenta in a typical Monte Carlo integration over momenta we concluded that the assumed independence of momenta at a vertex is correct in the limit of infinite spatial dimensions ($d \to \infty$). The results of the Gutzwiller approximation thus correspond to the evaluation of expectation values with the Gutzwiller wave function in the limit $d = \infty$. This immediately explained the quasiclassical nature of the Gutzwiller approximation. Most importantly, we had found that diagrammatic calculations in quantum many-body theory drastically simplify for $d \to \infty$. Clearly, the limit $d \to \infty$ was not only useful for the investigation of spin models, but also in the case of lattice fermion models.

5.1 Simplifications of diagrammatic quantum many-body theory

The simplifications of diagrammatic many-body theory for $d \to \infty$ are due to a collapse of irreducible diagrams in position space. This means that only site-diagonal ("local") diagrams (diagrams which only depend on a single site), remain [50, 51].[14] In particular, the irreducible self-energy is then completely local (Fig. 3).

To understand the reason for the diagrammatic collapse in $d \to \infty$ let us, for simplicity, consider diagrams where lines correspond to the single-particle density matrix $g^0_{ij,\sigma}$ as they enter in the calculation of expectation values with the Gutzwiller wave function (note that, since $g^0_{ij,\sigma} = \lim_{t\to 0^-} G^0_{ij,\sigma}(t)$, the following arguments are equally valid for the single-particle Green function $G^0_{ij,\sigma}(t)$ or its Fourier transform).

The single-particle density matrix $g^0_{ij,\sigma}$ may be interpreted as the quantum amplitude of the hopping of an electron with spin σ between sites $\boldsymbol{R}_i$ and $\boldsymbol{R}_j$. The square of its magnitude is therefore proportional to the *probability* of an electron to hop from $\boldsymbol{R}_j$ to a site $\boldsymbol{R}_i$. For nearest-neighbor sites $\boldsymbol{R}_i$, $\boldsymbol{R}_j$ on a lattice with coordination number Z this implies $|g^0_{ij,\sigma}|^2 \sim \mathcal{O}(1/Z)$,

[14] Gebhard later showed that in $d = \infty$ the calculation of expectation values with the Gutzwiller wave function can be performed even without diagrams [52]. This provided a direct link between the slave-boson mean-field theory and the results obtained with the Gutzwiller wave function in $d = \infty$. The latter approach was generalized by Gebhard and collaborators to multi-band Hubbard models, which can be used to describe the effect of correlations in real materials ("Gutzwiller density-functional theory") [53].

such that on a hypercubic lattice, where $Z = 2d$, and $d \to \infty$ one finds [50, 51]

$$g^0_{ij,\sigma} \sim \mathcal{O}\Big(\frac{1}{\sqrt{d}}\Big). \tag{21}$$

For general i, j one obtains [51, 54]

$$g^0_{ij,\sigma} \sim \mathcal{O}\Big(1/d^{\|\boldsymbol{R}_i - \boldsymbol{R}_j\|/2}\Big). \tag{22}$$

Here $\|\boldsymbol{R}\| = \sum_{n=1}^{d} |R_n|$ is the length of $\boldsymbol{R}$ in the "Manhattan metric", where electrons only hop along horizontal or vertical lines, but never along a diagonal; for further discussions of diagrammatic simplifications see ref. [55].

Consequences of the asymptotic d dependence of $g^0_{ij,\sigma}$ can be determined by examining the kinetic energy. For non-interacting electrons at $T = 0$ the expectation value of the kinetic energy is given by

$$E^0_{\rm kin} = -t \sum_{\langle \boldsymbol{R}_i, \boldsymbol{R}_j \rangle} \sum_{\sigma} g^0_{ij,\sigma}. \tag{23}$$

The sum over nearest neighbors leads to a factor $\mathcal{O}(Z)$ (which is $\mathcal{O}(d)$ for a hypercubic lattice). In view of the $1/\sqrt{d}$ dependence of $g^0_{ij,\sigma}$ for $d \to \infty$ it is therefore necessary to scale the nearest-neighbor hopping amplitude t as [50, 51]

$$t = \frac{t^*}{\sqrt{d}}, \; t^* = \text{const.}, \tag{24}$$

so that the kinetic energy remains finite for $d \to \infty$. The same result may be derived in a momentum-space formulation.[15] It is important to bear in mind that, although $g^0_{ij,\sigma}$ vanishes for $d \to \infty$, the electrons are still mobile. Indeed, even in the limit $d \to \infty$ the off-diagonal elements of $g^0_{ij,\sigma}$ contribute, since electrons may hop to $Z \sim \mathcal{O}(d)$ many nearest neighbors with amplitude $t^*/\sqrt{d}$.

5.2 The Hubbard model in $d = \infty$

A rescaling of the microscopic parameters of the Hubbard model with d is only required for the kinetic energy, since the interaction term is independent of the spatial dimension.[16] Altogether

[15] The need for the scaling (24) also follows from the density of states of non-interacting electrons. For nearest-neighbor hopping on a d-dimensional hypercubic lattice $\varepsilon_{\boldsymbol{k}}$ has the form $\varepsilon_{\boldsymbol{k}} = -2t \sum_{i=1}^{d} \cos k_i$ (here and in the following we set Planck's constant $\hbar$, Boltzmann's constant k_B, and the lattice spacing equal to unity). The density of states corresponding to $\varepsilon_{\boldsymbol{k}}$ is given by $N_d(\omega) = \sum_{\boldsymbol{k}} \delta(\omega - \varepsilon_{\boldsymbol{k}})$, which is the probability density for finding the value $\omega = \varepsilon_{\boldsymbol{k}}$ for a random choice of $\boldsymbol{k} = (k_1, \ldots, k_d)$. If the momenta k_i are chosen randomly, $\varepsilon_{\boldsymbol{k}}$ is the sum of d many independent (random) numbers $-2t \cos k_i$. The central limit theorem then implies that in the limit $d \to \infty$ the density of states is given by a Gaussian, i.e., $N_d(\omega) \stackrel{d\to\infty}{\longrightarrow} \frac{1}{2t\sqrt{\pi d}} \exp\Big[-\Big(\frac{\omega}{2t\sqrt{d}}\Big)^2\Big]$. Only if t is scaled with d as in (24) does one obtain a non-trivial density of states $N_\infty(\omega)$ in $d = \infty$ [56, 50] and thus a finite kinetic energy. The density of states on other types of lattices in $d = \infty$ can be calculated similarly [57, 58].

[16] Interactions beyond the Hubbard interaction, e.g., nearest-neighbor interactions such as $\hat{H}_{nn} = \sum_{\langle \boldsymbol{R}_i, \boldsymbol{R}_j \rangle} \sum_{\sigma\sigma'} V_{\sigma\sigma'} \hat{n}_{i\sigma} \hat{n}_{j\sigma'}$ have to be scaled, too, in the limit $d \to \infty$. In this case a scaling as in the Ising model, $V_{\sigma\sigma'} \to V^*_{\sigma\sigma'}/Z$, is required [59] ("classical scaling"). In $d = \infty$ non-local contributions therefore reduce to their (static) Hartree substitute and only the Hubbard interaction remains dynamical.

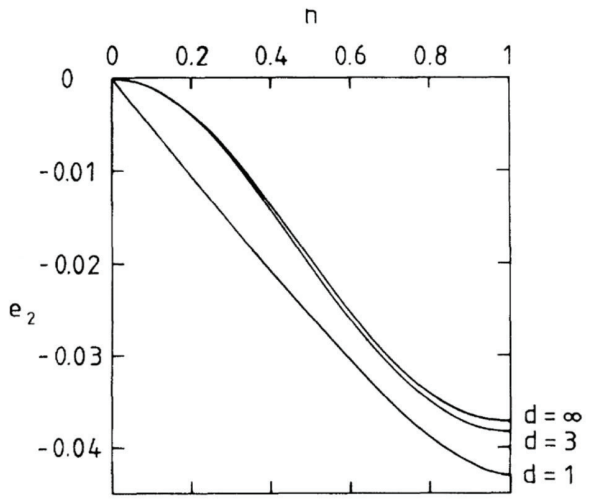


Fig. 4: *Correlation energy of the Hubbard model in second-order Goldstone perturbation theory in U in units of $2U^2/|\varepsilon_0|$ vs. density n in dimensions $d = 1, 3, \infty$. Here ε_0 is the kinetic energy for $U = 0$ and $n = 1$; adapted from ref. [50].*

this implies that only the Hubbard Hamiltonian with a rescaled kinetic energy

$$\hat{H} = -\frac{t^*}{\sqrt{d}} \sum_{\langle \boldsymbol{R}_i, \boldsymbol{R}_j \rangle} \sum_{\sigma} \hat{c}^\dagger_{i\sigma} \hat{c}_{j\sigma} + U \sum_{\boldsymbol{R}_i} \hat{n}_{i\uparrow} \hat{n}_{i\downarrow} \tag{25}$$

has a non-trivial $d \to \infty$ limit where both the kinetic energy and the interaction contribute (namely, it is the *competition* between the two terms which leads to interesting many-body physics). Therefore, even in $d = \infty$ the Hubbard model describes nontrivial correlations among the fermions. This is already evident in the evaluation of the second-order diagram in Goldstone perturbation theory for the correlation energy at weak coupling [50]. The integral over the three internal momenta (which, in $d = 3$, lead to nine integrals) reduces to a single integral in $d = \infty$. Obviously, calculations are much simpler in $d = \infty$ than in finite dimensions. More importantly, the results for the energy obtained in $d = \infty$ turn out to be very close to those in $d = 3$ (Fig. 4) and therefore provide a computationally simple, but quantitatively reliable approximation.

The simplifications in calculations for quantum lattice models such as the Hubbard model in infinite dimensions arise from the fact that energies are randomized by umklapp processes generated when lattice momenta are added [50]. Hence the energies become mutually independent, which allows one to replace the momentum integrations by energy integrations over the density of states. In other words, in $d = \infty$ the momentum conservation constraint at a vertex may be ignored.

With these results Walter and I had demonstrated [50] that microscopic calculations for correlated lattice fermions in $d = \infty$ dimensions were useful and very promising. Subsequently Müller-Hartmann [59] showed that in infinite dimensions the self-energy is $\boldsymbol{k}$-independent, i.e., local in position space, as in the Gutzwiller approximation, but remains dynamical

$$\Sigma_\sigma(\boldsymbol{k}, \omega) \overset{d\to\infty}{\equiv} \Sigma_\sigma(\omega), \tag{26}$$

whereby typical Fermi liquid features are preserved [60]. This result may be understood as follows [61, 62]: The influence of an interaction between particles on their motion is described quite generally by a complex, spatially dependent and dynamical field, the self-energy $\Sigma_\sigma(\boldsymbol{k},\omega)$. On a lattice with a very large number of nearest neighbors the *spatial* dependence of this field becomes increasingly unimportant and vanishes completely in $d=\infty$, as in the mean-field theory of the Ising model. So the field becomes a mean field in position space but retains its full dynamics.[17] Furthermore, Schweitzer and Czycholl [65] found that calculations for the periodic Anderson model also simplify in high dimensions, and Brandt and Mielsch [66] derived the exact solution of the Falicov-Kimball model in infinite dimensions by mapping the lattice problem onto a solvable atomic problem in a generalized, time-dependent external field; they also indicated that, in principle, such a mapping was even possible for the Hubbard model.[18]
Due to the $\boldsymbol{k}$-independence of the irreducible self-energy the most important obstacle for diagrammatic calculations in finite dimensions $d\geq 1$, namely the integration over intermediate momenta, is removed. At the same time the limit $d\to\infty$ does not affect the dynamics of the system. Hence, in spite of the simplifications in position or momentum space, the many-electron problem retains its full dynamics in $d=\infty$.

5.2.1 Single-particle propagator and spectral function

In $d=\infty$ the single-particle propagator of an interacting lattice fermion system (the "lattice Green function") at $T=0$ is then given by

$$G_{\boldsymbol{k},\sigma}(\omega)=\frac{1}{\omega-\varepsilon_{\boldsymbol{k}}+\mu-\Sigma_\sigma(\omega)}. \tag{27}$$

The $\boldsymbol{k}$-dependence of $G_{\boldsymbol{k}}(\omega)$ is now entirely due to the energy dispersion $\varepsilon_{\boldsymbol{k}}$ of the *non*-interacting particles. This means that in a homogeneous system described by the propagator

$$G_{ij,\sigma}(\omega)=L^{-1}\sum_{\boldsymbol{k}}G_{\boldsymbol{k},\sigma}(\omega)e^{i\boldsymbol{k}\cdot(\boldsymbol{R}_i-\boldsymbol{R}_j)} \tag{28}$$

its local part, $G_{ii,\sigma}\equiv G_\sigma$, is determined by

$$G_\sigma(\omega)=L^{-1}\sum_{\boldsymbol{k}}G_{\boldsymbol{k},\sigma}(\omega)=\int\limits_{-\infty}^{\infty}dE\,\frac{N_0(E)}{\omega-E+\mu-\Sigma_\sigma(\omega)}, \tag{29}$$

where $N_0(E)$ is the density of states of the non-interacting system. The spectral function of the interacting system (also often called density of states) is given by

$$A_\sigma(\omega)=-\frac{1}{\pi}\mathrm{Im}\,G_\sigma(\omega+i0^+). \tag{30}$$

[17] In this respect there is a direct analogy to non-interacting electrons in the present of static ("quenched") disorder, where the self-energy also becomes $\boldsymbol{k}$-independent in the limit $d\to\infty$ and plays the role of a coherent potential. The "coherent potential approximation" [43] is a single-site theory where an electron moves through an effective medium described by the self-energy $\Sigma_\sigma(\omega)$ that becomes exact in $d=\infty$ [61,63,64]. In the case of the Hubbard model in the limit $d\to\infty$ the coherent potential is much more complicated due to the explicit interaction between the particles (see footnote 21).

[18] Alternatively, it can be shown that in the limit $Z\to\infty$ the dynamics of the Falicov-Kimball model reduces to that of a non-interacting, tight-binding model on a Bethe lattice with coordination number $Z=3$ which can be solved analytically [67].

5.2.2 $\boldsymbol{k}$-independence of the self-energy and Fermi liquid behavior

The $\boldsymbol{k}$-independence of the self-energy allows one to make contact with Fermi liquid theory [60]. In general, i.e., even when Σ has a $\boldsymbol{k}$-dependence, the Fermi surface is defined by the $\omega = 0$ limit of the denominator of (27) (in the paramagnetic phase we can suppress the spin index)

$$\varepsilon_{\boldsymbol{k}} + \Sigma_{\boldsymbol{k}}(0) = E_F. \tag{31}$$

According to Luttinger and Ward [68] the volume within the Fermi surface is not changed by interactions, provided the latter can be treated in perturbation theory.[19] This is expressed by

$$n = \sum_{\boldsymbol{k}\sigma} \Theta\big(E_F - \varepsilon_{\boldsymbol{k}} - \Sigma_{\boldsymbol{k}}(0)\big), \tag{32}$$

where n is the electron density and $\Theta(x)$ is the step function. The $\boldsymbol{k}$-dependence of $\Sigma_{\boldsymbol{k}}(0)$ in (31) implies that, in spite of (32), the shape of the Fermi surface of the interacting system will be quite different from that of the non-interacting system, except for the rotationally invariant case $\varepsilon_{\boldsymbol{k}} = f(|\boldsymbol{k}|)$. By contrast, for lattice fermion models in $d = \infty$, where $\Sigma_{\boldsymbol{k}}(\omega) \equiv \Sigma(\omega)$, the Fermi surface itself, and hence the enclosed volume, is not changed by the interaction. The Fermi energy is simply shifted uniformly from its non-interacting value E_F^0 to $E_F = E_F^0 + \Sigma(0)$, to keep n in (32) constant. Thus $G(0)$, the $\omega = 0$ value of the local lattice Green function, and the spectral function $A(0) = -\frac{1}{\pi}\mathrm{Im}\, G(i0^+)$ are not changed by the interaction at all. This "pinning behavior" is well-known from the single-impurity Anderson model [70]. A renormalization of $N(0)$ can only be due to a $\boldsymbol{k}$-dependence of Σ.
For $\omega \to 0$ the self-energy has the property [60]

$$\mathrm{Im}\ \Sigma(\omega) \propto \omega^2, \tag{33}$$

which implies Fermi liquid behavior. The effective mass of the quasiparticles

$$\frac{m^*}{m} = 1 - \left.\frac{d\Sigma}{d\omega}\right|_{\omega=0} \tag{34}$$

$$= 1 + \frac{1}{\pi}\int_{-\infty}^{\infty} d\omega\, \frac{\mathrm{Im}\,\Sigma(\omega{+}i0^-)}{\omega^2} \geq 1 \tag{35}$$

is seen to be enhanced by the interaction. In particular, the momentum distribution

$$n_{\boldsymbol{k}} = \frac{1}{\pi}\int_{-\infty}^{0} d\omega\, \mathrm{Im}\, G_{\boldsymbol{k}}(\omega) \tag{36}$$

has a discontinuity at the Fermi surface given by $n_{k_F^-} - n_{k_F^+} = (m^*/m)^{-1}$, where $k_F^\pm = k_F \pm 0^+$.

[19] Recently, necessary and sufficient conditions for the validity of Luttinger's theorem [68] based on the Atiyah-Singer index theorem were derived, by which the topological robustness of a generalized Fermi surface may be quantified [69].

6 Dynamical mean-field theory for correlated electrons

The diagrammatic simplifications of quantum many-body theory for lattice fermions in $d = \infty$ provide the basis for the construction of a comprehensive mean-field theory of the Hubbard model which is diagrammatically controlled and whose free energy has no unphysical singularities. The construction is based on the scaled Hamiltonian (25). The self-energy is then momentum independent but retains its frequency dependence and thereby describes the full many-body dynamics of the interacting system. This is in contrast to Hartree(-Fock) theory where the self-energy acts only as a static potential. The resulting theory is both mean-field-like and dynamical and therefore represents a *dynamical* mean-field theory (DMFT) for lattice fermions which is able to describe genuine correlation effects as will be discussed in this section.

6.1 The self-consistent equations

In $d = \infty$ lattice fermion models with a local interaction effectively reduce to a single site embedded in a dynamical mean field provided by the other interacting fermions as illustrated in Fig. 5. The self-consistent DMFT equations can be derived in different ways depending on the physical interpretation of the correlation problem emerging in the limit $d, Z \to \infty$ [61, 71, 72]; for a discussion see ref. [55]. The mapping of the lattice electron problem onto a single-impurity Anderson model with a self-consistency condition in $d = \infty$ introduced by Georges and Kotliar [71], which was also employed by Jarrell [72], turned out to be the most useful approach,[20] since it made a connection with the well-studied theory of quantum impurities [70], for whose solution efficient numerical codes such as the quantum Monte Carlo (QMC) method [73] had already been developed and were readily available.[21] For a detailed discussion of the foundations of DMFT see the review by Georges, Kotliar, Krauth, and Rozenberg [74] and the lecture by Kollar at the Jülich Autumn School 2018 [75]; an introductory presentation can be found in ref. [76].

For $T > 0$ the self-consistent DMFT equations are given by:

(I) the *local propagator* $G_\sigma(i\omega_n)$, which is expressed by a functional integral as

$$G_\sigma(i\omega_n) = -\frac{1}{\mathcal{Z}} \int \prod_\sigma Dc_\sigma^* Dc_\sigma \, [c_\sigma(i\omega_n) c_\sigma^*(i\omega_n)] \, \exp[-S_{\rm loc}] \tag{37}$$

with the partition function

$$\mathcal{Z} = \int \prod_\sigma Dc_\sigma^* Dc_\sigma \, \exp[-S_{\rm loc}] \tag{38}$$

[20] The mapping itself can be performed without approximation, but leads to a complicated coupling between the impurity and the bath which makes the solution generally intractable. However, the problem can be solved in the limit $d \to \infty$ when the momentum dependence of the self-energy drops out.

[21] Alternatively, Janiš derived the self-consistent DMFT equations already in 1991 by generalizing the coherent potential approximation (CPA) [61]. In the CPA quenched disorder acting on non-interacting electrons is averaged and produces a mean field, the "coherent potential". In the case of the Hubbard model in $d = \infty$ the fluctuations generated by the Hubbard interaction may be treated as "annealed" disorder acting on non-interacting electrons [62] which, after averaging, produce a mean field, the self-energy. Numerical solutions of the DMFT equations starting from the CPA point of view have not been developed so far.

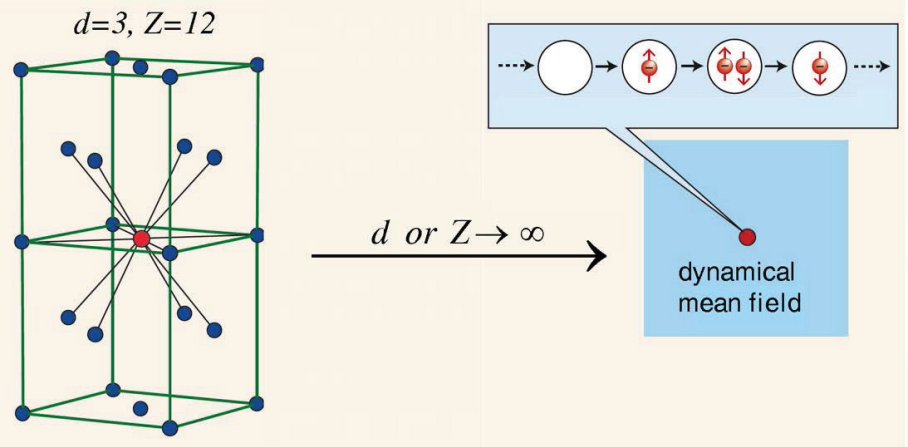


Fig. 5: *In the limit d or $Z \to \infty$ the Hubbard model effectively reduces to a dynamical single-site problem which may be viewed as a lattice site embedded in a $\boldsymbol{k}$-independent, dynamical fermionic mean field. Electrons can hop from the mean field onto this site and back, and interact on the site as in the original Hubbard model (see Fig.1). The local dynamics of the electrons is independent of the dimension or coordination number and therefore remains unchanged.*

and the local action

$$S_{\rm loc} \;=\; -\int_0^\beta d\tau_1 \int_0^\beta d\tau_2 \sum_\sigma c_\sigma^*(\tau_1)\, \mathcal{G}_\sigma^{-1}(\tau_1{-}\tau_2)\, c_\sigma(\tau_2) \;+\; U \int_0^\beta d\tau\, c_\uparrow^*(\tau) c_\uparrow(\tau) c_\downarrow^*(\tau) c_\downarrow(\tau). \quad (39)$$

Here $\mathcal{G}_\sigma$ is the effective local propagator (also called "bath Green function", or "Weiss mean field"[22]), which is defined by a Dyson equation

$$\mathcal{G}_\sigma(i\omega_n) = \big[[G_\sigma(i\omega_n)]^{-1} + \Sigma_\sigma(i\omega_n)\big]^{-1}. \quad (40)$$

Furthermore, by identifying the local propagator (37) with the Hilbert transform of the lattice Green function

$$G_{\boldsymbol{k}\,\sigma}(i\omega_n) = \frac{1}{i\omega_n - \varepsilon_{\boldsymbol{k}} + \mu - \Sigma_\sigma(i\omega_n)}, \quad (41)$$

(which is exact in $d = \infty$ [74]), one obtains
(II) the *self-consistency condition*

$$G_\sigma(i\omega_n) = \frac{1}{L}\sum_{\boldsymbol{k}} G_{\boldsymbol{k}\,\sigma}(i\omega_n) = \int_{-\infty}^{\infty} d\varepsilon\, \frac{N(\omega)}{i\omega_n - \varepsilon + \mu - \Sigma_\sigma(i\omega_n)} \quad (42)$$

$$= G_\sigma^0\big(i\omega_n{-}\Sigma_\sigma(i\omega_n)\big). \quad (43)$$

In (42) the ionic lattice enters only through the density of states of the non-interacting electrons. Eq. (43) illustrates the mean-field nature of the DMFT equations very clearly: the local Green function of the interacting system is given by the non-interacting Green function G_σ^0 at the shifted energy $i\omega_n{-}\Sigma_\sigma(i\omega_n)$, which is the energy measured relative to that of the surrounding fermionic bath, the dynamical mean field $\Sigma_\sigma(i\omega_n)$.

[22] This expresses the fact that $\mathcal{G}$ describes the coupling of a single site to the rest of the system, similar to the Weiss mean-field $h_{\rm MF}$ in the mean-field theory of the Ising model (see section 3.2.1). However, in the case of the DMFT the mean field depends on the frequency, i.e., is dynamical. It should be noted that, in principle, both local functions $\mathcal{G}_\sigma(i\omega_n)$ and $\Sigma_\sigma(i\omega_n)$ can be viewed as a dynamical mean field since both enter in the bilinear term of the local action (39).

6.1.1 Solving the self-consistent equations

The self-consistent DMFT equations can be solved iteratively: starting with an initial guess for the self-energy $\Sigma_\sigma(i\omega_n)$ one obtains the local propagator $G_\sigma(i\omega_n)$ from (42) and thereby the bath Green function $\mathcal{G}_\sigma(i\omega_n)$ from (40). This determines the local action (39) which is needed to compute a new value for the local propagator $G_\sigma(i\omega_n)$ from (37). By employing the old self-energy a new bath Green function $\mathcal{G}_\sigma$ is calculated and so on, until convergence is reached.

It should be stressed that although the DMFT corresponds to an effectively local problem, the propagator $G_{\boldsymbol{k}}(\omega)$ depends on the crystal momentum $\boldsymbol{k}$ through the dispersion relation $\varepsilon_{\boldsymbol{k}}$ of the non-interacting electrons. But there is no *additional* momentum-dependence through the self-energy, since this quantity is local within DMFT.

Solutions of the self-consistent DMFT equations require the extensive application of numerical methods, in particular quantum Monte Carlo (QMC) simulations [72, 74] with continuous-time QMC [77] still as the method of choice, the numerical renormalization group [78], the density matrix renormalization group [79], exact diagonalization [74], Lanczos procedures [80], and solvers based on matrix product states [81] or tensor networks [82]. Here the recent development of impurity solvers making use of machine learning [83] and quantum computers [84] open new perspectives.

6.2 Application of DMFT to the Hubbard model

In DMFT the mean field is dynamical, whereby local quantum fluctuations are fully taken into account, but is local (i.e., spatially independent) because of the infinitely many neighbors of every lattice site. The only approximation of this "single-site DMFT" when applied in $d < \infty$ is the neglect of the $\boldsymbol{k}$-dependence of the self-energy. DMFT provides a comprehensive, non-perturbative, thermodynamically consistent and diagrammatically controlled approximation scheme for the investigation of correlated lattice models at all interaction strengths, densities, and temperatures [74, 76], and can resolve even very low energy scales.

Intensive theoretical investigations of the Hubbard model and related correlation models using DMFT over the last three decades have provided a wealth of new insights into the physics described by this fundamental fermionic interaction model. In this subsection only a few exemplary results will be discussed; more detailed presentations can be found in refs. [74, 55], and the lecture notes of the Jülich Autumn Schools in 2011, 2014, 2018, and 2022 [12].

Most importantly, with DMFT it is possible to compute electronic correlation effects quantitatively in such a way that they can be tested experimentally, for example, by electron spectroscopies. Namely, DMFT describes the correlation induced transfer of spectral weight and the finite lifetime of quasiparticles through the real and imaginary part of the self-energy, respectively. This greatly helps to understand and characterize the Mott metal-insulator transition (MIT) to be discussed next.

6.2.1 Metal-insulator transitions

Mott-Hubbard transition The interaction-driven transition between a paramagnetic metal and a paramagnetic insulator, first discussed by Mott [85] and referred to as "Mott metal-insulator transition" (MIT), or "Mott-Hubbard MIT" when studied within the Hubbard model, is one of the most intriguing phenomena in condensed matter physics [86, 87]. This transition is a consequence of the quantum-mechanical competition between the kinetic energy of the electrons and their interaction U: the kinetic energy prefers the electrons to be mobile (a wave effect) which invariably leads to their interaction (a particle effect). For large values of U doubly occupied sites become energetically too costly. The system can reduce its total energy by localizing the electrons, which leads to a MIT. Here the DMFT provided detailed insights into the nature of the Mott-Hubbard-MIT for all values of the interaction U and temperature T [74, 88, 76, 55]. A microscopic investigation of the Mott MIT obtained within DMFT from a Fermi-liquid point of view was performed only recently [89].

While at small U the interacting system can be described by coherent quasiparticles whose spectral function ("density of states" (DOS)) still resembles that of the free electrons, the DOS in the Mott insulating state consists of two separate, incoherent "Hubbard bands" whose centers are separated approximately by the energy U (here we discuss only the half filled case without magnetic order). At intermediate values of U the spectrum then has a characteristic three-peak structure which is qualitatively similar to that of the single-impurity Anderson model [90] and which is a consequence of the three possible occupations of a lattice site: empty, singly occupied (up or down), and doubly occupied.

At $T = 0$ the width of the quasiparticle peak vanishes at a critical value of U which is of the order of the band width. So the Mott-Hubbard MIT occurs at intermediate coupling and therefore belongs to the hard problems in many-body theory, where most analytic approaches fail and investigations have to rely on numerical methods. Therefore several features of the Mott-Hubbard MIT near the transition point are still not sufficiently understood even within DMFT. Actually, it was recently argued that the Mott-Hubbard transition in the infinite-dimensional single-band Hubbard model may be understood as a topological phase transition, where the insulating state is the topological phase, and the transition from the metallic (Fermi liquid) to the insulating state involves domain wall dissociation [91].

At $T > 0$ the Mott-Hubbard MIT is found to be first order and is associated with a hysteresis region in the interaction range $U_{c1} < U < U_{c2}$ where U_{c1} and U_{c2} are the values at which the insulating and metallic solution, respectively, vanish [74, 88]; for more detailed discussions see refs. [74, 76, 55]. The hysteresis region terminates at a critical point, above which the transition becomes a smooth crossover from a "bad metal" to a "bad insulator"; for a schematic plot of the phase diagram see fig. 3 of ref. [76]. Transport in the incoherent region above the critical point shows remarkably rich properties, including scaling behavior [92]. The highly non-perturbative nature of the Mott MIT is illustrated by the fact that the MIT at $T = 0$ is an accumulation point of an infinite number of vertex divergence lines [93].

Mott-Hubbard MITs are found, for example, in transition metal oxides with partially filled

bands. For such systems band theory typically predicts metallic behavior. One of the most famous examples is V_2O_3 doped with Ti or Cr [94]. However, it is now known that certain organic materials are better realizations of the single-band Hubbard model without magnetic order and allow for more controlled investigations of the Mott MIT and the Mott state [95].

Metal-insulator transitions in the presence of disorder DMFT also provides a theoretical framework for the investigation of correlated electrons in the presence of disorder. In the absence of interactions, when the effect of local disorder is taken into account through the arithmetic mean of the local DOS (LDOS), DMFT is equivalent to the coherent potential approximation (CPA) [63, 64]; for a discussion see ref. [55]. However, CPA cannot describe Anderson localization. To overcome this deficiency a variant of the DMFT was formulated where the *geometrically* averaged LDOS is computed from the solutions of the self-consistent stochastic DMFT equations and is then fed into the self-consistency cycle [96]. This corresponds to a "typical medium theory" which is able to reproduce the Anderson transition of non-interacting electrons. By implementing this scheme into DMFT to study the properties of disordered electrons in the presence of interactions it is possible to compute the phase diagram of the Anderson-Hubbard model [97].

6.2.2 Metallic ferromagnetism

The Hubbard model was introduced in 1963 [17–19] in an attempt to explain metallic ferromagnetism in $3d$ metals such as Fe, Co, and Ni starting from a microscopic point of view. However, at that time investigations of the model employed severe, uncontrolled approximations. Therefore it was uncertain for a long time whether the Hubbard model can explain band ferromagnetism at realistic temperatures, electron densities, and interaction strengths in $d > 1$ at all. Using DMFT it was found that on generalized fcc-type lattices in $d = \infty$ (i.e., on "frustrated" lattices with large spectral weight at the lower band edge) the Hubbard model indeed predicts metallic ferromagnetic phases in large regions of the phase diagram [58, 98]. In the paramagnetic phase the susceptibility χ_F obeys a Curie-Weiss law [99], where the Curie temperature T_C is much lower than that obtained by Stoner theory, due to many-body effects. In the ferromagnetic phase the magnetization M is consistent with a Brillouin function as originally derived for localized spins, even for a *non-integer* magneton number as in $3d$ transition metals [58]. Therefore, DMFT accounts for the behavior of both the magnetization and the susceptibility of band ferromagnets [98]; see section 6.1 of my 2018 lecture notes [75]. Like the Mott MIT, metallic ferromagnetism is a hard intermediate-coupling many-electron problem.

6.2.3 Topological properties of correlated electron systems

The interest in non-trivial topological properties of electronic systems sparked by the theory of the quantum Hall effect, greatly increased when it was realized that the spin-orbit interaction can generate topologically insulating behavior [100]. Initially, investigations focused on topological features of non-interacting systems. But during the last decade the influence of

electronic interactions on these topological properties received more and more attention. Here DMFT turned out to be a useful tool. For example, DMFT was employed to study interaction effects in two-dimensional topological insulators [101], to analyze the robustness of the Chern number in the Haldane-Hubbard model [102], and to investigate the topological quantization of the Hall conductivity of correlated electrons at $T > 0$ [103]. Furthermore, to better understand the topological phase transition from a Weyl-semimetal to a Mott insulator the topological properties of quasiparticle bands were computed [104]. DMFT also made it possible to explore topological phase transitions in the Kitaev model in a magnetic field and to calculate the corresponding phase diagrams [105]. Correlation-induced topological effects can even arise from non-Hermitian properties of the single-particle spectrum in equilibrium systems [106]. Furthermore, it was demonstrated that a topologically nontrivial multiorbital Hubbard model remains well-defined and nontrivial in the limit $d \to \infty$ for arbitrary, but even, d [107]. Most recently, DMFT studies of the two-dimensional Hubbard model showed that correlated altermagnets can host Dirac points and topological phases [108].

6.2.4 Nonequilibrium DMFT

The study of correlated electrons out of equilibrium by employing a generalization of the DMFT has become another fascinating new research area [109]. Nonequilibrium DMFT is able to explain the results of time-resolved electron spectroscopy experiments, where femtosecond pulses are now available in a wide frequency range. In such experiments a probe is excited and the subsequent relaxation is studied. Thereby it was found, for example, that doubly occupied sites in the photo-excited quasi-2d transition-metal dichalcogenide 1T-TaS_2 show an ultrafast dynamics [110]. Such excitations may even result in long-lived, metastable ("hidden") states [111]. Quite generally, photo-induced nonequilibrium states in Mott insulators provide valuable information on correlation effects and metastable states of matter [112].

6.3 Beyond DMFT

Mean-field approximations provide useful information on the general physical properties of many-body problems. In particular, DMFT with its dynamical but local self-energy has been a breakthrough for the investigation and explanation of electronic correlation effects in models and materials. Although it is an approximation when used in $d < \infty$, experiments with cold atoms in optical lattices demonstrated that DMFT can be remarkably accurate in $d = 3$ [113]. A dynamical, local self-energy was also shown to be well justified in iron pnictides and chalcogenides [114] as well as in Sr_2RuO_4 [115]. Nevertheless mean-field results can neither explain correlation phenomena occurring on finite length scales or the critical behavior at thermal or quantum phase transitions, nor unconventional superconductivity observed in finite-dimensional systems. In such cases it is necessary to go beyond mean-field theory.

6.3.1 $1/d$ corrections

For mean-field theories derived in the limit $d \to \infty$ corrections can be obtained, at least in principle, by performing an expansion in the parameter $1/d$ around the mean-field results.[23]
An early strategy to include intersite quantum fluctuations into DMFT is "extended DMFT" (EDMFT) [116], where the interaction strength of a nearest-neighbor density-density interaction is scaled such that its fluctuation part contributes even in the large d limit.
Systematic calculations of $1/d$-corrections to the DMFT start with a Luttinger-Ward functional of the non-local Green function $G_{ij,\sigma}(i\omega_n)$, from which the non-local self-energy $\Sigma_{ij,\sigma}(i\omega_n)$ is obtained by functional derivative. To calculate first-order corrections in $1/d$ one needs to consider a pair of nearest-neighbor sites [117]. This generalizes the single-impurity problem of the DMFT to a two-impurity problem. It is then possible, in principle, to formulate a self-consistent, thermodynamically consistent approximation which is correct to order $1/d$ [117]. This scheme requires an exact cancellation of certain diagrams in the approximation. Unfortunately, numerical computations within this approach are unstable and can easily lead to acausal solutions. Although the scheme was modified such that the diagrammatic cancellation is assured at each iteration step [118] and thereby provided causal solutions in test calculations for the Hubbard model, acausal behavior cannot be ruled out in general. Therefore it is still not clear whether, and how, controlled and thermodynamically consistent $1/d$ expansions around DMFT can be constructed. So far, analytic calculations in this directions were not further pursued in view of the successes of numerical cluster approaches which, although not systematic in $1/d$, are explicitly causal [119] (see below).

6.3.2 Non-local extensions

There are different, mostly numerical, techniques to include non-local correlations into the DMFT; for a review see ref. [120]; in the following we mention three approaches:

Cluster extensions These methods incorporate short-range spatial correlations by solving an impurity problem for a cluster of sites rather than a single site. The dynamical cluster approximation (DCA) [121] systematically improves the accuracy by increasing the cluster size in momentum space, while the cellular DMFT (CDMFT) [122] works in real space. In both approaches the cluster is self-consistently embedded in a dynamical mean field. Thereby it has become possible to compute, for example, typical features of unconventional superconductivity in the Hubbard model in $d = 2$, such as the interplay of antiferromagnetism and d-wave pairing as well as pseudogap behavior [119], but also signatures of Anderson localization in disordered systems [123].

Diagrammatic generalizations By extending the DMFT on a diagrammatic level through the inclusion of non-local contributions, corrections to the local self-energy of the DMFT can

[23] For a discussion of the calculation of $1/d$ corrections to the Weiss mean-field theory of the Ising model, the Gutzwiller approximation, and the coherent potential approximation see section 7 of ref. [33].

be calculated explicitly. In particular, the dynamical vertex approximation (DΓA) [124] incorporates momentum-dependent vertex corrections beyond DMFT, while the dual fermion approach [125] introduces auxiliary fermions to capture long-range correlations. These approximations provided new insights into the mechanism of superconductivity arising from purely repulsive interactions, e.g., in the Kondo lattice [126] and Hubbard model [127]. In particular, in the Hubbard model a specific set of local particle-particle diagrams was identified which describe a strong screening of the bare interaction at low frequencies. Thereby antiferromagnetic spin fluctuations are suppressed, which in turn reduce the pairing interaction. Thus dynamical vertex corrections were found to lower T_c strongly [127]. With these approaches it is possible to determine critical behavior near thermal ($T > 0$) [128] and quantum phase transitions ($T = 0$) [129].

Functional renormalization group (fRG) The fRG method [130] systematically integrates out energy scales and captures collective fluctuations, which can be combined with DMFT to describe nonlocal correlations. In the DMF^{2}RG approach [131] the fRG flow does not start from the bare action of the system, but rather from the DMFT solution. Local correlations are thus included from the beginning, and nonlocal correlations are generated by the fRG flow, as demonstrated for the two-dimensional Hubbard model [131].

7 Understanding correlated materials with DMFT

It took several decades to develop theoretical techniques that made it possible to understand basic properties of the single-band Hubbard model. During this time first-principles investigations into the much more complicated many-body problem of correlated electron *materials* were out of reach. The electronic properties of solids were mainly studied within density-functional theory (DFT) [132], e.g., in the local density approximation (LDA) [133], the generalized gradient approximation (GGA) [134], and the LDA+U method [135]. Those approaches can describe the ground state properties of many simple elements and semiconductors, and even of some insulators, quite accurately, and often predict the magnetic and orbital properties [133] as well as the crystal structures of many solids correctly [136]. However, they fail to describe the electronic and structural properties of correlated paramagnetic materials since they miss characteristic features of correlated electron systems such as heavy quasiparticle behavior and Mott physics. DMFT changed this situation completely.

7.1 DFT+DMFT and GW+DMFT

The computational scheme introduced by Anisimov *et al.* [137] and Lichtenstein and Katsnelson [138], which merges material-specific DFT-based approximations with the many-body DMFT, provides a powerful new method for the microscopic computation of the electronic, magnetic, and structural properties of correlated materials from first principles even at finite temperatures [139–143]. This theoretical method is now often denoted by DFT+DMFT (or,

more specifically, LDA+DMFT, GGA+DMFT, etc.). In particular, this approach naturally accounts for the existence of local moments in the paramagnetic phase. By construction, DFT+DMFT includes the correct quasiparticle physics and the corresponding energetics, and reproduces the DFT results in the limit of weak Coulomb interaction U [144]. Most importantly, DFT+DMFT describes the correlation-induced many-body dynamics of strongly correlated electron materials at all values of the Coulomb interaction and doping.
As in the case of the single-band Hubbard model the many-body model of correlated materials constructed within the DFT+DMFT scheme consists of two parts: an effective kinetic energy obtained by DFT which describes the material-specific band structure of the uncorrelated electrons, and the local interactions between the electrons in the same orbital as well as in different orbitals. Here the static contribution of the electronic interactions already included in the DFT-approximations must be subtracted to avoid double counting [137–142]. Such a "double counting" correction is not necessary in the fully diagrammatic, but computationally very demanding GW+DMFT approach, where the LDA/GGA input is replaced by the GW approximation [145]. The resulting many-particle problem with its numerous energy bands and local interactions is then solved within DMFT, typically by CT-QMC.

7.2 Applications

7.2.1 Bulk materials

DFT+DMFT has been remarkably successful in the investigation of correlated materials, including transition metals and their oxides, manganites, fullerenes, Bechgaard salts, f-electron materials, magnetic superconductors, and Heusler alloys [139–142].
In particular, the application of DFT+DMFT led to the discovery of novel physical mechanisms and correlation phenomena. Take, for example, the Mott MIT. Within the single-band Hubbard model the Mott MIT was originally explained as a transition where the effective mass of quasiparticles diverges ("Brinkman-Rice scenario") [41]. When DMFT had made it possible to examine multi-band models, an orbitally-selective Mott MIT was identified [146]. Then, with the advent of DFT+DMFT, a site-selective Mott MIT was discovered in Fe_2O_3 with its numerous energy bands and local interactions [147].
In the following we illustrate the DFT+DMFT approach by its application to two paradigmatic materials, $SrVO_3$ and Fe.

$SrVO_3$: three-peak spectral function Transition metal oxides are an ideal laboratory for the study of electronic correlations in solids. Spectroscopic studies typically find a pronounced lower Hubbard band in the photoemission spectra which cannot be explained by conventional band-structure theory. $SrVO_3$ is a particularly simple correlated material due to its $3d^1$ configuration and its purely cubic crystal structure with one vanadium ion per unit cell. The cubic symmetry of the crystal field splits the fivefold degenerate $3d$ orbital into a threefold degenerate t_{2g} orbital and a twofold degenerate e_g orbital at higher energies. In the simplest approximation only the local interaction between the electrons in the t_{2g} orbitals is included. By employing

a variant of the LDA it is possible to compute the strength of the local Coulomb repulsion ($U \simeq 5.5$ eV) and the Hund's rule coupling ($J \simeq 1.0$ eV) [148]. Using these values the electronic band structure is calculated within LDA. The correlated electron problem defined in this way is solved numerically within DMFT. The spectral function shows the characteristic three-peak structure of a correlated metal (lower Hubbard band, quasiparticle peak, upper Hubbard band) [148, 149]. This was confirmed experimentally using electron spectroscopies [148, 150]. Recently it was pointed out that oxygen vacancy states created by UV or x-ray irradiation can strongly affect the line shapes of the lower Hubbard band and the quasiparticle peak [151], which must be taken into account in quantitative interpretations of those peaks.

Fe: electronic correlations and structural stability Iron (Fe) exhibits a rich phase diagram. Under ambient conditions Fe is ferromagnetic and has a bcc crystal structure (α phase). At the Curie temperature $T_C \sim 1043$ K the α phase becomes paramagnetic but retains its bcc structure. Only when the temperature is further increased to $T_{\text{struct}} \sim 1185$ K does a structural phase transition to a fcc structure (γ phase) take place. At $T \sim 1670$ K a transition to a second bcc structure (δ phase) occurs. DFT+DMFT calculations for ferromagnetic bcc Fe provide a semi-quantitative description of several physical properties of that phase (at least sufficiently far from the Curie point) and demonstrate that electronic correlations play an important role [152].[24] This approach also clarified the microscopic origin of the magnetic exchange interactions in the ferromagnetic phase [155]. While DFT band-structure methods provide qualitatively correct results for several electronic and structural properties of iron [156], their application in the case of the bcc-to-fcc phase transition predicts a simultaneous transition of the structural and the magnetic state. In fact, without magnetization standard band-structure methods find bcc iron to be unstable [157]. These discrepancies can been resolved by using DFT+DMFT to compute total energies [154, 158]. Thereby one obtains values of the lattice constant, unit cell volume, and bulk modulus of paramagnetic α iron which are in good quantitative agreement with experiment [154]. In particular, DFT+DMFT calculations of the equilibrium crystal structure and phase stability of iron find that the bcc-to-fcc phase transition indeed takes place at a temperature well above the magnetic transition (at about 1.3 T_C) and correctly determine the phonon dispersion and Debye temperature [154]. This approach is also of interest for geophysical studies, namely to explore iron and nickel at Earth's core conditions [159].

Furthermore, the study of Fe-based pnictides and chalcogenides led to the important insight that in metallic multi-orbital materials the intra-atomic exchange J can also induce strong correlations [160]. Clearly DMFT-based approaches will be very useful for the future design of correlated materials [161], such as materials with a high thermopower for thermoelectric devices which can convert waste heat into electric energy [162].

[24] In these investigations the lattice structure was assumed to be given and fixed. The question regarding the stability of the lattice structure in the presence of electronic correlations was studied, for example, in the case of plutonium [153] and iron at ambient pressure [154].

7.2.2 Surfaces, layers, and nanostructures

During the last few years DMFT investigations of inhomogeneous systems greatly improved our understanding of correlation effects at surfaces and interfaces, in thin films and multi-layered nanostructures [163], infinite layer nickelates [164], and twisted bilayer graphene [165]. This also opened new insights into potential functionalities of such structures and their application in electronic devices. DMFT has been extended to study correlations also in finite systems such as nanoscopic conductors and molecules [166]. In this way many-body effects were shown to be important even in biological matter [167].

8 Conclusions

The solution of the Hubbard model in $d = \infty$, which corresponds to a dynamical mean-field theory (DMFT) of correlated lattice fermions, has become the generic mean-field theory of correlated electrons. It provides a comprehensive, non-perturbative and thermodynamically consistent approximation scheme for the investigation of correlated fermions, especially electrons in solids and cold fermionic atoms in optical lattices, in finite dimensions. Non-local extensions of the DMFT now also allow to explain correlation effects which occur on the scale of several lattice constants and at thermal and quantum phase transitions. Most importantly, the combination of DMFT with methods for the computation of electronic band structures has led to a powerful new theoretical framework for the realistic study of correlated materials. The further development of this approach and its applications is the subject of current research.

References

[1] D.I. Khomskii: *Transition Metal Compounds* (Cambridge University Press, 2024)

[2] M.B. Maple, J. Phys. Soc. Jpn **74**, 222 (2005)

[3] D.M. Kennes, M. Claassen, L. Xian, A. Georges, A.J. Millis, J. Hone, C.R. Dean, D.N. Basov, A.N. Pasupathy, and A. Rubio, Nat. Phys. **17**, 155 (2021)

[4] N. Grewe and F. Steglich, in: K.A. Gschneidner Jr. and L. Eyring (eds.): *Handbook on the Physics and Chemistry of Rare Earths*, Vol. **14**, (North Holland, 1991), p. 343

[5] J.R. Schrieffer (ed.): *Handbook of High-Temperature Superconductivity* (Springer, 2007)

[6] E. Dagotto: *Nanoscale Phase Separation and Collossal Magnetoresistance* (Springer, 2002)

[7] M. Imada, A. Fujimori, and Y. Tokura, Rev. Mod. Phys. **70**, 1039 (1998)

[8] H.L. Stormer, D.C. Tsui, and A.C. Gossard, Rev. Mod. Phys. **71**, 298 (1999)

[9] H. v. Löhneysen, A. Rosch, M. Vojta, and P. Wölfle, Rev. Mod. Phys. **79**, 1015 (2007)

[10] Y. Tokura, Phys. Today **56**, No. 7, 50 (2003); E. Dagotto, Science **309**, 257 (2005)

[11] Z. Hennighausen and S. Kar, Electron. Struct. **3**, 014004 (2021)

[12] The Lecture Notes of the annual Jülich Autumn Schools on Correlated Electrons published by E. Pavarini, E. Koch and co-editors since 2011 provide extensive information on correlated electron systems and theoretical techniques for their investigation. [`https://www.cond-mat.de/events/correl.html`]

[13] W. Heisenberg, Z. Phys. **49**, 619 (1928)

[14] F. Bloch, Z. Phys. **57**, 545 (1929)

[15] L. Hoddeson, G. Baym, and M. Eckert, Rev. Mod. Phys. **59**, 287 (1987)

[16] D. Pines: *The Many-Body Problem* (W.A. Benjamin, Inc., Reading, 1962)

[17] M.C. Gutzwiller, Phys. Rev. Lett. **10**, 159 (1963)

[18] J. Hubbard, Proc. Roy. Soc. London A **276**, 238 (1963)

[19] J. Kanamori, Prog. Theor. Phys. **30**, 275 (1963)

[20] D. Jaksch, C. Bruder, J.I. Cirac, C.W. Gardiner, and P. Zoller, Phys. Rev. Lett. **81** 3108 (1998); I. Bloch, J. Dalibard, and W. Zwerger, Rev. Mod. Phys. **80**, 885 (2008)

[21] P.W. Anderson, Phys. Rev. **115**, 2 (1959)

[22] P.W. Anderson, Phys. Rev. **124**, 41 (1961)

[23] P.A. Wolff, Phys. Rev. **124**, 1030 (1961)

[24] M. Kollar, R. Strack, and D. Vollhardt, Phys. Rev. B **53**, 9225 (1996)

[25] E. Lieb and F.Y. Wu, Phys. Rev. Lett. **20**, 1445 (1968)

[26] Y.-F. Song, Y. Deng, Y.-Y. He, Phys. Rev. B **111**, 035123 (2025)

[27] S. Stanisic, J.L. Bosse, F.M. Gambetta, R.A. Santos, W. Mruczkiewicz, T.E. O'Brien, E. Ostby, and A. Montanaro, Nat. Commun. **13**, 5743 (2022);
A. Jafarizadeh, F. Pollmann, and A. Gammon-Smith, arXiv:2408.14543

[28] R. Peierls, Contemp. Phys. **21**, 3 (1980)

[29] E. Wigner, Phys. Rev. **46**, 1002 (1934)

[30] R. Brout, Phys. Rev. **118**, 1009 (1960)

[31] M.E. Fisher and D.S. Gaunt, Phys. Rev. **133**, A224 (1964)

[32] E. Ising, Z. Phys. **31**, 253 (1925)

[33] D. Vollhardt, in E. Pavarini, E. Koch, A. Lichtenstein, and D. Vollhardt (eds.): *Dynamical Mean-Field Theory of Correlated Electrons*, vol. 12 (Forschungszentrum Jülich, 2022) [https://www.cond-mat.de/events/correl22/manuscripts/]

[34] W. Langer, M. Plischke, and Mattis, Phys. Rev. Lett. **23**, 1448 (1969);
K. Dichtel, R.J. Jelitto, and H. Koppe, Z. Phys. **246**, 248 (1971)

[35] E. Feenberg: *Theory of Quantum Fluids* (Academic, New York, 1969);
V.R. Pandharipande and R.B. Wiringa, Rev. Mod. Phys. **51**, 821 (1979);
P. Fulde: *Electron Correlations in Molecules and Solids* (Springer, Berlin, 2002)

[36] M.C. Gutzwiller, Phys. Rev. **137**, A1726 (1965)

[37] P. Fazekas: *Lecture Notes on Electron Correlation and Magnetism* (World Scientific, Singapore, 1999)

[38] T. Ogawa, K. Kanda, and T. Matsubara, Prog. Theor. Phys. **53**, 614 (1975)

[39] D. Vollhardt, Rev. Mod. Phys. **56**, 99 (1984)

[40] P.G.J. van Dongen and D. Vollhardt, Phys. Rev. B **40**, 7252 (1989)

[41] W.F. Brinkman and T.M. Rice, Phys. Rev. B **2**, 4302 (1970)

[42] J. Hubbard, Proc. Roy. Soc. London A **281**, 401 (1964)

[43] R.J. Elliott, J.A. Krumhansl, and P.L. Leath, Rev. Mod. Phys. **46**, 465 (1974)

[44] P.W. Anderson and W.F. Brinkman, in K.H. Bennemann and J.B. Ketterson (eds.): *The Physics of Liquid and Solid Helium*, Part II, (Wiley, New York, 1978), p. 177

[45] D. Vollhardt, in E. Pavarini, E. Koch, D. Vollhardt, A. Lichtenstein (eds.): *DMFT at 25: Infinite Dimensions*, vol. 4 (Forschungszentrum Jülich, 2014) [https://www.cond-mat.de/events/correl14/manuscripts/]

[46] H.A. Razafimandimby, Z. Phys. B: Condens. Matter **49**, 33 (1982)

[47] For a personal account by Andrei Ruckenstein of the developments leading to the formulation of the Kotliar-Ruckenstein slave-boson mean-field theory see https://aspenphys.org/presidential-essay-from-andrei-ruckenstein/

[48] G. Kotliar and A.E. Ruckenstein, Phys. Rev. Lett. **57**, 1362 (1986)

[49] W. Metzner and D. Vollhardt, Phys. Rev. Lett. **59**, 121 (1987); W. Metzner and D. Vollhardt, Phys. Rev. B **37**, 7382 (1988); Erratum: *ibid.* **39**, 12339 (1989)

[50] W. Metzner and D. Vollhardt, Phys. Rev. Lett. **62**, 324 (1989)

[51] W. Metzner, Z. Phys. B: Condens. Matter **77**, 253 (1989)

[52] F. Gebhard, Phys. Rev. B **41**, 9452 (1990)

[53] J. Bünemann, F. Gebhard, and W. Weber, Found. Phys. **30**, 2011 (2000);
T. Schickling, J. Bünemann, F. Gebhard, and W. Weber, New J. Phys. **16**, 93034 (2014)

[54] P.G.J. van Dongen, F. Gebhard, D. Vollhardt, Z. Phys. B: Condens. Matter **76**, 199 (1989)

[55] D. Vollhardt, in A. Avella and F. Mancini (eds.): *Lectures on the Physics of Strongly Correlated Systems XIV*, *AIP Conference Proceedings*, vol. 1297, (American Institute of Physics, Melville, 2010), p. 339; [http://arxiv.org/abs/1004.5069v3]

[56] U. Wolff, Nucl. Phys. B **225**, 391 (1983)

[57] E. Müller-Hartmann, in E. Talik and J. Szade (eds.): *Proc. of the V. Symp. Phys. of Metals*, (Poland, 1991), p. 22; G.S. Uhrig, Phys. Rev. Lett. **77**, 3629 (1996)

[58] M. Ulmke, Euro. Phys. J. B **1**, 301 (1998)

[59] E. Müller-Hartmann, Z. Phys. B: Condens. Matter **74**, 507 (1989)

[60] E. Müller-Hartmann, Z. Phys. B: Condens. Matter **76**, 211 (1989)

[61] V. Janiš, Z. Phys. B: Condens. Matter **83**, 227 (1991)

[62] V. Janiš and D. Vollhardt, Int. J. Mod. Phys. **B6**, 731 (1992)

[63] R. Vlaming and D. Vollhardt, Phys. Rev. B **45**, 4637 (1992)

[64] V. Janiš and D. Vollhardt Phys. Rev. B **46**, 15712 (1992)

[65] H. Schweitzer and G. Czycholl, Solid State Commun. **69**, 171 (1989)

[66] U. Brandt and C. Mielsch, Z. Phys. B: Condens. Matter **75**, 365 (1989)

[67] P.G.J. van Dongen and D. Vollhardt, Phys. Rev. Lett. **65**, 1663 (1990)

[68] J.M. Luttinger and J.C. Ward, Phys. Rev. **118**, 1417 (1960);
J.M. Luttinger, Phys. Rev. **119**, 1153 (1960)

[69] J.T. Heath and K.S. Bedell, New J. Phys. **22** 063011 (2020)

[70] A.C. Hewson: *The Kondo Problem to Heavy Fermions* (Cambridge Univ. Press, 1997)

[71] A. Georges and G. Kotliar, Phys. Rev. B **45**, 6479 (1992)

[72] M. Jarrell, Phys. Rev. Lett. **69**, 168 (1992)

[73] J.E. Hirsch and R.M. Fye, Phys. Rev. Lett. **56**, 2521 (1986)

[74] A. Georges, G. Kotliar, W. Krauth, and M.J. Rozenberg, Rev. Mod. Phys. **68**, 13 (1996)

[75] E. Pavarini, E. Koch, A. Lichtenstein, and D. Vollhardt (eds.): *DMFT: From Infinite Dimensions to Real Materials*, vol. 8 (Forschungszentrum Jülich, 2018) [https://www.cond-mat.de/events/correl18/manuscripts/]

[76] G. Kotliar and D. Vollhardt, Phys. Today **57**, 53 (2004)

[77] E. Gull, A.J. Millis, A.I. Lichtenstein, A.N. Rubtsov, M. Troyer, P. Werner, Rev. Mod. Phys. **83**, 349 (2011)

[78] R. Bulla, T.A. Costi, and Th. Pruschke, Rev. Mod. Phys. **80**, 395 (2008)

[79] K. Hallberg, D.J. García, P.S. Cornaglia, J.I. Facio, and Y. Núñez-Fernández, EPL **112**, 17001 (2015)

[80] E. Koch, G. Sangiovanni, and O. Gunnarsson, Phys. Rev. B **78**, 115102 (2008); Y. Lu and M.W. Haverkort, Eur. Phys. J. Spec. Top. **226**, 2549 (2017)

[81] A. Holzner, A. Weichselbaum, and J. von Delft, Phys. Rev. B **81**, 125126 (2010); N.-O. Linden, M. Zingl, C. Hubig, O. Parcollet, and U. Schollwöck, Phys. Rev. B **101**, 041101(R) (2020)

[82] D. Bauernfeind, M. Zingl, R. Triebl, M. Aichhorn, and H.G. Evertz, Phys. Rev. X **7**, 031013 (2017)

[83] L.-F. Arsenault, A. Lopez-Bezanilla, O.A. von Lilienfeld, and A.J. Millis, Phys. Rev. B **90**, 155136 (2014); E. Sheridan, C. Rhodes, F. Jamet, I. Rungger, and C. Weber, Phys. Rev. B **104**, 205120 (2021)

[84] J. Selisko, M. Amsler, C. Wever, Y. Kawashima, G. Samsonidze, R. Ul Haq, F. Tacchino, I. Tavernelli, and T. Eckl, arXiv:2404.09527; C. Bertrand, P. Besserve, M. Ferrero, and T. Ayral, arXiv:2412.13711

[85] N.F. Mott, Proc. Phys. Soc. London, Ser. A **62**, 416 (1949); N.F. Mott, Rev. Mod. Phys. **40**, 677 (1968)

[86] N.F. Mott: *Metal-Insulator Transitions* (Taylor and Francis, London, 1990), 2nd edition

[87] M. Imada, A. Fujimori, and Y. Tokura, Rev. Mod. Phys. **70**, 1039 (1998)

[88] R. Bulla, Phys. Rev. Lett. **83**, 136 (1999); M.J. Rozenberg, R. Chitra, and G. Kotliar, Phys. Rev. Lett. **83**, 3498 (1999); J. Joo and V. Oudovenko, Phys. Rev. B **64**, 193102 (2001); R. Bulla, T.A. Costi, and D. Vollhardt, Phys. Rev. B **64**, 045103 (2001); N. Blümer: *Metal-Insulator Transition and Optical Conductivity in High Dimensions* (Shaker Verlag, Aachen, 2003)

[89] F. Krien, E.G.C.P. van Loon, M.I. Katsnelson, A.I. Lichtenstein, and M. Capone, Phys. Rev. B **99**, 245128 (2019)

[90] O. Gunnarsson and K. Schönhammer, Phys. Rev. B **31**, 4815 (1985); R. Bulla, A.C. Hewson, and Th. Pruschke, J. Phys.: Condens. Matter **10**, 8365 (1998)

[91] S. Sen, P.J. Wong, and A.K. Mitchell, Phys. Rev. B **102**, 081110 (2020)

[92] H. Terletska, J. Vučičević, D. Tanasković, and V. Dobrosavljević, Phys. Rev. Lett. **107**, 026401 (2011); J. Vučičević, H. Terletska, D. Tanasković, and V. Dobrosavljević, Phys. Rev. B **88**, 075143 (2013)

[93] M. Pelz, S. Adler, M. Reitner, A. Toschi, Phys. Rev. B **108** 155101 (2023)

[94] D.B. McWhan, A. Menth, J.P. Remeika, W.F. Brinkman, T.M. Rice, Phys. Rev. B **7**, 1920 (1973); P. Limelette, A. Georges, D. Jerome, P. Wzietek, P. Metcalf, J.M. Honig, Science **302**, 89 (2003); P. Hansmann, A. Toschi, G. Sangiovanni, T. Saha-Dasgupta, S. Lupi, M. Marsi, K. Held, Phys. Status Solidi B **250**, 1251 (2013); J.C. Leiner, H.O. Jeschke, R. Valentí, S. Zhang, A.T. Savici, J.Y.Y. Lin, M.B. Stone, M.D. Lumsden, Jiawang Hong, O. Delaire, Wei Bao, C.L. Broholm, Phys. Rev. X **9**, 011035 (2019)

[95] P. Limelette, P. Wzietek, S. Florens, A. Georges, T.A. Costi, C. Pasquier, D. Jérome, C. Mézière, and P. Batail, Phys. Rev. Lett. **91**, 016401 (2003); F. Kagawa, T. Itou, K. Miyagawa, and K. Kanoda, Phys. Rev. B **69**, 064511 (2004); A. Pustogow, Y. Saito, A. Löhle, M.S. Alonso, A. Kawamoto, V. Dobrosavljević, M. Dressel, and S. Fratini, Nat. Commun. **12**, 1571 (2021)

[96] V. Dobrosavljević and G. Kotliar, Phys. Rev. Lett. **78**, 3943 (1997); V. Dobrosavljević, A.A. Pastor, and B.K. Nikolić, Europhys. Lett. **62**, 76 (2003); S. Mahmoudian, S. Tang, and V. Dobrosavljević, Phys. Rev. B **92**, 144202 (2015)

[97] K. Byczuk, W. Hofstetter, and D. Vollhardt, Phys. Rev. Lett. **94**, 056404 (2005); *ibid.* **102**, 146403 (2009); K. Byczuk, W. Hofstetter, and D. Vollhardt, in E. Abrahams (ed.): *Fifty Years of Anderson Localization* (World Scientific, Singapore, 2010), p. 473 [reprinted in Int. J. Mod. Phys. B **24**, 1727 (2010)]

[98] D. Vollhardt, N. Blümer, K. Held, and M. Kollar, Lecture Notes in Physics **580**, 191 (Springer, Heidelberg, 2001)

[99] K. Byczuk and D. Vollhardt, Phys. Rev. B **65**, 134433 (2002)

[100] M.Z. Hasan and C.L. Kane, Rev. Mod. Phys. **82**, 3045 (2010)

[101] Y. Tada, R. Peters, M. Oshikawa, A. Koga, N. Kawakami, and S. Fujimoto, Phys. Rev. B **85**, 165138 (2012)

[102] T. Mertz, K. Zantout, and R. Valentí, Phys. Rev. B **100**, 125111 (2019)

[103] A.A. Markov, G. Rohringer, and A.N. Rubtsov, Phys. Rev. B **100**, 115102 (2019)

[104] B. Irsigler, T. Grass, J.-H. Zheng, M. Barbier, and W. Hofstetter, Phys. Rev. B **103**, 125132 (2021)

[105] S. Liang, M.-H. Jiang, W. Chen, J.-X. Li, and Q.-H. Wang, Phys. Rev. B **98**, 054433 (2018)

[106] T. Yoshida, R. Peters, and N. Kawakami, Phys. Rev. B **98**, 035141 (2018); Y. Nagai, Y. Qi, H. Isobe, V. Kozii, L. Fu, Phys. Rev. Lett. **125**, 227204 (2020)

[107] D. Krüger and M. Potthoff, Phys. Rev. Lett. **126**, 196401 (2021)

[108] L. Del Re, arXiv:2408.14288

[109] H. Aoki, N. Tsuji, M. Eckstein, M. Kollar, T. Oka, and P. Werner, Rev. Mod. Phys. **86**, 779 (2014)

[110] M. Ligges, I. Avigo, D. Golež, H.U.R. Strand, Y. Beyazit, K. Hanff, F. Diekmann, L. Stojchevska, M. Kalläne, P. Zhou, K. Rossnagel, M. Eckstein, P. Werner, and U. Bovensiepen, Phys. Rev. Lett. **120**, 166401 (2018); Erratum: *ibid.* **122**, 159901 (2019)

[111] J. Li, H.U.R. Strand, P. Werner, and M. Eckstein, Nat. Commun. **9**, 4581 (2018)

[112] Y. Murakami, D. Golež, M. Eckstein, and P. Werner, arXiv:2310.05201

[113] U. Schneider, L. Hackermüller, S. Will, Th. Best, I. Bloch, T.A. Costi, R.W. Helmes, D. Rasch, A. Rosch, Science **322**, 1520 (2008)

[114] P. Sémon, K. Haule, and G. Kotliar, Phys. Rev. B **95**, 195115 (2017)

[115] A. Tamai, M. Zingl, E. Rozbicki, E. Cappelli, S. Riccò, A. de la Torre, S. McKeown Walker, F.Y. Bruno, P.D.C. King, W. Meevasana, M. Shi, M. Radović, N.C. Plumb, A.S. Gibbs, A.P. Mackenzie, C. Berthod, H. Strand, M. Kim, A. Georges, and F. Baumberger, Phys. Rev. X **9**, 021048 (2019)

[116] Q. Si and J.L. Smith (1996), Phys. Rev. Lett. **77**, 3391 (1996); J.L. Smith and Q. Si, Phys. Rev. B **61**, 5184 (2000); R. Chitra and G. Kotliar, Phys. Rev. Lett. **84**, 3678 (2000); P. Sun and G. Kotliar, Phys. Rev. B **66**, 085120 (2002)

[117] A. Schiller and K. Ingersent, Phys. Rev. Lett. **75**, 113 (1995)

[118] G. Zaránd, D.L. Cox, and A. Schiller, Phys. Rev. B **62**, R16227 (2000)

[119] Th. Maier, M. Jarrell, Th. Pruschke, and M.H. Hettler, Rev. Mod. Phys. **77**, 1027 (2005)

[120] G. Rohringer, H. Hafermann, A. Toschi, A.A. Katanin, A.E. Antipov, M.I. Katsnelson, A.I. Lichtenstein, A.N. Rubtsov, and K. Held, Rev. Mod. Phys. **90**, 025003 (2018)

[121] M.H. Hettler, A.N. Tahvildar-Zadeh, M. Jarrell, Th. Pruschke, and H.R. Krishnamurthy, Phys. Rev. B **58**, R7475 (1998)

[122] A.I. Lichtenstein, and M.I. Katsnelson, Phys. Rev. B **62**, R9283 (2000); G. Kotliar, S.Y. Savrasov, G. Pálsson, and G. Biroli, Phys. Rev. Lett. **87**, 186401 (2001)

[123] C.E. Ekuma, H. Terletska, K.-M. Tam, Z.-Y. Meng, J. Moreno, and M. Jarrell, Phys. Rev. B **89**, 081107(R) (2014); H. Terletska, Y. Zhang, K.M. Tam, T. Berlijn, L. Chioncel, N.S. Vidhyadhiraja, and M. Jarrell, Appl. Sci. **8**, 2401 (2018)

[124] A. Toschi, A.A. Katanin, and K. Held, Phys Rev. B **75**, 045118 (2007)

[125] A.N. Rubtsov, M.I. Katsnelson, and A.I. Lichtenstein, Phys. Rev. B **77**, 033101 (2008)

[126] J. Otsuki, Phys. Rev. Lett. **115**, 036404 (2015)

[127] M. Kitatani, T. Schäfer, H. Aoki, and K. Held, Phys Rev. B **99**, 041115(R) (2019)

[128] T. Schäfer, A.A. Katanin, K. Held, and A. Toschi, Phys. Rev. Lett. **119**, 046402 (2017)

[129] D. Hirschmeier, H. Hafermann, and A.I. Lichtenstein, Phys. Rev. B **97**, 115150 (2018); T. Schäfer, A.A. Katanin, M. Kitatani, A. Toschi, and K. Held, Phys. Rev. Lett. **122**, 227201 (2019)

[130] W. Metzner, M. Salmhofer, C. Honerkamp, V. Meden, and K. Schönhammer, Rev. Mod. Phys. **84**, 299 (2012)

[131] C. Taranto, S. Andergassen, J. Bauer, K. Held, A. Katanin, W. Metzner, G. Rohringer, and A. Toschi, Phys. Rev. Lett. **112**, 196402 (2014); D. Vilardi, C. Taranto, and W. Metzner, Phys. Rev. B **99**, 104501 (2019)

[132] P. Hohenberg and W. Kohn, Phys. Rev. B **136**, 864 (1964); W. Kohn and L.J. Sham, Phys. Rev. **140**, A1133 (1965)

[133] R.O. Jones and O. Gunnarsson, Rev. Mod. Phys. **61**, 689 (1989)

[134] J.P. Perdew, K. Burke, and M. Ernzerhof, Phys. Rev. Lett. **77**, 3865 (1996)

[135] V.I. Anisimov, J. Zaanen, and O.K. Andersen, Phys. Rev. B **44**, 943 (1991)

[136] S. Baroni, S. de Gironcoli, A.D. Corso, and P. Giannozzi, Rev. Mod. Phys. **73**, 515 (2001)

[137] V.I. Anisimov, A.I. Poteryaev, M.A. Korotin, A.O. Anokhin, and G. Kotliar, J. Phys.: Condens. Matter **9**, 7359 (1997)

[138] A.I. Lichtenstein and M.I. Katsnelson, Phys. Rev. B **57**, 6884 (1998)

[139] K. Held, I.A. Nekrasov, G. Keller, V. Eyert, N. Blümer, A.K. McMahan, R.T. Scalettar, Th. Pruschke, V.I. Anisimov, and D. Vollhardt, Psi-k Newsletter **56**, 65 (2003) [reprinted in Phys. Status Solidi B **243**, 2599 (2006)]; K. Held, Adv. Phys. **56**, 829 (2007)

[140] G. Kotliar, S.Y. Savrasov, K. Haule, V.S. Oudovenko, O. Parcollet, and C.A. Marianetti, Rev. Mod. Phys. **78**, 865 (2006)

[141] M.I. Katsnelson, V. Yu. Irkhin, L. Chioncel, A.I. Lichtenstein, and R.A. de Groot, Rev. Mod. Phys. **80**, 315 (2008)

[142] D. Vollhardt and A.I. Lichtenstein (eds.): *Dynamical Mean-Field Approach with Predictive Power for Strongly Correlated Materials*, Eur. Phys. J. Spec. Top. **226** (2017)

[143] D. Vollhardt, JPS Conf. Proc. **30**, 011001 (2020)

[144] A. Carta, I. Timrov, P. Mlkvik, A. Hampel, C. Ederer, arXiv:2411.03937

[145] S. Biermann, F. Aryasetiawan, and A. Georges, Phys. Rev. Lett. **90**, 086402 (2003); S. Biermann, J. Phys.: Condens. Matter **26**, 173202 (2014); J.M. Tomczak, P. Liu, A. Toschi, G. Kresse, and K. Held, Eur. Phys. J. Spec. Top. **226**, 2565 (2017)

[146] L. de'Medici, A. Georges, and S. Biermann, Phys. Rev. B **72**, 205124 (2005)

[147] E. Greenberg, I. Leonov, S. Layek, Z. Konopkova, M.P. Pasternak, L. Dubrovinsky, R. Jeanloz, I.A. Abrikosov, and G. Kh. Rozenberg, Phys. Rev. X **8**, 031059 (2018)

[148] A. Sekiyama, H. Fujiwara, S. Imada, S. Suga, H. Eisaki, S.I. Uchida, K. Takegahara, H. Harima, Y. Saitoh, I.A. Nekrasov, G. Keller, D.E. Kondakov, A.V. Kozhevnikov, Th. Pruschke, K. Held, D. Vollhardt, and V.I. Anisimov, Phys. Rev. Lett. **93**, 156402 (2004); I.A. Nekrasov, G. Keller, D.E. Kondakov, A.V. Kozhevnikov, Th. Pruschke, K. Held, D. Vollhardt, and V.I. Anisimov, Phys. Rev. B **72**, 155106 (2005); I.A. Nekrasov, K. Held, G. Keller, D.E. Kondakov, Th. Pruschke, M. Kollar, O.K. Andersen, V.I. Anisimov, and D. Vollhardt, Phys. Rev. B **73**, 155112 (2006)

[149] E. Pavarini, S. Biermann, A. Poteryaev, A.I. Lichtenstein, A. Georges, and O.K. Andersen, Phys. Rev. Lett. **92**, 176403 (2004)

[150] I.H. Inoue, I. Hase, Y. Aiura, A. Fujimori, K. Morikawa, T. Mizokawa, Y. Haruyama, T. Maruyama, and Y. Nishihara, Physica C **235-240**, 1007 (1994)

[151] M. Sing, H.O. Jeschke, F. Lechermann, Valentí, and R. Claessen, Eur. Phys. J. Spec. Top. **226**, 2457 (2017)

[152] A.I. Lichtenstein, M.I. Katsnelson, and G. Kotliar, Phys. Rev. Lett. **87**, 067205 (2001); J. Sánchez-Barriga, J. Fink, V. Boni, I. Di Marco, J. Braun, J. Minár, A. Varykhalov, O. Rader, V. Bellini, F. Manghi, H. Ebert, M.I. Katsnelson, A.I. Lichtenstein, O. Eriksson, W. Eberhardt, and H.A. Dürr, Phys. Rev. Lett. **103**, 267203 (2009)

[153] X. Dai, S.Y. Savrasov, G. Kotliar, A. Migliori, H. Ledbetter, and E. Abrahams, Science **300**, 953 (2003)

[154] I. Leonov, A.I. Poteryaev, V.I. Anisimov, and D. Vollhardt, Phys. Rev. Lett. **106**, 106405 (2011); I. Leonov, A.I. Poteryaev, V.I. Anisimov, and D. Vollhardt, Phys. Rev. B **85**, R020401 (2012); I. Leonov, A.I. Poteryaev, Y.N. Gornostyrev, A.I. Lichtenstein, M.I. Katsnelson, V.I. Anisimov, and D. Vollhardt, Sci. Rep. **4**, 5585 (2014); J. Kuneš, I. Leonov, P. Augustinský, V. Křápek, M. Kollar, and D. Vollhardt, Eur. Phys. J. Spec. Top. **226**, 2641 (2017)

[155] Y.O. Kvashnin, R. Cardias, A. Szilva, I. Di Marco, M.I. Katsnelson, A.I. Lichtenstein, L. Nordström, A.B. Klautau, and O. Eriksson, Phys. Rev. Lett. **116**, 217202 (2016);

A.A. Katanin, A.S. Belozerov, A.I. Lichtenstein, and M.I. Katsnelson, Phys. Rev. B **107**, 235118 (2023)

[156] D.J. Singh, W.E. Pickett, and H. Krakauer, Phys. Rev. B **43**, 11628 (1991); S.V. Okatov, A.R. Kuznetsov, Y.N. Gornostyrev, V.N. Urtsev, and M.I. Katsnelson, Phys. Rev. B **79**, 094111 (2009);

[157] H.C. Hsueh, J. Crain, G.Y. Guo, H.Y. Chen, C.C. Lee, K.P. Chang, and H.L. Shih, Phys. Rev. B **66**, 052420 (2002)

[158] H. Park, A.J. Millis, and C.A. Marianetti, Phys. Rev. B **90**, 235103 (2014)

[159] A. Hausoel, M. Karolak, E. Şaşıoğlu, A. Lichtenstein, K. Held, A. Katanin, A. Toschi, and G. Sangiovanni, Nat. Commun. **8**, 16062 (2017); L.V. Pourovskii, J. Phys.: Condens. Matter **31**, 373001 (2019)

[160] K. Haule and G. Kotliar, New. J. Phys. **11**, 025021 (2009); A. Georges, L de'Medici, and J. Mravlje, Ann. Rev. Condens. Matter Phys. **4**, 137 (2013); D. Guterding, S. Backes, M. Tomić, H.O. Jeschke, and R. Valentí, Phys. Status Solidi B **254**, 1600164 (2017)

[161] R. Adler, C.-J. Kang, C.-H. Yee, and G. Kotliar, Rep. Prog. Phys. **82**, 012504 (2019)

[162] G.G. Pálsson and G. Kotliar, Phys. Rev. Lett. **80**, 4775 (1998); P. Wissgott, A. Toschi, H. Usui, K. Kuroki, and K. Held, Phys. Rev. B **82**, 201106(R) (2010); W. Xu, K. Haule, and G. Kotliar, Phys. Rev. Lett. **111**, 036401 (2013); M. Zingl, G.J. Kraberger, and M. Aichhorn, Phys. Rev. Mater. **3**, 075404 (2019)

[163] M.J. Han, X. Wang, C.A. Marianetti, A.J. Millis, Phys. Rev. Lett. **107**, 206804 (2011); J.K. Freericks, *Transport in multilayered nanostructures – The dynamical mean-field approach*, 2nd edition (Imperial College Press, London, 2016); Z. Zhong, M. Wallerberger, J.M. Tomczak, C. Taranto, N. Parragh, A. Toschi, G. Sangiovanni, K. Held, Phys. Rev. Lett. **114**, 246401 (2015); F. Lechermann, Phys. Rev. Mater. **2**, 085004 (2018)

[164] H. Chen, A. Hampel, J. Karp, F. Lechermann, A. Millis, Front. Phys. **10**, 835942 (2022)

[165] G. Rai, L. Crippa, D. Călugăru, H. Hu, F. Paoletti, L. de'Medici, A. Georges, B.A. Bernevig, R. Valentí, G. Sangiovanni, T. Wehling, Phys. Rev. X **14**, 031045 (2024)

[166] D. Jacob, K. Haule, and G. Kotliar, Phys. Rev. B **82**, 195115 (2010); L. Chioncel, C. Morari, A. Östlin, W.H. Appelt, A. Droghetti, M.M. Radonjić, I. Rungger, L. Vitos, U. Eckern, A.V. Postnikov, Phys. Rev. B **92**, 054431 (2015); M. Schüler, S. Barthel, T. Wehling, M. Karolak, A. Valli, and G. Sangiovanni, Eur. Phys. J. Spec. Top. **226**, 2615 (2017); P. Pudleiner, A. Kauch, K. Held, and G. Li, Phys. Rev. B **100**, 075108 (2019)

[167] C. Weber, D.D. O'Regan, N.D.M. Hine, P.B. Littlewood, G. Kotliar, and M.C. Payne, Phys. Rev. Lett. **110**, 106402 (2013); M.A. al-Badri, E. Linscott, A. Georges, D.J. Cole, and C. Weber, Commun. Phys. **3**, 4 (2020)

2 Density Functional Theory for the Sceptical

Robert O. Jones
Peter-Grünberg-Institut PGI-1
Forschungszentrum Jülich

Contents

1 Introduction **2**

2 The electron density as basic variable **3**

3 An "approximate practical method" **6**

4 Electron density functional formalism **7**
4.1 Single-particle description of a many-electron system. 8
4.2 Exchange-correlation energy $E_{\rm xc}$ and the xc-hole 10

5 Local density approximation (LDA) and extensions **11**
5.1 Three examples 12
5.2 Spin systems. LSD approximation 15
5.3 Shortcomings of LD/LSD approximations 16
5.4 "Jacob's Ladder" 17
5.5 Functional approximations: current status 19

6 Broken symmetry. Connection to strong correlation? **20**
6.1 Broken symmetry in general 20
6.2 Symmetry-broken systems: H_2, Cr_2, Be_2 21

7 Concluding remarks **23**

E. Pavarini, E. Koch, A. Lichtenstein, and D. Vollhardt (eds.)
Understanding Correlated Materials with DMFT
Modeling and Simulation Vol. 15
Forschungszentrum Jülich, 2025, ISBN 978-3-95806-813-1
http://www.cond-mat.de/events/correl25

1 Introduction

> Density Functional Theory:
> "Almost the right answer, for almost the right reason, at almost the right price,
> for almost all systems of interest"
> (J.P. Perdew) [1, p. 194]

There will be people in the audience who will say immediately that "strongly correlated" systems must be exceptions, since they are often viewed as those that are not described well by electron density functional theory (DFT) theory. Many seminars and publications on the subject mention at the outset the widespread use of DFT in materials, and they may even quote Walter Kohn: "For periodic solids it is sometimes referred to as the standard model" [2]. It is then a short step to listing the systems where DF results with standard approximations are unacceptable (a "metallic" transition metal oxide insulator, almost anything to do with rare earth or actinide elements, ...), emphasizing the importance of describing such "strongly correlated" materials correctly [3].[1] DFT is nevertheless an essential part of this school. It is used widely in materials science and chemistry and provides useful results for countless systems for which the exact wave function cannot be computed. We shall see that physical insight can be obtained and *why* approximations used in DF calculations can give sensible answers far from their regions of obvious validity. Some features of the results, particularly the orbitals, are essential input for "strongly correlated" methods. We shall also see that improvements in the approximations needed in density functional calculations are now closing the distance to the strongly correlated world.

The origins of DF theory go back to the early years of quantum mechanics in the late 1920s. Thomas [4] and Fermi [5] recognized the electron density as a basic variable, and Dirac [6] showed already in 1930 that the state of an atom can be determined completely within Hartree-Fock theory by its one-particle reduced density matrix; we do not need to specify the wave function. We follow here the early history of density-related methods to the single-particle equations of Kohn and Sham in 1965. In its modern form, the DF formalism shows that ground state properties of a system of electrons in an external field can be determined, in principle, from a knowledge of the *density distribution* $n(\mathbf{r})$ alone. Much of the work in materials science and chemistry focuses on the *structure* and cohesive energies and on a property for which DF calculations are particularly valuable: the total energy E of a system of electrons in the presence of ions located at $\mathbf{R}_{\rm I}$.

Accurate calculations of the entire energy surface $E(\mathbf{R}_{\rm I})$ are possible only for systems with very few atoms, and this function generally has vast numbers of maxima and minima at unknown locations. The lowest energy, however, corresponds to the ground state *structure*, and paths between minima are essential to our studies of chemical reactions, including their activation

[1] An example can be found in the Preface of the 2012 Autumn School: "Density functional theory (DFT) is considered the Standard Model of solid state physics. The state-of-the-art approximations to DFT, the local-density approximation (LDA) or its simple extensions, fail, however, even qualitatively, for strongly correlated systems."

barriers. When I read the autobiography of Francis Crick [7], I was taken by his observation

> "If you want to understand *function*, study *structure*."

and have used it ever since. This relationship may be self-evident to molecular biologists and most chemists, but it is also true in other areas. The DF approach allows us to calculate $E(R_{\rm I})$, and hence the structure and many related properties, without using experimental input. If you are more interested in "real materials" than in mathematical models, this is a crucial advantage for strongly correlated materials as well.

Density functional theory is seen today as "the workhorse of quantum chemistry and materials science" [8], and it remains uncertain as to why it was resisted by the chemical community with great stubbornness for several decades. I have written about this matter elsewhere [9, 10] and shall not discuss it further here. However, a recent conference (Stockholm, 7–8 November 2024) was devoted to this question, and the seminars of leading DFT experts (Perdew, Baerends, Becke, Burke, Grimme, Head-Gordon, Savin,...) can be viewed online [11]. If you want to find out what really happened in the bleak years until DFT broke through in chemistry, watch [12].

There are many books and review articles on density functional theory, and I mention just two where I was involved [10, 13]. A long article with 70 authors, including many who played important roles in the development of DFT, surveys many important problems [8]. The focus in the present article is on *electron* density functional theory; DF methods in classical systems and nuclei are surveyed briefly in [10]. Symmetry breaking in density functional theory, in combination with the continuing improvement in approximate functional forms, may provide a direct link to the strongly correlated world and is discussed in Sec. 6.

2 The electron density as basic variable

The development of quantum mechanics after its introduction in 1925 was extremely rapid. Methods for finding approximate solutions of the Schrödinger equation followed soon after the equations were published in 1926 and have had a profound effect on chemistry and condensed matter physics ever since.

The "Hartree approximation" to the many-electron wave function is a product of single-particle functions,

$$\Psi(\mathbf{r}_1, \mathbf{r}_2, \ldots) = \psi_1(\mathbf{r}_1) \cdots \psi_N(\mathbf{r}_N) \tag{1}$$

where each $\psi_i(\mathbf{r}_i)$ satisfies a one-electron Schrödinger equation with a potential term arising from the average field of the other electrons. Hartree [14] introduced the idea of a "self-consistent field", with specific reference to the core and valence electrons, but the approximation (1) is not mentioned in any of his papers. Slater [15] and Fock [16] recognized immediately, however, that the product wave function (1) in conjunction with the variational principle led to a generalization of the method that would apply to systems more complex than atoms. They showed that replacing (1) by a determinant of such functions [15, 16] led to equations that were not much more complicated than those of Hartree, while satisfying the Pauli exclusion principle. These determinantal functions, which had been used in discussions of atoms [17] and

ferromagnetism [18], are known today as "Slater determinants", and the resulting "Hartree-Fock equations" have formed the basis of most discussions of atomic and molecular structure since.
In 1929 Dirac wrote [19]:

> "The general theory of quantum mechanics is now almost complete... The underlying physical laws necessary for the mathematical theory of a large part of physics and the whole of chemistry are thus completely known, and the difficulty is only that the exact application of these laws leads to equations much too complicated to be soluble. It therefore becomes desirable that approximate practical methods of applying quantum mechanics should be developed, which can lead to an explanation of the main features of complex atomic systems without too much computation."

I cannot think of a better short description of density functional theory than an "approximate practical method of applying quantum mechanics" to explain "complex atomic systems". I was not the only one who ignored the point "without too much computation."
Dirac [19] also sought to improve the model of Thomas [4] and Fermi [5] for calculating atomic properties based purely on the electron density $n(r)$. In the first "density functional theory", Thomas and Fermi assumed that the electrons form a homogeneous electron gas satisfying Fermi statistics and the kinetic energy has a simple dependence on the density $n(r)$. The TF equations are:

$$\frac{5}{3}C_k n(\mathbf{r})^{\frac{2}{3}} + e^2 \int d\mathbf{r}' \, \frac{n(\mathbf{r}')}{|\mathbf{r}-\mathbf{r}'|} + V_{\rm ext}(\mathbf{r}) + \lambda = 0\,, \tag{2}$$

where $C_k = 3\hbar^2(3\pi^2)^{\frac{2}{3}}/(10m)$, $V_{\rm ext}$ is the external potential, and λ is the Lagrange multiplier related to the constraint of constant particle number. Dirac noted the necessity of incorporating "exchange" phenomena, as in the Hartree-Fock approach [19], and he included these effects in the "Thomas atom" [6] by means of the potential

$$V_{\rm x}^{\rm Dirac} = -\left(\frac{1}{\pi}\right)\left(3\pi^2 n(\mathbf{r})\right)^{\frac{1}{3}}. \tag{3}$$

This term was derived for a homogeneous gas of density n and should be valid for weak spatial variations of $n(\mathbf{r})$.[2] The modified TF equation is often referred to as the "Thomas-Fermi-Dirac" equation.
The Thomas-Fermi method is a genuine "density functional" theory, in that the energy is related directly to the electron density. With its extensions, it provides a rough description of the charge density and the electrostatic potential of atoms, and its mathematical properties have attracted considerable attention [20,21]. However, it has severe deficiencies: The charge density is infinite at the nucleus and decays as r^{-6}, not exponentially, far from it. Teller [22] and others also showed that TF theory does not bind atoms to form molecules or solids, which rules out its use in chemistry or materials science. There is also no shell structure in the TF atom, so that the

[2] The exchange energy in a homogeneous (spin-polarized!) electron gas had been derived by Bloch [18] in 1929.

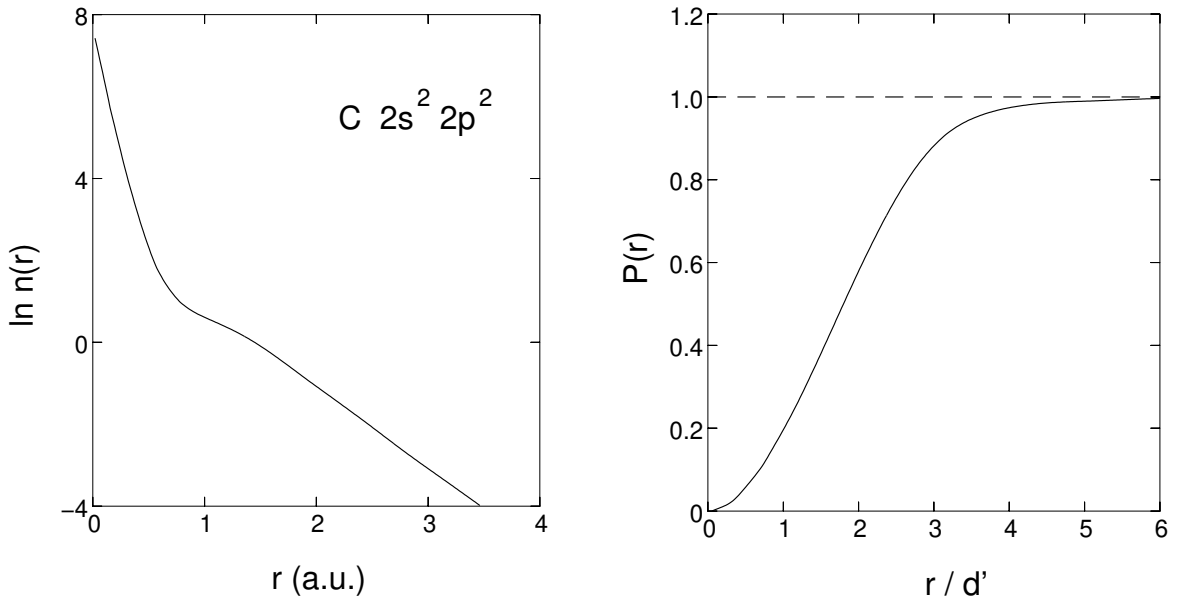


Fig. 1: *(left) Logarithm of spherical average of density in ground state of C atom as a function of the distance from the nucleus (atomic units [13]; (right) Probability that electrons in Na metal with parallel spins are r/d' apart ($d'^3 = V_0/(3\pi^2)$, V_0 is the atomic volume). After Wigner and Seitz [25].)*

.

periodic variation of many properties with changing atomic number Z cannot be reproduced, no ferromagnetism [13], and atoms *shrink* with increasing Z (as $Z^{-1/3}$) [23]. Nevertheless, it may be useful in the context of very dense matter [10].

One point made by Dirac [6], however, has been emphasized by many advocates of the DF method over the years, even if we were unaware of his words of over 80 years ago:

> "Each three-dimensional wave function will give rise to a certain electric density. This electric density is really a matrix, like all dynamical variables in the quantum theory. By adding the electric densities from all the wave functions we can obtain the total electric density for the atom. If we adopt the equations of the self-consistent field as amended for exchange, then this total electric density (the matrix) has one important property, namely, if the value of the total electric density at any time is given, then its value at any later time is determined by the equations of motion. This means that *the whole state of the atom is completely determined by this electric density; it is not necessary to specify the individual three-dimensional wave functions that make up the total electric density.* Thus one can deal with any number of electrons by working with just one matrix density function."

The italics are in the original. The derivation is based on the "self-consistent field" or Hartree-Fock approximation, and the "matrix density function" is known today as the one-particle reduced density matrix, but the observation that the density follows the equations of motion is much in the spirit of the theorem of Ehrenfest, who had proved in 1927 that the acceleration of a quantum wave packet that does not spread satisfied Newton's equations of motion [24].

The central role played by the density means that we must know what it looks like in real systems. Fig. 1 shows that the spherically averaged *density* in the ground state of the carbon atom falls monotonically from the nucleus and does not show the radial oscillations that occur if we plot $r^2 n(r)$. The charge density in small molecules is also rather featureless, with maxima at the nuclei, saddle points along the bonds, and a generally monotonic decay from both. The electron density in molecules and solids also shows relatively small departures from the overlapped densities of the constituent atoms. Energy differences, including binding, ionization, and cohesive energies, are the focus of much DF work and result from subtle changes in relatively featureless density distributions.

3 An "approximate practical method"

The basis of a quantum theory of atoms, molecules, and solids was in place at the beginning of the 1930's. Hans Bethe was another participant in this adventure and looked back on the time in this way:

> "The basic structure of quantum mechanics, quantum mechanics without relativity, that basic structure is finished ... The understanding of atoms, molecules, the chemical bond, and so on, that was all complete by 1928." [26, p. 78]

Linear combinations of atomic orbitals formed molecular orbitals, from which determinantal functions could be constructed, and linear combinations of determinants ("configuration interaction") would provide approximations to the complete wave function. Dirac had noted already, however, that this procedure could not be implemented in practice, so that approximations are essential. Furthermore, numerical techniques for solving the Schrödinger equation in extended systems were still to be developed.

Wigner and Seitz [25] developed a method for treating the self-consistent problems in crystals, and the "Wigner-Seitz cell" is known to all condensed matter physicists. The first application to metallic sodium used a pseudopotential for the Na ion, and calculations of the lattice constant, cohesive energy, and compressibility gave satisfactory results. Of particular interest for our purposes, however, is the calculation of the probability of finding electrons with parallel spins a distance r apart (Fig. 1 (right)). This function obtains its half-value for $r = 1.79\,d'$ or $0.460\,d$ for a body-centered cubic lattice with cube edge d, which is close to the radius of the "Wigner-Seitz sphere" $(3/8\pi)^{\frac{1}{3}}\,d = 0.492\,d$. The exclusion principle means then that two electrons with parallel pins will very rarely be at the same ion. This argument does not depend significantly on the potential and should apply to a Fermi gas subject to periodic boundary conditions [25]. The corresponding curves for spin up and spin down electrons, as well as for both spins combined, were discussed in the 1934 review article of Slater [27].

The picture that results is simple and appealing: the exclusion principle means that an electron with a given spin produces a surrounding region where there is a deficiency of charge of the same spin. This region contains unit charge and is referred to as the "Fermi" [25] or

"exchange" hole [28]. In the Hartree-Fock scheme, the exchange hole is different for each electronic function, but Slater [28] developed a simplified "exchange potential" that depended only on the density:

$$V_{\mathrm{x}}^{\mathrm{Slater}} = -\left(\frac{3}{2\pi}\right)\left(3\pi^2 n(r)\right)^{\frac{1}{3}}. \tag{4}$$

The Slater approximation (4) was proposed at the time that electronic computers were becoming available for electronic structure calculations and proved to be very useful in practice. Methods for solving the Schrödinger equation had been developed—but not implemented—somewhat earlier, including the augmented plane wave (APW) [29] and Korringa-Kohn-Rostoker approaches [30, 31].

The exchange potential of Slater (4) is 3/2 times that derived by Dirac and Bloch (3) for a homogeneous electron gas, but Slater [32] pointed out that an effective potential proportional to the cube root of the density could be obtained by arguments based on the exchange hole that do not depend on the free electron gas arguments used in the original derivation [28]. The exchange hole discussed above for a spin up electron contains a single electron. If we assume that it can be approximated by a sphere of radius $R_\uparrow$, then

$$\left(\frac{4\pi}{3}\right) R_\uparrow^3 \, n_\uparrow \stackrel{!}{=} 1 \;\rightsquigarrow\; R_\uparrow = \left(\frac{3}{4\pi n_\uparrow}\right)^{\frac{1}{3}} \tag{5}$$

where $n_\uparrow$ is the density of spin up electrons. Since the electrostatic potential at the center of such a spherical charge is proportional to $1/R_\uparrow$, the exchange potential will be proportional to $n_\uparrow^{\frac{1}{3}}$. This argument was used by Slater to counter a misconception (unfortunately still widespread) that local density approximations based on the homogeneous electron gas are only appropriate if the electron density is nearly homogeneous.

In 1954, Gáspár [33] questioned the prefactor of the effective exchange potential (Eq. 4). If one varies the spin orbitals to minimize the total energy in the Thomas-Fermi-Dirac form, one obtains a coefficient just $\frac{2}{3}$ as large. Gáspár applied this approximation to the Cu^+ ion and found good agreement with Hartree-Fock eigenfunctions and eigenvalues. Slater noted that Gáspár's method was "more reasonable than mine" [34], but the larger value was used in most calculations in the following years.

4 Electron density functional formalism

The variational principle on the energy was the basis of the derivation of the density functional formalism given by Hohenberg and Kohn (HK) [35]. First, they showed that there is a one-to-one relationship between the external potential $V_{\mathrm{ext}}(\mathbf{r})$ and the (nondegenerate) ground state (GS) wave function Ψ, and then that there is a one-to-one relationship between Ψ and the ground state density $n(\mathbf{r})$ of an N-electron system,

$$n(\mathbf{r}) = N \int d\mathbf{r}_2 \cdots d\mathbf{r}_N \, \Psi^*(\mathbf{r}, \mathbf{r}_2, \ldots, \mathbf{r}_N) \, \Psi(\mathbf{r}, \mathbf{r}_2, \ldots, \mathbf{r}_N) \; , \tag{6}$$

where the spin coordinates are not shown explicitly. Knowledge of the density then determines the external potential to within a constant, so that all terms in the Hamiltonian are known. Since the Hamiltonian operator determines completely all states of the system, $n(\mathbf{r})$ determines excited states as well as the ground state.

These ideas can be applied to the total energy using the variational principle. For this purpose, HK defined the functional $F[n(\mathbf{r})]$, which is "universal" in the sense that it is valid for any external potential $V_{\rm ext}$,

$$F[n] = \big\langle \Psi_n \big| T + V_{\rm ee} \big| \Psi_n \big\rangle, \tag{7}$$

and showed that the energy functional $E[n, V_{\rm ext}]$ satisfies a variational principle:

$$E_{\rm GS} = \min_{n(\mathbf{r})} E[n, V_{\rm ext}], \tag{8}$$

where

$$E[n, V_{\rm ext}] = \int d\mathbf{r}\, V_{\rm ext}(\mathbf{r})\, n(\mathbf{r}) + F[n]. \tag{9}$$

The minimization is performed in HK over all non-degenerate densities that can be derived from the ground state of some external potential ("V-representable"). Levy [36] generalized this to a minimization over all densities, including degeneracies.

The generalization to finite temperatures was carried out soon after the work of Hohenberg and Kohn [35]. Mermin [37] showed that, in a grand canonical ensemble at given temperature T and chemical potential μ, the equilibrium density is determined by the external potential $V_{\rm ext}$, and the equilibrium density minimizes the grand potential. Single-particle equations can be derived for a fictitious system with kinetic energy T_0 and entropy S_0, with $E_{\rm xc}$ replaced by the exchange-correlation contribution to the free energy.

4.1 Single-particle description of a many-electron system.

The task of finding good approximations to the energy functional $E[n]$ is simplified greatly if we use the decomposition introduced by Kohn and Sham [38],

$$E[n] = T_0[n] + \int d\mathbf{r}\, n(\mathbf{r}) \Big(V_{\rm ext}(\mathbf{r}) + \frac{1}{2}\Phi(\mathbf{r}) \Big) + E_{\rm xc}[n]. \tag{10}$$

T_0 is the kinetic energy that a system with density n would have if there were no electron-electron interactions, Φ is the classical Coulomb potential for electrons, and $E_{\rm xc}$ *defines* the exchange-correlation energy. T_0 is not the true kinetic energy T, but it is of comparable magnitude. Its treatment without approximation removes many deficiencies of the Thomas-Fermi approach, such as the lack of a shell structure of atoms or the absence of chemical bonding in molecules and solids. In the expression (10) all terms other than the exchange-correlation energy $E_{\rm xc}$ can be evaluated exactly, so that approximations for this term are crucial in density functional applications.

The variational principle applied to (10) yields

$$\frac{\delta E[n]}{\delta n(\mathbf{r})} = \frac{\delta T_0}{\delta n(\mathbf{r})} + V_{\rm ext}(\mathbf{r}) + \Phi(\mathbf{r}) + \frac{\delta E_{\rm xc}[n]}{\delta n(\mathbf{r})} = \mu, \tag{11}$$

where μ is the Lagrange multiplier associated with the requirement of constant particle number: $\int d\mathbf{r}\ \delta n(\mathbf{r}) = 0$, and the functional derivative is defined as

$$\delta F = \int d\mathbf{r} \left(\frac{\delta F}{\delta n(\mathbf{r})} \right) \delta n(\mathbf{r}) \ . \tag{12}$$

If we compare this with the corresponding equation for a system with an effective potential $V(\mathbf{r})$ but *without* electron-electron interactions,

$$\frac{\delta E[n]}{\delta n(\mathbf{r})} = \frac{\delta T_0}{\delta n(\mathbf{r})} + V(\mathbf{r}) = \mu, \tag{13}$$

we see that the mathematical problems are identical, provided that

$$V(\mathbf{r}) = V_{\rm ext}(\mathbf{r}) + \Phi(\mathbf{r}) + \frac{\delta E_{\rm xc}[n]}{\delta n(\mathbf{r})}. \tag{14}$$

The solution of (Eq. 13) can be found by solving the Schrödinger equation for *non-interacting* particles,

$$\left(-\frac{1}{2}\nabla^2 + V(\mathbf{r}) \right) \psi_i(\mathbf{r}) = \varepsilon_i \psi_i(\mathbf{r}), \tag{15}$$

yielding

$$n(\mathbf{r}) = \sum_{i=1}^{N} f_i \left| \psi_i(\mathbf{r}) \right|^2 \tag{16}$$

where f_i are occupation numbers ($0 \leq f_i \leq 1$) corresponding to the relevant Slater determinant. We have mapped the original problem onto finding the solution of a *non-linear* equation, since the Hamiltonian in (15) is a function of its own eigenvectors. The equation must be solved iteratively (self-consistently) to satisfy the condition (14).

The solution of this system of equations leads to the energy and density of the lowest state, and all quantities derivable from them. The formalism can be generalized to the lowest state with a given symmetry [39]. Instead of seeking these quantities by determining the wave function of the system of interacting electrons, the DF method reduces the problem to the solution of a single-particle equation of Hartree form. In contrast to the Hartree-Fock potential,

$$V_{\rm HF}\ \psi(\mathbf{r}) = \int d\mathbf{r}'\ V_{\rm HF}(\mathbf{r}, \mathbf{r}')\ \psi(\mathbf{r}'), \tag{17}$$

the effective potential, $V(\mathbf{r})$ is a *local* (i.e., multiplicative) operator. It is worth noting that the non-interacting particles are still Fermions, and the Pauli principle must be satisfied.

The numerical advantages of solving the Kohn-Sham equations [38] are obvious. Efficient methods exist for solving single-particle Schrödinger-like equations with a local effective potential, and there is no restriction to small systems. With a local approximation to $E_{\rm xc}$, the equations can be solved as readily as the Hartree equations. Unlike the Thomas-Fermi method, where the large kinetic energy term is approximated, the valence kinetic energy and the core-valence and valence-valence electrostatic interactions are treated exactly. However, $E_{\rm xc}$ is the difference between the *exact* energy and terms we can evaluate exactly, and approximations are unavoidable.

4.2 Exchange-correlation energy $E_{\rm xc}$ and the xc-hole

Kohn and Sham [38] proposed using the "local density (LD) approximation"

$$E_{\rm xc}^{\rm LD} = \int d\mathbf{r}\, n(\mathbf{r})\, \varepsilon_{\rm xc}[n(\mathbf{r})], \tag{18}$$

where $\varepsilon_{\rm xc}[n]$ is the exchange and correlation energy per particle of a homogeneous electron gas with density n. This approximation is exact in the limits of slowly varying densities and very high densities. The electron density in molecules and solids is generally far from that of a homogeneous electron gas, and the validity of calculations based on properties of a gas of constant density has often been questioned. We now discuss some general properties of $E_{\rm xc}$ using arguments closely related to the "exchange hole" picture of Wigner and Seitz [25] and Slater [28, 32].

The crucial simplification in the density functional scheme is the relationship between the interacting system, whose energy and density we seek, and the fictitious, non-interacting system for which we solve (Eq. 15, 16). This can be studied by considering the interaction $\lambda/|\mathbf{r}-\mathbf{r}'|$ and varying λ from 0 (non-interacting system) to 1 (physical system). This is done in the presence of an external potential V_λ [39], such that the ground state of the Hamiltonian

$$H_\lambda = -\frac{1}{2}\nabla^2 + V_{\rm ext}(\mathbf{r}) + V_\lambda + \lambda V_{\rm ee} \tag{19}$$

has density $n(\mathbf{r})$ for all λ. The exchange-correlation energy of the interacting system can then be expressed as an integral over the coupling constant λ [40]:

$$E_{\rm xc} = \frac{1}{2}\int d\mathbf{r}\, n(\mathbf{r}) \int d\mathbf{r}'\, \frac{1}{|\mathbf{r}-\mathbf{r}'|}\, n_{\rm xc}(\mathbf{r}, \mathbf{r}'-\mathbf{r}), \tag{20}$$

with

$$n_{\rm xc}(\mathbf{r}, \mathbf{r}'-\mathbf{r}) \equiv n(\mathbf{r}') \int_0^1 d\lambda \left(g(\mathbf{r}, \mathbf{r}', \lambda) - 1\right). \tag{21}$$

The function $g(\mathbf{r}, \mathbf{r}', \lambda)$ is the pair correlation function of the system with density $n(\mathbf{r})$ and Coulomb interaction $\lambda V_{\rm ee}$. The exchange-correlation hole $n_{\rm xc}$ describes the fact that an electron at point $\mathbf{r}$ reduces the probability of finding one at $\mathbf{r}'$, and $E_{\rm xc}$ is simply the energy resulting from the interaction between an electron and its exchange-correlation hole. This is a straightforward generalization of the work of Wigner and Seitz [25] and Slater [28] discussed above.

Second, the isotropic nature of the Coulomb interaction $V_{\rm ee}$ has important consequences. A variable substitution $\mathbf{R} \equiv \mathbf{r}'-\mathbf{r}$ in (20) yields

$$E_{\rm xc} = \frac{1}{2}\int d\mathbf{r}\, n(\mathbf{r}) \int_0^\infty dR\, R^2\, \frac{1}{R} \int d\Omega\, n_{\rm xc}(\mathbf{r}, \mathbf{R}). \tag{22}$$

Equation (22) shows that the xc-energy depends only on the spherical average of $n_{\rm xc}(\mathbf{r}, \mathbf{R})$, so that approximations for $E_{\rm xc}$ can still give an *exact* value, even if the description of the non-spherical parts of $n_{\rm xc}$ is quite inaccurate. The energy depends on certain averages over the hole, and this implies a systematic partial cancellation of errors in the LSD approximation. Third, the

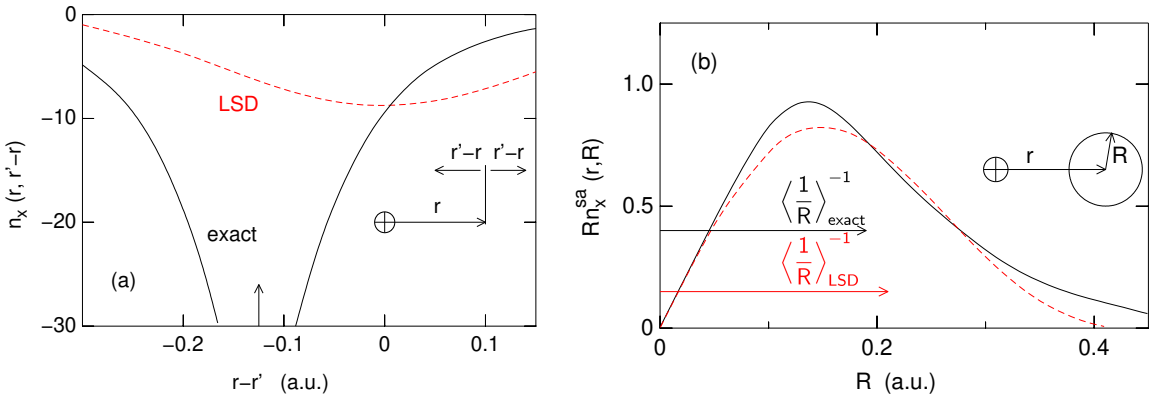


Fig. 2: *Magnitude of exact (solid) and LSD (red, dashed) exchange holes* $n_{\rm xc}(\mathbf{r}, \mathbf{r}'-\mathbf{r})$ *for spin up electron in N atom for* $\mathbf{r} = 0.13$ *a.u. (a) Hole along line through nucleus (arrow) and electron* ($\mathbf{r}-\mathbf{r}' = 0$)*. (b) spherical averages of holes, and* $\langle 1/\mathbf{R}\rangle$ *[Eq. (24)] (from [13]).*

definition of the pair-correlation function leads to a sum-rule requiring that the xc-hole contains one electron, i.e. for all $\mathbf{r}$,

$$\int d\mathbf{r}'\, n_{\rm xc}(\mathbf{r}, \mathbf{r}'-\mathbf{r}) = -1. \tag{23}$$

This means that we can consider $-n_{\rm xc}(\mathbf{r}, \mathbf{r}'-\mathbf{r})$ as a normalized weight factor and define the radius of the xc-hole locally for a particular value of $\mathbf{r}$,

$$\left\langle \frac{1}{\mathbf{R}} \right\rangle_{\mathbf{r}} = -\int d\mathbf{R}\, \frac{n_{\rm xc}(\mathbf{r}, \mathbf{R})}{|\mathbf{R}|}. \tag{24}$$

This leads to

$$E_{\rm xc} = -\frac{1}{2}\int d\mathbf{r}\, n(\mathbf{r}) \left\langle \frac{1}{\mathbf{R}} \right\rangle_{\mathbf{r}}. \tag{25}$$

Provided Equation (23) is satisfied, $E_{\rm xc}$ is determined by the first moment of a function whose second moment we know exactly and depends only weakly on the details of $n_{\rm xc}$ [39]. Provided that the spherical average of the exchange-correlation hole is correct, approximations to $E_{\rm xc}$ can then lead to good total energies, even if other details are described very poorly. This is shown by the example in Fig. 2, where the exchange hole in a nitrogen atom is shown for a representative value of $\mathbf{r}$ for both the local density and exact (Hartree-Fock) cases. The holes are qualitatively different: The LD hole is spherically symmetric and centred on the electron, while the exact hole has a large weight at the nucleus and is very asymmetric. Nevertheless, the spherical averages are very similar, and the exchange energies differ by only around 10%.

5 Local density approximation (LDA) and extensions

The early expectations of the LDA were very modest. John Perdew noted:

> "One of the authors (J.P.P.) was told by W. Kohn (personal communication) that he anticipated the LDA to be only slightly more accurate than the Hartree approximation ($E_{xc} = 0$) that was widely used in condensed matter physics in 1965." [1, p. 196]

In fact, the original paper of Kohn and Sham [38] found good reasons for this:

> "In atoms and molecules one can distinguish three regions: (1) . . . , (2) . . . (3) The 'surface' of atoms and the overlap regions in molecules. Here our approximation [LDA] has no validity and therefore we expect this region to be the main source of error. We do not expect an accurate description of chemical binding " [38].

Hindsight is always much sharper, of course, but Kohn was certainly correct in noticing:

> "I believe that formal DFT would have been of very little interest if there had not been a simple and very practical approximation for E_{xc}, the LDA, which has yielded surprisingly accurate results" [41].

5.1 Three examples

We discuss here three cases where the LDA and a simple extension gave interesting and unexpected results.

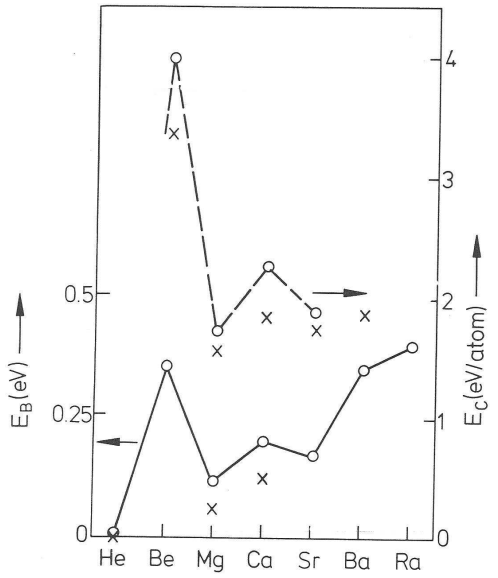
5.1.1 Group 2 dimers: He_2, Be_2, Mg_2, Ca_2, . . .

The group 2 elements have a particularly simple structure of the valence electrons: a closed shell of s-electrons, ns^2. When two such atoms approach each other, there is again a closed shell configuration $\sigma_g^2\sigma_u^2$, with an equal number of electrons in bonding an antibonding orbitals ("bond order" zero). Prior to the first DF calculations, the accepted picture was that binding was only possible in the presence of London dispersion forces, which increase as the atomic polarizability increases. This was consistent with available experimental data at the time, which showed an increase in binding energies from $He_2 \rightarrow Mg_2 \rightarrow Ca_2$, Be_2 having not yet been identified experimentally (Fig. 3). All Hartree-Fock and correlated wave function calculations on Be_2 to that time gave no binding or a weak minimum at large interatomic separation (~ 4.5 Å).

The prediction of DF calculations that the Be_2 dimer should not only exist, but should be more stable than Mg_2 [42], was treated by many in the "correlated wave function" world as evidence that DF calculations were unreliable. Nevertheless, the zigzag behavior in the binding energies is also present in the bulk cohesive energies (Fig. 3), and a calculation one year later using correlated wave functions [43] also gave a similar bond length, shorter than widely expected, and a larger binding energy than in Mg_2. The essential correctness of the DF prediction was finally confirmed experimentally five years later [44]. More details of this saga are provided in [9].

5.1.2 Phosphorus clusters: P_n

The combination of DF calculations with molecular dynamics (DF/MD, Car-Parrinello method [45] made simulations of bulk systems at elevated temperatures possible, and simulated annealing techniques could be used to study the energy surfaces of molecules and clusters. The use



Mg_2	Expt	HF	DF
R_e (Å)	3.89	–	3.81
ω_e (cm^{-1})	51.12	–	80
E_B (eV)	0.052	–	0.11

Ca_2	Expt	HF	DF
R_e (Å)	4.28	–	4.30
ω_e (cm^{-1})	64.93	–	80
E_B (eV)	0.13 ± 0.02	–	0.20

Be_2	Expt[a]	HF	ICF[b]	DF
R_e (Å)	2.45	–	2.49 ± 0.02	2.57
ω_e (cm^{-1})	~ 250	–	–	300
E_B (eV)	–	–	0.10 ± 0.01	0.35

[a] V.E. Bondybey and J.H. English, J. Chem. Phys. **80**, 568 (1984)

[b] B. Liu and A.D. McLean, J. Chem. Phys. **72**, 3418 (1980)

Fig. 3: *(left) binding energies of diatomic molecules (left scale, eV) and cohesive energies of bulk metals (right scale, eV per atom). Crosses: experimental values, as available ca. 1980. (right) spectroscopic constants of group 2 dimers [42].*

of molecular dynamics provides an element of randomness needed if one is to avoid biasing the search for cluster structures.

Four-atom clusters of phosphorus were among the first atomic clusters to be studied using gas-phase electron diffraction [46]. The most stable form of P_4 is tetrahedral, but a second, "butterfly" (C_{2v}) form has a much higher energy, but also a much larger region where it is the nearest local minimum to a given arrangement of four P atoms. The only larger cluster to have been studied in any detail was the cubic (O_h) form of P_8. This was an obvious choice for the valence configuration of P ($3s^2 3p^3$), with three p-orbitals at 90° to each other, but it was noted that the stability of this structure relative to two P_4 tetrahedra was remarkably low.

The reason became clear after DF calculations [47] showed that an unexpected C_{2v} structure had a much (1.7 eV) lower energy than the cube. Other structures were found for P_5 to P_8 that were confirmed by calculations with more traditional methods and by subsequent experiments. The "butterfly" form can be seen as a component of many larger clusters.

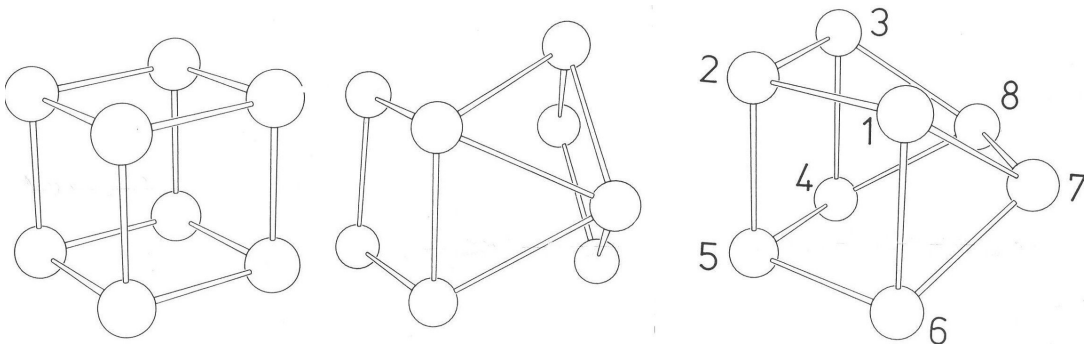


Fig. 4: *Molecular dynamics and simulated annealing of P_8 from the cubic (O_h) to a C_2 structure to the most stable (C_{2v}) form [47].*

5.1.3 Liquid bismuth

An example from the condensed matter world is provided by extensive DF/MD simulations using the PBEsol functional approximation [48] (over 500 atoms, up to 100 ps) of liquid bismuth at four temperatures between 573 K and 1023 K). These simulations have provided details of the dynamical structure factor, the dispersion of longitudinal and transverse collective modes, and related properties. Agreement with available inelastic x-ray and neutron scattering data and with previous simulations is remarkably good [49].

The density fluctuations in the liquid can be described by the intermediate scattering function

$$F(q,t) = \left\langle \mathrm{Re}\left(n(q,t{+}t_0)\, n(q,t_0) \right) \right\rangle , \tag{26}$$

where $\langle \ldots \rangle$ denote averages over all reference times t_0, and $n(q,t)$ is a Fourier component of the density,

$$n(q,t) = \frac{1}{\sqrt{N}} \sum_i \exp(i\vec{q}{\cdot}\vec{r}_i). \tag{27}$$

The index i runs over all particles, whose total number is N. The dynamical structure factor $S(q,\omega)$ is the Fourier transform of $F(q,t)$

$$S(q,\omega) = \frac{1}{2\pi} \int dt\; F(q,t) \exp(i\omega t). \tag{28}$$

Calculations of structure factors and related functions involve averages over all equivalent q vectors with $\mathrm{q} = |q|$. In Fig. 5, we compare the calculated [49] and experimental [50] structure factors $S(q,\omega/S(q)$ for liquid Bi at 573 K.

The current autocorrelation function $C(q,t)$ can be calculated directly from the Fourier transform of the particle current $J(q,t)$, which has a longitudinal component

$$J_L(q,t) = \frac{1}{\sqrt{N}} \sum_i \vec{q}{\cdot}\vec{v}_i \; \exp(i\vec{q}{\cdot}\vec{r}_i) \tag{29}$$

and a transverse component

$$J_T(\vec{q},t) = \frac{1}{\sqrt{N}} \sum_i \vec{q}{\times}\vec{v}_i \; \exp(i\vec{q}{\cdot}\vec{r}_i). \tag{30}$$

The longitudinal component of the current autocorrelation function is

$$C_L(q,t) = \left\langle \mathrm{Re}\left(J_L(q,t{+}t_0)\, J_L(q,t_0) \right) \right\rangle \tag{31}$$

with a transverse component

$$C_T(q,t) = \frac{1}{2} \left\langle \mathrm{Re}\left(J_T(q,t{+}t_0)\, J_T(q,t_0) \right) \right\rangle . \tag{32}$$

A variety of experimental probes, including x-rays and neutrons, couple to longitudinal density fluctuations, but provide no direct information about transverse fluctuations. The shear viscosity η is a rare transport property that couples to the transverse momentum and can be calculated from $C_T(q,t)$ [49]. The results are 573 K: 1.86 (1.65) mPa s; 773 K: 1.42 (1.18) mPa s; 923 K: 1.11 (1.06) mPa s; 1023 K: 1.08 (0.94) mPa s, where the values in brackets are experimental values interpolated from the tables of Assael *et al.* [51]. Given the scatter in the experimental data of different groups, the agreement is very satisfactory.

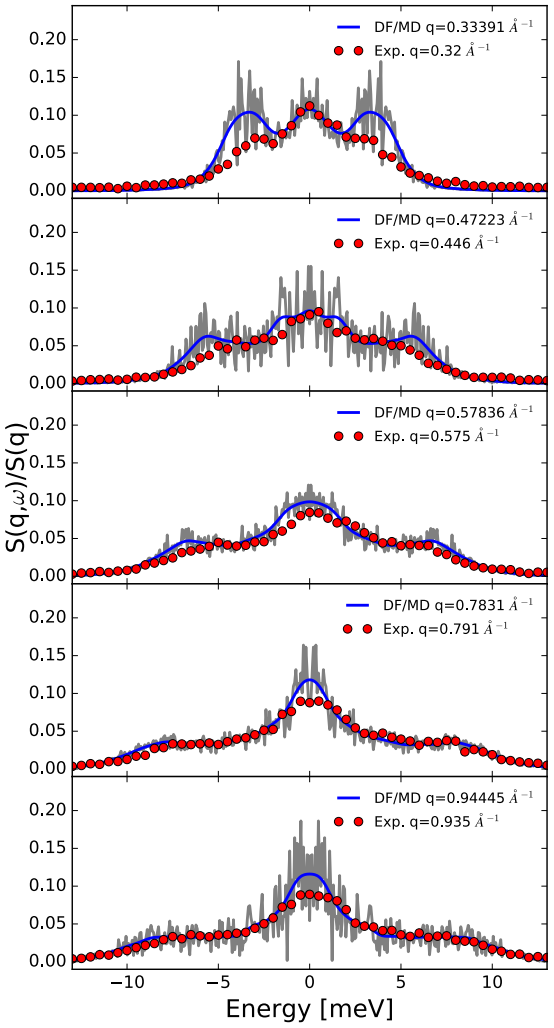


Fig. 5: *Ratio of dynamical to static structure factors, $S(q,\omega)/S(q)$, for selected q-values at 573 K [49]. Grey: DF/MD results, blue: DF/MD with 3 meV Gaussian broadening, red: experimental IXS [50].*

5.2 Spin systems. LSD approximation

Spin plays a minor role in the systems we have just considered: the Be atom and the beryllium dimer are closed-shell systems, as are P_4 and P_8 clusters, and the lowest-lying state of liquid Bi with an even number of atoms is also spin-free. The extension to spin systems [52] or an external magnetic field requires the introduction of the spin indices α of the one-electron operators $\psi_\alpha(\mathbf{r})$ and replacing V_{ext} by $V_{\text{ext}}^{\alpha\beta}(\mathbf{r})$, and the charge density $n(\mathbf{r})$ by the density matrix $n_{\alpha\beta}(\mathbf{r}) = \langle\Psi|\psi_\beta^\dagger(\mathbf{r})\psi_\alpha(\mathbf{r})|\Psi\rangle$. All ground state properties are functionals of $n_{\alpha\beta}$, and E is stationary with respect to variations in $n_{\alpha\beta}$. The expression for the energy E_{xc} is analogous to Equations (20,21).

The generalization of the LDA to spin-polarized systems is known as the local spin density (LSD) approximation:

$$E_{\text{xc}}^{\text{LSD}} = \int d\mathbf{r}\, n(\mathbf{r})\, \varepsilon_{\text{xc}}[n_\uparrow(\mathbf{r}), n_\downarrow(\mathbf{r})], \tag{33}$$

where $\varepsilon_{\rm xc}[n_\uparrow, n_\downarrow]$ is the exchange and correlation energy per particle of a homogeneous, spin-polarized electron gas with spin-up and spin-down densities $n_\uparrow$ and $n_\downarrow$, respectively.[3]
The "Xα" approximation

$$E_{\rm x}^{{\rm X}\alpha} = -\frac{3}{2}\alpha C \int d\mathbf{r} \left(\big(n_\uparrow(\mathbf{r})\big)^{4/3} + \big(n_\downarrow(\mathbf{r})\big)^{4/3} \right), \tag{34}$$

where $C = 3(3/4\pi)^{1/3}$, was used in numerous calculations in the late 1960s and 1970s. The α-dependence of energy differences for a given atom or molecule is weak for values near $2/3$, the value of Bloch [18], Dirac [6], Gáspár [33] and Kohn and Sham [38]. The usual physical interpretation of $n_\uparrow(\mathbf{r})$ and $n_\downarrow(\mathbf{r})$ is that $n_\uparrow(\mathbf{r})+n_\downarrow(\mathbf{r})$ is the total density $n(\mathbf{r})$, and $n_\uparrow(\mathbf{r})-n_\downarrow(\mathbf{r})$ is the spin magnetization density.

5.3 Shortcomings of LD/LSD approximations

5.3.1 Self-interaction correction

A particularly obvious defect of the LDA is evident when one considers a system containing only one electron, since the contribution to the total energy (Eq. 10) contains a spurious "self-interaction" of the electron with itself. If we knew the exact functional E_{xc}, it would cancel the direct Coulomb energy in (10). Perdew and Zunger [53] developed an approximation for correcting the SIC to the LSD or any approximation to the exchange-correlation energy

$$E_{xc}^{SIC} = E_{xc}^{LSD}(n_\uparrow, n_\downarrow) - \sum_{\alpha\sigma} \delta_{\alpha\sigma} \ , \tag{35}$$

where

$$\delta_{\alpha\sigma} = \frac{1}{2}\int d\mathbf{r} \int d\mathbf{r}' \, \frac{n_{\alpha\sigma}(\mathbf{r}) n_{\alpha\sigma}(\mathbf{r}')}{|\mathbf{r}-\mathbf{r}'|} + E_{xc}^{LSD}[n_{\alpha\sigma}, 0] \ , \tag{36}$$

where E_{xc}^{LSD} is the energy functional in the LSD approximation and $\delta_{\alpha\sigma}$ is the SIC correction for the orbital α with spin σ and charge density $n_{\alpha\sigma}$. The last term is the LSD approximation to the exchange and correlation energy of a fully spin polarized system with density $n_{\alpha\sigma}$. This functional is exact for a one-electron system, and it was shown that it led to much better total energies for atoms [53, 54]. However, energy differences, such as the sd-promotion energies in atoms, showed little improvement, and the substantial improvement in total energies was shown to result from a better description of the most tightly bound core electrons [54]. These are the least relevant for many problems, including chemical bonding.

5.3.2 Further problems

Most of the early DF calculations on small clusters and molecules used the LD (Eq. 18) and/or LSD (Eq. 33) approximations. The results were often encouraging and provided insight into interesting physical problems, but it was soon clear that local density calculations can lead to

[3] The calculation by Bloch [18] in 1929 of ferromagnetism in a free-electron model of a metal was the first where the exchange energy was expressed as the sum of terms proportional to $n_\uparrow^{4/3}$ and $n_\downarrow^{4/3}$.

unacceptable results. Examples include the overbinding of many molecules, the exchange energy difference between states with different nodal structures, e.g. the sp-promotion energies in first-row atoms, particularly O and F, and the sd-promotion energies in transition element atoms [55]. The Kohn-Sham eigenvalues often underestimate measured optical band gaps significantly.

Better approximations were needed, and corrections involving density gradients were soon available for the correlation [56, 57] and exchange energies [58], where the semi-empirical approximation of Becke [58] had the correct asymptotic behavior for atoms. Hybrid functionals including exact exchange were introduced by Becke in 1993 [59]. This form of E_{x} has three parameters, and its combination with E_{c} of Lee, Yang, and Parr [57] (B3LYP) is still one of the most common approximations used in chemical applications.

Many other empirical and hybrid functionals have been developed since, with parameters usually fit to thermochemical data for particular groups of molecules. The use of experimental data for fitting functional forms provided additional parameters that led to improvement over LD and LSD results [60], and the use of "training sets" of atomic and molecular systems to optimize the parameters improved the calculated results for particular sets of molecules [61]. Caution is advised when applying "well-trained" functional forms to systems of a different nature.

Dispersion forces—the weak, non-local interactions between closed shells systems—are a particular problem for DF approximations (DFA). The long-range interaction between separated atoms or molecules is absent, and yet the LD approximation *overestimates* the binding energy in many such systems, e.g. He_2 and other group 2 dimers [42]. The development of a functional that changes seamlessly on going from weakly interacting units to a combined system remains an important goal. Langreth and coworkers [62], for example, developed a functional that incorporates results for electron gas slabs and the electron gas itself and is free of experimental input. Empirical corrections to DF results have been studied by Grimme and coworkers [63, 64, and references therein] and are very widely used.

"Strongly correlated" systems often involve transition element or rare earth atoms, and the potential energy can dominate over the kinetic energy. Local density approximations can lead to poor descriptions of these materials, and ways of avoiding these problems is the topic of this school. A common approach has been to add an on-site Coulomb repulsion ("Hubbard U") in the "LSD+U" scheme [65]. The parameter U can be estimated within a DF framework [66] or fit to experiment. We shall return to these systems below.

5.4 "Jacob's Ladder"

An alternative path has been followed by others, particular Perdew and collaborators, who developed a sequence ("Jacob's ladder") of approximations without experimental input, where each "rung" builds on the experience of lower levels and satisfies additional physical constraints (Fig. 6). This approach is systematic and not empirical [67]. Starting with a proof of the existence of a functional, one can derive formally exact relationships that can be used as constraints on approximate forms. If these forms are flexible enough, we can fit their free parameters to

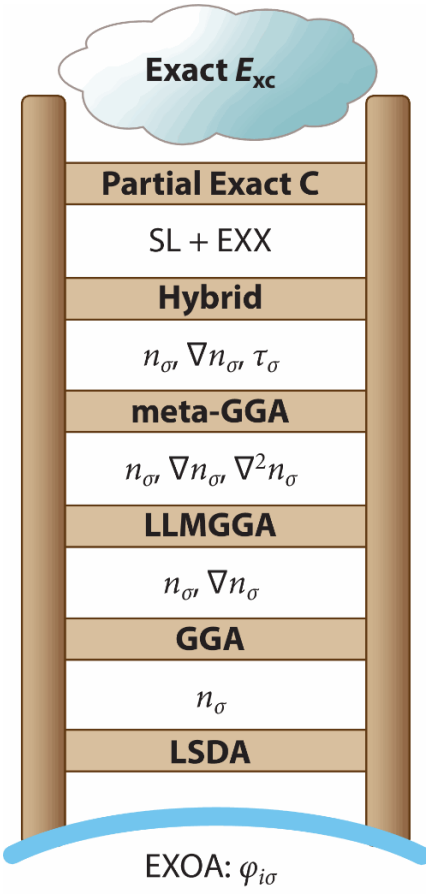


Fig. 6: *Jacob's ladder hierarchy of density functional approximations. For each quantity, the spin index σ equals $\uparrow, \downarrow$. Abbreviations: EXOA, exchange-only approximation; EXX, exact exchange; GGA, generalized gradient approximation; LLMGGA, Laplacian level meta-generalized gradient approximation; LSDA, local spin-density approximation; meta-GGA, meta-generalized gradient approximation; SL, semi-local; xc, exchange correlation. Reproduced from [1], ©2023 The Authors, published by Annual Reviews)*

appropriate norms of energies or densities. These should not include binding energies, which are always susceptible to error cancellation between exchange and correlation.
If we consider the class of semilocal (SL) density functional approximations

$$E_{xc}^{SL}[n_\uparrow, n_\downarrow] = \int d\mathbf{r}\, \varepsilon_{xc}^{SL}(n_\uparrow, n_\downarrow, \ldots; \mathbf{r})\,, \tag{37}$$

there are 17 known constraints that must be satisfied, with another four if we consider nonlocal approximations, which are typically two-point functionals [1]. A detailed explanation of these constraints is given in [1].
In this spirit, the gradient corrected form of Perdew, Burke, and Ernzerhof [68] (PBE) incorporates the LSD form below it, and the "meta-GGA" form of Tao, Perdew, Staroverov, and Scuseria (TPSS) [69], where $n_\uparrow$ and $n_\downarrow$ are joined by their gradients and the kinetic energy density of the occupied Kohn-Sham orbitals, builds on both. The complexity of the calculations increases as one climbs the "ladder" [70], while the physical content may well seem less transparent.

5.5 Functional approximations: current status

Hundreds of functional approximations have been developed over the years, although the number in widespread use is limited. The LDA is still used for its simplicity, PBE is used in many molecular calculations, PBEsol gives improved geometries in extended systems, and B3LYP is very widely used in chemistry. A broad survey of DFA in chemistry [71] came to the conclusion that "ultimately, today's state-of-the-art functionals are close to achieving the level of accuracy desired for a broad range of chemical applications, and the principal remaining limitations are associated with systems that exhibit significant self-interaction/delocalization errors and/or strong correlation effects" [71].

Geometrical arrangements are often the goal of DF calculations, but band gaps in the energy eigenvalue spectrum are also important. A database of 473 semiconductors and insulators has been used to benchmark over 30 exchange-correlation energy functionals according to the calculated band gaps. Meta-GGAs and hybrid functionals generally gave the best results [72].

The choice of functional approximation is not the only variable in a calculation; we must also write a program or use one of the many now available. The reproducibility in DF calculations in solids has been studied in some detail [73], with the reassuring conclusion that "most of the commonly used codes and methods are now found to predict essentially identical results."

The agreement with experiment generally improves, as we shall see in the case of the ladder from LDA $\rightarrow$ PBE $\rightarrow$ r^{2}SCAN [74], the most recent of the family of strongly constrained and appropriately normed ("SCAN" [75]) functionals of Perdew and coworkers. A rather thorough comparison of r^{2}SCAN results with other DFA [1] provides an encouraging picture, not only for the developers of the approximation. Formation enthalpies are improved, self-interaction errors are reduced,[4] and the Hubbard-U values needed to fit experimental data are lower. SCAN recognizes without adjustment that undoped La_2CuO_4 is an antiferromagnetic insulator and its Sr-doped counterpart is metallic, which is not the case for most other DFA. r^{2}SCAN predicts an essentially constant magnetization as the structure of NiO is varied, which is consistent with experiment and an improvement over the GGA functionals PBE and PBEsol [77].

Density functional calculations also predict the electronic density distribution, and Medvedev *et al.* [67] noted some years ago that many (empirically fitted) functionals developed since the year 2000 lead to improved energies but *densities* that are further from the exact results. An extensive study of dipole moments of small molecules calculated using coupled-cluster theory with up to triple excitations showed that the best performing of the 88 DFA tested were of comparable accuracy [78]. Hybrid functionals performed best, although it is a little disconcerting that some modern DFA performed little better than LDA.

A very recent study of 26 molecules with up to four atoms compared the charge distribution in DF calculations with Hartree-Fock and with 12 widely-used DFA with the densities obtained from coupled-cluster (single and double excitations) calculations [79]. This work showed that modern DFA can provide highly accurate charge densities, particularly in the case of meta-GGA

[4] Recent studies of the sd-promotion energies in transition metal atoms [76] suggest that the Perdew-Zunger [53] model for SIC induces a significant error in these atoms.

and hybrid functionals. These DFA outperform Hartree-Fock for simple, sp-bonded molecules near their equilibrium geometries. The only functional that was worse than Hartree-Fock was LDA. Particularly striking was the finding that "the functionals that adhere to theoretical constraints, such as SCAN and r^{2}SCAN, produced the most consistent results across all error measures. In contrast, empirically designed functionals exhibited a significantly larger spread in at least one error measure, emphasizing the importance of adhering to physically rigorous constraints for achieving consistently accurate charge densities" [79].

6 Broken symmetry. Connection to strong correlation?

> "We can now propose a definition of strong correlation: Strong correlation in a symmetry-constrained wave function is any correlation between electrons that results in an exceptionally structured electron-pair density, or is otherwise qualitatively different from the "normal" Coulomb correlation found in simple sp-bonded materials in their ground states near equilibrium nuclear geometries... This definition has little in common with "everything that DFT gets wrong."
> J.P. Perdew *et al.* (2021) [80]

> "The focus on quantum materials has raised questions on the fitness of density functional theory for the description of the basic physics of such strongly correlated systems. Recent studies point to another possibility: the perceived limitations are often not a failure of the density functional theory per se, but rather a failure to break symmetry."
> A. Zunger (2022) [81]

Can it really be true that a symmetry-broken version of density functional theory is able to handle some "strongly correlated" problems? We now look at simple examples of symmetry breaking in density functional calculations.

6.1 Broken symmetry in general

We have noted that the Hamiltonian in Eq. (15) is a function of its own eigenvectors, so must be solved iteratively to satisfy the condition (14). The non-linearity means that solutions may not be unique and may break essential symmetries of the system, often connected with phase transitions. Additional correlations may occur. Such considerations can suggest new physical processes or provide new insight, but the broken-symmetry wave functions do not have the symmetry of the original system, so that many results cannot be compared directly with experiment. General group-theoretical techniques that have been developed to restore the original symmetry are reviewed in [82] and apply also to the extension of the restricted Hartree-Fock (RHF) approach, where the single Slater determinant wave function is constrained to have the underlying molecular symmetry, to the unrestricted Hartree-Fock (UHF) approach, where it is not. A

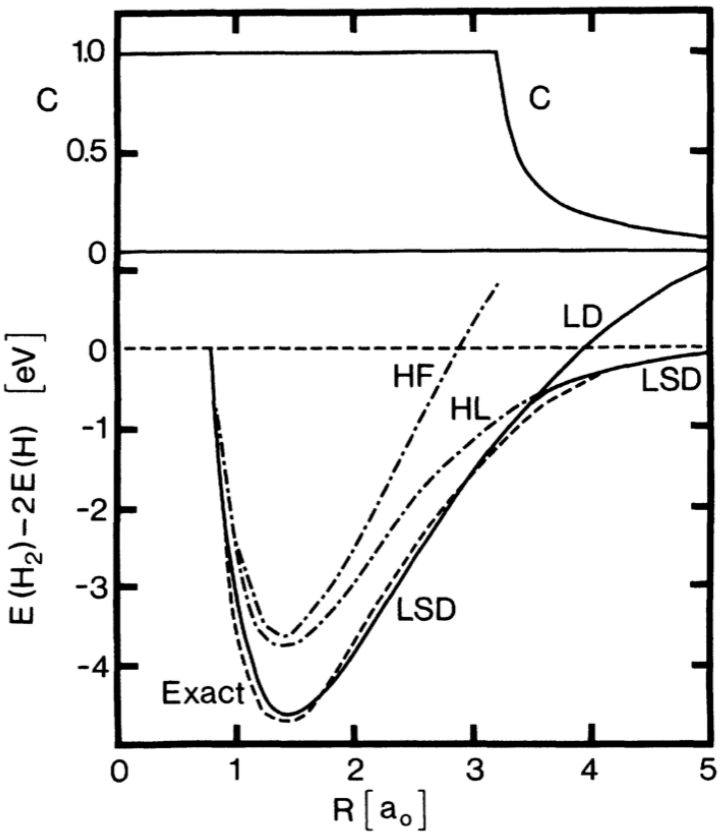


Fig. 7: *Energy of the hydrogen molecule as a function of the internuclear distance. The full curves show the results in the LD and LSD approximations, which differ for $R \geq 3.2$ The dashed curve gives the accurate result of Ref. [84]. The upper part of the figure shows the quantity c in Eq. (38), which gives the degree of spin polarization. For $c = 1$, the system is unpolarized. Reproduced with permission from [39]. ©1976 American Physical Society.*

single Slater determinant of different orbitals for different spins, for example, is not a satisfactory eigenfunction of the total spin operator $\langle S^2 \rangle$, and the ground state can be contaminated by excited states [83].

6.2 Symmetry-broken systems: H_2, Cr_2, Be_2 ...

One of the earliest DF calculations of a molecule, now 50 years ago, was the study of the ground state ($^1\Sigma_g^+$) of H_2 by Gunnarsson and Lundqvist [39]. The results for several approaches are shown in Fig. 7 and include the Hartree-Fock (HF), Heitler-London (HL), local density (LD), and the numerically exact result [84].

The LSD curve is obtained by assuming that the two orbitals contributing to the spin density are $\psi_{i\alpha} = \Phi_i \xi_\alpha$, where ξ_α is a spin function and

$$\Phi_i(\mathbf{r}) = [\phi_i(\mathbf{r}) + c\phi_j(\mathbf{r})]/(1 + 2cS + c^2)^{1/2}, \quad (i, j = a, b, i \neq j) \tag{38}$$

with $S = \int d\mathbf{r}\ \phi_a(\mathbf{r})\phi_b(\mathbf{r})$. This means that the spin polarization can be different for atoms a and b. The LSD curve follows the exact curve closely and allows dissociation into two neutral

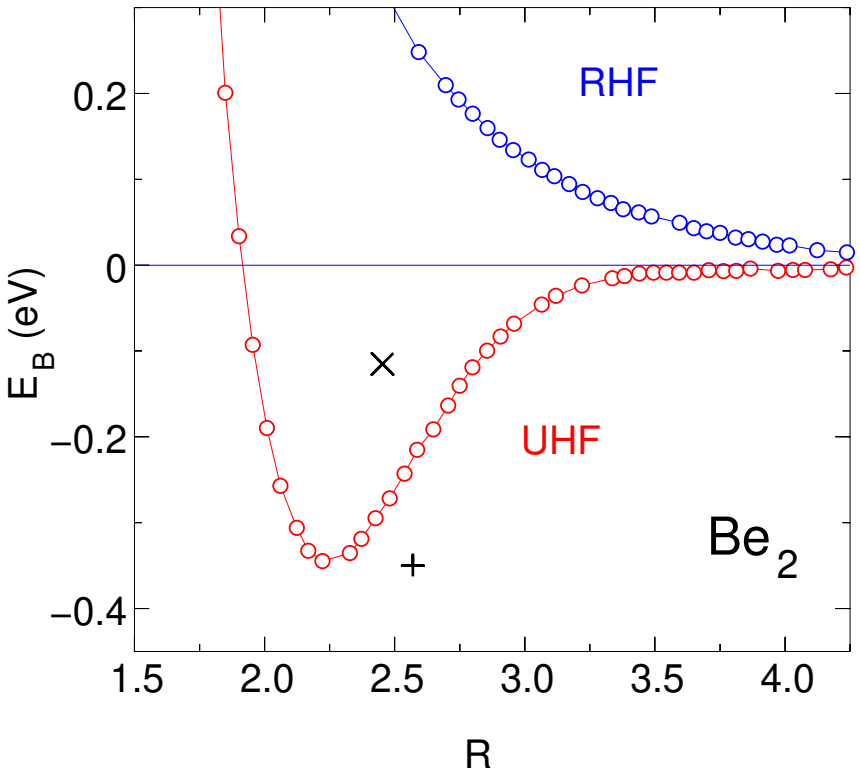


Fig. 8: *Restricted (blue) and unrestricted (red) Hartree-Fock calculations for Be_2 (after [93]). ×: correlated wave function results of [43], +: LDA results [42].*

H atoms with opposite spin. The degree of spin polarization is given by the value of c (Fig. 7, upper), and the symmetry-broken state has a lower energy than the LD calculation for $r > 3.2$ Å. The fact that a large part of correlation effects can be described by a single determinantal wave function with broken-symmetry orbitals and projection to an eigenstate of total spin was pointed out first by Coulson and Fischer [85].

The transition point depends on the DFA used, both for closed-shell [86] and open-shell molecules [87]. This electronic instability corresponds to the Mott transition in solids [88], where the broken-symmetry solutions are described as spin- or charge-density waves. Spin waves were identified much earlier by Bloch [89].

The first density functional calculations on transition metal dimers [90] considered only states with the full symmetry of the molecule, and it was difficult to make a clear prediction of the ground state of Cr_2, where the balance between favoring the occupation of bonding orbitals and having a high-spin state is delicate. This study overlooked the possibility of antiferromagnetic coupling in these systems [91, and references therein]. It is possible to describe a ladder of spin states by constructing states of mixed spin symmetry and lower space symmetry.

We have seen that DF calculations for the beryllium dimer [42] led to an unexpectedly short bond length (2.57 Å). Previous Hartree-Fock calculations had led to a repulsive curve and no binding, but these were restricted HF calculations that required the wave function to have the full molecular symmetry. Unrestricted HF calculations [92], however, showed a weak minimum (depth 0.26 eV, interatomic separation $\sim$ 2.3 Å). In Fig. 8, we show very recent (and much

more accurate) RHF and UHF calculations for Be_2 [93], as well as the minimum energies and separations found in density functional [42] and correlated wave function calculations [43]. One can only speculate about the course of events if the UHF result had been known *before* the DF results.

The quotations at the beginning of this section suggest that the broken-symmetry ideas we have just discussed could be useful in addressing some long-running problems in the density functional description of strongly-correlated systems, e.g., transition metal monoxides such as FeO and NiO. It has now been shown [77, 94] that the antiferromagnetic, insulating phase in these materials can be described well if the unit cell is chosen to allow antiferromagnetic order. The smallest unit cell has a single transition element atom, so that the local magnetic moment is zero, not just the global magnetization. It should be noted that the energy eigenvalues in general and band gaps in particular do not agree with experiment. This can be improved by adding about 20 % "exact exchange" to the r^2-SCAN functional or by adding a Hubbard-U.

7 Concluding remarks

Density functional theory has a long and fascinating history involving some of the best known names in physics and has become, without dispute, the "workhorse of quantum chemistry and materials science" [8]. This is a remarkable result for a method that has experienced much opposition. The theoretical chemistry community took many years to be convinced of its usefulness, and its dismissal by a leading condensed matter theorist, Philip Anderson, as the "Great Solid State Physics Dream Machine" did little to help its establishment in the wider condensed matter community. Its difficulties in the past to describe "strongly correlated" materials led to their definition in terms of this failure.

I concluded my lecture at the 2013 School with the following lines:

> "I end with a note of caution for the 'strongly correlated' community, Few theoretical chemists thought that DF calculations were relevant to understanding the electronic structure of molecules, but local density approximations (and their modifications) have given far better results than *anyone* expected. It was shown *afterwards* why approximations to E_{xc} could give good results for density distributions far from those where they are obviously valid. Perhaps DF theory has some real surprises in store for the 'strongly correlated' world." [95]

Developments in the recent past seem to bear this out. The remarkable improvement in the results from DFA that satisfy increasing numbers of physical constraints has been accompanied by a new focus on broken symmetry wave functions as a way to study some of the problems involving strong correlations. I was not expecting either development, but I am optimistic about the future of both.

References

[1] A.D. Kaplan, M. Levy, and J.P. Perdew, Ann. Rev. Phys. Chem. **74**, 193 (2023)

[2] W. Kohn, Rev. Mod. Phys. **71**, 1253 (1999)

[3] P.W. Anderson: *More and different. Notes from a thoughtful curmudgeon* (World Scientific, Singapore, 2011)

[4] L.H. Thomas, Proc. Camb. Phil. Soc. **23**, 542 (1927)

[5] E. Fermi, Z. Physik **48**, 73 (1928)

[6] P.A.M. Dirac, Proc. Camb. Phil. Soc. **26**, 376 (1930)

[7] F.H.C. Crick, *What mad pursuit* (Penguin, London, 1988), p. 150

[8] A.M. Teale, T. Helgaker, and A. Savin, Phys. Chem. Chem. Phys. **24** 28700 (2022) *DFT exchange: sharing perspectives on the workhorse of quantum chemistry and materials science*

[9] R.O. Jones in A. Avella, F. Mancini, (eds.): *Strongly Correlated Systems*, Springer Series in Solid-State Sciences 171 (Springer, Heidelberg, 2012), pp. 1–28

[10] R.O. Jones, Rev. Mod. Phys. **87**, 897 (2015)

[11] *DFT in Chemistry – Dispute at Inception and Rise to Prominence*, lectures at Royal Swedish Academy of Sciences, Stockholm, 7–8 November 2024
`https://www.youtube.com/playlist?list=PLSs3YyR66CkoFV8s32tDfccLFvfvvug2Z`

[12] R.O. Jones, *50 years of density functional theory*, in [11]

[13] R.O. Jones and O. Gunnarsson, Rev. Mod. Phys. **61**, 689 (1989)

[14] D.R. Hartree, Proc. Camb. Phil. Soc. **24**, 89,111 (1928)

[15] J.C. Slater, Phys. Rev. **35**, 210 (1930)

[16] V. Fock, Z. Physik **61**, 126 (1930)

[17] J.C. Slater, Phys. Rev. **34**, 1293 (1929)

[18] F. Bloch, Z. Physik **57**, 545 (1929)

[19] P.A.M. Dirac, Proc. Roy. Soc. (London) A **123**, 714 (1929)

[20] E.H. Lieb, Rev. Mod. Phys. **53**, 601 (1981)

[21] L. Spruch, Rev. Mod. Phys. **63**, 151 (1991)

[22] E. Teller, Rev. Mod. Phys. **34**, 627 (1962)

[23] E.H. Lieb and B. Simon, Phys. Rev. Lett. **31**, 681 (1973)

[24] P. Ehrenfest, Z. Physik A **45**, 455 (1927)

[25] E. Wigner and F. Seitz, Phys. Rev. **43**, 804 (1933); Phys. Rev. **46**, 509 (1934)

[26] H. Bethe in J. Horgan: *The End of Science*, (Addison-Wesley, Reading, MA, 1996)

[27] J.C. Slater, Rev. Mod. Phys. **6**, 209 (1934)

[28] J.C. Slater, Phys. Rev. **81**, 385 (1951)

[29] J.C. Slater, Phys. Rev. **51**, 846 (1937)

[30] J. Korringa, Physica **13**, 392 (1947)

[31] W. Kohn and N. Rostoker, Phys. Rev. **94**, 111 (1954)

[32] J.C. Slater, Phys. Rev. **165**, 658 (1968)

[33] R. Gáspár, Acta Phys. Hung. **3**, 263 (1954)

[34] J.C. Slater, in R. Daudel, B. Pullman (Eds.): *The World of Quantum Chemistry* (D. Reidel, Dordrecht, 1974), pp. 3–15

[35] P. Hohenberg and W. Kohn, Phys.Rev. **136**, B864 (1964)

[36] M. Levy, Proc. Nat. Acad. Sci. (USA), **76**, 6062 (1979)

[37] N.D. Mermin, Phys. Rev. **137**, A1441 (1965)

[38] W. Kohn and L.J. Sham, Phys. Rev. **140**, A1133 (1965)

[39] O. Gunnarsson and B.I. Lundqvist, Phys. Rev. B **13**, 4274 (1976)

[40] J. Harris and R.O. Jones, J. Phys. F **4**, 1170 (1974)

[41] W. Kohn in E.K.U. Gross and R.M. Dreizler (Eds.): *Density Functional Theory* (Plenum, New York, 1995) p. 3

[42] R.O. Jones, J. Chem. Phys. **71**, 1300 (1979)

[43] B. Liu and A.D. McLean, J. Chem. Phys. **72**, 3418 (1980)

[44] V.W. Bondybey and J.H. English, J. Chem. Phys. **80**, 568 (1984)

[45] R. Car and M. Parrinello, Phys. Rev. Lett. **55**, 2471 (1985)

[46] L.R. Maxwell, S.B. Hendricks, and V.M. Mosley, J. Chem. Phys. **3**, 699 (1935)

[47] R.O. Jones and D. Hohl, J. Chem. Phys. **92**, 6710 (1990)

[48] J.P. Perdew, A. Ruzsinsky, G.I. Csonka, O.A. Vydrov, G.E. Scuseria, L.A. Konstantin, X. Zhou, and K. Burke, Phys. Rev. Lett. **100**, 136406 (2008)

[49] M. Ropo, J. Akola, and R.O. Jones, J. Chem. Phys. **145**, 184502 (2016)

[50] M. Inui, Y. Kajihara, S. Munejiri, S. Hosokawa, A. Chiba, K. Ohara, S. Tsutsui, and A.Q.R. Baron, Phys. Rev. B **92**, 054206 (2015)

[51] M.J. Assael, A.E. Kalyva, K.D. Antoniadis, R.M. Banish, I. Egry, J.T. Wu, E. Kashnitz, and W.A. Wakeham, High Temp.-High Pressures **41**, 161 (2012)

[52] U. von Barth and L. Hedin, J. Phys. C: Solid State Phys. **5**, 1629 (1972)

[53] J.P. Perdew and A. Zunger, Phys. Rev. B **23**, 5048 (1981)

[54] O. Gunnarsson and R.O. Jones, Solid State Commun. **37**, 249 (1981)

[55] O. Gunnarsson and R.O. Jones, Phys. Rev. B **31**, 7588 (1985)

[56] J.P. Perdew, Phys. Rev. B **33**, 8822 (1986)

[57] C.T. Lee, W.T. Yang, and R.G. Parr, Phys. Rev. B **37**, 785 (1988)

[58] A.D. Becke, Phys. Rev. A **38**, 3098 (1988)

[59] A.D. Becke, J. Chem. Phys. **98**, 5648 (1993)

[60] A.D. Boese and N.C. Handy, J. Chem. Phys. **114**, 5497 (2001)

[61] Y. Zhao and D.G. Truhlar, Acc. Chem. Res. **41**, 157 (2008), and references therein

[62] M. Dion, H. Rydberg, E. Schröder, D.C. Langreth, and B.I. Lundqvist, Phys. Rev. Lett. **92**, 246401 (2004)

[63] S. Grimme, J. Antony, S. Ehrlich, and H. Krieg, J. Chem. Phys. **132**, 154104 (2010)

[64] S. Grimme, A. Hansen, S. Ehlert, and J.M. Mewes, J. Chem. Phys. **154**, 064103 (2021)

[65] V.I. Anisimov, F. Aryasetiawan, and A.I. Lichtenstein, J. Phys.: Condens. Matter **9**, 767 (1997)

[66] M. Cococcioni and S. de Gironcoli, Phys. Rev. B **71**, 035105 (2005), and references therein

[67] M.G. Medvedev, I.S. Bushmarinov, J. Sun, J.P. Perdew, and K.A. Lyssenko, Science **355**, 49 (2017)

[68] J.P. Perdew, K. Burke, and M. Ernzerhof, Phys. Rev. Lett. **77**, 3865 (1996)

[69] J. Tao, J.P. Perdew, V.N. Staroverov, and G.E. Scuseria, Phys. Rev. Lett. **91**, 146401 (2003)

[70] See, for example, F. Furche and J.P. Perdew, J. Chem. Phys. **124**, 044103 (2006)

[71] N. Mardirossian and M. Head-Gordon, Mol. Phys. **115**, 2315 (2017)

[72] P. Borlido, J. Schmidt, A,W, Huran, F. Tran, M.A.L. Marques, and S, Botti, npj Computational Materials **6**, 96 (2020)

[73] K. Lejaeghere *et al.*, Science **351**, 1415 (2016)

[74] J.W. Furness, A.D. Kaplan, J. Ning, J.P. Perdew, and J. Sun, J. Phys. Chem. Lett. **11**, 8208 (2020)

[75] J. Sun, A. Ruzsinszky, and J.P. Perdew, Phys. Rev. Lett. **115**, 036401 (2015)

[76] R. Maniar, P.B. Shukla, J.K. Johnson, K.A. Jackson, and J.P. Perdew, Proc. Nat. Acad. Sci. USA **122**, e2418305122 (2025)

[77] M.J. DelloStritto, A.D. Kaplan, J.P. Perdew, and M.L. Klein, APL Mater. **11**, 060702 (2023)

[78] D. Hait and M. Head-Gordon, J. Chem. Theory Comput. **14**, 1969 (2018)

[79] M. Gubler, M.R. Schäfer, J. Behler, and S. Goedeker, J. Chem. Phys. **162**, 094103 (2025)

[80] J.P. Perdew, A. Ruzsinszky, J. Sun, N.K. Nepal, and A.D. Kaplan, Proc. Natl. Acad. Sci. USA **118**, e2017850118 (2021)

[81] A. Zunger, Nat. Comput. Sci. **2**, 529 (2022)

[82] J.A. Sheikh, J. Dobaczewski, P. Ring, L.M. Robledo, and C. Yannouleas, J. Phys. G: Nucl. Part. Phys. **48**, 123001 (2021)

[83] H. Fukutome, Int. J. Quantum Chem. **20**, 955 (1981)

[84] W. Kołos and C.J. Roothaan, Rev. Mod. Phys. **32**, 219 (1960)

[85] C.A. Coulson and I. Fischer, Phil. Mag. **40**, 386 (1949)

[86] R. Bauernschmitt and R. Ahlrichs, J. Chem. Phys. **104**, 9047 (1996)

[87] C.D. Sherrill, M.S. Lee, and M. Head-Gordon, Chem. Phys. Lett. **302**, 425 (1999)

[88] N.F. Mott, Proc. Phys. Soc. Lond. **62**, 416 (1949)

[89] F. Bloch, Z. Physik **61**, 206 (1930)

[90] J. Harris and R.O. Jones, J. Chem. Phys. **70**, 830 (1979)

[91] L. Noodleman and E.R. Davidson, Chem. Phys. **109**, 131 (1986)

[92] M.B. Lepetit and J.P. Malrieu, Chem. Phys. Lett. **169**, 285 (1990)

[93] G.B. Bacskay, Molecules **30**, 1154 (2025)

[94] G. Trimarchi, Z. Wang, and A. Zunger, Phys. Rev. B **97**, 035107 (2018)

[95] R.O. Jones, "Density Functional Theory for Emergents", in E. Pavarini, E. Koch, and U. Schollwöck (Eds.): *Emergent Phenomena in Correlated Matter*, Reihe Modeling and Simulation, Vol. 2 (Forschungszentrum Jülich, 2013)
https://www.cond-mat.de/events/correl13/manuscripts/jones.pdf

3 Dynamical Mean-Field Theory for Materials

Eva Pavarini
Peter Grünberg Institute
Forschungszentrum Jülich

Contents

1 Introduction **2**

2 From DMFT to LDA+DMFT **5**
2.1 DMFT for a toy model: The Hubbard dimer 5
2.2 Non-local Coulomb interaction 13
2.3 Quantum-impurity solvers: Continuous-time quantum Monte Carlo 15
2.4 Hartree-Fock (LDA+U) versus DMFT approximation 20
2.5 DMFT for the one-band Hubbard model 25
2.6 DMFT for multi-orbital models 28

3 Building materials-specific many-body models **30**
3.1 Model construction 30
3.2 Localization of the basis and range of the Coulomb interaction 33
3.3 Hubbard Hamiltonians for t_{2g} and e_g systems 34
3.4 Spin-orbit interaction and effects of the basis choice 35
3.5 Non-spherical Coulomb terms and double-counting correction 38

4 Understanding correlated materials with DMFT **40**

5 Conclusion and outlook **42**

A Hubbard dimer and Anderson molecule **43**

B Lehmann representation of the local Green function **47**

E. Pavarini, E. Koch, A. Lichtenstein, and D. Vollhardt (eds.)
Understanding Correlated Materials with DMFT
Modeling and Simulation Vol. 15
Forschungszentrum Jülich, 2025, ISBN 978-3-95806-813-1
http://www.cond-mat.de/events/correl25

1 Introduction

In 1965, when the two founding papers [1] of density-functional theory (DFT) had just been published in the Physical Review, very few could recognize the revolution in the making. Efficient techniques for materials science applications were missing and computers were not that powerful. And yet in 50 years, thanks to remarkable ideas, novel algorithms and steady advance in computational power, brilliant minds brought DFT to its present splendor, making it the *standard model* of condensed matter physics. In 1998, in his Nobel lecture [2], Walter Kohn, described the most important contributions of DFT to science with these words

> *The first is in the area of fundamental understanding. Theoretical chemists and physicists, following the path of the Schrödinger equation, have become accustomed to think in a truncated Hilbert space of single particle orbitals. The spectacular advances achieved in this way attest to the fruitfulness of this perspective. However, when very high accuracy is required, so many Slater determinants are required (in some calculations up to* $\sim 10^9$*!) that comprehension becomes difficult.*

DFT changed the focus from the N-electron ground-state wavefunction $\Psi(\boldsymbol{r}_1, \ldots, \boldsymbol{r}_N)$ to a three-dimensional variable, the electronic ground-state density $n(\boldsymbol{r})$, or other directly measurable quantities, such as response functions. These, within a given approximation of the DFT exchange-correlation functional, could be calculated *from first principles*, i.e., using as input the type of atoms involved and, at most, their positions. In practice, $n(\boldsymbol{r})$ is obtained by mapping the actual many-body problem onto an auxiliary single-electron Hamiltonian with the same ground-state electron density, the Kohn-Sham Hamiltonian. The associated Kohn-Sham eigenvalues are thus in principle merely Lagrange multipliers. Remarkably, however, the big success of DFT came, in part, from bold applications of the theory beyond its actual realm of validity. To general surprise, the Kohn-Sham eigenvalues turned out to be in many cases excellent approximations to the actual elementary excitations of a given material. Early on it became clear, however, that this Ansatz fails qualitatively for a whole category of systems, those in which local Coulomb repulsion effects are large, also known as *strongly-correlated materials*. Paradoxically, in describing strong-correlation phenomena, simple models describing generic features of the microscopic mechanism are much more effective than DFT-based materials-specific calculations. This happens, e.g., for the Kondo effect, heavy-fermion behavior, or the metal-insulator transition. Thus criticisms arose. Particularly outspoken in this contest was another Nobel laureate, P.W. Anderson, who emphasized the emergent nature of a true many-body phenomenon [3]. Emergent states typically elude a simple mapping to an effective non-interacting system. For a while, two apparently incompatible philosophies thus coexisted. The first-principles school identified in the materials dependence the essential ingredient for understanding the real world, and tried to correct the failures of the practical implementations of DFT by corrections, often ad hoc, of the exchange-correlation potential. Instead, the many-body models school identified canonical models which explain specific emergent phenomena, dismissing the materials dependence as non-relevant, non-generic detail. In the last three decades these different world-views started to merge, and it became apparent that both sides were right and wrong at the same time. While the

local Coulomb repulsion is indeed key, materials aspects turn out to be essential for understanding real correlated materials. In hindsight, we can now put this debate in a different perspective. The electronic many-body problem, in the non-relativistic limit and in the Born-Oppenheimer approximation, is described by the Hamiltonian

$$\hat{H}_e = -\frac{1}{2}\sum_i \nabla_i^2 - \sum_i \sum_\alpha \frac{Z_\alpha}{|\boldsymbol{r}_i - \boldsymbol{R}_\alpha|} + \sum_{i>j} \frac{1}{|\boldsymbol{r}_i - \boldsymbol{r}_j|} + \sum_{\alpha>\alpha'} \frac{Z_\alpha Z_{\alpha'}}{|\boldsymbol{R}_\alpha - \boldsymbol{R}_{\alpha'}|}, \tag{1}$$

where $\{\boldsymbol{r}_i\}$ are electron coordinates, $\{\boldsymbol{R}_\alpha\}$ nuclear coordinates and Z_α the nuclear charges. Using a complete one-electron basis, for example the basis $\{\varphi_a(\boldsymbol{r})\}$, where $\{a\}$ are the quantum numbers, we can write this Hamiltonian in second quantization as

$$\hat{H}_e = \underbrace{-\sum_{ab} t_{ab}\, c_a^\dagger c_b}_{\hat{H}_0} + \underbrace{\frac{1}{2}\sum_{aa'bb'} U_{aa'bb'}\; c_a^\dagger c_{a'}^\dagger c_{b'} c_b}_{\hat{H}_U}. \tag{2}$$

Here the hopping integrals are given by

$$t_{ab} = -\int d\mathbf{r}\; \overline{\varphi_a}(\boldsymbol{r}) \left(-\frac{1}{2}\nabla^2 \underbrace{- \sum_\alpha \frac{Z_\alpha}{|\boldsymbol{r} - \boldsymbol{R}_\alpha|}}_{v_{\rm en}(\boldsymbol{r})} \right) \varphi_b(\boldsymbol{r}), \tag{3}$$

while the elements of the Coulomb tensor are

$$U_{aa'bb'} = \int d\mathbf{r}_2 \int d\mathbf{r}_2\; \overline{\varphi_a}(\boldsymbol{r}_1)\, \overline{\varphi_{a'}}(\boldsymbol{r}_2)\; \frac{1}{|\boldsymbol{r}_1 - \boldsymbol{r}_2|}\; \varphi_{b'}(\boldsymbol{r}_2)\, \varphi_b(\boldsymbol{r}_1). \tag{4}$$

In principle, all complete one-electron bases are equivalent. In practice, since, in the general case, we cannot solve the N-electron problem exactly, some bases are better than others. One possible choice for the basis are the Kohn-Sham orbitals, $\{\varphi_a^{\rm KS}(\boldsymbol{r})\}$, obtained, e.g., in the local density approximation (LDA) or its simple extensions.[1] In this case, it is useful to replace the electron-nuclei interaction $v_{\rm en}(\boldsymbol{r})$ with the DFT potential $v_R(\boldsymbol{r})$, which includes in addition the Hartree term $v_{\rm H}(\boldsymbol{r})$ and the (approximate) exchange-correlation potential $v_{\rm xc}(\boldsymbol{r})$

$$v_{\rm R}(\boldsymbol{r}) = v_{\rm en}(\boldsymbol{r}) + \underbrace{\int d\mathbf{r}'\; \frac{n(\boldsymbol{r}')}{|\boldsymbol{r} - \boldsymbol{r}'|}}_{v_{\rm H}(\boldsymbol{r})} + v_{\rm xc}(\boldsymbol{r}) \tag{5}$$

so that

$$\tilde{t}_{ab} = -\int d\mathbf{r}\; \overline{\varphi_a^{\rm KS}}(\boldsymbol{r}) \left(-\frac{1}{2}\nabla^2 + v_{\rm R}(\boldsymbol{r}) \right) \varphi_b^{\rm KS}(\boldsymbol{r}). \tag{6}$$

To avoid double counting (DC), we have, however, to subtract from $\hat{H}_U$ the term $\hat{H}_{\rm DC}$, which describes the Coulomb terms already included in the hopping integrals

$$\hat{H}_e = \underbrace{-\sum_{ab} \tilde{t}_{ab}\, c_a^\dagger c_b}_{\hat{H}_0 = \hat{H}_e^{\rm LDA}} + \underbrace{\frac{1}{2}\sum_{aba'b'} \tilde{U}_{aa'bb'}\; c_a^\dagger c_{a'}^\dagger c_{b'} c_b - \hat{H}_{\rm DC}}_{\Delta \hat{H}_U}. \tag{7}$$

[1] For the purpose of many-body calculations the differences between LDA, GGA or their simple extensions are in practice negligible; for simplicity, in the rest of the lecture, we thus adopt LDA as representative functional.

For weakly-correlated systems, in the Kohn-Sham basis, the effects included in $\Delta\hat{H}_U$ can, in first approximation, either be neglected or treated as a perturbation. This implies that $\hat{H}_e^{\rm LDA} \sim \hat{H}_{\rm eff}$, where $\hat{H}_{\rm eff}$ is the effective model which provides a good description of the system (at least) at low energy, and which describes emergent effective "elementary particles" and their interactions. Hypothetically, one could imagine that $\hat{H}_{\rm eff}$ is obtained via a canonical transformation, so that $\hat{H}_{\rm eff} \sim \hat{S}^{-1}\hat{H}_e\,\hat{S}$, although the exact form of the operator $\hat{S}$ is unknown.
A defining feature of strong-correlation effects is that they cannot be described via a single-electron Hamiltonian, however. A model of form $\hat{H}_e^{\rm LDA}$ does not describe correctly the Mott metal-insulator transition, no matter what the specific values of the parameters $\tilde{t}_{ab}$ are.[2] Thus for strongly-correlated systems the low-energy effective model must have a different form. For Mott systems a canonical Hamiltonian is the Hubbard model

$$\hat{H} = -\sum_{\sigma}\sum_{ii'} t^{i,i'} c^{\dagger}_{i\sigma} c_{i'\sigma} + U\sum_{i} \hat{n}_{i\uparrow}\hat{n}_{i\downarrow}, \tag{8}$$

which includes, in addition to a single-electron term, the on-site Coulomb repulsion. This Hamiltonian captures the essence of the Mott transition. At half filling, for $U = 0$ it describes a paramagnetic metal, and for $t^{i,i'}(1-\delta_{i,i'})=0$ an insulating set of paramagnetic atoms. Unfortunately, differently from Hamiltonians of type $\hat{H}_e^{\rm LDA}$, Hubbard-like models cannot be solved exactly in the general case. Remarkably, till 30 years ago, no method for describing the complete phase diagram of (8) in one coherent framework, including the paramagnetic insulating phase, was actually known. This changed between 1989 and 1992, when the dynamical mean-field theory (DMFT) was developed [4–7]. The key idea of DMFT consists in mapping the Hubbard model onto a self-consistent *auxiliary quantum-impurity problem*, which can be solved exactly. The mapping is based on the *local dynamical self-energy approximation*, very good for realistic three-dimensional lattices—and becoming exact in the infinite coordination limit [4, 5].
DMFT was initially applied to simple cases, due to limitations in model building, computational power, and numerical methods for solving the auxiliary impurity problem (the quantum impurity solvers). In the last thirty years remarkable progress lifted many of these limitations. First, reliable schemes to build realistic low-energy materials-specific Hubbard-like models have been devised, in particular using Kohn-Sham localized Wannier functions. This is impressive, given that we do not know the exact operator $\hat{S}$ which gives the effective low-energy Hamiltonian, and thus a truly systematic derivation is not possible. Second, key advances in quantum impurity solvers and increasingly more powerful supercomputers made it possible to study always more complex many-body Hamiltonians. The approach which emerged, consisting in solving within DMFT materials-specific many-body Hamiltonians constructed via LDA, is known as the LDA+DMFT method [8–10]. This technique (and its extensions) is now the state-of-the-art for describing strongly-correlated materials. In this lecture I will outline the basic ideas on which the method is based, its successes and its limitations.

[2] One can obtain an insulator by reducing the symmetry, e.g, by increasing the size of the primitive cell. This Slater-type insulator has however different properties than a Mott-type insulator.

2 From DMFT to LDA+DMFT

In this section we introduce the basics of dynamical mean-field theory. We start from a case for which we can perform analytic calculations, the two-site Hubbard Hamiltonian. This is a toy model; it is also the worst case for DMFT, since the coordination number is the lowest possible. It is nonetheless very useful in order to explain how the method works. Next we extend the formalism to the one-band and then to the multi-orbital Hubbard Hamiltonian. For three-dimensional lattices the coordination number is typically large and thus DMFT is an excellent approximation. In Sec. 3 we describe state-of-the-art schemes to construct materials-specific many-body models. They are based on Kohn-Sham Wannier orbitals, calculated, e.g, using the LDA functional. The solution of such models via DMFT defines the LDA+DMFT method.

2.1 DMFT for a toy model: The Hubbard dimer

The two-site Hubbard model is given by

$$\hat{H} = \varepsilon_d \sum_{i\sigma} \hat{n}_{i\sigma} - t \sum_{\sigma} \left(c^\dagger_{1\sigma} c_{2\sigma} + c^\dagger_{2\sigma} c_{1\sigma} \right) + U \sum_i \hat{n}_{i\uparrow} \hat{n}_{i\downarrow}, \tag{9}$$

with $i = 1, 2$. The ground state for $N = 2$ electrons (half filling) is the singlet[3]

$$|G\rangle_H = \frac{a_2(t,U)}{\sqrt{2}} \left(c^\dagger_{1\uparrow} c^\dagger_{2\downarrow} - c^\dagger_{1\downarrow} c^\dagger_{2\uparrow} \right) |0\rangle + \frac{a_1(t,U)}{\sqrt{2}} \left(c^\dagger_{1\uparrow} c^\dagger_{1\downarrow} + c^\dagger_{2\uparrow} c^\dagger_{2\downarrow} \right) |0\rangle \tag{10}$$

with

$$a_1^2(t,U) = \frac{1}{\Delta(t,U)} \frac{\Delta(t,U) - U}{2}, \qquad a_2^2(t,U) = \frac{4t^2}{\Delta(t,U)} \frac{2}{\Delta(t,U) - U}, \tag{11}$$

and

$$\Delta(t,U) = \sqrt{U^2 + 16t^2}. \tag{12}$$

The energy of this state is

$$E_0(2) = 2\varepsilon_d + \frac{1}{2} \left(U - \Delta(t,U) \right). \tag{13}$$

In the $T \to 0$ limit, using the Lehmann representation (see Appendix B), one can show that the local Matsubara Green function for spin σ takes then the form

$$\begin{aligned} G^\sigma_{i,i}(i\nu_n) = \frac{1}{4} \Bigg(& \frac{1 + w(t,U)}{i\nu_n - \big(\underbrace{E_0(2) - \varepsilon_d + t - \mu}_{E_0(2) - E_-(1) - \mu} \big)} + \frac{1 - w(t,U)}{i\nu_n - \big(\underbrace{-E_0(2) + U + 3\varepsilon_d + t - \mu}_{E_+(3) - E_0(2) - \mu} \big)} \\ & + \frac{1 - w(t,U)}{i\nu_n - \big(\underbrace{E_0(2) - \varepsilon_d - t - \mu}_{E_0(2) - E_+(1) - \mu} \big)} + \frac{1 + w(t,U)}{i\nu_n - \big(\underbrace{-E_0(2) + U + 3\varepsilon_d - t - \mu}_{E_-(3) - E_0(2) - \mu} \big)} \Bigg), \end{aligned} \tag{14}$$

[3] Eigenstates and eigenvalues of the Hubbard dimer for arbitrary filling can be found in Appendix A.

where $\nu_n = \pi(2n+1)/\beta$ are fermionic Matsubara frequencies and $\mu = \varepsilon_d + U/2$ is the chemical potential. The weights are

$$w_\pm(t,U) = \frac{1}{4}\big(1 \pm w(t,U)\big), \tag{15}$$

$$w(t,U) = 2a_1(t,U)a_2(t,U) = \frac{4t}{\Delta(t,U)}\,. \tag{16}$$

The local Green function can be rewritten as the average of the Green function for the bonding ($k=0$) and the anti-bonding state ($k=\pi$), i.e.,

$$G^\sigma_{i,i}(i\nu_n) = \frac{1}{2}\Bigg(\underbrace{\frac{1}{i\nu_n + \mu - \varepsilon_d + t - \Sigma^\sigma(0;i\nu_n)}}_{G^\sigma(0;i\nu_n)} + \underbrace{\frac{1}{i\nu_n + \mu - \varepsilon_d - t - \Sigma^\sigma(\pi;i\nu_n)}}_{G^\sigma(\pi;i\nu_n)}\Bigg). \tag{17}$$

The self-energy is given by

$$\Sigma^\sigma(k;i\nu_n) = \frac{U}{2} + \frac{U^2}{4}\frac{1}{i\nu_n + \mu - \varepsilon_d - \frac{U}{2} - \; e^{ik}\; 3t}\,. \tag{18}$$

The self-energies $\Sigma^\sigma(0;i\nu_n)$ and $\Sigma^\sigma(\pi;i\nu_n)$ differ due to the phase $e^{ik} = \pm 1$ in their denominators. The local self-energy is, by definition, the average of the two

$$\begin{aligned}\Sigma^\sigma_l(i\nu_n) = \frac{1}{2}\Big(\Sigma^\sigma(\pi;i\nu_n) + \Sigma^\sigma(0;i\nu_n)\Big) &= \frac{U}{2} + \frac{U^2}{4}\,\frac{i\nu_n + \mu - \varepsilon_d - \frac{U}{2}}{(i\nu_n + \mu - \varepsilon_d - \frac{U}{2})^2 - (3t)^2} \\ &= \frac{U}{2} + \frac{U^2}{4}\,\frac{i\nu_n}{(i\nu_n)^2 - (3t)^2}\end{aligned} \tag{19}$$

The difference

$$\begin{aligned}\Delta\Sigma^\sigma_l(i\nu_n) = \frac{1}{2}\Big(\Sigma^\sigma(\pi;i\nu_n) - \Sigma^\sigma(0;i\nu_n)\Big) &= \frac{U^2}{4}\,\frac{3t}{(i\nu_n + \mu - \varepsilon_d - \frac{U}{2})^2 - (3t)^2} \\ &= \frac{U^2}{4}\,\frac{3t}{(i\nu_n)^2 - (3t)^2},\end{aligned} \tag{20}$$

thus measures the importance of non-local effects; it would be zero if the self-energy was independent of k. Next we define the hybridization function

$$F^\sigma(i\nu_n) = \frac{\big(t + \Delta\Sigma^\sigma_l(i\nu_n)\big)^2}{i\nu_n + \mu - \varepsilon_d - \Sigma^\sigma_l(i\nu_n)} \tag{21}$$

which for $U = 0$ becomes

$$F^\sigma_0(i\nu_n) = \frac{t^2}{i\nu_n}. \tag{22}$$

By using these definitions, we can rewrite the local Green function as

$$G^\sigma_{i,i}(i\nu_n) = \frac{1}{i\nu_n + \mu - \varepsilon_d - F^\sigma(i\nu_n) - \Sigma^\sigma_l(i\nu_n)}. \tag{23}$$

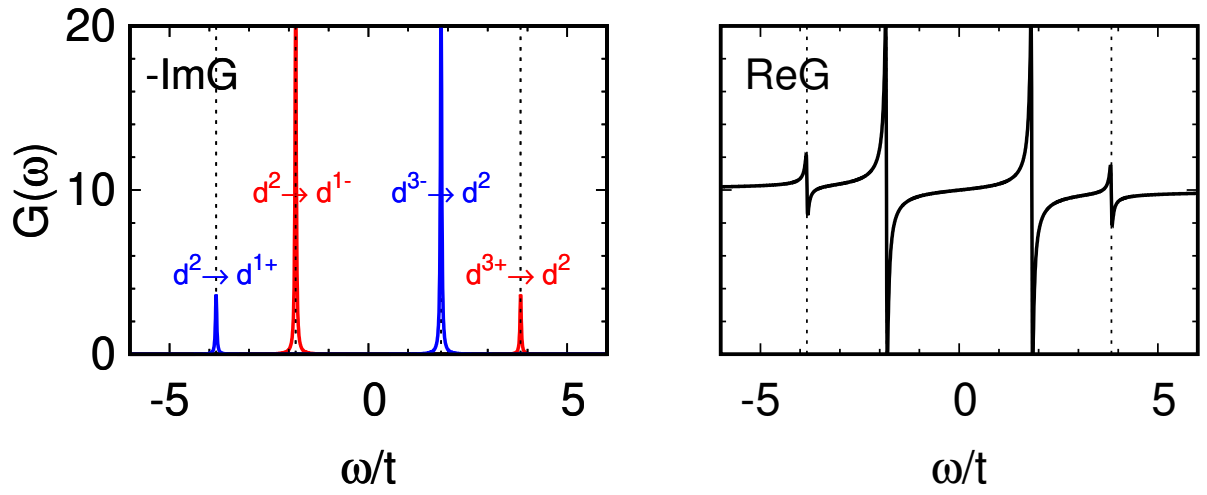


Fig. 1: *Hubbard dimer: Imaginary (left) and real (right) part of the retarded Green function, obtained setting $i\nu_n \to \omega + i\delta$ (analytic continuation) in Eq. (14). Red lines: $k = 0$ contribution. Blue lines: $k = \pi$ contribution. Dashed lines: Poles of the retarded Green function. Parameters: $t = 1, U = 4$. The weight of the poles yielding the smaller peaks, $w_-(t, U)$, defined in Eq. (15), goes to zero for $U \to 0$. In the atomic limit, instead, all four poles have the same weight; the energies of the two positive (negative) poles become identical, however.*

The associated retarded Green function, obtained via analytic continuation ($i\nu_n \to \omega + i\delta$), is shown in Fig. 1. It is important to point out that, as one may see from the formulas just discussed, the local Green function and the local self-energy satisfy the *local Dyson equation*

$$\Sigma_l^\sigma(i\nu_n) = \frac{1}{\mathfrak{G}_{i,i}^\sigma(i\nu_n)} - \frac{1}{G_{i,i}^\sigma(i\nu_n)}\,, \tag{24}$$

where $\mathfrak{G}_{i,i}^\sigma(i\nu_n)$ is given by

$$\mathfrak{G}_{i,i}^\sigma(i\nu_n) = \frac{1}{i\nu_n + \mu - \varepsilon_d - F^\sigma(i\nu_n)}\,. \tag{25}$$

Thus, one could think of mapping the Hubbard dimer into an auxiliary quantum-impurity model, chosen such that, within certain approximations, the impurity Green function is as close as possible to the local Green function of the original problem. How can we do this? Let us adopt as auxiliary model the Anderson molecule

$$\hat{H}^{\mathrm{A}} = \varepsilon_s \sum_\sigma \hat{n}_{s\sigma} - t \sum_\sigma \left(c_{d\sigma}^\dagger c_{s\sigma} + c_{s\sigma}^\dagger c_{d\sigma} \right) + \varepsilon_d \sum_\sigma \hat{n}_{d\sigma} + U \hat{n}_{d\uparrow} \hat{n}_{d\downarrow}, \tag{26}$$

where s labels the uncorrelated bath site and d the correlated quantum-impurity site. The first constraint would be that Hamiltonian (26) has a ground state with the same occupations of the 2-site Hubbard model, i.e., at half filling, $n_d = n_s = 1$. Such a *self-consistency condition* is satisfied if $\varepsilon_s = \mu = \varepsilon_d + U/2$. This can be understood by comparing the Hamiltonian matrices of the two models in the Hilbert space with $N = 2$ electrons. To this end, we first order the

two-electron states of the Hubbard dimer as

$$
\begin{aligned}
|1\rangle &= c^\dagger_{1\uparrow}c^\dagger_{2\uparrow}|0\rangle, & |4\rangle &= \tfrac{1}{\sqrt{2}}\big(c^\dagger_{1\uparrow}c^\dagger_{2\downarrow} - c^\dagger_{1\downarrow}c^\dagger_{2\uparrow}\big)|0\rangle,\\
|2\rangle &= c^\dagger_{1\downarrow}c^\dagger_{2\downarrow}|0\rangle, & |5\rangle &= c^\dagger_{1\uparrow}c^\dagger_{1\downarrow}|0\rangle,\\
|3\rangle &= \tfrac{1}{\sqrt{2}}\big(c^\dagger_{1\uparrow}c^\dagger_{2\downarrow} + c^\dagger_{1\downarrow}c^\dagger_{2\uparrow}\big)|0\rangle, & |6\rangle &= c^\dagger_{2\uparrow}c^\dagger_{2\downarrow}|0\rangle.
\end{aligned}
\tag{27}
$$

In this basis the Hamiltonian of the Hubbard dimer has the matrix form

$$
\hat{H}_2(\varepsilon_d, U, t) = \begin{pmatrix}
2\varepsilon_d & 0 & 0 & 0 & 0 & 0\\
0 & 2\varepsilon_d & 0 & 0 & 0 & 0\\
0 & 0 & 2\varepsilon_d & 0 & 0 & 0\\
0 & 0 & 0 & 2\varepsilon_d & -\sqrt{2}t & -\sqrt{2}t\\
0 & 0 & 0 & -\sqrt{2}t & 2\varepsilon_d{+}U & 0\\
0 & 0 & 0 & -\sqrt{2}t & 0 & 2\varepsilon_d{+}U
\end{pmatrix}.
\tag{28}
$$

The ground state, the singlet given in Eq. (10), can be obtained by diagonalizing the lower 3×3 block. For the Anderson molecule, ordering the basis in the same way ($1 \to d, 2 \to s$), this Hamiltonian becomes

$$
\hat{H}^A_2(\varepsilon_d, U, t; \varepsilon_s) = \begin{pmatrix}
\varepsilon_d{+}\varepsilon_s & 0 & 0 & 0 & 0 & 0\\
0 & \varepsilon_d{+}\varepsilon_s & 0 & 0 & 0 & 0\\
0 & 0 & \varepsilon_d{+}\varepsilon_s & 0 & 0 & 0\\
0 & 0 & 0 & \varepsilon_d{+}\varepsilon_s & -\sqrt{2}t & -\sqrt{2}t\\
0 & 0 & 0 & -\sqrt{2}t & 2\varepsilon_d{+}U & 0\\
0 & 0 & 0 & -\sqrt{2}t & 0 & 2\varepsilon_s
\end{pmatrix}.
\tag{29}
$$

Comparing the lower 3×3 block of $\hat{H}^A_2(\varepsilon_d, U, t; \varepsilon_s)$ with the corresponding block of $\hat{H}_2(\varepsilon_d, U, t)$ we can see that, unless $\varepsilon_s = \mu = \varepsilon_d + U/2$, the two doubly occupied states $|5\rangle$ and $|6\rangle$ have different energies and thus the two sites $i = 1, 2$ are differently occupied in the ground state. By setting $\varepsilon_s = \mu$ we find that

$$
\hat{H}^A_2(\varepsilon_d, U, t; \mu) = \hat{H}_2(\varepsilon_d{+}\tfrac{U}{4}, \tfrac{U}{2}, t).
\tag{30}
$$

The $N = 2$ ground state of $\hat{H}^A_2(\varepsilon_d, U, t; \mu)$ has thus the form of the ground-state for the Hubbard dimer

$$
|G\rangle_A = \frac{a_2(t, U/2)}{\sqrt{2}}\big(c^\dagger_{d\uparrow}c^\dagger_{s\downarrow} - c^\dagger_{d\downarrow}c^\dagger_{s\uparrow}\big)|0\rangle + \frac{a_1(t, U/2)}{\sqrt{2}}\big(c^\dagger_{d\uparrow}c^\dagger_{d\downarrow} + c^\dagger_{s\uparrow}c^\dagger_{s\downarrow}\big)|0\rangle,
\tag{31}
$$

and the condition $n_s = n_d = 1$ is satisfied. Since $\varepsilon_s \neq \varepsilon_d$, however, the eigenstates of $\hat{H}^{\rm A}$ for one electron ($N = 1$) or one hole ($N = 3$) are not the bonding and antibonding states of the

Hubbard dimer.[4] The impurity Green function is then given by

$$G^{\sigma}_{d,d}(i\nu_n) = \frac{1}{4}\Bigg(\frac{1+w'(t,U)}{i\nu_n - \big(E_0(2) - E_-(1) - \mu\big)} + \frac{1-w'(t,U)}{i\nu_n - \big(E_+(3) - E_0(2) - \mu\big)} \\ \frac{1-w'(t,U)}{i\nu_n - \big(E_0(2) - E_+(1) - \mu\big)} + \frac{1+w'(t,U)}{i\nu_n - \big(E_-(3) - E_0(2) - \mu\big)}\Bigg), \tag{32}$$

where

$$E_0(2) - E_\pm(1) - \mu = -\Big(E_\pm(3) - E_0(2) - \mu\Big) = -\frac{1}{4}\Big(2\Delta(t,U/2) \pm \Delta(t,U)\Big) \tag{33}$$

and

$$w'(t,U) = \frac{1}{2}\frac{32t^2 - U^2}{\Delta(t,U)\Delta(t,U/2)}\,. \tag{34}$$

After some rearrangement we obtain a much simpler expression

$$G^{\sigma}_{d,d}(i\nu_n) = \frac{1}{i\nu_n + \mu - \varepsilon_d - \mathcal{F}^{\sigma}_0(i\nu_n) - \Sigma^{\sigma}_A(i\nu_n)}\,. \tag{35}$$

The impurity self-energy equals the local self-energy of the Hubbard dimer

$$\Sigma^{\sigma}_A(i\nu_n) = \frac{U}{2} + \frac{U^2}{4}\frac{i\nu_n}{(i\nu_n)^2 - (3t)^2}\,, \tag{36}$$

as one may see comparing it to equation (19). The hybridization function is given by

$$\mathcal{F}^{\sigma}_0(i\nu_n) = \frac{t^2}{i\nu_n}\,, \tag{37}$$

as for the non-interacting Hubbard dimer, Eq. (22). For $U = 0$, $G^{\sigma}_{d,d}(i\nu_n)$ equals the non-interacting impurity Green function

$$G^{0\sigma}_{d,d}(i\nu_n) = \frac{1}{i\nu_n + \mu - \varepsilon_d - \mathcal{F}^{\sigma}_0(i\nu_n)}\,. \tag{38}$$

The impurity Green function thus satisfies the *impurity Dyson equation*

$$\Sigma^{\sigma}_A(i\nu_n) = \frac{1}{G^{0\sigma}_{d,d}(i\nu_n)} - \frac{1}{G^{\sigma}_{d,d}(i\nu_n)}\,. \tag{39}$$

In Fig. 2 we show the retarded impurity Green function of the Anderson molecule (orange, right panels) and the retarded local Green function of the 2-site Hubbard model, both in the local self-energy approximation (blue, right panels) and exact (blue, left panels). Comparing left and right panels we can see that setting $\Delta\Sigma^{\sigma}_l(\omega) = 0$ yields large errors. The right panels demonstrate, however, that the spectral function of the Anderson molecule is quite similar to the

[4]The complete list of eigenvalues and eigenvectors of the Anderson molecule for $\varepsilon_s = \varepsilon_d + U/2$ and arbitrary electron number N can be found in Appendix A.

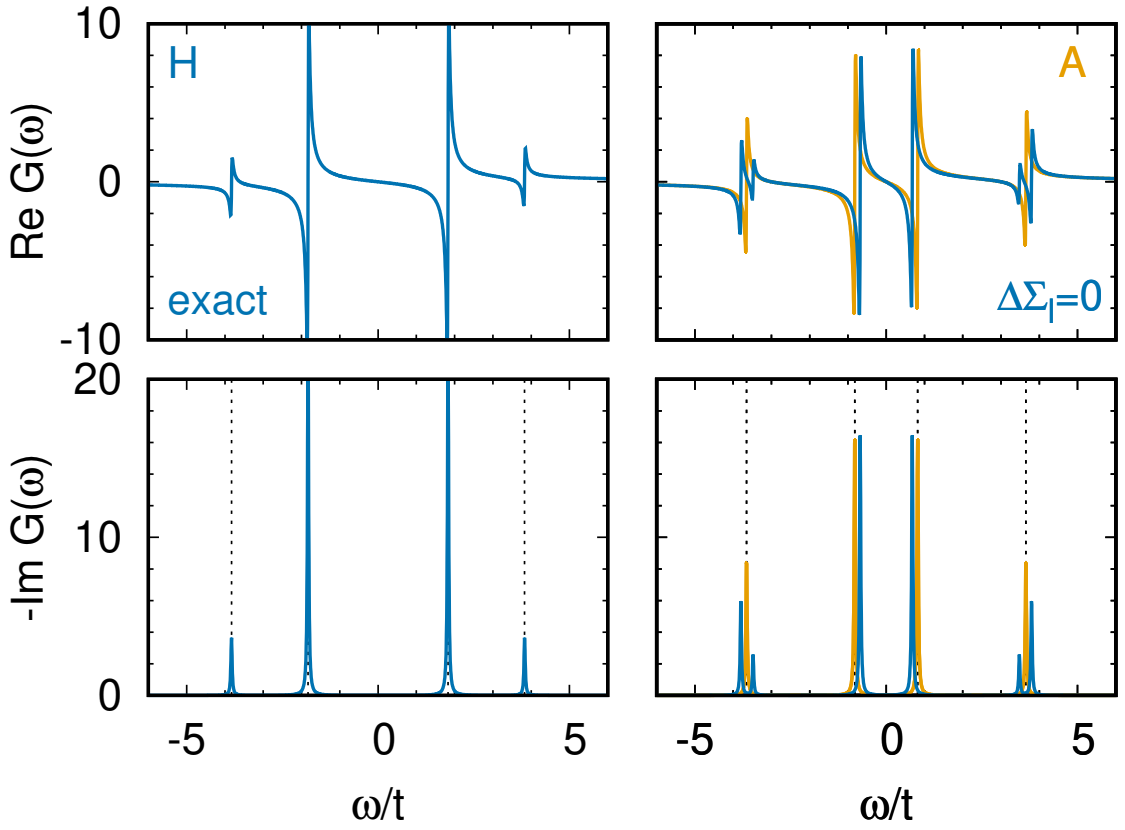


Fig. 2: *Retarded Green function of the Hubbard dimer ($t = 1, U = 4$) and of the Anderson molecule ($\varepsilon_s = \varepsilon_d + U/2$) in the zero temperature limit. Left panels: Hubbard dimer, exact Green function. Right panels, blue: Hubbard dimer in the local self-energy approximation, i.e., with $\Delta\Sigma_l^\sigma(\omega) = 0$. Right panels, orange: Anderson molecule. Dashed lines: Poles for the Hubbard dimer (left) or the Anderson molecule (right).*

one of the Hubbard dimer with $\Delta\Sigma_l^\sigma(\omega) = 0$. The small remaining deviations come from the fact that, for the Hubbard dimer, in the impurity Dyson equation, the non-interacting impurity Green function is replaced by $\mathfrak{G}_{i,i}^\sigma(i\nu_n)$ in the local self-energy approximation, i.e., by the *bath* Green function

$$\mathcal{G}_{i,i}^\sigma(i\nu_n) = \frac{1}{i\nu_n + \mu - \varepsilon_d - \mathcal{F}_l^\sigma(i\nu_n)}\,, \tag{40}$$

where

$$\mathcal{F}_l^\sigma(i\nu_n) = \frac{t^2}{i\nu_n + \mu - \varepsilon_d - \Sigma_A^\sigma(i\nu_n)}\,. \tag{41}$$

We are now in the position of explaining how DMFT works for the Hamiltonian of the Hubbard dimer, choosing the Anderson molecule Hamiltonian (26) as the auxiliary quantum-impurity model. The procedure can be split in the following steps

1. Build the initial quantum impurity model with $G_{d,d}^{0\sigma}(i\nu_n) = G_{i,i}^{0\sigma}(i\nu_n)$. The initial bath is thus defined by energy $\varepsilon_s = \varepsilon_d$ and hopping t.

2. Calculate the local Green function $G^{\sigma}_{d,d}(i\nu_n)$ for the auxiliary model.

3. Use the local Dyson equation to calculate the impurity self-energy

$$\Sigma^{\sigma}_{A}(i\nu_n) = \frac{1}{G^{0\sigma}_{d,d}(i\nu_n)} - \frac{1}{G^{\sigma}_{d,d}(i\nu_n)} \, .$$

4. Calculate the local Green function of the Hubbard dimer setting the self-energy equal to the one of the quantum-impurity model

$$G^{\sigma}_{i,i}(i\nu_n) \sim \frac{1}{2}\left(\frac{1}{i\nu_n + \mu - \varepsilon_d + t - \Sigma^{\sigma}_{A}(i\nu_n)} + \frac{1}{i\nu_n + \mu - \varepsilon_d - t - \Sigma^{\sigma}_{A}(i\nu_n)} \right) .$$

5. Calculate a new bath Green function $\mathcal{G}^{\sigma}_{i,i}(i\nu_n)$ from the local Dyson equation

$$\mathcal{G}^{\sigma}_{i,i}(i\nu_n) = \frac{1}{\Sigma^{\sigma}_{A}(i\nu_n) + 1/G^{\sigma}_{i,i}(i\nu_n)} \, .$$

6. Build a new $G^{0\sigma}_{d,d}(i\nu_n)$ from $\mathcal{G}^{\sigma}_{i,i}(i\nu_n)$.

7. Restart from the second step.

8. Iterate till self-consistency, i.e., here till $n^{\sigma}_{d} = n^{\sigma}_{i}$ and $\Sigma^{\sigma}_{A}(i\nu_n)$ does not change any more.

The Anderson molecule satisfies the self-consistency requirements for $\varepsilon_s = \mu$. The remaining difference between $G^{\sigma}_{d,d}(i\nu_n)$, the impurity Green function, and $G^{\sigma}_{i,i}(i\nu_n)$, the local Green function of the Hubbard dimer in the local self-energy approximation, arises from the difference in the associated hybridization functions

$$\Delta\mathcal{F}_l(i\nu_n) = \mathcal{F}^{\sigma}_{l}(i\nu_n) - \mathcal{F}^{\sigma}_{0}(i\nu_n) = t^2 p^2 \left(-\frac{2}{i\nu_n} + \frac{1}{i\nu_n - \varepsilon_a} + \frac{1}{i\nu_n + \varepsilon_a} \right) \tag{42}$$

where $p^2 = U^2/8\varepsilon_a^2$ and $\varepsilon_a = \sqrt{9t^2 + U^2/4}$. The error made is small, however, as shown in the right panels of Fig. 2. To further improve we would have to modify the auxiliary model adding more bath sites. Staying with the Anderson molecule, in Fig. 3 we compare in more detail its spectral function with the exact spectral function of the Hubbard dimer. The figure emphasizes several important conclusions. The top right panel reminds us that DMFT is not a good approximation for molecular complexes with two (or few) correlated sites. This is because in such systems the coordination number is the lowest possible, the worst case for dynamical mean-field theory. In three-dimensional crystals, instead, the coordination number is typically large enough to make dynamical mean-field theory an excellent approximation. The bottom left panel of Fig. 3 shows that, in the local-self-energy approximation, the agreement between Anderson and Hubbard Green functions is very good for any U value. This indicates that when the local-self-energy approximation (hence DMFT) works well, as in the case of three-dimensional crystals, it can be successfully used to study the behavior of a given system as a function of U. Leaving for a moment DMFT aside, the two bottom panels of Fig. 3 show that

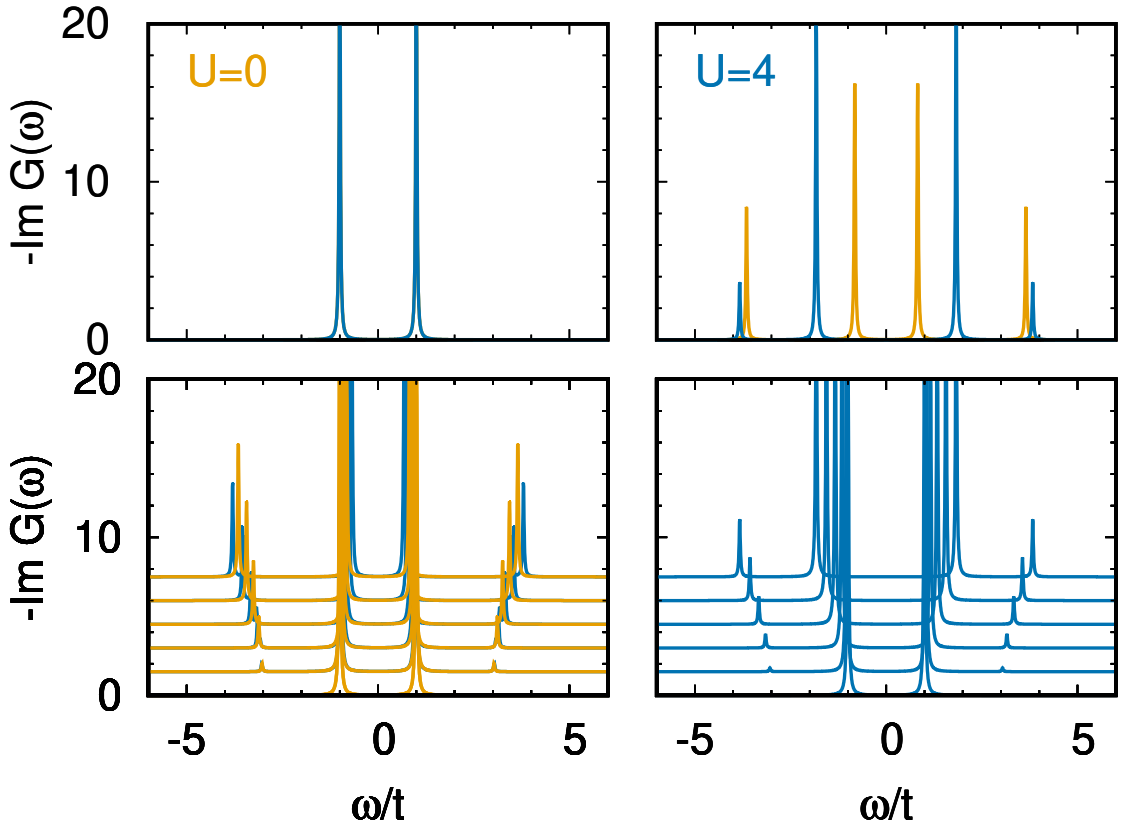


Fig. 3: *Imaginary part of the retarded Green function of the Anderson molecule (orange) and Hubbard dimer (blue) in the zero temperature limit. In the bottom left panel the local self-energy approximation is adopted for the Hubbard dimer; in all other cases the exact Green function of the Hubbard dimer is shown. Parameters:* $t = 1$, $\varepsilon_s = \mu$. *Top:* $U = 0$ *(left) and* $U = 4t$ *(right). Bottom: Evolution with increasing* U *from* 0 *to* $4t$ *in equal steps.*

the evolution with U is different for the impurity Green function of the Anderson molecule and the exact local Green function of the Hubbard dimer. Anticipating the discussion of later sections, if we compare to the spectral function of the actual *lattice* Hubbard model, we could say that the Hubbard dimer captures well the evolution of the Hubbard bands and the gap in the large-U limit. On the other hand, the Anderson molecule partially captures the behavior of the central "quasi-particle" or "Kondo" peak, although the Kondo effect itself is unrealistically described; as a matter of fact, the Kondo energy gain (the "Kondo temperature") is perturbative ($\propto t^2/U$) in the case of the Anderson molecule, while it is exponentially small for a Kondo impurity in a metallic bath. This also points to the possible shortcomings of calculations in which the DMFT quantum-impurity model for the *lattice* Hubbard model is solved via exact diagonalization, however using a single bath site or very few; this is sufficient in the limit of large gap,[5] but is bound to eventually fail approaching the metallic regime. Indeed, this failure is one of the reasons why the solution of the Kondo problem required the development of—at the time new—non-perturbative techniques such as the numerical renormalization group.

[5]For a discussion of bath parametrization in exact diagonalization and the actual convergence with the number of bath sites for the lattice Hubbard model see Ref. [11].

2.2 Non-local Coulomb interaction

In Sec. 2.1 we have seen that the local Coulomb interaction gives rise, *alone*, to non-local self-energy terms, which can be very important. What is, instead, the effect of the non-local part of the Coulomb interaction? For a Hubbard dimer, extending the Coulomb interaction to first neighbors leads to the Hamiltonian

$$\begin{aligned}\hat{H} =& \varepsilon_d \sum_{i\sigma} \hat{n}_{i\sigma} - t \sum_{\sigma} \left(c^\dagger_{1\sigma} c_{2\sigma} + c^\dagger_{2\sigma} c_{1\sigma}\right) + U \sum_{i=1,2} \hat{n}_{i\uparrow}\hat{n}_{i\downarrow} \\ &+ \sum_{\sigma\sigma'} \left(V - 2J_V - J_V\,\delta_{\sigma\sigma'}\right) \hat{n}_{1\sigma}\hat{n}_{2\sigma'} - J_V \sum_{i\neq i'} \left(c^\dagger_{i\uparrow} c_{i\downarrow} c^\dagger_{i'\downarrow} c_{i'\uparrow} + c^\dagger_{i'\uparrow} c^\dagger_{i'\downarrow} c_{i\uparrow} c_{i\downarrow}\right), \end{aligned} \tag{43}$$

where the parameters in the last two terms are the intersite direct (V) and exchange (J_V) Coulomb interaction. For two electrons the Hamiltonian, in a matrix form, becomes

$$\hat{H}_2^{\rm NL} = \begin{pmatrix} 2\varepsilon_d{+}V{-}3J_V & 0 & 0 & 0 & 0 & 0 \\ 0 & 2\varepsilon_d{+}V{-}3J_V & 0 & 0 & 0 & 0 \\ 0 & 0 & 2\varepsilon_d{+}V{-}3J_V & 0 & 0 & 0 \\ 0 & 0 & 0 & 2\varepsilon_d{+}V{-}J_V & -\sqrt{2}t & -\sqrt{2}t \\ 0 & 0 & 0 & -\sqrt{2}t & 2\varepsilon_d{+}U & -J_V \\ 0 & 0 & 0 & -\sqrt{2}t & -J_V & 2\varepsilon_d{+}U \end{pmatrix},$$

where the basis is defined in Eq. (27). In the atomic ($t = 0$) limit, the triplet states, $|1\rangle$, $|2\rangle$ and $|3\rangle$, have lower energy than the singlet states, $|4\rangle$, $|5\rangle$ and $|6\rangle$, as one can see by comparing the diagonal elements of the upper and lower 3×3 block of the matrix $\hat{H}_2^{\rm NL}$ here above. This is due to the fact that J_V is positive (ferromagnetic) and $V < U$. The triplet can remain the ground multiplet even for finite t. If, however, J_V is sufficiently small, the ground state is a singlet, as in the case $V{=}J_V{=}0$. Setting for simplicity $J_V = 0$, we notice that $\hat{H}_2^{\rm NL} = \hat{H}_2(\varepsilon'_d, U', t)$, where the right-hand-side term is the $N{=}2$-electron Hamiltonian of the $J_V{=}V{=}0$ Hubbard dimer, Eq. (28), with parameters $\varepsilon'_d = \varepsilon_d + V/2$ and $U'{=}U{-}V$. The $N{=}2$ ground state is thus still given by Eq. (10), provided that we replace U with U' in the coefficients. Eventually, in the limiting case $U{=}V$, $\hat{H}_2^{\rm NL}$ equals the corresponding Hamiltonian of an effective non-correlated dimer, $\hat{H}_2(\varepsilon'_d, 0, t)$. What happens away from half filling? For $N{=}1$ electrons, eigenvectors and eigenvalues are the same as in the $V{=}0$ case; for $N{=}3$ electrons all energies are shifted by $2V$. Summarizing, we can obtain the Green function for $V \neq 0$ from Eq. (14) setting

$$\begin{aligned} E_\pm(N{=}1, U; V) &= E_\pm(N{=}1, U; 0) &&= \varepsilon_d \pm t \\ E_\pm(N{=}3, U; V) &= E_\pm(N{=}3, U; 0) + 2V &&= 3\varepsilon_d \pm t + U + 2V \\ E_0(N{=}2, U; V) &= E_0(N{=}2, U{-}V; 0) + V &&= E_0(2, U{-}V) + V \\ \mu(U; V) &= \mu(U) + V &&= \mu + V \\ w_\pm(t, U; V) &= w_\pm(t, U{-}V; 0). \end{aligned}$$

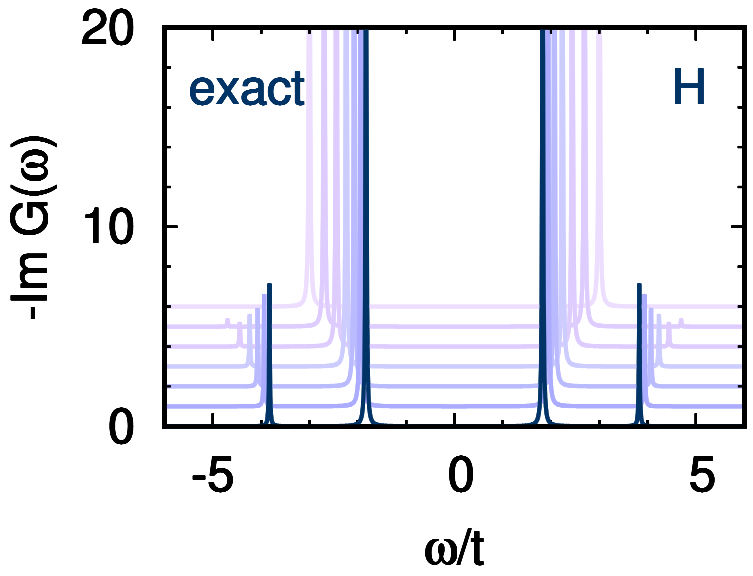


Fig. 4: *Imaginary part of the retarded Green function of the Hubbard dimer in the zero temperature limit ($U = 4$, $t = 1$), increasing the intersite Coulomb repulsion V from 0 to $V = U = 4$ in equal steps; we have set $J_V = 0$. The dark blue line corresponds to $V = 0$.*

Thus we have, recalling that $U' = U - V$,

$$G^{\sigma}_{i,i}(i\nu_n) = \frac{w_+(t,U')}{i\nu_n - \left(E'_0(2) - \frac{1}{2}V - \varepsilon_d + t - \mu'\right)} + \frac{w_-(t,U')}{i\nu_n - \left(-E'_0(2) + U' + \frac{1}{2}V + 3\varepsilon_d + t - \mu'\right)}$$
$$+ \frac{w_-(t,U')}{i\nu_n - \left(E'_0(2) - \frac{1}{2}V - \varepsilon_d - t - \mu'\right)} + \frac{w_+(t,U')}{i\nu_n - \left(-E'_0(2) + U' + \frac{1}{2}V + 3\varepsilon_d - t - \mu'\right)}\,, \qquad (44)$$

where we set $\mu' = \mu - V/2 = 2\varepsilon_d + U'/2$ and $E'_0(2) = E_0(2, U')$. The associated spectral function is shown in Fig. 4. The figure illustrates that increasing V from 0 to U makes the spectra progressively closer to the one of a non-correlated system. Eventually, for $U{=}V$, only two poles contribute, since $w_-(t, U') = 0$. In this limit, the spectral function is identical to the one of the non-interacting Hubbard dimer, however with an enhanced effective hopping, $t \longrightarrow t + V/2$. We can thus say that, in first approximation, the (positive) intersite coupling V effectively reduces the strength of correlations in the Hubbard dimer. In conclusion, the case of the Hubbard dimer explains why *strong-correlation* effects typically appear when the *local term of the electron-electron repulsion dominates*, i.e., when it is much larger than long-range terms. A hypothetical system in which the Coulomb interaction strength is independent on the distance between sites (for the dimer, $U{=}V$) is likely to be already well described via an *effective weakly correlated model*. Of course, in real materials, the effects of long-range Coulomb repulsion can be much more complicated than in the two-site model just discussed, but the general considerations made here remain true even in realistic cases.

2.3 Quantum-impurity solvers: Continuous-time quantum Monte Carlo

For the case of the Anderson molecule exact diagonalization is the simplest quantum-impurity solver and the one that provides most insights. Methods based on quantum Monte Carlo (QMC) sampling are often, however, the only option for realistic multi-orbital and/or multi-site models. Thus, here we explain how to obtain the impurity Green function of the Anderson molecule via hybridization-expansion continuous-time QMC [12], a very successful QMC-based quantum-impurity solver. In this approach, the first step consists in splitting the Hamiltonian into bath ($\hat{H}_{\rm bath}$), hybridization ($\hat{H}_{\rm hyb}$), and local ($\hat{H}_{\rm loc}$) terms

$$\hat{H}^{\rm A} = \underbrace{\varepsilon_s \sum_\sigma \hat{n}_{s\sigma}}_{\hat{H}_{\rm bath}} \underbrace{-t \sum_\sigma \left(c^\dagger_{d\sigma} c_{s\sigma} + c^\dagger_{s\sigma} c_{d\sigma} \right)}_{\hat{H}_{\rm hyb}} + \underbrace{\varepsilon_d \sum_\sigma \hat{n}_{d\sigma} + U \hat{n}_{d\uparrow} \hat{n}_{d\downarrow}}_{\hat{H}_{\rm loc}} . \tag{45}$$

Next, we write the partition function Z as a perturbation series in the hybridization. To this end, we define $\hat{H}_0 = \hat{H}_{\rm bath} + \hat{H}_{\rm loc}$ and rewrite the partition function as

$$Z = {\rm Tr} \left(e^{-\beta(\hat{H}_0 - \mu \hat{N})} \hat{V}(\beta) \right) \tag{46}$$

where the operator $\hat{V}(\beta)$ is given by

$$\hat{V}(\beta) = e^{\beta(\hat{H}_0 - \mu \hat{N})} \, e^{-\beta(\hat{H}_0 + \hat{H}_{\rm hyb} - \mu \hat{N})} = \sum_m \underbrace{\int_0^\beta d\tau_1 \cdots \int_{\tau_{m-1}}^\beta d\tau_m}_{\int d\boldsymbol{\tau}^m} \underbrace{(-1)^m \prod_{l=m}^1 \hat{H}_{\rm hyb}(\tau_l)}_{\hat{O}^m(\boldsymbol{\tau})} , \tag{47}$$

and

$$\hat{H}_{\rm hyb}(\tau_l) = e^{\tau_l(\hat{H}_0 - \mu \hat{N})} \, \hat{H}_{\rm hyb} \, e^{-\tau_l(\hat{H}_0 - \mu \hat{N})} = -t \sum_\sigma \left(c^\dagger_{d\sigma_l}(\tau_l) c_{s\sigma_l}(\tau_l) + c^\dagger_{s\sigma_l}(\tau_l) c_{d\sigma_l}(\tau_l) \right). \tag{48}$$

In this expansion, the only terms that contribute to the trace are even order ones ($m = 2k$) and they are products of impurity (d) and bath (s) creator-annihilator pairs. We can thus rewrite

$$\int d\boldsymbol{\tau}^{2k} \longrightarrow \int d\boldsymbol{\tau}^k \int d\bar{\boldsymbol{\tau}}^k \quad \text{and} \qquad \hat{O}^{2k}(\boldsymbol{\tau}) \longrightarrow \sum_{\boldsymbol{\sigma}, \bar{\boldsymbol{\sigma}}} \hat{O}^{2k}_{\boldsymbol{\sigma}, \bar{\boldsymbol{\sigma}}}(\boldsymbol{\tau}, \bar{\boldsymbol{\tau}}) \tag{49}$$

where

$$\hat{O}^{2k}_{\boldsymbol{\sigma}, \bar{\boldsymbol{\sigma}}}(\boldsymbol{\tau}, \bar{\boldsymbol{\tau}}) = (t)^{2k} \prod_{i=1}^k \left(c^\dagger_{d\bar{\sigma}_i}(\bar{\tau}_i) c_{s\bar{\sigma}_i}(\bar{\tau}_i) c^\dagger_{s\sigma_i}(\tau_i) c_{d\sigma_i}(\tau_i) \right). \tag{50}$$

The vector $\boldsymbol{\sigma} = (\sigma_1, \sigma_2, ..., \sigma_k)$ gives the spins $\{\sigma_i\}$ associated with the k impurity annihilators at imaginary times $\{\tau_i\}$, while $\bar{\boldsymbol{\sigma}} = (\bar{\sigma}_1, \bar{\sigma}_2, ..., \bar{\sigma}_k)$ gives the spins $\{\bar{\sigma}_i\}$ associated with the k impurity creators at imaginary times $\{\bar{\tau}_i\}$. It follows that the local and bath traces can be

decoupled and the partition function can be rewritten as

$$\frac{Z}{Z_{\rm bath}} = \sum_k \int d\boldsymbol{\tau}^k \int d\bar{\boldsymbol{\tau}}^k \sum_{\boldsymbol{\sigma},\bar{\boldsymbol{\sigma}}} d^k_{\bar{\boldsymbol{\sigma}},\boldsymbol{\sigma}}(\boldsymbol{\tau},\bar{\boldsymbol{\tau}})\, t^k_{\boldsymbol{\sigma},\bar{\boldsymbol{\sigma}}}(\boldsymbol{\tau},\bar{\boldsymbol{\tau}}) \tag{51}$$

$$d^k_{\bar{\boldsymbol{\sigma}},\boldsymbol{\sigma}}(\boldsymbol{\tau},\bar{\boldsymbol{\tau}}) = \frac{t^{2k}}{Z_{\rm bath}}\, {\rm Tr}_{\rm bath}\left(e^{-\beta(\hat{H}_{\rm bath}-\mu\hat{N}_s)}\mathcal{T}\prod_{i=k}^1 c^\dagger_{s\sigma_i}(\tau_i)c_{s\bar{\sigma}_i}(\bar{\tau}_i)\right) \tag{52}$$

$$t^k_{\boldsymbol{\sigma},\bar{\boldsymbol{\sigma}}}(\boldsymbol{\tau},\bar{\boldsymbol{\tau}}) = {\rm Tr}_{\rm loc}\left(e^{-\beta(\hat{H}_{\rm loc}-\mu\hat{N}_d)}\mathcal{T}\prod_{i=k}^1 c_{d\sigma_i}(\tau_i)c^\dagger_{d\bar{\sigma}_i}(\bar{\tau}_i)\right), \tag{53}$$

where $Z_{\rm bath} = 1 + 2e^{-\beta(\varepsilon_s-\mu)} + e^{-2\beta(\varepsilon_s-\mu)}$ and

$$c_{d\sigma}(\tau) = e^{\tau(\hat{H}_{\rm loc}-\mu\hat{N}_d)}c_{d\sigma}e^{-\tau(\hat{H}_{\rm loc}-\mu\hat{N}_d)}, \qquad c_{s\sigma}(\tau) = e^{\tau(\hat{H}_{\rm bath}-\mu\hat{N}_s)}c_{s\sigma}e^{-\tau(\hat{H}_{\rm bath}-\mu\hat{N}_s)}.$$

The trace involving only bath operators is simple to calculate, since $\hat{H}_{\rm bath}$ describes an independent-electron problem for which Wick's theorem holds. It is given by the determinant

$$d^k_{\bar{\boldsymbol{\sigma}},\boldsymbol{\sigma}}(\boldsymbol{\tau},\bar{\boldsymbol{\tau}}) = \det\left(\mathcal{F}^k_{\bar{\boldsymbol{\sigma}},\boldsymbol{\sigma}}(\boldsymbol{\tau},\bar{\boldsymbol{\tau}})\right) \tag{54}$$

of the $k\times k$ non-interacting hybridization-function matrix, with elements

$$\left(\mathcal{F}^k_{\bar{\boldsymbol{\sigma}},\boldsymbol{\sigma}}(\boldsymbol{\tau},\bar{\boldsymbol{\tau}})\right)_{i',i} = \mathcal{F}^0_{\bar{\sigma}_{i'},\sigma_i}(\bar{\tau}_{i'}-\tau_i) \tag{55}$$

where

$$\mathcal{F}^0_{\bar{\sigma},\sigma}(\tau) = \delta_{\bar{\sigma},\sigma}\,\frac{t^2}{1+e^{-\beta(\varepsilon_s-\mu)}} \times \begin{cases} -e^{-\tau(\varepsilon_s-\mu)} & \tau > 0, \\ +e^{-(\beta+\tau)(\varepsilon_s-\mu)} & \tau < 0. \end{cases} \tag{56}$$

This is the imaginary time Fourier transform of the hybridization function introduced previously

$$\mathcal{F}^0_{\bar{\sigma},\sigma}(i\nu_n) = \frac{t^2}{i\nu_n - (\varepsilon_s-\mu)}\,\delta_{\bar{\sigma},\sigma}. \tag{57}$$

The calculation of the local trace is in general more complicated. In the case discussed here, the Hamiltonian does not flip spins. Thus only terms with an equal number of creation and annihilation operators *per spin* contribute to the local trace, and we can express the partition function in expansion orders per spin, k_σ. This yields [13]

$$\frac{Z}{Z_{\rm bath}} = \left(\prod_\sigma \sum_{k_\sigma=0}^\infty \int d\boldsymbol{\tau}_\sigma^{k_\sigma} \int d\bar{\boldsymbol{\tau}}_\sigma^{k_\sigma}\right) d^k_{\bar{\boldsymbol{\sigma}},\boldsymbol{\sigma}}(\boldsymbol{\tau},\bar{\boldsymbol{\tau}})\, t^k_{\boldsymbol{\sigma},\bar{\boldsymbol{\sigma}}}(\boldsymbol{\tau},\bar{\boldsymbol{\tau}}) \tag{58}$$

where the vectors $\boldsymbol{\sigma} = (\boldsymbol{\sigma}_\uparrow,\boldsymbol{\sigma}_\downarrow)$ and $\bar{\boldsymbol{\sigma}} = (\bar{\boldsymbol{\sigma}}_\uparrow,\bar{\boldsymbol{\sigma}}_\downarrow)$ have $(k_\uparrow,k_\downarrow)$ components, and for each k_σ component $\sigma_i = \bar{\sigma}_i = \sigma$. Thus

$$t^k_{\boldsymbol{\sigma},\bar{\boldsymbol{\sigma}}}(\boldsymbol{\tau},\bar{\boldsymbol{\tau}}) = {\rm Tr}_{\rm loc}\left(e^{-\beta(\hat{H}_{\rm loc}-\mu\hat{N}_d)}\,\mathcal{T}\prod\nolimits_\sigma\prod\nolimits_{i=k_\sigma}^1 c_{d\sigma}(\tau_{\sigma_i})c^\dagger_{d\sigma}(\bar{\tau}_{\bar{\sigma}_i})\right). \tag{59}$$

The latter can be calculated analytically. To do this, first we parametrize all configurations for a given spin via a timeline $[0,\beta)$ plus a number of creator/annihilator pairs which define segments

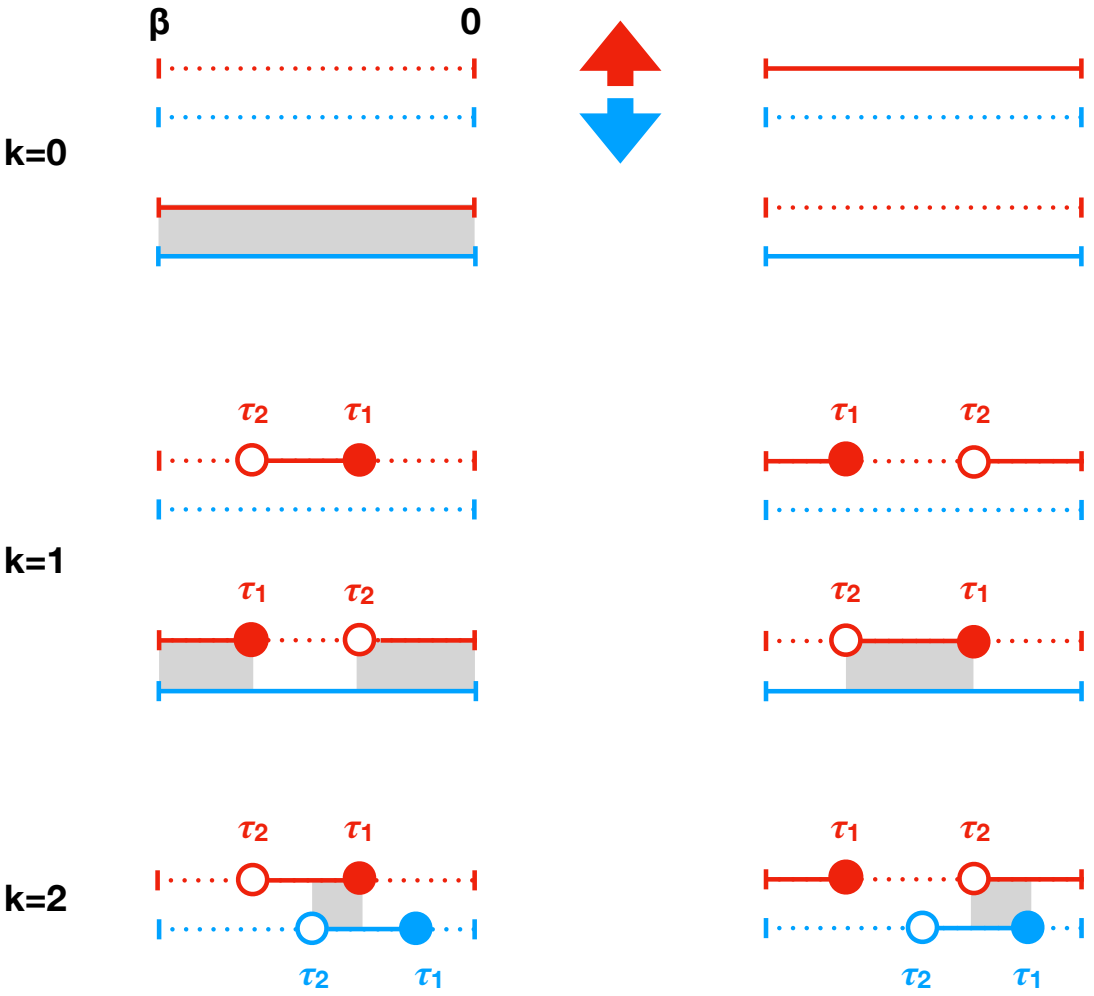


Fig. 5: *Representative configurations contributing to the local trace at zeroth, first and second order. The timelines for spin up are red and those for spin down are blue. The filled circles correspond to the insertion of a creator (time τ_1), and the empty circles to the insertion of an annihilator (time τ_2). Dotted lines represent the vacuum state for a given spin, full lines the occupied state. The grey boxes indicate the regions in which $l_{\uparrow,\downarrow} \neq 0$.*

on the timeline. At zeroth order two possible configurations exist per spin, an empty timeline, which corresponds to the vacuum state $|0\rangle$, and a full timeline, which corresponds to the state $c^\dagger_{d\sigma}|0\rangle$. A given configuration yields, at order $k = k_\uparrow + k_\downarrow$

$$t^k_{\sigma,\bar{\sigma}}(\boldsymbol{\tau},\bar{\boldsymbol{\tau}}) = \left(\prod_\sigma s^{k_\sigma}_\sigma\right) e^{-\sum_{\sigma\sigma'}((\varepsilon_d-\mu)\delta_{\sigma\sigma'}+\frac{U}{2}(1-\delta_{\sigma,\sigma'}))l_{\sigma,\sigma'}} \tag{60}$$

where $l_{\sigma,\sigma'}$ is the length of the overlap of the τ segments for spins σ and σ', respectively, while $s_\sigma = \mathrm{sign}(\tau_{\sigma_1} - \bar{\tau}_{\sigma_1})$ is the fermionic sign. Possible configurations at order $k = 0, 1, 2$ are shown in Fig. 5. At order $k = 0$, summing up the contribution of the four configurations shown in Fig. 5 yields the local partition function $Z_{\mathrm{loc}} = 1 + 2e^{-\beta(\varepsilon_d-\mu)} + e^{-\beta(2(\varepsilon_d-\mu)+U)}$. Order $k = 1$ is already more complicated. Setting $\varepsilon_s = \mu$ as in the self-consistent solution, the contribution

to the bath trace in this case is

$$d^1_{\bar\sigma\sigma}(\tau_1,\tau_2) = \mathcal{F}^0_{\bar\sigma\sigma}(\tau_1,\tau_2) = -\frac{t^2}{2}\delta_{\sigma,\bar\sigma}\ \mathrm{sign}(\tau_1-\tau_2). \tag{61}$$

The local trace at the same order is instead given by

$$t^1_{\sigma\bar\sigma}(\tau_2,\tau_1) = \mathrm{Tr}_{\rm loc}\Big(e^{-\beta(\hat H_{\rm loc}-\mu\hat N_d)}\mathcal{T}c_{d\sigma}(\tau_2)c^\dagger_{d\sigma}(\tau_1)\Big). \tag{62}$$

We can now calculate the contribution at half filling of the four $k=1$ configurations shown in Fig. 5. In the case $k_\uparrow = 1$ and $k_\downarrow = 0$ we have, going from left to right in each row

$$t^1_{\uparrow\uparrow}(\tau_2,\tau_1) = \begin{cases} +e^{-(\tau_2-\tau_1)(\varepsilon_d-\mu)} & = +e^{+\tau_{21}U/2} \\ -e^{-(\beta-(\tau_1-\tau_2))(\varepsilon_d-\mu)} & = -e^{(\beta+\tau_{21})U/2} \\ -e^{-\beta(2(\varepsilon_d-\mu)+U)+(\tau_1-\tau_2)(\varepsilon_d-\mu+U)} & = -e^{-\tau_{21}U/2} \\ +e^{-(\tau_2-\tau_1)(\varepsilon_d-\mu+U)-\beta(\varepsilon_d-\mu)} & = +e^{(\beta-\tau_{21})U/2} \end{cases} \tag{63}$$

where $\tau_{21} = \tau_2 - \tau_1$ and $\mu = \varepsilon_d + U/2$. Similar results can be obtained for $k_\uparrow = 0$ and $k_\downarrow = 1$. Summing up all terms up to order one we find

$$\begin{aligned} \frac{Z}{Z_{\rm bath}} &\sim Z_{\rm loc} + \sum_\sigma \int_0^\beta d\tau_2 \int_0^\beta d\tau_1\, d^1_{\sigma\sigma}(\tau_1,\tau_2)\, t^1_{\sigma\sigma}(\tau_2,\tau_1) \\ &\sim Z_{\rm loc}\left(1 - \beta\,\frac{1-e^{\frac{\beta U}{2}}}{1+e^{\frac{\beta U}{2}}}\frac{2t^2}{U}\right). \end{aligned} \tag{64}$$

The exact formula of the partition function can be obtained from the eigenvalues and eigenvectors in Appendix A

$$\frac{Z}{Z_{\rm bath}} = Z_{\rm loc}\frac{3(1+e^{\frac{\beta U}{2}}) + e^{\frac{\beta U}{4}}\left(4e^{-\frac{\beta\Delta(t,U)}{4}} + 4e^{+\frac{\beta\Delta(t,U)}{4}} + e^{+\frac{\beta\Delta(t,U/2)}{2}} + e^{-\frac{\beta\Delta(t,U/2)}{2}}\right)}{8\big(1+e^{\frac{\beta U}{2}}\big)}. \tag{65}$$

Its Taylor expansion in powers of t/U yields, at second order, the expression above. Going back to Eq. (62), one can observe that, for $k=1$, the local trace is proportional to the local Green function, $G^\sigma_{d,d}(\tau)$. Indeed, $G^\sigma_{d,d}(\tau)$ can be calculated using the configurations just described—provided that we start from $k=1$ and we divide by the hybridization function. More specifically, for $k=1$ and $\tau > 0$ we have

$$G^\sigma_{d,d}(\tau) \sim -\frac{1}{\beta}\int_0^\beta\int_0^\beta \underbrace{d\tau_2 d\tau_1\, d^1_{\sigma\sigma}(\tau_1,\tau_2)t^1_{\sigma\sigma}(\tau_2,\tau_1)}_{w^1}\ \delta\big(\tau-(\tau_2-\tau_1)\big)\ \frac{1}{\mathcal{F}^0_{\sigma\sigma}(\tau_1-\tau_2)}. \tag{66}$$

We are now ready to generalize to arbitrary order. Taking all k values into account, the partition function can be expressed as the sum over all configurations $\{c\}$, i.e., in short

$$Z = \sum_c w_c = \sum_c |w_c|\ \mathrm{sign}\ w_c. \tag{67}$$

In a compact form, we can write $w_c = d\boldsymbol{\tau}_c \; d_c \; t_c$ where $d\boldsymbol{\tau}_c = \prod_\sigma \prod_i^{k_\sigma} d\tau_{\sigma_i} d\bar{\tau}_{\bar{\sigma}_i}$, and d_c and t_c are the bath and local traces for the configuration c. This expression of the partition function shows that we can interpret $|w_c|$ as the sampling weight of configuration c. A generic observable $\hat{O}$ can then be obtained as the Monte Carlo average on a finite number of configurations N_c

$$\langle \hat{O} \rangle = \frac{\sum_c \langle \hat{O} \rangle_c |w_c| \,\mathrm{sign}\, w_c}{\sum_c |w_c| \,\mathrm{sign}\, w_c} = \frac{\sum_c \mathrm{sign}\, w_c \langle \hat{O} \rangle_c \, |w_c| / \sum_c |w_c|}{\sum_c \mathrm{sign}\, w_c \, |w_c| / \sum_c |w_c|} \approx \frac{\frac{1}{N_c} \sum_c^{N_c} \langle \hat{O} \rangle_c \,\mathrm{sign}\, w_c}{\frac{1}{N_c} \sum_c \mathrm{sign}\, w_c}. \quad (68)$$

The term $\frac{1}{N_c} \sum_c \mathrm{sign}\; w_c$ in the denominator is the average fermionic sign. When this is small, much longer runs are required to obtain data of the same quality; eventually the computational time can become so long that the calculation is unfeasible—in these cases we have a sign problem. In practice, the QMC simulation starts from a random configuration c. Next we propose an update $c \to c'$. Within the Metropolis algorithm, the acceptance ratio is

$$R_{c \to c'} = \min\left(1, \frac{p_{c' \to c}}{p_{c \to c'}} \frac{|w_{c'}|}{|w_c|}\right) \quad (69)$$

where $p_{c \to c'}$ is the proposal probability for the update $c \to c'$. In the approach described here, known as *segment solver*, the basic updates are addition and removal of segments, antisegments (segments winding over the borders of the timeline, see Fig. 5), or complete lines. As example, let us consider the insertion of a segment for spin σ. A segment is made by a creator and an annihilator. The creator is inserted at time τ_{in}; the move is rejected if τ_{in} is in a region where a segment exists. If created, the segment can have at most length $l_{\max}$, given by the distance between τ_{in} and the time at which the next creator is, hence

$$p_{c \to c'} = \frac{d\bar{\tau}}{\beta} \frac{d\tau}{l_{\max}} \,. \quad (70)$$

The proposal probability of the reverse move (removing a segment) is instead given by the inverse of the number of existing segments

$$p_{c' \to c} = \frac{1}{k_\sigma + 1} \,. \quad (71)$$

The acceptance ratio for the insertion of a segment becomes then

$$R_{c \to c'} = \min\left(1, \frac{\beta l_{max}}{k_\sigma + 1} \left| \frac{d_{c'}}{d_c} \frac{t_{c'}}{t_c} \right| \right). \quad (72)$$

For the impurity Green function, here the most important observable, the direct average yields

$$\langle \hat{O} \rangle_c = \langle G^\sigma_{d,d} \rangle_c = \sum_{\sigma'} \sum_{i=1}^{k_\sigma} \sum_{j=1}^{k_\sigma} \Delta(\tau, \tau_{\sigma' j} - \bar{\tau}_{\sigma' j}) \left(M^{k'_\sigma}\right)_{\sigma' j, \sigma' i} \delta_{\sigma, \sigma_{\sigma' j}} \delta_{\sigma, \bar{\sigma}_{\sigma' i}} \quad (73)$$

where $M^k = \left(\mathcal{F}^k\right)^{-1}$ is the inverse of the hybridization matrix and

$$\Delta(\tau, \tau') = -\frac{1}{\beta} \begin{cases} \delta(\tau - \tau') & \tau' > 0 \\ -\delta(\tau - (\tau' + \beta)) & \tau' < 0 \end{cases} . \quad (74)$$

One can verify that at order $k = 1$ this indeed returns Eq. (66).

2.4 Hartree-Fock (LDA+U) versus DMFT approximation

Let us now compare the exact solution of the Hubbard dimer with the result of the Hartree-Fock (HF) approximation, which is the basis of the LDA+U method. It consists in replacing

$$\hat{H}_U = U \sum_i \hat{n}_{i\uparrow}\hat{n}_{i\downarrow} \rightarrow \hat{H}_U^{\rm HF} = U \sum_i \left(\hat{n}_{i\uparrow}\bar{n}_{i\downarrow} + \hat{n}_{i\downarrow}\bar{n}_{i\uparrow} - \bar{n}_{i\uparrow}\bar{n}_{i\downarrow}\right), \tag{75}$$

where $\bar{n}_{i\sigma}$ is the HF expectation value of the operator $\hat{n}_{i\sigma}$. It is convenient to define

$$\begin{aligned} n_i &= \bar{n}_{i\uparrow}+\bar{n}_{i\downarrow} & n &= \frac{1}{2}\left(n_1+n_2\right) & \delta n &= \frac{1}{2}\left(n_1-n_2\right) \\ m_i &= \frac{1}{2}\left(\bar{n}_{i\uparrow}-\bar{n}_{i\downarrow}\right) & m_+ &= \frac{1}{2}\left(m_1+m_2\right) & m_- &= \frac{1}{2}\left(m_1-m_2\right) \end{aligned}$$

Inverting these relations, in the absence of charge disproportionation ($\delta n = 0$), we find

$$\bar{n}_{i\uparrow} = \left(m_+ + (-1)^{i-1} m_-\right) + n/2 \qquad \bar{n}_{i\downarrow} = -\left(m_+ + (-1)^{i-1} m_-\right) + n/2\,.$$

The Hartree-Fock version of the Hubbard dimer Hamiltonian equals the non-interacting Hamiltonian plus a shift of the on-site level. This shift depends on the site and the spin

$$\hat{H}_{\rm HF} = \sum_{i\sigma} \left(\varepsilon_d + \Delta_{i\sigma}\right)\hat{n}_{i\sigma} - t \sum_{\sigma} \left(c^\dagger_{1\sigma} c_{2\sigma} + c^\dagger_{2\sigma} c_{1\sigma}\right) - \Delta_0 \tag{76}$$

$$\Delta_0 = 2U \left(\frac{n^2}{4} - m_+^2 - m_-^2\right) \tag{77}$$

$$\Delta_{i\sigma} = U \left(\frac{1}{2} n - \sigma \left(m_+ + (-1)^{i-1} m_-\right)\right), \tag{78}$$

where $\sigma = +1$ for spin up and $\sigma = -1$ for spin down. Thus we can write immediately the local Green function matrix for site i. It is convenient to use the site basis, hence, to calculate the matrix $G^\sigma_{i,i'}(i\nu_n)$. Then we have

$$G^\sigma_{i,i}(i\nu_n) = \begin{pmatrix} i\nu_n - \left(\varepsilon_d - \mu + \Sigma^\sigma_{1,1}(i\nu_n)\right) & t \\ t & i\nu_n - \left(\varepsilon_d - \mu + \Sigma^\sigma_{2,2}(i\nu_n)\right) \end{pmatrix}^{-1}_{i,i} \tag{79}$$

where we introduced the diagonal self-energy matrix $\Sigma^\sigma_{i,i'}(i\nu_n) = \Delta_{i\sigma}\,\delta_{i,i'}$. This shows that the Hartree-Fock self-energy is not dependent on the frequency, i.e., Hartree-Fock is a *static* mean-field approach. The value of the parameters m_+ and m_- have to be found solving the *self-consistent equations*

$$\bar{n}_{i\sigma} = \langle \hat{n}_{i\sigma} \rangle = \frac{1}{\beta} \sum_n e^{-i\nu_n 0^-} G^\sigma_{i,i}(i\nu_n) = G^\sigma_{i,i}(0^-). \tag{80}$$

Since the exact ground state of the Hubbard dimer is a singlet, let us consider first the antiferromagnetic Hartree-Fock solution ($m_+{=}0$ and $m_-{\neq}0$). In this case, the Hartree-Fock self-energy depends on the site and the interaction couples states with different k. This becomes

clear rewriting the Green-function matrix in the basis of the bonding ($k = 0$) and anti-bonding ($k = \pi$) creation/annihilation operators

$$G^{\sigma}(i\nu_n) = \frac{1}{2}\begin{pmatrix} i\nu_n - \big(\varepsilon_d - t - \mu + \frac{1}{2}\sum_i \Sigma_{i\sigma}(i\nu_n)\big) & \frac{1}{2}\sum_i (-1)^{i-1}\Sigma_{i\sigma}(i\nu_n) \\ \frac{1}{2}\sum_i (-1)^{i-1}\Sigma_{i\sigma}(i\nu_n) & i\nu_n - \big(\varepsilon_d + t - \mu + \frac{1}{2}\sum_i \Sigma_{i\sigma}(i\nu_n)\big) \end{pmatrix}^{-1}. \quad (81)$$

The diagonal terms of the matrix $\Sigma^{\sigma}_{k,k'}(i\nu_n)$ are thus identical

$$\Sigma^{\sigma}_{0,0}(i\nu_n) = \Sigma^{\sigma}_{\pi,\pi}(i\nu_n) = \frac{1}{2}\big(\Sigma^{\sigma}_{1,1}(i\nu_n) + \Sigma^{\sigma}_{2,2}(i\nu_n)\big). \quad (82)$$

The off-diagonal terms $\Sigma^{\sigma}_{0,\pi}(i\nu_n)$ and $\Sigma^{\sigma}_{\pi,0}(i\nu_n)$ are not zero, however. This tells us that, by introducing the antiferromagnetic HF correction, we lower the symmetry of the system. Let us now calculate explicitly the eigenstates for different fillings. It is sufficient to diagonalize $\hat{H}_1$, the Hamiltonian in the 1-electron sector; the many-electron states can be obtained by filling the one-electron states respecting the Pauli principle. The Hamiltonian $\hat{H}_1$ can be written as $\hat{H}_1 = \hat{H}'_1 + \varepsilon_d \hat{N} - \Delta_0$, and, in the antiferromagnetic case we then have

$$\hat{H}'_1 = \begin{pmatrix} U\big(\frac{1}{2}n - m_-\big) & -t & 0 & 0 \\ -t & U\big(\frac{1}{2}n + m_-\big) & 0 & 0 \\ 0 & 0 & U\big(\frac{1}{2}n + m_-\big) & -t \\ 0 & 0 & -t & U\big(\frac{1}{2}n - m_-\big) \end{pmatrix}. \quad (83)$$

This leads to the (normalized) states

$\lvert 1\rangle_l$	$E_l(1)$
$\lvert 1\rangle_3 = a_2\lvert 1, 1/2, \uparrow\rangle_1 - a_1\lvert 1, 1/2, \uparrow\rangle_2$	$\varepsilon_0(1) + \Delta_1(t,U)$
$\lvert 1\rangle_2 = a_1\lvert 1, 1/2, \downarrow\rangle_1 - a_2\lvert 1, 1/2, \downarrow\rangle_2$	$\varepsilon_0(1) + \Delta_1(t,U)$
$\lvert 1\rangle_1 = a_1\lvert 1, 1/2, \uparrow\rangle_1 + a_2\lvert 1, 1/2, \uparrow\rangle_2$	$\varepsilon_0(1) - \Delta_1(t,U)$
$\lvert 1\rangle_0 = a_2\lvert 1, 1/2, \downarrow\rangle_1 + a_1\lvert 1, 1/2, \downarrow\rangle_2$	$\varepsilon_0(1) - \Delta_1(t,U)$

where $\varepsilon_0(1) = \varepsilon_d + U\big(1/2 + 2m_-^2 - n^2/2\big)$ and $a_1^2 = \frac{1}{2}\left(1 + \frac{Um_-}{\Delta_1(t,U)}\right)$, while $\Delta_1(t,U) = \sqrt{(m_- U)^2 + t^2}$. At half filling, if we assume that only the ground doublet is occupied, solving the self-consistent equations (80) yields

$$m_- = 0 \quad \text{or} \quad m_- = \frac{1}{2}\sqrt{1 - \frac{4t^2}{U^2}}\,. \quad (84)$$

As a result, for the non-trivial solution ($m_- \neq 0$), the gap at half filling is $E_g^{\mathrm{HF}} = 2\Delta_1(t,U) = U$. In Fig. 6, Hartree-Fock and exact spectral function are compared for a specific parameter choice. Looking at the size of the gap only, one could naively infer that, for the case shown, Hartree-Fock is an excellent approximation, better than DMFT (see Fig. 3, top-right panel). This would

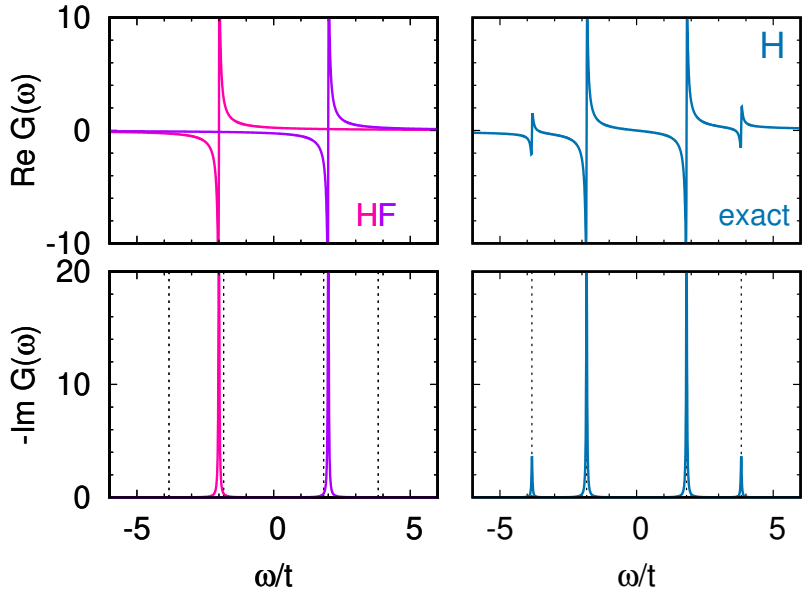


Fig. 6: *Local retarded Green function $G^\sigma(\omega)$ of the Hubbard dimer ($t = 1, U = 4$) at half filling and in the zero temperature limit. Left: Antiferromagnetic Hartree-Fock (HF) approximation; green and violet distinguish $G^\uparrow(\omega)$ and $G^\downarrow(\omega)$ at a given site. Right: Exact local Green function, for which $G^\uparrow(\omega) = G^\downarrow(\omega)$. Dashed lines: Poles of the exact local Green function.*

be, however, the wrong conclusion. Although, due to the small coordination number, in this specific case, DMFT indeed sizably underestimates the gap, it nevertheless captures the essential nature of the ground state. Instead, while HF, in this specific case,[6] gives an almost exact gap, it does it via a qualitatively incorrect description (antiferromagnetic instead of singlet ground state). Increasing the coordination number, DMFT approaches the exact solution both in the paramagnetic and magnetic phase, while HF does not. Let us analyze in more detail the differences between the HF approximation and the exact solution of the Hubbard dimer. The HF Hamiltonian for two electrons is given by $\hat{H}_2 = \hat{H}_2' + \varepsilon_d \hat{N} - \Delta_0$, and

$$\hat{H}_2' = \begin{pmatrix} U & 0 & 0 & -2Um_- & 0 & 0 \\ 0 & U(1-2m_+) & 0 & 0 & 0 & 0 \\ 0 & 0 & U(1+2m_+) & 0 & 0 & 0 \\ -2Um_- & 0 & 0 & U & -\sqrt{2}t & -\sqrt{2}t \\ 0 & 0 & 0 & -\sqrt{2}t & U & 0 \\ 0 & 0 & 0 & -\sqrt{2}t & 0 & U \end{pmatrix} . \quad (85)$$

[6] In real materials the Hartree-Fock approximation often overestimates the size of the gap, however.

For m_+=0 and $m_- \neq 0$ (antiferromagnetic solution) the eigenvalues and eigenvectors are

$\|2\rangle_l$	$E_l(2)$
$\|2\rangle_5 = \frac{1}{\sqrt{2}}\Big(\|2,0,0\rangle_0 + a_2\|2,1,0\rangle - \frac{a_1}{\sqrt{2}}\big(\|2,0,0\rangle_1 + \|2,0,0\rangle_2\big)\Big)$	$\varepsilon_0(2) + 2\Delta_1(t,U)$
$\|2\rangle_4 = \frac{1}{\sqrt{2}}\big(\|2,0,0\rangle_1 - \|2,0,0\rangle_2\big)$	$\varepsilon_0(2)$
$\|2\rangle_3 = \|2,1,1\rangle$	$\varepsilon_0(2)$
$\|2\rangle_2 = \|2,1,-1\rangle$	$\varepsilon_0(2)$
$\|2\rangle_1 = a_1\|2,1,0\rangle + a_2\frac{1}{\sqrt{2}}\big(\|2,0,0\rangle_1 + \|2,0,0\rangle_2\big)$	$\varepsilon_0(2)$
$\|2\rangle_0 = \frac{1}{\sqrt{2}}\Big(\|2,0,0\rangle_0 - a_2\|2,1,0\rangle + \frac{a_1}{\sqrt{2}}\big(\|2,0,0\rangle_1 + \|2,0,0\rangle_2\big)\Big)$	$\varepsilon_0(2) - 2\Delta_1(t,U)$

where $\varepsilon_0(2)$=$2\varepsilon_d + U\big(1+2m_-^2 - n^2/2\big)$, and $a_1^2 = t^2/\Delta_1^2(t,U)$. The antiferromagnetic Hartree-Fock ground state has an overlap with the correct ground state, however incorrectly mixes triplet and singlet states, thus breaking the rotational symmetry of the model. For this reason, its energy, in the large U limit, is $2\varepsilon_d - 2t^2/U$ and not $2\varepsilon_d - 4t^2/U$ as in the exact case.
For the ferromagnetic solution of the Hartree-Fock equations (m_-=0 and $m_+ \neq 0$) the eigenvalues and eigenvectors are instead

$\|2\rangle_l$	$E_l(2)$
$\|2\rangle_5 = \|2,1,-1\rangle$	$\varepsilon_0^+(2) + 2Um_+$
$\|2\rangle_4 = \frac{1}{\sqrt{2}}\Big(\|2,0,0\rangle_0 - \frac{1}{\sqrt{2}}\big(\|2,0,0\rangle_1 + \|2,0,0\rangle_2\big)\Big)$	$\varepsilon_0^+(2) + 2t$
$\|2\rangle_3 = \frac{1}{\sqrt{2}}\big(\|2,0,0\rangle_1 - \|2,0,0\rangle_2\big)$	$\varepsilon_0^+(2)$
$\|2\rangle_2 = \|2,1,\ \ 0\rangle$	$\varepsilon_0^+(2)$
$\|2\rangle_1 = \frac{1}{\sqrt{2}}\Big(\|2,0,0\rangle_0 + \frac{1}{\sqrt{2}}\big(\|2,0,0\rangle_1 + \|2,0,0\rangle_2\big)\Big)$	$\varepsilon_0^+(2) - 2t$
$\|2\rangle_0 = \|2,1,\ \ 1\rangle$	$\varepsilon_0^+(2) - 2Um_+$

where $\varepsilon_0^+(2)$=$2\varepsilon_d + U(1 + 2m_+^2 - n^2/2)$. The ferromagnetic Hartree-Fock correction thus yields an incorrect sequence of levels; the ground state for large U/t, indicated as $|2\rangle_0$ in the table, has no overlap with the exact ground state of the Hubbard dimer. It is, instead, one of the states of the first excited triplet. An important observation is that, despite the errors, the energy difference between ferro- and antiferro-magnetic ground state is

$$E_{\rm F} - E_{\rm AF} \sim \frac{2t^2}{U}, \tag{86}$$

which is indeed the correct value in the small t/U limit. It does not correspond, however, to the actual singlet-triplet excitation energy, $\Gamma \sim 4t^2/U$.

We can now directly compare the **Hartree-Fock** and the **dynamical mean-field approximation** for the two-site Hubbard model. Both approaches are based on the solution of self-consistent mean-field-type equations, and therefore they are both mean-field methods. In Hartree-Fock the self-energy is frequency-independent (static), while in DMFT depends on the frequency (dynamical). In Hartree-Fock the self-energy can be site-dependent, as we have seen in the antiferromagnetic case. In DMFT, allowing for a site-dependent self-energy leads to cluster or cluster-like extensions of the method. If the same unit cell is used in DMFT and Hartree-Fock, we can identify another relation between the two methods. In the infinite-frequency limit, the DMFT self-energy equals the Hartree-Fock self-energy. This can be shown analytically in a simple way. For the case of the two-site Hubbard model, the expansion of the local lattice Green function at high frequency in the local-self-energy approximation is

$$G^\sigma_{i,i}(i\nu_n) = \frac{1}{i\nu_n} - \frac{\big(\mu - \varepsilon_d - \Sigma^\sigma_l(\infty)\big)}{(i\nu_n)^2} + \mathcal{O}\bigg(\frac{1}{(i\nu_n)^3}\bigg). \tag{87}$$

Instead, the expansion of the impurity Green-function can be written as

$$\begin{aligned} G^\sigma_{d,d}(i\nu_n) &= \int_0^\beta d\tau\, e^{i\nu_n\tau} G^\sigma_{d,d}(\tau) \\ &= \frac{1}{i\nu_n}\int_0^\beta d\tau \frac{de^{i\nu_n\tau}}{d\tau} G^\sigma_{d,d}(\tau) = \frac{1}{i\nu_n}\bigg(- G^\sigma_{d,d}(\beta^-) - G^\sigma_{d,d}(0^+) - \int_0^\beta d\tau\, e^{i\nu_n\tau}\frac{dG^\sigma_{d,d}(\tau)}{d\tau}\bigg) \\ &= \frac{1}{i\nu_n} + \frac{1}{(i\nu_n)^2}\bigg(\frac{dG^\sigma_{d,d}(\tau)}{d\tau}\bigg|_{\beta^-} + \frac{dG^\sigma_{d,d}(\tau)}{d\tau}\bigg|_{0^+} + \int_0^\beta d\tau\, e^{i\nu_n\tau}\frac{d^2G^\sigma_{d,d}(\tau)}{d\tau^2}\bigg) \\ &= \frac{1}{i\nu_n} + \frac{\frac{dG^\sigma_{d,d}(\tau)}{d\tau}\Big|_{\beta^-} + \frac{dG^\sigma_{d,d}(\tau)}{d\tau}\Big|_{0^+}}{(i\nu_n)^2} + \mathcal{O}\bigg(\frac{1}{(i\nu_n)^3}\bigg) \end{aligned} \tag{88}$$

where

$$\frac{dG^\sigma_{d,d}(\tau)}{d\tau}\bigg|_{\beta^-} + \frac{dG^\sigma_{d,d}(\tau)}{d\tau}\bigg|_{0^+} = -\bigg\langle\Big\{\big[\hat{H}_A - \mu\hat{N},\, c_{d\sigma}\big],\, c^\dagger_{d\sigma}\Big\}\bigg\rangle = -\mu + \varepsilon_d + U\langle\hat{n}_{-\sigma}\rangle. \tag{89}$$

From this result we can conclude that, assuming self-consistency has been reached,

$$\Sigma^\sigma_l(\infty) = U\langle\hat{n}_{-\sigma}\rangle. \tag{90}$$

This is exactly the Hartree-Fock expression of the self-energy that we found earlier, and indeed equals the **infinite-frequency limit** of the DMFT self-energy we previously calculated; however, the occupations $\langle\hat{n}_{-\sigma}\rangle$ in DMFT and Hartree-Fock calculations are typically not the same. In the case of the dimer, DMFT yields $\langle\hat{n}_{-\sigma}\rangle{=}1/2$; this would correspond in Hartree-Fock to a (trivial) solution in which the self-energy merely shifts all the energy levels by the same amount, and has therefore no relevant effects. These conclusions also apply to the LDA+U method, which is based on the Hartree-Fock treatment of the local Coulomb interaction. A more detailed discussion of differences and relation between the LDA+U and LDA+DMFT method can be found in my chapter in Ref. [14].

2.5 DMFT for the one-band Hubbard model

The Hubbard Hamiltonian (8) is in principle the simplest model for the description of the Mott metal-insulator transition. In the tight-binding approximation it becomes

$$\hat{H} = \varepsilon_d \sum_{\sigma i} \hat{n}_{i\sigma} - t \sum_{\sigma \langle ii' \rangle} c^\dagger_{i\sigma} c_{i'\sigma} + U \sum_i \hat{n}_{i\uparrow} \hat{n}_{i\downarrow}, \tag{91}$$

where $\langle ii' \rangle$ is a sum over first neighbors. As discussed in the introduction, for $U{=}0$, at half-filling, this Hamiltonian describes a metallic band. For $t{=}0$ it describes an insulating collection of disconnected atoms. Somewhere in between, at a critical value of t/U, a metal to insulator transition must occur. In this section we will discuss the DMFT solution of (91) and the picture of the metal-insulator transition emerging from it. The first step consists in mapping the original many-body Hamiltonian into an effective quantum-impurity model, such as the Anderson Hamiltonian

$$\hat{H}^A = \underbrace{\sum_{\boldsymbol{k}\sigma} \varepsilon^s_{\boldsymbol{k}} \hat{n}_{\boldsymbol{k}\sigma}}_{\hat{H}_{\rm bath}} + \underbrace{\sum_{\boldsymbol{k}\sigma} \left(V^s_{\boldsymbol{k}} c^\dagger_{\boldsymbol{k}\sigma} c_{d\sigma} + \text{h.c.} \right)}_{\hat{H}_{\rm hyb}} + \underbrace{\varepsilon_d \sum_\sigma \hat{n}_{d\sigma} + U \hat{n}_{d\uparrow} \hat{n}_{d\downarrow}}_{\hat{H}_{\rm imp}}. \tag{92}$$

In this model the on-site Coulomb repulsion U appears only in the impurity Hamiltonian, $\hat{H}_{\rm imp}$, while the terms $\hat{H}_{\rm bath}$ and $\hat{H}_{\rm hyb}$, describe, respectively, the bath and the bath-impurity hybridization. In the next step, the quantum-impurity model is solved. Differently from the case of the Anderson molecule, this cannot be done analytically. It requires non-perturbative numerical methods, such as exact diagonalization, the numerical renormalization group, density-matrix renormalization group or QMC. Here we describe the DMFT self-consistency loop for a QMC quantum-impurity solver. Solving the quantum-impurity model yields the impurity Green function $G^\sigma_{d,d}(i\nu_n)$. From the impurity Dyson equation we can calculate the impurity self-energy

$$\Sigma^\sigma_A(i\nu_n) = \left(G^{0\sigma}_{d,d}(i\nu_n)\right)^{-1} - \left(G^\sigma_{d,d}(i\nu_n)\right)^{-1}. \tag{93}$$

Next, we adopt the local self-energy approximation, i.e., we assume that the self-energy of the Hubbard model equals the impurity self-energy. Then, the local Green function is given by

$$G^\sigma_{i_c,i_c}(i\nu_n) = \frac{1}{N_{\boldsymbol{k}}} \sum_{\boldsymbol{k}} \frac{1}{i\nu_n + \mu - \varepsilon_{\boldsymbol{k}} - \Sigma^\sigma_A(i\nu_n)}, \tag{94}$$

where $N_{\boldsymbol{k}}$ is the number of $\boldsymbol{k}$ points. The local Dyson equation is used once more, this time to calculate the bath Green function $\mathcal{G}^\sigma(i\nu_n)$, which in turn defines a new quantum-impurity model. This procedure is repeated until self-consistency is reached, i.e., the number of electrons is correct and the self-energy does not change anymore (within a given numerical accuracy). In this situation we have

$$G^\sigma_{i_c,i_c}(i\nu_n) \sim G^\sigma_{d,d}(i\nu_n). \tag{95}$$

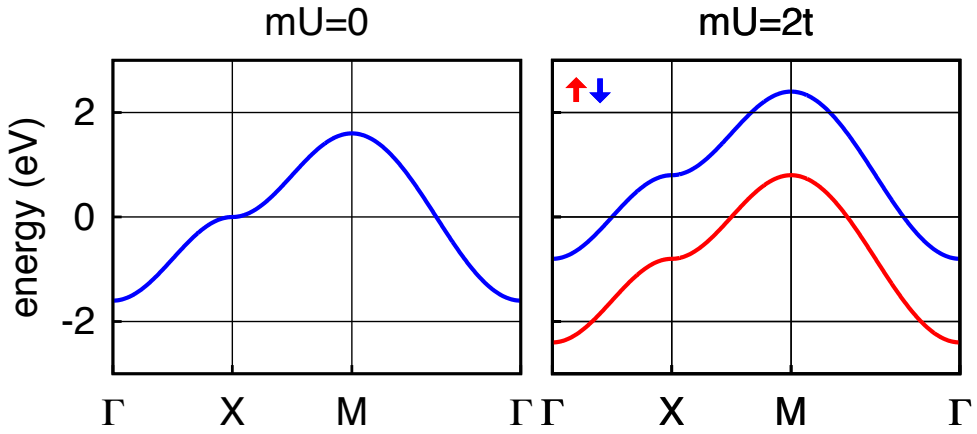


Fig. 7: *The metal-insulator transition in ferromagnetic Hartree-Fock. The calculation is for a square lattice tight-binding model with dispersion* $\varepsilon_{\boldsymbol{k}} = -2t(\cos k_x + \cos k_y)$.

It is important to underline that self-consistency is key to the success of DMFT in describing the metal-to-insulator transition. This can, perhaps, be best understood looking once more at the effects of self-consistency in a simpler approach, the static mean-field Hartree-Fock method.[7] If we chose the same primitive cell as in DMFT, the Hartree-Fock self-energy matrix is

$$\Sigma^{\sigma}_{i,i'}(i\nu_n) = U\left(\frac{n}{2} - \sigma m\right)\delta_{i,i'}, \tag{96}$$

where $\sigma = +1$ for spin up and $\sigma = -1$ for spin down and $m{=}m_+{=}(n_\uparrow - n_\downarrow)/2$, with $n_\sigma{=}n_{i\sigma}$. The approximation is then identical to replacing the Hubbard Hamiltonian with

$$\hat{H}_{\rm HF} = \sum_{\boldsymbol{k}\sigma}\left[\varepsilon_{\boldsymbol{k}} + U\left(\frac{1}{2} - \sigma m\right)\right]\hat{n}_{\boldsymbol{k}\sigma}. \tag{97}$$

This shows that $h_{\rm eff}{=}2Um$ plays the role of an effective magnetic field (Weiss field). The self-consistency criterion is

$$\bar{n}_\sigma = \bar{n}_{i\sigma} = \langle\hat{n}_{i\sigma}\rangle_{\rm HF}\,, \tag{98}$$

where the expectation value $\langle\hat{n}_{i\sigma}\rangle_{\rm HF}$ is calculated using the Hamiltonian $\hat{H}_{\rm HF}$, which in turn depends on $\bar{n}_\sigma$ via m. This gives the self-consistency equation

$$m = \frac{1}{2}\frac{1}{N_{\boldsymbol{k}}}\sum_{\boldsymbol{k}\sigma}\frac{\sigma e^{-\beta(\varepsilon_{\boldsymbol{k}}+U(\frac{1}{2}-\sigma m)-\mu)}}{1+e^{-\beta(\varepsilon_{\boldsymbol{k}}+U(\frac{1}{2}-\sigma m)-\mu)}}\,. \tag{99}$$

If we set $m{=}0$ the equation is satisfied; for such a trivial solution the static mean-field correction in Eq. (97) merely redefines the chemical potential and has therefore no effect. For sufficiently large U, however, a non-trivial solution ($m \neq 0$) can be found. If $m \neq 0$ the spin up and spin down bands split, and eventually a gap can open. This is shown in Fig. 7. The static mean-field correction in Eq. (97) equals the contribution of the Hartree diagram to the self-energy, $\Sigma^{\sigma}_{\rm H}(i\nu_n){=}U\bar{n}_{-\sigma}$. In many-body perturbation theory, however, $\bar{n}_\sigma{=}1/2$, i.e., $m{=}0$.

[7] Keeping in mind that many self-consistent solutions obtained with the Hartree-Fock method are spurious.

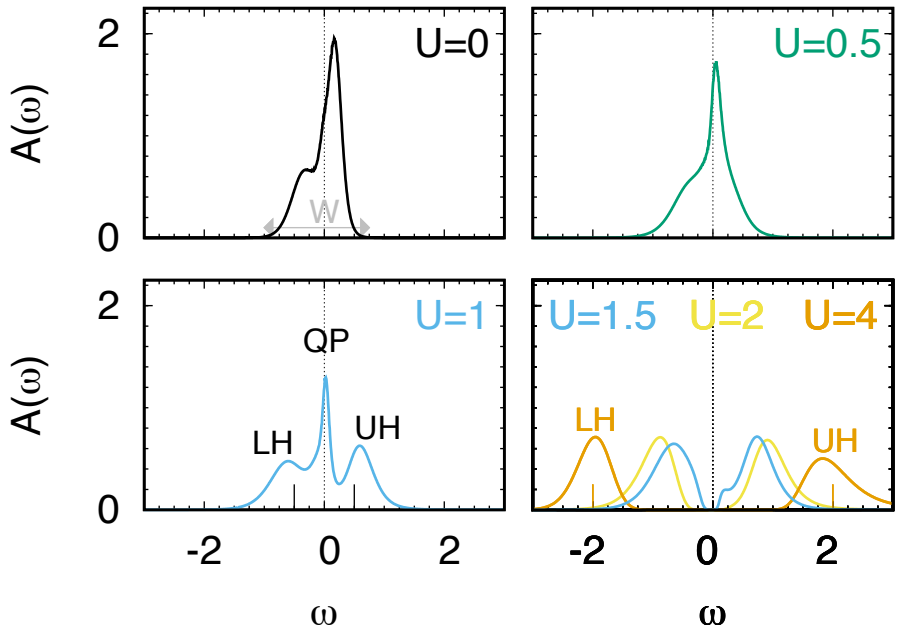


Fig. 8: *$VOMoO_4$: LDA+DMFT spectral function at finite temperature for $0 \leq U \leq 4$. Energies are in eV and spectral functions in states/spin/eV. The calculations have been done using a continuous-time hybridization-expansion QMC solver [13]. A detailed LDA+DMFT study of the electronic and magnetic properties of $VOMoO_4$ can be found in Ref. [15].*

In the self-consistent static mean-field approximation, instead, m can differ from zero, and a phenomenon not described by the mere Hartree diagram can be captured, ferromagnetism in a correlated metal. If mU is larger than the bandwidth, the system can even become an insulator. In DMFT the role of the Weiss mean field is played by the bath Green function $\mathcal{G}^{\sigma}_{i,i}(i\nu_n)$. The emerging picture of the Mott transition is described in Fig. 8 for a representative single-band material. In the $U{=}0$ limit, the spectral function $A_0(\omega)$ is metallic at half filling (top left panel). For finite U, if we set $\Sigma^{\sigma}_A(\omega){=}0$ as initial guess, the DMFT self-consistency loop starts with $A(\omega){=}A_0(\omega)$. For small U/t, the *converged* spectral function $A(\omega)$ is still similar to $A_0(\omega)$. This can be seen comparing the $U{=}0.5$ and $U{=}0$ panels in Fig. 8. Further increasing U/t, sizable spectral weight is transferred from the zero-energy quasi-particle peak to the lower (LH) and upper (UH) Hubbard bands, centered at $\omega \sim \pm U/2$. This can be observed in the $U = 1$ panel of Fig. 8. The system is still metallic, but with strongly renormalized masses and short lifetimes, reflected in the narrow quasi-particle (QP) peak. Finally, for U larger than a critical value ($U \geq 1.5$ in the figure) a gap opens and the system becomes a Mott insulator. When this happens the self-energy diverges at low frequency, where

$$\Sigma^{\sigma}_A(\omega + i0^+) \sim \frac{U}{2} + \frac{U^2}{4}\frac{a(t,U)}{\omega + i0^+}. \tag{100}$$

In the large U/t limit the gap increases linearly with the Coulomb repulsion, i.e., $E_g(1) \sim U{-}W$, where W is the bandwidth.

2.6 DMFT for multi-orbital models

The multi-orbital Hubbard-like Hamiltonian has the form

$$\hat{H} = \hat{H}_0 + \hat{H}_U \tag{101}$$

$$\hat{H}_0 = -\sum_{ii'}\sum_{\sigma\sigma'}\sum_{mm'} t^{i,i'}_{m\sigma,m'\sigma'}\, c^\dagger_{im\sigma} c_{i'm'\sigma'} \tag{102}$$

$$\hat{H}_U = \frac{1}{2}\sum_{i}\sum_{\sigma\sigma'}\sum_{mm'}\sum_{pp'} U_{mpm'p'}\, c^\dagger_{im\sigma} c^\dagger_{ip\sigma'} c_{ip'\sigma'} c_{im'\sigma}, \tag{103}$$

where m, m' and p, p' are different orbitals and the Coulomb tensor is local. The DMFT approach can be extended to solve models of this form, mapping them to multi-orbital quantum-impurity models. The main changes with respect to the formalism introduced in the previous section are then the following

$$\varepsilon_{\boldsymbol{k}} \to (H_{\boldsymbol{k}})_{m\sigma,m'\sigma'} \qquad (i\nu_n+\mu) \to (i\nu_n+\mu)\,\hat{1}_{m\sigma,m'\sigma'}$$

$$t^{i,i'} \to t^{i,i'}_{m\sigma,m'\sigma'} \qquad \varepsilon_d \to \varepsilon^{i,i'}_{m\sigma,m'\sigma'} = -t^{i,i}_{m\sigma,m'\sigma'}$$

where $\hat{1}$ is the identity matrix. As a consequence, the local Green function, the bath Green function, the hybridization function, and the self-energy also become matrices

$$\mathcal{G}^\sigma(i\nu_n) \to \mathcal{G}^{\sigma,\sigma'}_{m,m'}(i\nu_n) \qquad G^\sigma(i\nu_n) \to G^{\sigma,\sigma'}_{m,m'}(i\nu_n) \qquad \Sigma^\sigma(i\nu_n) \to \Sigma^{\sigma,\sigma'}_{m,m'}(i\nu_n).$$

The corresponding generalization of the self-consistency loop is shown schematically in Fig. 9. Although the extension of DMFT to Hubbard models with many orbitals might appear straightforward, in practice it is not. The bottleneck is the solution of the generalized multi-orbital quantum-impurity problem. The most flexible solvers available so far are all based on QMC. Despite being flexible, QMC-based approaches have limitations. These can be classified in two types. First, with increasing the number of degrees of freedom, calculations become very quickly computationally too expensive—how quickly depends on the specific QMC algorithm used and the actual implementation. Thus, typically, going beyond a limited number of orbitals and reaching the zero-temperature limit is unfeasible in practice. The second type of limitation is more severe. Increasing the number of degrees of freedom leads, eventually, to the infamous sign problem; when this happens, QMC calculations cannot be performed at all. In order to deal with limitations of the first type, it is crucial to restrict QMC calculations to the essential degrees of freedom; furthermore, we should exploit symmetries, develop fast algorithms and use the power of massively-parallel supercomputers to reduce the actual computational time. For the second type of problems not a lot can be done; nevertheless, it has been shown that a severe sign problem might appear earlier with some basis choices than with others [13]. Although eventually we cannot escape it, this suggests that the model set up can be used as a tool to expand the moderate sign-problem zone. For what concerns symmetries, in the paramagnetic case and in absence of spin-orbit interaction or external fields, an obvious symmetry to exploit

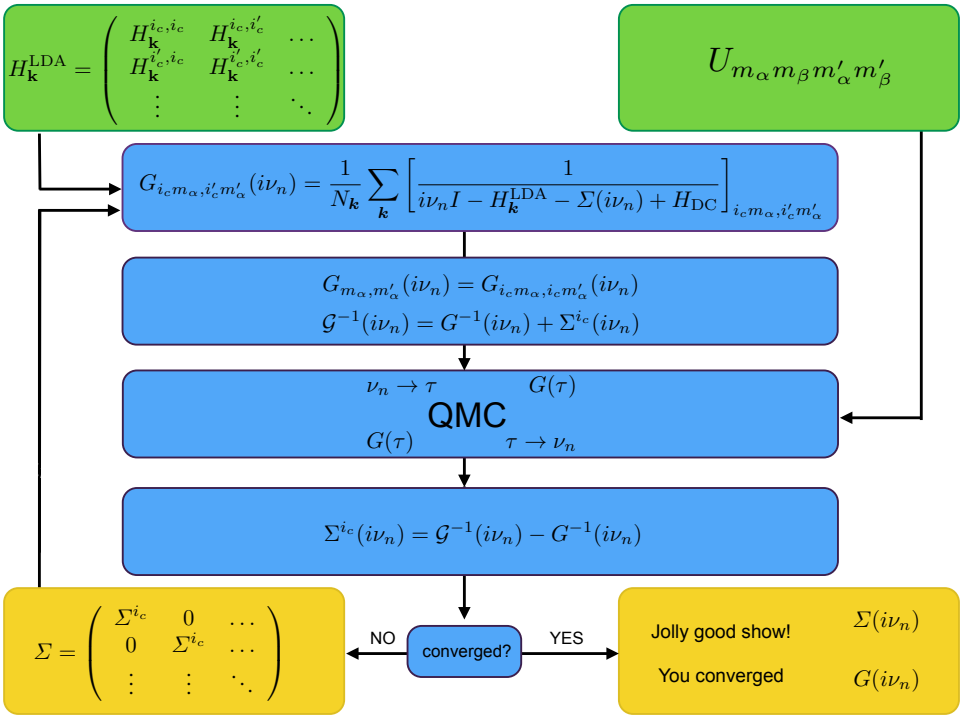


Fig. 9: *LDA+DMFT self-consistency loop. The one-electron Hamiltonian is built in the basis of Bloch states obtained from localized Wannier functions, for example in the local-density approximation (LDA); this gives* $H^{\rm LDA}_{\boldsymbol{k}}$. *The set* $\{i_c\}$ *labels the equivalent correlated sites inside the unit cell. The local Green-function matrix is at first calculated using an initial guess for the self-energy matrix. The bath Green-function matrix is then obtained via the Dyson equation and used to construct an effective quantum-impurity model. The latter is solved via a quantum-impurity solver, here quantum Monte Carlo (QMC). This yields the impurity Green-function matrix. Through the Dyson equation the self-energy is then obtained, and the procedure is repeated until self-consistency is reached.*

is the rotational invariance of spins, from which follows

$$A^{\sigma,\sigma'}_{m,m'}(i\nu_n) = \delta_{\sigma,\sigma'}\, A_{m,m'}(i\nu_n), \tag{104}$$

where $A = \mathcal{G}, G, \Sigma$. In addition, if we use a basis of real functions, the local Green-function matrices are real and symmetric in imaginary time τ, hence

$$A^{\sigma,\sigma'}_{m,m'}(i\nu_n) = \delta_{\sigma,\sigma'}\, A_{m,m'}(i\nu_n) = \delta_{\sigma,\sigma'}\, A_{m',m}(i\nu_n). \tag{105}$$

Finally, often the unit cell contains several equivalent correlated sites, indicated as $\{i_c\}$ in Fig. 9. In order to avoid expensive cluster calculations, we can use space-group symmetries to construct the matrices $\mathcal{G}, G, \Sigma$ at a given site i'_c from the corresponding matrices at an equivalent site, e.g., $i_c = 1$. Space-group symmetries also tell us if some matrix elements are zero. For example, for a model with only t_{2g} (or only e_g) states, in cubic symmetry, in the paramagnetic case and in absence of spin-orbit interaction or external fields, we have

$$A^{\sigma,\sigma'}_{m,m'}(i\nu_n) = \delta_{\sigma,\sigma'}\, A_{m,m}(i\nu_n)\, \delta_{m,m'}. \tag{106}$$

3 Building materials-specific many-body models

3.1 Model construction

How do we build realistic Hubbard-like models for correlated materials? The state-of-the art approach relies on constructing, for a given system, *materials-specific* Kohn-Sham Wannier functions $\varphi^{\rm KS}_{im\sigma}(\boldsymbol{r})$. These can be obtained via electronic structure calculations based on density-functional theory [8–10], e.g., in the LDA approximation.[8] After we constructed the complete one-electron basis, the first steps in model-building are those described in the introduction. We recall here the essential points and then discuss the next stage. The many-body Hamiltonian can be expressed as $\hat{H} = \hat{H}_0 + \hat{H}_U - \hat{H}_{\rm DC}$, with $\hat{H}_0 = \hat{H}^{\rm LDA}$ and

$$\hat{H}_0 = -\sum_{ii'}\sum_{\sigma\sigma'}\sum_{mm'} t^{i,i'}_{m\sigma,m'\sigma'} c^\dagger_{im\sigma} c_{i'm'\sigma'}, \tag{107}$$

$$\hat{H}_U = \frac{1}{2}\sum_{ii'jj'}\sum_{\sigma\sigma'}\sum_{mm'pp'} U^{iji'j'}_{mp\,m'p'} c^\dagger_{im\sigma} c^\dagger_{jp\sigma'} c_{j'p'\sigma'} c_{i'm'\sigma}. \tag{108}$$

The hopping integrals in $\hat{H}_0$ are calculated replacing the electron-nuclei interaction, $v_{\rm en}(\boldsymbol{r})$, with the self-consistent DFT reference potential, $v_{\rm R}(\boldsymbol{r}) = v_{\rm en}(\boldsymbol{r}) + v_{\rm H}(\boldsymbol{r}) + v_{\rm xc}(\boldsymbol{r})$, defined in Eq. (5). The latter includes the long-range Hartree term, $v_{\rm H}(\boldsymbol{r})$, and the exchange-correlation contribution, $v_{\rm xc}(\boldsymbol{r})$; to avoid including the *effects* of these terms twice, we thus introduce the double-counting correction, $\hat{H}_{\rm DC}$, so that

$$\hat{H}_U \to \Delta\hat{H}_U = \hat{H}_U - \hat{H}_{\rm DC}.$$

Unfortunately we do not know which important correlation effects are included in $\hat{H}_0$ via $v_{\rm R}(\boldsymbol{r})$, and therefore the exact expression of $\Delta\hat{H}_U$ is also unknown. The remarkable successes of the LDA suggest, however, that in many materials the LDA is overall a good approximation, and therefore, in those systems at least, the term $\Delta\hat{H}_U$ can be completely neglected. What about strongly-correlated materials? Even in correlated systems, most likely, the LDA works rather well for the delocalized electrons or in describing the average or the long-range Coulomb effects. Thus one can think of separating the electrons into two categories: *uncorrelated* (or light) and *correlated* (or heavy); only for the latter we do take the correction $\Delta\hat{H}_U$ into account explicitly, assuming furthermore that $\Delta\hat{H}_U$ is local or almost local [8], since we know that it is the local term which is responsible for most non-trivial many-body effects. Typically, correlated electrons are those that partially retain their atomic character, e.g., those that originate from localized d and f shells; for convenience, here we assume that in a given system they stem from a single atomic shell l (e.g., d for transition-metal oxides or f for heavy-fermion systems) and label their states with the atomic quantum numbers l and $m = -l, \ldots, l$ of that shell. Thus

$$U^{iji'j'}_{mp\,m'p'} \sim \begin{cases} U^l_{mp\,m'p'} & iji'j' = iiii \quad \wedge \quad mp, m'p' \in l \\ 0 & iji'j' \neq iiii \quad \vee \quad mp, m'p' \notin l. \end{cases}$$

[8] Using GGA or similar functionals in place of LDA yields minor differences in the many-body Hamiltonian; on the other hand, using LDA+U or similar approximations yields Hartree-Fock-like effects that would have to be subtracted via the double-counting correction.

Within this approximation $\Delta\hat{H}_U$ is replaced by $\Delta\hat{H}^l_U = \hat{H}^l_U - \hat{H}^l_{\rm DC}$, where $\hat{H}^l_{\rm DC}$ is, e.g., given by the static mean-field contribution of $\hat{H}^l_U$. There is a drawback in this procedure, however. By splitting electrons into light and heavy, we implicitly assume that the main effect of the latter is the renormalization or *screening* of parameters for the former, in particular of the Coulomb interaction. The computation of screening effects remains, unfortunately, a challenge. The calculation of exact screening would require the solution of the original many-body problem, taking all degrees of freedom into account, an impossible task. Commonly-used approximate schemes are the constrained LDA approximation (cLDA) and the constrained random-phase approximation (RPA) [8–10]. Both methods give reasonable estimates of screened Coulomb parameters for DMFT calculations. Typically cRPA calculations include more screening channels and are performed for less localized bases than cLDA calculations; thus cRPA parameters turn out to be often smaller than cLDA ones. To some extent, the difference can be taken as an estimate of the error bar.

After we have selected the electrons for which we think it is necessary to include explicitly the Hubbard correction, in order to build the final Hamiltonian for DMFT calculations, it is often convenient to integrate out or *downfold*, in part or completely, the weakly correlated states. There are different degrees of downfolding. The two opposite extreme limits are (i) *no downfolding*, i.e., keeping explicitly in the Hamiltonian all weakly-correlated states (ii) *massive downfolding*, i.e., downfold all weakly correlated states. If we perform massive downfolding, e.g., downfold to the d (or e_g or t_{2g}) bands at the Fermi level, the Hamiltonian relevant for DMFT takes a simpler form. The LDA part is limited to the selected orbitals or bands, which, in the ideal case, are decoupled from the rest

$$\hat{H}^{\rm LDA} = -\sum_{ii'}\sum_{\sigma\sigma'}\sum_{m_\alpha m'_\alpha} t^{i,i'}_{m_\alpha\sigma,m'_\alpha\sigma'}\, c^\dagger_{im_\alpha\sigma}\, c_{i'm'_\alpha\sigma'}. \tag{109}$$

The local *screened* Coulomb interaction for this set of orbitals is the on-site tensor

$$\hat{H}^l_U = \frac{1}{2}\sum_{i}\sum_{\sigma\sigma'}\sum_{m_\alpha m'_\alpha}\sum_{m_\beta m'_\beta} U_{m_\alpha m_\beta m'_\alpha m'_\beta}\, c^\dagger_{im_\alpha\sigma} c^\dagger_{im_\beta\sigma'} c_{im'_\beta\sigma'} c_{im'_\alpha\sigma}. \tag{110}$$

It is important to point out that the level of downfolding does not modify the hardness of the quantum-impurity problem. If, for example, in studying a transition-metal oxide, we plan to treat only $3d$ bands as correlated, it does not matter if we perform calculations with a Hamiltonian containing also, e.g., O p states, or we rather downfold all states but the $3d$ and work with a set of Wannier basis spanning the $3d$-like bands only. The number of correlated orbitals in the quantum-impurity problem is the same.[9]

One advantage of massive downfolding is that the double-counting correction typically becomes a shift of the chemical potential, and it is therefore not necessary to calculate it explicitly. A second important advantage is that the interpretation of the final results is simpler. Instead, a disadvantage is that the basis functions are less localized, and therefore the approximation of the Coulomb interaction to a local operator might be less justified, and in some cases it might be

[9] The choice might influence how severe the QMC sign problem is, however.

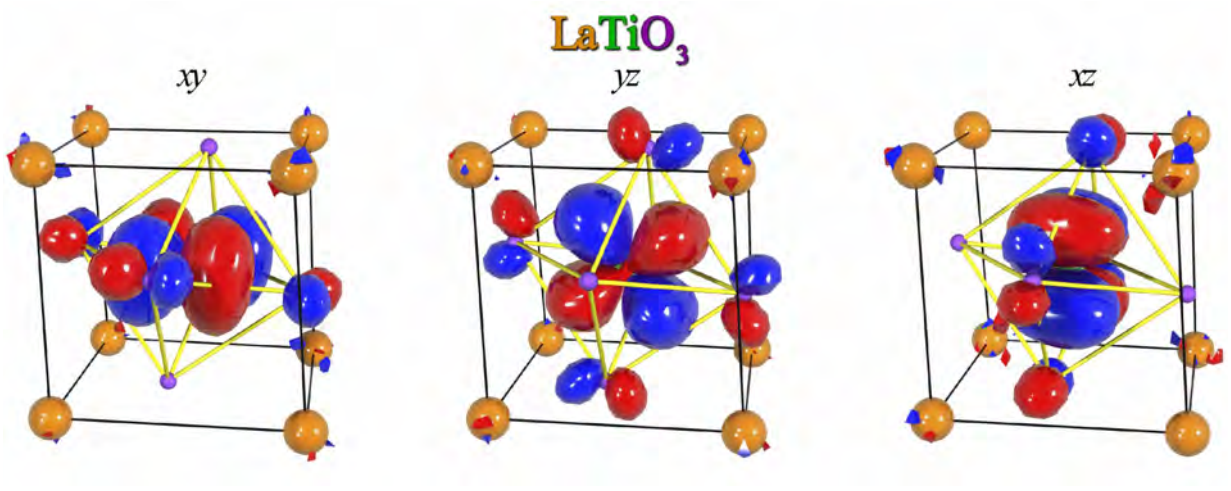


Fig. 10: *NMTO Wannier-like orbitals for t_{2g} states in $LaTiO_3$ obtained via massive downfolding to the t_{2g} bands. The t_{2g}-like orbitals have O p tails at the neighboring O sites reflecting the distortions of the lattice. The figure has been taken from Ref. [16].*

necessary to include non-local Coulomb terms. The effect of downfolding on the localization of Wannier functions is illustrated for example in Fig. 10. Finally, another disadvantage of massive downfolding is that the energy window in which the model is valid is more narrow.

Considering all advantages and disadvantages, what is then the best way of performing DMFT calculations? There is no universal answer to this question; it depends on the problem we are trying to solve and the system we are studying. Independently of the degree of downfolding we choose, it is important to point out that a clear advantage of Wannier functions in general is that they carry information about the lattice, bonding, chemistry and distortions. This can be seen once more in Fig. 10, where orbitals are tilted and deformed by the actual structure and chemistry of the compound. Indeed, one might naively think of using a "universal" basis, for example atomic functions, the same for all systems, and thus calculating the hopping integrals using simply the electron-nuclei interaction $v_{en}(\boldsymbol{r})$. Besides the complications arising from the lack of orthogonality, such a basis has no built-in materials-specific information, except lattice positions. It is therefore a worse starting point to describe the electronic structure, even in the absence of correlations; larger basis sets are required to reach the same accuracy. From the point of view of LDA+DMFT, an advantage of a universal basis would be that it is free from double-counting corrections; on the other hand, however, exactly because we do not use the LDA potential and LDA orbitals to calculate the hopping integrals, we also cannot count on the successes of LDA in the description of average and long-range Coulomb effects. For these reasons *ab-initio* Wannier functions remain so far the basis of choice. They can be built via the Nth-Order Muffin-Tin Orbital (NMTO) method [16], the maximal-localization scheme [17], or projectors. Fig. 10 shows examples of NMTO-based Wannier functions.

3.2 Localization of the basis and range of the Coulomb interaction

No matter what construction procedure is used, a common characteristic of *ab-initio* Wannier functions is that they are site-centered and localized.[10] A question naturally arises: How crucial is it to use localized functions as one-electron basis? This is an important point, since we have seen that strong-correlation effects arise in systems in which the on-site Coulomb interaction is much larger than longer-range terms. Let us consider therefore two opposite extreme limits. The first is the case in which the basis functions are independent of the lattice position (i.e., they are totally delocalized). For such a basis choice the Coulomb interaction parameters would be the same for every couple of lattice sites, no matter how distant. Thus a Hubbard-like model would be hard to justify. In the second extreme case, we adopt a hypothetical basis so localized that $\psi_{im\sigma}(\boldsymbol{r})\overline{\psi_{i'm'\sigma'}}(\boldsymbol{r}) \sim \delta_{i,i'}\delta(\boldsymbol{r}-\boldsymbol{T}_i)$. Even for such a basis choice, the unscreened Coulomb interaction is *not* local. It is given by

$$U^{iji'j'}_{mp\,m'p'} \propto \frac{\delta_{i,i'}\delta_{j,j'}}{|\boldsymbol{T}_i-\boldsymbol{T}_j|}\,, \tag{111}$$

hence it decays slowly with distance, although the (divergent) on-site term dominates. More generally, we can conclude that by increasing the localization of the basis we enhance the importance of the on-site Coulomb repulsion with respect to long-range terms; this better justifies Hubbard-like models—although we have to remember that most of the long-range part of the Coulomb interaction is in any case subtracted via the double-counting correction $\hat{H}_{\rm DC}$. The extreme case of the $\delta(\boldsymbol{r}-\boldsymbol{T}_i)$ functions also illustrates, however, how far we can go. A major problem with the extremely localized basis discussed above is that it would make it impossible to properly describe bonding, since the hopping integrals would be zero. Although such a basis is, of course, never used to build many-body models, there is a tempting approximation that has similar flaws. If one uses DFT-based electronic-structure techniques that tile the space in interstitial and *non*-overlapping atomic spheres (e.g., the LAPW method), it is tempting to use as basis for correlated electrons the atomic functions *defined inside the atomic spheres*. These functions are, by construction, much more localized than Wannier orbitals (even when no downfolding is performed in the Wannier construction). However, they *do not form a complete basis set* in the space of square-integrable functions. This is obvious because such a basis does not even span the LDA bands; to reproduce the bands we need, in addition, functions defined in the interstitial region. This is illustrated in Fig. 11 for a simple example of two quantum well potentials.[11] We therefore cannot use it to write the many-body Hamiltonian in the usual form $\hat{H}_0 + \hat{H}_U$. In conclusion, a basis which, as *ab-initio* Wannier functions, is complete and indeed spans the bands, is better justified, although we somewhat lose in localization.

[10] Differences in localizations between the various construction procedures are actually small for the purpose of many-body calculations, provided that the same bands are spanned with the same accuracy.

[11] Another, but less severe, problem of atomic sphere truncations is that the results will depend on the sphere size, in particular when atomic spheres are small.

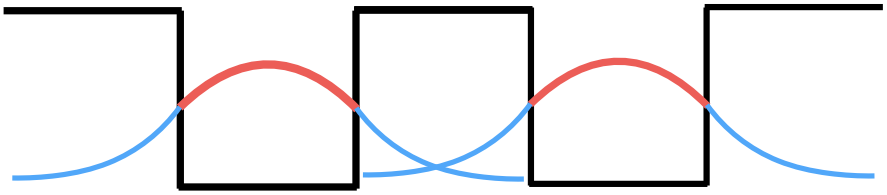


Fig. 11: *The problem of two quantum wells. The figure shows (schematically) for each well the wavefunction of a bound state. If we consider only the part of the wavefunction inside its own well (red in the figure), the differential overlap (and hence the hopping integral) between functions centered on different wells would be zero.*

3.3 Hubbard Hamiltonians for t_{2g} and e_g systems

Several strongly-correlated transition-metal oxides can be described via minimal materials-specific Hubbard-like models which involve only t_{2g} or only e_g bands. A representative system of this kind is the layered perovskite Sr_2RuO_4 with the $4d\ t_{2g}^4$ electronic configuration. Its crystal structure is shown in Fig. 12 (left side), together with the associated LDA bands crossing the Fermi level (top-right panel). Due to the layered structure the xz and yz bands are quasi one-dimensional and the xy band is quasi two-dimensional. Thus, the t_{2g} bands give rise, in first approximation, to a Fermi surface made of four crossing lines (from the xz, yz bands) and a circle (from the xy band), shown schematically in the bottom-right panel of Fig. 12. Experimentally, Sr_2RuO_4 is a correlated metal down to 1.5 K; below this temperature it becomes an anomalous superconductor. Other representative cases of t_{2g} systems are the Mott insulating perovskites $LaTiO_3$ and $YTiO_3$, with the electronic configuration $3d\ t_{2g}^1$. A paradigmatic e_g system is instead the orbitally ordered insulator $KCuF_3$, with the electronic configuration $t_{2g}^6 e_g^3$. For all these materials, if we massively downfold all LDA bands but the t_{2g} (or the e_g), the resulting 3-band (or 2-band) generalized Hubbard model takes the form

$$\begin{aligned}\hat{H} = &\sum_{i\sigma}\sum_{mm'} \varepsilon_{m,m'}\, c^\dagger_{im\sigma} c_{im'\sigma} - \sum_{\sigma}\sum_{i\neq i'}\sum_{mm'} t^{i,i'}_{m,m'}\, c^\dagger_{im\sigma} c_{i'm'\sigma} \\ &+ U\sum_{i\,m} \hat{n}_{im\uparrow}\hat{n}_{im\downarrow} + \frac{1}{2}\sum_{\substack{i\sigma\sigma' \\ m\neq m'}} \left(U - 2J - J\delta_{\sigma,\sigma'}\right) \hat{n}_{im\sigma}\hat{n}_{im'\sigma'} \\ &- J\sum_{i\ m\neq m'} \left(c^\dagger_{im\uparrow} c^\dagger_{im\downarrow} c_{im'\uparrow} c_{im'\downarrow} + c^\dagger_{im\uparrow} c_{im\downarrow} c^\dagger_{im'\downarrow} c_{im'\uparrow} \right), \end{aligned} \tag{112}$$

where $m, m' = xy, yz, xz$ for t_{2g} and $m, m' = 3z^2{-}r^2, x^2{-}y^2$ for e_g. The parameters U and J are the direct and exchange screened Coulomb integrals. The Coulomb interaction $\hat{H}_U$ is here assumed to have full $O(3)$ rotational symmetry, as in the atomic limit.[12] The first two terms of

[12] A derivation of the Coulomb interaction tensor for the free atom can be found in my chapter in Ref. [8]. There the difference in the values of U and J for the t_{2g} and e_g orbitals is also discussed.

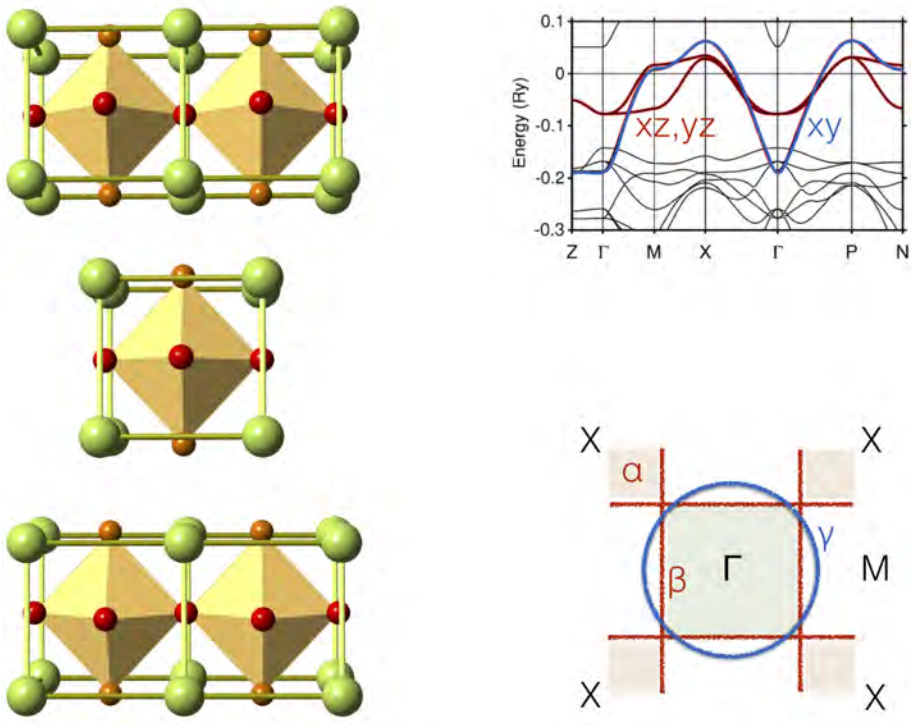


Fig. 12: *Left: Crystal structure of the tetragonal layered perovskite Sr_2RuO_4. Right: Low-energy LDA band structure (top) and schematic representation of the associated Fermi surface (bottom). The band structure was calculated using the Nth-Order Muffin-Tin Orbital (NMTO) method. The figure is rearranged from Ref. [18].*

$\hat{H}_U$ are the so-called density-density terms, and the last two are the pair-hopping and spin-flip interactions. We dropped the double-counting correction $\hat{H}_{\rm DC}$, which in this case is a mere shift of the chemical potential. The energies $\varepsilon_{m,m'}$ are the elements of the crystal-field matrix. In the case of cubic symmetry, the crystal-field matrix, the self-energy, the Green function and the spectral function are all diagonal in orbital space. For low-symmetry systems, however, this is not true. It can be seen in Fig. 13, which shows the diagonal and off-diagonal elements of the spectral-function matrix for the orthorhombic Mott insulator $YTiO_3$.

3.4 Spin-orbit interaction and effects of the basis choice

In many interesting systems the spin-orbit interaction $\hat{H}_{\rm SO}$ plays an important role. In the atomic limit, for the d shells the spin-orbit interaction is

$$\hat{H}_{\rm SO} = \sum_{\mu} \lambda_\mu \sum_{mm'} \sum_{\sigma\sigma'} \epsilon^{\mu}_{m\sigma,m'\sigma'}\, c^{\dagger}_{m\sigma} c_{m'\sigma'}, \qquad \epsilon^{\mu}_{m\sigma,m'\sigma'} = \langle m\sigma | l_\mu s_\mu | m'\sigma' \rangle, \tag{113}$$

where $\mu = x, y, z$, and λ_μ are the spin-orbit couplings, with $\lambda_\mu = \lambda$ in $O(3)$ symmetry, and

$$\lambda \sim g\mu_B^2 \left\langle \frac{1}{r}\frac{d}{dr} v_R(r) \right\rangle . \tag{114}$$

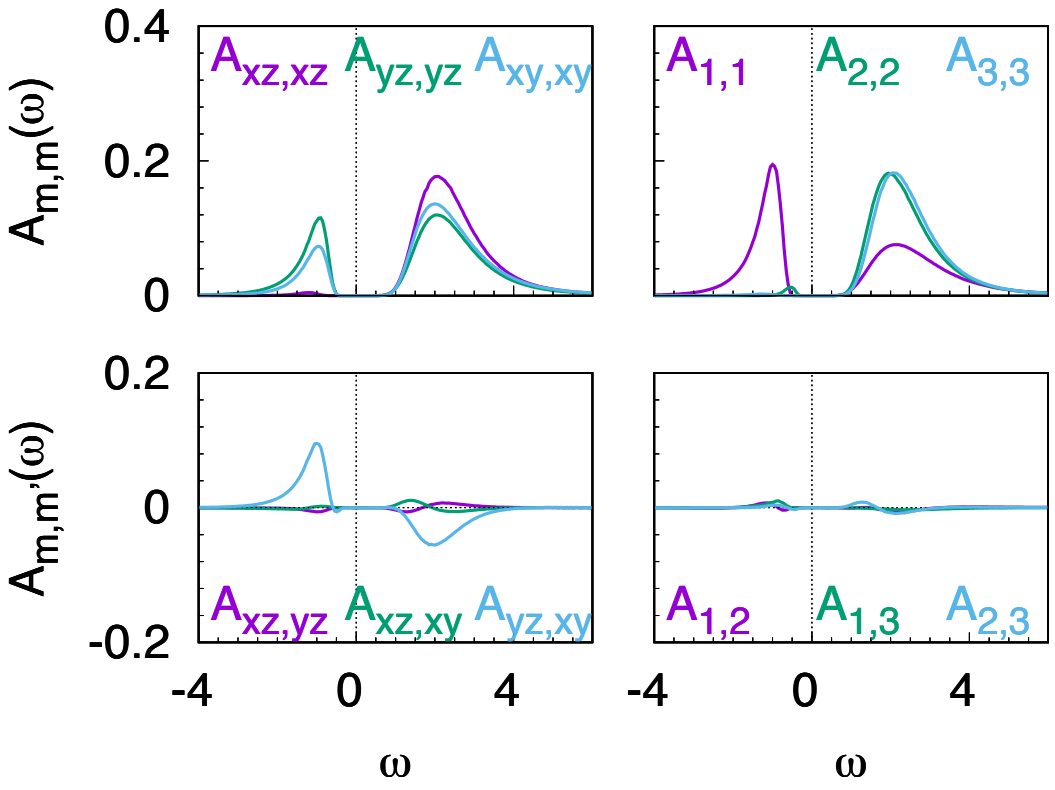


Fig. 13: *The LDA+DMFT spectral function matrix of the orbitally-ordered t_{2g}^1 system $YTiO_3$, in the (xz, yz, xy) basis (left panels) and in the crystal-field basis (right panels) [16, 19].*

For a given material, the on-site one-electron Hamiltonian is thus the matrix $\hat{\varepsilon}$ with elements $\hat{\varepsilon}_{m\sigma,m'\sigma'} = \varepsilon_{m,m'} + \sum_\mu \lambda_\mu \epsilon^\mu_{m\sigma,m'\sigma'}$, where the terms $\varepsilon_{m,m'}$ arise from the crystal field. More specifically, for a t_{2g} system with tetragonal site symmetry we have

$$\hat{\varepsilon} = \begin{pmatrix} \varepsilon_{xy} & 0 & 0 & 0 & \frac{\lambda_y}{2} & -\frac{i\lambda_x}{2} \\ 0 & \varepsilon_{yz} & \frac{i\lambda_z}{2} & -\frac{\lambda_y}{2} & 0 & 0 \\ 0 & -\frac{i\lambda_z}{2} & \varepsilon_{xz} & \frac{i\lambda_x}{2} & 0 & 0 \\ 0 & -\frac{\lambda_y}{2} & -\frac{i\lambda_x}{2} & \varepsilon_{xy} & 0 & 0 \\ \frac{\lambda_y}{2} & 0 & 0 & 0 & \varepsilon_{yz} & -\frac{i\lambda_z}{2} \\ \frac{i\lambda_x}{2} & 0 & 0 & 0 & \frac{i\lambda_z}{2} & \varepsilon_{xz} \end{pmatrix}. \tag{115}$$

Although $\hat{H}_{\rm SO}$ looks like an innocent one-body term, it turns out that, for materials, simulations including this term are more difficult. This has two reasons: (i) QMC calculations involve Green function matrices of larger size, e.g., 6×6 as in the case just discussed, hence they are from the start computationally more demanding; (ii) QMC calculations are often hampered by a much stronger sign problem; even when it can be tamed, this often happens at the price of further increasing the computational time. Thus, specific basis choices and approximations are used. A possible approach consists in working in the basis that diagonalizes the non-interacting local Green function or the non-interacting local Hamiltonian; such a choice is known to reduce

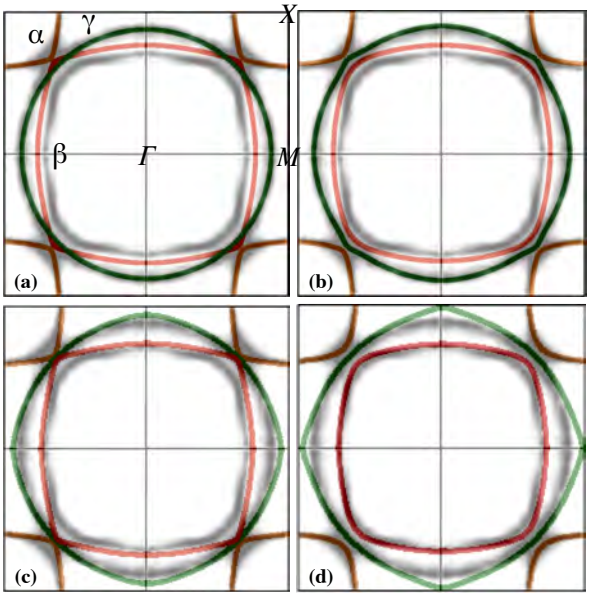


Fig. 14: *Fermi surface of Sr_2RuO_4 calculated with LDA (a), LDA+SO (b), LDA+DMFT (c) and LDA+SO+DMFT (d). Figure from [20]. The grey maps are experimental results from Ref. [23].*

the sign problem, as was first shown in Ref. [13] for the case without spin-orbit interaction. For a system with tetragonal symmetry, the states that diagonalize the local Green function belong either to the Γ_6 or to the Γ_7 irreducible representations, both 2-dimensional. There are two (coupled) Γ_7 representations, defining the space $\Gamma_7' \oplus \Gamma_7''$. The analytic expression of these states can be found in Refs. [18, 20, 21]. The transformation to the $\Gamma_6 \oplus \Gamma_7' \oplus \Gamma_7''$ basis is, of course, in principle, a mere basis change. Approximations are made, however, if all off-diagonal elements of the Green function are set to zero or the Coulomb tensor is truncated to further tame the sign problem or to reduce the computational time.

It has to be noticed that the Coulomb interaction of the t_{2g} Hubbard Hamiltonian is *only invariant under orthogonal transformations* of the basis. Thus if we change basis to the Γ_6-Γ_7'-Γ_7'' representation, the form of the interaction tensor changes. The exact expression of the Coulomb tensor in the total angular momentum basis (i.e., the one relevant when the t_{2g} crystal-field splitting is zero) can be found in Ref. [22]. For the Coulomb interaction tensor in the basis of spherical harmonics you can instead look the derivation in Ref. [8].

In the presence of crystal-field splitting, if the spin-orbit interaction is small in comparison, it is often preferable to perform the calculations in the t_{2g} basis. To this end, it is key to make QMC codes very efficient in order to reduce as much as possible statistical errors and increase the average sign. Exact LDA+SO+DMFT calculations in the t_{2g} basis have been successfully performed, e.g., for Sr_2RuO_4, using an interaction-expansion continuous-time quantum Monte Carlo solver, and an orbital-dependent phase which makes the Green function matrix real [20, 21]. This approach allowed us to study, for example, the effects of the spin-orbit interaction on the Fermi surface without approximations. The results are shown in Fig. 14 in comparison with experimental data; we will discuss them in the next section.

3.5 Non-spherical Coulomb terms and double-counting correction

While for a free atom the Coulomb tensor is spherical (symmetry $O(3)$), in a material the screened Coulomb tensor has, in general, the symmetry of the lattice. Taking into account non-spherical Coulomb terms is, in general hard, both because they make QMC calculations more difficult and can worsen the sign problem, and because in their presence the double-counting correction has to be explicitly accounted for, even when massive downfolding is used. For these reasons they are typically neglected. Recently it was shown that they can play, however, a very important role for the Fermi surface [20]. Let us therefore discuss how the double-counting correction can be treated with and without such terms, following the approach of Ref. [20]. One of the classical approximations for the double-counting correction is the so called "around mean-field" approximation. The idea is that LDA describes well the average Coulomb term, in the absence of orbital polarization. This is equivalent to using as double-counting correction the Hartree term of the Coulomb interaction tensor, i.e., the operator

$$\begin{aligned}\hat{H}_{\rm U}^{\rm DC} = & U\sum_{m}\left(\hat{n}_{m\uparrow}\bar{n}_{m\downarrow}+\bar{n}_{m\uparrow}\hat{n}_{m\downarrow}\right)+(U{-}2J)\sum_{m\neq m'}\left(\hat{n}_{m\uparrow}\bar{n}_{m'\downarrow}+\bar{n}_{m\uparrow}\hat{n}_{m'\downarrow}\right)\\ & +(U{-}3J)\sum_{\sigma}\sum_{m>m'}\left(\hat{n}_{m\sigma}\bar{n}_{m'\sigma}+\bar{n}_{m\sigma}\hat{n}_{m'\sigma}\right)-\mu\hat{N}_d \\ & -U\sum_{m}\bar{n}_{m\uparrow}\bar{n}_{m\downarrow}+(U{-}2J)\sum_{m\neq m'}\bar{n}_{m\uparrow}\bar{n}_{m'\downarrow}+(U{-}3J)\sum_{\sigma}\sum_{m>m'}\bar{n}_{m\sigma}\bar{n}_{m'\sigma}\end{aligned} \tag{116}$$

where $\bar{n}_{m\sigma} = n/d$, if n is the number of the correlated electrons per site and d the orbital degeneracy. Within this approximation we have, after collecting all terms,

$$\begin{aligned}\hat{H}_{\rm U}^{\rm DC} =& (\delta\mu{-}\mu)\hat{N}_d-\frac{n^2}{d}\big(U\,(2d{-}1)-5\,(d{-}1)\,\big)\\ \delta\mu =& \frac{n}{d}\big(U(2d{-}1)-5J(d{-}1)\big).\end{aligned}$$

If we perform massive downfolding to the correlated bands, as previously mentioned, this is merely a shift of the chemical potential and can therefore be neglected. Let us now consider the case in which the Coulomb interaction has an additional term that does not change the average U but has tetragonal symmetry

$$\Delta\hat{H}_U = \frac{\Delta U}{3}\left(2\hat{n}_{xy\uparrow}\hat{n}_{xy\downarrow}-\hat{n}_{xz\uparrow}\hat{n}_{xz\downarrow}-\hat{n}_{yz\uparrow}\hat{n}_{yz\downarrow}\right)$$

We can now use the around mean-field approximation for this term as well. We find

$$\begin{aligned}\Delta\hat{H}_U^{\rm DC} &= \frac{n}{6}\frac{\Delta U}{3}\sum_{\sigma}\left(2\hat{n}_{xy\sigma}{-}\hat{n}_{xz\sigma}{-}\hat{n}_{yz\sigma}\right)=\frac{n}{6}\Delta U\sum_{\sigma}\hat{n}_{xy\sigma}-\delta\mu'\hat{N}\\ \delta\mu' &= \frac{n}{6}\frac{\Delta U}{3}.\end{aligned}$$

This term, in addition to a shift of the chemical potential, yields an effective change of the crystal-field splitting $\varepsilon_{\rm CF}$, and has therefore to be accounted for explicitly.

How does ΔU change the Fermi surface of Sr_2RuO_4? The Fermi surface is determined by the poles of the Green function at zero frequency. These depend on the non-interacting Hamiltonian and the self-energy matrix at zero frequency. In the Fermi-liquid regime, and within the DMFT approximation, the effect of the self-energy is merely to modify the on-site part of the Hamiltonian, i.e., the crystal-field splitting $\varepsilon_{\mathrm{CF}} = \varepsilon_{xz/yz} - \varepsilon_{xy}$ and the spin-orbit couplings λ_μ

$$\varepsilon_{\mathrm{CF}} \to \varepsilon_{\mathrm{CF}} + \Delta\varepsilon_{\mathrm{CF}}(0),$$

$$\lambda_\mu \to \lambda_\mu + \Delta\lambda_\mu(0).$$

Both $\Delta\varepsilon_{\mathrm{CF}}(0)$ and $\Delta\lambda_\mu(0)$ are positive for Sr_2RuO_4, and lead to an almost doubling of the LDA parameters. The positive $\Delta\varepsilon_{\mathrm{CF}}(0)$ shrinks the β sheet (xz/yz bands) and enlarges the γ (xy band) sheet. This can be understood from the schematic Fermi surface and the LDA band structure in Fig. 12. Enhancing the crystal-field splitting corresponds to slightly moving the xy band downwards and the xz/yz bands upwards with respect to the Fermi level. The enhancement of the spin-orbit couplings has a large Hartree-Fock component [21], since the spin-orbit interaction yields a small but finite off-diagonal occupation matrix. For an $O(3)$-symmetric Coulomb tensor, the Hartree-Fock enhancement of the spin-orbit coupling is thus

$$\begin{aligned}
\frac{\Delta\lambda_z}{2} &= \quad i\big(U{-}3J\big)\, n^{\uparrow\uparrow}_{xz,yz} \\
\frac{\Delta\lambda_y}{2} &= -\,\big(U{-}3J\big)\, n^{\uparrow\downarrow}_{xy,yz}, \\
\frac{\Delta\lambda_x}{2} &= -i\big(U{-}3J\big)\, n^{\uparrow\downarrow}_{xz,xy},
\end{aligned}$$

where $n^{\sigma\sigma'}_{m,m'}$ are the off-diagonal elements of the density matrix. The Coulomb-enhanced spin-orbit coupling improves the agreement with the experimental Fermi surface at the degeneracy points (e.g., along the Γ-X direction). The agreement with ARPES data, however, further deteriorates for the γ sheet. This can be seen in Fig. 14, in which the LDA and LDA+DMFT Fermi surface are shown on top of ARPES data from Ref. [23].

Including correlation effects has thus two opposite effects: on the one hand, the agreement with experiments improves (with respect to LDA) for the β sheet; on the other hand, it deteriorates for the γ sheet. This can be seen comparing either panels (a) and (c) or panels (b) and (d) in Fig. 14. Introducing tetragonal Coulomb terms, and in particular the term ΔU, however, reduces the crystal-field enhancement to

$$\varepsilon_{\mathrm{CF}} \to \varepsilon_{\mathrm{CF}} + \Delta\varepsilon'_{\mathrm{CF}}(0),$$

where $\Delta\varepsilon'_{\mathrm{CF}}(0)$ becomes almost zero for cRPA-based estimates of ΔU. This leads to an almost perfect Fermi surface, as shown in Fig. 15. Non-spherical Coulomb terms turn out to be more important for properties that reflect the point symmetry of the lattice, like the Fermi surface, than for properties that average over orbitals, like the total spectral function [21].

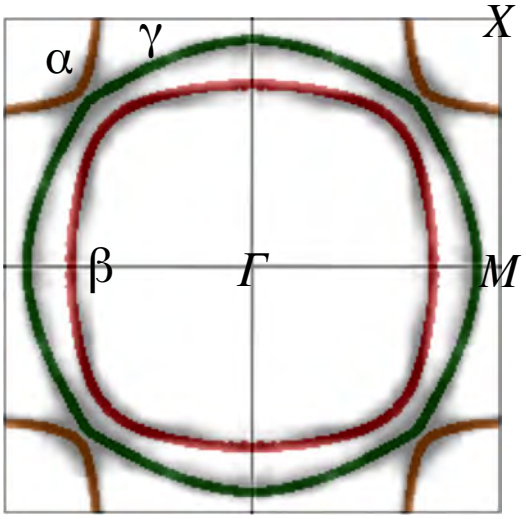


Fig. 15: *The LDA+SO+DMFT Fermi surface of Sr_2RuO_4 calculated including the effects of the non-spherical Coulomb term ΔU. Figure from [20].*

4 Understanding correlated materials with DMFT

The ultimate test for a method is the actual advance it brings in solving outstanding problems. The LDA+DMFT approach has proven very successful, advancing qualitatively our understanding of the physics of strongly-correlated materials. This has two reasons. From the many-body side, the success of the method is rooted in the fact that dynamical mean-field theory captures exactly key limits: non-interacting limit, atomic limit, single-impurity limit, infinite dimension limit. It also describes very well phases with different characteristics: paramagnetism, long-range order, metallic and insulating phase. Thus DMFT can be used to explore transitions/crossovers from one corner to another of the phase diagram, building a coherent picture as a function of both internal and external parameters (e.g., U, J, doping and temperature). This differs from static mean-field approaches, such as the LDA+U method; the latter only captures the behavior in a specific corner of the phase diagram (and typically merely the ground state), e.g., long-range magnetic order[13] or, if one uses large supercells, spin-glass-like phases. This limitation makes static mean-field approaches unsuitable to study, e.g., the effects of temperature or external parameters, and for identifying a mechanism behind a certain phenomenon, or finding the onset of a Mott phase. From the materials-dependence side, by constructing many-body models from Kohn-Sham Wannier functions, the LDA+DMFT technique builds on the shoulders of the most successful theory for materials, DFT. In order to illustrate the success of LDA+DMFT, here I will briefly review two paradigmatic examples.

[13] It should be noted that LDA+U is less accurate than DMFT also in capturing long-range order. This is because LDA+U is based on the Hartree-Fock approximation; as we have seen for the Hubbard dimer, it is, therefore, the static (high-frequency) limit of LDA+DMFT. All results from LDA+U are thus by construction contained in LDA+DMFT, provided that, of course, calculations are performed for the same Hamiltonian, the same basis and the same unit cell. Unlike LDA+U, however, LDA+DMFT also captures correctly dynamical fluctuations and actual phase transitions. See Ref. [14] for more details. Long-range order is well described in DMFT via a local cluster with the size of the (enlarged) broken-symmetry unit cell, without additional computational cost.

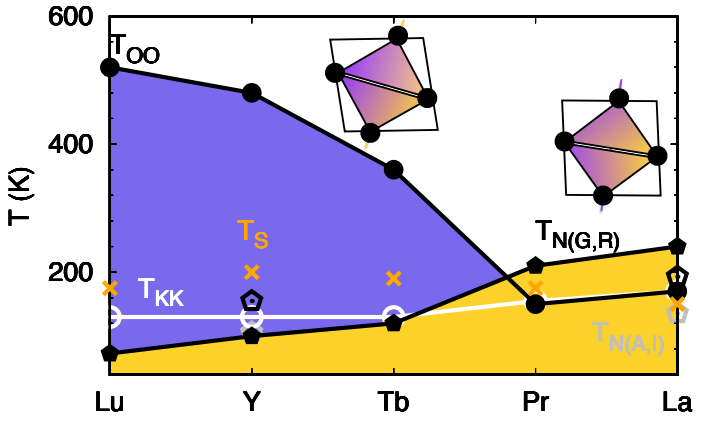


Fig. 16: *Inversion of magnetic and orbital transition in the $ReVO_3$ series with increasing rare-earth (Re) ionic radius. While in most orbitally ordered systems the magnetic transition occurs at lower temperature than the orbital transition (T_N<T_{OO}), in the $ReVO_3$ series $T_N \gtrsim T_{OO}$ for large rare-earth (Re) radius. Figure from [35].*

The first is unravelling the importance of **crystal-field splitting** in determining low-energy properties of strongly-correlated systems. The metal-insulator Mott transition arises, in the simplest picture, from the competition between the bandwidth, W, and the on-site Coulomb repulsion, U. This competition is well captured by the single-band Hubbard model; however, the latter is typically insufficient for understanding the complex behavior displayed by actual correlated materials. One reason is the importance of multi-orbital effects. Pioneering works based on lattice QMC calculations for the multi-band Hubbard model have indeed shown that orbital degeneracy strongly influence the size of the Mott gap [24, 25]. Accounting for multi-orbital effects strongly complicates the matter from the viewpoint of theory: realistic models have many unknown independent parameters and are considerably more difficult to solve. The LDA+DMFT approach provided the first framework to study multi-orbital phenomena systematically in a realistic setting. One of the early success of the method was to show that, contrarily to what was often assumed, small details do matter. A crystal-field splitting much smaller than the bandwidth can favor the Mott metal-insulator transition. In fact, everything else remaining the same, the crystal-field splitting reduces orbital degeneracy, thereby modifying the correlation strength. This insight explained the metal-insulator transition in the series of $3d^1$ perovskites: $SrVO_3$ (metal), $CaVO_3$ (metal), $LaTiO_3$ (small gap insulator), $YTiO_3$ (insulator) [19]. Important crystal-field effects are now recognized in most correlated materials. They have been key to settle several hot debates, e.g., to understand the complex phase diagram of layered $Ca_{2-x}Sr_xRuO_4$ ruthenates [26]. More recently, it was shown that the crystal-field splitting and its subtle interplay with the **spin-orbit interaction** is crucial for determining the correlation strength, the shape of the Fermi surface and the effective masses [20–22, 27].

The second success story is unravelling the **origin of orbital ordering** in materials. More than fifty years ago, thanks to seminal works of Kugel and Khomskii [28], it became clear that orbital degrees of freedom play a key role in the properties of strongly-correlated Mott insulators; in particular, they can give rise to orbital ordering via many-body super-exchange interactions [29,

30]. For a long time it was however hotly debated if, in actual materials, it is Kugel-Khomskii (KK) super-exchange or rather the Jahn-Teller effect that control the onset of orbital ordering. This is a classical case of a chicken-and-egg problem, with two theoretical mechanisms leading to the same final state. The systems for which super-exchange-driven orbital ordering was initially proposed were the e_g perovskites $KCuF_3$ and $LaMnO_3$. Combining DMFT with a novel disentanglement scheme [31], it became possible to solve the problem. It was shown that, in $KCuF_3$ and $LaMnO_3$, the KK super-exchange interaction, although strong, is not sufficiently large to drive alone orbital ordering at experimental temperatures [31, 32]. More recently, it was shown that t_{2g} systems are more likely than e_g materials to exhibit super-exchange-driven orbital ordering; $LaVO_3$ was then identified as the first clear-cut case of a Kugel-Khomskii material [33, 34]. This lead to the solution of another long-standing problem: the origin of the puzzling inversion of magnetic and orbital transition in the $ReVO_3$ series with increasing rare-earth (Re) ionic radius, see Fig. 16 and Refs. [34, 35]. Furthermore, as a byproduct, it was shown that DMFT and super-exchange theory can be successfully combined to pinpoint the nature of spin-orbital phases. This can be done via a general scheme for constructing **exact materials-specific super-exchange Hamiltonians** in an irreducible tensor basis [33–35]; the latter provides at the same time analytic expressions and numerical results. This scheme can be used for the realistic description of all KK-type super-exchange phenomena, static (e.g., orbital ordering) and dynamical (e.g., spin-orbital excitations, orbital and spin liquid behavior).

5 Conclusion and outlook

The LDA+DMFT approach and its extension has proven very successful for describing correlated materials. In the last decades, it also became very versatile. It is now possible, e.g., to study multi-orbital models including the full Coulomb vertex and the spin-orbit interaction, and to calculate response functions or bosonic excitations. Still, several challenges remain. Models with more than a few orbitals or sites and out-of-equilibrium phenomena are still, e.g., hard to study. Furthermore, since the birth of DFT, Moore's law constantly helped as much as new algorithms in extending the frontier; that has come now slowly to a halt.

Quantum computers and artificial intelligence, or new, not yet foreseeable, technological advances might help us in the future. The present deceleration, however, urges us to think to what we should strive for. It is perhaps easier to discuss first what we *do not* need. We do not need a magical calculating machine that gives us answers with no explanations. Reproducing the data is, of course, the aim of theory, but not the only goal. As scientists we need to know why. The danger of giving this question up is evident if we look back at the historical controversy between copernican and ptolemaic system. At the time, the ptolemaic system was the one which agreed better with experiments. Indeed, it had been fine-tuned along the years, via a series of ad hoc assumptions. The copernican system was initially not performing so well, among others because it was based on circular orbits. But, at the end, it is the copernican system that made a contribution to science, by identifying the correct picture.

Appendices

A Hubbard dimer and Anderson molecule

The Hamiltonian of the **Hubbard dimer** is given by

$$\hat{H} = \varepsilon_d \sum_{\sigma} \sum_{i=1,2} n_{i\sigma} - t \sum_{\sigma} \left(c^{\dagger}_{1\sigma} c_{2\sigma} + c^{\dagger}_{2\sigma} c_{1\sigma} \right) + U \sum_{i=1,2} \hat{n}_{i\uparrow} \hat{n}_{i\downarrow}.$$

It commutes with the number of electron operator $\hat{N}$, with the total spin $\hat{S}$, and with $\hat{S}_z$. Thus we can express the many-body states in the atomic limit as

$\lvert N, S, S_z \rangle$			N	S	$E(N,S)$
$\lvert 0,0,0 \rangle$	$=$	$\lvert 0 \rangle$	0	0	0
$\lvert 1, \frac{1}{2}, \sigma \rangle_1$	$=$	$c^{\dagger}_{1\sigma} \lvert 0 \rangle$	1	$\frac{1}{2}$	ε_d
$\lvert 1, \frac{1}{2}, \sigma \rangle_2$	$=$	$c^{\dagger}_{2\sigma} \lvert 0 \rangle$	1	$\frac{1}{2}$	ε_d
$\lvert 2,1,1 \rangle$	$=$	$c^{\dagger}_{2\uparrow} c^{\dagger}_{1\uparrow} \lvert 0 \rangle$	2	1	$2\varepsilon_d$
$\lvert 2,1,-1 \rangle$	$=$	$c^{\dagger}_{2\downarrow} c^{\dagger}_{1\downarrow} \lvert 0 \rangle$	2	1	$2\varepsilon_d$
$\lvert 2,1,0 \rangle$	$=$	$\frac{1}{\sqrt{2}} \left(c^{\dagger}_{1\uparrow} c^{\dagger}_{2\downarrow} + c^{\dagger}_{1\downarrow} c^{\dagger}_{2\uparrow} \right) \lvert 0 \rangle$	2	1	$2\varepsilon_d$
$\lvert 2,0,0 \rangle_0$	$=$	$\frac{1}{\sqrt{2}} \left(c^{\dagger}_{1\uparrow} c^{\dagger}_{2\downarrow} - c^{\dagger}_{1\downarrow} c^{\dagger}_{2\uparrow} \right) \lvert 0 \rangle$	2	0	$2\varepsilon_d$
$\lvert 2,0,0 \rangle_1$	$=$	$c^{\dagger}_{1\uparrow} c^{\dagger}_{1\downarrow} \lvert 0 \rangle$	2	0	$2\varepsilon_d + U$
$\lvert 2,0,0 \rangle_2$	$=$	$c^{\dagger}_{2\uparrow} c^{\dagger}_{2\downarrow} \lvert 0 \rangle$	2	0	$2\varepsilon_d + U$
$\lvert 3, \frac{1}{2}, \sigma \rangle_1$	$=$	$c^{\dagger}_{1\sigma} c^{\dagger}_{2\uparrow} c^{\dagger}_{2\downarrow} \lvert 0 \rangle$	3	$\frac{1}{2}$	$3\varepsilon_d + U$
$\lvert 3, \frac{1}{2}, \sigma \rangle_2$	$=$	$c^{\dagger}_{2\sigma} c^{\dagger}_{1\uparrow} c^{\dagger}_{1\downarrow} \lvert 0 \rangle$	3	$\frac{1}{2}$	$3\varepsilon_d + U$
$\lvert 4,0,0 \rangle$	$=$	$c^{\dagger}_{1\uparrow} c^{\dagger}_{1\downarrow} c^{\dagger}_{2\uparrow} c^{\dagger}_{2\downarrow} \lvert 0 \rangle$	4	0	$4\varepsilon_d + 2U$

Let us order the $N = 1$ states as in the table above, first the spin up and then spin down block. For finite t the Hamiltonian matrix for $N = 1$ electrons takes then the form

$$\hat{H}_1 = \begin{pmatrix} \varepsilon_d & -t & 0 & 0 \\ -t & \varepsilon_d & 0 & 0 \\ 0 & 0 & \varepsilon_d & -t \\ 0 & 0 & -t & \varepsilon_d \end{pmatrix}.$$

This matrix can be easily diagonalized and yields the *bonding* $(-)$ and *antibonding* $(+)$ states

$\|1,S,S_z\rangle_\alpha$		$E_\alpha(1,S)$	$d_\alpha(1,S)$
$\|1,\frac{1}{2},\sigma\rangle_+$	$= \frac{1}{\sqrt{2}}\big(\|1,\frac{1}{2},\sigma\rangle_1 - \|1,\frac{1}{2},\sigma\rangle_2\big)$	$\varepsilon_d + t$	2
$\|1,\frac{1}{2},\sigma\rangle_-$	$= \frac{1}{\sqrt{2}}\big(\|1,\frac{1}{2},\sigma\rangle_1 + \|1,\frac{1}{2},\sigma\rangle_2\big)$	$\varepsilon_d - t$	2

where $d_\alpha(N)$ is the spin degeneracy of the α manifold.
For $N = 2$ electrons (half filling), the hopping integrals only couple the three $S = 0$ states, and therefore the Hamiltonian matrix is given by

$$\hat{H}_2 = \begin{pmatrix} 2\varepsilon_d & 0 & 0 & 0 & 0 & 0 \\ 0 & 2\varepsilon_d & 0 & 0 & 0 & 0 \\ 0 & 0 & 2\varepsilon_d & 0 & 0 & 0 \\ 0 & 0 & 0 & 2\varepsilon_d & -\sqrt{2}t & -\sqrt{2}t \\ 0 & 0 & 0 & -\sqrt{2}t & 2\varepsilon_d{+}U & 0 \\ 0 & 0 & 0 & -\sqrt{2}t & 0 & 2\varepsilon_d{+}U \end{pmatrix}.$$

The eigenvalues and the corresponding eigenvectors are

$\|2,S,S_z\rangle_\alpha$		$E_\alpha(2,S)$	$d_\alpha(2,S)$
$\|2,0,0\rangle_+$	$= a_1\|2,0,0\rangle_0 - \frac{a_2}{\sqrt{2}}\big(\|2,0,0\rangle_1 + \|2,0,0\rangle_2\big)$	$2\varepsilon_d + \frac{1}{2}\,(U{+}\Delta(t,U))$	1
$\|2,0,0\rangle_o$	$= \frac{1}{\sqrt{2}}\big(\|2,0,0\rangle_1 - \|2,0,0\rangle_2\big)$	$2\varepsilon_d + U$	1
$\|2,1,m\rangle_o$	$= \|2,1,m\rangle$	$2\varepsilon_d$	3
$\|2,0,0\rangle_-$	$= a_2\|2,0,0\rangle_0 + \frac{a_1}{\sqrt{2}}\big(\|2,0,0\rangle_1 + \|2,0,0\rangle_2\big)$	$2\varepsilon_d + \frac{1}{2}\,(U{-}\Delta(t,U))$	1

where

$$\Delta(t,U) = \sqrt{U^2 + 16t^2},$$

and

$$a_1^2 = a_1^2(t,U) = \frac{1}{\Delta(t,U)}\frac{\Delta(t,U) - U}{2} \qquad a_2^2 = a_2^2(t,U) = \frac{4t^2}{\Delta(t,U)}\frac{2}{\Delta(t,U) - U}\,,$$

so that $a_1 a_2 = 2t/\Delta(t,U)$. For $U = 0$ we have $a_1 = a_2 = 1/\sqrt{2}$, and the two states $|2,0,0\rangle_-$ and $|2,0,0\rangle_+$ become, respectively, the state with two electrons in the bonding orbital and the state with two electrons in the antibonding orbital; they have energy $E_\pm(2,0) = 2\varepsilon_d \pm 2t$; the remaining states have energy $2\varepsilon_d$ and are non-bonding. For $t > 0$, the ground state is unique and it is always the singlet $|2,0,0\rangle_-$; in the large U limit its energy is

$$E_-(2,0) \sim 2\varepsilon_d - 4t^2/U.$$

In this limit the energy difference between the first excited state, a triplet state, and the singlet ground state is thus equal to the Heisenberg antiferromagnetic coupling

$$E_o(2,1) - E_-(2,0) \sim 4t^2/U = \Gamma.$$

Finally, for $N = 3$ electrons, eigenstates and eigenvectors are

$\lvert 3, S, S_z\rangle_\alpha$		$E_\alpha(3)$	$d_\alpha(3,S)$
$\lvert 3, \frac{1}{2}, \sigma\rangle_+$	$= \frac{1}{\sqrt{2}}\big(\lvert 1, \frac{1}{2}, \sigma\rangle_1 + \lvert 1, \frac{1}{2}, \sigma\rangle_2\big)$	$3\varepsilon_d{+}U + t$	2
$\lvert 3, \frac{1}{2}, \sigma\rangle_-$	$= \frac{1}{\sqrt{2}}\big(\lvert 1, \frac{1}{2}, \sigma\rangle_1 - \lvert 1, \frac{1}{2}, \sigma\rangle_2\big)$	$3\varepsilon_d{+}U - t$	2

If we exchange holes and electrons, the $N{=}3$ case is identical to the $N{=}1$ electron case. This is due to the particle-hole symmetry of the model.

The Hamiltonian of the **Anderson molecule** is given by

$$\hat{H} = \varepsilon_s \sum_\sigma \hat{n}_{2\sigma} - t \sum_\sigma \left(c^\dagger_{1\sigma} c_{2\sigma} + c^\dagger_{2\sigma} c_{1\sigma}\right) + \varepsilon_d \sum_\sigma \hat{n}_{1\sigma} + U \hat{n}_{1\uparrow}\hat{n}_{1\downarrow}.$$

In the atomic limit, its eigenstates states can be classified as

$\lvert N, S, S_z\rangle$			N	S	$E(N,S)$
$\lvert 0,0,0\rangle$	$=$	$\lvert 0\rangle$	0	0	0
$\lvert 1, \frac{1}{2}, \sigma\rangle_1$	$=$	$c^\dagger_{1\sigma}\lvert 0\rangle$	1	$\frac{1}{2}$	ε_d
$\lvert 1, \frac{1}{2}, \sigma\rangle_2$	$=$	$c^\dagger_{2\sigma}\lvert 0\rangle$	1	$\frac{1}{2}$	ε_s
$\lvert 2,1,1\rangle$	$=$	$c^\dagger_{2\uparrow}c^\dagger_{1\uparrow}\lvert 0\rangle$	2	1	$\varepsilon_d + \varepsilon_s$
$\lvert 2,1,-1\rangle$	$=$	$c^\dagger_{2\downarrow}c^\dagger_{1\downarrow}\lvert 0\rangle$	2	1	$\varepsilon_d + \varepsilon_s$
$\lvert 2,1,0\rangle$	$=$	$\frac{1}{\sqrt{2}}\big(c^\dagger_{1\uparrow}c^\dagger_{2\downarrow} + c^\dagger_{1\downarrow}c^\dagger_{2\uparrow}\big)\lvert 0\rangle$	2	1	$\varepsilon_d + \varepsilon_s$
$\lvert 2,0,0\rangle_0$	$=$	$\frac{1}{\sqrt{2}}\big(c^\dagger_{1\uparrow}c^\dagger_{2\downarrow} - c^\dagger_{1\downarrow}c^\dagger_{2\uparrow}\big)\lvert 0\rangle$	2	0	$\varepsilon_d + \varepsilon_s$
$\lvert 2,0,0\rangle_1$	$=$	$c^\dagger_{1\uparrow}c^\dagger_{1\downarrow}\lvert 0\rangle$	2	0	$2\varepsilon_d + U$
$\lvert 2,0,0\rangle_2$	$=$	$c^\dagger_{2\uparrow}c^\dagger_{2\downarrow}\lvert 0\rangle$	2	0	$2\varepsilon_s$
$\lvert 3, \frac{1}{2}, \sigma\rangle_1$	$=$	$c^\dagger_{1\sigma}c^\dagger_{2\uparrow}c^\dagger_{2\downarrow}\lvert 0\rangle$	3	$\frac{1}{2}$	$\varepsilon_d + 2\varepsilon_s$
$\lvert 3, \frac{1}{2}, \sigma\rangle_2$	$=$	$c^\dagger_{2\sigma}c^\dagger_{1\uparrow}c^\dagger_{1\downarrow}\lvert 0\rangle$	3	$\frac{1}{2}$	$2\varepsilon_d + \varepsilon_s + U$
$\lvert 4,0,0\rangle$	$=$	$c^\dagger_{1\uparrow}c^\dagger_{1\downarrow}c^\dagger_{2\uparrow}c^\dagger_{2\downarrow}\lvert 0\rangle$	4	0	$2\varepsilon_d + 2\varepsilon_s + U$

For $N = 1$ electrons the Hamiltonian can be written in the matrix form

$$\hat{H}_1 = \begin{pmatrix} \varepsilon_d & -t & 0 & 0 \\ -t & \varepsilon_s & 0 & 0 \\ 0 & 0 & \varepsilon_d & -t \\ 0 & 0 & -t & \varepsilon_s \end{pmatrix}.$$

The eigenstates are thus

$\|1, S, S_z\rangle_\alpha$	$E_\alpha(1, S)$	$d_\alpha(1, S)$
$\|1, \frac{1}{2}, \sigma\rangle_+ = \alpha_1 \|1, \frac{1}{2}, \sigma\rangle_1 - \alpha_2 \|1, \frac{1}{2}, \sigma\rangle_2$	$\frac{1}{2}\big(\varepsilon_d + \varepsilon_s + \sqrt{(\varepsilon_d - \varepsilon_s)^2 + 4t^2}\big)$	2
$\|1, \frac{1}{2}, \sigma\rangle_- = \alpha_2 \|1, \frac{1}{2}, \sigma\rangle_1 + \alpha_1 \|1, \frac{1}{2}, \sigma\rangle_2$	$\frac{1}{2}\big(\varepsilon_d + \varepsilon_s - \sqrt{(\varepsilon_d - \varepsilon_s)^2 + 4t^2}\big)$	2

where $d_\alpha(N)$ is the spin degeneracy of the α manifold. For $\varepsilon_s = \varepsilon_d + U/2$ the eigenvalues are

$$E_\pm(1, S) = \varepsilon_d + \frac{1}{4}\big(U \pm \Delta(U, t)\big),$$

while the coefficients are $\alpha_1 = a_1(t, U)$ and $\alpha_2 = a_2(t, U)$.
For N=2 electrons, the hopping integrals only couple the S=0 states. The Hamiltonian is

$$\hat{H}_2 = \begin{pmatrix} \varepsilon_d{+}\varepsilon_s & 0 & 0 & 0 & 0 & 0 \\ 0 & \varepsilon_d{+}\varepsilon_s & 0 & 0 & 0 & 0 \\ 0 & 0 & \varepsilon_d{+}\varepsilon_s & 0 & 0 & 0 \\ 0 & 0 & 0 & \varepsilon_d{+}\varepsilon_s & -\sqrt{2}t & -\sqrt{2}t \\ 0 & 0 & 0 & -\sqrt{2}t & 2\varepsilon_d{+}U & 0 \\ 0 & 0 & 0 & -\sqrt{2}t & 0 & 2\varepsilon_s \end{pmatrix}$$

For $\varepsilon_s = \varepsilon_d + U/2$ the eigenvalues and the corresponding eigenvectors are

$\|2, S, S_z\rangle_\alpha$	$E_\alpha(2, S)$	$d_\alpha(2, S)$
$\|2,0,0\rangle_+ = b_1 \|2,0,0\rangle_0 - \frac{b_2}{\sqrt{2}}\big(\|2,0,0\rangle_1 + \|2,0,0\rangle_2\big)$	$2\varepsilon_d + \frac{U}{2} + \frac{1}{4}\big(U{+}2\Delta(t, \frac{U}{2})\big)$	1
$\|2,0,0\rangle_o = \frac{1}{\sqrt{2}}\big(\|2,0,0\rangle_1 - \|2,0,0\rangle_2\big)$	$2\varepsilon_d + U$	1
$\|2,1,m\rangle_o = \|2,1,m\rangle$	$2\varepsilon_d + \frac{U}{2}$	3
$\|2,0,0\rangle_- = b_2 \|2,0,0\rangle_0 + \frac{b_1}{\sqrt{2}}\big(\|2,0,0\rangle_1 + \|2,0,0\rangle_2\big)$	$2\varepsilon_d + \frac{U}{2} + \frac{1}{4}\big(U{-}2\Delta(t, \frac{U}{2})\big)$	1

where $b_1 = a_1(t, U/2)$ and $b_2 = a_2(t, U/2)$. These states have the same form as in the case of the Hubbard dimer; the ground state energy and the weight of doubly occupied states in $|2, 0, 0\rangle_-$ differ, however. Finally, for $N = 3$ electrons, the eigenstates are

$\|3, S, S_z\rangle_\alpha$	$E_\alpha(3, S)$	$d_\alpha(3, S)$
$\|3, \frac{1}{2}, \sigma\rangle_+ = \alpha_2 \|1, \frac{1}{2}, \sigma\rangle_1 + \alpha_1 \|1, \frac{1}{2}, \sigma\rangle_2$	$3\varepsilon_d + U + \frac{1}{4}\big(U{+}\Delta(t, U)\big)$	2
$\|3, \frac{1}{2}, \sigma\rangle_- = \alpha_1 \|1, \frac{1}{2}, \sigma\rangle_1 - \alpha_2 \|1, \frac{1}{2}, \sigma\rangle_2$	$3\varepsilon_d + U + \frac{1}{4}\big(U{-}\Delta(t, U)\big)$	2

B Lehmann representation of the local Green function

For a single-orbital model, the local Matsubara Green function for a given site i is defined as

$$G^{\sigma}_{i,i}(i\nu_n) = -\int_0^{\beta} d\tau\, e^{i\nu_n\tau}\big\langle \mathcal{T} c_{i\sigma}(\tau)c^{\dagger}_{i\sigma}(0)\big\rangle, \tag{117}$$

where $\mathcal{T}$ is the time-ordering operator, $\beta = 1/k_BT$, and ν_n a fermionic Matsubara frequency. Let us assume to know all eigenstates $|N_l\rangle$ and their energy $E_l(N)$, for arbitrary number of electrons N. Thus, formally

$$G^{\sigma}_{i,i}(i\nu_n) = -\frac{1}{Z}\sum_{Nl}\int_0^{\beta} d\tau\, e^{i\nu_n\tau}e^{-\Delta E_l(N)\beta}\langle N_l|c_{i\sigma}(\tau)c^{\dagger}_{i\sigma}(0)|N_l\rangle, \tag{118}$$

where $Z = \sum_{Nl} e^{-\Delta E_l(N)\beta}$ is the partition function, $\Delta E_l(N){=}E_l(N){-}\mu N$ with μ the chemical potential, and $c^{\dagger}_{i\sigma}(0) = c^{\dagger}_{i\sigma}$. We now insert a complete set of states, obtaining

$$\begin{aligned} G^{\sigma}_{i,i}(i\nu_n) &= -\frac{1}{Z}\sum_{ll'NN'}\int_0^{\beta} d\tau\, e^{i\nu_n\tau}e^{-\Delta E_l(N)\beta}\langle N_l|c_{i\sigma}(\tau)|N'_{l'}\rangle\langle N'_{l'}|c^{\dagger}_{i\sigma}|N_l\rangle \\ &= -\frac{1}{Z}\sum_{ll'NN'}\int_0^{\beta} d\tau\, e^{-\Delta E_l(N)\beta}e^{(i\nu_n+\Delta E_l(N)-\Delta E_{l'}(N'))\tau}\left|\langle N'_{l'}|c^{\dagger}_{i\sigma}|N_l\rangle\right|^2 \\ &= \frac{1}{Z}\sum_{ll'NN'}\frac{e^{-\Delta E_{l'}(N')\beta}+e^{-\Delta E_l(N)\beta}}{i\nu_n+\Delta E_l(N){-}\Delta E_{l'}(N')}\left|\langle N'_{l'}|c^{\dagger}_{i\sigma}|N_l\rangle\right|^2. \end{aligned} \tag{119}$$

Due to the weight $\left|\langle N'_{l'}|c^{\dagger}_{i\sigma}(0)|N_l\rangle\right|^2$ only the terms for which $N' = N{+}1$ contribute. Thus, after exchanging the labels $l'N' \leftrightarrow lN$ in the first addend, we obtain the Lehmann representation

$$G^{\sigma}_{i,i}(i\nu_n){=}\sum_{ll'N}\frac{e^{-\beta\Delta E_l(N)}}{Z}\left(\frac{\left|\langle(N{-}1)_{l'}|c_{i\sigma}|N_l\rangle\right|^2}{i\nu_n-\Delta E_l(N){+}\Delta E_{l'}(N{-}1)}{+}\frac{\left|\langle(N{+}1)_{l'}|c^{\dagger}_{i\sigma}|N_l\rangle\right|^2}{i\nu_n-\Delta E_{l'}(N{+}1){+}\Delta E_l(N)}\right).$$

Let us consider as example the atomic limit of the Hubbard model at half filling (for which $\mu{=}\varepsilon_d{+}U/2$). In this case all sites are decoupled; there are four eigenstates per site, the vacuum $|0\rangle$, with $\Delta E(0) = 0$, the doublet $|1_\sigma\rangle = c^{\dagger}_{i\sigma}|0\rangle$, with $\Delta E_\sigma(1) = -U/2$, and the doubly-occupied singlet $|2\rangle = c^{\dagger}_{i\uparrow}c^{\dagger}_{i\downarrow}|0\rangle$, with $\Delta E(2) = 0$. Furthermore, $Z = 2\big(1+e^{\beta U/2}\big)$ and

$$\left|\langle(N{-}1)_{l'}|c_{i\sigma}|N_l\rangle\right|^2{=}\begin{cases}1 & \text{if } |N_l\rangle{=}|2\rangle\vee|1_\sigma\rangle\\ 0 & \text{otherwise}\end{cases}\qquad \left|\langle(N{+}1)_{l'}|c^{\dagger}_{i\sigma}|N_l\rangle\right|^2{=}\begin{cases}1 & \text{if } |N_l\rangle{=}|0\rangle\vee|1_{-\sigma}\rangle\\ 0 & \text{otherwise}\end{cases}$$

Thus, after summing up the four non-zero contributions, we find

$$G^{\sigma}_{i,i}(\nu_n) = \frac{1}{2}\left(\frac{1}{i\nu_n+U/2}+\frac{1}{i\nu_n-U/2}\right). \tag{120}$$

References

[1] P. Hohenberg and W. Kohn, Phys. Rev. **136**, B864 (1964);
W. Kohn and L.J. Sham, Phys. Rev. **140**, A1133 (1965)

[2] W. Kohn, Rev. Mod. Phys. **71**, 1253 (1999)

[3] P.W. Anderson: *More and different – Notes from a thoughtful curmudgeon*
(World Scientific, Singapore, 2011)

[4] W. Metzner and D. Vollhardt, Phys. Rev. Lett. **62**, 324 (1989)

[5] E. Müller-Hartmann, Z. Phys. B **74**, 507 (1989);
Z. Phys. B **76**, 211 (1989); Int. J. Mod. Phys. B **3**, 2169 (1989)

[6] A. Georges and G. Kotliar, Phys. Rev. B **45**, 6479 (1992)

[7] M. Jarrell, Phys. Rev. Lett. **69**, 168 (1992)

[8] E. Pavarini, E. Koch, D. Vollhardt, A. Lichtenstein (eds.):
The LDA+DMFT approach to strongly-correlated materials,
Reihe Modeling and Simulation, Vol. 1 (Forschungszentrum Jülich, 2011)
`http://www.cond-mat.de/events/correl11`

[9] E. Pavarini, E. Koch, A. Lichtenstein, D. Vollhardt (eds.):
DMFT at 25: Infinite dimensions,
Reihe Modeling and Simulation, Vol. 4 (Forschungszentrum Jülich, 2014)
`http://www.cond-mat.de/events/correl14`

[10] E. Pavarini, E. Koch, A. Lichtenstein, D. Vollhardt (eds.):
DMFT: From infinite dimensions to real materials,
Reihe Modeling and Simulation, Vol. 8 (Forschungszentrum Jülich, 2018)
`http://www.cond-mat.de/events/correl18`

[11] E. Koch, G. Sangiovanni, and O. Gunnarsson, Phys. Rev. B **78**, 115102 (2008)

[12] E. Gull, A.J. Millis, A.I. Lichtenstein, A.N. Rubtsov, M. Troyer, and P. Werner,
Rev. Mod. Phys. **83**, 349 (2011)

[13] A. Flesch, E. Gorelov, E. Koch, E. Pavarini, Phys. Rev. B **87**, 195141 (2013)

[14] E. Pavarini, E. Koch, R. Scalettar, and R.M. Martin (eds.):
The physics of correlated insulators, metals, and superconductors
Reihe Modeling and Simulation, Vol. 7 (Forschungszentrum Jülich, 2017)
`http://www.cond-mat.de/events/correl17`

[15] A. Kiani and E. Pavarini, Phys. Rev. B **94**, 075112 (2016)

[16] E. Pavarini, A. Yamasaki, J. Nuss, and O.K. Andersen,
New. J. Phys **7**, 188 (2005)

[17] N. Marzari, A.A. Mostofi, J.R. Yates, I. Souza, and D. Vanderbilt,
Rev. Mod. Phys. **84**, 1419 (2012)

[18] G. Zhang and E. Pavarini, Phys. Status Solidi RRL **12**, 1800211 (2018)

[19] E. Pavarini, S. Biermann, A. Poteryaev, A.I. Lichtenstein, A. Georges, and O.K. Andersen,
Phys. Rev. Lett. **92**, 176403 (2004)

[20] G. Zhang, E. Gorelov, E. Sarvestani, and E. Pavarini, Phys. Rev. Lett. **116**, 106402 (2016)

[21] E. Sarvestani, G. Zhang, E. Gorelov, and E. Pavarini, Phys. Rev. B **97**, 085141 (2018)

[22] G. Zhang and E. Pavarini, Phys. Rev. B **99**, 125102 (2019)

[23] A. Damascelli, D.H. Lu, K.M. Shen, N.P. Armitage, F. Ronning, D.L. Feng, C. Kim,
Z.-X. Shen, T. Kimura, Y. Tokura, Z.Q. Mao, and Y. Maeno,
Phys. Rev. Lett. **85**, 5194 (2000)

[24] O. Gunnarsson, E. Koch, and R.M. Martin, Phys. Rev. B **56**, 1146 (1996)

[25] E. Koch, O. Gunnarsson, and R.M. Martin, Phys. Rev. B **60**, 15714 (1999)

[26] E. Gorelov, M. Karolak, T.O. Wehling, F. Lechermann, A.I. Lichtenstein, E. Pavarini,
Phys. Rev. Lett. **104**, 226401 (2010)

[27] N. Samani, G. Zhang and E. Pavarini, Phys. Rev. Lett. **132**, 236505 (2024)

[28] K.I. Kugel and D.I. Khomskii, Zh. Eksp. Teor. Fiz. **64**, 1429 (1973)
[Sov. Phys. JETP **37**, 725 (1973)]

[29] D.I. Khomskii, *Transition metal compounds*, Cambridge University Press (2014)

[30] E. Pavarini and E. Koch (eds.): *Orbital physics in correlated matter*,
Reihe Modeling and Simulation, Vol. 13 (Forschungszentrum Jülich, 2023)
`http://www.cond-mat.de/events/correl23`

[31] E. Pavarini, E. Koch, and A.I. Lichtenstein, Phys. Rev. Lett. **101**, 266405 (2008)

[32] E. Pavarini and E. Koch, Phys. Rev. Lett. **104**, 086402 (2010)

[33] X-J. Zhang, E. Koch and E. Pavarini, Phys. Rev. B **105**, 115104 (2022)

[34] X-J. Zhang, E. Koch and E. Pavarini, Phys. Rev. B **106**, 115110 (2022)

[35] X-J. Zhang, E. Koch and E. Pavarini, Phys. Rev. Lett. **135**, 026508 (2025)

4 Hund's Metal Physics in the Iron-Based Superconductors

Luca de' Medici
Ecole Supérieure de Physique et Chimie Industrielles de la Ville de Paris
20 rue Vauquelin, 75005 Paris, France

Contents

1 Introduction **2**

2 Essentials about Fe-based superconductors **4**

3 Modeling Fe-based superconductors **5**

4 Slave-spin mean-field **10**

5 Hund's metal physics **12**

6 The working mechanism of Hund's induced correlations **15**

7 Conclusions **20**

E. Pavarini, E. Koch, A. Lichtenstein, and D. Vollhardt (eds.)
Understanding Correlated Materials with DMFT
Modeling and Simulation Vol. 15
Forschungszentrum Jülich, 2025, ISBN 978-3-95806-813-1
http://www.cond-mat.de/events/correl25

1 Introduction

Iron-based superconductors (Fe-SC) are one of the many "quantum materials"[1] that are keeping the international research community busy in the recent years. In order to understand, and possibly boost, their superconductivity, a necessary step is understanding their normal metallic phase that turns superconductive below the critical temperature.

This has been characterized as a Hund's metal [1], and this paradigm now applies successfully to many other materials [2].

The name comes from the correlations in the electronic states that are due to the tendency of electrons to distribute themselves on different orbital states with their spins aligned. This energetic convenience, in isolated atoms, is known as a set of rules, the famous "Hund's rules". The fact that these rules have an impact on gases and insulating solids is well known. That they can have strong influence on metallic phases is a much more recent realization [3].

Band theory is the basic approach to crystalline solids, and within it electronic properties of solids are calculated using independent electrons. That is, the electron-electron repulsion is taken into account effectively (differently depending on the specific technique that is used: i.e. Hartree-Fock, any flavor of Density-Functional Theory-DFT, etc.) as an external potential acting on single particles, and the wavefunctions of the eigenstates are Slater determinants of Bloch single-particle eigenfunctions. Each Bloch wavefunction is a plane wave modulating a periodic function which, in some materials, can be quite localized around the lattice sites for the conduction bands. For these materials often band theory is particularly bad in predicting many electronic properties, this being an indication that the independent particle approximation of the wavefunctions is not good enough, and one has to use a more refined scheme. By definition electrons in these materials are called correlated.

The local part of the Bloch wavefunction can be expanded on a local basis, a customary choice being that of (orthonormal) maximally-localized Wannier functions [4] with given s/p/d or f orbital symmetries. In the Slater determinant the weight of the different local configurations (i.e. the coefficient in front of each possible product of local basis functions in the sum) will be dictated by the weights of these orbitals in the Bloch functions. No preference can arise in the wavefunction for specific collective configurations of the electrons on a given site, i.e., high or low total spin, charge or orbital state: these correlations are absent in band theory. Methods that introduce these correlations are needed for modeling these materials correctly, among which indeed are the Fe-SC, as is illustrated in Fig. 1. The plot shows in blue the experimentally measured Sommerfeld coefficient (the slope of the electronic specific heat as a function of temperature at low temperatures) across a range of Fe-SC, each square being a different single-crystal sample. This quantity can be calculated within band theory (DFT) and the results are plotted in black. The discrepancy between theory and experiments is apparent, all the more moving towards the left side of the diagram, indicating an increasing impact of

[1] Quantum materials is an "umbrella term" encompassing materials showing interesting non-trivial quantum properties, among which unconventional superconductivity has certainly a prominent spot.
`https://en.wikipedia.org/wiki/Quantum_materials`

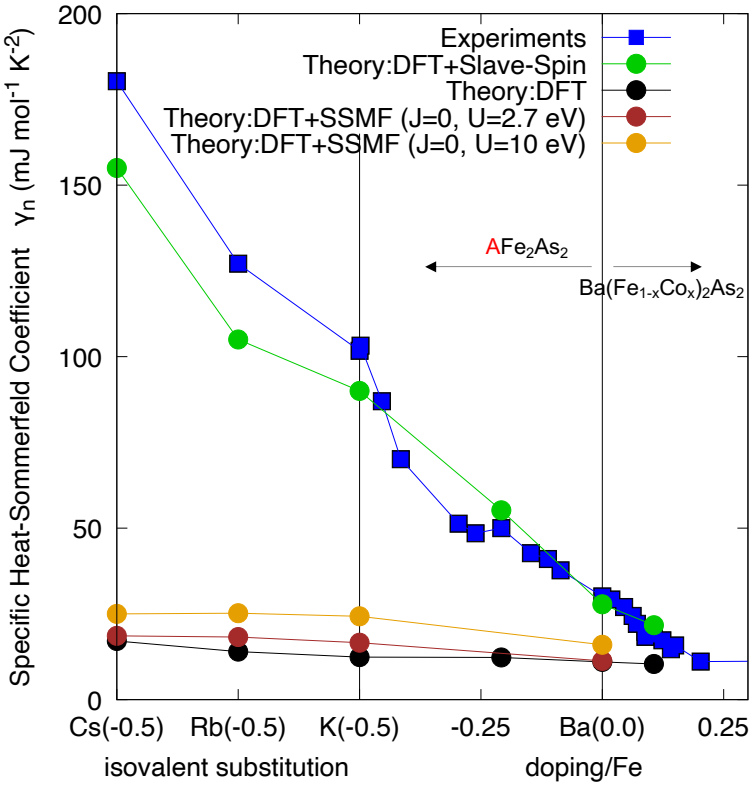
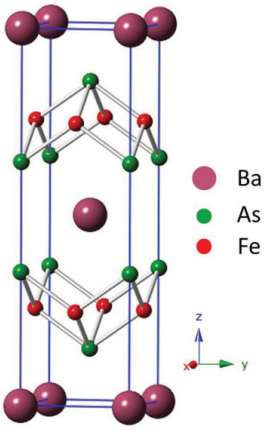


Fig. 1: *Sommerfeld coefficient, i.e., the coefficient γ of the low-T electronic specific heat ($C_V \sim \gamma T + \cdots$) of the normal metallic phases in the "122" family of Fe-based superconductors. Its mother compound, $BaFe_2As_2$ can be electron doped with the substitution of Co for Fe, and hole-doped replacing Ba with K, yielding the level of doping reported on the x-axis. The hole-doped end members AFe_2As_2 (A=K, Rb, Cs) are isovalent. Experimental values are reported in blue, while DFT-GGA results are in black, the discrepancy highlighting the strongly correlated nature of these materials. DFT+Slave-spin mean-field (in green) calculations performed with a single choice of the interaction values ($U = 2.7\,eV$, $J/U = 0.25$) are able to reproduce the whole trend by including dynamical local correlations. Switching off only the Hund's coupling J (brown) makes the results fall back towards the uncorrelated ones, no matter how large (even unphysically large—dark yellow) the value of the Coulomb interaction U is chosen, demonstrating the predominant role of Hund's coupling in these materials.*

the neglected correlations. The results of an approach including them (DFT+Slave-Spin mean-field, reported in green) captures the whole series of experiments instead, proving the point. Neglecting specifically the aforementioned Hund's rules in the approach, even when including the more familiar charge correlations (i.e. the tendency of electrons to avoid packing on the same site, reported in yellow and brown as "J=0") results in a spectacular fall back close to the band-theory results, demonstrating that Hund's physics is the key player here.

In this chapter we will try to break down this calculation to inspect its gears and to gain—also through some simplified models—insight into why and when Hund's physics is important and a material can be rightfully seen as a Hund's metal.[2]

[2]I gave previously a lecture at the Jülich school of 2017 entitled "Hund's metals, explained". Both lectures' subject is Hund's metal physics and they both address its importance in the Fe-SC. I have tried, however, to maintain the information overlap between the two lectures to a minimum, making them maximally complementary.



Compound	$a = b$(Å)	c(Å)	z_{As}
$BaFe_2As_2$	3.9625	13.0168	0.3545
KFe_2As_2	3.844	13.916	0.35249
$RbFe_2As_2$	3.873	14.459	0.34748
$CsFe_2As_2$	3.905	15.126	0.34189

Fig. 2: *Structure of the AFe_2As_2 compounds (here A=Ba), and structural parameters determined by X-ray diffraction. (F. Hardy, private communication)*

2 Essentials about Fe-based superconductors

Here an essential outline of Fe-SC will be given, without any attempt of neither a historical account nor a review of the literature (for which two nice starting points are Refs. [5, 6]).

- Fe-SC are materials including planes of Fe atoms forming a square lattice with ligands in the middle of the squares, alternatively slightly above and below the level of the plane. The ligands can be Pnictogens (As, P) or Chalcogens (S, Se, Te), giving rise to the two groups of Iron Pnictides and Iron Chalcogenides, respectively. Several different families exist in these two groups depending on the spacer layers between these planes. Most of the action happens in the Fe-ligand plane, which motivates the common physics of these materials despite their chemical variations. We will focus on the "122" family, taking the name from the stoichiometric formula AFe_2As_2 (where A can be Ba, K, Rb, Cs),[3] where the spacer layer hosts only the cation A (see Fig. 2). Their symmetry is tetragonal (i.e., the conventional unit cell has equal dimensions a=b in the x and y directions, but not in the z direction), with orthorhombic distortions (i.e. $a \neq b$) happening at low temperatures in some cases.

- The striking feature that makes this family extremely interesting is that it can be chemically tuned in a very fine way. Isovalent substitutions (P for As) can be used to apply chemical pressure, while others can be used to tune the electronic density. Using formal oxidation states Ba^{2+} and As^{3-} gives to Iron the valence Fe^{2+}, which since the Fe has the ground state configuration [Ar]$3d^6 4s^2$ means that it will host 6 electrons in the $3d$-orbitals on average. Substituting Fe with Co (but also with Ni) introduces extra electrons, whereas the substitution of Ba with K introduces extra holes, and all the compositions between the stoichiometric $BaFe_2As_2$ and KFe_2As_2 can be obtained, thus providing the very fine phase diagram reported in Fig. 3. Given that the formal oxidation state for the alkaline elements is K^{1+}, the average number of electron hosted on Fe diminishes to 5.5. As said the end member KFe_2As_2 has isovalent siblings with K replaced by Rb or Cs.

[3] And also Na, Ca and Sr which we will not address here.

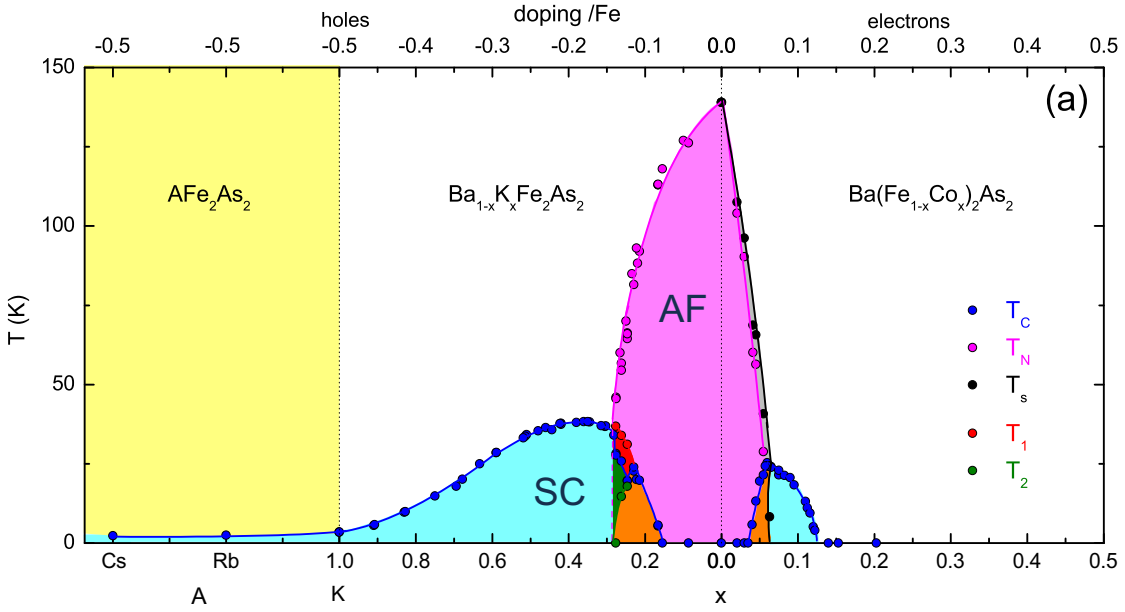


Fig. 3: *Phase diagram of electron and hole-doped $BaFe_2As_2$ (where Fe is formally in the $3d^6$ configuration at stoichiometry), and of the end-members of the family (yellow area, with Fe in the formal $3d^{5.5}$ configuration) AFe_2As_2 (A=K,Rb,Cs). The white/yellow zone of the phase diagram is paramagnetic and metallic, AF indicates a collinear metallic antiferromagnetic phase, SC indicates superconductivity. Other colors indicate coexistent phases. (adapted from [7])*

- In the phase diagram three main phases are present: a metallic "normal" phase for all compounds at high temperatures, turning into an antiferromagnetic metal (with reduced orthorhombic symmetry) or into a superconductor, depending on the composition, below the respective critical temperatures. The metallic phases are standard Fermi liquids, showing, e.g., a T^2 dependence of the resistivity, saturating Pauli magnetic susceptibility and T-linear specific heat (of which the slope is reported in Fig. 1) at low temperature. The maximal critical temperature for superconductivity varies across the families, it tops at ~ 40 K for the 122 family, while the record for a bulk Fe-SC is ~ 56 K for the "1111" family. Monolayer FeSe on a $SrTiO_3$ substrate was reported having $T_c > 65$ K.

3 Modeling Fe-based superconductors

Ab-initio modeling of Fe-SC can be straightforwardly performed within DFT, using the experimental structural parameters determined by X-ray diffraction (reported in Fig. 2). For AFe_2As_2 the Bravais lattice is body-centered, space group $I4/mmm$ in the tetragonal phases (turning to $Fmmm$ in the orthorhombic phases). The bandstructures obtained with the PBE-GGA functional are reported in Fig. 4 (green curves in the right panels). The plots focus on a range of a few eV around the Fermi level, on the conduction bands which are responsible of the electronic properties of these materials and which, as it is visible on the left panels, have mostly a character of Fe $3d$-orbitals.

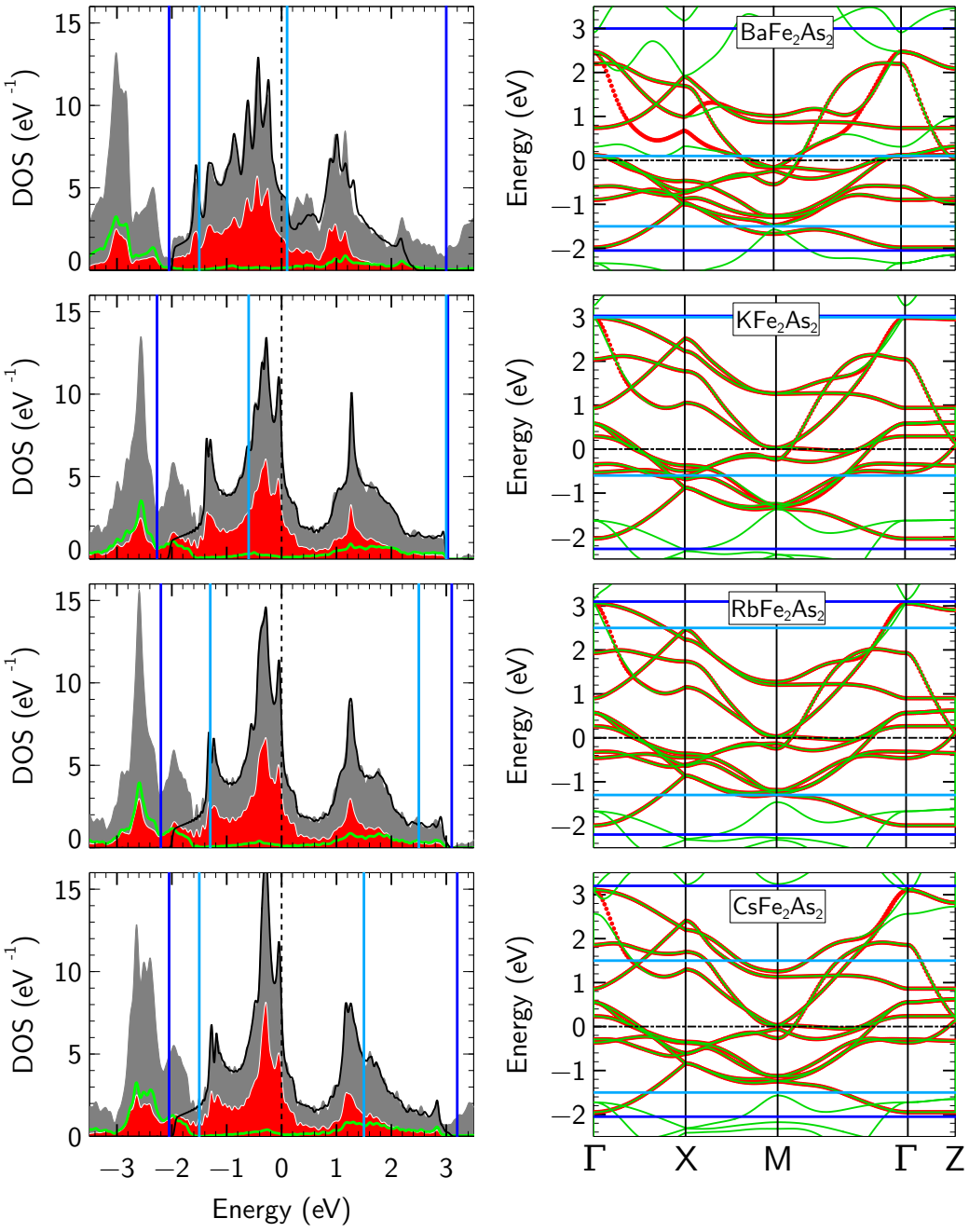


Fig. 4: *Electronic structure and maximally-localized Wannier function fitting of the conduction bands for the main stoichiometric compounds of the 122 family. Right panels: the DFT bandstructure—zoomed in to an energy range of a few eV around the Fermi level—is reported in green on a path in the Brillouin zone of the tetragonal BCC lattice. The fit of these bands with 5 Wannier d-orbitals centered on each Fe atom is drawn in red. Left panels: the total DFT DOS in this energy range is reported in grey. The contribution of each of the two Fe atoms is in red, while that of the As ligands is in green. The black line is the DOS of the tight-binding Wannier model. The dark and light blue lines define the outer and the inner ("frozen") windows for the Wannier90 procedure for obtaining MLWF and the tight-binding model for each compound. (courtesy of Pablo Villar Arribi [8])*

Three main comments are in order, on the DFT bandstructures:

1. Most of the bands have little dispersion in the z-direction (Γ–Z path in these figures), owing to the relatively bi-dimensional nature of these materials. Thus, the resulting Fermi surfaces will have little evolution along z and can be well characterized by looking at their cuts in the k_z=0 plane (path Γ–X–M–Γ). Importantly, the bands in $BaFe_2As_2$ cross the Fermi level around the center of the Brillouin zone Γ and near its corner M, creating there hole pockets and electron pockets, respectively. This *semi-metallic* nature of the mother compounds is shared among all the families of Fe-SC, and is observed in ARPES experiments. The various pockets are similar in size and shape and this creates quasi-nesting conditions boosting the magnetic susceptibility, which explains the arising of the magnetic phases and provides a natural mechanism for unconventional superconductivity mediated by spin fluctuations [5].

   Since the substitution of Ba with alkalines diminishes the electrons in the system the Fermi level moves down in these compounds, making the hole-pockets larger, while the electron pockets essentially empty out and leave little features in the Fermi surface around the M point.

2. Despite the Fermi surfaces matching qualitatively the experiments, the measured dispersion of the conduction bands is much smaller than the calculated bandstructure by at least a factor of 2 to 3. This is a typical sign that dynamical correlations are important, since the dressed quasiparticles replacing the bare electronic excitations of independent electrons have a larger mass and smaller velocity, thus mainly "squeezing" the dispersions around the Fermi level. Moreover it is seen that bands where the Fe t_{2g} (and in particular the d_{xy}) orbital character is dominant are substantially more strongly renormalized than the others, indicating the *selective* strength of the correlations among the different electrons.[4] This band-theory/experiment mismatch is smaller for the electron-doped compounds but larger the more hole doping is introduced. It is strikingly illustrated in the value of the Sommerfeld coefficient γ discussed in the introduction and shown in Fig. 1. Indeed, $\gamma = \pi^2 k_B^2 / 3N^*(E_F)$ is proportional to the density of states (DOS) of the quasiparticles at the Fermi level $N^*(E_F)$, which increases with the aforementioned mass increase due to dynamical correlations. In cases of selective correlations the most correlated electrons can make the DOS very large even in the presence of other much less correlated electrons. For a doping of 0.5 holes/Fe (i.e., for KFe_2As_2 and its isovalent siblings) correlations are very strong and very selective.

3. Taking into account local dynamical correlations, as we will see in the following, does not cure *all* quantitative discrepancies between theory and experiments [1], however. Indeed the Fermi pockets have typically a larger size in calculation than in experiments, and in some cases a pocket is present in the DFT result whereas the band responsible

[4] Both the experimental and the theoretical aspects of the orbital selectivity of Fe-SC's correlation strength were discussed in depth in the lecture of 2017.

for it is seen in ARPES data away from E_F. This mismatch can obviously alter the estimate of many low-energy electronic properties (for example the value of $N^*(E_F)$, the nesting properties, etc.). In semi-metals as the Fe-SC this is a typical outcome of the self-interaction, a known issue of LDA or GGA flavors of DFT, absent in Hartree-Fock. As a matter of fact improving the treatment of the exchange energy beyond standard DFT can cure it and improve the calculation of the Fermi surface and of the related properties (see Ref. [9] and references therein).

In order to include dynamical correlations in the modeling, the electron-electron interaction has to be treated beyond the mean-field level. The (screened) Coulomb interaction decaying quickly with the distance, it is customary to expand it on a basis of localized functions, which is also very efficient in describing the one-body part of the Hamiltonian, since as we mentioned previously the electronic density associated to the conduction bands is quite concentrated around the lattice ions. One such orthonormal basis is that of the maximally-localized Wannier functions (MLWF) that can be optimized so to best parametrize eigenstates and eigenfunctions in the conduction bands of the DFT solution [4]. Their character is mainly Fe-$3d$ as we said, with some contribution from the $4p$-electrons of the ligands. A natural choice is then to use a set of 5 basis functions of d-like symmetry on each Fe ion, and 3 basis functions of p-like symmetry on each ligand ion, a total of 16 functions per unit cell. This p-d ***model*** is more accurate but of greater complexity than the customary ***d-model***, i.e., the alternative choice of introducing only 5 basis functions of d-like symmetry on each Fe ion. These functions cannot be as localized as in the p-d model, but reduce the number of interaction parameters in the model.
Once chosen[5] the basis of Wannier functions $w_m(r-R_i)$ the Hamiltonian of the conduction electrons reads

$$H = \sum_{ijmm'\sigma} t_{ij}^{mm'}\, d^\dagger_{im\sigma} d_{jm'\sigma} + \frac{1}{2}\sum_{ijkl}\sum_{mm'nn'}\sum_{\sigma\sigma'} V_{ijkl}^{mm'nn'}\, d^\dagger_{im\sigma} d^\dagger_{jm'\sigma'} d_{kn'\sigma'} d_{ln\sigma} \tag{1}$$

where $d^\dagger_{im\sigma}$ is the creation operator of an electron with spin σ in the state whose wavefunction is $w_m(r-R_i)$, and

$$t_{ij}^{mm'} = \int d\mathbf{r}\, w_m^*(\mathbf{r}-\mathbf{R}_i)\left(-\frac{\hbar^2}{2m_e}\nabla^2 + V_{\text{eff}}(\mathbf{r})\right) w_{m'}(\mathbf{r}-\mathbf{R}_j) \tag{2}$$

and

$$V_{ijkl}^{mm'nn'} = \int d\mathbf{r} d\mathbf{r}'\, w_m^*(\mathbf{r}-\mathbf{R}_i) w_{m'}^*(\mathbf{r}'-\mathbf{R}_j)\, W(\mathbf{r},\mathbf{r}',\omega{=}0)\, w_n(\mathbf{r}'-\mathbf{R}_k) w_{n'}(\mathbf{r}-\mathbf{R}_l) \tag{3}$$

where $V_{\text{eff}}(\mathbf{r})$ is the effective one-body potential used in the band-theory calculation (e.g. the Kohn-Sham potential in DFT) and $W(\mathbf{r},\mathbf{r}',\omega{=}0)$ is the low-frequency limit of the Coulomb

[5] A technical point is worth stressing for obtaining an optimal basis of MLWF, using, e.g., the publicly available code Wannier90: Two windows of energy need to be defined in order to have a faithful representation of the conduction bands *and* localized basis functions. An outer window encompasses all the bands to be fitted, whereas an inner ("frozen") window enforces the part to be reproduced exactly [4]. In Fig. 4 well-working choices for these windows are indicated by dark and light blue lines respectively for each of the compounds, both in the left and in the right panels. These were used in defining the models we utilize in the following.

interaction $e^2/|\mathbf{r}-\mathbf{r}'|$ screened by all the excitation processes to and within the bands that are not included in this low-energy model. It can be calculated in different frameworks, a customary choice being constrained-RPA approximation (c-RPA). For most Fe-SC, c-RPA calculations were reported in Ref. [10].

Owing to the localized nature of the Wannier functions and to the rapid decay of the screened interaction with distance, a common simplifying choice is to retain only the local terms of the interaction, i.e., $V^{mm'nn'} \equiv V^{mm'nn'}_{ijkl}\delta_{ij}\delta_{jk}\delta_{kl}$. This gives rise to a *multi-orbital Hubbard model*.

Among the matrix elements of the local interaction a typical choice (exact in some limits, e.g., in the presence of a large cubic field splitting that allows one to treat the three t_{2g} orbitals separately from the two e_g orbitals [3]) is to retain only the terms containing the integrals $U_{mn} \equiv V^{mmnn}$, and $J_{mn} \equiv V^{mnmn}$ (with $n \neq m$) and, defining U as the average of the U_{mm} and J the average of the J_{mn} for $n \neq m$ over the orbitals, to finally write down the *Kanamori interaction*[6]

$$\begin{aligned} H_{\text{int}} &= U\sum_{im}\tilde{n}_{im\uparrow}\tilde{n}_{im\downarrow} + (U-2J)\sum_{im\neq m'}\tilde{n}_{im\uparrow}\tilde{n}_{im'\downarrow} + (U-3J)\sum_{im<m',\sigma}\tilde{n}_{im\sigma}\tilde{n}_{im'\sigma} \\ &- J\sum_{im\neq m'} d^\dagger_{im\uparrow}d_{im\downarrow}\,d^\dagger_{im'\downarrow}d_{im'\uparrow} + J\sum_{im\neq m'} d^\dagger_{im\uparrow}d^\dagger_{im\downarrow}\,d_{im'\downarrow}d_{im'\uparrow}, \end{aligned} \tag{4}$$

where $n_{im\sigma} \equiv d^\dagger_{im\sigma}d_{im\sigma}$ is the number operator and $\tilde{n}_{im\sigma} \equiv n_{im\sigma}-\frac{1}{2}$ its particle-hole symmetric version.[7] J being the parameter favoring the spin alignment and the distribution of electrons on different orbitals, is called the "Hund's coupling".

Solving and exploring this Hubbard-Kanamori model for the Fe-SC is still a formidable task. However it can be done in several frameworks. Indeed several approaches and levels of perturbation theory in the interaction are the methods of choice, able to explore instabilities of the DFT bandstructures towards the various broken symmetry phases found in the phase diagrams of these materials. The strength of the correlations, however, as we have previously highlighted, casts some doubts on the quantitative (and in several important cases qualitative) validity of such approaches. Also, typically calculated values of U range from 2.5 to 4.2 eV (J is typically smaller, i.e., $J/U = 0.12\ldots0.15$) which is of the order of the DFT bandwidth (see, e.g., Fig. 4). We here expose the results of non-perturbative methods, thus not assuming a small interaction as a starting point in any way.

One such methods is Dynamical Mean-Field Theory (DMFT), presented in this book in the chapter by Eva Pavarini. Here we will rather expose the Slave-spin mean-field (SSMF) method, which can be seen as a simpler dynamical mean-field technique providing orbital-selective band renormalization and giving direct analytical access on the mechanisms behind it.

[6] Here it is seen that the off-diagonal elements of U_{mn} are not used. Indeed it is found that they are typically close to $U-2J$ (an exact relation in some cases) which is then taken as a further simplifying assumption.

[7] This form of the interaction implies a shift of the chemical potential, of no physical meaning. A shift of the chemical potential is implied anyway because of the double counting of the interaction already included in $V_{\text{eff}}(r)$, which is not an issue in the d-model formulation for this reason.

4 Slave-spin mean-field

In the slave-spin representation, the original fermionic model is mapped on an auxiliary model having both fermions and spin variables on a lattice. That is, to every local electronic one-particle state (created by $d^\dagger_{im\sigma}$) are associated in the auxiliary, larger Hilbert space, both a fermionic state (created by $f^\dagger_{im\sigma}$) and a spin-1/2 variable, of z-component $S^z_{im\sigma}$ (and flipped by $S^\pm_{im\sigma}$). They both carry the same indices of the original d fermion, and the slave-spin has no special relation—and should not be confused—with the physical spin. An occupied local state $|1\rangle_d$ in the original space is then associated, in the auxiliary Hilbert space, to the direct product of the occupied state for the corresponding f fermion and to the "up" (that we indicate with 1) state of the associated "slave"-spin $|1\rangle_f|1\rangle_s$. Likewise an empty d-state $|0\rangle_d$ is associated to the empty fermionic state and the "down" (that we indicate with 0) state of the slave spin $|0\rangle_f|0\rangle_s$. These "physical" states satisfy the operatorial relation

$$f^\dagger_{im\sigma} f_{im\sigma} = S^z_{im\sigma} + \frac{1}{2}, \tag{5}$$

which can be used to distinguish them from the remaining combinations $|1\rangle_f|0\rangle_s$ and $|0\rangle_f|1\rangle_s$ which have no physical counterpart.

This is apparently a complication, but it turns out that approximations performed on the larger space can be less severe than if applied directly to the original system.

The operators of the original space are mapped on operators having the same matrix elements between the physical states of the larger space, while their action on the unphysical states can be chosen freely, in principle. In practice this freedom is used to gauge approximated treatments, e.g., to reproduce known limits and possibly yield the most physical results.

Hence the number operator $n_{im\sigma} = d^\dagger_{im\sigma} d_{im\sigma}$ can be equivalently mapped into the number operator for the pseudo-fermions $n^f_{im\sigma} = f^\dagger_{im\sigma} f_{im\sigma}$ or into $S^z_{im\sigma} + \frac{1}{2}$, which, because of Eq. (5), gives the same result by construction on the physical states. The interaction Hamiltonian Eq. (4) then, for which we customarily consider only the density-density terms,[8] can be written in terms of the S^z operators only

$$H^s_{\text{int}} = \sum_i H^s_{\text{int}}[i] = U \sum_{im} S^z_{im\uparrow} S^z_{im\downarrow} + (U-2J) \sum_{im\neq m'} S^z_{im\uparrow} S^z_{im'\downarrow} + (U-3J) \sum_{im<m'\sigma} S^z_{im\sigma} S^z_{im'\sigma}. \tag{6}$$

The one-body part instead involves both slave-spins and pseudofermions, since the off-diagonal destruction (creation) operator $d^{(\dagger)}_{im\sigma}$ is expressed by $f^{(\dagger)}_{im\sigma} O^{(\dagger)}_{im\sigma}$. The general form of the $O_{im\sigma}$ operator is $O_{im\sigma} = S^-_{im\sigma} + c_{im\sigma} S^+_{im\sigma}$, where $c_{im\sigma}$ is an arbitrary gauge embodying the aforementioned freedom. We choose $c_{im\sigma} = \frac{1}{\sqrt{\langle \hat{n}^f_{im\sigma}\rangle_f (1-\langle \hat{n}^f_{im\sigma}\rangle_f)}} - 1$, which, within the present mean-field approximation, can be shown to reproduce the non-interacting limit. Then the total Hamiltonian of our model in the auxiliary Hilbert space reads $H = H_0 + H^s_{\text{int}}$ with

$$H_0 = \sum_{i\neq jmm'\sigma} t^{mm'}_{ij} f^\dagger_{im\sigma} f_{jm'\sigma} O^\dagger_{im\sigma} O_{jm'\sigma} + \sum_{im\sigma} \varepsilon_m f^\dagger_{im\sigma} f_{im\sigma}, \tag{7}$$

[8] Using the full Kanamori form, thus including the spin-flip and pair-hopping terms that we here neglect, does not alter qualitatively any of the analysis or conclusions exposed in this chapter. The differences are merely quantitative ones.

where we have singled out the local terms in the one-body part of Eq. (1) as $t_{ii}^{mm'} = \varepsilon_m \delta_{mm'}$.

The mapping is thus far exact if we could project out all unphysical states strictly enforcing the constraint Eq. (5). In the SSMF scheme three approximations are instead performed. First, we mean-field decouple slave-spin and pseudofermion so that we are left with a non-interacting fermionic Hamiltonian, and a lattice spin model where several slave-spins interact on site and are also coupled to the slave-spins of neighboring sites. Second, we perform a mean-field decoupling of the slave-spin lattice system in the spirit of a Weiss mean-field, and thus we are left with a single-site spin Hamiltonian in an effective field. Third, we treat the constraint on average, with site-independent (and spin-independent, since we address the paramagnetic phases here) Lagrange multipliers λ_m, adjusted so that $\langle n_{m\sigma}^f \rangle = \langle S_{m\sigma}^z \rangle + \frac{1}{2}, \forall i, m, \sigma$. Details of this procedure can be found, e.g., in Ref. [11] and references therein.

The resulting mean-field Hamiltonian is $H - \mu N = H_s + H_f - \mu N$, with

$$H_f - \mu N = \sum_{i \neq j m m' \sigma} \sqrt{Z_m Z_{m'}}\, t_{ij}^{mm'}\, f_{im\sigma}^\dagger f_{jm'\sigma} + \sum_{im\sigma} (\varepsilon_m - \lambda_m + \lambda_m^0 - \mu) f_{im\sigma}^\dagger f_{im\sigma}\,, \tag{8}$$

and $H_s = \sum_i H_s^i$ with

$$H_s^i = \sum_{m\sigma} \big(h_m O_{m\sigma}^\dagger + H.c.\big) + \lambda_m \big(S_{m\sigma}^z + \frac{1}{2}\big) + H_{\text{int}}^s[i]\,, \tag{9}$$

where the self-consistent parameters are

$$Z_m = |\langle O_{m\sigma} \rangle|^2, \tag{10}$$

$$h_m = \sum_{j \neq i, m'} t_{ij}^{mm'} \sqrt{Z_{m'}} \langle f_{im\sigma}^\dagger f_{jm'\sigma} \rangle \tag{11}$$

$$\lambda_m^0 = h_m \sqrt{Z_m}\, \frac{2\langle \hat{n}_m^f \rangle - 1}{\langle \hat{n}_m^f \rangle \big(1 - \langle \hat{n}_m^f \rangle\big)} \tag{12}$$

the latter being a shift due to the mean-field procedure, which reduces to λ_m, and thus cancels it, in the non-interacting limit [11].

Solving these equations iteratively until convergence yields the renormalized quasiparticle Hamiltonian Eq. (8), the bandstructure of which can be compared with the quasiparticle bands measured in ARPES. In particular the orbitally-resolved quasiparticle weight Z_m is the inverse of the orbitally-resolved mass enhancement, and $\varepsilon_m - \lambda_m + \lambda_m^0$ can be seen as a renormalized local orbital energy.

The slave-spin Hamiltonian is still a many-body Hamiltonian that can be used to calculate local correlation functions, here we will see the (z component of the) total local magnetic moment $\Big\langle \big(\sum_m (S_{im\uparrow}^z - S_{im\downarrow}^z) \big)^2 \Big\rangle$.

5 Hund's metal physics

Application of the SSMF to the multiorbital Hubbard models[9] for $A\mathrm{Fe_2As_2}$ with A=Ba, K, Rb, and Cs leads to the results reported in Fig. 5. All the plotted quantities show a clear crossover as a function of U between a weak-coupling and a strong-coupling behavior.
For the lower range of U all the quasiparticle weight Z_m are grouped, weakly dependent on U and barely smaller than 1, their non-interacting value. Analogously, the orbital-resolved mass enhancements, which are exactly their inverse, lie barely above 1 for the whole range. Also the renormalized orbital energies evolve smoothly and the local magnetic moment remains near its small non-interacting value.
All quantities change rapidly around the crossover value of U, and above it one sees a completely different behavior: The Z_m have spread and dropped to small values below (some way below) 0.5, and correspondingly the mass-enhancements are very selective and reach very high values (extremely high for the t_{2g} orbitals and in particular d_{xy}); the renormalized orbital energies have rearranged and now are very close to one-another, while the local magnetic moment has risen and is now very close to its saturation value 5/2. This behavior is the *Hund's metal*.
It is to be noted that the crossover is sharper and happens earlier for the alkaline compounds A=K, Rb, Cs than for $\mathrm{BaFe_2As_2}$. This is mainly due to the difference in the average electron density. As said the alkaline compounds host 5.5 electrons/Fe on average while $\mathrm{BaFe_2As_2}$ has 6 electrons/Fe (and indeed the chemical potentials in the calculations are adjusted so to keep these densities at all interactions). The sharpness of the crossover culminates at half-filling where it converges with the Mott transition. This implies that the Hund's metal is a zone at U larger than the U_c for the Mott transition at half-filling that can be entered both increasing the interaction strength and reducing the doping towards half-filling. In other words the Hund's metal is the doped Mott insulator in presence of sizeable Hund's coupling.
This behavior is clearly understood when analyzing the same features in a 5-orbital Hubbard-Kanamori model of featureless simplified bands (i.e. ε_m=0 for all orbitals and $t_{ij}^{m,m'} = t\,\delta_{m,m'}$ for i nearest neighbor of j on an infinitely-dimensional Bethe lattice, that has a semicircular DOS of half-bandwidth D=$2t$). As visible in Fig. 6, the characteristic crossover [2, 3] to the Hund's metal reported for all integer fillings from n=8.0 to n=5.0 (half-filling)[10] clearly becomes sharper the more half-filling is approached, and is obviously connected to the Mott transition at half-filling (yellow sharp drop). This strong-correlation behavior being connected to the prevalence of high-spin local configurations favored by J, as outlined previously, it is instructive to plot the relative weight of these configurations compared to the others. Indeed for $U/D = 3.0$ and $J/U = 0.25$ it is visible that the high-spin configurations of each sector dominate (i.e. compared to the other configurations with the same number of electrons), and all the more the closer the system is to half-filling.

[9] In these calculations as a function of U a fixed ratio $J/U = 0.25$ was kept. Indeed, it was shown [12, 13] that the physical results for the Kanamori interaction with $J/U = 0.12 \div 0.15$ as estimated by c-RPA are best reproduced in SSMF increasing the ratio to $J/U = 0.25$.

[10] The model being particle-hole symmetric the curves are also representative of the filling between n=2.0 and n=5.0.

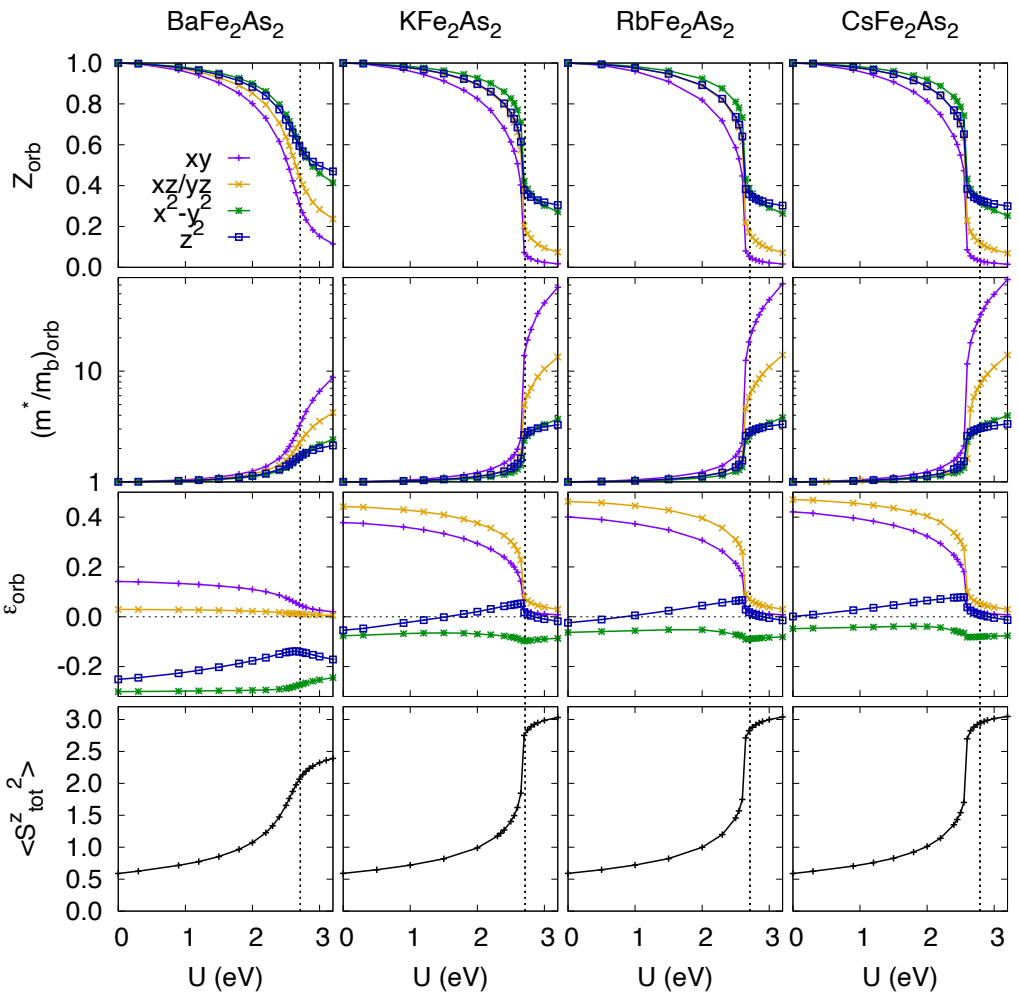


Fig. 5: *Slave-spin mean-field results for AFe_2As_2 with A=Ba, K, Rb, Cs as a function of the interaction strength U (for J/U=0.25). From top to bottom rows: orbitally-resolved quasiparticle weights Z_m, orbitally-resolved mass enhancements $(m^*/m_b)_m = 1/Z_m$ (log scale), renormalized orbital energies and z-component of the local magnetic moment. A clear crossover from a normal metal to the Hund's metal behavior is visible just below the dashed line, which marks the interaction value (close to the one calculated in c-RPA) used for the calculations reported in Fig. 1. The crossover is sharper and happens faster in the calculations for the alkaline compounds (5.5 electrons/Fe) than for $BaFe_2As_2$ (6 electrons/Fe), owing to the influence of the half-filled Mott insulator. (courtesy of Pablo Villar Arribi [8])*

It is clear that both for the realistic calculations and for those in the idealized model, Hund's coupling triggers a behavior where the local high-spin configurations prevail and the quasiparticle weight becomes small (and the mass enhancement large) and selective, all the more for filling near half, but *only* for values of the interaction strength larger than the critical value for the Mott transition at half-filling. It is worth noticing that the Mott insulating states at all the other fillings play very little role in the zone of the phase diagram we are discussing (where the interaction strength U is of the order of the bandwidth or even smaller), relevant to the Fe-SC, because they are sent at much higher critical U values. Conversely the role of the Mott insulator at half filling is clearly dominant, and it seems to act as a catalyst for the Hund's metal, amplifying its features with its proximity.

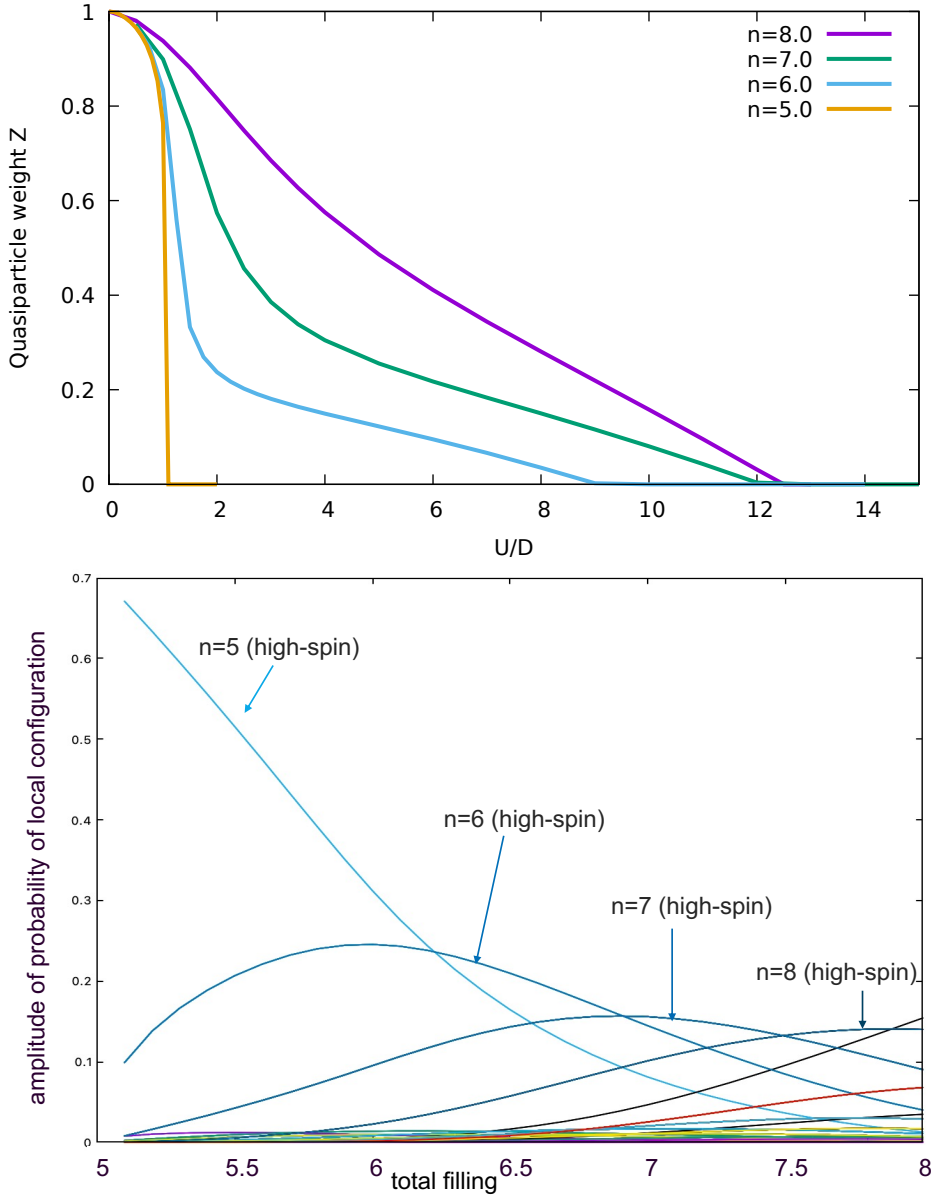


Fig. 6: *5-orbital Hubbard Kanamori model with $J/U = 0.25$. Upper panel: quasiparticle weight Z as a function of the interaction strength U for the integer fillings between half-filling (n=5.0) up to 8 electrons per site, showing the increasing sharpness of the crossover with the proximity to the Mott transition at half-filling. Lower panel: relative weight of the high-spin configuration with the indicated number of electrons in the ground state of the slave-spin Hamiltonian as a function of the filling of the system for $U/D = 3.0$. The weights for all other configurations are also plotted in this graph, most being indistinguishable from the x-axis. (adapted from [14])*

But why is it so? Why is Hund's coupling so efficient in inducing a Mott insulator at half-filling and why are correlations in its proximity so much stronger than at J=0? We can gain this insight by inspecting a few analytical results that can be obtained within SSMF in these idealized models.

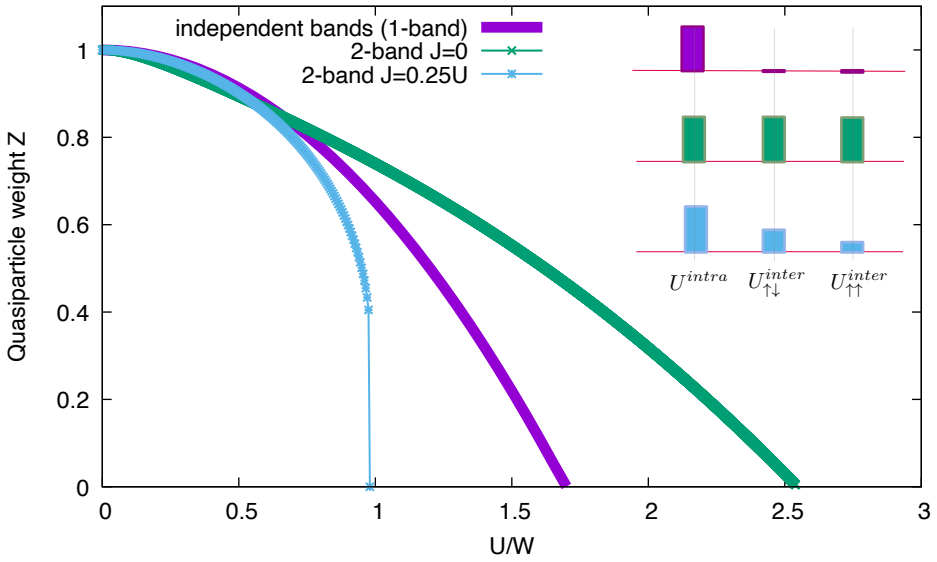


Fig. 7: *Mott transition in the half-filled Hubbard model studied with SSMF (or equivalently Gutzwiller approximation or slave-boson mean-field). Independent bands (purple line) compared with two bands in absence (green) and in presence (light blue) of Hund's coupling J. It might surprise that at strong coupling the second case is less correlated then the first, and the third more correlated than the second, despite the opposite overall trend in the inter-orbital interaction strength (columns sketched on the right). [14]*

6 The working mechanism of Hund's induced correlations

The counter-intuitive nature of Hund's induced correlations can be illustrated by the following simplified paradoxical puzzle, summarized by Fig. 7. Let's imagine a half-filled multi-orbital Hubbard band with featureless bands (as before we can take a semi-circular DOS of bandwidth $W = 2D$, i.e., $D(\varepsilon) \equiv \frac{2}{\pi D}\sqrt{(1-(\frac{\varepsilon}{D})^2)}$) and no inter-orbital hopping.

- If all inter-orbital interaction is switched off too one obtains a collection of single-band Hubbard models, not talking to each other. Their behavior, in particular with respect to the Mott transition will be that of a one-band model (purple line in the figure). Its critical coupling for the Mott transition in SSMF (and in Gutzwiller approximation or slave-boson mean-field) is $U_c = -16\bar{\varepsilon}$, where $\bar{\varepsilon}$ is the bare delocalization ("kinetic") energy at half-filling, i.e., $\bar{\varepsilon} \equiv \int_{-D}^{0} d\varepsilon\, \varepsilon\, D(\varepsilon) \simeq -0.2122D$. As visible in the figure this gives $U_c \simeq 3.4\, D \simeq 1.7\, W$.

- Let's now *turn on* the interaction between the different orbitals. Let's focus for simplicity on the two-orbital case. At J=0 the electrons in the two orbitals will add to their intra-orbital repulsion U and inter-orbital repulsion U to electrons in the other orbital irrespectively of their spin orientation. One might naively expect that this additional repulsion makes the system more correlated. This is however not the case: as visible in the figure (green line) the quasiparticle weight lies systematically above that of independent bands for moderate to strong interactions, and the Mott transition happens at much larger $U_c \simeq 2.5W$!

- Even more puzzling, let's now *reduce* the inter-orbital interaction compared to the intra-orbital one, and even more so for electrons with parallel spins. This is exactly what is done for finite Hund's coupling J/U. Again one might expect this reduction in the electronic repulsion to de-correlate the system, but one finds the opposite. The quasiparticle weight lies below the one for $J{=}0$ at moderate to strong interactions, and the Mott transition happens precipitously at a much smaller $U_c \simeq W$!

The puzzle is solved by the explicit calculation of U_c, that can be effected analytically in SSMF for any number M of orbitals both for $J{=}0$ and finite J. It turns out that a naive balance between bare kinetic energy and interaction strength is not enough to understand the degree of correlation of the system. The energy and degeneracy of local multiplets and the processes available for fluctuating between different charge states are of importance instead, and these are tuned by Hund's coupling, as we are going to see now.

In the slave-spin mean-field approximation[11] a Mott insulator is a solution in which $Z_m = 0$. By the self-consistency equation Eq. (11), this implies $h_m = 0$. Thus in proximity of a Mott insulator a perturbative treatment in h_m of the slave-spin problem can be performed.
In the half-filled, particle-hole symmetric case with no crystal-field splitting (i.e. $\varepsilon_m = 0$), $\mu{=}\lambda_m{=}\lambda^0_m{=}0$ and $c_m{=}1$. Then the unperturbed Hamiltonian is simply $H^s_{\text{int}}[i]$ from Eq. (6).
At $T{=}0$ we only need the ground state of this Hamiltonian, which will have a different degeneracy d_0 depending on the value of J, so later on we will distinguish the $J{=}0$ from the finite J case. The perturbing Hamiltonian is

$$V \equiv H^i_s - H^s_{\text{int}}[i] = 2h \sum_{m\sigma} 2S^x_{m\sigma} = 2h \sum_{m\sigma} \left(S^+_{m\sigma} + S^-_{m\sigma}\right), \tag{13}$$

where $h \equiv h_m$ is here equal for all the M orbitals. It simply flips any of the slave-spins.
It removes the ground state degeneracy at the second order in h (the perturbation has no matrix elements within the degenerate subspace), and in order to obtain the "correct" unperturbed ground state $\left|\phi^{(0)}_0\right\rangle$ (the one to which the perturbed ground state tends for $h \to 0$) one has to diagonalize the matrix $H' \equiv V\left(E_0{-}H^s_{\text{int}}\right)^{-1}V$ in the degenerate subspace, where E_0 is the unperturbed ground state energy. The ground state ket will have a correction at the linear order instead, which according to standard perturbation theory reads: $\left|\phi^{(1)}_0\right\rangle = \left|\phi^{(0)}_0\right\rangle + \sum_{|s\rangle\neq|\phi_0\rangle} \langle s|\left(E_0{-}H^s_{\text{int}}\right)^{-1}V\left|\phi^{(0)}_0\right\rangle|s\rangle$.
The self-consistency condition Eq. (11) is needed to determine the solution of the mean-field equations, and in the present case simplifies to

$$h = \sqrt{Z_m}\bar{\varepsilon}\,. \tag{14}$$

$\sqrt{Z_m} = \left\langle 2S^x_{m\sigma}\right\rangle$ is itself a function of h, and this relation determines the self-consistent value of h for a given set of physical parameters. The critical parameters for the Mott transition are found when the solution goes to $h{=}0$, so the linear term in h is enough.

[11] In the presentation of the slave-spin analytical calculations we follow closely the Appendix of Ref. [15]

A particularly relevant and insightful quantity to calculate then is

$$4hM\langle 2S^x_{m\sigma}\rangle = \langle V\rangle = \langle \phi_0^{(1)}|V|\phi_0^{(1)}\rangle = 2\langle \phi_0^{(0)}\big|V\big(E_0{-}H^s_{\rm int}\big)^{-1}V\big|\phi_0^{(0)}\rangle, \tag{15}$$

(where we used explicitly the fact that $\langle \phi_0^{(0)}|V|\phi_0^{(0)}\rangle = 0$).
Eq. (15) illustrates that $\langle V\rangle$ (and thus $\langle 2S^x_{m\sigma}\rangle$) counts the number of ways in which flipping any two slave-spins brings the ground state into (a state having overlap with) itself, weighed by $2/(E_0{-}E_S)$, twice the inverse of the (negative) energy difference between the ground state and the intermediate excited state.
In physical terms this tracks the number of processes by which a particle can hop onto a neighboring site and back to any of the spin-orbitals still turning the ground state into (having overlap with) itself [16]. This is in strict analogy with the perturbative arguments determining Kondo coupling of an impurity in a bath which through dynamical mean-field theory describes the itinerancy of particles in a lattice model [3].
Now these processes are enhanced in presence of large degeneracy of the energy multiplets. We illustrate this in the following by comparing the case at $J{=}0$ with that for finite J.

- *$J{=}0$, $SU(2M)$ symmetry*

At $J=0$, up to a constant shift, $H^s_{\rm int}[i] = U/2\big(\sum_{m\sigma} S^z_{m\sigma}\big)^2 = U/2\big(S^z_{tot}\big)^2$. The system has an even number $2M$ of slave-spins on each site, hence any state with $S^z_{tot}=0$ is a ground state. Owing to the $SU(2M)$ symmetry of the $J=0$ problem, there are $d_0 = \binom{2M}{M}$ such states ($|S^z_{tot}{=}0;\, l\,\rangle$, for $l{=}1\dots d_0$) , corresponding to the number of ways to take half of the $2M$ slave-spins up and half down. Physically this corresponds to the ways of putting M particles in $2M$ spin-orbitals, owing to the half-filling of the system.
All the states with one flipped spin are $U/2$ higher in energy from the ground state and hence one can diagonalize $H' = -2V^2/U$. The lowest-energy eigenstate of the restriction of H' to the unperturbed degenerate manifold is

$$\big|\phi_0^{(0)}\big\rangle = \frac{1}{\sqrt{d_0}}\sum_{l=1}^{d_0}\big|S^z_{tot}{=}0;\, l\,\big\rangle \tag{16}$$

i.e., the linear combination of all the degenerate basis states in the ground state manifold with all plus signs. This can be easily checked by inspection. Indeed H' flips down any of the M spins pointing up, and then flips up any of the now $M{+}1$ spins pointing down. The analogous process takes place starting with a flip up. This makes $2M(M{+}1)$ possible processes. The fact that *all of the* d_0 degenerate basis states with M spins up and M spins down are included in the linear combination ensures that all these "exchange" processes are active. The plus signs in the linear combination also ensures that all the corresponding $-U/2$ contributions add up, generating the lowest possible energy.
This, by inserting $|\phi_0^{(0)}\rangle$ into Eq. (15) results in

$$\langle 2S^x_{m\sigma}\rangle = -\frac{8h}{U}(M{+}1) \tag{17}$$

- *$J\neq 0$ with density-density interaction, Z_2 symmetry*

For $J \neq 0$, $H^s_{\text{int}}[i]$, Eq. (6), splits the manifold with $S^z=0$ and for the case of density-density only interaction the ground state is *only two times degenerate*.[12] The two degenerate states are $|1,\dots,1,0,\dots,0\rangle$, with all M slave spins corresponding to spin-orbitals $m\uparrow$ —in our ket notation the first M of all the $2M$ slave-spins—pointing "up" (1, in our notation) and the remaining ones pointing "down" (0 in our notation), or the inverse $|0,\dots,0,1,\dots,1\rangle$.
The excitation energy of the states that can be reached by flipping one spin starting from the ground state and flipped back to it is $U_{\text{eff}}/2$ with $U_{\text{eff}} = U + (M-1)J$, so the matrix to be diagonalized to find the "correct" unperturbed ground state is the restriction of $H' = -2V^2/U_{\text{eff}}$.
This degeneracy is split at order h^{2M}, but the "correct" unperturbed ground state is still the linear combination of these two basis states with the plus sign

$$\left|\phi_0^{(0)}\right\rangle = \frac{1}{\sqrt{2}}\big(|1,\dots,1,0,\dots,0\rangle + |0,\dots,0,1,\dots,1\rangle\big). \tag{18}$$

However to leading order h^2 only $2M$ processes are active: those flipping twice a given slave spin. Thus inserting $\left|\phi_0^{(0)}\right\rangle$ into Eq. (15) gives

$$\langle 2S^x_{m\sigma}\rangle = -\frac{8h}{U_{\text{eff}}} = -\frac{8h}{U+(M-1)J} \tag{19}$$

which, for any $M \geq 2$, is much smaller than in the $J=0$ case.
Using this in the self-consistency condition Eq. (14) and eliminating h one can solve for the critical interaction for the Mott transition

$$U_c = \begin{cases} 8(M+1)|\bar{\varepsilon}|, & J=0, \quad \forall M \quad (\text{including } M=1) \\ 8|\bar{\varepsilon}| - (M-1)J & J\neq 0 \quad \text{and} \quad M\geq 2 \end{cases} \tag{20}$$

the latter relation being equivalent to say that to $U_c^{\text{eff}} = 8|\bar{\varepsilon}|$.

These results illustrate our point that the degeneracy of the ground state and of the multiplets visited by charge fluctuations enhance the itinerancy, through the activation of extra hopping channels.
This is the reason for the reduction of correlations in a multi-orbital system in absence of Hund's coupling, indeed in that case the U_c grows with the number of orbitals M.
Hund's coupling changes the situation, and increases the correlation strength for two reasons, as obvious comparing the expressions eqs. (17) and (19):

1. it reduces the number of processes contributing to $\langle V\rangle$ (and thus to $\langle 2S^x_{m\sigma}\rangle$), thus eliminating the $M+1$ prefactor,

2. increases the value of U^{eff}, thus increasing the cost for charge fluctuations, and weighing more the denominator in Eq. (19).

[12] In the case of full Kanamori interaction, including the spin-flip and pair-hopping terms, the degeneracy of the ground-state multiplet is not as reduced. However it is still much smaller than for the $J=0$ case. Thus our treatment, albeit quantitatively not exact, is qualitatively representative also of the Kanamori case.

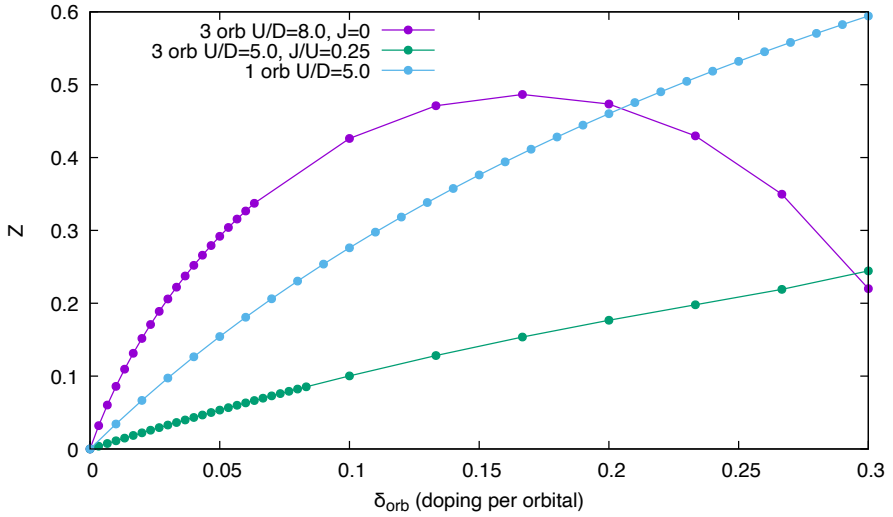


Fig. 8: *Doping dependence of the quasiparticle weight for doped half-filled Mott insulators: a 3-orbital Hubbard model with and without Hund's coupling J is compared to the single-band case. Visibly, the multi-orbital case with J=0 is less correlated than the single-band case (even for the considerably larger value of U, chosen so to be well beyond $Uc(J{=}0)$). The multi-orbital case in presence of J is much more strongly correlated than both (even more so when considering the* total *doping and not the doping* per orbital *as shown here). The parallel with the behavior of Z at half-filling as a function of $U < U_c$ plotted in Fig.7 is obvious, for the reasons explained in the main text. (adapted from [14])*

These two aspects were explored from DMFT perspective in Ref. [17]. Here we have shown explicitly the mechanism at work through an analytical calculation, showing how the many-body hopping channels participate to the geometrical factor enhancing or reducing U_c. In this respect it is worth mentioning that away from integer fillings other than half the reason 1 above still applies, while reason 2 does not. In fact $U^{\rm eff} = U{+}3J$ in these cases, thus rather pushing U_c away. Nevertheless in most of the U range correlations are found enhanced because of reason 1.

A further interesting point is that here with the same formalism the dependence of the quasi-particle weight Z on the doping for a doped Mott insulator can be obtained. After a similar calculation and for the same reasons as above one gets

$$Z = \begin{cases} \frac{M+1}{\sqrt{1-U_c/U}}\,\delta_{\rm orb}, & J=0, \quad \forall M \quad (\text{including } M{=}1) \\ \frac{1}{\sqrt{1-U_c^{\rm eff}/U^{\rm eff}}}\,\delta_{\rm orb} & J\neq 0 \quad \text{and} \quad M\geq 2 \end{cases} \tag{21}$$

where $\delta_{\rm orb} = \delta/M$ is the *doping per orbital*.
Typical behaviors are illustrated in Fig. 8 for a three-orbital Hubbard model. As it happens, for the half-filled metal, also in the present case of a doped Mott insulator, for the same conditions of doping, the multi-orbital case with J=0 is much less correlated than the single-band case. The multi-orbital model in presence of J is instead much more correlated than the single band case. It is to be noted, by the way, that the plot compares the models at the same doping *per orbital*. As a function of the total doping in the model the multi-orbital case is then even more strongly correlated than it appears on this plot, compared to a typical single-band doped Mott insulator.

Thus overall not only the half-filled Mott insulating state is strongly favored by Hund's coupling, given the strong reduction of U_c due to J, but also the correlations, when doping this Mott insulating state, are enhanced and decrease more slowly with doping than in the case without J. This is, in essence, the reason why Hund's metal physics is so relevant for Fe-SC, and all the more the closer to half-filling they are, as anticipated at the end of section 5.

7 Conclusions

In this lecture we have discussed the way in which the Hund's metal paradigm helps understanding the metallic phases in Fe-based superconductors, hopefully clarifying the ground on which high-Tc superconductivity prospers. We have detailed the way in which realistic DFT+slave-spin mean-field calculations are performed, and how they capture extremely well the behavior of the strong electronic correlations characterizing these phases. We have then exposed the gears inside the calculations, using simplified models—yet having all the essential features of the realistic simulations—in order to show explicitly how Hund's coupling enhances the correlations. We have hopefully given an intuitive justification to its influence that can initially appear counter-intuitive. In particular we have shown how, rather than a simple "arm wrestling" between bare kinetic energy of the electrons and their interaction strength, correlations should be viewed as a result of the available channels for charge fluctuations, and their energy cost, both of which are heavily tuned by Hund's coupling.

Before closing, we should mention that our calculations were all formally done at zero temperature. They are indeed fully representative of the low-but-finite-temperature Fermi-liquid phases encountered in Fe-SC that we have discussed. However more and equally rich Hund's metal physics [18] unveils when raising the temperature, in particular when crossing the Fermi-liquid coherence temperature, both in Fe-SC and in other Hund's metals, and in the related model calculations [2].

Furthermore, we have not even tried to touch upon other crucial aspects of the physics of Fe-SC that are impacted by Hund's coupling. The magnetic phases found in these materials are influenced by the balance between Hund's coupling and non-local exchange mechanisms, while nematicity [19] and superconductivity [20–22] might be amplified by Hund's metal correlations. Some of these aspects are still an ongoing research frontier, and could be interesting material for a future lecture.

References

[1] Z.P. Yin, K. Haule, and G. Kotliar, Nat. Mater. **10**, 932 (2011)

[2] A. Georges and G. Kotliar, Physics Today **77**, 46 (2024)

[3] A. Georges, L. de' Medici, and J. Mravlje,
Annu. Rev. Condens. Matter Physics **4**, 137 (2013)

[4] N. Marzari, A.A. Mostofi, J.R. Yates, I. Souza, and D. Vanderbilt,
Rev. Mod. Phys. **84**, 1419 (2012)

[5] A.V. Chubukov and P.J. Hirschfeld, Physics Today **68**, 46 (2015)

[6] Q. Si and N.E. Hussey, Physics Today **76**, 34 (2023)

[7] F. Hardy, A.E. Böhmer, L. de' Medici, M. Capone, G. Giovannetti, R. Eder, L. Wang,
M. He, T. Wolf, P. Schweiss, R. Heid, A. Herbig, P. Adelmann, R.A. Fisher, and
C. Meingast, Phys. Rev. B **94**, 205113 (2016)

[8] P. Villar Arribi: *Heavy fermions and Hund's metals in iron-based superconductors*
(Ph.D. thesis, Université Grenoble Alpes, 2018)
`https://theses.hal.science/tel-02151075/`

[9] T. Gorni, P. Villar Arribi, M. Casula, and L. de' Medici, Phys. Rev. B **104**, 014507 (2021)

[10] T. Miyake, K. Nakamura, R. Arita, and M. Imada, J. Phys. Soc. Jpn. **79**, 044705 (2010)

[11] M. Crispino, M. Chatzieleftheriou, T. Gorni, and L. de' Medici,
Phys. Rev. B **107**, 155149 (2023)

[12] L. Fanfarillo and E. Bascones, Phys. Rev. B **92**, 075136 (2015)

[13] L. de' Medici and M. Capone: *Modeling Many-Body Physics with Slave-Spin Mean-Field:
Mott and Hund's Physics in Fe-Superconductors* (Springer, Cham, 2017), pp. 115–185.

[14] L. de' Medici, in preparation (2025)

[15] M. Chatzieleftheriou, M. Berović, P. Villar Arribi, M. Capone, and L. de' Medici,
Phys. Rev. B **102**, 205127 (2020)

[16] O. Gunnarsson, E. Koch, and R.M. Martin, Phys. Rev. B **54**, R11026 (1996)

[17] L. de' Medici, J. Mravlje, and A. Georges, Phys. Rev. Lett. **107**, 256401 (2011)

[18] P. Werner, E. Gull, M. Troyer, and A.J. Millis, Phys. Rev. Lett. **101**, 166405 (2008)

[19] L. Fanfarillo, G. Giovannetti, M. Capone, and E. Bascones,
Phys. Rev. B **95**, 144511 (2017)

[20] L. de' Medici, Phys. Rev. Lett. **118**, 167003 (2017)

[21] S. Hoshino and P. Werner, Phys. Rev. Lett. **115**, 247001 (2015)

[22] L. Fanfarillo, A. Valli, and M. Capone, Phys. Rev. Lett. **125**, 177001 (2020)

5 DMFT for Moiré Systems

Tim Wehling
Universität Hamburg
Notkestraße 9-11, 22607 Hamburg

Contents

1 Strong correlations and superconductivity in moiré systems **2**
1.1 Graphene-based moiré materials 4
1.2 Transition metal dichalcogenide moiré systems 6

2 Model building for moiré systems:
From moiré band structures to correlated electron lattice models **7**
2.1 Γ valley twisted TMD moiré bilayers 7
2.2 Twisted bilayer graphene 13
2.3 Twisted bilayer WSe_2 19

3 DMFT studies of correlations in moiré systems **21**
3.1 Twisted bilayer graphene 22
3.2 Twisted bilayer WSe_2 25

4 Summary **26**

E. Pavarini, E. Koch, A. Lichtenstein, and D. Vollhardt (eds.)
Understanding Correlated Materials with DMFT
Modeling and Simulation Vol. 15
Forschungszentrum Jülich, 2025, ISBN 978-3-95806-813-1
http://www.cond-mat.de/events/correl25

1 Strong correlations and superconductivity in moiré systems

Two-dimensional (2D) materials are crystalline solids consisting of a single or a few layers of atoms arranged in a flat, planar structure [1, 2]. Unlike conventional three-dimensional materials, which extend in all spatial directions, 2D materials are confined to just two dimensions. The most well-known example is graphene, a single layer of carbon atoms arranged in a honeycomb lattice. Graphene sparked strong interest for its mere existence as a 2D crystal seemingly violating the Mermin Wagner theorem and from early on also for its special electronic properties with low-energy electronic quasiparticles behaving like massless Dirac fermions [3, 4].
Since then, a wide family of 2D materials has been explored, including transition metal dichalcogenides (TMDs), hexagonal boron nitride (h-BN), and phosphorene, realizing a variety of atomically thin systems including metals, semimetals, semiconductors, insulators, superconductors, topological insulators etc. An especially exciting development in the field of 2D materials is the controlled stacking of different monolayers, which enables the creation of van der Waals heterostructures—artificial materials formed by layering 2D crystals without the constraints of lattice matching [1, 2].
When two layers with slightly mismatched lattice constants or a small twist angle θ between them are stacked, they produce a moiré pattern — a long-wavelength modulation pattern — resulting from the superposition of the two atomic lattices as can be seen from Fig.1. The moiré periodicity can significantly modify the electronic properties of the system by acting as a periodic potential or as a periodically modulated interlayer tunneling at the emergent length scale defined by the moiré lattice.
In particular, twisted bilayer graphene (TBG) near the so-called "magic angle" ($\sim 1.1^\circ$) hosts flat topological electronic bands, which dramatically enhance electron-electron interactions, leading to correlated insulating states and even superconductivity [5–7]. Similar moiré-induced correlation phenomena have since also been observed in heterostructures based on TMDs [8–11], establishing moiré engineering as a versatile platform for exploring strongly correlated and topological phases of matter [7, 12, 13].
The enhancement of correlation effects in moiré structures can be rationalized from the follow-

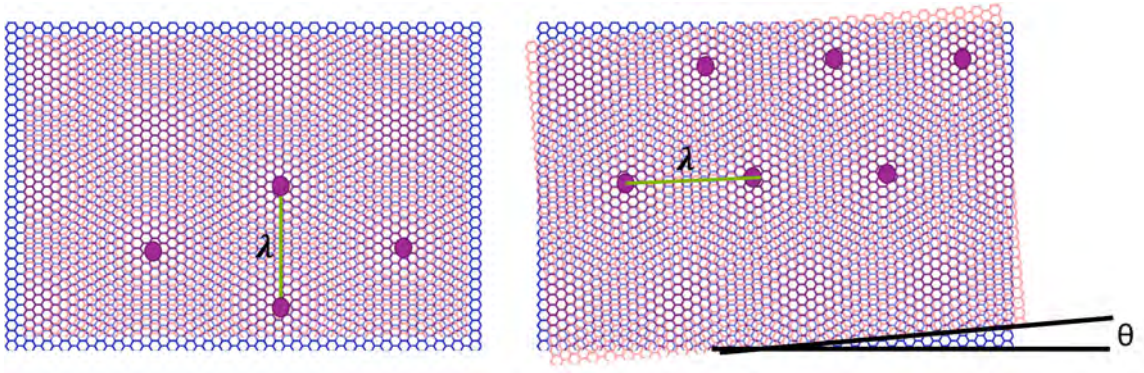


Fig. 1: *Moiré superlattices in van der Waals heterostructures from lattice mismatch (left) and twisting (right) of the 2D constituent layers.*

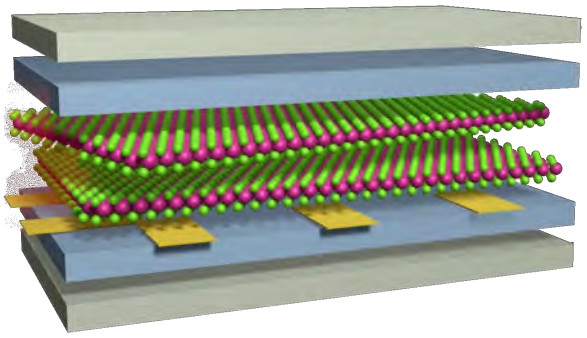


Fig. 2: *Typical experimental setup to realize and probe electronic correlation phenomena in moiré systems: a twisted 2D bilayer giving rise to the actual moiré structure is sandwiched between dielectric spacer layers, often hBN (blue), and outer gate electrodes (gray). The gate electrodes allow to apply vertical electric fields and to dope the sample via the field effect. The dielectric environment controls the effective strength of Coulomb interactions in the active 2D moiré bilayer.*

ing argument. The moiré periodicity is associated the characteristic length scale of the moiré lattice constant λ. For twisted bilayers of the same material, the length scale λ follows from the twist angle θ and the original lattice constant a according to

$$\lambda(\theta) = a/(2\sin(\theta/2)) \approx a/\theta,$$

where the latter relation holds at small twist angles. Assuming now a parabolic dispersion for the electrons, we arrive at the following scaling of the band width W and the Coulomb interaction U with twist angle

$$\left.\begin{aligned} W &\sim \frac{\hbar^2}{2m}\frac{1}{\lambda^2} \propto \theta^2 \\ U &\sim \frac{e^2}{\kappa}\frac{1}{\lambda} \propto \theta \end{aligned}\right\} \Rightarrow \frac{U}{W} \propto \frac{1}{\theta}\,. \tag{1}$$

Typical experiments on electron correlations in 2D material moiré structures are based on setups as depicted in Fig. 1, which lead to a quite remarkable tunability in comparison to conventional bulk systems: tuning twist angle and the dielectric environment (κ in Eq. (1)) allows to control the relative strength of electron correlations in the moiré system, while the gate voltages allow for wide tuning of the filling and reshaping of band structures as we will see.

In this chapter, we give an overview of correlated electron physics in moiré systems, starting with a selection of experimental observations of strong correlation effects and superconductivity in van der Waals based moiré systems. Afterwards we will turn towards the theoretical description of these phenomena focusing on moiré band structures and the modeling of correlation effects in these in graphene and TMD based moiré systems.

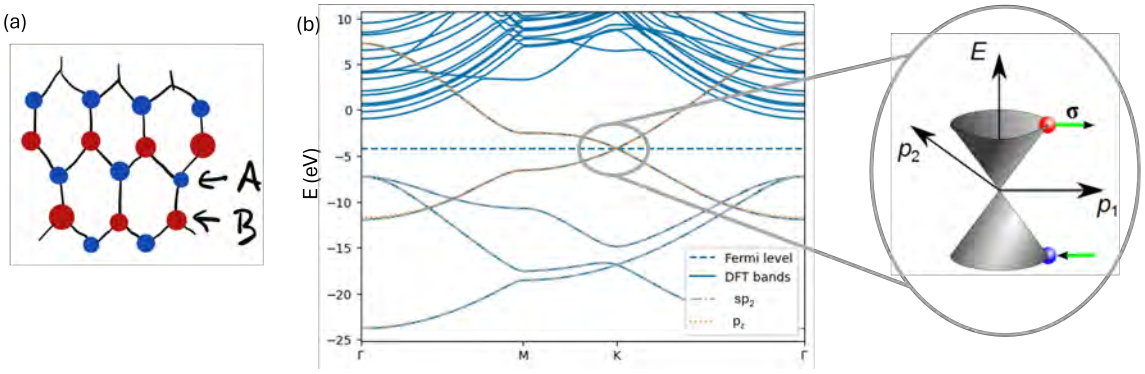


Fig. 3: *Crystal structure (a) and electronic band structure with close up view around the Fermi level of monolayer graphene (b). The low-energy electronic states are described by a Dirac equation with inherent pseudospin degree of freedom resulting from the two-sublattice structure of graphene (see sublattices A and B marked in panel a). The nodal points in the band structure are referred to as Dirac points. Electrons acquire a Berry phase of $\pm\pi$ upon encircling the Dirac points at K (K').*

1.1 Graphene-based moiré materials

The band structure of monolayer graphene is shown in Fig. 3. The bands around the Fermi level are made up from Carbon p_z orbitals and exhibit a bandwidth of more than 10 eV. The low-energy quasiparticles are near the Brillouin zone corners $\pm K = K, K'$ and described by a Dirac Hamiltonian: $H_D = \hbar v_f \mathbf{k} \cdot \boldsymbol{\sigma}$, where v_f is the Fermi velocity, $\mathbf{k}$ is the crystal momentum and $\boldsymbol{\sigma} = (\sigma_x, \pm\sigma_y)$ is a vector of Pauli matrices. Here, the Pauli matrices refer to a pseudospin describing the sublattice degree of freedom in graphene, i.e., the degree of freedom for electrons to reside in honeycomb sublattice A or B. The Brillouin zone regions around K and K' are called "valleys" and the corresponding band degeneracy points are called Dirac points. The pseudospin of the electrons rotates in the x-y-plane and the wave function picks up a Berry phase of $\pm\pi$, when encircling the Dirac points at $\pm K$ in momentum space. This Berry phase will turn out to bestow bands in twisted bilayer graphene with a distinct topology that needs to be accounted for properly modeling of the correlated electron physics.

The strength of Mott-Hubbard type correlations in pure monolayer graphene has been assessed on the basis of interaction parameters derived from the constrained Random Phase Approximation (cRPA) [14, 15]. While the local Hubbard repulsion in free standing graphene reaches the scale of the band width, it turns out that screening by sizeable non-local interaction terms quenches Mott Hubbard correlations leading to a ratio of effective interaction to hopping $\tilde{U}/t \approx 1.6$ [15], which far below the value for the Mott transition on the honeycomb lattice $U^{\mathrm{Mott}}/t \approx 8$ and also smaller than the value of $U^{\mathrm{AMF}}/t \approx 3.5$ for the transition into a sublattice antiferromagnet. Taken together, charge neutral monolayer graphene is thus a Dirac material with characteristic Berry phase imprinted to the dispersion relation featuring weak electron correlations in the Mott Hubbard sense.

This situation changes drastically, when two graphene layers are stacked on top of each other with a twist angle on the order of 1.1° —referred to as the "magic angle". A representative dop-

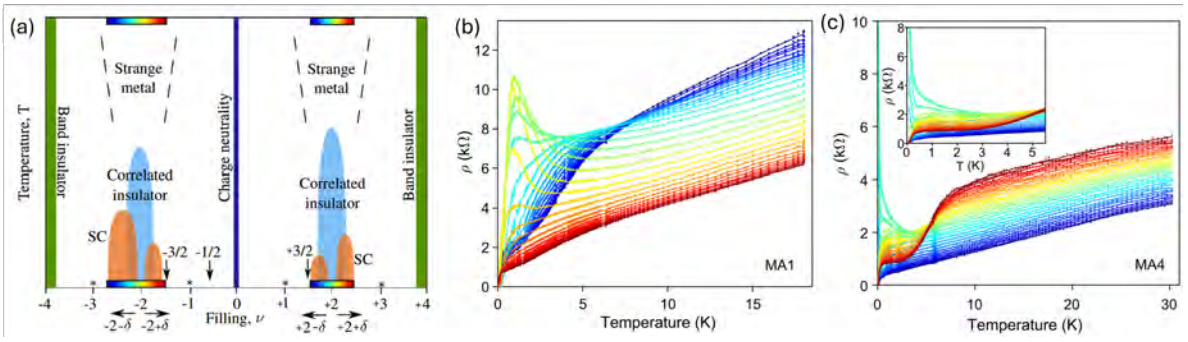


Fig. 4: *Phase diagram of near magic angle TBG as derived from transport experiments of Ref [16]. (a) Schematic phase diagram for magic angle TBG as a function of temperature and filling ν exhibiting superconducting regions (orange), correlated insulating states (light blue) and strange metal behavior with T-linear resistivity. (b,c) Experimentally measured resistivity (ρ) measured on two different TBG devices ("MA1", "MA4") with twist angles of $\theta = 1.16°$ and $1.18°$, respectively, as function of temperature for different fillings close to $\nu = \pm 2$ illustrate the manifestation of the strange metal, correlated insulating and superconducting states in electronic transport. The horizontal color bars in the left and right panel of the phase diagrams in (a) correspond to the transport data shown (b) and (c), respectively. Adapted from Ref. [16].*

ing and temperature dependent phase diagram is shown in Fig. 4. It is derived from transport experiments of Ref. [16] and is qualitatively in line with several other studies [5–7, 12, 17–20]. At low temperatures highly resistive states ("correlated insulators") emerge next to superconducting states—both of which are absent in the monolayer constituents. Close to the correlated insulators, there is a region featuring unusual transport behavior including linear-in-temperature resistivity referred to as strange metal phase. This phase diagram is indeed quite similar to cuprates and other correlated electron systems.

A large body of theoretical and experimental work has been ongoing to understand the electronic phase diagram of TBG. Taking together experiments like Refs. [5,6,16–22] the following overarching picture can drawn:

- Superconductivity emerges on the scale of roughly 1 K in certain filling ranges.
- Correlated insulating states occur at some integer fillings.
- The doping regions where superconductivity occurs and the integer fillings where the insulating states occurs are sample dependent.
- There is a temperature controlled fade out of insulating behavior (at integer ν) and an onset of incoherent metallic behavior (for wider filling ranges) around 5–20 K.
- Different kinds of spontaneous symmetry breaking such as orbital ferromagnets or intervalley coherent states with characteristic sublattice interference patterns occur below characteristic temperatures on the order of 5 K.

TBG is indeed only one representative of a larger family of graphene-based multilayer moiré systems featuring similar correlation effects and (enhanced) superconductivity [23].

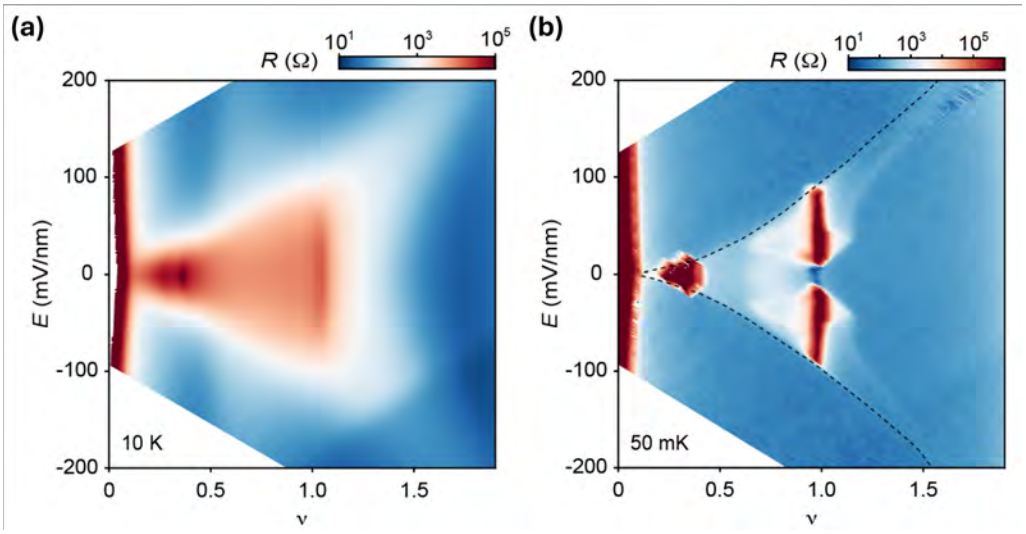


Fig. 5: *Emergent electronic phases in $tWSe_2$ as manifesting in transport experiments of Ref. [10]. The moiré band structure of the system is tunable by vertical displacement fields E. The longitudinal resistance R of $tWSe_2$ at twist angle $3.65°$ is shown as a function of displacement field E and filling ν at 10 K (a) and 50 mK (b). From Y. Xia, Z. Han, K. Watanabe, T. Taniguchi, J. Shan, and K. F. Mak: Unconventional Superconductivity in Twisted Bilayer WSe_2, arXiv:2405.14784. Copyrighted under CC BY-NC-ND 4.0.*

We will discuss in section 2.2 how interference of electronic states from the different bilayers modulated by the moiré pattern of TBG can lead to flat bands with extremely narrow bandwidths, where the kinetic energy of charge carriers is strongly suppressed thereby promoting electronic correlation effects. We will also work out how modeling of these correlation effects can be achieved focusing in particular on studies employing dynamical mean-field theory.

1.2 Transition metal dichalcogenide moiré systems

The emergence of 2D moiré superlattices in van der Waals stacks is very general and not limited to graphene-based systems. Correspondingly, moiré flat band physics has been explored in multiple platforms particularly TMDs [8–13].

In their monolayer form TMDs MX_2 with M$\in \{\mathrm{Mo}, \mathrm{W}\}$ and X$\in \{\mathrm{S}, \mathrm{Se}\}$ are semiconductors with quasi particle band gaps on the order of eV. These materials are structurally similar to graphene by also having honeycomb lattice structures, where now one sublattice is filled by the metal atoms M and the other sublattice by the chalcogens X (c.f. Fig. 12). The moiré physics emerges here upon building multilayer structures with a lattice mismatch (heterobilayers) or twist angle (hetero- and homobilayers). Several correlated states including correlated insulators [8,24,25] featuring rich multi-orbital physics [26] and quantum critical behavior [27,28] as well as topological Kondo physics [29] have been reported. Early experiments on $5.0°$ twisted WSe_2 hinted at the existence of superconducting phases in moiré TMDs [8] but the situation remained controversial. Recent experiments on $3.65°$ [10] and $5.1°$ [11] twisted bilayer WSe_2 ($tWSe_2$) reported evidence for superconductivity, albeit at significantly lower critical temperatures than [8].

We illustrate in Fig. 5 the resistivity of twisted bilayer WSe_2 at twist angle 3.65° [10] measured as function of doping and displacement field for two different temperatures, 10 K and 50 mK. At 10 K, there is a strong asymmetry of the resistivity around $\nu = 1$ and particularly enhanced scattering right at $\nu = 1$. Lowering the temperature to 50 mK, one sees, highly resistive insulating states at $\nu = 1$ for a certain region of displacement fields and a low-resistance metallic state in between. Right at the boundary of the metallic and the insulating states near $\nu = 1$, a zero resistance superconducting states occurs. Again, as in the 10 K, there is a strong doping asymmetry around $\nu = 1$. Transitions between all these different phases are tunable by doping ν, vertical displacement field E_z and additionally temperature.

2 Model building for moiré systems: From moiré band structures to correlated electron lattice models

In this section, we will exemplify the quenching of kinetic energy and formation of flat bands in moiré systems with three examples: (i) In MoS_2, WS_2 and $MoSe_2$ twisted bilayers Mott Hubbard correlations and spin fluctuations emerge in the Γ valley. This case is particularly simple and illustrates most clearly how, spatially modulated potentials and interlayer hybridization quench kinetic energy and give way to strong electron correlations in systems of formerly weakly correlated semiconducting constituents. Afterwards, we will turn towards the experimentally particularly relevant cases of twisted bilayer graphene (ii) and twisted WSe_2 bilayers, where moiré minibands stemming from the K and K' valley, carry distinct Berry curvature, leading to an interplay of electron correlations and topology. Along with these example cases we illustrate model building and practical implementations of dynamical mean-field based simulations of correlation effects.

2.1 Γ valley twisted TMD moiré bilayers

For moiré superlattices from semiconducting or semimetallic constituents, the emergent electronic states can be effectively described by continuum model Hamiltonians, in which the exact commensurability between the moiré pattern and the underlying atomic lattice is not essential. In bulk WS_2, MoS_2 and $MoSe_2$ and also corresponding non-twisted bilayers, the valence band maximum is located at the Γ point and composed of layer-antibonding states that are separated from other states by hundreds of meV. This motivates the following one-band continuum model [30]

$$H = -\frac{\hbar^2 k^2}{2m^*} + V_{\mathrm{M}}(\mathbf{r}), \tag{2}$$

where m^* is the effective mass and $V_{\mathrm{M}}(\mathbf{r})$ is the moiré potential felt by the holes near the valence band maximum at Γ. A standard way to obtain an estimate of the moiré potential is to assess which contributions to $V_{\mathrm{M}}(\mathbf{r})$ would be allowed by the system's symmetry and fit these contributions then to ab initio calculations.

The analysis of Ref. [30] shows that the twisted TMD homobilayers impose the dihedral symmetry D_6 on $V_{\mathrm{M}}(\mathbf{r})$. Time-reversal symmetry implies that $V_{\mathrm{M}}(\mathbf{r})$ must be real. Finally, $V_{\mathrm{M}}(\mathbf{r})$ is periodic with the moiré superlattice, which motivates the following plane-wave expansion

$$V_{\mathrm{M}}(\mathbf{r}) = \sum_{s=1}^{3} \sum_{j=1}^{6} V^s \mathrm{e}^{i(\mathbf{g}_j^s \cdot \mathbf{r} + \phi^s)}. \tag{3}$$

Here, s is the s-th shell of six moiré reciprocal lattice vectors $\mathbf{g}_j^s = \mathcal{R}_{(j-1)\pi/3}\mathbf{G}^s$ ($j = 1, \ldots, 6$) with $\mathcal{R}_\alpha$ being the two-dimensional (2D) rotation matrix about an angle α. The phase factors ϕ^s are constrained by symmetry to be either 0 or π. As shown in Ref. [30], the potential $V_{\mathrm{M}}(\mathbf{r})$ is well-captured by the three leading Fourier components. Thus, the Hamiltonian describing twisted TMDs is indeed a "real material" implementation of the textbook problem of nearly free electrons in a periodic potential.

The D_6 symmetry together with the moiré periodicity further demands that the high symmetry Wyckoff positions corresponding to the regions with AA stacking or regions with AB/BA stacking are extrema of the potential $V_{\mathrm{M}}(\mathbf{r})$. The DFT calculations of Ref. [30] show that the valence band maximum in the Bernal stacked regions (AB, BA) is higher in energy than in the AA regions. The low-energy moiré bands in Γ-valley TMD homobilayers are therefore generated by orbitals sitting on the honeycomb lattice formed by the AB/BA regions and Γ-valley TMDs homobilayers can be viewed as a moiré pendant of graphene.

The moiré lattice translation symmetry implies that Bloch's theorem applies on the moiré scale with moiré crystal momentum, $\mathbf{k}$, being a good quantum number. The single particle Hamiltonian from Eq. (2) is thus diagonal in $\mathbf{k}$ and takes the following form in the basis of plane waves $|\mathbf{k}+\mathbf{G}\rangle$

$$\langle \mathbf{k}+\mathbf{G}| \, H \, |\mathbf{k}+\mathbf{G}'\rangle = -\frac{\hbar^2|\mathbf{k}+\mathbf{G}|^2}{2m^*}\delta_{\mathbf{G},\mathbf{G}'} + V_{\mathrm{M}}(\mathbf{G}-\mathbf{G}'). \tag{4}$$

Here, $\mathbf{G}$ denotes vectors from the moiré reciprocal lattice, respectively and $V_{\mathrm{M}}(\mathbf{G}-\mathbf{G}')$ is the Fourier transform of $V_{\mathrm{M}}(\mathbf{r})$. Diagonalization of the Hamiltonian from Eq. (4) yields the plane-wave expansion coefficients $c^\alpha_{\mathbf{kG}}$ of the eigenstates

$$|\Phi^\alpha_{\mathbf{k}}\rangle = \sum_{\mathbf{G}} c^\alpha_{\mathbf{kG}} \, |\mathbf{k}+\mathbf{G}\rangle \, , \tag{5}$$

where α is the band index. These eigenstates are expanded up to a plane-wave cutoff G_{c}, which depends in practice on the twist angle θ. This "program" to deal with the moiré minibands is analogous to plane wave expansions of Bloch states in conventional solids.

In Fig. 6 we show the band structures for Γ-valley twisted TMDCs at twist angles in the range $1^\circ < \theta < 5^\circ$. The zero energy is defined as the top of the valence band. For this twist angle range it turns out to be sufficient to use $G_c = 4$–$5\, G^{\mathrm{M}}$, where $G^{\mathrm{M}} = |\mathbf{G}^{\mathrm{M}}_{1,2}|$, i.e., the solving the continuum models is numerically rather "light-weight".

From the valence band edge, two flat bands emerge which touch at Dirac points in the corners of the moiré Brillouin zone. We refer to these bands as "flat Dirac bands". Their shape is very similar in shape to the dispersion of graphene albeit at a completely different energy scale.

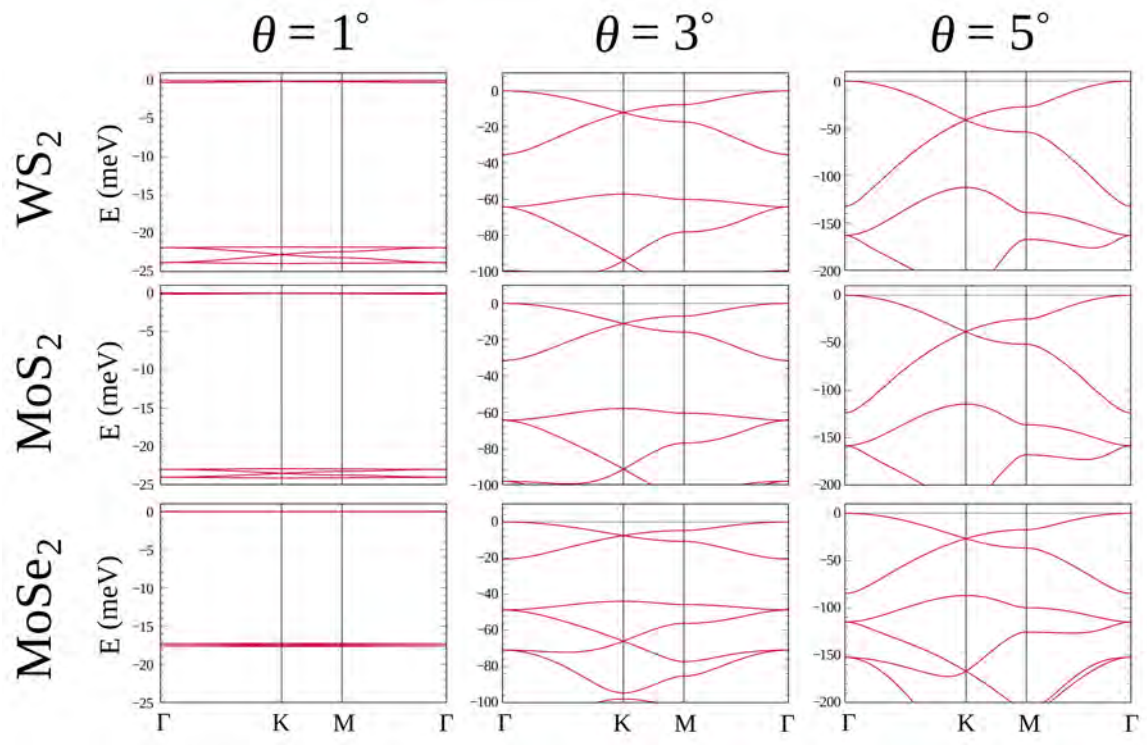


Fig. 6: *Band structures for the Γ-valley twisted TMDCs, WS_2 (top row), MoS_2 (middle row), and $MoSe_2$ (bottom row). We show the low-energy band evolution for the twist angle range $1^\circ < \theta < 5^\circ$. From Ref. [32].*

This is well understandable from the honeycomb form of the moiré potential, which resembles graphene. The flat Dirac bands are well isolated from other higher energy bands for $\theta < 5^\circ$ and their bandwidth increases approximately quadratically with the twist angle.

A decisive step in the model building for the treatment of strong electron correlations, is the formulation of lattice models describing the low-energy electronic degrees of freedom. For the case at hand, a Wannierization procedure analogously to conventional bulk systems is expedient. Based on our observations we construct a Wannier Hamiltonian for the isolated flat Dirac bands via projection [31] with one orbital per site for each moiré sublattice [32], where the AB and BA regions of the moiré play the role of the A and B sublattice sites in a honeycomb lattice.

We proceed, thus, with trial orbitals $|g^m\rangle$ (e.g. Gaussian orbitals) centered on sublattice sites $m \in \{\mathrm{A}, \mathrm{B}\}$ of the unit cell at the origin in real space, which are then projected onto the space spanned by the low energy Dirac bands to yield new states

$$|\phi^m_{\mathbf{k}}\rangle = \sum_\alpha |\Phi^\alpha_{\mathbf{k}}\rangle \langle \Phi^\alpha_{\mathbf{k}}|g^m\rangle \,. \tag{6}$$

By this step, we arrive at states $|\phi^m_{\mathbf{k}}\rangle$ spanning the space of the flat Dirac bands with a smooth gauge in $\mathbf{k}$-space. However, $\{|\phi^m_{\mathbf{k}}\rangle\}$ are not necessarily orthonormal. Using the projection matrix $P^{\alpha m}_{\mathbf{k}} = \langle \Phi^\alpha_{\mathbf{k}}|g^m\rangle$ we obtain the overlap matrix

$$S^{mn}_{\mathbf{k}} = \langle \phi^m_{\mathbf{k}}|\phi^n_{\mathbf{k}}\rangle = \left(P^\dagger_{\mathbf{k}} P_{\mathbf{k}}\right)^{mn} , \tag{7}$$

which is finally used to calculate the orthonormalized smooth gauge Bloch states via Löwdin orthonormalization at every $\boldsymbol{k}$

$$|\tilde{\psi}_{m\boldsymbol{k}}\rangle = \sum_{n\in\{A,B\}} |\phi_{n\boldsymbol{k}}\rangle \left(S^{-1/2}(\boldsymbol{k})\right)_{nm} . \tag{8}$$

Since the $|\tilde{\psi}_{m\boldsymbol{k}}\rangle$ exhibit a smooth gauge in $\boldsymbol{k}$-space, a Fourier transformation yields finally the desired Wannier functions in real space. The the m^{th} Wannier function in unit cell $\boldsymbol{R}$ reads

$$|\boldsymbol{R}m\rangle = \frac{A_M}{(2\pi)^2} \int_{mBZ} d\boldsymbol{k}\, e^{-i\boldsymbol{k}\cdot\boldsymbol{R}} |\tilde{\psi}_{m\boldsymbol{k}}\rangle , \tag{9}$$

with A_M being the moiré unit cell area and the integral running over the moiré Brillouin zone. Taking matrix elements of the original continuum model Hamiltonian H, Eqs. (2)–(4), w.r.t. the Wannier functions, yield the hopping and on-site matrix elements of a tight-binding description of the moiré band structure:

$$h_{\boldsymbol{R}n,\boldsymbol{R'}m} = \langle \boldsymbol{R}n|H|\boldsymbol{R'}m\rangle . \tag{10}$$

The following steps need to be implemented for actual calculations as, e.g., detailed in the supplement of Ref. [32]:

- Choose localized projector orbitals and obtain their plane-wave expansion:

$$|g^m\rangle = g^m_{\mathbf{k},\mathbf{G}} \,|\mathbf{k}{+}\mathbf{G}\rangle .$$

- Obtain plane wave expansion coefficients $c^\alpha_{\mathbf{kG}}$ of the eigenstates of the continuum model from diagonalization of the continuum model, Eq. (4), in $\mathbf{k}$-space:

$$|\Phi^\alpha_{\mathbf{k}}\rangle = \sum_{\mathbf{G}} c^\alpha_{\mathbf{kG}} \,|\mathbf{k}{+}\mathbf{G}\rangle .$$

- Calculate projector matrix for each $\mathbf{k}$:

$$P^{\alpha m}_{\mathbf{k}} = \langle \Phi^\alpha_{\mathbf{k}}|g^m\rangle = \sum_{\mathbf{G}} (c^\alpha_{\mathbf{kG}})^\dagger g^m_{\mathbf{kG}}.$$

- Calculate plane-wave expansion coefficients of the smooth gauge states $|\phi^m_{\mathbf{k}}\rangle = \sum_{\mathbf{G}} \phi^m_{\mathbf{kG}} \,|\mathbf{k}{+}\mathbf{G}\rangle$:

$$\phi^m_{\mathbf{kG}} = \sum_\alpha c^\alpha_{\mathbf{kG}} P^{\alpha m}_{\mathbf{k}} .$$

- Calculate overlap matrix $(S_{\mathbf{k}})^{nm}$ via Eq. (7).

- Calculate the plane-wave expansion coefficients of the orthonormalized smooth gauge Bloch states $|\tilde{\Phi}^m_{\mathbf{k}}\rangle = \sum_{\mathbf{G}} \tilde{c}^m_{\mathbf{kG}} \,|\mathbf{k}{+}\mathbf{G}\rangle$:

$$\tilde{c}^m_{\mathbf{kG}} = \sum_n \phi^n_{\mathbf{kG}} \cdot \left(S^{-1/2}_{\mathbf{k}}\right)^{nm} .$$

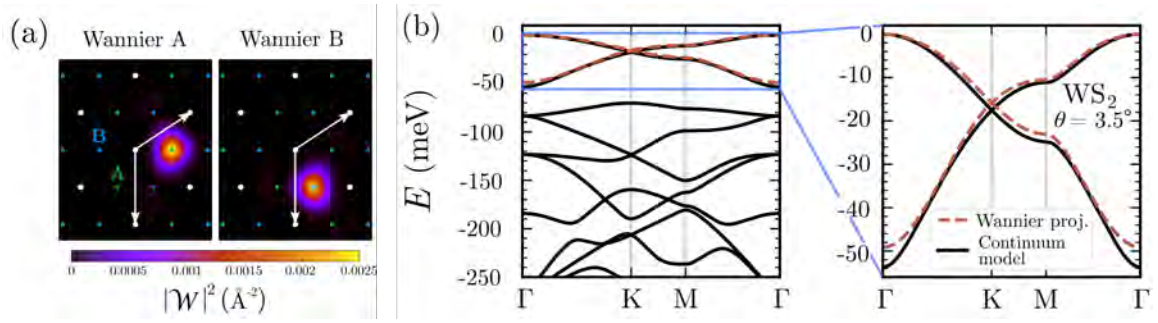


Fig. 7: *Wannier tight-binding model for twisted WS_2 at 3.5°. (a) Probability densities $|\mathcal{W}_m(\mathbf{r})|^2$ for Wannier orbitals centered in the sublattices A (green dots) and B (blue dots). White dots denote the Bravais lattice $\mathbf{R}$ and white arrows are the moiré lattice vectors. (b) Band structure of twisted bilayer WS_2 at the twist angle of $\theta = 3.5°$ from the continuum model (black solid line) and from the Wannier tight-binding model (red dashed line) of the two highest valence bands, where the hopping has been truncated after the third-nearest-neighbor terms. The right panel shows a zoom to the flat Dirac bands. From Ref. [32]*

- Obtain Wannier functions in real space:

$$\mathcal{W}_{\mathbf{R}m}(\mathbf{r}) = \langle \mathbf{r}|\tilde{\Phi}^m_{\mathbf{k}}\rangle = \frac{1}{N_{\mathbf{k}}\sqrt{A_{\mathrm{M}}}} \sum_{\mathbf{k}} \sum_{\mathbf{G}} \tilde{c}^m_{\mathbf{kG}} \mathrm{e}^{i\mathbf{K}\cdot(\mathbf{r}-\mathbf{R})} \ ,$$

  where the Brillouin zone integral from Eq. (9) is discretized with $N_{\mathbf{k}}$ points sampling the moiré Brillouin zone.

- Calculate Hamiltonian in Wannier basis by projecting the continuum Hamiltonian onto the orthonormalized smooth gauge Bloch states $|\tilde{\Phi}^m\rangle$:

$$\tilde{H}^{mn}_{\mathbf{k}} = \langle \tilde{\Phi}^m_{\mathbf{k}}|H|\tilde{\Phi}^n_{\mathbf{k}}\rangle \equiv \sum_{\mathbf{G},\mathbf{G}'} \left(\tilde{c}^m_{\mathbf{kG}}\right)^\dagger H_{\mathbf{kGG}'}\, \tilde{c}^n_{\mathbf{kG}'},$$

  where $H_{\mathbf{kGG}'}$ are the matrix elements of the Hamiltonian in Eq. (4).

- Fourier transform $\tilde{H}^{mn}_{\mathbf{k}}$ to obtain hopping matrix elements.

Performing this procedure for the two topmost Dirac bands resulting from the continuum model of Ref. [30] for twisted bilayer WS_2 at twist angle $3.5°$ yields the Wannier orbitals shown in Fig. 7(a). The two Wannier orbitals at sublattice $m \in \{A, B\}$ are well-localized on the scale of the moiré lattice.

The band structures from the continuum model and the Wannier tight binding model are compared in Fig. 7(b). We see that including up to three nearest-neighbor hoppings is sufficient to describe the upmost bands from the continuum model quite accurately.

For correlated electron modeling, one has to include also the interaction terms, i.e., usually Coulomb and electron-phonon interactions, to the model. We focus here on the Coulomb interactions.

Two ingredients are needed for that: the Wannier functions $\mathcal{W}_{\mathbf{R}m}(\mathbf{r})$ and an interaction kernel $V_{\text{eff}}(\mathbf{r})$ describing the effective appropriately screened Coulomb interaction. With these the (density-density part of the) Coulomb interaction matrix reads

$$W_{\mathbf{R},mn} = \iint d^2\mathbf{r}\, d^2\mathbf{r}'\; V_{\text{eff}}(\mathbf{r}-\mathbf{r}')\rho_{\mathbf{R}m}(\mathbf{r})\rho_{\mathbf{0}n}(\mathbf{r}'), \tag{11}$$

where $\rho_{\mathbf{R}m}(\mathbf{r}) = |\mathcal{W}_{\mathbf{R}m}(\mathbf{r})|^2$. In $V_{\text{eff}}(\mathbf{r})$ different screening contributions have to be accounted for: (i) the external screening by the dielectric environment and distant gate electrodes present in typical devices (Fig. 2), (ii) internal screening taking place in the tWS_2 bilayer, where one has to exclude those screening channels that will be later generated also in the many-body treatment of the low-energy model. While this partial internal screening has been discussed in some works like Ref. [33], a full analysis remains an open issue to date. A widely employed approximation is currently to use the Coulomb interaction screened by the TMDC bilayer in its undoped state and the dielectric environment for $V_{\text{eff}}(\mathbf{r})$.

To estimate the upper and lower bounds for the effective interaction within this approximation one can consider the following in two limiting cases for the dielectric environment: free-standing twisted bilayers, for which the external screening is minimal, and a metallic gate in direct contact with the twisted bilayers, for which the external screening is maximal [32, 33].

For practical calculations, it is helpful to start from an Ohno potential

$$V_{\text{Ohno}}(\mathbf{r}) = \frac{e^2}{\sqrt{r^2+\xi^2}} \tag{12}$$

which regularizes the bare Coulomb interaction e^2/r at a short wavelength cut-off. For tWS_2 a natural cut-off is given by the spacial extent of the W d-orbitals, i.e., $\xi \approx 1$ Å. The effect of screening is easiest included in reciprocal space, so the effective interaction is $V_{\text{eff}}(\mathbf{r})$ then calculated from the inverse Fourier transformation of

$$V_{\text{eff}}(\mathbf{q}) = \frac{V_{\text{Ohno}}(\mathbf{q})}{\epsilon(\mathbf{q})} = \frac{2\pi e^2}{\epsilon(\mathbf{q})q}\mathrm{e}^{-q\xi}\,, \tag{13}$$

where $\epsilon(\mathbf{q})$ is the dielectric function that encodes the environmental screening effect. The two limiting cases, free-standing ('fs') and metal in direct contact ('m'), correspond to the effective dielectric functions [33]

$$\epsilon_{\text{fs}}(\mathbf{q}) = \kappa\frac{1-\tilde{\kappa}\mathrm{e}^{-qh}}{1+\tilde{\kappa}\,\mathrm{e}^{-qh}} \quad \text{and} \quad \epsilon_{\text{m}}(\mathbf{q}) = \kappa\coth\frac{qh}{2}\,. \tag{14}$$

Here, $\kappa \approx 10$ is the internal screening of the undoped TMDC bilayer, $h \approx 13$ Å is the bilayer height, and $\tilde{\kappa} = (\kappa-1)/(\kappa+1)$.

In Fig. 8(a) we plot the on-site and nearest-neighbor interactions, $U = W_{\mathbf{0},AA} = W_{\mathbf{0},BB}$ and $V = W_{\mathbf{0},AB}$, at different twist angles θ for the two limiting cases for WS_2. For for a metal gate in direct contact with the twisted WS_2 bilayer, the nearest-neighbor interaction V_{m} is on the order of 1 meV and not included in the plot.

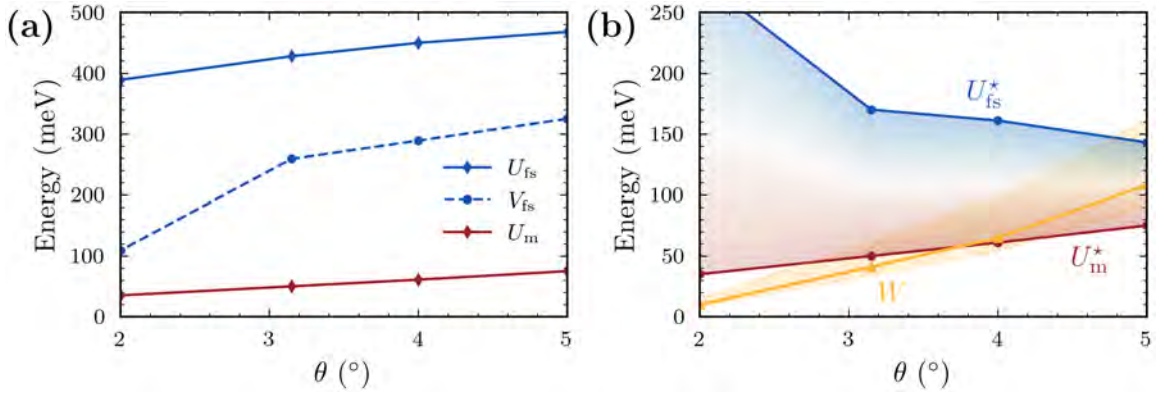


Fig. 8: *Estimated Coulomb interactions in different dielectric environments for twisted WS_2 bilayers. (a) Local and nearest-neighbor Coulomb interaction U and V in two dielectric environments, free-standing twisted bilayer ('fs', red line) and metallic gate in direct contact with the twisted bilayer ('m', blue line) as function of twist angle θ. (b) Effective local Hubbard interactions $U^\star = U - V$ and bandwidth W (orange line). The blue-red shaded region describes the possible values that $U^\star$ can take depending on the dielectric environmental setup. From Ref. [32].*

The resulting extended Hubbard models can be mapped onto a local Hubbard model with effective local interaction $U^\star$ by making the assumption $U^\star \approx U - V$ [15]. Fig. 8(b) shows $U^\star$ in comparison to the bandwidth W.

A realistic value for $U^\star$ in Γ-valley twisted TMDCs will fall inside the shaded regions between the limiting cases $U^\star_{\rm fs}$ and $U^\star_{\rm m}$, which depends on the experimental setup and which can be tuned by changing the dielectric environment.

Intriguing correlated electron physics with metal-insulator transitions, different kinds of spontaneous symmetry breaking including superconductivity is expected to be most prominent, where characteristic Coulomb and kinetic energy scales are on the same order of magnitude. Fig. 8 shows that twisted TMD bilayers in typical experimental setups will allow to widely tune the effective interaction strength and to reach regimes of Coulomb and kinetic energies being on the same scale.

Given the experimental state of the field we proceed with the more complex cases of twisted bilayer graphene and twisted WSe_2, where moiré flat bands occur due to interlayer hybridization at the corners of the Brillouin and where bands with finite Chern numbers are involved.

2.2 Twisted bilayer graphene

Twisted bilayer graphene (TBG) is a striking example, where the theoretical prediction [34, 35] of correlation effects predated their experimental realization [5, 6] but where the actual understanding of the system poses an outstanding challenge to theory. It illustrates thus the bidirectionality of the interplay between theory and experiment.

To rationalize the emergence of flat bands in TBG, we follow Refs. [5, 34, 35] and the corresponding cartoon shown in Fig. 9. In the absence of any interlayer coupling, the low-energy

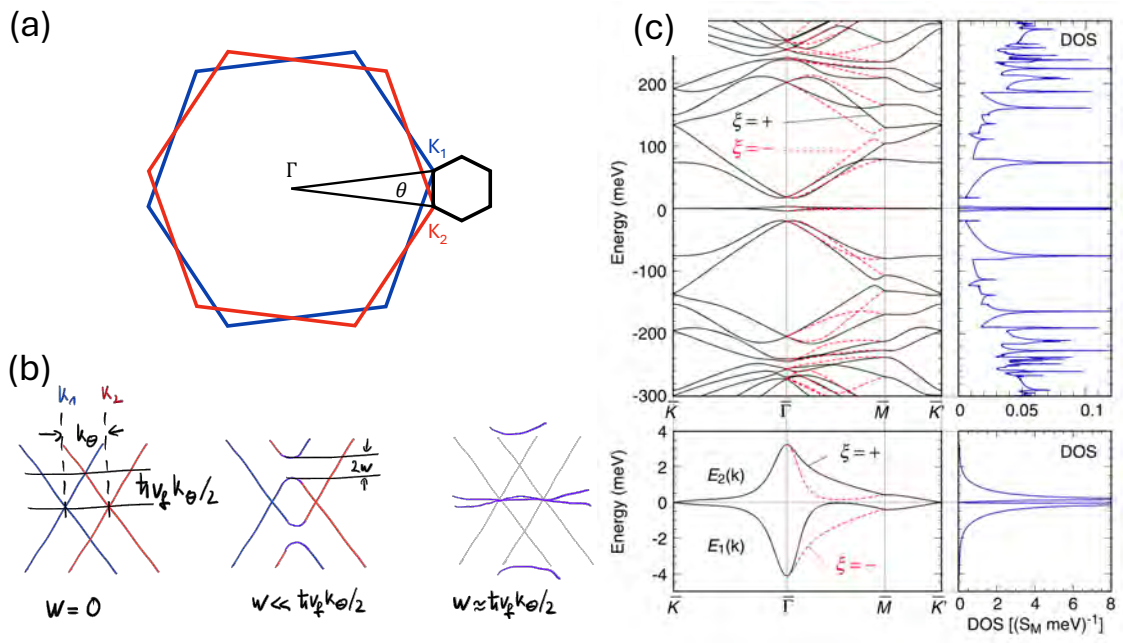


Fig. 9: *Moiré Brillouin zone and flat bands in magic angle TBG. (a) The moiré mini Brillouin zone is constructed from the difference between the two K (or K') wavevectors from the two layers. (b) Hybridization between Dirac cones within each valley leads to flat bands near the magic angle. Illustration of the two Dirac bands from the two layers contributing the low-energy states in each valley. The cases of vanishing interlayer hybridization (left panel), small hybridization ($2w \ll \hbar v_f k_\theta$, middle panel), and hybridization $2w \approx \hbar v_f k_\theta$ (right panel) leading to complete band flattening at the magic angle are shown. (c) Band structure and the density of states of TBG at the magic angle $\theta = 1.05°$ as obtained from the continuum model of Ref. [36]. The lower panel is the enlarged plot of the flat-band region. The black solid line and red dashed line represent the energy bands of valleys, K and K' respectively. Panel (c) from Ref. [36].*

band structure in each valley would be made up of two Dirac cones, one stemming from the lower and one stemming from the upper layer, which are rotated about the Brillouin zone center by the twist angle θ. The difference between the two rotated K (or K') wavevectors gives rise to the moiré Brillouin zone, which is shown as a small hexagon in Fig. 9(a). While the Dirac cones near either of the K or K' valleys mix through interlayer hybridization, the coupling between distant Dirac cones is suppressed and "valley" remains a good quantum number.

The interlayer hybridization leads to energy gaps that open near the intersection of the Dirac cones and a renormalization of the Fermi velocity. Indeed, a series of "magic" twist angles θ emerges, where the Fermi velocity at the Dirac points vanishes.

The flattening of the energy bands near the first (and experimentally most relevant) magic angle can be understood qualitatively from the competition between the intralayer kinetic energy and the interlayer hybridization as depicted in Fig. 9(b): When the hybridization energy $2w$ becomes comparable to the intralayer kinetic energy associated with the twist induced momentum offset between the Dirac points $\hbar v_f k_\theta$, the lower of the hybridized states are pushed to zero energy leading to band flattening and the first magic angle. With $w \approx 110$ meV [35], one arrives at $\theta_M = 1.05°$ for the first magic angle.

In Fig. 9c we show a band structure and density of states (DOS) of TBG at this "magic" angle $\theta_M = 1.05^\circ$ [36]. The flat bands have a bandwidth on the order of $10\,\mathrm{meV}$ and are well separated in energy from higher-energy dispersive bands.

A usual route towards modeling the correlated states of TBG would be to proceed along the lines of the previous section, i.e., to build a Wannier tight-binding model for the flat bands and then to incorporate interactions. Typically, the relevant orbitals for the tight-binding model can be inferred from chemical intuition or from the projected density of states for the relevant bands. This approach does not work in the case of TBG, as we will see following closely Ref. [37]: One finds that the local density states for the flat bands is strongly peaked to the AA regions of the moiré [5], which form a triangular lattice. It would thus seem natural to consider a real-space model starting from effective orbitals centered at the AA sites, which corresponds to a tight-binding model defined on the triangular lattice. Treating the two valleys separately, one would arrive at a model with two orbitals localized to each of the triangular sites (i.e., AA regions of the moiré pattern).

However, such a model contradicts symmetry requirements [37] as can be seen from the band structure of TBG shown in Fig. 9(c): Per valley we have two low-energy flat bands. These are nondegenerate at Γ but exhibit (indeed symmetry-protected) Dirac points at $\mathrm{K_M}$ and $\mathrm{K'_M}$. This pattern of degeneracies allows to infer the symmetries and Wyckoff positions of the involved orbitals. A triangular-lattice model respecting all symmetries of TBG would always lead to a situation where the two bands are either nondegenerate at all high-symmetry Brillouin zone points (Γ, $\mathrm{K_M}$, $\mathrm{K'_M}$), or all three points are Dirac points. Both patterns are inconsistent with the low-energy band structure of TBG, which rules out all "pure" triangular-lattice models [37]. Indeed, the degeneracies found in the low energy band of magic angle TBG match exactly those found in monolayer graphene. This indicates (and one can indeed show) that any tight-binding model describing the flat bands alone must correspond to orbitals sitting on a honeycomb lattice. There seems to be thus a contradiction: symmetry arguments imply Wannier centers at a honeycomb lattice, while the local density of states derived from the flat band sector peaks at triangular lattice site.

One can attempt to reconcile this problem in different ways: first, one could allow for extended Wannier functions with nontrivial shapes, where each orbital is centered at a honeycomb site (i.e., the AB/BA regions of the moiré pattern) but the weight of the orbitals is mainly localized at AA sites. Corresponding Wannier constructions have been pursued, e.g., in Ref. [36] and lead to orbitals that resemble (three-lobed) fidget spinners. Such orbitals bring along several problems: long ranged hopping, multiple sizeable non-local non-density-density general four fermion interaction terms in the Coulomb tensor, which are problematic in the DMFT context, breaking of interlayer mirror symmetries, and an incorrect representation of the topology [37].

The latter issue arises very generally when constructing tight-binding representations of moiré systems, where multiple valleys away from the Γ-point of the original single layer constituents are involved [13]. In the case of graphene it can be understood as follows.

There is a Berry phase of $\pm\pi$ for any closed loop encircling a single Dirac point. This is also the case in monolayer graphene. In monolayer graphene the Berry phase of the Dirac point at K and

K' carry opposite sign and do not obstruct any tight-binding representation of the monolayer graphene bands. In contrast, in MA-TBG the two inequivalent Dirac points stemming from the different layers but same valley as entering the single-valley model have the same winding number and thus do not add up to zero. However, the total winding number of the Dirac points arising in any (sufficiently symmetric) two-band tight-binding model would necessarily be zero. So, a tight-binding model with two localized Wannier functions per valley only, that reproduces two flat bands, preserves valley quantum numbers and TBG symmetries must not exist.
There is however a second route that turned out successful for the formulation of lattice models that respect the symmetries of MA-TBG, the topology of the low-energy flat band sector and that yield finally models that are accessible to correlated electron techniques such as DMFT. This route is based on extending the single particle Hilbert space beyond the flat band manifold. Two flavors of this route exist.

- "All Wannier models": here all degrees of freedom entering the modeling are represented through Wannier orbitals. In particular, a formulation based on two correlated and eight non-correlated orbitals per valley [38, 39] turned out successful for DMFT modeling of TBG [40]. We will discuss this approach in the context of $tWSe_2$ in section 2.3.

- "Topological heavy fermion" [41] and "projector models" [42]: in these models the correlated orbitals (i.e. two per valley) are represented in real space through proper Wannier orbitals but the additional weakly correlated electronic states contributing to the model are represented in $\mathbf{k}$-space.

We will follow here the discussion of the topological heavy fermion model for TBG along the lines of Ref. [41], noting that the resultant model will be very similar to the projector based modeling of Ref. [42]. The concept of projector based modeling is widely used in complex multiband situations arising also in bulk systems [43].
Since it is impossible to obtain a symmetry and topology respecting tight-binding model for the two flat bands alone, the idea of the topological heavy fermion model is to involve the spectral weight missing for a proper Wannierization from higher lying bands [41]. The detailed symmetry analysis performed in Ref. [41] indeed shows that this is possible by using four additional bands and working with $p_x \pm ip_y$ trial orbitals located at the triangular lattice formed by the AA sites to carry most (but not all spectral weight) of the flat bands. The overlaps of Gaussian shaped $p_x \pm ip_y$-trial orbitals and the Bloch bands of TBG are visualized in Fig. 10(b). We see that the trial orbitals are supported by the flat band states at $\mathbf{k}$ away from Γ_M and by the lowest higher-energy bands around Γ_M. Wannierization starting from the $p_x \pm ip_y$-projectors leads to maximally localized Wannier functions with density as depicted in the inset of Fig. 10(b). The resultant Wannier functions span 96% of the flat bands and are well-localized [41].
Yet, the remaining 4% of spectral weight of the low-energy bands are very important for the phase diagram of TBG. To recover the low-energy bands including their symmetry and topology correctly, we have to augment the model with further states. We start from the continuum model Hamiltonian of TBG, H_{BM}, which is of referred to as the "Bistritzer MacDonald" (BM)

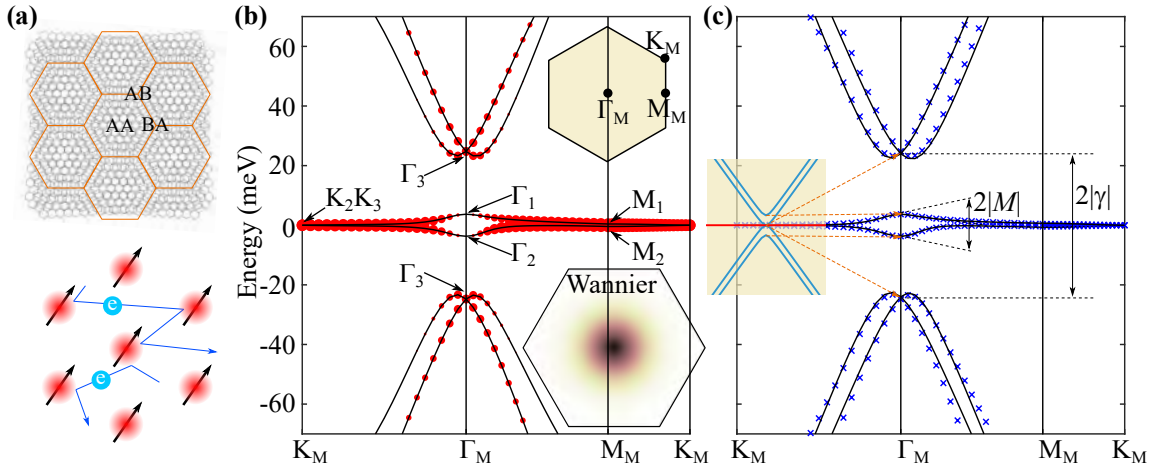


Fig. 10: *(a) An illustration of the moiré unit cell of TBG and the topological heavy fermion model, where the localized electrons (f-orbitals in the AA-stacking regions) hybridize with itinerant c-electrons carrying the topology. (b) The band structure of the magic angle TBG model obtained from the BM continuum model of Ref. [35]. The moiré Brillouin zone is illustrated in the upper inset. The overlaps between the Bloch states and trial f-orbitals are represented by the red circles. The density profile of the Wannier functions from Ref. [41] for the f-orbitals is shown in the lower inset. (c) Comparison of bands from the topological heavy fermion model (black lines) to the full continuum model bands (blue crosses). The inset shows the c- (blue) and f-bands (red) in the decoupled limit. Orange dashed lines indicate the evolution of energy levels as the f-c coupling is turned on. From Ref. [41].*

model [35, 41]. We define the projector onto the space spanned by the WFs as $\mathbb{P}$, the projector into the lowest six bands (per spin and valley) as $\mathbb{I}$, and divide the low energy BM Hamiltonian H_{BM} into four parts: $H^{(f)} = \mathbb{P}H_{BM}\mathbb{P}$, $H^{(c)} = \mathbb{Q}H_{BM}\mathbb{Q}$, $H^{(fc)} = \mathbb{P}H_{BM}\mathbb{Q}$, $H^{(cf)} = H^{(fc)\dagger}$, where $\mathbb{Q} = \mathbb{I} - \mathbb{P}$, $H^{(c)}$ is the remaining Hamiltonian, and $H^{(fc)} + \text{h.c.}$ is the coupling between WFs and the remaining states [41].

Since the hopping between neighboring Wannier centers is extremely weak ($\sim$0.1 meV) and it is neglected in many works: $H^{(f)} \to 0$. The analysis performed in Ref. [41] then shows that the Hamiltonian describing the six lowest energy bands then takes the form

$$H^K_{HF}(\mathbf{k}) = \begin{pmatrix} H^{(c)} & H^{(cf)} \\ H^{(fc)} & H^{(f)} \end{pmatrix} = \begin{pmatrix} 0 & v\mathbf{k}\cdot(\sigma_0, i\sigma_3) & \gamma\sigma_0 + v'\mathbf{k}\cdot\boldsymbol{\sigma} \\ v\mathbf{k}\cdot(\sigma_0, -i\sigma_3) & M\sigma_1 & 0 \\ \gamma\sigma_0 + v'\mathbf{k}\cdot\boldsymbol{\sigma} & 0 & 0 \end{pmatrix}. \quad (15)$$

Choosing the parameters $v_\star$=$-$4.303 eV·Å, M=3.697 meV, γ=$-$24.75 meV, $v'_\star$=1.622 eV·Å, the low-energy band structure of TBG turns out to be well-matched by the Hamiltonian of Eq. (15) (see Fig. 9(c)).

In the model reproduced here, the Wannier functions are strongly localized and hybridize with delocalized topological highly dispersive electronic states. These states are usually referred to as f- and c-electrons, respectively. This situation resembles heavy fermion materials and the model of Eq. (15) is named "topological heavy fermion (THF) model" of TBG [41].

2.2.1 Coulomb interaction in the topological heavy fermion model

From the construction of the THF model the wave functions of the f states and the c states are known and one can obtain all Coulomb matrix elements as required for modeling of electronic correlation effects.

The f electrons have a real-space and a k-space representation, while the c-electron have a k-space representation only. This needs to be taken into account when calculating the Coulomb integrals.

We note here two points that are of particular importance, when deriving Coulomb terms for moiré systems. First, the Coulomb interaction of 2D materials can be strongly impacted and controlled by the dielectric environment of the material—a concept sometimes called Coulomb engineering. Experiments on TBG typically work with single or doubled gate structures, where the actual TBG layer is separated by hBN spacer layers from metallic some gate electrodes. An appropriately screened Coulomb interaction to enter a low energy model of TBG should account for both, the internal and the external screening [33]. The Coulomb interaction derived in Ref. [41] accounts for screening by the hBN and a typical double gate structure (cf. Fig.2).

For this configuration one arrives at the following Coulomb interaction terms in the THF model

$$\hat{H}_I = \hat{H}_{U_1} + \hat{H}_J + \hat{H}_{U_2} + \hat{H}_V + \hat{H}_W \tag{16}$$

$\hat{H}_{U_1} = \frac{U_1}{2} \sum_{\mathbf{R}} :\rho^f_{\mathbf{R}}: :\rho^f_{\mathbf{R}}:$ are the on-site interactions of f-electrons with $\rho^f_{\mathbf{R}}$ being the f-electron density operator at site $\mathbf{R}$ and the colon symbols represent the normal ordered operator with respect to the normal state. $\hat{H}_J$ is a ferromagnetic exchange coupling between the f- and the c-electrons. Using a typical setup for MATBG, Ref. [41] finds $U_1 = 57.95\,\text{meV}$ and $J = 16.38\,\text{meV}$ setting the scale of $\hat{H}_J$. The other three terms in $\hat{H}_I$ are: H_{U_2}, the repulsion ($\sim 2.3\,\text{meV}$) between nearest neighbor f-electrons, H_V, the repulsion ($\sim 48\,\text{meV}$) between c-electrons, and H_W, the repulsion ($\sim 47\,\text{meV}$) between c- and f-electrons.

A usually adopted approximation motivated by the respective band widths of the c- and f-electrons is to treat only the local f-f interactions ($\hat{H}_{U_1}$) dynamically but all other interactions at a static Hartree(-Fock) level. Then, $H_{U_2} + H_V + H_W$ will effectively only shift the band energies of the entire c- and f-block relative to each other.

From the numbers above it becomes clear that the Hartree terms relating to H_V and H_W are by no means small. Indeed, there are substantial shifts between the f- and the c-block upon changing the filling as can be seen from the Hartree Fock band structures taken from Ref. [41], which we reproduce here in Fig. 11. Thus, when attempting to model electronic correlation phenomena, it is very important to consider also these additional interaction terms.

2.2.2 DMFT implementation for twisted bilayer graphene

We follow now [44] to explain, how one can proceed from the THF model towards practical DMFT simulations of TBG. First, we split the total Hamiltonian into a static and a dynamic

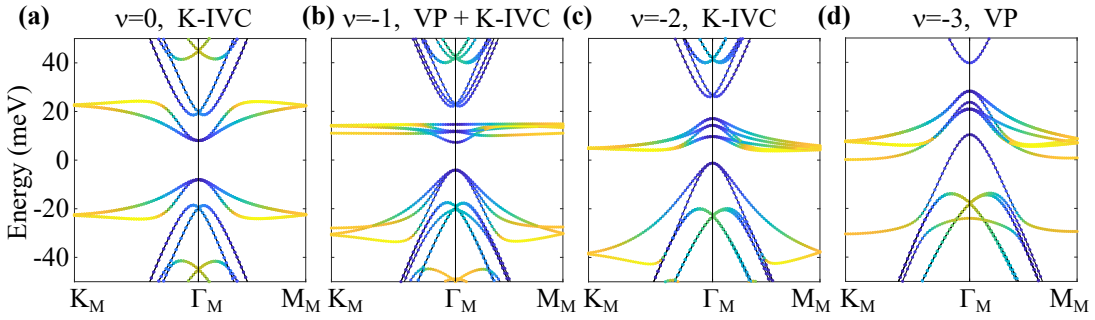


Fig. 11: *Band structure obtained from Hartree Fock solutions of the topological heavy fermion model at fillings $\nu = 0, -1, -2, -3$. The color of the bands represents their orbital composition with f-electron states printed in yellow and c-electrons states in blue. From Ref. [41].*

part,

$$\hat{H}_{\text{stat}} = \hat{H}_c + \hat{H}_{fc} + \hat{H}_W^{MF} + \hat{H}_V^{MF} + \hat{H}_J^{MF} - 3.5U \sum_{\alpha\eta\sigma} f^\dagger_{\alpha\eta\sigma} f_{\alpha\eta\sigma}, \tag{17}$$

$$\hat{H}_{\text{dyn}} = \frac{U}{2} \sum_{(\alpha\eta\sigma)\neq(\alpha'\eta'\sigma')} f^\dagger_{\alpha\eta\sigma} f_{\alpha\eta\sigma} f^\dagger_{\alpha'\eta'\sigma'} f_{\alpha'\eta'\sigma'}. \tag{18}$$

The superscript MF represents a static mean-field decoupled interaction term (Hartree+Fock for $\hat{H}_W^{MF}$ and $\hat{H}_J^{MF}$ and Hartree for $\hat{H}_V^{MF}$).
$\hat{H}_{\text{stat}}$ plays the role of the lattice Hamiltonian in the DMFT calculation. It must be self-consistently determined, as the mean-field decoupled interaction terms depend on the system's density matrix ρ. $\hat{H}_{\text{dyn}}$ acts on the f-subspace only and induces a frequency-dependent self-energy in the f-subspace. The self-energy for the f-sector is obtained from solving the impurity problem arising in DMFT with some appropriate solver. For the TBG problem at hand continuous-time quantum Monte Carlo (CT-QMC) hybridization expansion solvers turn out to be practicable [44]. Importantly, one has to converge two nested self-consistency loops: the DMFT self-consistency for the self-energy Σ of the f-subspace and the Hartree-Fock self-consistency setting $\hat{H}_W^{MF}$, $\hat{H}_J^{MF}$ and $\hat{H}_V^{MF}$. This computational scheme thus resembles charge-self-consistent DMFT calculations known from the DFT+DMFT context.

2.3 Twisted bilayer WSe_2

Twisted bilayer WSe_2 has been demonstrated experimentally to host intriguing correlated electron physics including metal insulator transitions in close vicinity to superconductivity as explained in section 1.2.
Here, the moiré bands emerge at the valence band edge in the K and K' valley, i.e., at non-time reversal invariant points of the Brillouin zone, with the valley index being a good quantum number in the band structure part of the moiré Hamiltonian. This situation is akin to TBG. Again, the moiré bands for each valley can carry finite Chern numbers, while Chern numbers from opposite valleys would cancel. Thus, also here topology can obstruct Wannierization and impact the emergent electron correlations by enforcing admixture of different orbitals to, e.g., the highest moiré band.

We lay out here, the "all Wannier model" approach for model building mentioned already for TBG. We follow closely Refs. [45, 46] giving an application to twisted WSe_2. The procedure is to (i) start from a large-scale model (here a continuum model), (ii) build proper Wannier functions, and (iii) obtain appropriate interaction terms to arrive at an extended multiorbital Hubbard model.

The non-interacting electronic structure of hole-doped tWSe_2 is accurately described by a continuum model in which the spin-valley locked holes of both monolayers are treated within an effective mass approximation, and are coupled by moiré potentials and interlayer tunneling. For the spin-up sector of the K the continuum Hamiltonian is a matrix in layer space reading

$$H(\boldsymbol{k}) = \begin{pmatrix} (\boldsymbol{k}-\kappa)^2/2m^* + \Delta_+(\boldsymbol{r}) & T_M(\boldsymbol{r}) \\ T_M^\dagger(\boldsymbol{r}) & (\boldsymbol{k}-\kappa')^2/2m^* + \Delta_-(\boldsymbol{r}) \end{pmatrix} + \begin{pmatrix} E_z & 0 \\ 0 & -E_z \end{pmatrix}. \tag{19}$$

Here, m^* is the hole effective mass from the WSe_2 monolayer and E_z accounts for external out-of-plane electric fields in the form of a layer-dependent potential. The κ and κ' points denote the position of the K-point coming from the top and bottom layer, respectively, which are displaced due to the twist. The intra- and inter-layer moiré couplings read $\Delta_\pm(\boldsymbol{r}) = V \sum_{\boldsymbol{g}\in\hexagon} \cos(\boldsymbol{g}\cdot\boldsymbol{r} \pm \psi)$ and $T_M(\boldsymbol{r}) = w\left(1 + e^{i\boldsymbol{g}_1\cdot\boldsymbol{r}} + e^{i\boldsymbol{g}_2\cdot\boldsymbol{r}}\right)$ [47]. The parameters V, ψ, and w characterizing the moiré couplings can be obtained by fitting Eq. (19) to large-scale *ab-initio* calculations [48] and are given in Refs. [45–47].[1]

For the DMFT modeling we seek a Wannier representation of the topmost valence bands. A symmetry analysis [49, 50] suggests a model with three Wannier orbitals per valley and unit cell, where one of these is centered at triangular lattice site T, having weight on both layers, as well as the others at two honeycomb lattice sites $H_{1,2}$ with dominant weight on either one of the layers as depicted in Fig. 12.

In the twist angle range $3.5^\circ < \theta < 5^\circ$, however, the Chern number sequence of the first three valence bands of tWSe_2 in valley $\nu = \pm 1$ is (ν, ν, ν) for the parameters of Ref. [48], prohibiting an exponential localization of these three bands alone onto the (in total three) T and $H_{1,2}$ sites. To resolve this issue, one can adapt the "single shot" Wannierization procedure outlined in section 2.1 in the following way [31, 39, 46, 51]: Instead of having as many Bloch states as Wannier states, we consider Bloch states from the entire valence band manifold for the projection. For a proper subspace selection, the Bloch states will be weighted according to their energy.

The construction works as follows: We start we N trial orbitals $|g^m\rangle$ and replace the projection of Eq. (6) by an energy-weighted "projection"[2]

$$|\phi_{\boldsymbol{k}}^m\rangle = \sum_{\alpha=1}^{M} |\Phi_{\boldsymbol{k}}^\alpha\rangle\, w_{\alpha\boldsymbol{k}}\, \langle \Phi_{\boldsymbol{k}}^\alpha | g^m\rangle\,. \tag{20}$$

The sum involves more Bloch states $|\Phi_{\boldsymbol{k}}^\alpha\rangle$ (i.e. eigenstates of the Hamiltonian H from Eq. (19)) than trial functions $M > N$ and $w_{\alpha\boldsymbol{k}} \in [0, 1]$ is a weighting factor for the Bloch states to

[1] The '$\hexagon$' denotes the set of the first shell of moiré reciprocal lattice vectors, and $\boldsymbol{g}_{1,2}$ are two reciprocal lattice vectors in the first shell rotated by 60° with respect to each other.

[2] We note that Eq. (20) is not a projection in the strict mathematical sense.

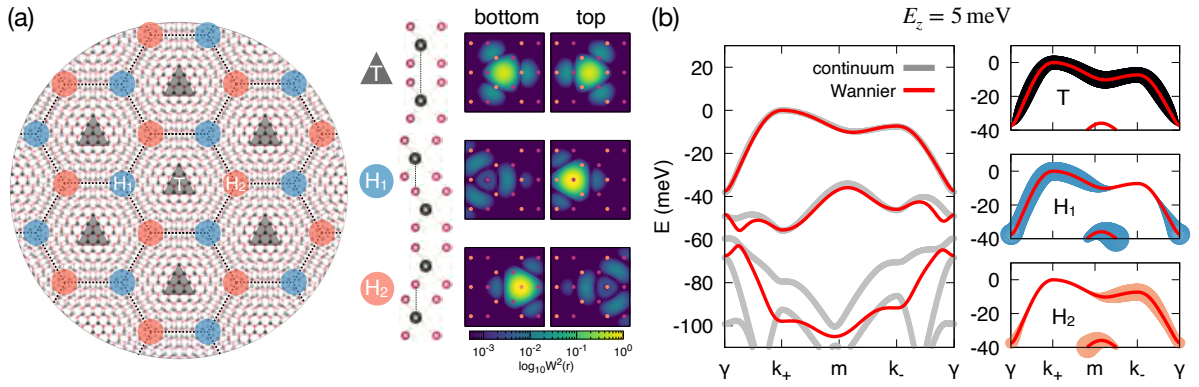


Fig. 12: *(a) Sketch of the local stacking regions, MM (T), MX (H_1), and XM (H_2), in the moiré lattice of $tWSe_2$ and the corresponding Wannier functions on the top layer and the bottom layer at $E_z = 0$. (b) Three-orbital Wannier bands for one valley/spin ($\sigma = \uparrow$) overlaid with continuum model bands at $E_z = 5$ meV along with the corresponding spectral weight of Wannier orbitals in the topmost band. The opposite valley/spin ($\sigma = \downarrow$) states are obtained via time-reversal conjugation of the $\uparrow$ states. Adapted from Ref. [45].*

facilitate band disentanglement. For the example of $tWSe_2$, Ref. [46] applied an exponential weighting scheme

$$w_\alpha(\boldsymbol{k}) = e^{-|\epsilon_\alpha(\boldsymbol{k})|/\eta} \tag{21}$$

with $\eta = 80\,\mathrm{meV}$.

The choice of a proper trial functions and of a proper weighting scheme is indeed central to the model building. Once, both is achieved, one can continue from Eq. (20) with the standard Wannierization scheme [31] outlined in section 2.1. Hereby, when obtaining the overlap matrix according to Eq. (7), one can either calculate $S^{mn}_{\mathbf{k}}$ with an explicit representation of the $|\phi^m_{\boldsymbol{k}}\rangle$ from Eq. (20) or using adapted "projector" matrices $P^{\alpha m}_{\mathbf{k}} = w_\alpha(\boldsymbol{k})\,\langle \Phi^\alpha_{\mathbf{k}} | g^m \rangle$.

For the case of twisted bilayer WSe_2 at twist angle $3.15°$, Fig. 12 shows the Wannier functions resulting from this adapted procedure and a comparison between the continuum model and the three orbital Wannier model. We see that the topmost moiré band is well reproduced by the Wannier model and that indeed all three orbitals contribute to this topmost band. The third continuum band does not match the third Wannier model band. Indeed, admixtures of states from the fourth and higher bands are essential for a three-orbital description, which has to yield an overall vanishing *total* Chern number in contrast to the three lowest lying bands of the continuum model. The lattice model reproduced here, has been used to analyze electron correlations and spontaneous symmetry breaking in twisted WSe_2 bilayers in Refs. [45, 46, 52].

3 DMFT studies of correlations in moiré systems

There are two major differences in DMFT of modeling moiré quantum materials as compared to bulk systems: (i) the more complex model building (cf. section 2) and (ii) the experimental tunabilities particularly via gate voltages allowing to change the number of electrons by as much as one electron (or even more) per (moiré) unit cell. Due to the latter it is often critical to account

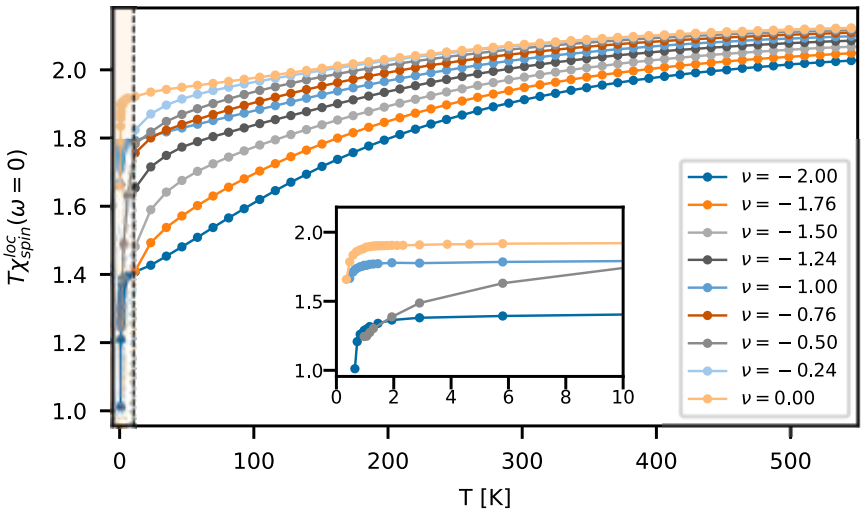


Fig. 13: *Local static spin susceptibility in the symmetric phase of TBG as a function of temperature. The shaded region of the main panel, delimited by the black dashed line is enlarged in the inset and illustrates the Curie-Weiss susceptibility plateau, associated with the presence of local moments at integer fillings. From Ref. [44].*

of charge self-consistency in the modeling. In the following we exemplify some insights that can be gained from the DMFT and related many-electron modeling of TBG and $tWSe_2$. This section is not meant to be exhaustive review of the field but more an introduction showcasing some phenomena that can be understood from many-body modeling of moiré systems.

3.1 Twisted bilayer graphene

DMFT studies using all Wannier models [40, 53], projector techniques [42] and the topological heavy fermion model [44,54–56] of TBG gave explanations and deeper understanding of several correlation effects seen in TBG experiments.

To understand the physics taking place across the temperature scale from $\mathcal{O}(100\,\mathrm{K})$ down to $\mathcal{O}(5\,\mathrm{K})$ we consider the spin-susceptibility and follow closely the discussion from Ref. [44]: In a non-interacting system, we would expect a Pauli type behavior, $\chi^{\mathrm{loc}}_{\mathrm{spin}}(T) \sim const.$, for the temperature dependence of the local spin susceptibility. In an interacting system, local (iso)spin moments are formed when charge fluctuations are suppressed due to Coulomb energy penalties. This reflects in the Curie-like behavior of the local spin susceptibility $\chi^{\mathrm{loc}}_{\mathrm{spin}}(T) \sim 1/T$. From deviations of $\chi^{\mathrm{loc}}_{\mathrm{spin}}(T)$ from the Curie law, one can identify two temperature scales: T_{K}, below which Kondo screening takes place, and T_{Moments}, above which thermally activated charge fluctuations set in. In the simplest case of a one-orbital model, charge fluctuations lead to the doubly-occupied and empty sectors contributing significantly to the partition function. This range of very high temperatures, known as *free orbital regime*, is associated with a decrease in the $1/T$-coefficient of $\chi^{\mathrm{loc}}_{\mathrm{spin}}(T)$ and an increase in entropy from $\sim \log 2$ to $\sim \log 4$, reflecting the higher number of contributing local eigenstates.

TBG features deviations from this picture in the low and in the high temperature limit. This is a consequence of the multi-orbital structure of the narrow bands manifold combined with

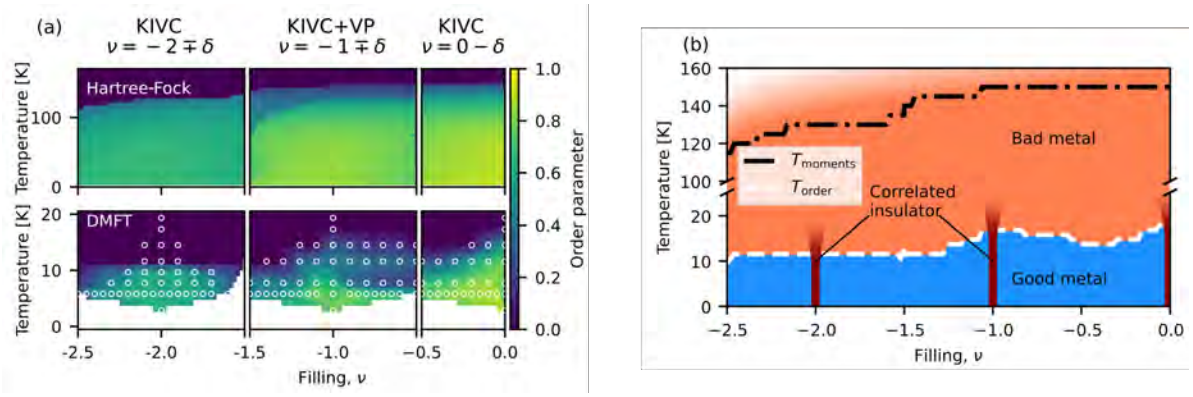


Fig. 14: *(a) The magnitude of the symmetry-breaking order parameter at various fillings and temperatures. In the bottom panel, white circles represent numerical data points from DMFT simulations with linear interpolation in between. The top panel shows the same quantity from a Hartree-Fock simulation (note the different vertical scale). In the dark blue regions, the self-consistency loop flows to the symmetric state, indicating that the symmetry-broken solution does not exist. (b) A schematic filling-temperature phase diagram: thermally activated charge fluctuations are frozen below the Hartree-Fock ordering temperature ($T_{moments}$), allowing local moments to progressively form in the orange region. These local moments order below the DMFT ordering temperature (T_{order}) in the blue region. The DMFT ordering temperature marks the boundary between a bad metal and an order-facilitated good metal at fractional fillings. The correlated insulators at integer fillings emerging below T_{order} (dark red) fade into the bad metal above T_{order}. From Ref. [44].*

the absence of an interaction term enforcing the Hund's rules. We show $T \cdot \chi^{\mathrm{loc}}_{\mathrm{spin}}(\omega{=}0)$, which quantifies the fluctuating local moment, obtained from DMFT in the symmetric phase in Fig. 13. As can be seen from the inset, TBG at integer filling shows Curie-like behavior (i.e. the curve is horizontal) all the way down to 1–2 K. The susceptibility deviates from clear Curie behavior for all fillings when considering the temperature scale $\mathcal{O}(100\,\mathrm{K})$. The deviation from the Curie law at low-temperatures signals Kondo screening, which sets in at $\sim 2\,\mathrm{K}$ at integer filling and at higher temperatures at fractional fillings.

DMFT allows to assess the interplay of spontaneous symmetry breaking and dynamical correlations by analyzing in which part of the temperature-doping phase space a symmetry broken state is a stable solution of the self-consistency condition. A comparison, of temperature and doping dependent isospin order obtained from DMFT and Hartree Fock is given in Fig. 14. In DMFT, the system flows to the symmetric phase under the self-consistency loop for sufficiently high temperature, while order set in below threshold temperatures of $\mathcal{O}(10\,\mathrm{K})$. The ordering temperatures predicted by Hartree-Fock are an order of magnitude higher ($\sim$ 100–150 K; see upper panel of Fig. 14(a)).

The DMFT simulations show that long-range order is suppressed by local dynamic fluctuations down to about 10 K. Order is most prominent at integer fillings resulting in dome-shaped ordered regions peaked around integer fillings as seen in the lower panel of Fig. 14.

The Hartree-Fock ordering temperature encodes the onset of thermally activated charge fluctuations. Above this temperature thermal smearing results in the Hartree-Fock equations converging to the symmetric unpolarized solution. Since Hartree-Fock neglects dynamic fluctuations,

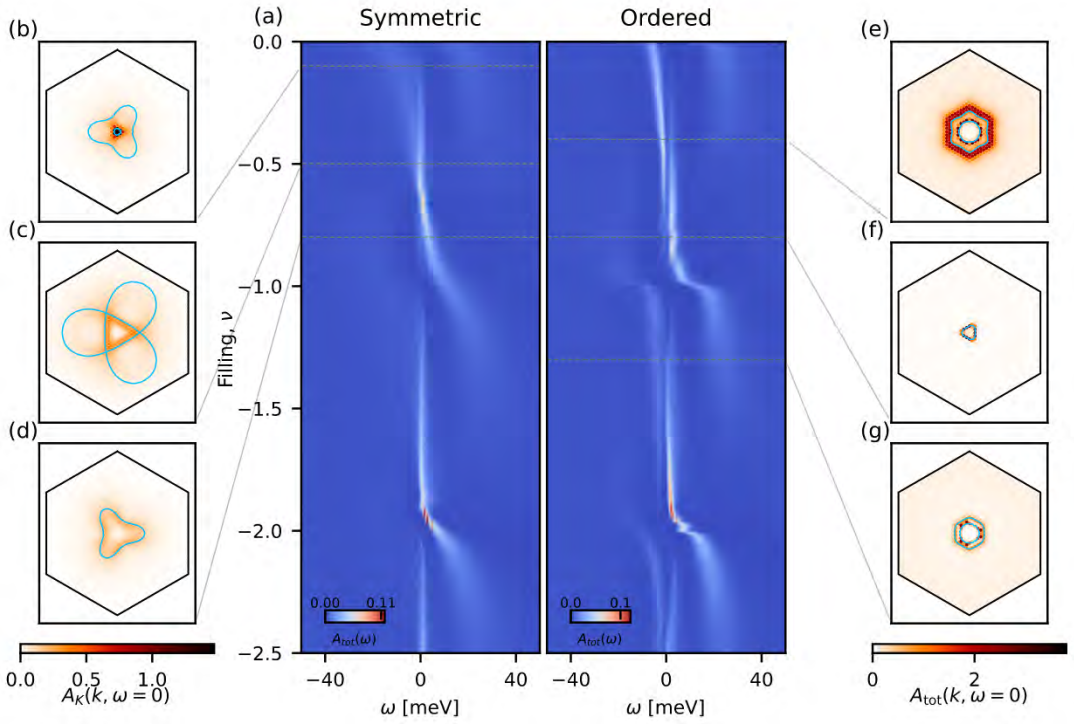


Fig. 15: *(a) The momentum-integrated spectral function $A_{tot}(\omega)$ 5.8 K in the symmetric phase (left) and in the ordered phase (right) as a function of hole doping. The electron-doped side (with respect to CNP) is related to the hole-doped side by a particle-hole transformation. (b)-(d) The K-valley–projected zero-energy spectral function in the first moiré Brillouin zone in the symmetric phase at select fillings. (e)-(g) The full zero-energy spectral function in the first moiré Brillouin zone in the ordered state at select fillings. The light blue lines mark the zeros of the effective Hamiltonian as identified by a quasiparticle analysis. From Ref. [44]*

moments order immediately upon formation. Therefore, the temperature range between the Hartree-Fock and DMFT ordering temperatures is the regime of fluctuating local moments at integer fillings. Correspondingly, in this temperature range, the local spin susceptibility follows the Curie-Weiss law as seen in Fig. 13. Near half-integer filling an intermediate valence regime with quantum charge fluctuations between two neighboring sectors is realized below the Hartree-Fock ordering temperature preventing the identification of well-defined local moments. Taken together, this analysis shows the formation of local spin and valley isospin moments around 100 K for integer fillings, intermediate valence behavior in between and the ordering of the local isospin moments around 10 K [44].

DMFT naturally yields electronic spectral functions. In Fig. 15(a), we show the momentum-integrated spectral function of TBG as a function of filling in the symmetric and symmetry-broken phases. In both cases, there is a depletion of spectral weight at the Fermi level for integer ν. In the symmetry broken states there are even full gaps at integer ν, which explain the correlated insulating states in experiments. Upon sweeping the filling through a larger range, there is a cascadic reshuffling of the low-energy spectral weight upon changing ν by an integer value. These are the *cascade transitions* that have been seen experimentally with scanning tunneling spectroscopy (STS) [57]. These cascades have been consistently seen in DMFT studies using pure Wannier [40] and the topological heavy fermion model [44].

The symmetry-broken state behaves the same way except that there is fine low-energy structure, owing to isospin order. In particular, the zero-energy peak at fractional fillings, made up primarily of f-spectral weight, is split by a feedback effect from the exchange interaction $\hat{H}_J$.
Further phenomena, that can be understood from DMFT modeling of TBG include compressibilities, details of the metal insulator transitions taking place in TBG, and doping as well as temperature dependencies of quasi particle scattering rates [44]. The latter becomes clear from the k-resolved plots of the zero energy spectral weight in Fig. 15: For the symmetric state we see largely incoherent "blurry" spectral weight in space, while there much sharper Fermi contours emerge upon ordering in the system. I.e., there is "coherence from order" upon lowering the temperature in TBG, which also explains the Pomeranchuk physics observed in experiments of Refs. [58, 59].
Overall, DMFT draws the phase diagram as shown in Fig. 14(b): Below the ordering temperature of $\sim$10 K, there are insulators at integer fillings and a good metal featuring well-defined coherent quasiparticles at fractional fillings. Above the ordering temperature, the spectral weight at the Fermi level is generically incoherent, indicating a bad metal [44].

3.2 Twisted bilayer WSe_2

For $tWSe_2$, several aspects of the experiments reported in Refs. [8, 10, 11] can be understood, based on the three orbital Wannier model discussed in section 2.3. Ref. [46] performed a functional renormalization group study of this model and finds an interplay of so-called intervalley-coherent antiferromagnetic order with superconductivity. The phase boundaries as function of displacement field and doping are in good agreement with experimental observations particularly for twist angle $\sim 5^\circ$. Taken together with the Hartree Fock study of Ref. [52], it is very plausible that in the regime of twist angles $\sim 5^\circ$ a Slater-type mechanism leads to the intervalley-coherent antiferromagnetic order for certain parts of the phase diagram, while corresponding dynamical quantum fluctuations act as pairing glue for the superconducting state that emerges upon suppression of the intervalley-coherent antiferromagnetic order. Yet, temperature dependencies remain to be explored and understood here.
For twist angles of 3.5° stronger electron correlations are expected. Ref. [45] reports a DMFT study of this system and reveals the importance of orbital polarization effects, which are strongly enhanced by Coulomb interactions: a correlated metal competes with three distinct site-polarized correlated insulators that are controllable by displacement field and dielectric constant. The insulators turn out to be charge transfer insulators, which are characterized by a strong differentiation between orbitals with regard to the correlation strength which naturally explain key experimental observations including the displacement field driven metal-to-insulator transitions, transport asymmetry, and a coherence-incoherence crossover and importantly temperature dependencies of transport.
Thus, the situation is currently such that different approaches (Hartree Fock, fRG, DMFT) explain different aspects of the correlated electron physics emerging in $tWSe_2$, while a full unified theory explaining all experiments consistently remains to be developed.

4 Summary

Moiré systems constitute an emerging platform for electronic quantum matter, where electron correlations arise on the length scale of the moiré superlattice. Particularly interesting is the connection between correlation phenomena and topology observed across various moiré systems, including twisted graphene structures and transition metal dichalcogenide multilayers. Both platforms exhibit rich multiorbital physics, manifested in flat electronic bands characterized by nontrivial Berry curvature and quantum geometry.
The fact that electronic correlations emerge at mesoscopic length scales enables extensive tunability via gate voltages, twist angles, and the dielectric environment. This tunability is highly advantageous for both understanding and controlling correlated electronic phases, as well as for the development of quantitative theories of correlated electron systems. These prospects have spurred extensive efforts toward many-body modeling of moiré quantum matter, including DMFT.
From a practitioner's perspective, DMFT modeling of moiré systems can be conducted in close analogy to that of conventional solids, provided that special attention is paid to the following aspects:

1. **Model Construction:** It is essential to derive faithful, well-localized Wannier functions that accurately describe the correlated orbitals. The effective low-energy model must respect the system's underlying topology and symmetries.

2. **Coulomb Interactions:** Moiré systems are typically embedded in complex dielectric environments, which have to be accounted for in the derivation of appropriate Coulomb interaction tensors.

3. **Charge Self-Consistency and Long-Range Interactions:** The filling of moiré minibands can be widely tuned—by as much as one or more electrons per moiré unit cell—using gate voltages. This variability leads to substantial effects arising from the interplay between local and non-local Coulomb terms in multi-orbital and/or multi-site systems, which must be accurately captured in charge self-consistent DMFT calculations.

The field is now approaching a quantitative understanding of the phase diagrams, excitation spectra, and transport properties of moiré systems. In this context, DMFT has proven capable of delivering semi-quantitative insights into thermodynamic observables and spectral properties, as illustrated in section 3. Key open challenges include achieving a precise and quantitative understanding of superconductivity, quantum criticality, and strange metal behavior in moiré systems, as well as incorporating non-local correlation effects.

References

[1] A.K. Geim and I.V. Grigorieva, Nature **499**, 419 (2013)

[2] K.S. Novoselov, A. Mishchenko, A. Carvalho, and A.H.C. Neto, Science **353**, aac9439 (2016)

[3] A.H. Castro Neto, F. Guinea, N.M.R. Peres, K.S. Novoselov, and A.K. Geim, Rev. Mod. Phys. **81**, 109 (2009)

[4] M.I. Katsnelson: *The Physics of Graphene* (Cambridge University Press, 2020), 2 ed.

[5] Y. Cao, V. Fatemi, A. Demir, S. Fang, S.L. Tomarken, J.Y. Luo, J.D. Sanchez-Yamagishi, K. Watanabe, T. Taniguchi, E. Kaxiras, R.C. Ashoori, and P. Jarillo-Herrero, Nature **556**, 80 (2018)

[6] Y. Cao, V. Fatemi, S. Fang, K. Watanabe, T. Taniguchi, E. Kaxiras, and P. Jarillo-Herrero, Nature **556**, 43 (2018)

[7] L. Balents, C.R. Dean, D.K. Efetov, and A.F. Young, Nat. Phys. **16**, 725 (2020)

[8] L. Wang, E.-M. Shih, A. Ghiotto, L. Xian, D.A. Rhodes, C. Tan, M. Claassen, D.M. Kennes, Y. Bai, B. Kim, K. Watanabe, T. Taniguchi, X. Zhu, J. Hone, A. Rubio, A.N. Pasupathy, and C.R. Dean, Nat. Mater. **19**, 861 (2020)

[9] K.F. Mak and J. Shan, Nat. Nanotechnol. **17**, 686 (2022)

[10] Y. Xia, Z. Han, K. Watanabe, T. Taniguchi, J. Shan, and K.F. Mak, Nature **637**, 833 (2025)

[11] Y. Guo, J. Pack, J. Swann, L. Holtzman, M. Cothrine, K. Watanabe, T. Taniguchi, D.G. Mandrus, K. Barmak, J. Hone, A.J. Millis, A. Pasupathy, and C.R. Dean, Nature **637**, 839 (2025)

[12] K.P. Nuckolls and A. Yazdani, Nat. Rev. Mater. **9**, 460 (2024)

[13] P.C. Adak, S. Sinha, A. Agarwal, and M.M. Deshmukh, Nat. Rev. Mater. **9**, 481 (2024)

[14] T.O. Wehling, E. Şaşıoğlu, C. Friedrich, A.I. Lichtenstein, M.I. Katsnelson, and S. Blügel, Phys. Rev. Lett. **106**, 236805 (2011)

[15] M. Schüler, M. Rösner, T.O. Wehling, A.I. Lichtenstein, and M.I. Katsnelson, Phys. Rev. Lett. **111**, 036601 (2013)

[16] Y. Cao, D. Chowdhury, D. Rodan-Legrain, O. Rubies-Bigorda, K. Watanabe, T. Taniguchi, T. Senthil, and P. Jarillo-Herrero, Phys. Rev. Lett. **124**, 076801 (2020)

[17] X. Lu, P. Stepanov, W. Yang, M. Xie, M.A. Aamir, I. Das, C. Urgell, K. Watanabe, T. Taniguchi, G. Zhang, A. Bachtold, A.H. MacDonald, and D.K. Efetov, Nature **574**, 653 (2019)

[18] M. Yankowitz, S. Chen, H. Polshyn, Y. Zhang, K. Watanabe, T. Taniguchi, D. Graf, A.F. Young, and C.R. Dean, Science **363**, 1059 (2019)

[19] H. Polshyn, M. Yankowitz, S. Chen, Y. Zhang, K. Watanabe, T. Taniguchi, C.R. Dean, and A.F. Young, Nat. Phys. **15**, 1011 (2019)

[20] S. Wu, Z. Zhang, K. Watanabe, T. Taniguchi, and E.Y. Andrei, Nat. Mater. **20**, 488 (2021)

[21] M. Serlin, C.L. Tschirhart, H. Polshyn, Y. Zhang, J. Zhu, K. Watanabe, T. Taniguchi, L. Balents, and A.F. Young, Science **367**, 900 (2020)

[22] K.P. Nuckolls, R.L. Lee, M. Oh, D. Wong, T. Soejima, J.P. Hong, D. Călugăru, J. Herzog-Arbeitman, B.A. Bernevig, K. Watanabe, T. Taniguchi, N. Regnault, M.P. Zaletel, and A. Yazdani, Nature **620**, 525 (2023)

[23] Y. Zhang, R. Polski, C. Lewandowski, A. Thomson, Y. Peng, Y. Choi, H. Kim, K. Watanabe, T. Taniguchi, J. Alicea, F. von Oppen, G. Refael, and S. Nadj-Perge, Science **377**, 1538 (2022)

[24] Y. Xu, S. Liu, D.A. Rhodes, K. Watanabe, T. Taniguchi, J. Hone, V. Elser, K.F. Mak, and J. Shan, Nature **587**, 214 (2020)

[25] X. Huang, T. Wang, S. Miao, C. Wang, Z. Li, Z. Lian, T. Taniguchi, K. Watanabe, S. Okamoto, D. Xiao *et al.*, Nat. Phys. **17**, 715 (2021)

[26] S. Ryee and T.O. Wehling, Nano Lett. **23**, 573 (2023)

[27] A. Ghiotto, E.-M. Shih, G.S. Pereira, D.A. Rhodes, B. Kim, J. Zang, A.J. Millis, K. Watanabe, T. Taniguchi, J.C. Hone *et al.*, Nature **597**, 345 (2021)

[28] T. Li, S. Jiang, L. Li, Y. Zhang, K. Kang, J. Zhu, K. Watanabe, T. Taniguchi, D. Chowdhury, L. Fu *et al.*, Nature **597**, 350 (2021)

[29] W. Zhao, B. Shen, Z. Tao, Z. Han, K. Kang, K. Watanabe, T. Taniguchi, K.F. Mak, and J. Shan, Nature **616**, 61 (2023)

[30] M. Angeli and A.H. MacDonald, Proc. Natl. Acad. Sci. **118** (2021)

[31] N. Marzari, A.A. Mostofi, J.R. Yates, I. Souza, and D. Vanderbilt, Rev. Mod. Phys. **84**, 1419 (2012)

[32] N. Witt, J.M. Pizarro, J. Berges, T. Nomoto, R. Arita, and T.O. Wehling, Phys. Rev. B **105**, L241109 (2022)

[33] J.M. Pizarro, M. Rösner, R. Thomale, R. Valentí, and T.O. Wehling, Phys. Rev. B **100**, 161102 (2019)

[34] J.M.B. Lopes dos Santos, N.M.R. Peres, and A.H. Castro Neto, Phys. Rev. Lett. **99**, 256802 (2007)

[35] R. Bistritzer and A.H. MacDonald, Proc Natl Acad Sci USA **108**, 12233 (2011)

[36] M. Koshino, N.F. Yuan, T. Koretsune, M. Ochi, K. Kuroki, and L. Fu, Phys. Rev. X **8**, 031087 (2018)

[37] H.C. Po, L. Zou, A. Vishwanath, and T. Senthil, Phys. Rev. X **8**, 031089 (2018)

[38] H.C. Po, L. Zou, T. Senthil, and A. Vishwanath, Phys. Rev. B **99**, 195455 (2019)

[39] S. Carr, S. Fang, H.C. Po, A. Vishwanath, and E. Kaxiras, Phys. Rev. Res. **1**, 033072 (2019)

[40] A. Datta, M.J. Calderón, A. Camjayi, and E. Bascones, Nat. Commun. **14**, 5036 (2023)

[41] Z.-D. Song and B.A. Bernevig, Phys. Rev. Lett. **129**, 047601 (2022)

[42] M. Haule, E.Y. Andrei, and K. Haule, arXiv:1901.09852

[43] B. Amadon, F. Lechermann, A. Georges, F. Jollet, T.O. Wehling, and A.I. Lichtenstein, Phys. Rev. B **77**, 205112 (2008)

[44] G. Rai, L. Crippa, D. Călugăru, H. Hu, F. Paoletti, L. de' Medici, A. Georges, B.A. Bernevig, R. Valentí, G. Sangiovanni, and T. Wehling, Phys. Rev. X **14**, 031045 (2024)

[45] S. Ryee, L. Klebl, G. Rai, A. Fischer, V. Crépel, L. Xian, A. Rubio, D.M. Kennes, R. Valentí, A.J. Millis, A. Georges, and T.O. Wehling, arXiv:2506.22325

[46] A. Fischer, L. Klebl, V. Crépel, S. Ryee, A. Rubio, L. Xian, T.O. Wehling, A. Georges, D.M. Kennes, and A.J. Millis, arXiv:2412.14296

[47] F. Wu, T. Lovorn, E. Tutuc, I. Martin, and A. MacDonald, Phys. Rev. Lett. **122**, 086402 (2019)

[48] T. Devakul, V. Crépel, Y. Zhang, and L. Fu, Nat. Commun. **12**, 6730 (2021)

[49] V. Crépel and A. Millis, Phys. Rev. Res. **6**, 033127 (2024)

[50] W.-X. Qiu, B. Li, X.-J. Luo, and F. Wu, Phys. Rev. X **13**, 041026 (2023)

[51] A. Fischer, L. Klebl, D.M. Kennes, and T.O. Wehling, arXiv:2407.02576

[52] D. Muñoz-Segovia, V. Crépel, R. Queiroz, and A.J. Millis, arXiv:2503.11763

[53] M.J. Calderón, A. Camjayi, A. Datta, and E. Bascones, arXiv:2412.20855

[54] H. Hu, G. Rai, L. Crippa, J. Herzog-Arbeitman, D. Călugăru, T. Wehling, G. Sangiovanni, R. Valentí, A.M. Tsvelik, and B.A. Bernevig, Phys. Rev. Lett. **131**, 166501 (2023)

[55] G.-D. Zhou, Y.-J. Wang, N. Tong, and Z.-D. Song, Phys. Rev. B **109**, 045419 (2024)

[56] Y.-J. Wang, G.-D. Zhou, S.-Y. Peng, B. Lian, and Z.-D. Song, Phys. Rev. Lett. **133**, 146001 (2024)

[57] D. Wong, K.P. Nuckolls, M. Oh, B. Lian, Y. Xie, S. Jeon, K. Watanabe, T. Taniguchi, B.A. Bernevig, and A. Yazdani, Nature **582**, 198 (2020)

[58] Y. Saito, F. Yang, J. Ge, X. Liu, T. Taniguchi, K. Watanabe, J.I.A. Li, E. Berg, and A.F. Young, Nature **592**, 220 (2021)

[59] A. Rozen, J.M. Park, U. Zondiner, Y. Cao, D. Rodan-Legrain, T. Taniguchi, K. Watanabe, Y. Oreg, A. Stern, E. Berg, P. Jarillo-Herrero, and S. Ilani, Nature **592**, 214 (2021)

6 Effect of Charge Self-Consistency in Calculations for Transition-Metal Oxides

Claude Ederer
Materials Theory
ETH Zürich

Contents

1 Introduction **2**

2 Charge self-consistent DFT+DMFT **4**
2.1 Definition of the correlated subspace and Wannier functions 4
2.2 The DFT+DMFT self-consistency cycle 6
2.3 Local interaction Hamiltonian and double counting correction 11

3 Transition metal oxides in a nutshell **12**

4 Examples **15**
4.1 Orbital polarization in $CaVO_3$ 15
4.2 Potential charge disproportionation in $SrCrO_3$ 18

5 Summary and conclusions **25**

E. Pavarini, E. Koch, A. Lichtenstein, and D. Vollhardt (eds.)
Understanding Correlated Materials with DMFT
Modeling and Simulation Vol. 15
Forschungszentrum Jülich, 2025, ISBN 978-3-95806-813-1
http://www.cond-mat.de/events/correl25

1 Introduction

Soon after the emergence of dynamical mean-field theory (DMFT) as a powerful approach to address models of interacting fermions on a lattice, the idea emerged to combine DMFT also with realistic electronic structure calculations using density functional theory (DFT) in the local density approximation (LDA) [1, 2]. Thereby, the auxiliary independent-particle Kohn-Sham (KS) band-structure obtained within LDA is taken as a "zeroth order" approximation to the interacting problem [1]. After constructing a minimal tight-binding (TB) representation of the most relevant bands, a local electron-electron interaction is added to the corresponding Hamiltonian, resulting in a realistic materials-specific multi-orbital Hubbard model. For the case of transition metal (TM) oxides or related materials, these "most relevant bands" generally consist of partially filled bands around the Fermi level with dominant TM d orbital character, and sometimes also of bands with strong O p orbital character. Thus, a TB representation of these bands is typically based on localized d-like orbitals centered on the TM sites, and potentially also p-like orbitals on the O atoms or other anionic ligands.

The basic idea is similar in spirit to the DFT+U method [3,4], where the underlying energy functional and the KS potential are supplemented by terms explicitly describing the local electron-electron interaction within a subset of electrons, typically corresponding to localized d or f states. However, while the local interaction within DFT+U is treated on the level of a *static* mean-field approximation, within the DFT+DMFT approach the resulting multi-band Hubbard model is treated by considering a *dynamical* mean-field.[1] Thereby, each interacting site on the lattice is viewed as an individual atom that is embedded in an effective bath. Thus, the bath in principle consists of all other atoms in the system. Electrons can dynamically fluctuate between the selected atom and the bath. Electrons on the atom interact with each other via the local electron-electron interaction, while electrons in the bath are considered as non-interacting. Thus, the original lattice problem is mapped to an Anderson-type impurity problem. However, since the bath of this effective impurity problem indeed consists of all other sites, which are either equivalent to the selected site or connected to it via their respective effective baths, the bath itself is related to the solution of the impurity problem via a self-consistency condition.

The fact that this approach has evolved into a powerful method that is nowadays also applied to the treatment of rather complex materials systems involving, e.g., heterostructures, surfaces, or point defects (see, e.g., [5–7]), is closely tied to the availability of efficient and accurate computational methods to solve the corresponding Anderson impurity problem(s). Various examples of such *impurity solvers* have been discussed in other lecture notes within this series and therefore will not be discussed here. We just note that the effect of the bath, the hybridization between the bath and the impurity site, and the non-interacting part of the local Hamiltonian, are encoded in the form of a non-interacting local Green function, the so-called *Weiss field*, $\mathcal{G}_0$, usually expressed in a basis of suitable localized orbitals. The impurity solver then takes $\mathcal{G}_0$ as

[1] In these lecture notes, we use the term "DFT+DMFT" instead of the more traditional "LDA+DMFT", acknowledging the fact that many calculations are nowadays using DFT functionals based on the generalized gradient approximation or other semi-local exchange correlation (xc) functionals. Thus, "DFT" in "DFT+DMFT" should be read as "DFT using some approximate semi-local xc functional".

input, together with the specific form of the local interaction Hamiltonian, $\hat{H}_{\text{int}}$, and computes the full one-particle Green function of the impurity, G^{imp} as well as the local impurity self energy, Σ^{imp}, which are related via the Dyson equation $(G^{\text{imp}})^{-1} = \mathcal{G}_0^{-1} - \Sigma^{\text{imp}}$. The impurity self energy is then used as purely local approximation to the self energy of the original lattice problem, and a new estimate of the Weiss field can be obtained from the local component of the lattice Green function. This procedure, described in more detail in Sec. 2, is then repeated until a self-consistent solution is obtained, such that the local part of the lattice Green function becomes identical to the impurity Green function.

In most realistic cases, the DMFT treatment of the local interaction results in a redistribution of electrons compared to the underlying initial DFT calculation. For example, in systems where a local crystal field splitting lifts the degeneracy between partially filled d levels, electrons can be redistributed between the different non-degenerate orbitals, and in complex crystal structures, where several inequivalent atomic sites are mapped on different effective impurity problems, electrons can be redistributed between different sites. This redistribution of electrons corresponds to a change in the electronic charge density of the system, which consequently also changes the KS potential that was used in the initial DFT calculation, and thus also the corresponding band structure changes compared to the initial bandstructure that was used to construct the multi-orbital Hubbard model for the DMFT treatment. Therefore, in order to arrive at a truly realistic and potentially also quantitative and predictive method for the treatment of complex correlated materials, an additional self-consistency over the charge density is required. Furthermore, if quantities related to total energy differences are of interest, then the condition for stationarity of the underlying energy functional also demands *charge self-consistency*.

However, charge self-consistency increases the required computational effort and simultaneously also increases the complexity of the computational scheme, since DFT calculations have to be performed for which the KS potential is calculated from an externally modified charge density, and the information about this modified charge density has to be transferred from the DMFT part of the calculation to the DFT code that is used. Therefore, in practice, charge self-consistency is often neglected in favor of so-called "one-shot" calculations, where the DMFT calculation is essentially a "post-processing" of the DFT results, and the DFT calculation is merely providing a fixed input to the DMFT part. It is therefore essential to be aware of the potential limitations of such one-shot calculations, and to recognize cases that require the full charge self-consistent treatment.

In these lecture notes, we present several case studies of DFT+DMFT calculations for specific materials where charge self-consistency is important and leads to noticeable differences from the one-shot results. However, before discussing the various examples in Sec. 4, we start with a detailed description of the charge self-consistent DFT+DMFT approach, which is presented in Sec. 2. Thereby, we emphasize a clear and transparent definition of what represents "the most relevant bands", and show how all relevant quantities can be transformed back and forth between the KS Bloch basis and the localized orbitals centered on the relevant sites, which is required for a fully charge self-consistent treatment. We also briefly discuss how the DFT+DMFT approach can be derived from a specific approximation to the Gibbs free energy functional, providing

a solid theoretical foundation of the method. Then, before discussing the several examples demonstrating the effect of charge self-consistency, a brief summary of the most relevant aspects of TM oxides is provided in Sec. 3, which is intended to help to better understand the different materials aspects in the various case studies.

2 Charge self-consistent DFT+DMFT

2.1 Definition of the correlated subspace and Wannier functions

The main conceptual idea behind DFT+DMFT as a "first principles"-based method for quantitative materials-specific electronic structure calculations, is based on a separation of the electronic degrees of freedom into a strongly interacting and a weakly interacting part. The basic assumption is, that the weakly interacting subspace, which makes up the largest part of the electronic Hilbert space, is well described by DFT using standard local or semi-local exchange-correlation functionals, and that only a small subset of electronic degrees of freedom, the *correlated subspace*, $\mathcal{C}$, requires a more sophisticated treatment of the local electron-electron interaction. The correlated subspace typically involves partially filled bands around the Fermi level corresponding to relatively localized orbital degrees of freedom. The assumption that a more sophisticated treatment is only necessary for a small subset of electrons, is of course to some extent also a matter of necessity, since a full treatment of all electronic degrees of freedom within DMFT (or another more advanced computational many-body approach) is not realistically feasible.

In the case of transition metal oxides, the correlated subspace typically consists of the "d electrons" corresponding to the transition metal ions with partially filled d shell, or of a subset thereof, such as, e.g., either the e_g or t_{2g} subshells in systems with a pronounced octahedral crystal field splitting. However, it should be noted that, as discussed also in some detail in Sec. 3, there is some ambiguity what is meant by the "d electrons" in a specific material, reflecting the fact that local angular momentum is not a good quantum number in a periodic solid. The choice of the correlated subspace for a specific material is therefore always to some degree based on physical and chemical intuition, or other specific insights on what are the most important degrees of freedom that require a treatment beyond conventional DFT. The obtained results will generally depend on this choice. Nevertheless, in many cases it has been found that even somewhat different but reasonable choices can lead to consistent results.

The correlated subspace is typically defined in terms of a set of orthogonal spatially localized orbitals, $|\phi_{m\mathbf{T}}\rangle$, centered on specific sites within each crystallographic unit cell, in the following called the "correlated sites". $\mathbf{T}$ is a vector of the underlying Bravais lattice and indicates the crystallographic unit cell where the corresponding orbital is located, while m represents the orbital character including spin. In cases with more than one correlated site per unit cell, m indicates both the specific site within the unit cell as well as the corresponding orbital character. For transition metal oxides, the correlated sites typically coincide with the positions of the transition metal cations.

It is convenient to work with Bloch sums, i.e., Fourier transforms, of the local orbitals, defined

as follows

$$|\phi_{m\mathbf{k}}\rangle = \sum_{\mathbf{T}} e^{i\mathbf{k}\cdot\mathbf{T}}|\phi_{m\mathbf{T}}\rangle \quad \leftrightarrow \quad |\phi_{m\mathbf{T}}\rangle = \frac{V}{(2\pi)^3}\int_{\mathrm{BZ}} d\mathbf{k}\, e^{-i\mathbf{k}\cdot\mathbf{T}}|\phi_{m\mathbf{k}}\rangle, \tag{1}$$

where the integral over $\mathbf{k}$ is taken over the Brillouin zone (BZ) of the crystal and V is the unit cell volume. Since in practice one always works with a finite set of KS Bloch states, $|\psi_{\nu\mathbf{k}}\rangle$, corresponding to a finite number of bands (indexed by ν), an arbitrary orbital generally cannot be exactly represented in this Bloch basis. Consequently, the projections of a set of given *trial orbitals* into this restricted Bloch space $\mathcal{R}$:

$$|\phi^{(\mathcal{R})}_{m\mathbf{k}}\rangle = \sum_{\nu\in\mathcal{R}} |\psi_{\nu\mathbf{k}}\rangle\langle\psi_{\nu\mathbf{k}}|\phi_{m\mathbf{k}}\rangle, \tag{2}$$

are not necessarily orthogonal to each other, even if the original trial orbitals were. However the set of $|\phi^{(\mathcal{R})}_{m\mathbf{k}}\rangle$ can always be subsequently orthogonalized, using, e.g., Löwdin orthonormalization (see, e.g., [8]). Furthermore, only the projection of $|\phi_{m\mathbf{k}}\rangle$ into $\mathcal{R}$ is relevant for the DFT+DMFT treatment. Therefore, in the following we always use the orthonormalized projections, $|\phi^{(\mathcal{R})}_{m\mathbf{k}}\rangle$, of the original trial orbitals as our local orbital basis, and we drop the superscript $\mathcal{R}$ again for ease of notation. Thus, from now on we can assume that the $|\phi_{m\mathbf{k}}\rangle$ form an orthonormal basis and are completely representable in $\mathcal{R}$.

A set of localized orbitals that exhibits this property automatically by construction are *Wannier functions* [8], defined as

$$|w_{m\mathbf{T}}\rangle = \frac{V}{(2\pi)^3}\int_{\mathrm{BZ}} d\mathbf{k}\, e^{-i\mathbf{k}\cdot\mathbf{T}} \sum_{\nu} U^{(\mathbf{k})}_{\nu m}|\psi_{\nu\mathbf{k}}\rangle = \frac{V}{(2\pi)^3}\int_{\mathrm{BZ}} d\mathbf{k}\, e^{-i\mathbf{k}\cdot\mathbf{T}}|w_{m\mathbf{k}}\rangle. \tag{3}$$

The functions $|w_{m\mathbf{k}}\rangle = \sum_\nu U^{(\mathbf{k})}_{\nu m}|\psi_{\nu\mathbf{k}}\rangle$ are equivalent to the Bloch sums $|\phi_{m\mathbf{k}}\rangle$ defined from the local orbitals $|\phi_{m\mathbf{T}}\rangle$ and are sometimes called "$\mathbf{k}$-space Wannier functions" or "remixed Bloch states", since they are defined as a linear combination of the Kohn-Sham eigenfunctions corresponding to a set of bands at the same $\mathbf{k}$-point. Specific Wannier functions are defined by a specific choice of the matrices $U^{(\mathbf{k})}_{\nu m}$. In fact, the procedure described above, i.e., projecting some localized trial orbitals on the Bloch space with subsequent Löwdin orthonormalization, is one widely-used approach to obtain Wannier functions, which then typically closely resemble the orbital character of the initial trial orbitals. Such Wannier functions have been termed "Wannier functions via projection" or "projected Wannier functions" [8]. Another wide-spread possibility is to minimize the total quadratic spatial spread of the Wannier functions, leading to so-called *maximally localized Wannier functions* (MLWFs) [8]. In this case, Wannier functions defined via projections are often used as starting point for the spread minimization and thus the resulting MLWFs typically also closely resemble the orbital character of the initial trial orbitals.

The summation over the band index ν in Eq. (3) is often further restricted to only a specific group of bands, which can either be completely isolated from other bands at lower and higher energies, or is defined within a certain energy window around the Fermi level. The resulting subspace is called the *Wannier space*, $\mathcal{W}$, and is a subset of $\mathcal{R}$. If the number of Bloch states

in the sum in Eq. (3) matches the number of Wannier functions, i.e., if the dimension of the correlated subspace $\mathcal{C}$ is identical to that of the Wannier space $\mathcal{W}$, then the matrices $U^{(\mathbf{k})}_{\nu m}$ are square unitary matrices for each $\mathbf{k}$, and the two subspaces are in fact identical. If the number of Bloch functions in the sum is larger than the number of Wannier functions (which is generally the case for bands that are "entangled" with other bands at lower and/or higher energies), then $\mathcal{C}$ is a subspace of $\mathcal{W}$. In this case, $\left(U^{(\mathbf{k})\dagger}\,U^{(\mathbf{k})}\right)_{mm'}=\delta_{mm'}$ still holds, while $\left(U^{(\mathbf{k})}U^{(\mathbf{k})\dagger}\right)_{\nu\nu'}\neq\delta_{\nu\nu'}$, reflecting the fact that the transformation from the Bloch to the Wannier states is well-defined, whereas the inverse transformation is not.
The relation between the localized orbitals and the Kohn-Sham Bloch states can also be encoded via so-called *projector functions*

$$P_{m\nu}(\mathbf{k}) = \left\langle \phi_{m,\mathbf{T}=0} \middle| \psi_{\nu\mathbf{k}} \right\rangle. \tag{4}$$

These projector functions are equivalent to the matrices $U^{(\mathbf{k})}_{\nu m}$ in Eq. (3), with $P_{m\nu}(\mathbf{k}) = (U^{(\mathbf{k})}_{\nu m})^*$. To be consistent with a large part of the DFT+DMFT literature, from now on we use the projector functions $P_{m\nu}(\mathbf{k})$ to define the transformation between the set of local orbitals $|\phi_{m\mathbf{k}}\rangle$ and the Kohn-Sham Bloch functions $|\psi_{\nu\mathbf{k}}\rangle$. However, we note that these local orbitals, under the condition that they are orthogonal and fully represented within $\mathcal{W}$, are nothing but Wannier functions, and can also be expressed according to Eq. (3). Analogous to what is discussed above, the projector functions are square unitary matrices if $\mathcal{C} = \mathcal{W}$, i.e. $P(\mathbf{k})\cdot P^\dagger(\mathbf{k}) = P^\dagger(\mathbf{k})\cdot P(\mathbf{k}) = \mathbb{1}$. Otherwise, $\left(P(\mathbf{k})\cdot P^\dagger(\mathbf{k})\right)_{mm'} = \delta_{mm'}$ still holds, but $\left(P^\dagger(\mathbf{k})\cdot P(\mathbf{k})\right)_{\nu\nu'} \neq \delta_{\nu\nu'}$.
Finally, we summarize the different Hilbert spaces that we have defined: i) the restricted Bloch space, $\mathcal{R}$, which contains all the Kohn-Sham states obtained in the DFT calculation. This generally comprises all occupied and a certain number of unoccupied bands. ii) the Wannier space, $\mathcal{W}$, which contains only the Kohn-Sham states that enter the definition of the local orbitals, and iii) the correlated subspace, $\mathcal{C}$, which is spanned by the local orbitals centered on the correlated sites, and in which the effective DMFT local impurity problem is formulated. Thereby, $\mathcal{C}$ is a subspace of $\mathcal{W}$, which is a subspace of $\mathcal{R}$, i.e., $\mathcal{C} \subseteq \mathcal{W} \subseteq \mathcal{R}$. In the following, mostly $\mathcal{C}$ and $\mathcal{W}$ are relevant for the DFT+DMFT treatment, whereas the part of $\mathcal{R}$ that is not contained in $\mathcal{W}$ is only indirectly affected through the change of the KS potential in the case of a charge self-consistent calculation.

2.2 The DFT+DMFT self-consistency cycle

The central quantity that is evaluated within the DFT+DMFT approach is the one-particle lattice Green function, which, expressed in the KS Bloch basis, can be written as

$$\left[G^{-1}(\mathbf{k}, i\omega_n)\right]_{\nu\nu'} = (i\omega_n + \mu - \epsilon_{\nu\mathbf{k}})\,\delta_{\nu\nu'} - \Delta\Sigma_{\nu\nu'}(\mathbf{k}, i\omega_n). \tag{5}$$

Here, ω_n is the n-th Matsubara frequency, $\omega_n = (2n+1)\pi/\beta$, with the inverse temperature $\beta = 1/T$, μ is the chemical potential, $\epsilon_{\nu\mathbf{k}}$ is the Kohn-Sham eigenvalue corresponding to $|\psi_{\nu\mathbf{k}}\rangle$, and $\Delta\Sigma_{\nu\nu'}(\mathbf{k}, i\omega_n)$ is the DMFT self-energy correction expressed in the KS basis.

The self energy correction is obtained by solving the effective impurity problems on the symmetry-inequivalent correlated sites, which are formulated in terms of the local orbital basis. The resulting impurity self energies, $\Sigma^{\text{imp}}_{mm'}(i\omega_n)$, are then *upfolded* into the Bloch basis using the projector functions $P_{m\nu}(\mathbf{k})$

$$\Delta\Sigma_{\nu\nu'}(\mathbf{k}, i\omega_n) = \sum_{mm'} [P^\dagger(\mathbf{k})]_{\nu m}\, \Delta\Sigma_{mm'}(i\omega_n)\, P_{m'\nu'}(\mathbf{k}). \tag{6}$$

Note that here a potential non-unitarity of the transformation from $\mathcal{C}$ to $\mathcal{W}$ is not a problem, since $\Delta\Sigma$ is zero by definition outside of $\mathcal{C}$. Before upfolding, one usually subtracts a double counting (DC) correction from the impurity self-energy, which is meant to contain all contributions of the local interaction within the correlated subspace that are already included in the KS potential, i.e. $\Delta\Sigma_{mm'}(i\omega_n) = \Sigma^{\text{imp}}_{mm'}(i\omega_n) - \Sigma^{\text{DC}}_{mm'}$. Typically, the DC correction is just taken to be a rigid shift of the local potential that depends on the total occupation of the local orbitals on that site, i.e., $\Sigma^{\text{DC}}_{mm'}$ is diagonal in m and depends only on the specific site related to m but not on its actual orbital character (remember that we defined m to denote both orbital character and correlated site). A specific expression for $\Sigma^{\text{DC}}_{mm'}$ is given in Sec. 2.3. Note also that the self energy in the local orbital basis is $\mathbf{k}$-independent, due to the purely local character of the effective impurity problem, whereas it gains some $\mathbf{k}$-dependence in the upfolded Bloch basis.

After performing the matrix inversion of Eq. (5) to obtain $G_{\nu\nu'}(\mathbf{k}, i\omega_n)$, the local Green function corresponding to the correlated sites is obtained by *downfolding* again back to the local orbital basis

$$G^{\text{loc}}_{mm'}(i\omega_n) = \frac{V}{(2\pi)^3} \sum_{\nu\nu'} \int d\mathbf{k}\, P_{m\nu}(\mathbf{k}) G_{\nu\nu'}(\mathbf{k}, i\omega_n) [P^\dagger(\mathbf{k})]_{\nu' m'}\,. \tag{7}$$

Here, the summation over ν and ν' can in principle be restricted over $\mathcal{W}$, since outside of $\mathcal{W}$ the projector functions are zero by definition.

The local Weiss field defining the effective local impurity problem(s) is then obtained through the Dyson equation $\mathcal{G}_0^{-1} = (G^{\text{loc}})^{-1} + \Sigma^{\text{imp}}$ (with all quantities defined as local matrices in $\mathcal{C}$, i.e., m and m' always correspond to the same correlated site). Since Σ^{imp} is in turn obtained by solving the corresponding quantum impurity problem, this defines a closed set of equations, and a self-consistent solution of this set of equations is found iteratively, as schematically depicted by the "inner" cycle in Fig. 1. If self-consistency is achieved in this inner loop, then the impurity self-energy Σ^{imp} that is obtained by solving the impurity model(s) is identical to the one from the previous iteration step that was used obtain the corresponding Weiss field(s), $\mathcal{G}_0$, and each impurity Green function is identical to the corresponding local component of the downfolded lattice Green function.

The procedure described so far corresponds to the usual DMFT self-consistency cycle for a fixed single particle Hamiltonian defined by the KS band energies $\epsilon_{\nu\mathbf{k}}$. However, since these band energies are calculated for the KS potential, and since the KS potential depends on the underlying charge density, an additional self-consistency with respect to this charge density is required.

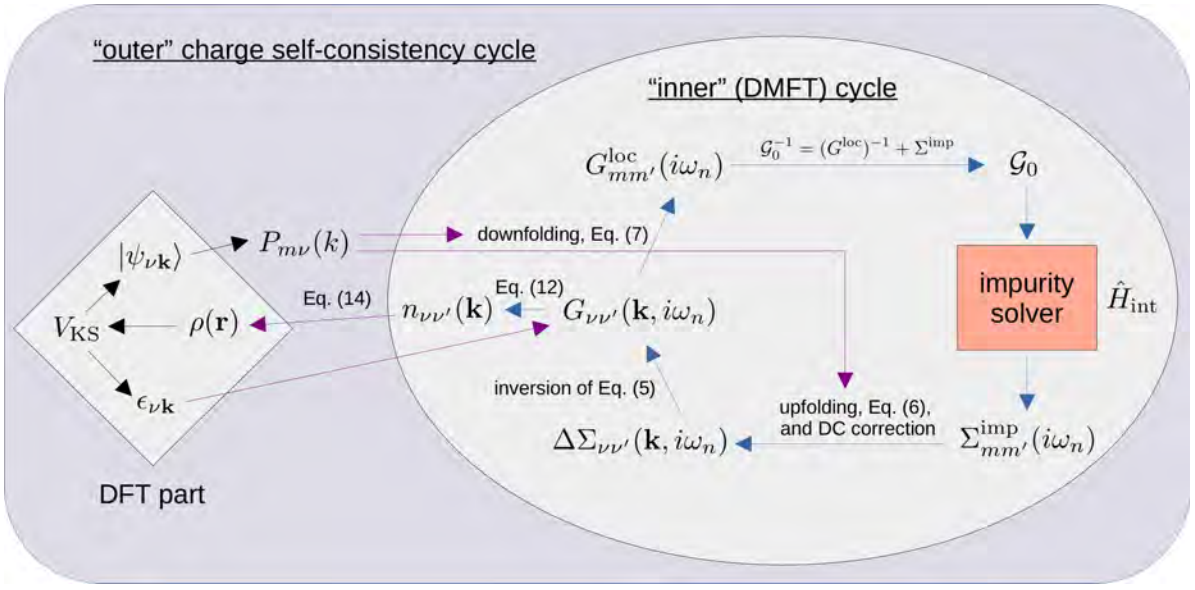


Fig. 1: *Schematic depiction of the full DFT+DMFT self-consistency cycle. The "inner loop" ensures self-consistency between the effective impurity Green function(s) and the local component(s) of the lattice Green function, while the "outer loop"ensures charge self-consistency. From the DFT perspective, the inner loop can also be viewed as a more elaborate way to obtain the occupations $n_{\nu\nu'}(\mathbf{k})$ from the solution of the KS equations.*

The charge density[2] can be obtained from the Green function in its real-space representation by summing over all Matsubara frequencies

$$\rho(\mathbf{r}) = \frac{1}{\beta} \sum_n G(\mathbf{r}, \mathbf{r}, i\omega_m). \tag{8}$$

This can easily be seen from the fundamental definition of the imaginary-time Green function in terms of field operators $\hat{\psi}(\mathbf{r}, \tau)$

$$G(\mathbf{r}, \mathbf{r}'; \tau) = -\Big\langle \hat{T}_\tau \big(\hat{\psi}(\mathbf{r}, 0) \hat{\psi}^\dagger(\mathbf{r}', \tau) \big) \Big\rangle, \tag{9}$$

where τ is imaginary time and $\hat{T}_\tau$ is the corresponding time-ordering operator. Thus, $\rho(\mathbf{r}) = G(\mathbf{r}, \mathbf{r}'; \tau{=}0^+)$, which, after Fourier transforming to Matsubara frequencies, leads to Eq. (8). Within the basis of KS Bloch states, Eq. (8) can be written as

$$\rho(\mathbf{r}) = \frac{1}{\beta} \sum_n \sum_{\nu\nu'} \frac{V}{(2\pi)^3} \int d\mathbf{k}\, \psi_{\nu\mathbf{k}}(\mathbf{r}) G_{\nu\nu'}(\mathbf{k}, i\omega_n) \psi^*_{\nu'\mathbf{k}}(\mathbf{r}) \tag{10}$$

$$= \sum_{\nu\nu'} \frac{V}{(2\pi)^3} \int d\mathbf{k}\, \psi_{\nu\mathbf{k}}(\mathbf{r}) n_{\nu\nu'}(\mathbf{k}) \psi_{\nu'\mathbf{k}}(\mathbf{r}), \tag{11}$$

where we used $\psi_{\nu\mathbf{k}}(\mathbf{r}) = \langle \mathbf{r} | \psi_{\nu\mathbf{k}} \rangle$ and also defined the density matrix

$$n_{\nu\nu'}(\mathbf{k}) = \frac{1}{\beta} \sum_n G_{\nu\nu'}(\mathbf{k}, i\omega_n). \tag{12}$$

[2]Note that we are not distinguishing between the (electronic) charge density and the corresponding particle density, i.e., we are using units where the electronic charge is equal to $+1$.

Without considering the self-energy correction, $\Delta\Sigma(\mathbf{k}, i\omega_n)$, in Eq. (5), $G(\mathbf{k}, i\omega_n)$ represents the uncorrected Kohn-Sham Green function, and the corresponding density matrix is diagonal in the KS basis, $n_{\nu\nu'}(\mathbf{k}) \rightarrow n^{\mathrm{KS}}_{\nu\mathbf{k}}\delta_{\nu\nu'}$. Eq. (11) then becomes equivalent to the usual way the charge density is obtained within KS DFT by summing over the occupied KS states, with the only (in practice irrelevant) difference that here the occupations also include a temperature (or β) dependent Fermi-smearing. Otherwise (and apart from a potential additional smearing to improve convergence on a finite $\mathbf{k}$ mesh), the KS occupations, $n^{\mathrm{KS}}_{\nu\mathbf{k}}$ are either one or zero, depending on whether the corresponding KS eigenvalue $\epsilon_{\nu\mathbf{k}}$ is below or above the Fermi level, μ^{KS}, where μ^{KS} is determined by the condition that the number of occupied KS states in the BZ matches the number of electrons in the crystallographic unit cell.

If the self-energy correction is included in Eq. (5), and the full DFT+DMFT lattice Green function is used in Eq. (12), then the resulting density matrix is generally not diagonal any more in the original Kohn-Sham basis. However, for practical implementations, it is often advantageous to define a unitary transformation between all the KS states included in $\mathcal{W}$ that diagonalizes the corrected density matrix at each $\mathbf{k}$ point

$$\sum_{\nu\nu'}[V^{\dagger}(\mathbf{k})]_{\mu\nu}n_{\nu\nu'}(\mathbf{k})V_{\nu'\mu'}(\mathbf{k}) = \tilde{n}_{\mu\mathbf{k}}\delta_{\mu\mu'}\,. \tag{13}$$

Then, the charge density can be calculated from the transformed Bloch functions, $|\tilde{\psi}_{\mu\mathbf{k}}\rangle$, as usual using diagonal occupations

$$\rho(\mathbf{r}) = \sum_{\mu}\frac{V}{(2\pi)^3}\int d\mathbf{k}\,\tilde{n}_{\mu\mathbf{k}}|\tilde{\psi}_{\mu\mathbf{k}}(\mathbf{r})|^2, \tag{14}$$

with

$$\tilde{\psi}_{\mu\mathbf{k}}(\mathbf{r}) = \sum_{\nu}\psi_{\nu\mathbf{k}}(\mathbf{r})V_{\nu\mu}\,. \tag{15}$$

This has the advantage that, after transforming the KS Bloch functions according to Eq. (15), the existing subroutines or functions already included in the DFT code can be used to evaluate the corrected charge density.

In order to ensure full charge self-consistency, another ("outer") iterative loop is added to the computational procedure, as also indicated in Fig. 1, where the KS states and corresponding band energies are recalculated from the KS potential, V_{KS}, evaluated from the corrected charge density obtained from the (inner) DMFT self-consistency loop. In practice, a suitable mixing-scheme is typically applied to ensure or accelerate convergence of the iterative procedure.

If full charge self-consistency is achieved, then the system of electrons, which is divided into a strongly correlated and a weakly correlated part, with the local electron-electron interaction within the correlated subspace explicitly treated within DMFT, and all other interactions incorporated in the KS potential, gives rise to exactly the same density that is used to obtain this KS potential. The KS potential, in turn, defines the KS bandstructure that enters the self-consistent effective bath for the DMFT impurity problem(s).

While this approach appears conceptually reasonable, physically transparent, and, in the charge self-consistent case, also internally consistent, so far the presentation of the DFT+DMFT method

was mostly based on heuristic considerations. However, the DFT+DMFT approach can also be put on a solid theoretical foundation within the conceptual framework of *spectral density functional theory* [9], which is based on an effective action formalism of quantum field theory. A rigorous derivation of the DFT+DMFT approach within this conceptual framework goes beyond the scope of these lecture notes. In the following, we therefore just briefly sketch some of the main ideas.

The starting point is the generic problem of electrons in an external potential, interacting with each other via a Coulombic, i.e., two-particle, interaction. Different approximate treatments of this generic problem can then be constructed by (i) choosing different "observables" to describe the system, (ii) dividing the Gibbs free energy functional into that corresponding to a simpler "reference system" and a remaining "interaction" part, and (iii) finding a good approximation for the interaction part as a functional of the chosen observables. Thereby, the reference system includes a "constraining field" that ensures that the reference system has the same expectation value for the chosen observables as the original interacting electron system. This allows to formulate DFT, DFT+U, and DFT+DMFT all within the same conceptual framework, differing mainly by the choice of the basic observables and the approximations used for the functional representing the unknown part of the interaction energy.

Specifically, DFT is based on the electron density as the central observable and the interaction energy is written as sum of the exactly known Hartree energy and the unknown exchange-correlation energy functional, $E_{\text{xc}}[\rho(\mathbf{r})]$, for which accurate and practically useful approximations exist. The reference system is the system of non-interaction KS electrons and the KS potential takes the role of the constraining field, ensuring that the density of the KS system is identical to that of the original interacting system.

In the case of the DFT+DMFT approach, the local part of the one-particle Green function is chosen as an additional observable, in combination with the electronic charge density, and the interaction part of the Gibbs free energy is written as a sum of the Hartree energy, the usual DFT exchange-correlation energy functional, the interaction energy of the electrons corresponding to the correlated subspace, and a DC correction. The first two terms are functionals of the density, while the last two terms are expressed as functionals of the local Green function. The DMFT approximation then corresponds to considering only purely local diagrams in the evaluation of the interaction energy within the correlated subspace, and the impurity self-energy (or, equivalently, the Weiss field) represents the constraining field for the local Green function.

The formal derivation of the DFT+DMFT approach within the conceptual framework of spectral density functional theory, ensures that the self-consistent solution for the charge density and local Green function correspond to a stationary point of the underlying free energy functional. The total energy within DFT+DMFT can then be obtained by taking the zero temperature limit of the free energy [9]

$$E_{\text{DFT+DMFT}} = E_{\text{DFT}}[\rho(\mathbf{r})] + \langle \hat{H}_{\text{int}} \rangle - E_{\text{DC}}[G^{\text{loc}}] \,. \tag{16}$$

Note that E_{DFT} is usually evaluated within the DFT code and includes the *band energy*, i.e., the total energy of the KS electrons, plus additional terms that are all explicit functionals of

$\rho(\mathbf{r})$. Thus, the total energy reported by the DFT code needs to be corrected for the change in the band energy, by considering the occupations of the KS states according to Eq. (12). The interaction energy within the correlated subspace, $\langle \hat{H}_{\text{int}} \rangle$, can be evaluated using the Galitskii-Migdal formula

$$\langle \hat{H}_{\text{int}} \rangle = \frac{1}{2\beta} \sum_{n,m,m'} \Sigma^{\text{imp}}_{mm'}(i\omega_n)\, G^{\text{loc}}_{m'm}(i\omega_n)\,, \tag{17}$$

and a specific expression for the DC correction E_{DC} is given in Sec. 2.3.

2.3 Local interaction Hamiltonian and double counting correction

There are still two aspects which have been left open up to now. This is the definition of the local interaction Hamiltonian, $\hat{H}_{\text{int}}$, entering the effective DMFT impurity problem, and the question of how to properly define the double counting correction in terms of Σ^{DC} and $E_{\text{DC}}[G^{\text{loc}}]$.
The generic form of a local two-particle interaction, expressed in the local orbital basis of the correlated subspace, is given by

$$\hat{H}_{\text{int}} = \frac{1}{2} \sum_{\{m\}\sigma\sigma'} U_{mm'm''m'''}\, \hat{c}^\dagger_{m\sigma} \hat{c}^\dagger_{m''\sigma'} \hat{c}_{m'''\sigma'} \hat{c}_{m'\sigma}\,, \tag{18}$$

where $\hat{c}^\dagger_{m\sigma}$ is the creation operator corresponding to an electron in orbital $|\phi_{m\mathbf{T}}\rangle$ with spin σ. Note that we have used spin-independent local orbitals, and all creation and annihilation operators in Eq. (18) are meant to correspond to the same site, so that we can drop the index $\mathbf{T}$ for simplicity and we can interpret the index m as indicating only the corresponding orbital character. The matrix elements $U_{mm'm''m'''}$ are defined as

$$U_{mm'm''m'''} = \int d\mathbf{r} \int d\mathbf{r}'\, \phi^*_m(\mathbf{r}) \phi^*_{m''}(\mathbf{r}')\, V_{\text{ee}}(\mathbf{r},\mathbf{r}')\, \phi_{m'}(\mathbf{r}) \phi_{m'''}(\mathbf{r}')\,, \tag{19}$$

where $V_{\text{ee}}(\mathbf{r},\mathbf{r}')$ represents the (screened) local electron-electron interaction experienced by the electrons within the correlated subspace.
In practice, one usually uses a simplified parametrization for the interaction tensor $U_{mm'm''m'''}$. Specifically, for the examples discussed in Sec. 4, a so-called Kanamori parametrization is used (see, e.g., Ref. [10]), which contains only two independent parameters U and J, representing the average inter-orbital Coulomb interaction and the local Hund's exchange, respectively, and the interaction Hamiltonian becomes

$$\begin{aligned} \hat{H}_{\text{int}} = U \sum_m \hat{n}_{m\uparrow}\hat{n}_{m\downarrow} + (U-2J) \sum_{m\neq m'} \hat{n}_{m\uparrow}\hat{n}_{m'\downarrow} + (U-3J) \sum_{m\neq m',\sigma} \hat{n}_{m\sigma}\hat{n}_{m'\sigma} \\ -J \sum_{m\neq m'} \hat{c}^\dagger_{m\uparrow}\hat{c}_{m\downarrow}\hat{c}^\dagger_{m'\downarrow}\hat{c}_{m'\uparrow} + J \sum_{m\neq m'} \hat{c}^\dagger_{m\uparrow}\hat{c}^\dagger_{m\downarrow}\hat{c}_{m'\downarrow}\hat{c}_{m'\uparrow}\,, \end{aligned} \tag{20}$$

where, $\hat{n}_{m\sigma} = \hat{c}^\dagger_{m\sigma}\hat{c}_{m\sigma}$. The Kanamori form corresponds to the most general form of $\hat{H}_{\text{int}}$ for the case of a three-fold degenerate t_{2g} or two-fold degenerate e_g subshell within cubic symmetry, but is also used as approximate form in cases where these degeneracies are lifted. Another

parametrization of $\hat{H}_{\text{int}}$ that is often used for calculations involving the full five-orbital d shell, is the so-called Slater parameterization (see, e.g., Refs. [3, 4]).
We note that the calculation of realistic materials- and orbital-specific screened interaction parameters, i.e., the calculation of specific values for U and J in Eq. (20), or of the full interaction tensor in Eq. (19), is an active research area (see other lecture notes in this series). To arrive at a potentially quantitative and predictive method, the "first principles" calculation of such screened interaction parameters is of course highly desirable. Nevertheless, it should be noted that sometimes it can also be instructive to vary, e.g., U and J within certain limits to better analyze the underlying physics.
Finally, we also provide the specific form of the DC correction that was used in the DFT+DMFT calculations discussed in Sec. 4. Generally, an exact definition of $E_{\text{DC}}[G^{\text{loc}}]$ is ill-defined. The DFT exchange correlation functional is a complicated functional of the total density, that does not allow to simply separate off the contributions corresponding to the local interaction of the correlated subspace. Therefore, in practice, heuristic forms are used to account for the DC correction. A widely used form, also used in the examples discussed in Sec. 4, is based on the so-called "fully localized limit" [11, 12], which assumes $E_{\text{DC}} = \frac{\bar{U}}{2} N(N-1)$, where N is the total number of electrons occupying the correlated subspace on the corresponding site, and $\bar{U}$ is the local interaction strength averaged over all orbitals and spins. The corresponding self-energy correction is then defined as $\Sigma^{\text{DC}}_{mm'} = \frac{\delta E_{\text{DC}}}{\delta n_{mm'}} = U\left(N - \frac{1}{2}\right) \delta_{mm'}$, where $n_{mm'}$ represents the local density matrix within $\mathcal{C}$. For more details, see, e.g., Ref. [12].

3 Transition metal oxides in a nutshell

In this section, we briefly summarize some basic properties of TM oxides that are important to better understand the materials-specific examples discussed in the next section. In fact, many aspects of TM oxides and related TM compounds can be understood from some simple general considerations about their electronic structure.
The electronic bands around the Fermi level (or around the insulating gap) that govern the low energy properties of TM oxides are usually dominated by states with strong TM d and O p orbital character and can be understood to emerge from the heteropolar covalent bonds formed by the corresponding atomic orbitals. In a somewhat simplified but intuitive picture, this band formation can be understood as a two-step process. First, the hybridization between atomic TM d and O p orbitals gives rise to molecular-orbital-like states located around the corresponding ionic sites, as shown schematically in Fig. 2. Then, the molecular-orbital-like states at different sites hybridize to form extended Bloch states, leading to an energetic broadening of the molecular-orbital-like levels into wider "energy bands".
The energy difference between the atomic TM d and O p states is called the *charge transfer energy*. In most cases, the TM d states are higher in energy than the O p states, corresponding to a positive charge transfer energy. However, the charge transfer energy generally decreases from the lighter to the heavier TM cations in the same row of the periodic table, and thus some nickelates or cuprates can also be characterized as negative charge transfer systems. For a

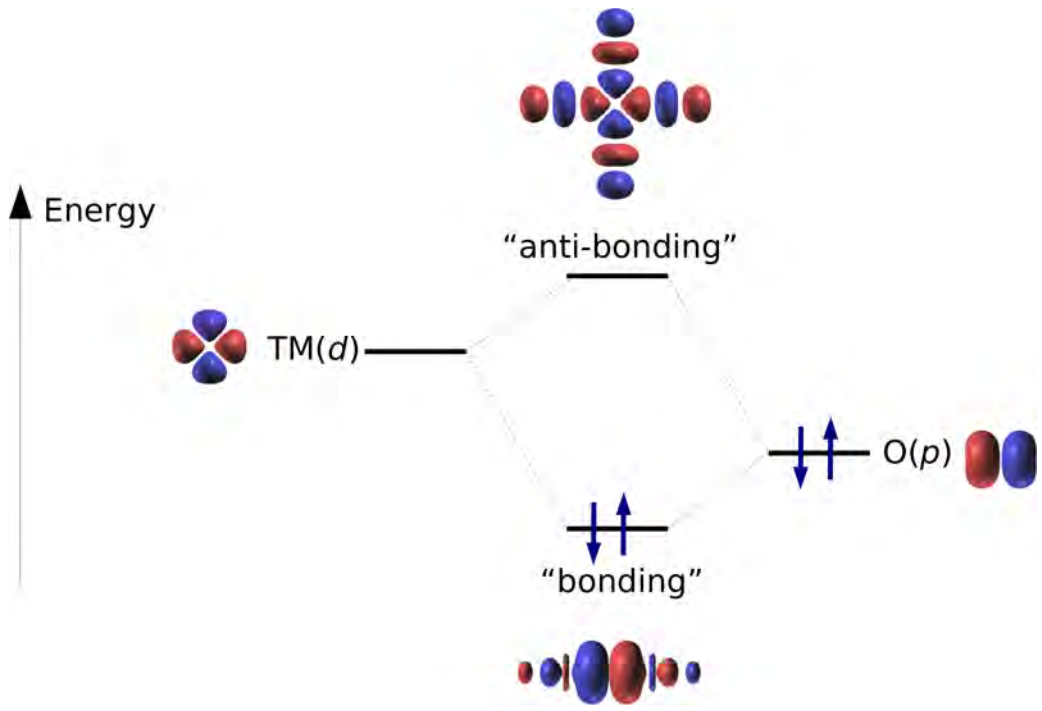


Fig. 2: *Schematic depiction of the formation of a heteropolar covalent bond between atomic orbitals with TM d and O p character, leading to "anti-bonding" and "bonding" molecular-orbital-like states. The depicted orbitals are Wannier functions obtained for $SrVO_3$ by considering different energy windows containing the corresponding bands (see Fig. 3 and the description in the main text).*

positive charge transfer energy, the higher-lying molecular-orbital-like states formed from the hybridization between TM d and O p states have a larger contribution of the TM d atomic orbitals and correspond to an anti-bonding linear combination of the two types of atomic orbitals, while the lower-lying states are dominated by O p contributions and correspond to a bonding combination.

If the charge transfer energy is large enough compared to the width of the bands that form from the overlap or "hopping" between the molecular-orbital-like states located at different sites, then the corresponding bands remain isolated from each other energetically, and can be clearly assigned to the different orbital characters. Fig. 3(a) shows the example of the cubic perovskite $SrVO_3$, with clearly separated groups of bands corresponding, from lower to higher energies, to a dominant O p, V t_{2g}, and V e_g orbital character, respectively (indicated in purple, red, and green in Fig. 3(a)). Note that typically, if one refers for example to the "t_{2g} bands" in $SrVO_3$, then one in fact refers to the group of bands with dominant V t_{2g} orbital character that correspond to the anti-bonding states resulting from the hybridization between atomic V t_{2g} and O p orbitals.

If one now constructs Wannier functions separately from the different groups of bands in Fig. 3(a), using atomic orbitals with the corresponding dominant orbital character as the initial trial orbitals, the resulting Wannier functions exactly resemble the molecular-orbital-like states discussed above for the corresponding group of bands. This is schematically depicted in

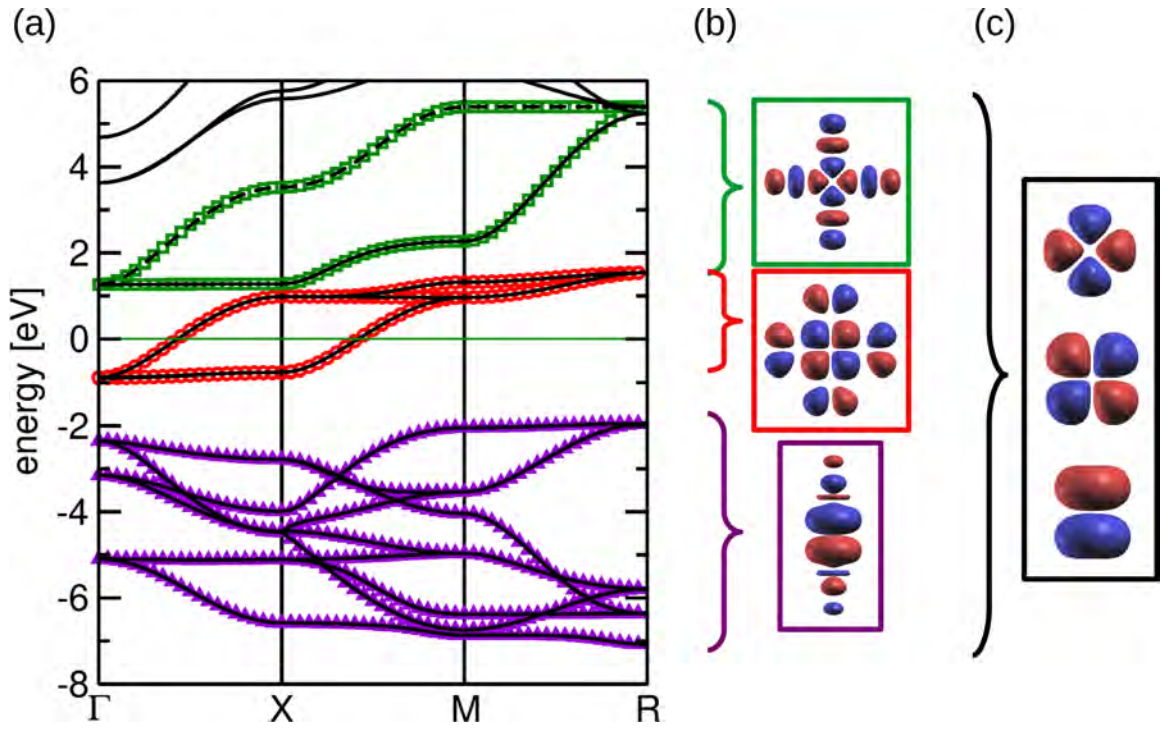


Fig. 3: *(a) KS band structure of $SrVO_3$. The dominant orbital characters of the different isolated groups of bands are indicated by colors, with purple, red, and green corresponding to O p, V t_{2g}, and V e_g dominated bands. (b) and (c) indicate typical Wannier functions obtained by either restricting $\mathcal{W}$ to individual groups of bands or defining $\mathcal{W}$ to span the whole energy window of V d and O p dominated bands.*

Fig. 3(b). For example, for the "t_{2g} bands" in $SrVO_3$, the Wannier functions correspond to anti-bonding linear combinations of an atomic t_{2g} orbital centered at the V site and the π-oriented O p orbitals on the surrounding oxygen ligands. The weight of these "oxygen tails" in the Wannier functions generally increases with decreasing energy separation from the O p dominated bands, i.e., they increase with decreasing (positive) charge transfer energy.

Often, DFT+DMFT calculations are performed using only a minimal correlated subspace with $\mathcal{C} = \mathcal{W}$ restricted to an isolated group of bands immediately around the Fermi level, e.g., the t_{2g} bands in $SrVO_3$. The Wannier orbitals that span the corresponding "frontier" bands are sometimes (and in the following) referred to as "frontier orbitals".

Alternatively, one can also use a Wannier space, $\mathcal{W}$, spanning the whole group of TM d and O p dominated bands. This usually results in Wannier orbitals that closely resemble atomic TM d and O p orbitals,[3] as schematically depicted in Fig. 3(c) for the example of $SrVO_3$. The correlated subspace, $\mathcal{C}$, is then often defined in terms of only the corresponding TM d-like Wannier functions.

[3]Note, however, that Wannier functions in a solid can never strictly be separated in a radial and angular part, as local angular momentum is not a good quantum number.

4 Examples

Before discussing three specific examples for the effect of charge self-consistency, we briefly comment on the case of cubic $SrVO_3$, which is often used as a typical benchmark system to test new DFT+DMFT implementations or extensions to more advanced features. This is related to both its highly symmetric cubic crystal structure as well as its simple and prototypical KS band structure, exhibiting clearly separated groups of bands, as seen in Fig. 3(a). Since the Fermi level cuts through the group of V t_{2g} bands, consistent with the nominal d^1 electron configuration of the V^{4+} cation, one often restricts the Wannier space, $\mathcal{W}$, for the DMFT treatment to only these three V t_{2g} bands (with $\mathcal{C} = \mathcal{W}$), as already discussed in Sec. 3. In this case, the orbital occupations (summed over the two spin projections) are exactly equal to $1/3$, due to the degeneracy of the three t_{2g} levels within cubic symmetry combined with the total filling of the corresponding bands by exactly one electron. Thus, even though a DFT+DMFT calculation will change, e.g., the features of the spectral function compared to the pure DFT treatment, the occupations within the correlated subspace will remain fixed to $1/3$.[4] This means that also the charge density remains identical to the DFT ground state charge density, so that in this case a one-shot calculation is in fact already charge-self-consistent.

Thus, charge self-consistent calculations become only relevant if the occupations are not fixed by the specific symmetry of the system and the total electron count within $\mathcal{C}$. For example, if one extends $\mathcal{W}$ to also include the O p-dominated bands at slightly lower energies, and defines $\mathcal{C}$ in terms of V-centered t_{2g}-like Wannier orbitals constructed from all bands within $\mathcal{W}$, then, even though all three V t_{2g} Wannier orbitals will still have identical occupations due to the cubic symmetry of the system, the total electron count within $\mathcal{C}$ is not fixed any more and electrons can be redistributed between $\mathcal{C}$ and the rest of $\mathcal{W}$ that is not contained in $\mathcal{C}$. This redistribution can then lead to subtle changes in the charge density.

In the following subsections, we focus on two cases where the electron redistribution is more pronounced and leads to noticeable differences between the one-shot results and that of a charge self-consistent DFT+DMFT calculation. All examples employ a definition of the correlated subspace and of the corresponding basis orbitals such that $\mathcal{C} \approx \mathcal{W}$, and $\mathcal{W}$ is isolated from other groups of bands towards lower energies. Thus, since the energy window spanned by $\mathcal{C}$ and $\mathcal{W}$ also includes the Fermi level, the electron count in $\mathcal{C}$ is fixed.[5] The resulting charge redistribution within $\mathcal{C}$ in these examples is therefore always related to the presence of symmetry-inequivalent orbitals or sites.

4.1 Orbital polarization in $CaVO_3$

Our first example is the moderately correlated metal $CaVO_3$, which is closely related to $SrVO_3$. In both materials, the V^{4+} cation exhibits a nominal d^1 electron configuration, but in contrast

[4] Here, we are excluding the possibility of a *spontaneous symmetry breaking* which can always be suppressed in the calculation by appropriate averaging/symmetrizing over equivalent orbitals.

[5] In the examples where $\mathcal{W}$ is not strictly identical to $\mathcal{C}$, the (very) small part of $\mathcal{W}$ that is not included in $\mathcal{C}$ always remains completely unoccupied.

to the perfectly cubic case of $SrVO_3$, the degeneracy of the t_{2g} levels in $CaVO_3$ is lifted due to the orthorhombic distortion of the underlying perovskite crystal structure [see Fig. 4(a)]. The energetic splitting of the t_{2g} levels leads to a (partial) orbital polarization, which is strongly affected by the local interaction and also influences the material's vicinity to a potential Mott metal-insulator transition. This orbital polarization can be further enhanced in thin films of $CaVO_3$ epitaxially grown on a suitable substrate. The mismatch of the lattice constant with that of the substrate material creates a biaxial in-plane strain, which results in a strong additional tetragonal component to the local crystal field on the V sites. Under tensile strain, i.e., if the in-plane lattice constant of the substrate is larger than that of the thin film material, this lowers the energy of the d_{xy} level relative to the other two t_{2g} states. An order-of-magnitude reduction of the resistivity has indeed been reported for $CaVO_3$ thin films grown epitaxially on $SrTiO_3$ [13, 14], for which the corresponding lattice mismatch corresponds to a nominal tensile strain of about 3.5 %.

Fig. 4(c) compares results obtained from charge-self-consistent (CSC) DFT+DMFT calculations with corresponding "one-shot" (OS) calculations for $CaVO_3$ under 4 % tensile epitaxial strain as a function of the local inter-orbital Hubbard interaction U. These calculations have been performed using a basis of three V-centered t_{2g}-like "frontier orbitals" (*cf.* Sec. 3) constructed from the isolated group of bands around the Fermi energy with dominant V t_{2g} character [see Fig. 4(b)].

In both one-shot and charge self-consistent calculations, the system is metallic for small U, indicated by the nonzero spectral weight around zero frequency, evaluated as $\bar{A}(0)=-\frac{\beta}{\pi}\mathrm{Tr}[G(\beta/2)]$, and shown in the lower panel of Fig. 4(c). With increasing U, the system then exhibits a transition to an insulating state, indicated by $\bar{A}(0) \approx 0$. The critical U for this metal-insulator transition is 0.3 eV larger in the charge self-consistent calculation compared to the one-shot result. This increase in the critical U can be related to a strong suppression of the orbital polarization, visible in the upper panel of Fig. 4(c). In the one-shot case, the system becomes nearly completely polarized in the insulating state, with one of the three t_{2g} orbitals nearly completely filled and the other two nearly completely empty. In the charge self-consistent calculation, the orbital polarization is much weaker, even though there is still a clear preferential occupation of one orbital compared to the other two. The partial suppression of orbital polarization in the charge self-consistent case can be understood from the fact that a full occupation of one t_{2g} orbital leads to a strong asymmetry in the charge distribution around the V cation, which then increases the Hartree potential for that particular t_{2g} orbital relative to the other two. This, in turn, will partially counteract the strain-related lowering of the corresponding crystal-field level in the KS potential, and thus reduce the orbital polarization relative to the one-shot result.

Even though the difference in the critical U for the metal-insulator transition between the one-shot and charge self-consistent calculation is not very large, the strong reduction of the orbital polarization can be important for an accurate description of, e.g., spectral properties. Furthermore, this example already highlights a general theme that will also be observed in the next example, i.e., that if the local interaction in DMFT tends to "polarize" the system, either locally between orbitals or also in between different sites, the resulting asymmetric or inhomogeneous

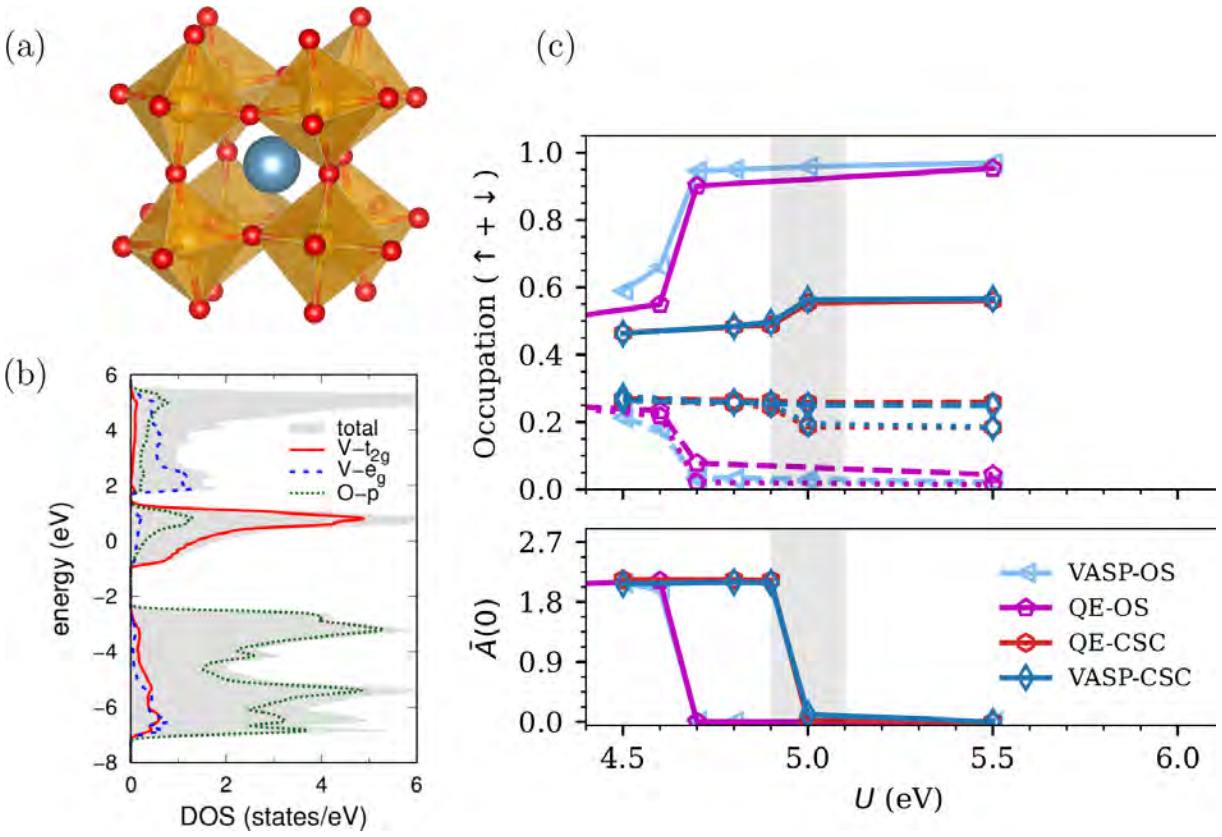


Fig. 4: *(a) Orthorhombically distorted perovskite structure of $CaVO_3$, exhibiting small collective tilts/rotations of the oxygen octahedra around the cubic axes. V atoms and their surrounding coordination octahedra are shown in orange, while O (Ca) atoms are shown in red (blue). (b) KS density of states (DOS) of $CaVO_3$. The total DOS as well as projections on selected atomic orbitals are shown. (c) Spin-summed orbital occupations of the three V t_{2g} frontier orbitals (upper panel), with different orbitals indicated by different line-styles, and zero frequency spectral weight (lower panel) in $CaVO_3$ under 4 % tensile strain obtained from different DFT+DMFT calculations as a function of the Hubbard U. Label QE (VASP) refers to an implementation based on Quantum Espresso (the Vienna Ab-Initio Simulation Package) in combination with TRIQS/solid_dmft [15], while CSC (OS) refers to a charge self-consistent (one-shot) calculation. Subfigure (b) is taken from Ref. [5]. Subfigure (c) courtesy of S. Beck.*

charge distribution is usually disfavored by the strong Hartree interaction included in the KS potential. Consequently, the corresponding polarization is reduced in a charge self-consistent calculation compared to the one-shot case.

Fig. 4(c) also compares two different implementations of the DFT+DMFT self-consistency cycle, one using the "Vienna Ab-Initio Simulation Package" (VASP) and a correlated subspace basis constructed from projection to localized orbitals (PLO) [16], the other based on Quantum ESPRESSO and Wannier orbitals obtained with the Wannier90 code [17]. One can see that the two implementations give nearly identical results, with small differences visible mainly for the orbital occupations in the one-shot case. These small differences can be assigned to the small differences in the definition of the corresponding local orbitals, but the overall quantitative agreement between the two cases is indeed very good.

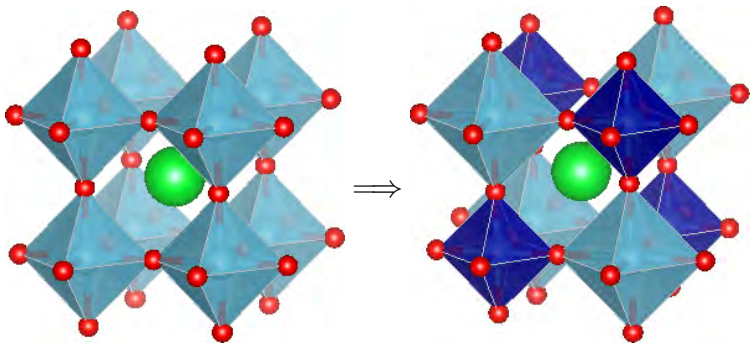


Fig. 5: *Schematic depiction of the octahedral breathing mode distortion of the perovskite structure observed in $CaFeO_3$ and the rare earth nickelates. The oxygen octahedra around the more (less) occupied sites increase (decrease) in volume, resulting in a three-dimensional checkerboard-like spatial arrangement.*

4.2 Potential charge disproportionation in $SrCrO_3$

In the previous example, a charge redistribution occurs between different orbitals centered on the same site. The example discussed in this section involves a charge redistribution between different sites. This is relevant for materials exhibiting *charge ordering* or *charge disproportionation*. Here, we use the former term for a situation where a TM cation has a non-integer average nominal valence, such as, e.g., in magnetite, Fe_3O_4, or in the compositionally doped manganites, $(R,A)MnO_3$, where R is a trivalent rare-earth cation and A a divalent alkaline-earth cation. In contrast, we use the term *charge disproportionation* to refer to situations, where a TM cation has an integer nominal valence, but the corresponding valence state is unfavorable, and can disproportionate into states with higher and lower valence than the average one. One example for a TM oxide exhibiting such charge disproportionation is $CaFeO_3$ [18], where the nominal Fe^{4+} cation disproportionates into a combination of Fe^{3+} and Fe^{5+}, corresponding to a change in the electron configuration according to $2d^4 \rightarrow d^5 + d^3$. Another example is the series of perovskite rare-earth nickelates, $RNiO_3$, where R again indicates a trivalent rare earth cation including also Y and Lu [19]. In this series, the nominal Ni^{3+} cation disproportionates into Ni^{2+} and Ni^{4+}, corresponding to a change in the electron configuration according to $2d^7 \rightarrow d^8 + d^6$.

In both $CaFeO_3$ and the rare earth nickelates, the charge disproportionation occurs below a transition temperature and is accompanied by a metal-insulator transition and a symmetry reduction related to the ordering of the inequivalent disproportionated TM cations on the B sites of the underlying perovskite structure. Furthermore, the disproportionation also couples to a structural distortion that can be understood as a "breathing", i.e., a volume change, of the oxygen octahedra surrounding the inequivalent TM cations, with the octahedra of the more occupied TM cations increasing in volume and the ones corresponding to the less occupied TM cations decreasing (see Fig. 5).

The picture of a "charge" disproportionation in these systems has also been questioned, based on the observation that the actual charge differences, defined, e.g., by integrating the DFT charge density up to some radius within a sphere around the TM sites, is much smaller than the nominal

difference of two electrons. It has therefore been suggested that an interpretation in terms of *ligand holes* could be more appropriate, where the electron configuration around, e.g., the Ni site in $R\mathrm{NiO}_3$ in the undisproportionated state is better described as d^8L, where L represents a hole distributed over the surrounding oxygen ligands. The disproportionation is then interpreted as $2d^8L \rightarrow d^8 + d^8L^2$, with two ligand holes localizing around one of the inequivalent Ni sites. Since the ligand holes are spatially distributed over the surrounding octahedron, the corresponding change in the actual charge density is minimal [20, 21].

Here, we take the viewpoint that, at least in the present context, local charges within a solid are best defined in terms of occupations of suitably defined atom-centered orbitals or Wannier functions. In this case, the ligand hole and "d-only" pictures of electronic disproportionation are just two sides of the same coin, which simply correspond to using different basis sets to describe the same phenomenon. Specifically, a description in terms of a minimal correlated subspace consisting of TM-centered frontier Wannier functions results in orbital occupations that closely resemble the "d-only" picture of charge disproportionation in terms of the formal valence states [22, 23]. On the other hand, a correlated subspace defined in terms of more localized atomic-orbital-like Wannier functions spanning the whole energy window of the TM d and O p dominated bands corresponds more closely to the ligand-hole picture. Since in the following, we analyze DFT+DMFT calculations that employ a frontier orbital basis, we consequently discuss the corresponding results in terms of the d-only picture based on the formal charge states.

Getting back to our example for charge self-consistent DFT+DMFT calculations, we note that in both examples mentioned so far, the disproportionation takes place in the e_g subshell of the TM cation. In the case of the nickelates, the t_{2g} states always remain completely filled and the charge disproportionation can also be described as $2e_g^1 \rightarrow e_g^2 + e_g^0$. Similarly, in CaFeO_3 the Fe always remains in a high-spin state where the t_{2g} orbitals are half-filled with three electrons with the same spin character, and the occupation of the e_g states changes in the same way as in the nickelates.

It is therefore interesting to ask whether charge disproportionation can also occur purely within the t_{2g} subshell. Indeed, model studies considering a generic three-band Hubbard model with an average filling of two electrons per site have found a disproportionated insulating phase in a regime where $U-3J < 0$, i.e., where the local Hubbard interaction is strongly screened while the Hund's interaction remains relatively strong [24, 25]. In this regime, the Hund's interaction dominates over the Hubbard repulsion and it becomes favorable to accumulate a maximum number of electrons with the same spin on the same site, resulting in a charge disproportionation according to $3d^2 \rightarrow 2d^3 + d^0$. The disproportion is thus slightly more complex compared to CaFeO_3 and the nickelates, since the number of d^3 sites is twice the number of empty sites.

Potential candidate materials to observe this physics, are the perovskite chromates $A\mathrm{CrO}_3$, where A can be Ca, Sr, or Pb, and the formal valence of the Cr^{4+} cation corresponds to a d^2 configuration with two electrons in the t_{2g} subshell. In fact, a possible charge disproportionation of the Cr cation has been reported for PbCrO_3 [26, 27], but other reports point more towards a disproportionation of the Pb cations into Pb^{2+} and Pb^{4+}, with all Cr cations in their most fa-

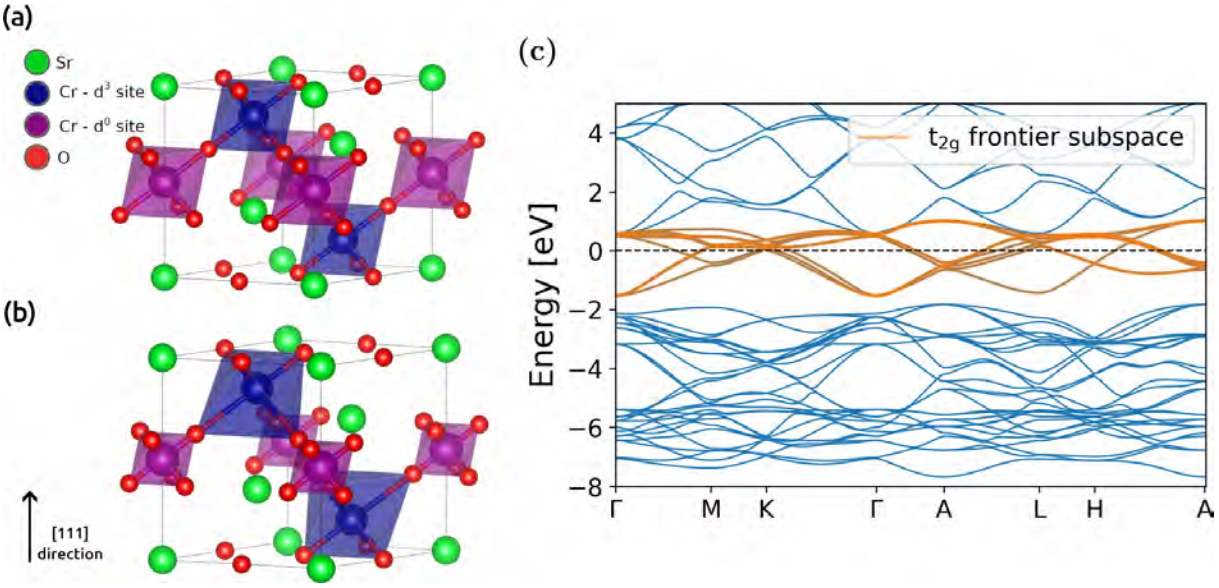


Fig. 6: *(a) Spatial arrangement of the charge disproportionated sites assumed in the DFT+DMFT calculations for $SrCrO_3$, corresponding of a layering along the pseudo-cubic [111] direction, whereby two Cr^{3+} layers (d^3 sites) periodically alternate with one Cr^{6+} layer (d^0 sites), indicated by blue and purple octahedra, respectively. (b) Structural distortion related to the charge disproportionation. The blue Cr^{3+} octahedra expand and distort, while the Cr^{6+} octahedra shrink but essentially keep their perfect octahedral shape. (c) KS bandstructure (blue lines) of cubic $SrCrO_3$ in the energy region around the Fermi level. The orange lines represent the dispersion recalculated from the frontier Wannier functions spanning the correlated Cr t_{2g} subspace. All subfigures are taken from Ref. [35].*

vorable Cr^{3+} oxidation state [28]. Here, we therefore discuss the simpler case of $SrCrO_3$ where the A site cation is definitely divalent, and for which a simple ideal cubic perovskite structure has been reported at ambient conditions. Nevertheless, conflicting experimental reports still exist on the metallic or insulating character of $SrCrO_3$, and on the presence of magnetic order at lower temperatures, see, e.g., Refs. [29–32]. Recently, a potential metal-insulator transition has been reported in thin films of $SrCrO_3$ under tensile strain conditions [33]. While the transition from metallic to insulating behavior under tensile strain can in principle be explained by the emergence of orbital order and a Jahn-Teller distortion [34], a charge disproportionation of the Cr cations could provide an alternative scenario, which has been explored using charge self-consistent DFT+DMFT [35].

The spatial arrangement of potential d^3 and d^0 sites in these DFT+DMFT calculations is depicted in Fig. 6(a). It corresponds to a periodic layering along the [111] direction of the underlying cubic perovskite structure. Two potential d^3 layers are followed by one potential d^0 layer. Here, the term "potential" simply means that the two effective impurity problems corresponding to the potential d^3 and d^0 sites are solved independently (albeit of course coupled through the usual self-consistency condition), and thus allow for a spontaneous electronic symmetry breaking between these otherwise crystallographically equivalent sites. Fig. 6(c) shows the KS band structure of cubic $SrCrO_3$ in the corresponding supercell, with the correlated Cr t_{2g} frontier sub-

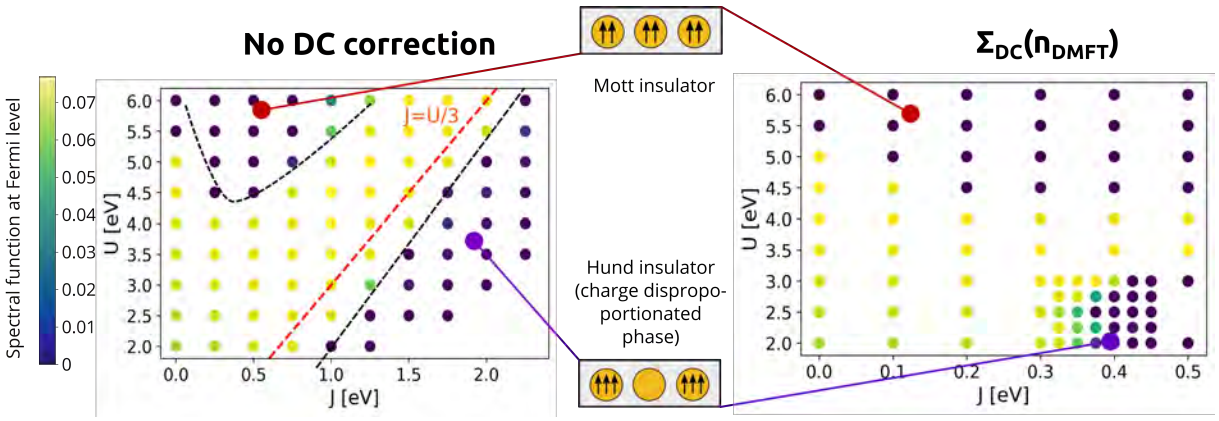


Fig. 7: *Spectral weight around zero frequency, $\bar{A}(0)$, as function of interaction parameters U and J, obtained from different DFT+DMFT one-shot calculations. The left phase diagram corresponds to using DFT occupations to evaluate the DC correction (which in the present case is equivalent to using no DC correction). For the phase diagram on the right, DMFT occupations are used for the DC correction. The regions corresponding to the homogeneous Mott insulator and the charge-disproportionated insulator are indicated. Figure is adapted from Ref. [35] courtesy of A. Carta.*

space indicated by the band dispersion that was recalculated from the corresponding Wannier functions. One can see that these bands are only minimally entangled with the Cr e_g bands at higher energies, and the essentially perfect match with the underlying KS bands indicates that $\mathcal{C} \approx \mathcal{W}$.

We first discuss the results of the corresponding one-shot calculations shown in Fig. 7, where the spectral weight around zero frequency, $\bar{A}(0)$, is plotted as function of the interaction parameters U and J. Here, one has to face an ambiguity of such one-shot calculations, which is whether the total site occupations used for the DC correction are evaluated from the initial DFT occupations or from the occupations obtained after the DMFT treatment of the local interaction. In the present case, these occupations differ substantially in the charge-disproportionated region of the U-J phase diagram. Specifically, the "DFT occupations" are always identical for all Cr sites, since no charge disproportionation occurs in the DFT calculation and thus all sites remain symmetry-equivalent. On the other hand, in the region of the phase diagram where $U-3J < 0$ and charge disproportionation is obtained within DMFT, the difference in the "DMFT occupations" between the nominal d^3 and d^0 sites is typically $\Delta n > 2.6$. This is rather close to the nominal charge difference of 3 electrons, exemplifying that the frontier orbital treatment indeed maps nearly perfectly on the d-only picture of charge disproportionation based on the formal valence states.

Using DFT occupations to evaluate the DC correction is in this case equivalent to not considering any DC correction at all. Since all Cr sites are equally occupied within DFT, the DC correction results in identical shifts of the local potential of each site, which, in the present frontier orbital treatment with $\mathcal{C} = \mathcal{W}$, is simply absorbed by a rigid shift of the chemical potential. The U-J phase diagram on the left side of Fig. 7, labeled "no DC correction", corresponds to

that case, and is essentially identical to the corresponding phase diagram of a generic three-band Hubbard model [24]. There are two distinct insulating phase indicated by $\bar{A}(0) \approx 0$. The conventional Mott-insulating phase, where all Cr sites are equally occupied by two electrons, appears at large $U \gtrsim 4.5\,\text{eV}$. The critical U for the transition into this Mott-insulating phase decreases with J for $J \lesssim 0.5\,\text{eV}$, then increases with J for larger J (cf. Ref. [10]). In the region with $U-3J < 0$, the charge disproportionated phase appears (which was also termed "Hund's insulator" in Ref. [24]), where two of the Cr sites are occupied by nearly three electrons each and one Cr site is nearly empty. The two insulating phases are separated by a metallic region, which extends along the line $U = 3J$ even to very large U. This is the region of a strongly correlated "Hund's metal" [24, 10].

Using DMFT occupations to evaluate the DC correction leads to drastic changes in the corresponding phase diagram. While the overall topology remains the same as before, with a metallic region separating two distinct insulating regions, the region of the charge-disproportionated insulator now appears at significantly smaller J, and even in regions where $U-3J > 0$ (note the different scales of the J axes of the two phase diagrams in Fig. 7). This reflects the fact that now, as soon as a small difference in occupation of the different sites occurs in the DMFT self-consistency loop, the DC correction further lowers the local potential at the more occupied sites relative to that of the less occupied sites, and thus strongly reinforces the charge disproportionation.

As mentioned, the choice of whether to use DFT or DMFT occupations to evaluate the DC correction is ambiguous in a one-shot calculation. This ambiguity is of course a result of the missing charge self-consistency, and the observation that the two different possible choices lead to rather different results of course indicates a strong redistribution of electrons, which in the end calls for a charge self-consistent calculation. On the other hand, in a charge self-consistent calculation the only physically meaningful occupations are the DMFT occupations. These are also the occupations that determine the charge density used to evaluate the KS potential, and thus there is no ambiguity on the choice of occupations for the DC correction in the charge self-consistent case.

If one calculates an analogous phase diagram to the ones shown in Fig. 7 from charge self-consistent calculations, one finds that the charge-disproportionated insulating region in fact completely disappears from the phase diagram. While the Mott-insulating region, where the DMFT occupations are identical to the DFT ones, remains unaffected by the charge self-consistency, the metallic region now fills up the entire rest of the phase diagram, also in the region where $U-3J < 0$. Thus, similar to the previous example of $CaVO_3$, where the orbital polarization is strongly suppressed by the charge self-consistency, the "site polarization" in $SrCrO_3$ is also suppressed, even to an extent that it completely disappears. The strong charge accumulation around the Cr^{3+} sites after the first DFT+DMFT iteration step (which corresponds to a one-shot calculation using DMFT occupations for the DC correction) leads to a strong increase of the local Hartree potential in the second DFT step, which then strongly opposes the charge disproportionation and restores the homogeneous metallic solution with identical occupation on all sites.

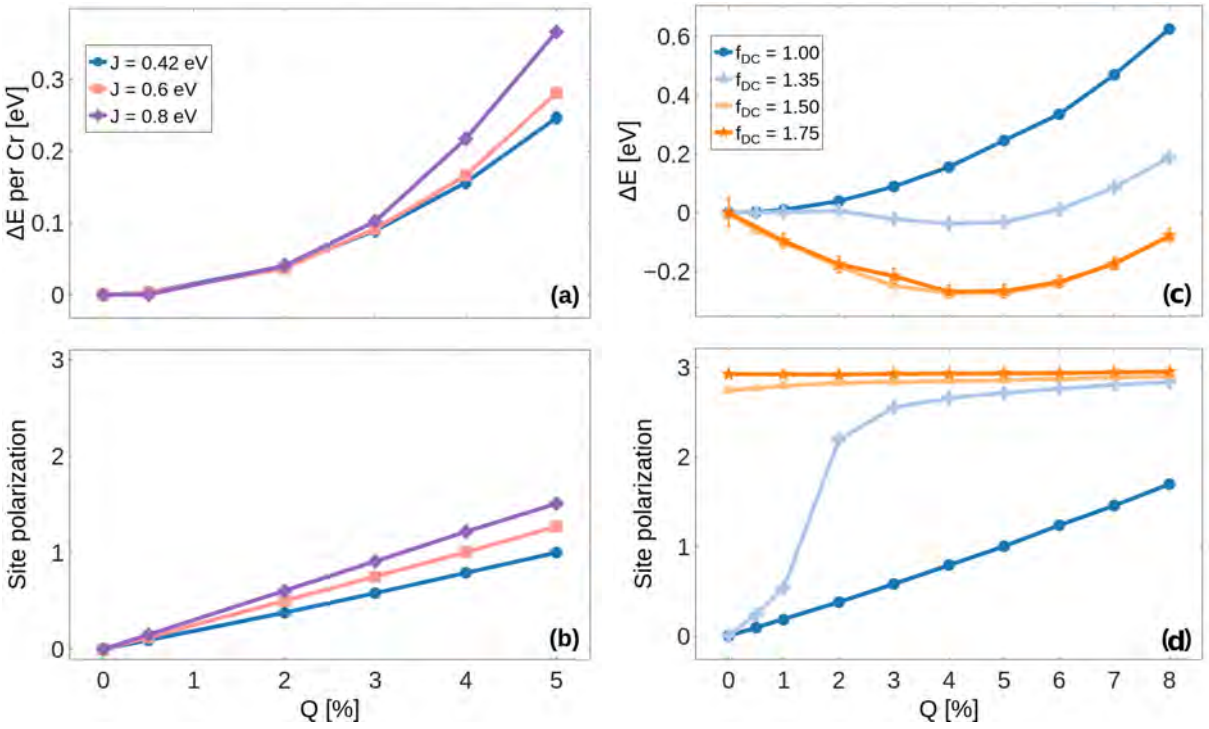


Fig. 8: *Total energy change, (a) and (c), as well as site polarization, (b) and (d), defined as difference in total occupation of the potential d^3 and d^0 sites, obtained from charge self-consistent DFT+DMFT calculations for $SrCrO_3$ as function of the structural breathing mode distortion depicted in Fig. 6(b). The amplitude of the distortion is measured in terms of the change in Cr-O bond length of the smaller octahedra relative to the undistorted case. Panels (a) and (b) are calculated using the standard form of the DC correction, $U = 2.7$ eV, and different values of J. Panels (c) and (d) are calculated using $U = 2.7$ eV, $J = 0.42$ eV, and the DC correction was scaled by f_{DC}. All subfigures are taken from Ref. [35].*

The charge self-consistent calculation thus indicates that $SrCrO_3$ does not exhibit any electronic instability towards spontaneous charge disproportionation.[6] However, as noted previously, in materials such as $CaFeO_3$ and the rare earth nickelates, the charge disproportionation always appears together with a structural distortion corresponding to a breathing of the oxygen octahedra around the TM cations (cf. Fig. 5). This raises the question of whether charge disproportionation in $SrCrO_3$ could also be stabilized by the coupling to an appropriate structural distortion.

An octahedral "breathing mode" compatible with the considered spatial arrangement of potential d^3 and d^0 sites is depicted in Fig. 6(b). Due to the connectivity of the octahedra and the fact that two layers of potential d^3 sites are next to each other, the volume expansion leads to a further distortion of these d^3 octahedra, corresponding to three longer and three shorter Cr^{3+}-O bond distances. On the other hand, the octahedra surrounding the potential d^0 sites can in principle keep their perfect octahedral shape.

Fig. 8 summarizes results of charge self-consistent DFT+DMFT calculations where the ampli-

[6] Since the corresponding region completely disappears from the charge self-consistent phase diagram, we do not even have to face the question which values of U and J would best describe real $SrCrO_3$.

tude of this breathing mode distortion has been varied and both the total energy and the "site polarization, i.e., the difference in total occupation between the nominal d^3 and d^0 sites have been monitored as function of the distortion amplitude. These calculations have been performed for $U = 2.7\,\text{eV}$, which is the value that has been calculated for t_{2g} frontier orbitals in $SrCrO_3$ using the constrained random phase approximation (cRPA) in Ref. [36]. Fig. 8(a) and (b) also shows the effect of varying the strength of the Hund's coupling J, with $J = 0.42\,\text{eV}$ being the calculated cRPA value from Ref. [36]. Note that these cRPA values of $U = 2.7\,\text{eV}$ and $J = 0.42\,\text{eV}$ would put $SrCrO_3$ in the charge disproportionated insulating region according to the one-shot phase diagram on the right side of Fig. 7. On the other hand, the results from the charge self-consistent calculations shown in Fig. 8 show that, even for significantly increased J, the total energy increases essentially quadratically with the structural distortion amplitude, showing no sign of a potential instability towards a distorted charge disproportionated state. This is also consistent with the behavior of the site polarization, which just exhibits an essentially linear response to the structural distortion that breaks the symmetry between the formerly equivalent Cr sites, with no sign of a potential electronic instability.

As discussed above, the DC correction can in principle strongly support a charge disproportionation, by further lowering the local potential of the more occupied sites relative to that of the less occupied sites. On the other hand, the resulting charge accumulation then strongly increases the local Hartree potential if the KS potential is recalculated from the DMFT occupations. Thus, whether charge disproportionation emerges or not, appears to be determined by the subtle balance between these two opposing tendencies. Thereby, one should remember that, as briefly discussed in Sec. 2.3, the DC correction as such is not defined exactly, and that commonly used expressions are mostly based on heuristic arguments and practical experience in their application to different materials systems. In fact, several cases have been identified, where the commonly used expressions for the DC correction do not seem to be completely appropriate, and a scaling of the DC correction is necessary to obtain good agreement with experimental observations [37–39].

Fig. 8(c) and (d) therefore show results of additional charge self-consistent calculations, where the DC correction is scaled by a factor $f_{\text{DC}} > 1$, while U and J are kept fixed to the cRPA values. It can be seen that for $f_{\text{DC}} = 1.35$, the simple linear response of the site polarization to the structural distortion is significantly altered, and a second minimum of the total energy appears for nonzero distortion. In this case, the site polarization exhibits a strong nonlinear increase for distortion amplitudes in the range 1–2 %, to values above 2 electrons, and then saturates for larger distortion to a value slightly below 3. The strong nonlinear increase of the site polarization is accompanied by a transition from metallic to insulating behavior in the spectral functions (not shown). Thus, scaling the DC correction by 35 % puts the system into a regime where the coupling between the structural distortion and the electronic instability stabilizes the charge disproportionated insulating state. For larger scaling, $f_{\text{DC}} \geq 1.5$, the electronic charge disproportionation even occurs again for zero structural distortion (as in the one-shot case), but the minimum of the total energy for nonzero distortion amplitude indicates that this will also stabilize a significant structural distortion.

So what can we finally learn from this example of potential charge disproportionation in $SrCrO_3$? First, it demonstrates nicely and instructively the effect of charge self-consistency, in particular the potential interplay between the DC correction and the change in the Hartree part of the KS potential due to the electron redistribution within DMFT. In the present case, this leads to a clear and rather drastic difference between the charge self-consistent calculation and the corresponding one-shot result. To some extent, the example also exposes the limitations of the current quantitative predictive capabilities of the DFT+DMFT approach, in this case related mostly to the conceptual difficulties in accurately defining the DC correction. On the other hand, even in view of this uncertainty, a required scaling of the DC correction by 35 % relative to the conventional expression appears relatively large, and thus an emergence of charge disproportionation in bulk stoichiometric $SrCrO_3$ is probably unlikely. Nevertheless, the calculations clearly show that $SrCrO_3$ is in fact on the verge of several electronic instabilities (also considering the possibility of orbital order and an accompanying Jahn-Teller distortion explored in Ref. [34]). This observation can provide a possible explanation for the partly conflicting experimental reports regarding its electronic and magnetic properties [29–32], and suggests the possibility to potentially tune $SrCrO_3$ into different insulating ground states by applying strain, substitutional doping, or nano-structuring.

5 Summary and conclusions

In these lecture notes, we have addressed the effect of charge self-consistency in DFT+DMFT calculations, with a special emphasis on TM oxides and related compounds. We have mostly focussed on the practical implementation of the different steps in the iterative computational procedure, summarized by the schematic workflow shown in Fig. 1, but we have also mentioned that the method can be derived rigorously as a stationary solution of a specific approximation to the Gibbs free energy functional in terms of the charge density and the local Green function corresponding to the correlated subspace.

An important aspect of the charge self-consistent procedure is a clear and transparent definition of the local orbitals that span the correlated subspace, which allows to downfold, respectively upfold, various quantities from the KS Bloch basis to the correlated subspace and vice versa. The effect of the DMFT treatment of the local interaction within the correlated subspace is then incorporated in the charge density via the upfolded DMFT occupations defined in Eq. (12). Thus, if these occupations change significantly compared to the initial DFT occupations, a charge self-consistent calculation is generally required.

The two examples discussed in Sec. 4 demonstrate that this is particular relevant in cases where electrons are redistributed within the correlated subspace, either between different non-degenerate orbitals on the same site or between different symmetry-inequivalent sites. This can then result in a strong competition between the tendency of the local correlations to favor an inhomogeneous distribution of electrons and the electrostatic Hartree interaction favoring a more homogeneous distribution.

All specific examples discussed in these lecture notes were based on a definition of the correlated subspace in terms of more or less isolated frontier bands, such that electrons can only be redistributed *within* the correlated subspace. Due to the significantly larger computational effort, charge self-consistent calculations based on a wider energy window, where $\mathcal{W}$ includes also, e.g., the bands with dominant O p character, and $\mathcal{C}$ includes all five d orbitals on the TM site, are sparse. In this case, an electron redistribution can also occur between $\mathcal{C}$ and the uncorrelated part of $\mathcal{W}$, and the DC correction also affects the energy difference between the TM d orbitals and the ligand states. In fact, it has been reported that in several such cases a similar scaling of the DC correction as described in Sec. 4.2 (albeit with $f_{\mathrm{DC}} < 1$) is required to obtain results that are consistent with experimental observations [38, 39]. However, a very recent report indicates that this might also be related to the fact that typically only the TM d orbitals are included in $\mathcal{C}$, while the ligand states remain uncorrected with respect to their KS energies obtained on the DFT level (using approximate semi-local exchange correlation functionals) [40]. Furthermore (to the best of the author's knowledge), no systematic studies on the effect of the charge density update (and its potential interplay with the effect of the DC correction) have been performed for DFT+DMFT calculations using a wide energy window, in particular not for systems involving a charge redistribution both within $\mathcal{C}$ and in between $\mathcal{C}$ and $\mathcal{W} \setminus \mathcal{C}$. Thus, there is still much to be learned on the effect of charge self-consistency and its importance to specific cases.

References

[1] A. Georges, G. Kotliar, W. Krauth, and M.J. Rozenberg, Rev. Mod. Phys. **68**, 13 (1996)

[2] V.I. Anisimov, A.I. Poteryaev, M.A. Korotin, A.O. Anokhin, and G. Kotliar, J. Phys.: Condens. Matter **9**, 7359 (1997)

[3] V.I. Anisimov, F. Aryasetiawan, and A.I. Lichtenstein, J. Phys.: Condens. Matter **9**, 767 (1997)

[4] B. Himmetoglu, A. Floris, S. de Gironcoli, and M. Cococcioni, Int. J. Quantum Chem. **114**, 14 (2014)

[5] S. Beck, G. Sclauzero, U. Chopra, and C. Ederer, Phys. Rev. B **97**, 075107 (2018)

[6] F. Lechermann, in W. Andreoni and S. Yip (Eds.): *Handbook of Materials Modeling* (Springer Cham, 2020), pp. 1099–1118

[7] J. Souto-Casares, N.A. Spaldin, and C. Ederer, Phys. Rev. Res. **3** (2021)

[8] N. Marzari, A.A. Mostofi, J.R. Yates, I. Souza, and D. Vanderbilt, Rev. Mod. Phys. **84**, 1419 (2012)

[9] G. Kotliar, S.Y. Savrasov, K. Haule, V.S. Oudovenko, O. Parcollet, and C.A. Marianetti, Rev. Mod. Phys. **78**, 865 (2006)

[10] A. Georges, L. de' Medici, and J. Mravlje, Annu. Rev. Condens. Matter Phys. **4**, 137 (2013)

[11] V.I. Anisimov, I.V. Solovyev, M.A. Korotin, M.T. Czyżyk, and G.A. Sawatzky, Phys. Rev. B **48**, 16929 (1993)

[12] K. Held, Adv. Phys. **56**, 829 (2007)

[13] M. Gu, J. Laverock, B. Chen, K.E. Smith, S.A. Wolf, and J. Lu, J. App. Phys. **113**, 133704 (2013)

[14] D.E. McNally, X. Lu, J. Pelliciari, S. Beck, M. Dantz, M. Naamneh, T. Shang, M. Medarde, C.W. Schneider, V.N. Strocov, E.V. Pomjakushina, C. Ederer, M. Radovic, and T. Schmitt, npj Quantum Mater. **4**, 6 (2019)

[15] M.E. Merkel, A. Carta, S. Beck, and A. Hampel, J. Open Source Software **7**, 4623 (2022)

[16] M. Schüler, O.E. Peil, G.J. Kraberger, R. Pordzik, M. Marsman, G. Kresse, T.O. Wehling, and M. Aichhorn, J. Phys.: Condens. Matter **30**, 475901 (2018)

[17] S. Beck, A. Hampel, O. Parcollet, C. Ederer, and A. Georges, J. Phys.: Condens. Matter **34**, 235601 (2022)

[18] M. Takano, N. Nakanishi, Y. Takeda, S. Naka, and T. Takada,
Mater. Res. Bull. **12**, 923 (1977)

[19] S. Catalano, M. Gibert, J. Fowlie, J. Íñiguez, J.-M. Triscone, and J. Kreisel,
Rep. Prog. Phys. **81**, 046501 (2018)

[20] H. Park, A.J. Millis, and C.A. Marianetti, Phys. Rev. Lett. **109**, 156402 (2012)

[21] S. Johnston, A. Mukherjee, I. Elfimov, M. Berciu, and G.A. Sawatzky,
Phys. Rev. Lett. **112**, 106404 (2014)

[22] A. Subedi, O.E. Peil, and A. Georges, Phys. Rev. B **91**, 075128 (2015)

[23] M.E. Merkel and C. Ederer, Phys. Rev. B **104**, 165135 (2021)

[24] A. Isidori, M. Berović, L. Fanfarillo, L. de' Medici, M. Fabrizio, and M. Capone,
Phys. Rev. Lett. **122**, 186401 (2019)

[25] S. Ryee, P. Sémon, M.J. Han, and S. Choi, npj Quantum Mater. **5**, 19 (2020)

[26] J. Cheng, K.E. Kweon, S.A. Larregola, Y. Ding, Y. Shirako, L.G. Marshall, Z.-Y. Li,
X. Li, A.M. dos Santos, M.R. Suchomel, K. Matsubayashi, Y. Uwatoko, G.S. Hwang,
J.B. Goodenough, and J.-S. Zhou, Proc. Natl. Acad. Sci. **112**, 1670 (2015)

[27] J. Zhao, S.-C. Haw, X. Wang, L. Cao, H.-J. Lin, C.-T. Chen, C.J. Sahle, A. Tanaka,
J.-M. Chen, C. Jin, Z. Hu, and L.H. Tjeng, Phys. Rev. B **107**, 024107 (2023)

[28] R. Yu, H. Hojo, T. Watanuki, M. Mizumaki, T. Mizokawa, K. Oka, H. Kim, A. Machida,
K. Sakaki, Y. Nakamura, A. Agui, D. Mori, Y. Inaguma, M. Schlipf, K.Z. Rushchanskii,
M. Ležaić, M. Matsuda, J. Ma, S. Calder, M. Isobe, Y. Ikuhara, and M. Azuma,
J. Am. Chem. Soc. **137**, 12719 (2015)

[29] J.-S. Zhou, C.-Q. Jin, Y.-W. Long, L.-X. Yang, and J.B. Goodenough,
Phys. Rev. Lett. **96**, 046408 (2006)

[30] L. Ortega-San-Martin, A.J. Williams, J. Rodgers, J.P. Attfield, G. Heymann, and
H. Huppertz, Phys. Rev. Lett. **99**, 255701 (2007)

[31] A.C. Komarek, T. Möller, M. Isobe, Y. Drees, H. Ulbrich, M. Azuma,
M.T. Fernández-Díaz, A. Senyshyn, M. Hoelzel, G. André, Y. Ueda,
M. Grüninger, and M. Braden, Phys. Rev. B **84**, 125114 (2011)

[32] Y. Long, L. Yang, Y. Lv, Q. Liu, C. Jin, J. Zhou, and J.B. Goodenough,
J. Phys: Condens. Matter **23**, 355601 (2011)

[33] G. Bertino, H.-C. Hsing, A. Gura, X. Chen, T. Sauyet, M. Liu, C.-Y. Nam, and M. Dawber,
arXiv:2104.02738

[34] A. Carta and C. Ederer, Phys. Rev. Mater. **6**, 075004 (2022)

[35] A. Carta, A. Panda, and C. Ederer, Phys. Rev. Res. **6**, 023240 (2024)

[36] L. Vaugier, H. Jiang, and S. Biermann, Phys. Rev. B **86**, 165105 (2012)

[37] M. Karolak, G. Ulm, T.W.V. Mazurenko, A. Poteryaev, and A. Lichtenstein, J. Electr. Spectr. Rel. Phenom. **181**, 11 (2010)

[38] H.T. Dang, X. Ai, A.J. Millis, and C.A. Marianetti, Phys. Rev. B **90**, 125114 (2014)

[39] H. Park, A.J. Millis, and C.A. Marianetti, Phys. Rev. B **89**, 245133 (2014)

[40] A. Carta, A. Panda, and C. Ederer, arXiv:2502.17229

7 A Perspective on Screened Coulomb Interactions from the constrained Random Phase Approximation

Jan M. Tomczak
Department of Physics, King's College London
Strand, London WC2R 2LS, UK

Contents

1 Introduction **2**

2 The random phase approximation (RPA) **2**
2.1 Derivation of the RPA in the context of screening 3
2.2 Diagrammatic representation 5
2.3 RPA for the electron-gas 8
2.4 Excitations encoded in χ^{RPA} 9
2.5 Properties of the plasmon 10
2.6 The excitation spectrum of the electron-gas within RPA 11
2.7 Static screening at long wavelengths 11
2.8 Use of the screened interaction W 12

3 The constrained RPA (cRPA) **17**
3.1 The one-particle part of the effective low-energy Hamiltonian 18
3.2 Interactions in the effective low-energy model 19
3.3 Caveats to how cRPA results are typically used 21

E. Pavarini, E. Koch, A. Lichtenstein, and D. Vollhardt (eds.)
Understanding Correlated Materials with DMFT
Modeling and Simulation Vol. 15
Forschungszentrum Jülich, 2025, ISBN 978-3-95806-813-1
http://www.cond-mat.de/events/correl25

1 Introduction

Electrons interact via the fundamental Coulomb force, which is long-ranged, strong, and universal. In a solid, the interaction an electron effectively experiences is often much weaker. This reduction arises from screening, the collective rearrangement of electrons in the material in response to a charge perturbation. As Anderson famously noted, "more is different" [1]: the collective behavior of many electrons cannot be reduced to pairwise interactions in isolation.
The constrained random phase approximation (cRPA), devised by Aryasetiawan *et al.* [2], provides a systematic framework for quantifying the screening in a materials-specific way. Crucially, cRPA allows one to disentangle screening processes arising from different energy scales. By separating screening contributions into low-energy (to be treated explicitly) and high-energy (to be integrated out) parts, cRPA yields effective interactions suited for use in low-energy settings, such as the Hubbard model. As such, this method has become a cornerstone in the realistic modeling of strongly correlated systems, bridging first-principles calculations and model Hamiltonians.
Several excellent reviews exist, in particular by Ferdi Aryasetiawan [3,4] from previous editions of the Jülich "Autumn School on Correlated Electrons". Highly recommended are also the reviews by Philipp Werner and Michele Casula [5] and by Silke Biermann [6].
The current notes require familiarity with elements of quantum-field theory for many-body systems (suitable books are, e.g., Refs. [7, 8]): The formalism of second quantization, (Matsubara) Greens functions, Wick's theorem, and Feynman rules will be employed.
The chapter is organized as follows. In Section 2 the random phase approximation (RPA) is introduced in the context of screening of the Coulomb interaction in a many-electron system. We will then derive simple results for the electron gas, the relevance of which will carry over to calculations of solids. We will briefly digress into discussing the GW approach, which will help us later to put into perspective how the effective interactions that cRPA provides typically are (or should be) used in higher-level many-body approaches.
Section 3 reviews the cRPA approach for the specific example of $SrVO_3$. We will discuss how an effective low-energy model for a subset of orbitals is obtained and compare its interaction to the bare as well as the fully screened interaction. Finally, we will contrast the level of material specificity contained in the cRPA interactions and how much of it is typically taken into account when solving the low-energy model.

2 The random phase approximation (RPA)

Broadly speaking, the random phase approximation[1] is a technique to approximately calculate susceptibilities χ of *interacting* systems. The principal advantage of the approach is that it only requires the explicit calculation of the system's free susceptibility, χ^0, i.e., the response in the absence of the inter-particle (Coulomb) interaction V. Nonetheless, the RPA suscepti-

[1]The RPA was originally introduced by Bohm and Pines in 1952. Details of the original derivation and the name the approach was given as a consequence is of little relevance today.

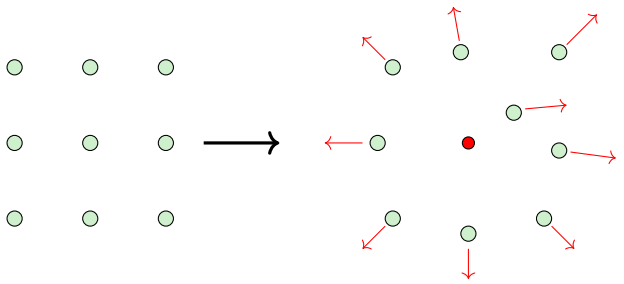


Fig. 1: *Coulomb repulsion in an electron gas* ○ ○ ○ *in presence of a (negative) test charge* ●. *The perturbation is mitigated (*screened*) as the system's density reacts to it.*

bility contains terms to all orders in the interaction strength by assembling an infinite series of Feynman diagrams from the building blocks χ^0 and V. Among others, the RPA can describe *collective* excitations (we will discuss the *plasmon*) and many-body renormalizations beyond Hartree-Fock (e.g., via the GW approach that we will sketch in Section 2.8).

2.1 Derivation of the RPA in the context of screening

The RPA is a fairly general approximation for susceptibilities associated with various degrees of freedom (e.g., spin, charge, or orbital in the context of solids). Here, we are interested in how the effect of a *fundamental* force between two particles (the Coulomb interaction) is modified if it is "simultaneously" experienced by a collection of many particles (electrons) that interact in a pairwise fashion from all to all. Imagine we subject our system of thus interacting electrons, which we describe with the Hamiltonian H, to an external perturbation V_t.

$$H_t = H + V_t \,. \tag{1}$$

We consider the case where $V_t = -\int d^3r\, \rho(\mathbf{r},t)\, V(\mathbf{r},t)$ is an explicitly time-dependent potential that describes the coupling of the system's charge density ρ to the (instantaneous) Coulomb interaction

$$V(\mathbf{r},t) = \frac{1}{4\pi\epsilon_0} \int d^3r' \frac{e^2}{|\mathbf{r}-\mathbf{r}'|}\, \rho_{\text{ext}}(\mathbf{r}')\, \delta(t) \tag{2}$$

arising from an *additional* external electron density $\rho_{\text{ext}}(\mathbf{r})$. Here, ϵ_0 is the permittivity of the vacuum. For example, $\rho_{\text{ext}}(\mathbf{r}') = \delta(\mathbf{r}')$ describes a single test charge at position $\mathbf{r}'$, see Fig. 1 for an illustration. The perturbation V_t will induce a change in the charge distribution of the original, unperturbed system. When Fourier-transforming to $\mathbf{q}$ and ω, this change is given by

$$\big\langle \delta\rho(\mathbf{q},\omega) \big\rangle = \big\langle \rho(\mathbf{q},\omega) \big\rangle - \big\langle \rho(\mathbf{q},\omega) \big\rangle_{V=0} = \frac{e^2}{\epsilon_0 q^2}\, \chi(\mathbf{q},\omega)\, \rho_{\text{ext}}(\mathbf{q},\omega) \tag{3}$$

where we used $\int d^3r \int d^3r' e^{i\mathbf{q}(\mathbf{r}-\mathbf{r}')}/|\mathbf{r}-\mathbf{r}'| = 4\pi/q^2$ for the Coulomb interaction. The response, or change in density, *screens* the perturbation: The extra charge density is accommodated by a rearrangement of the system's charge carriers, a process that effectively weakens the perturbation. The crucial idea now is to describe the external perturbation in a way that already accounts

(to an extent) for the system's reaction. The following Ansatz suggests itself

$$\big\langle \delta\rho(\mathbf{q},\omega)\big\rangle = \frac{e^2}{\epsilon_0 q^2}\,\tilde{\chi}(\mathbf{q},\omega)\big(\rho_{\text{ext}}(\mathbf{q},\omega) - \big\langle \delta\rho(\mathbf{q},\omega)\big\rangle\big). \tag{4}$$

In other words, we compute the response to a perturbation given by a modified "*screened*" external density, that we empirically choose as the original external density ρ_{ext}, *minus* the portion $\langle\delta\rho(\mathbf{q},\omega)\rangle$ of the system's charge that redistributes as a consequence of the initial "bare" perturbation. Since the perturbation has changed, also the response function is different from the one described by Eq. (3); we called it $\tilde{\chi}$. Note that (4) is a *self-consistent* equation: The anticipated change in density appears, both, on the left and on the right. Combining Eqs. (3) and (4), we obtain a relation between (a) the response χ to the *bare* perturbation and (b) the response $\tilde{\chi}$ to the *screened* perturbation

$$\chi(\mathbf{q},\omega) \;=\; \frac{\tilde{\chi}(\mathbf{q},\omega)}{1+\frac{e^2}{\epsilon_0 q^2}\tilde{\chi}(\mathbf{q},\omega)} \tag{5}$$

or, generalizing to an arbitrary interaction $V(\mathbf{q})$,

$$\chi(\mathbf{q},\omega) \;=\; \frac{\tilde{\chi}(\mathbf{q},\omega)}{1+V(\mathbf{q})\tilde{\chi}(\mathbf{q},\omega)}\,. \tag{6}$$

So far, we have not actually computed any susceptibility. We have only considered two settings that are, in principle, equivalent. The point now is that it stands to reason that *approximating* $\tilde{\chi}$ instead of χ is more promising, since the perturbation at its origin is, in a sense, weaker. That the perturbation is indeed effectively smaller can be seen as follows. We have

$$\big\langle \delta\rho(\mathbf{q},\omega)\big\rangle \overset{(4)}{=} V(\mathbf{q})\tilde{\chi}(\mathbf{q},\omega)\big(\rho_{\text{ext}}(\mathbf{q},\omega) - \big\langle \delta\rho(\mathbf{q},\omega)\big\rangle\big) \overset{(3)}{=} V(\mathbf{q})\chi(\mathbf{q},\omega)\rho_{\text{ext}}(\mathbf{q},\omega) \tag{7}$$

$$\equiv W(\mathbf{q},\omega)\tilde{\chi}(\mathbf{q},\omega)\rho_{\text{ext}}(\mathbf{q},\omega) \tag{8}$$

where we defined an effective interaction W, for which holds

$$W(\mathbf{q},\omega) = \frac{V(\mathbf{q})\chi(\mathbf{q},\omega)}{\tilde{\chi}(\mathbf{q},\omega)} \overset{(6)}{=} \frac{V(\mathbf{q})}{1+V(\mathbf{q})\tilde{\chi}(\mathbf{q},\omega)} = \epsilon^{-1}(\mathbf{q},\omega)V(\mathbf{q}) \leq V(\mathbf{q}) \tag{9}$$

where we introduced $\epsilon(\mathbf{q},\omega)$, the dielectric function, and the last inequality holds in the limit $(\mathbf{q}\to 0,\omega=0)$, since (as we will later show, see Eq. (47)) $\tilde{\chi}(\mathbf{q}\to 0,\omega=0)\geq 0$.
In the RPA, one performs the simplest possible approximation to the *screened* susceptibility: $\tilde{\chi} = \chi^0$. In other words, the screened response is approximated by the susceptibility of the *non-interacting* system. Consequently,

$$\chi^{\text{RPA}}(\mathbf{q},\omega) = \frac{\chi^0(\mathbf{q},\omega)}{1+V(\mathbf{q})\chi^0(\mathbf{q},\omega)} \tag{10}$$

$$W^{\text{RPA}}(\mathbf{q},\omega) = \frac{V(\mathbf{q})}{1+V(\mathbf{q})\chi^0(\mathbf{q},\omega)}\,. \tag{11}$$

While, now, the screened response that we will calculate is by construction independent of the inter-particle interaction, the RPA susceptibility depends on $V(\mathbf{q})$. However, this dependence

is merely *explicit*. Complicated two-particle expectation values for the interacting system are obviated, at the expense of including more complicated two-particle processes. As a consequence, we shall be able, in the following, to make use of Wick's theorem. This simplification allows the two-particle expectation, $\propto \langle c^\dagger\, cc^\dagger c\rangle$, to be factored into two one-particle expectation values, $\propto \langle c^\dagger c\rangle\langle c^\dagger c\rangle$, as for the purpose of the screened susceptibility we consider the electrons as non-interacting.[2]
For the following it will be useful to recall the geometric series, $\sum_{n=0}^{\infty} x^n = \frac{1}{1-x}$ for $|x| < 1$. Indeed, assuming convergence, we can rewrite the above RPA equations as a series expansion

$$\chi^{\mathrm{RPA}}(\mathbf{q},\omega) = \frac{\chi^0(\mathbf{q},\omega)}{1+V(\mathbf{q})\chi^0(\mathbf{q},\omega)} = \chi^0 + \chi^0(-V)\chi^0 + \dots \tag{12}$$

$$-W^{\mathrm{RPA}}(\mathbf{q},\omega) = \big[\underbrace{1+V(\mathbf{q})\chi^0(\mathbf{q},\omega)}_{\varepsilon(\mathbf{q},\omega)}\big]^{-1}(-V(\mathbf{q})) = \big[1+(-V)\chi^0+\dots\big](-V) \tag{13}$$

2.2 Diagrammatic representation

We will now make the connection to the description in terms of Feynman diagrams. In linear response theory (see, e.g., Refs [7, 8], the susceptibility that links a perturbation coupling to the system's charge density to its signatures in the same charge density can be written as

$$\chi^0(\mathbf{r},\mathbf{r}',t) = -\frac{1}{i\hbar}\Theta(t)\big\langle\big[\rho(\mathbf{r},t),\rho(\mathbf{r}',0)\big]\big\rangle_{H^0}. \tag{14}$$

Here, H^0 indicates that the free susceptibility is governed by an expectation value with respect to the non-interacting part of the system's Hamiltonian.
Making use of Wick's theorem, we can express χ^0 in terms of one-particle Green functions. For that, we first express the charge density in terms of field operators

$$\rho(\mathbf{r}) = \sum_\sigma \psi^\dagger_\sigma(\mathbf{r})\psi_\sigma(\mathbf{r}). \tag{15}$$

Here, $\psi^\dagger(\mathbf{r})$ creates an electron at a position $\mathbf{r}$ in continuum space. The connection with the perhaps more common formulation on a (discrete) lattice is made by introducing a basis set, e.g., in momentum-space $\{\varphi_{\mathbf{k}n}(\mathbf{r})\}$, whence

$$\psi_\sigma(\mathbf{r}) = \sum_{\mathbf{k}n} \varphi_{\mathbf{k}n}(\mathbf{r})c_{\mathbf{k}n\sigma}\,. \tag{16}$$

In the later parts of this section, we will study, for illustrative purposes, the charge response in the electron gas. We will therefore now assume a setting with a single band ($n = 1$) described

[2] Here, the RPA was derived through physical arguments for the density-density response. More generally, the RPA can be obtained through a truncation of the Green function's equation of motion (see, e.g., Ref. [7]): In the higher-order Green function that arises from the commutator with the interacting part of the Hamiltonian, one decouples the group of operators belonging, on the one hand, to the perturbation and, on the other hand, those from the particle-particle interaction in a mean-field fashion. Further, one approximates the arising expectation values by using only the non-interacting part of the Hamiltonian.

by plane waves, i.e., $\varphi_{\mathbf{k}}(\mathbf{r}) = \exp(i\mathbf{kr})$. While a more general formulation is of course possible (and used in practice), this setting will keep notation light. It follows that

$$\rho(\mathbf{r}) = \sum_{\sigma} \psi^{\dagger}_{\sigma}(\mathbf{r})\psi_{\sigma}(\mathbf{r}) = \sum_{\mathbf{k}\mathbf{k}'} c^{\dagger}_{\mathbf{k}\sigma} c_{\mathbf{k}'\sigma}\, e^{i(\mathbf{k}'-\mathbf{k})\mathbf{r}} = \sum_{\mathbf{k}\mathbf{q}\sigma} c^{\dagger}_{\mathbf{k}\sigma} c_{\mathbf{k}+\mathbf{q}\sigma}\, e^{i\mathbf{q}\mathbf{r}} \tag{17}$$

and writing χ in the Matsubara (imaginary time τ) formalism, we find

$$\chi^0(\mathbf{r},\mathbf{r}',\tau) = \sum_{\mathbf{k}\mathbf{q}\sigma}\sum_{\mathbf{k}'\mathbf{q}'\sigma'} \left\langle \mathcal{T}_\tau c^{\dagger}_{\mathbf{k}\sigma}(\tau) c_{\mathbf{k}+\mathbf{q}\sigma}(\tau) c^{\dagger}_{\mathbf{k}'\sigma'}(0) c_{\mathbf{k}'+\mathbf{q}'\sigma'}(0)\right\rangle_{H^0} e^{i\mathbf{q}\mathbf{r}} e^{i\mathbf{q}'\mathbf{r}'} \tag{18}$$

$$= \sum_{\mathbf{k}\mathbf{k}'\sigma\sigma' q} e^{i\mathbf{q}(\mathbf{r}-\mathbf{r}')} \left\langle \mathcal{T}_\tau c^{\dagger}_{\mathbf{k}\sigma}(\tau) c_{\mathbf{k}+\mathbf{q}\sigma}(\tau) c^{\dagger}_{\mathbf{k}'\sigma'}(0) c_{\mathbf{k}'-\mathbf{q}\sigma'}(0)\right\rangle_{H^0}. \tag{19}$$

Where we exploited momentum conservation, $\mathbf{k}+\mathbf{k}' = \mathbf{k}+\mathbf{q}+\mathbf{k}'+\mathbf{q}' \Leftrightarrow \mathbf{q}' = -\mathbf{q}$. Then, Wick's theorem tells us that there are two contractions that can be decoupled into pairs of Green functions

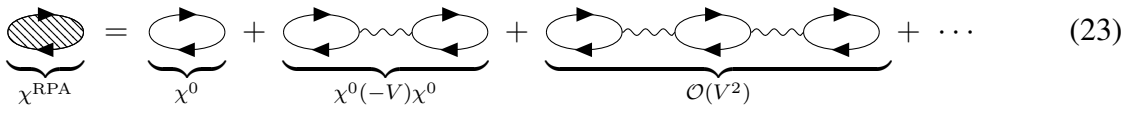
$$\chi^0(\mathbf{q},\tau) = \sum_{\mathbf{k}\mathbf{k}'\sigma\sigma'} \left\langle \mathcal{T}_\tau c^{\dagger}_{\mathbf{k}\sigma}(\tau) c_{\mathbf{k}+\mathbf{q}\sigma}(\tau) c^{\dagger}_{\mathbf{k}'\sigma'}(0) c_{\mathbf{k}'-\mathbf{q}\sigma'}(0)\right\rangle_{H^0} \tag{20}$$

$$= \sum_{\mathbf{k}\mathbf{k}'\sigma\sigma'} \underbrace{\left\langle \mathcal{T}_\tau c^{\dagger}_{\mathbf{k}\sigma}(\tau) c_{\mathbf{k}+\mathbf{q}\sigma}(\tau)\right\rangle}_{\delta_{\mathbf{q}\mathbf{0}}\, n_{\mathbf{k}\sigma}} \underbrace{\left\langle \mathcal{T}_\tau c^{\dagger}_{\mathbf{k}'\sigma'}(0) c_{\mathbf{k}'-\mathbf{q}\sigma'}(0)\right\rangle}_{\delta_{\mathbf{q}\mathbf{0}}\, n_{\mathbf{k}'\sigma'}} \tag{21}$$

$$+ \underbrace{\left\langle \mathcal{T}_\tau c^{\dagger}_{\mathbf{k}\sigma}(\tau) c_{\mathbf{k}'-\mathbf{q}\sigma'}(0)\right\rangle}_{G^0_{\mathbf{k}\,\sigma}(-\tau)} \underbrace{\left\langle \mathcal{T}_\tau c_{\mathbf{k}+\mathbf{q}\sigma}(\tau) c^{\dagger}_{\mathbf{k}'\sigma'}(0)\right\rangle}_{-G^0_{\mathbf{k}+\mathbf{q}}(\tau)\,\delta_{\mathbf{k}+\mathbf{q},\mathbf{k}'}\,\delta_{\sigma\sigma'}}$$

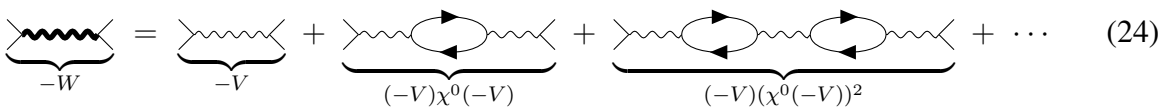
$$= \delta_{\mathbf{q}\mathbf{0}}\, n^2 - \sum_{\mathbf{k},\sigma} G^0_{\mathbf{k}\sigma}(-\tau)\, G^0_{\mathbf{k}+\mathbf{q}\sigma}(\tau) = \delta_{\mathbf{q}\mathbf{0}}\, n^2 + 0 \quad \underset{\mathbf{k},\,\sigma}{\overset{\mathbf{k}+\mathbf{q},\,\sigma}{\circlearrowright}}\ \tau\,. \tag{22}$$

The first term in Eq. (21) and following (where $n = \sum_{\mathbf{k}\sigma}\langle n_{\mathbf{k}\sigma}\rangle$) only contributes for $\mathbf{q} = 0$, i.e., it is uniform in space, $f(\mathbf{q}{=}0) = \int d^3r\, f(\mathbf{r})$. It is also τ-independent, i.e., static. Thus corresponding to a mere global shift of the origin of space, we will neglect this term. With only the bubble diagram remaining, and using Eq. (12), we see that the RPA consists of the following subset of 2-particle diagrams



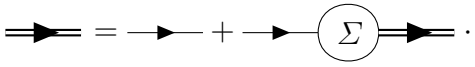
(23)

where the minus sign in front of V comes from the corresponding Feynman rule: one minus sign per power of the interaction. In turn, the screened interaction can be represented as



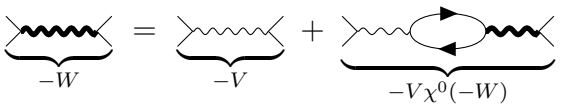
(24)

This (two-particle) series is similar to the (one-particle) Dyson equation for the one-particle Green function

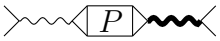


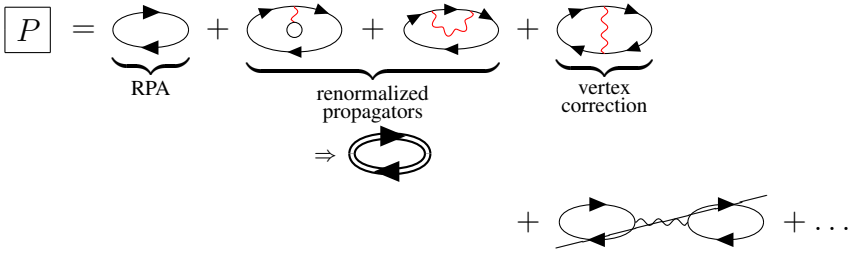
(25)

Indeed, in complete analogy, we can visualize Eq. (11) by



(26)

which is a so-called Bethe-Salpeter-equation (BSE), namely the one in the "particle-hole channel": Among the lines connecting V and W one points to the right and one to the left, corresponding to a particle propagating in time from 0 to τ and one propagating backwards in time, which we can alternatively identify as a hole propagating forward (cf. Eq. (22)).
The RPA is an approximation in that it contains only a subset of all possible two-particle diagrams. The general expression of the screened interaction, containing more or all diagrams, can be visualized by  where P is a place-holder for all possible, so-called polarization diagrams[3]



(27)

First, we note that the polarization only contains diagrams that are "V-irreducible". Indeed, diagrams that can be disconnected into two parts by cutting an interaction line (see, e.g., the stricken-out diagram above) are recursively generated in the BSE, Eq. (26), and have thus to be excluded in the polarization. This is in complete analogy to the irreducibility of the self-energy in terms of the propagator. There, the recursion in the Dyson equation generates diagrams that can be separated into two parts when cutting a Green function line. Second, the RPA is the lowest order approximation of the V-irreducible polarization. Higher order terms can be classified into two categories

1. Diagrams where individual Green function lines are dressed with self-energy insertions. These terms can be accounted for in so-called "bold" theories, where the free propagators G_0 (single line) are replaced with interacting Green functions (double line), see Eq. (27).

2. More complicated diagrams in which interactions couple different propagators. These terms are called "vertex corrections".

The RPA is non-perturbative in the sense that in the susceptibility, terms to all order in the interaction are generated (by virtue of the geometric series we do not have to compute them one-by-one). Still, as is evident from the above diagrams, there are contributions, again, at all orders, that are not included in the RPA. Therefore, the RPA is in practice still an approach best suited for weak coupling.

[3] In the cRPA and GW literature, instead of the charge-charge susceptibility χ, an object called the polarization $P = -\chi$ is used.

2.3 RPA for the electron-gas

2.3.1 Evaluation of χ^0

The evaluation of χ^0 is elementary in the Matsubara formalism

$$\chi^0(\mathbf{q},i\nu_n) = -2\sum_{\mathbf{k}}\sum_{i\omega_m}\frac{1}{\beta}G^0_{\mathbf{k}+\mathbf{q}}(i\omega_m+i\nu_n)\,G^0_{\mathbf{k}}(i\omega_m) \tag{28}$$

$$= -\frac{2}{\beta}\sum_{\mathbf{k}}\sum_{i\omega_m}\frac{1}{i\omega_m+i\nu_n-\varepsilon_{\mathbf{k}+\mathbf{q}}}\,\frac{1}{i\omega_m-\varepsilon_{\mathbf{k}}} \tag{29}$$

$$= -2\sum_{\mathbf{k}}\frac{1}{2\pi i}\oint dz\frac{f(z)}{(z+i\nu_n-\varepsilon_{\mathbf{k}+\mathbf{q}})(z-\varepsilon_{\mathbf{k}})} \tag{30}$$

$$= -2\sum_{\mathbf{k}}\frac{f(\varepsilon_{\mathbf{k}})-f(\varepsilon_{\mathbf{k}+\mathbf{q}})}{i\nu_n-(\varepsilon_{\mathbf{k}+\mathbf{q}}-\varepsilon_{\mathbf{k}})}, \tag{31}$$

where we used $\nu_n=\frac{2n\pi}{\beta}\rightarrow e^{i\beta\nu_n}=1\Rightarrow f(\varepsilon_{\mathbf{k}+\mathbf{q}}-i\nu)=f(\varepsilon_{\mathbf{k}+\mathbf{q}})$.Analytical continuation to real frequencies $i\nu\rightarrow\omega+i0^+$ leads to the (retarded) Lindhard function

$$\chi^0(\mathbf{q},\omega)=2\sum_{\mathbf{k}}\frac{f(\varepsilon_{\mathbf{k}+\mathbf{q}})-f(\varepsilon_{\mathbf{k}})}{\omega-(\varepsilon_{\mathbf{k}+\mathbf{q}}-\varepsilon_{\mathbf{k}})+i0^+}\,. \tag{32}$$

Quite generally, poles in propagators G or linear response susceptibilities χ describe eigenmodes of the system. Here, $\mathrm{Re}\,\chi^0(\mathbf{q},\omega)$ diverges for $\omega=\varepsilon_{\mathbf{k}+\mathbf{q}}-\varepsilon_{\mathbf{k}}>0$ if $\varepsilon_{\mathbf{k}}$ is an occupied and $\varepsilon_{\mathbf{k}+\mathbf{q}}$ an empty state, as dictated by the Fermi functions. One speaks of particle-hole excitations. These are illustrated in Fig. 2.

Had we allowed for the presence of multiple bands, n, we would have obtained a slightly more complicated Lindhard function of the form

$$\chi^0(\mathbf{q},\omega)=2\sum_{\mathbf{k}nn'}\Xi_{nn'}(\mathbf{k},\mathbf{q})\frac{f(\varepsilon_{\mathbf{k}+\mathbf{q}n'})-f(\varepsilon_{\mathbf{k}n})}{\omega-(\varepsilon_{\mathbf{k}+\mathbf{q}n'}-\varepsilon_{\mathbf{k}n})+i0^+} \tag{33}$$

where

$$\Xi_{nn'}(\mathbf{k},\mathbf{q})=\int d^3r\int\!d^3r'\,e^{-i\mathbf{q}(\mathbf{r}-\mathbf{r}')}\varphi^*_{\mathbf{k}n}(\mathbf{r})\varphi_{\mathbf{k}+\mathbf{q}n'}(\mathbf{r})\varphi^*_{\mathbf{k}+\mathbf{q}n'}(\mathbf{r}')\varphi_{\mathbf{k}n}(\mathbf{r}') \tag{34}$$

with the eigenfunctions $\varphi_{\mathbf{k}n}(\mathbf{r})=\langle\mathbf{r}|\mathbf{k}n\rangle$.

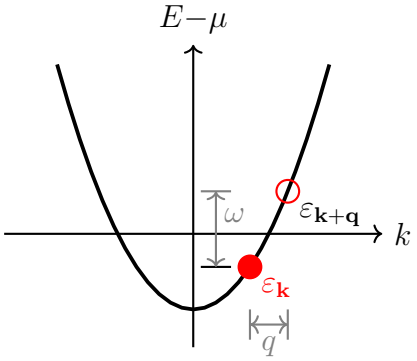


Fig. 2: *Particle-hole excitations. For an occupied state at $\varepsilon_{\mathbf{k}}$ and an unoccupied state at $\varepsilon_{\mathbf{k}+\mathbf{q}}$, the Lindhard function will have a pole for the indicated frequency $\omega>0$ and momentum $\mathbf{q}$.*

2.4 Excitations encoded in χ^{RPA}

What are the excitations encoded in the RPA susceptibility? For this, we perform in Fig. 3 a graphical analysis of

$$\chi^{\mathrm{RPA}}(\mathbf{q},\omega) = \frac{\chi^0(\mathbf{q},\omega)}{1+V(\mathbf{q})\chi^0(\mathbf{q},\omega)}\,. \tag{35}$$

at fixed momentum $\mathbf{q}$. The (real-part of the) RPA susceptibility diverges when the denominator cancels, i.e., $V(\mathbf{q})\chi^0(\mathbf{q},0) = -1$. First, we see that the poles of χ^0 translate into poles of χ^{RPA}. While individual poles are shifted, a dense continuum emerges in the thermodynamic limit that is shared between χ^0 and χ^{RPA}. This particle-hole continuum is confined by the possible values of $\varepsilon_{\mathbf{k}+\mathbf{q}}-\varepsilon_{\mathbf{k}}$: The *one-particle* spectrum available determines the energy/frequency range of these eigenmodes. The crucial observation now is that the $1/\omega$ decay in $\mathrm{Re}\,\chi^{RPA}$ causes an additional pole at $\omega = \omega_p$ *above* the one-particle continuum, whose existence hinges on the presence of the interaction V. This mode is called the *plasmon*. It corresponds to a quantum of *collective* plasma oscillations.

Classically, plasma oscillation can be understood as follows from electrodynamics: Consider a positively charged rigid and periodic ionic background, populated by negatively charged electrons. When electrons are displaced with respect to the ions, the Coulomb force tries to restore their equilibrium positions, acting as a "spring" causing the electrons to oscillate. Assuming an oscillating charge density $\rho(\omega) = \rho_0 \exp(-i\omega t)$, the continuity equation becomes $\nabla\cdot\mathbf{j} = -\partial\rho/\partial t = i\omega\rho(\omega)$. Combining with Ohm's law $\mathbf{j}(\omega) = \sigma(\omega)\mathbf{E}(\omega)$ and Gauss' law $\nabla\cdot\mathbf{E}(\omega) = \rho(\omega)/\epsilon_0$, one finds $i\omega\rho(\omega) = \sigma(\omega)\rho(\omega)/\epsilon_0$. For this equation to hold for an arbitrary $\rho(\omega)$ requires $\epsilon(\omega) \equiv 1 + i\sigma(\omega)/\epsilon_0\omega \stackrel{!}{=} 0$. According to Eq. (9), this is the same as demanding $1 + V(\mathbf{q})\chi^0(\mathbf{q},\omega) = 0$, which precisely holds for $\omega = \omega_p$, the plasmon! Above ω_p, absorption can no longer take place, and the system is transparent at those frequencies.

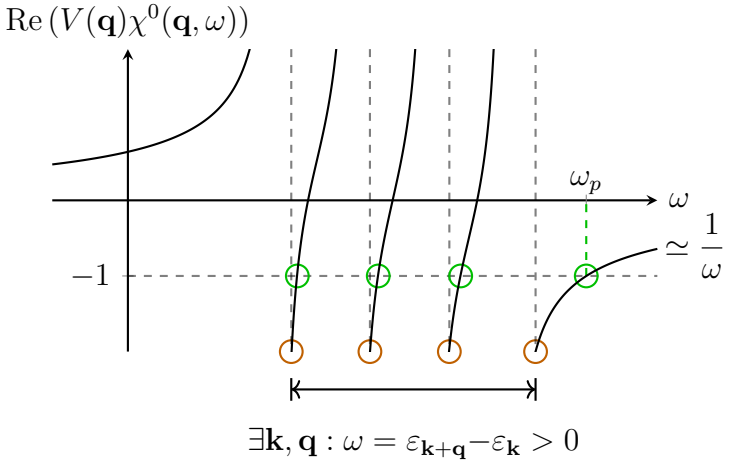


Fig. 3: *Eigenmodes encoded in the RPA susceptibility: The particle-hole continuum arising from accessible differences of one-particle energies,* $0 < \omega = \varepsilon_{\mathbf{k}+\mathbf{q}}-\varepsilon_{\mathbf{k}} < \omega_p$ *and the plasmon excitation in the electron gas.*

2.5 Properties of the plasmon

Consider $\chi(\mathbf{q},\omega)$ in the limit $\mathbf{q}\to 0$ at finite ω

$$\mathrm{Re}\,\chi^0(\mathbf{q},\omega) = -2\sum_{\mathbf{k}} \frac{f(\varepsilon_{\mathbf{k}}) - f(\varepsilon_{\mathbf{k}+\mathbf{q}})}{\omega - (\varepsilon_{\mathbf{k}+\mathbf{q}} - \varepsilon_{\mathbf{k}})} \tag{36}$$

$$= -2\sum_{\mathbf{k}} \left(\frac{f(\varepsilon_{\mathbf{k}})}{\omega - (\varepsilon_{\mathbf{k}+\mathbf{q}} - \varepsilon_{\mathbf{k}})} - \frac{f(\overbrace{\varepsilon_{-\mathbf{k}}}^{\varepsilon_{\mathbf{k}}})}{\omega - (\varepsilon_{-\mathbf{k}} - \varepsilon_{-\mathbf{k}-\mathbf{q}})} \right) \tag{37}$$

$$= -4\sum_{\mathbf{k}} f(\varepsilon_{\mathbf{k}}) \frac{(\varepsilon_{\mathbf{k}+\mathbf{q}} - \varepsilon_{\mathbf{k}})}{\omega^2 - (\varepsilon_{\mathbf{k}+\mathbf{q}} - \varepsilon_{\mathbf{k}})^2} \tag{38}$$

$$\overset{\mathbf{q}\to 0}{=} -\frac{2}{m\omega^2} \int \frac{d^3k}{(2\pi)^3}\, f(\varepsilon_{\mathbf{k}}) \big(\underbrace{2\,|\mathbf{k}|\,|\mathbf{q}|\cos\theta}_{=0 \text{ (angular integration)}} + \mathbf{q}^2 + \cdots \big) \tag{39}$$

$$= -\frac{n\mathbf{q}^2}{m\omega^2}, \tag{40}$$

where we made the replacement $k+q \to -k$ in the second term of Eq. (37), used the (even) symmetry of the dispersion $\varepsilon_{\mathbf{k}} = \hbar^2\mathbf{k}^2/2m = \varepsilon_{-\mathbf{k}}$,[4] and $n = 2\int \frac{d^3k}{(2\pi)^3} f(\varepsilon_{\mathbf{k}})$ is the number density of electrons. Neglecting $\mathrm{Im}\,\chi^{\mathrm{RPA}}$ in Eq. (10), this leads to

$$\chi^{\mathrm{RPA}}(\mathbf{q}\to 0,\omega) = \frac{-n\mathbf{q}^2/(m\omega^2)}{1 - V(\mathbf{q}) n\mathbf{q}^2/(m\omega^2)} = -\frac{n\mathbf{q}^2/m}{\omega^2 - \omega_p^2} \tag{41}$$

where, using the Coulomb interaction, $V(\mathbf{q}) = e^2/(\epsilon_0\mathbf{q}^2)$, we defined the plasma frequency

$$\omega_p = \sqrt{\frac{ne^2}{\epsilon_0 m}} > 0. \tag{42}$$

This limiting form of the RPA susceptibility clearly exposes the plasmon as an extra mode in the system. Typically, $\omega_p = \mathcal{O}(10\text{ eV})$. For example, in solid sodium, $\omega_p \approx 6$ eV [9].
Crucially, we note that the finite excitation energy for $q \to 0$ is intimately linked to the long-range nature of the Coulomb interaction (associated with the singularity of $V(q)$ at vanishing momentum). If the electrons were to interact via a short-range Yukawa interaction, $\frac{e^2}{\epsilon_0}\frac{1}{q^2+q_{\mathrm{TF}}^2}$ (with finite q_{TF}; see (46) below), (41) would yield a vanishing plasma frequency and a phenomenon known as "zero sound" emerges.[5]

[4] In the one-orbital case, $\varepsilon_{\mathbf{k}} = \varepsilon_{-\mathbf{k}}$ also holds (by virtue of Bloch's theorem) for dispersions on a lattice. For multi-orbital Hamiltonians, instead, inversion symmetry is required.

[5] The RPA procedure described here is very general. Applying the RPA formalism, e.g., to the spin-flip susceptibility of a ferromagnet, one finds a collective spin-excitation called the *magnon*, whose energy vanishes for $q \to 0$. In this case, the collective excitation is a so-called *Goldstone mode*: It is associated with the remaining all-up-or-all-down spin-flip freedom of the spontaneously broken spin-symmetry of the ferromagnetic state. Referring to the relativistic energy-momentum relation, $E = \sqrt{(pc)^2 + (m_0c^2)^2}$, zero sound and the magnon are called "massless" excitations ($m_0 = 0 \Rightarrow E \propto |p| \to 0\,(p \to 0)$), while the plasmon of the electron gas is a "massive" excitation.

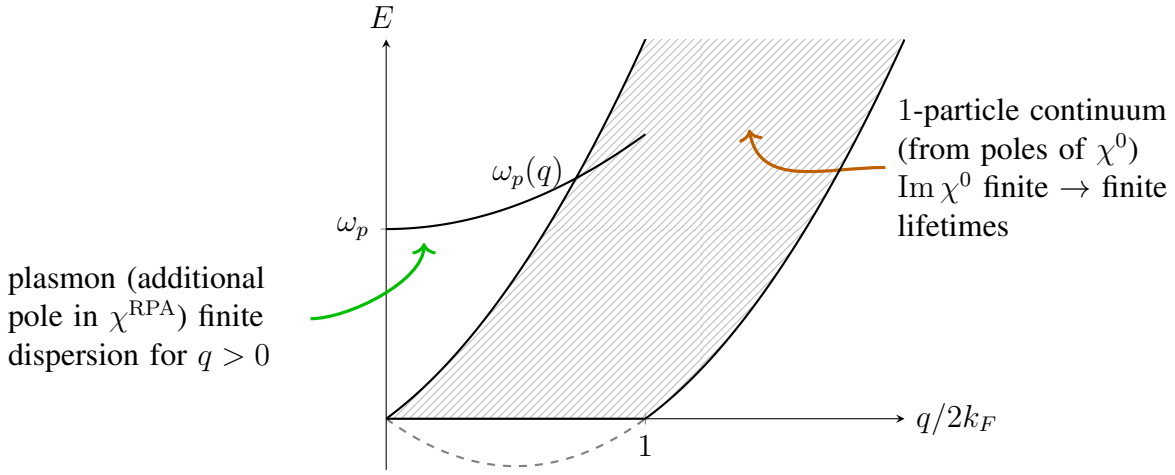


Fig. 4: *Excitation spectrum of the electron gas (in dimensions $d > 1$) within RPA. The shaded region delimits the particle-hole transitions between one-particle states, as already encoded in the free susceptibility. At small momentum q, there is an additional, collective mode: the plasmon. This excitation is a many-body effect. In fact, its existence requires the Coulomb repulsion between electrons.*

2.6 The excitation spectrum of the electron-gas within RPA

To put the *collective* plasmon mode into context to the particle-hole excitations described previously, we characterize their energy range. Transitions between one-particle states occur for poles in $\mathrm{Re}\,\chi^0$, i.e., for frequencies

$$\omega = \varepsilon_{\mathbf{k}+\mathbf{q}} - \varepsilon_{\mathbf{k}} = \frac{\hbar \mathbf{q}^2}{2m} + \frac{\hbar}{m} |\mathbf{k}|\,|\mathbf{q}| \cos\theta. \tag{43}$$

When we are in two or more dimensions, this yields a particle-hole continuum delimited by

$$\max(0, \frac{\hbar^2 q^2}{2m} - \frac{\hbar^2 k_F}{m} q) \leq \omega \leq \frac{\hbar^2 q^2}{2m} + \frac{\hbar^2 k_F}{m} q. \tag{44}$$

This range is visualized as a function of momentum q as the shaded region in Fig. 4. In particular, in the limit $q \rightarrow 0$, the particle-hole continuum vanishes (linearly). Consequently, for small momenta q, the "gapped" plasmon excitation lies far above the one-particle continuum.

2.7 Static screening (ω=0) in the long wavelength limit (q$\rightarrow$0)

We return to the motivation of these notes and study, how the response screens the Coulomb interaction within RPA. First, we specialize the Lindhard function to the static case (ω=0) in the long wavelength limit ($\mathbf{q}\rightarrow 0$). There,

$$\mathrm{Re}\,\chi^0(\mathbf{q}, \omega{=}0) = -2 \sum_{\mathbf{k}} \frac{f(\varepsilon_{\mathbf{k}}) - f(\varepsilon_{\mathbf{k}+\mathbf{q}})}{-(\varepsilon_{\mathbf{k}+\mathbf{q}} - \varepsilon_{\mathbf{k}})} \overset{\mathbf{q}\rightarrow 0}{=} 2 \sum_{\mathbf{k}} \left(-\frac{\partial f(\varepsilon_{\mathbf{k}})}{\partial \varepsilon_{\mathbf{k}}} \right) \overset{T=0}{=} N(0) \tag{45}$$

where we further assumed low temperatures and $N(0)$ is the value of the non-interacting system's density of states, $N(\varepsilon)=\sum_{\mathbf{k}\sigma}\delta(\varepsilon-\varepsilon_{\mathbf{k}})$, at the Fermi level. From this follows

$$W(|\mathbf{q}|\ll 1,\omega=0)=\frac{V(\mathbf{q})}{1+V(\mathbf{q})\chi^0(\mathbf{q},\omega=0)}=\frac{\frac{e^2}{\epsilon_0\mathbf{q}^2}}{1+\frac{e^2}{\epsilon_0\mathbf{q}^2}2N(0)}=\frac{e^2}{\epsilon_0}\frac{1}{\mathbf{q}^2+q_{\mathrm{TF}}^2}, \tag{46}$$

where $q_{\mathrm{TF}}=\sqrt{\frac{e^2}{\epsilon_0}N(0)}$ is the (inverse) Thomas-Fermi screening length. Fourier transforming this interaction to three-dimensional real-space, while assuming $W(|\mathbf{q}\ll 1,\omega=0)$ to be valid for all q, leads to the Yukawa potential

$$W(r)=\frac{e^2}{\epsilon_0\mathbf{r}}\,e^{-q_{\mathrm{TF}}|\mathbf{r}|}. \tag{47}$$

While the above derivation is approximate, this result provides important insights: In the presence of many particles interacting via the fundamental Coulomb force, the repulsion actually "felt" by the charge carriers is *screened*. Instead of a large and algebraically decaying interaction, $V(r)\propto 1/r$, the effective inter-electronic repulsion is reduced in magnitude and it becomes far more short-ranged. Note, in the present case of the electron gas, screening only occurs if the system is metallic ($N(0)>0$). Instead, in a solid, there are many bands or orbitals, both occupied and empty that contribute to χ^0, via inter-band transitions, see Eq. (33). Thus, while less efficient, screening also occurs in insulators.

The Yukawa form of the interaction can loosely be taken as a motivation of the Hubbard model. In its Hamiltonian the electron-electron interaction is assumed to be short-ranged to the extent that it is local.[6] Specifically, the Hubbard interaction takes the form $Un_{i\uparrow}n_{i\downarrow}$ with $n_{i\sigma}=c^\dagger_{i\sigma}c_{i\sigma}$: Only when electrons sit on the same lattice or atomic site i do they experience a repulsion U. The spin-structure of the interaction term is dictated by the Pauli principle because, in the absence of other quantum numbers (e.g., an orbital index), two electrons of the same spin cannot be present on the same site (at the same time).

2.8 The use of screened interactions: The GW approach

In Section 3 we will discuss how RPA-based techniques can be used to set up effective low-energy models from first principles. These models are typically cast into the form of a multi-orbital Hubbard Hamiltonian which is then solved with sophisticated many-body methods. However, there is great merit in directly using screened interactions W, of the kind that we just discussed. A popular and, at least formally, rather simple technique based on the screened interaction W is the GW approximation [10, 11]. Here, we will only provide two cartoon applications of this approach that will help us later to illustrate deficiencies in typical workflows for simulating correlated materials.

[6] It should be stressed that the Hubbard model is a lattice model. Hence, locality is to be understood in the sense of a Wannier orbital $\chi_{\mathbf{R}}(\mathbf{r})=\langle\mathbf{r}|\mathbf{R}\rangle$, i.e., as pertaining to a region in space surrounding a discrete position of an atomic site or unit-cell $\mathbf{R}$, instead of the point locality $\delta(\mathbf{r}-\mathbf{r}')$ in the continuum description of the electron gas.

As mentioned in the introduction, we cannot solve the full Hamiltonian that describes the solid we are interested in. One way to approximately simulate the system is the use of perturbation theory: We identify a parameter in the system, which, when set to zero, allows for a full solution of the problem. Then we perform a perturbative expansion in said parameter. At infinite order, we would describe the original problem exactly. The hope is, however, that if the parameter is small, a low-order expansion is sufficiently accurate.
Most frequently the interaction is considered as the perturbation to the exactly solvable non-interacting system. But which interaction to we perform our expansion in? The usual choice is the bare Coulomb interaction V. In that case, first-order perturbation theory amounts to the Hartree-Fock approximation. We could, however, make an expansion in terms of a screened interaction W. At infinite order, both expansions should yield identical results, but evaluations at finite order will differ. The argument for an expansion in W is, at least intuitively, straightforward: Screening reduces the interaction. The quantity we are expanding in is therefore a smaller parameter than the bare interaction—suggesting that a lower order in the expansion is sufficient than would be needed for the much larger bare interaction. Also, the RPA screening contains Feynman diagrams to all orders in the bare interaction, meaning that already a first-order expansion in W creates an infinite number of self-energy diagram. This first-order expansion is called the GW approximation. Diagrammatically, the GW self-energy is

$$\Sigma^{GW}_\sigma(\mathbf{k}, i\omega_n) = \quad = -\frac{1}{\beta}\sum_{i\omega_{n'},\mathbf{k}'} \underbrace{G^0(\mathbf{k}', i\omega_{n'})\, W(\mathbf{k}-\mathbf{k}', i\omega_n - i\omega_{n'})}_{\text{hence the name "}GW\text{"}} \tag{48}$$

$$= \quad + \quad + \quad + \ \ldots \tag{49}$$

We will now evaluate this GW diagram for two illustrative cases. Instead of computing the screened interaction, we will motivate typical forms of W for solid-state systems.

2.8.1 The non-local exchange self-energy

Let us first apply the GW approximation for the static, short-ranged (but still non-local!) Yukawa interaction from (46): $W(q) = \frac{e^2}{\epsilon_0}\frac{1}{q^2+q_{\mathrm{TF}}^2}$. For the sake of simplicity, we restrict the evaluation to one spatial dimension, set $T{=}0$, and assume a free-electron dispersion $\varepsilon_k = (\hbar k)^2/(2m)$ filled to the Fermi vector k_F. Then, an evaluation of the GW diagram is elementary, and yields

$$\Sigma(k) = (-1)^1(-1)^0 \sum_q \frac{1}{\beta}\sum_{n'} G^0(k{-}q, i\omega_{n'}) W(q) \tag{50}$$

$$= -\sum_q f(\varepsilon_{k-q}) W(q) \ = \ -\sum_{k'} \underbrace{f(\varepsilon_{k'})}_{\overset{T=0}{=}\theta(\varepsilon_{k_F}-\varepsilon_{k'})} W(k{-}k') \tag{51}$$

$$= -\frac{e^2}{\epsilon_0}\int_0^{k_F} dk' \, \frac{1}{(k{-}k')^2 + q_{\mathrm{TF}}^2} = \frac{e^2}{\epsilon_0 q_{\mathrm{TF}}}\left(\arctan\Big(\frac{k{-}k_F}{q_{\mathrm{TF}}}\Big) - \arctan\Big(\frac{k}{q_{\mathrm{TF}}}\Big)\right). \tag{52}$$

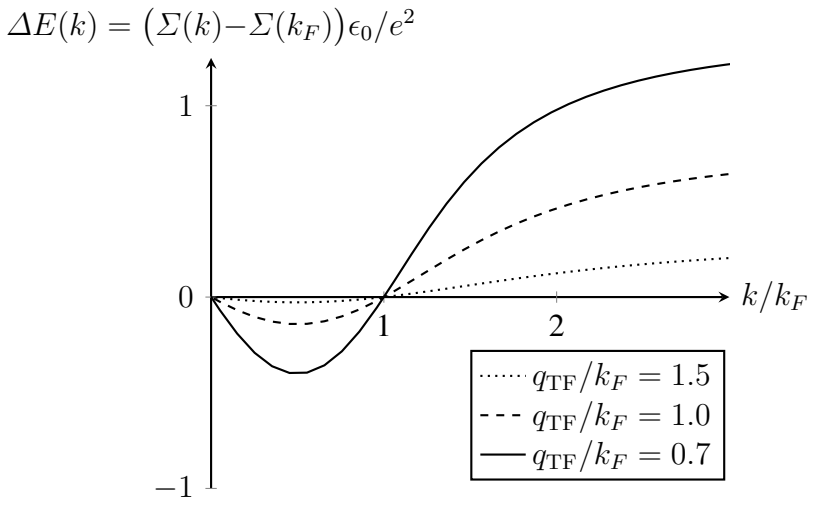


Fig. 5: *Momentum-dependence of the (toy-model's) exchange self-energy. Considering the renormalized energies, $\varepsilon_k \to \varepsilon_k + \Sigma(k)$, occupied states ($k < k_F$) are pushed down relatively to empty states ($k > k_F$), increasing the bandwidth or band-gap. Note: To conserve the particle number, the chemical potential has to adapt, e.g., in a coherent metal at $T{=}0$: $\mu \to \mu + \Sigma(k_F)$, which, here, we chose at the origin of energies.*

This self-energy, plotted in Figure 5, modifies the bare excitations ε_k in a way that is very different for occupied ($k/k_F < 1$) and for empty ($k/k_F > 1$) states. Indeed, in an effective dispersion, $\varepsilon_k \to \varepsilon_k + \Delta E(k)$, with $\Delta E(k) = \Sigma(k) - \Sigma(k_F)$, the former are pushed down, the latter are pushed upwards. Note that we added a chemical potential shift $\Sigma(k_F)$ to ΔE to assure conservation of particles (at $T{=}0$). This pulling away of states from the Fermi level enhances the bandwidth in a metal or the band-gap in a semiconductor.
This simplistic example highlights a crucial merit of the GW approximation, namely the non-local exchange contribution to the self-energy. Most notably, band gaps in semiconductors, such as Si or GaAs come out far too small in density-functional-based electronic structure methods. Through the mechanism illustrated here, the numerically more expensive GW approximation instead yields significantly larger and more accurate values for band gaps. This increase in kinetic energy (or band-gap) renders the system less correlated.

2.8.2 Self-energy from a dynamically screened interaction W

Screening is a dynamical process. Hence, the Lindhard function for χ^0, Eq. (32), the RPA susceptibility χ, Eq. (10), and the screened interaction W, Eq. (11), typically have a notable frequency dependence. A phenomenological form for the RPA screened interaction is[7]

$$W(\omega) = V + (V{-}U)\,\frac{\omega_p}{2}\left(\frac{1}{\omega{-}\omega_p + i0^+} - \frac{1}{\omega{+}\omega_p + i0^+}\right) = V + W_c(\omega) \tag{53}$$

[7]Note that the given $W(\omega)$ is the time-ordered version of the interaction, with which we could build Feynman diagrams with real frequencies. The relation to the retarded interaction $W^{\rm ret}(\omega)$ is $\mathrm{Re}\,W^{\rm ret}(\omega) = \mathrm{Re}\,W(\omega)$ and $\mathrm{Im}\,W^{ret}(\omega) = \mathrm{sgn}(\omega)\,\mathrm{Im}\,W(\omega)$.

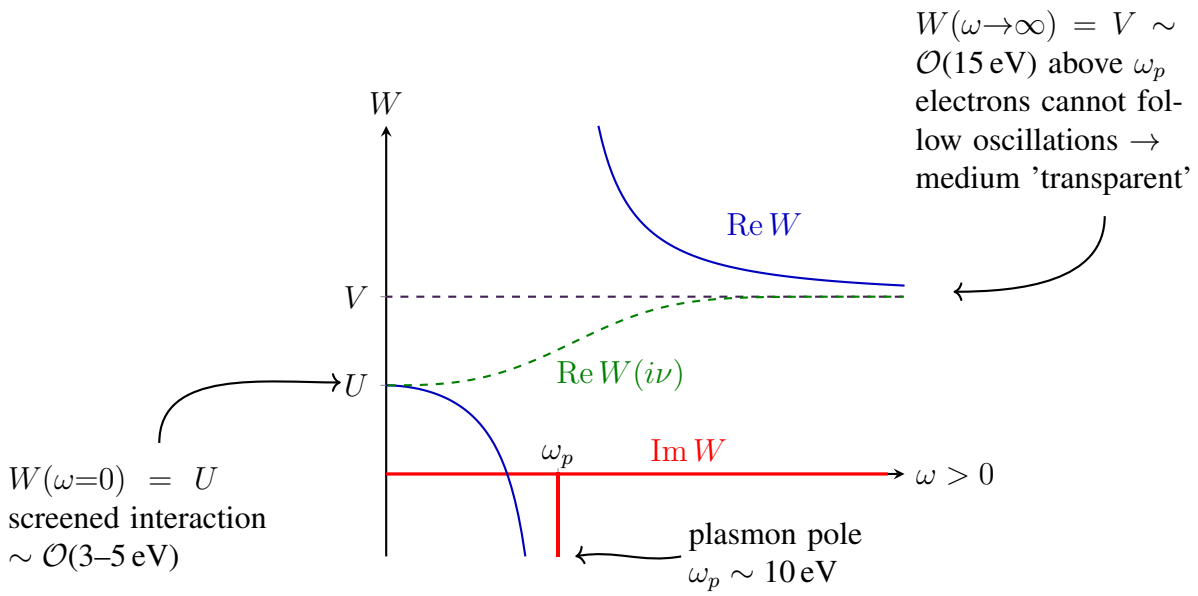


Fig. 6: *Phenomenological form of the frequency dependence of the RPA-screened interaction $W(\omega)$ on the real-axis. Also shown is the Matsubara counterpart $W(i\nu)$ which is purely real.*

that is illustrated in Figure 6: At large frequencies, screening is ineffective and the screened interaction approaches the bare Coulomb repulsion, $\text{Re}\,W(\omega{\to}\infty) \to V$. This can be understood from the electrodynamics point of view, already alluded to in Section 2.4: For frequencies above the plasma frequency ω_p, the system's electrons can no longer keep up with the fast pace of charge perturbations. The charges thus cease to mitigate the perturbation and the system becomes transparent. At the plasma frequency ω_p, which is a resonance (of the collective eigenmode) of the system, the interaction has a pole. Below ω_p, $\text{Re}\,W(\omega)$ is smaller than V and approaches a value $U < V$ in the static limit, as motivated by Thomas-Fermi theory above.

Comparing to the general form of the screened interaction in the RPA, Eq. (11), the expression above only accounts for the collective plasmon pole, not the electron-hole continuum arising from the Lindhard function. As such, it corresponds essentially to the $q \to 0$ limit for the electron gas discussed in Section 2.5. Further, in the case of a multi-band systems, inter-band transitions are neglected. Despite this limitation, Eq. (53) encodes well the overall shape of a screened interaction as computed from first principles, cf. Figures 6 and 9.
On the Matsubara axis, the dynamical part $W_c(\omega)$ of the interaction reads

$$W(i\nu) = \int d\omega \, \frac{-\frac{1}{\pi}\,\text{Im}\,W(\omega)}{i\nu - \omega} = g^2 \left(\frac{1}{i\nu - \omega_p} - \frac{1}{i\nu + \omega_p} \right) \tag{54}$$

with $g^2 = (V-U)\omega_p/2$.

Evaluation of the *GW* self-energy. Forgoing any complications of momentum-dependencies, let us assume a simplistic non-interacting electronic structure of a single level

$$H_0 = \varepsilon \sum_\sigma c_\sigma^\dagger c_\sigma \,. \tag{55}$$

Now, we have all the ingredients necessary to evaluate the GW diagram. We limit the calculation to the dynamical part of the interaction $W_c(\omega)$. Note also that, despite the name GW, the propagator in the diagram is the one of the non-interacting system, $G^0(i\omega_n)$.

$$\Sigma(i\omega_n) = -\frac{1}{\beta}\sum_{n'} G^0(i\omega_{n'})W_c(i\omega_n - i\omega_{n'}) \tag{56}$$

$$= -g^2\frac{1}{2\pi i}\oint dz \frac{f(z)}{z-\varepsilon}\left(\frac{1}{i\omega_n - z - \omega_p} - \frac{1}{i\omega_n - z + \omega_p}\right) \tag{57}$$

$$= -g^2\left(\frac{f(\varepsilon) - \overbrace{f(-\omega_p+i\omega_n)}^{-n_B(-\omega_p)\approx 1}}{i\omega_n - \varepsilon - \omega_p} - \frac{f(\varepsilon) + \overbrace{f(\omega_p+i\omega_n)}^{-n_B(+\omega_p)\approx 0}}{i\omega_n - \varepsilon + \omega_p}\right) \tag{58}$$

$$= -g^2\left(\frac{f(\varepsilon)-1}{i\omega_n - \varepsilon - \omega_p} - \frac{f(\varepsilon)}{i\omega_n - \varepsilon + \omega_p}\right). \tag{59}$$

Where we assumed $\omega_p \gg k_B T$. Let us further consider $\varepsilon \ll -1/\beta$, i.e., we require the state ε to be occupied, $f(\varepsilon) = 1$. Then the self-energy simplifies to

$$\Sigma(i\omega) = g^2\frac{1}{i\omega - \varepsilon + \omega_p} \overset{i\omega\to\omega+i0^+}{\longrightarrow} \Sigma(\omega) = g^2\frac{1}{\omega - \varepsilon + \omega_p + i0^+} \tag{60}$$

From this self-energy, we can obtain the excitation energies from the poles in the *interacting* Green function, $G(\omega) = [\omega - \varepsilon - \Sigma(\omega)]^{-1}$, i.e.,

$$\omega - \varepsilon - \mathrm{Re}\,\Sigma(\omega) \overset{!}{=} 0 \Leftrightarrow \omega - \varepsilon - \frac{g^2}{\omega - \varepsilon + \omega_p} = 0 \tag{61}$$

$$\rightarrow \omega_\pm = \varepsilon - \frac{\omega_p}{2} \pm \frac{\omega_p}{2}\sqrt{1 + \left(\frac{2g}{\omega_p}\right)^2} = \begin{cases} \varepsilon & + g^2/\omega_p \\ \varepsilon - \omega_p & - g^2/\omega_p \end{cases} + \mathcal{O}(g^4) \tag{62}$$

Hence, there are *two* peaks in the GW spectral function: ω_+ corresponds to the quasi-particle peak that shifts from its original position $\varepsilon < 0$ towards the Fermi level. In a solid with dispersive bands, this would correspond to a bandwidth narrowing. The other pole, ω_-, which for $g \ll \omega_p$ is at a distance of ω_p below the quasi-particle peak is the signature of the plasmon excitation encoded in $W(\omega)$.

The screened interaction thus causes a transfer of spectral weight from the quasi-particle peak to a plasmon satellite. We can estimate the transferred weight from the self-energy, akin to what is done in Fermi liquid theory. Indeed, assuming a form $\Sigma(\omega) = \Sigma(\omega{=}0) + (1 - \frac{1}{Z})\omega + \mathcal{O}(\omega^2)$ leads to a Green function $G(\omega) = \frac{1}{\omega - \varepsilon - \Sigma(\omega)} = \frac{Z}{\omega - Z(\varepsilon + \Sigma(0))} + G_{\mathrm{inc}}(\omega)$, where we have separated out incoherent contributions from higher energies into G_{inc}. Obtaining the quasi-particle weight Z from the derivative of the GW self-energy, we find[8]

$$Z = \left(1 - \frac{\partial\,\mathrm{Re}\,\Sigma}{\partial\omega}\right)^{-1}_{\omega=\varepsilon} = \left(1 + \frac{g^2}{(\omega_p - \varepsilon)^2}\right)^{-1} < 1 \tag{63}$$

[8] Alternatively, we could linearize around the bare level ε or the pole ω_+ instead of the Fermi level.

We see that spectral weight transfers, of magnitude $1-Z$, to the plasmon satellite that reduce the quasi-particle weight are large for states close to the Fermi level (small $|\varepsilon|$; $\varepsilon < 0$), large plasma frequency (ω_p; because $g^2 = (V-U)\omega_p/2$), and large screening effects (large $V-U$).[9]

The above two models illustrate the principal merits of the GW approximation:

1. the inclusion of momentum-dependent exchange contributions (that widen bandwidths) arising from non-local interactions

2. dynamical contributions (that cause bandwidth narrowing and satellite spectral features) originating from dynamical/retarded screening effects linked to the physics of plasmons.

3 The constrained RPA (cRPA)

For simulations of strongly correlated materials methodologies based on density-functional theory or the GW approximation are often insufficient. For example, the Mott transition and Kondo physics involve orbitals, typically from $3d$ and $4f$ shells, whose radial extent is small enough to reduce bandwidths to an extent that makes them comparable to the energy scale set by the Coulomb interaction. Then, interactions are no longer a perturbation to the almost-free electron picture and more sophisticated techniques have to be used. However, correlation effects are pronounced only for partially-filled orbitals that live close to the Fermi level. Further, higher-level many-body techniques commonly have an unfavorable scaling with the number of orbitals they can handle. Physics and methodological limitations thus suggest the use of effective setups that focus on a limited number of low-energy excitations. Identifying (or assuming) strong *local* interactions as dominating the physics allows for a further reduction of complexity, and, more often than not, the material problem is cast into the form of a multi-orbital Hubbard model. It is the workflow for this setting that we will describe in the following.

The overall goal is to devise a low-energy, few-orbital Hamiltonian that, when solved exactly, yields the same result for the degrees of freedom it contains as the exact solution of the initial full Hamiltonian of the solid [13]. Needless to say that exact solutions of neither the full nor the effective system are actually obtainable. The motivation is that for the model with less degrees of freedom, one could afford applying a more accurate methodology than would be possible for the initial Hamiltonian. A procedure that has become common practice is to seek the one-particle part of the desired low-energy Hamiltonian and its interaction terms *separately*.

[9] Clearly, the GW approximation is not exact. Thus, the question arises of how reliable it is. Incidentally, the electron-boson model, consisting of a spin-less level ε with the interaction $W(\omega)$ given, is exactly solvable [12]. The gist is that GW does well for the quasi-particle peak, $\omega_+^{\rm exact} = \varepsilon + g^2/\omega_p$ and $Z^{\rm exact} = e^{-(g/\omega_p)^2} = 1 - g^2/\omega_p^2 + g^4/(2\omega_p^4) + \ldots$, while the exact solution has infinitely many (instead of just one) plasmon satellites at $\omega_n^{\rm exact} = \varepsilon + g^2/\omega_p - n \times \omega_p$.

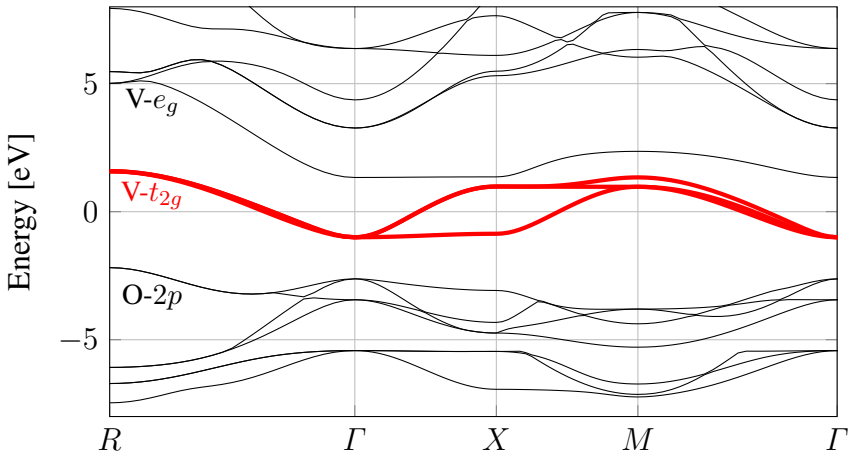


Fig. 7: *Band-structure of $SrVO_3$. DFT results (black) are overlaid with the bands of the maximally localized Wannier Hamiltonian for the vanadium t_{2g} orbitals (red). The Fermi level corresponds to the origin of energy.*

3.1 The one-particle part of the effective low-energy Hamiltonian

The starting point is a one-particle band-structure, e.g., obtained from density-functional theory-based approaches,[10] like the one shown in Figure 7 for the transition-metal oxide $SrVO_3$ or the sketch in Figure 8. We then identify a subset of bands (or an energy range) around the Fermi level that we believe to host the physics we wish to describe (e.g., the bands marked in red). We now interpret the dispersions of this target low-energy subspace as the one-particle ingredient to the interacting Hamiltonian that we seek. The assumption here is that DFT does not at all account for the physics that is to emerge from the interactions that we will supplement the dispersions with. Since the Kohn-Sham spectrum is a set of one-particle dispersions, the system's action is Gaussian and all undesired states can be integrated out. This procedure leads to a dynamical (or retarded) effective action for the small number of chosen states. A (static) Hamiltonian whose spectrum reproduces these low-energy dispersions can still be constructed through a linearization of this effective action, using or expanding on the idea of Löwdin downfolding [14]. A more elegant alternative is the use of (maximally localized) Wannier functions [15]. These functions, $\langle \mathbf{r}|\mathbf{R}L\rangle = \varphi_{\mathbf{R}L}(\mathbf{r})$, localized in a unit-cell R at the position of the atom hosting orbital L, are constructed from a subset of Bloch (or Kohn-Sham) states, $\psi_{\mathbf{k}n}(\mathbf{r})$ via a unitary transformation

$$\varphi_{\mathbf{R}L}(\mathbf{r}) = \frac{V}{2\pi}\int_{\mathrm{BZ}} d^3k\, e^{-i\mathbf{k}\mathbf{R}} \sum_n U^{(\mathbf{k})}_{nL}\psi_{\mathbf{k}n}(\mathbf{r}). \tag{64}$$

Essentially, Wannier orbitals are Fourier transforms of the Bloch eigenfunctions. However, (gauge) freedom allows for a unitary mixing instead of a mere 1-band (n) to 1-orbital (L) correspondence.[11] In maximally localized Wannier functions, this unitary ambiguity is used

[10] Although we remember that there is no actual justification for interpreting the auxiliary Kohn-Sham spectrum as the excitation energies of our system, empirically this works rather well.

[11] Complications may arise if the eliminated "high-energy" bands overlap or cross the low-energy sector. However, also for these situation a disentangling is possible, for details see Ref. [15].

to localize the Wannier function through minimization of the radial extent

$$\Omega = \sum_L \left(\langle \mathbf{R}L | \, \hat{\mathbf{R}}^2 \, | \mathbf{R}L \rangle - \left| \langle \mathbf{R}L | \, \hat{\mathbf{R}} \, | \mathbf{R}L \rangle \right|^2 \right), \tag{65}$$

where $\hat{\mathbf{R}}$ is the position operator. The Wannier orbitals are then used to construct the low-energy Hamiltonian, e.g., in real-space

$$H^0_{LL'}(\mathbf{R}) = \sum_{\mathbf{k}n} \varepsilon_{\mathbf{k}n} \, \langle \mathbf{0}L | \varphi_{\mathbf{k}n} \rangle \, \langle \varphi_{\mathbf{k}n} | \mathbf{R}L' \rangle = \sum_{\mathbf{k}} e^{-i\mathbf{k}\mathbf{R}} \left(U^{(\mathbf{k})^\dagger} \, \mathrm{diag}(\cdots \varepsilon_{\mathbf{k}n} \cdots) \, U^{(\mathbf{k})} \right)_{LL'} \tag{66}$$

As an example, we will discuss the transition-metal oxide $SrVO_3$. Strontium vanadate is a perfectly cubic perovskite in which Sr atoms sit at the corners of the cube, the V atom in the center and the O atoms at the face centers. The vanadium atom is thus surrounded by an oxygen octahedron, which causes a crystal-field that splits the V-$3d$ states into a low-lying t_{2g} triplet and a higher e_g doublet. With a nominal oxidation state of V^{4+}, the t_{2g} states are nominally filled with one electron. This partial filling places the t_{2g} states directly at the Fermi level, as can be seen in the DFT band-structure depicted in Figure 7. In the following, we shall be interested in constructing a low-energy model that solely comprises said t_{2g} states. If we were interested in the material's optical properties, say in the visual range, $\mathcal{O}$(1.6–3.3 eV), a setup that includes, at least, the O-$2p$ states and the V-e_g would be advisable.

Performing a Wannier projection onto the t_{2g} states provides us with the one-particle Hamiltonian, $H^0_{LL'}(\mathbf{k}) = \sum_{\mathbf{k}} \exp(i\mathbf{k}\mathbf{R}) H^0_{LL'}(\mathbf{R})$. Its eigenvalues trace the dispersion of the three t_{2g}-derived bands, as indicated by the red lines in Figure 7.

3.2 Interactions in the effective low-energy model

To compute the interacting part of the effective Hamiltonian, we need to account for the screening of all the states that we have eliminated. However, we do not want the *fully screened* interaction W that we have talked about before. We are seeking the *bare* interaction U of the effective Hamiltonian that describes the low-energy subspace. Indeed, maybe we want to perform perturbation theory in U or compute susceptibilities with beyond-RPA methods. So, the idea is to *constrain* the contributions to screening by eliminating all particle-hole transitions that occur within the target subspace, as detailed in (the caption of) Figure 8. This idea was pioneered by Ferdi Aryasetiawan *et al.* in Ref. [2][12] and is nowadays known as the *constrained random phase approximation (cRPA)*.

One thus separates the Lindhard function, Eq. (33), according to the start and end points of the particle-hole transitions into $\chi^0 = \chi^{0,\mathrm{high}} + \chi^{0,\mathrm{low}}$, where $\chi^{0,\mathrm{low}}$ contains all transitions that are confined to the low-energy subspace (red in Figure 8), and $\chi^{0,\mathrm{high}}$ all others. Then, we can define the *partially* screened interaction as

$$U(\mathbf{q},\omega) = \frac{V(\mathbf{q})}{1 + V(\mathbf{q}) \chi^{0,\mathrm{high}}(\mathbf{q},\omega)}, \tag{67}$$

[12] Worth mentioning are the some prequels [16, 17] and the sequel [18].

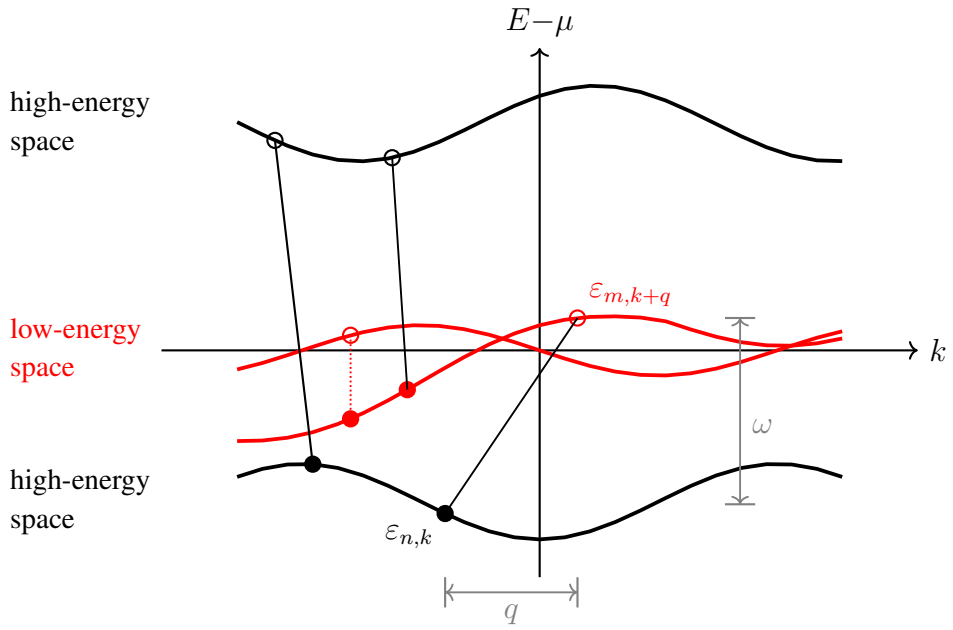


Fig. 8: *Contributions to the Lindhard function. The RPA employs as building block the free susceptibility, $\chi_0(\mathbf{q},\omega\geq 0)$, which sums up all possible transitions between (at $T=0$ occupied) states $\varepsilon_{n,k}$ and (empty) states $\varepsilon_{m,k+q}$. In cRPA, the band-structure is separated into high-energy (black) and low-energy (red) dispersions: We wish to eliminate the former, while the latter forms the one-particle ingredient to the effective Hamiltonian that we seek. To obtain an effective interaction for the low-energy subspace of orbital or bands, we constrain the contributing transitions to those that occur within the high-energy subspace, as well as transitions between the high-energy and the low-energy space. Examples for such transitions are indicated by solid black lines that connect an occupied state (solid circle) with an empty state (open circle). In other words, contributions to the screening that arise from transitions within the low-energy space are omitted. An example for such a transition is indicated by the red dotted line.*

and it is elementary to show that, when screening further, with $\chi^{0,\mathrm{low}}$, we recover the fully screened $W(\mathbf{q},\omega)=U(\mathbf{q},\omega)/(1+U(\mathbf{q},\omega)\chi^{0,\mathrm{low}}(\mathbf{q},\omega))$. To match up the interactions to the one-particle Hamiltonian, we transform the former into the Wannier basis [19],

$$V_{LL'}(\mathbf{R})=\langle L\mathbf{0},L'\mathbf{R}|\,V(\hat{\mathbf{R}})\,|L\mathbf{0},L'\mathbf{R}\rangle=e^2\int d^3r\int d^3r'\,\frac{|\varphi_{L\mathbf{0}}(\mathbf{r})|^2|\varphi_{L'\mathbf{R}}(\mathbf{r}')|^2}{|\mathbf{r}-\mathbf{r}'|} \tag{68}$$

$$U_{LL'}(\mathbf{R},\omega)=\int d^3r\int d^3r'\,|\varphi_{L\mathbf{0}}(\mathbf{r})|^2\left(\int d^3q\,e^{-i\mathbf{q}(\mathbf{r}-\mathbf{r}')}U(\mathbf{q},\omega)\right)|\varphi_{L'\mathbf{R}}(\mathbf{r}')|^2 \tag{69}$$

where, for simplicity, we limited ourselves to density-density type of interactions, $\propto n_{\mathbf{0}L}n_{\mathbf{R}L'}$. For $SrVO_3$, Figure 9 displays the resulting local ($\mathbf{R}$=0), intra-orbital ($L=L'\in\{1,2,3\}$; the t_{2g} are degenerate) interaction matrix elements in the Wannier basis: the bare interaction $V\in\mathbb{R}$, the partially screened cRPA Hubbard $U(\omega)$ and the fully screened RPA $W(\omega)$, where the latter two are complex at finite frequency. Looking at the static ($\omega=0$) limits, we see that screening with all electrons reduced the bare Coulomb interaction, $V=16.1\,\mathrm{eV}$, by more than one order of magnitude, to $W(0)=0.9\,\mathrm{eV}$. The effective interaction for the t_{2g} setup is still sizeable, $U(0)=3.5\,\mathrm{eV}$. From the inter-orbital matrix elements, we can further extract a Hund's rule coupling $J(\omega{=}0)=0.6\,\mathrm{eV}$.

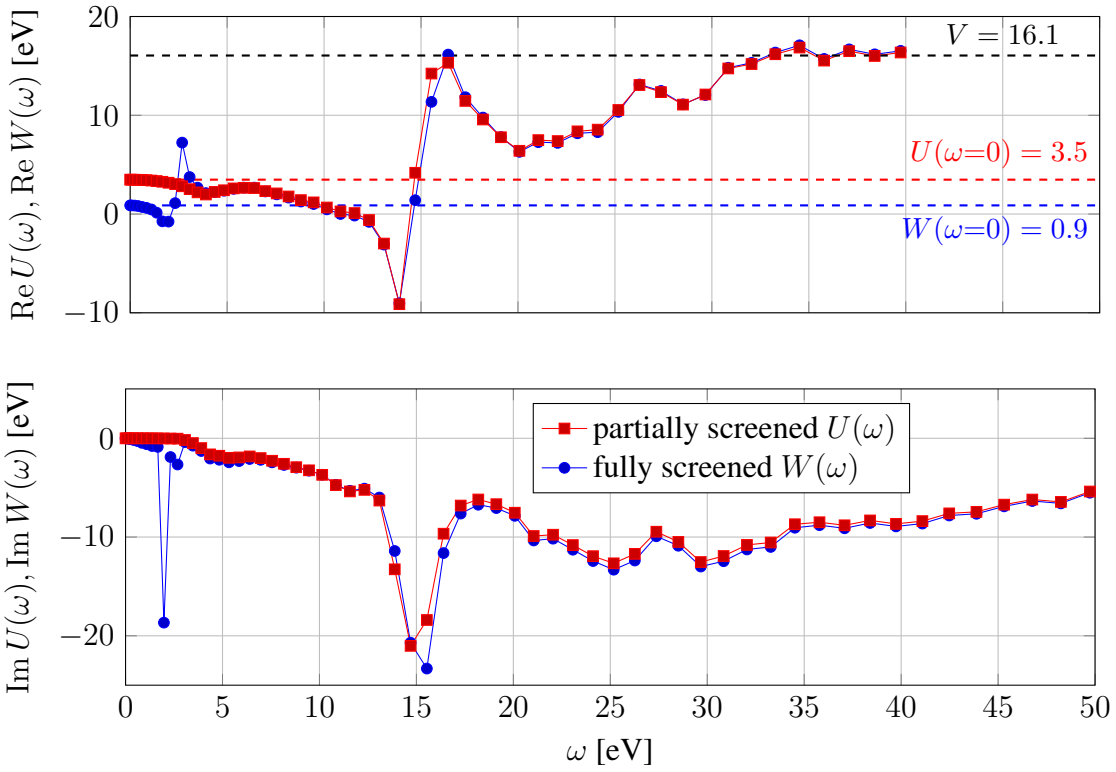


Fig. 9: *Local interactions of the t_{2g} orbitals of $SrVO_3$: the bare Coulomb interaction V (black dashed line; top panel), the RPA fully screened interaction $W(\omega)$ (blue circles; real (imaginary) part in top (bottom) panel); the cRPA partially screened Hubbard interaction $U(\omega)$ (red squares). All interactions refer to the on-site density-density intra-orbital matrix element in the t_{2g}-derived maximally localized Wannier basis. Increased screening contributions lead to the hierarchy $W(\omega{=}0) < U(\omega{=}0) < V$.*

The frequency dependence of U and W shares elements with the phenomenological plasmon-pole interaction shown in Figure 6: On top of a particle-hole background, we see in $U(\omega)$ [$W(\omega)$] one [two] plasmon resonances. The dominant one at $\omega \approx 15\,\mathrm{eV}$ corresponds to plasma oscillations that do not involve the V-$3d$ orbitals. This is corroborated by the fact that, electron-energy loss spectra (EELS: $\mathrm{Im}\,\epsilon^{-1}(\omega)$) of $SrTiO_3$ that nominally has one d-electron less, thus none at all, find a peak at the same frequency [20]. Instead, the low-energy plasma feature in $W(\omega{\approx}2\,\mathrm{eV})$ must derive from oscillations of the t_{2g} charge, as it is absent in $U(\omega)$ in which t_{2g} transitions are omitted.

This concludes our brief description of the setting up of the cRPA-based effective low-energy model, consisting of the one-particle Hamiltonian $H^0_{LL'}(\mathbf{k})$ and the interaction $U_{LL'}(\omega)$.

3.3 Caveats to how cRPA results are typically used

Here, we will not discuss critiques of the cRPA procedure outlined above, of which there are a few [21–23]. Rather, we will briefly point out deficiencies and skeletons in the closet in the way cRPA results are commonly used in, say, realistic dynamical mean-field theory (DFT+DMFT) calculations.

Dynamical interactions. Typically, DFT+DMFT simulations are performed with static interactions U instead of dynamical $U(\omega)$ ones. One might not have access to an *ab initio* computed $U(\omega)$. Also, impurity solvers that can work with retarded interactions are far less common and more expensive. A frequent procedure then is to simply use the cRPA interaction in the static limit $U(\omega{=}0)$, in the case of $SrVO_3$, $U(\omega{=}0) = 3.5\,\text{eV}$. However, it turns out that this interaction generates a mass enhancement far too small for simulations to match photoemission and specific-heat measurements. So, in various studies, the "solution" was to ramp up the interaction, in the case of $SrVO_3$, to $U = 5.0\,\text{eV}$ and mumble something about cRPA overestimating screening. Then, for $SrVO_3$, the effective mass enhancement, $m^*/m = Z^{-1} \approx 2$, comes out nicely indeed. Using the fictitiously enhanced U, half of the quasi-particle weight ($Z \approx 1/2$) is transferred to the *Hubbard bands* (cf. the chapters on DMFT in this book). But is this really the correct physics? In the GW model calculation in Section 2.8.2, we saw that a dynamical interaction (with a plasmon pole) caused a finite Z factor, Eq. (63), with spectral weight transferred to a *plasmon satellite*. Instead of artificially inflating the static U, could the plasmon peak or, generally, the frequency-dependence in $U(\omega)$ supply the missing mass-enhancement? Casula *et al.* [24], performing DFT+DMFT calculations with the *ab initio* $U(\omega)$ from Figure 9, answered this in the affirmative: They found the correct mass-enhancement as well has a lower Hubbard band in better agreement with experiment.

Non-local interactions. So, are DFT+DMFT calculations with $U(\omega)$ the ultimate answer? Reality turns out to be more complicated. While the occupied part of the spectrum (accessible from photoemission) comes out well for $SrVO_3$ using $U(\omega)$, an analysis [25] of the empty states suggests features are too close to the Fermi level. This time, the model calculation in Section 2.8.1 comes to the rescue: While screening reduces the range of the bare Coulomb interaction, the effective interaction experienced by the t_{2g} states is not strictly local (Hubbard-like). Then, a screened exchange contribution to the self-energy will widen the bandwidth, cf. Figure 5. With nominally 5/6 of the t_{2g} states being unoccupied, the anticipated increase in bandwidth will mostly be seen above the Fermi level. This insight is confirmed by GW [26] and so-called GW+DMFT calculations [27] for $SrVO_3$ [25, 28–33]. GW+DMFT combines the merits of both, GW (non-local exchange self-energy) and DMFT (dynamical local correlations).[13] From this vantage point, a provocative statement suggests itself [25]: The fact that DFT+DMFT calculations using $U(\omega{=}0)$ quite often do yield good results is owing to an error cancellation, the joint omission of mass renormalization from a dynamical $U(\omega)$ ($\rightarrow$ bandwidth narrowing) and non-local exchange contributions to the self-energy ($\rightarrow$ bandwidth widening).

One does not fit all. When applying many-body methods, such as DMFT, to materials, great care is taken to make the non-interacting part of the Hamiltonian as realistic as possible. Since correlations typically amplify any sort of polarization, it is indeed important to know whether,

[13] Note that a frequency-dependent local interaction can also be generated when treating non-local, say, nearest-neighbor interactions in the context of extended DMFT (EDMFT). For an instructive example using GW+(E)DMFT, see Ref. [34].

say, the t_{2g} orbitals in a transition-metal oxide are degenerate (as in metallic $SrVO_3$) or not (as in Mott-insulating $YTiO_3$) [35, 36]. Besides structural distortions in the bulk, also geometric constraints like a surface can lift degeneracies. For instance, in ultra-thin films of $SrVO_3$, this leads to a Mott-insulating state [37, 38] and a rich, orbital-physics driven phase diagram under doping [39].

The theoretical works cited in the preceding paragraph all used a static Hubbard U in their DMFT calculations. The additional caveat to mention here is that the *same* interaction was applied to all the (t_{2g}) orbitals. This is common practice. However, the Wannier functions, including their localization (Ω in Eq. (65)), will not be the same. Thus, already the matrix element of the bare interaction, V in Eq. (68), will differ from orbital to orbital. On top, the screening will be orbital-dependent as well. These differences in the interactions may enhance the degeneracy lifting in the non-interacting Hamiltonian. Or they could mitigate it.

The challenging truth is that correlated materials are extremely sensitive to minute details and trends are difficult to predict without explicit calculations. For instance, the dependence of the Hubbard U on external pressure or strain is highly-non-universal [40]: In the cuprate Bi_2CuO_4 pressure decreases U [41], while it goes up when straining La_2CuO_4 [42]. The fact that we are able to point this out is actually a sign of the field maturing. With methods such as the cRPA being available in more and more of the leading electronic structure packages, we are handed the tools for more realism and, hopefully, more quantitative predictions.

Acknowledgements

The author is indebted to Ferdi Aryasetiawan and Takashi Miyake who taught him the ropes of, among others, cRPA. Part of Section 2 derive from a chapter that the author wrote for the “Quantum field theory for many-body systems” course at TU Wien. Comments from my co-lecturers Karsten Held, Alessandro Toschi, and Anna Kauch are gratefully acknowledged. Special thanks go to Felix Höfenstock who in 2023 expertly turned my hand-written notes into LaTeX.

References

[1] P.W. Anderson, Science **177**, 393 (1972)

[2] F. Aryasetiawan, M. Imada, A. Georges, G. Kotliar, S. Biermann, and A.I. Lichtenstein, Phys. Rev. B **70**, 195104 (2004)

[3] F. Aryasetiawan, T. Miyake, and R. Sakuma in E. Pavarini, E. Koch, D. Vollhardt and A.I. Lichtenstein (eds.): *The LDA+DMFT approach to strongly correlated materials*, Modeling and Simulation, Vol. 1 (Forschungszentrum Jülich, 2011)

[4] F. Aryasetiawan in E. Pavarini, E. Koch, A. Lichtenstein, and D. Vollhardt (eds.): *DMFT: From Infinite Dimensions to Real Materials* Modeling and Simulation, Vol. 8 (Forschungszentrum Jülich, 2018)

[5] P. Werner and M. Casula, J. Phys.: Condens. Matter **28**, 383001 (2016)

[6] S. Biermann, J. Phys.: Condens. Matter **26**, 173202 (2014)

[7] W. Nolting: *Theoretical Physics 9: Fundamentals of Many-body Physics* (Springer, 2018)

[8] P. Coleman: *Introduction to Many-Body Physics* (Cambridge University Press, 2015)

[9] A. vom Felde, J. Sprösser-Prou, and J. Fink, Phys. Rev. B **40**, 10181 (1989)

[10] F. Aryasetiawan and O. Gunnarsson, **61**, 237 (1998)

[11] G. Onida, L. Reining, and A. Rubio, Rev. Mod. Phys. **74**, 601 (2002)

[12] D.C. Langreth, Phys. Rev. B **1**, 471 (1970)

[13] Y. Chang, E.G.C.P. van Loon, B. Eskridge, B. Busemeyer, M.A. Morales, C.E. Dreyer, A.J. Millis, S. Zhang, T.O. Wehling, L.K. Wagner, and M. Rösner, npj Comp. Mater. **10**, 129 (2024)

[14] P.-O. Löwdin, J. Chem. Phys. **19**, 1396 (1951)

[15] N. Marzari, A.A. Mostofi, J.R. Yates, I. Souza, and D. Vanderbilt, Rev. Mod. Phys. **84**, 1419 (2012)

[16] M. Springer and F. Aryasetiawan, Phys. Rev. B **57**, 4364 (1998)

[17] T. Kotani, J. Phys.: Condens. Matter **12**, 2413 (2000)

[18] F. Aryasetiawan, K. Karlsson, O. Jepsen, and U. Schönberger, Phys. Rev. B **74**, 125106 (2006)

[19] T. Miyake and F. Aryasetiawan, Phys. Rev. B **77**, 085122 (2008)

[20] S. Kohiki, M. Arai, H. Yoshikawa, S. Fukushima, M. Oku, and Y. Waseda, Phys. Rev. B **62**, 7964 (2000)

[21] Y. Nomura, M. Kaltak, K. Nakamura, C. Taranto, S. Sakai, A. Toschi, R. Arita, K. Held, G. Kresse, and M. Imada, Phys. Rev. B **86**, 085117 (2012)

[22] M. Kinza and C. Honerkamp, Phys. Rev. B **92**, 045113 (2015)

[23] E.G.C.P. van Loon, M. Rösner, M.I. Katsnelson, and T.O. Wehling, Phys. Rev. B **104**, 045134 (2021)

[24] M. Casula, A. Rubtsov, and S. Biermann, Phys. Rev. B **85**, 035115 (2012)

[25] J.M. Tomczak, M. Casula, T. Miyake, and S. Biermann, Phys. Rev. B **90**, 165138 (2014)

[26] T. Miyake, C. Martins, R. Sakuma, and F. Aryasetiawan, Phys. Rev. B **87**, 115110 (2013)

[27] S. Biermann, F. Aryasetiawan, and A. Georges, Phys. Rev. Lett. **90**, 086402 (2003)

[28] J.M. Tomczak, M. Casula, T. Miyake, F. Aryasetiawan, and S. Biermann, **100**, 67001 (2012)

[29] C. Taranto, M. Kaltak, N. Parragh, G. Sangiovanni, G. Kresse, A. Toschi, and K. Held, Phys. Rev. B **88**, 165119 (2013)

[30] R. Sakuma, P. Werner, and F. Aryasetiawan, Phys. Rev. B **88**, 235110 (2013)

[31] L. Boehnke, F. Nilsson, F. Aryasetiawan, and P. Werner, Phys. Rev. B **94**, 201106 (2016)

[32] J.M. Tomczak, P. Liu, A. Toschi, G. Kresse, and K. Held, Europ. Phys. J. Spec. Top. **226**, 2565 (2017)

[33] F. Nilsson, L. Boehnke, P. Werner, and F. Aryasetiawan, Phys. Rev. Mater. **1**, 043803 (2017)

[34] P. Hansmann, T. Ayral, L. Vaugier, P. Werner, and S. Biermann, Phys. Rev. Lett. **110**, 166401 (2013)

[35] E. Pavarini, S. Biermann, A. Poteryaev, A.I. Lichtenstein, A. Georges, and O.K. Andersen, Phys. Rev. Lett. **92**, 176403 (2004)

[36] E. Pavarini, A. Yamasaki, J. Nuss, and O.K. Andersen, New J. Phys. **7**, 188 (2005)

[37] K. Yoshimatsu, T. Okabe, H. Kumigashira, S. Okamoto, S. Aizaki, A. Fujimori, and M. Oshima, Phys. Rev. Lett. **104**, 147601 (2010)

[38] Z. Zhong, M. Wallerberger, J.M. Tomczak, C. Taranto, N. Parragh, A. Toschi, G. Sangiovanni, and K. Held, Phys. Rev. Lett. **114**, 246401 (2015)

[39] M. Pickem, J. Kaufmann, K. Held, and J.M. Tomczak, Phys. Rev. B **104**, 024307 (2021)

[40] J.M. Tomczak, T. Miyake, R. Sakuma, and F. Aryasetiawan, **79**, 235133 (2009)

[41] D. Di Sante, A. Hausoel, P. Barone, J.M. Tomczak, G. Sangiovanni, and R. Thomale, Phys. Rev. B **96**, 121106 (2017)

[42] O. Ivashko, M. Horio, W. Wan, N.B. Christensen, D.E. McNally, E. Paris, Y. Tseng, N.E. Shaik, H.M. Rønnow, H.I. Wei, C. Adamo, C. Lichtensteiger, M. Gibert, M.R. Beasley, K.M. Shen, J.M. Tomczak, T. Schmitt, and J. Chang, Nat. Commun. **10**, 786 (2019)

8 Dynamical Mean-Field Theory for Correlated Electrons with Disorder

Krzysztof Byczuk
Institute of Theoretical Physics, University of Warsaw
Pasteura 5, 02-093 Warszawa, Poland

Contents

1 Introduction **2**

2 Disordered systems, random variables, averages **3**
2.1 Models of disorder electrons 3
2.2 Average over disorder, most probable value 4
2.3 Generalized mean 5

3 Real-space dynamical mean-field theory **6**

4 Averaged DMFT **8**

5 DMFT and CPA **9**
5.1 CPA for non-interacting systems 9
5.2 Binary alloys and alloy band splitting 10
5.3 Mott-Hubbard transition at fractional filling in the binary alloy disordered Hubbard model 10
5.4 Ferromagnetism in the binary alloy disordered Hubbard model; disorder-induced enhancement of the Curie temperature 12

6 DMFT and TMT **14**
6.1 Typical medium theory for Anderson localization 14
6.2 Anderson localization in disordered Hubbard and Falicov-Kimball models . . . 15

7 Outlook **16**

A Proof of the alloy band splitting theorem **18**

E. Pavarini, E. Koch, A. Lichtenstein, and D. Vollhardt (eds.)
Understanding Correlated Materials with DMFT
Modeling and Simulation Vol. 15
Forschungszentrum Jülich, 2025, ISBN 978-3-95806-813-1
http://www.cond-mat.de/events/correl25

1 Introduction

For a classical observer the empty space, i.e., the vacuum, is perfectly regular with perfect translational and rotational symmetry. The vacuum is homogeneous and isotropic. Inserting particles into the vacuum breaks this perfect symmetry. However, if the particles are arranged in a regular fashion, there is still some symmetry in the system. For example, in case of perfect crystals, infinitely large, there is a discrete translational and a point group symmetry. In case of a single molecule or a cluster of molecules a discrete point group symmetry might be present. In the fascinating word of quasicrystals, the infinitely large system is not translationally symmetric but a certain point group symmetry is still present. These systems are regular, predictable and often exactly tractable in a mathematical description [1]. These regularities have been an inspiration for artists and architects for centuries around the word.

If there is a regularity in the nature there must be an irregularity as well [2]. Indeed, investigating systems very often one finds irregularities in the arrangements of atoms or molecules [3]. The hardest system in the nature, a diamond, is an arrangement of carbon atoms in a cube repeated infinitely many times in space. The perfect diamond is transparent and colorless insulator. If some randomly chosen carbons are replaced by nitrogens the diamond becomes a conductor, and is used in electronics, e.g., in transistors. When randomly substituting boron atoms for carbons a diamond becomes blueish but randomly deforming the perfect bond structure makes the crystal reddish. These defects in a diamond are welcome, making the crystal more rare and more visually intriguing and increase its price on the stock as well.

Irregularities are typically unrepeatable. But are present in most real physical systems. Their presence changes properties of the systems, sometimes along our intention but sometimes against it. As theoretical physicists we want to learn how to describe irregular systems mathematically [4].

In this lecture notes we will focus on some narrow aspects of irregular systems, namely on correlated electron (fermion) systems, and present how to combine the well know **dynamical mean-field theory** (DMFT) with mathematical theories tackling randomness. We start with defining various types of disordered systems on a model level within tight-binding approximations and discuss mathematical/statistical tools to describe such systems. We introduce systems with a binary disorder as well as with a continuous disorder. Both represent different situations in solid state physics. Next we will discuss a combination of the dynamical mean-field theory with the **coherent potential approximation** (CPA) for disordered systems. These are two *dynamical* mean-field type approximations to finite dimensional systems and are exact in infinite dimensions. As we will emphasize, both DMFT and CPA treats correlations and disorder on equal footing. We present two surprising results concerning the Curie temperature and the Mott-Hubbard **metal-insulator transition** (MIT) at fractional filling in the binary alloy systems. Further we will introduce the Anderson transition, a different kind of MIT triggered by randomness in the system. The DMFT is extended in such manner that the most probable realization is taken into account. This is a **typical medium theory** (TMT) which is combined with the DMFT, instead of the CPA, and predicts phase diagrams with different metallic and in-

sulating phases in correlated electron models, such as Hubbard and Falicov-Kimball ones. We will end with some short discussion of other developments where DMFT is used for disordered electrons, fermions and bosons, and comment on present approaches toward the many-body localization.

2 Disordered systems, random variables, averages

2.1 Models of disorder electrons

We shall consider model systems describing electrons moving in irregular crystals. Following the pioneering work of Anderson [5] we use the standard model, today known as the Anderson model, represented by a second-quantized Hamiltonian

$$\hat{H}_{\rm A} = \sum_{i\sigma} \varepsilon_i \, \hat{a}^\dagger_{i\sigma} \hat{a}_{i\sigma} + \sum_{ij\sigma} t_{ij} \, \hat{a}^\dagger_{i\sigma} \hat{a}_{j\sigma} \, , \tag{1}$$

where $\hat{a}_{i\sigma}$ ($\hat{a}^\dagger_{i\sigma}$) is an annihilation (creation) operator of an electron at lattice site $\mathbf{R}_i$, in a one particle Wannier basis, and with a spin $\sigma = \pm 1/2$ (in units with $\hbar$=1). Here the creation and annihilation operators obey standard anticommutation relations. The first term represents on-site energies ε_i and the second one a hopping t_{ij} of electrons between different lattice sites. It is the simplest tight-binding model describing electrons on a lattice. The interaction between electrons is absent for the moment.

For a perfectly regular uniform lattice system the on-site energies are the same on all lattice sites, i.e., $\varepsilon_i = \varepsilon$, and the hopping amplitudes t_{ij} are the same for the sites with the same distance $\|\mathbf{R}_i - \mathbf{R}_j\|$. For irregular, non-uniform systems the on-site energy may depend on the lattice site. For example, it can be a random number or it can be different but changed in a regular fashion. For example, in the presence of a uniform electric field along a one dimensional chain, the on-site energies are $\varepsilon_i = aE_0 i$, where a is a lattice constant and E_0 is an electric field intensity. In the following we are interested in cases where ε_i are random variables. Typically it is assumed that the probability distribution function factorizes and the random variables ε_i are independent

$$P(\varepsilon_1, ..., \varepsilon_{N_L}) = \prod_{i=1}^{N_L} p(\varepsilon_i), \tag{2}$$

where N_L is the number of lattice sites. In the original Anderson model [5] the hopping part was assumed to be regular. Nevertheless, one can extend the model by assuming that t_{ij} are random variables drawn from a certain probability distribution function. In the following we assume that any irregularity and randomness in the system appears due to random on-site energies ε_i.

The Anderson model (1) does not include any interaction between electrons. The simplest way to add an interaction is to write a Hubbard like Hamiltonian with the random on-site energies

$$\hat{H}_{\rm AH} = \sum_{i\sigma} \varepsilon_i \, \hat{n}_{i\sigma} + \sum_{ij\sigma} t_{ij} \, \hat{a}^\dagger_{i\sigma} \hat{a}_{j\sigma} + \sum_i U_i \, \hat{n}_{i\uparrow} \hat{n}_{i\downarrow}, \tag{3}$$

where $\hat{n}_{i\sigma} = \hat{a}^\dagger_{i\sigma}\hat{a}_{i\sigma}$ is the particle number operator and the projection of the spin is denoted by $\uparrow$ ($\downarrow$) symbols. This Anderson-Hubbard (AH) model describes itinerant electrons on a lattice and interacting when two fermions with opposite spins are occupying the same lattice site. The energy penalty $U_i > 0$ again can be a random variable, although in the Hubbard model and in the following notes it is assumed to be uniform, the same on all sites, $U_i = U$.
Another model with interacting fermions is the Falicov-Kimball one, a simplified version of the Hubbard model with particles with one spin projection immobile. The Anderson-Falicov-Kimball (AFK) Hamiltonian reads

$$\hat{H}_{\mathrm{AFK}} = \sum_i \varepsilon_i \hat{n}_i + \sum_{ij\sigma} t_{ij}\, \hat{e}^\dagger_i \hat{e}_j + \sum_i U_i\, \hat{n}_i \hat{f}^\dagger_i \hat{f}_i + \varepsilon_f \sum_i \hat{f}^\dagger_i \hat{f}_i, \tag{4}$$

where $\hat{n}_i = \hat{e}^\dagger_i \hat{e}_i$ is the particle number operator for itinerant spinless fermions and $\hat{f}_i$ ($\hat{f}^\dagger_i$) are annihilation (creation) fermion operators for immobile particles with on-site energy ε_f.

2.2 Average over disorder, most probable value

Imagine a system, described by one of the above Hamiltonian, with given and fixed on-site energies $\{\varepsilon_i\}_{i=1,\ldots,N_L}$. If we solve it exactly we can get information, for example, on thermodynamics of the system. The grand-canonical partition function $\Xi(T, N_L, \mu; \{\varepsilon_i\}) = \mathrm{Tr} e^{-\beta(\hat{H}-\mu\hat{N})}$, where μ is the chemical potential, $\beta = 1/k_B T$ is the inverse of temperature and k_B is the Boltzmann constant, will depend on particular realization of the on-site energies $\{\varepsilon_i\}$. The grand-canonical thermodynamic potential $\Omega(T, N_L, \mu; \{\varepsilon_i\}) = -k_B T \ln \Xi(T, N_L, \mu; \{\varepsilon_i\})$ and all other thermodynamic functions will be system dependent as well.
To overcome this difficulty, and to get some reliable information about the considered system we take a statistical average over $\{\varepsilon_i\}$. In most situations it is the *arithmetic average*, i.e., for an observable $O(\{\varepsilon_i\})$ we determine

$$\big\langle O(\{\varepsilon_i\})\big\rangle = \int \prod_{i=1}^{N_L} O(\{\varepsilon_i\})\, p(\varepsilon_i)\, d\varepsilon_i \tag{5}$$

according to the central limit theorem [6], for infinitely many ($N_L \to \infty$), independent random variables $\{\varepsilon_i\}$. It is a well founded approach for systems which are self-averaging. It means that the sample-to-sample fluctuations

$$\Delta_{N_L}(O) = \frac{\langle O^2\rangle - \langle O\rangle^2}{\langle O\rangle^2} \tag{6}$$

vanish when $N_L \to \infty$.
In taking an average there are two possibilities, one can take the average of the grand-canonical partition function $\big\langle \Xi(T, N_L, \mu; \{\varepsilon_i\})\big\rangle$. This situation is called an *annealed disorder*. Another option is to average a physical quantity, like the grand-canonical thermodynamic potential $\big\langle \Omega(T, N_L, \mu; \{\varepsilon_i\}\big\rangle$. This case is named a *quenched disorder* [7]. Unless it is specified otherwise, we will consider here only a quenched type of the disorder.

In nature most systems are self-averaging. Then the ergodic hypothesis is valid and we can use a standard statistical mechanics and arithmetic averaging over the disorder to study such systems in equilibrium. The early work of Anderson [5] put attention to non-ergodic systems, where the concept of statistical averaging does not hold. Anderson described the situation, where in a disordered system the one-particle wave function is localized in a finite subspace of the system. Then, in the dynamical unitary evolution, the quantum system cannot penetrate the whole phase space and cannot probe all possible disorder realizations. Such a system is named an *Anderson insulator*. The ergodic hypothesis cannot be applied and sample-to-sample fluctuations are finite even in the thermodynamic limit. To describe mathematically such non-self-averaging systems we need to focus on the *most probable values* of observables studied on them. This is a *typical* behavior of the system and the one expected to occur in practice.
The prediction of the most probable behavior is difficult. It requires the whole histogram or the whole probability distribution function for a give observable. It requires to solve the Hamiltonian for very many realization of the disorder. For noninteracting models it is demanding but possible, e.g. [8]. For interacting models in large systems it is challenging even today to get good statistics.
Therefore we take a different approach and use a different way of statistical averaging over disorder. We will use a *geometric average* which belongs to generalized means in the probability theory.

2.3 Generalized mean

Consider a single random variable y and a function $f = f(y)$, which is invertible, i.e., $f^{-1}(y)$ exists. The generalized f-mean (average) is defined as

$$\big\langle y \big\rangle_f = f^{-1}\big(\langle f(y)\rangle\big), \tag{7}$$

where the average inside is the arithmetic average $\big\langle f(y)\big\rangle = \int dy\, f(y)\, p(y)$ with the probability distribution function $p(y)$ [9]. The f-mean satisfies the usual axioms, required to hold for any useful mean in mathematics [9]. In particular, if we select $f(y) = \ln y$, such an f-mean is the geometric mean or geometric average, i.e.

$$\langle y \rangle_{\ln} = e^{\langle \ln y \rangle}. \tag{8}$$

The popular average in mathematics is the Hölder mean, where $f(y) = y^p$ and p is a number. This Hölder, or p-mean

$$\langle y \rangle_p = \left[\int dy\, y^p\, p(y) \right]^{\frac{1}{p}} \tag{9}$$

is parametrized by a single number p. Like the arithmetic mean, the Hölder mean is a homogeneous function of y and has a block property, i.e., $\langle xy \rangle_p = \langle x \rangle_p \langle y \rangle_p$ if x and y are independent random variables. In particular, if $p{=}{-}\infty$ this mean gives the possible minimum of y. Other choices, $p{=}{-}1$ gives a *harmonic mean*, $p{=}0$ gives the geometric mean, $p{=}1$ gives the arithmetic mean, $p{=}2$ gives a *quadratic mean*, and $p{=}\infty$ gives the possible maximum of y.

Which mean gives the best approximation, in particular when the disorder is very strong and drives the system far from the self-averaging limit, is a matter of investigation. For example, many biological and social processes are modeled by the log-normal probability distribution function, for which the geometric average gives the most probable value of the random variable [10, 11]. The same is also true for conductors in series with random resistances.

3 Real-space dynamical mean-field theory

The coherent potential approximation was formulated in 1960's [12], and much earlier than the dynamical mean-field theory, developed in 1990's [13]. However, there are many similarities in these two approaches and, in fact, for correlated electrons models with local disorder the CPA and the DMFT are combined within a singe theoretical approach.

A common denominator between CPA and DMFT is that both are local theories, with local self-energies, depending only on frequencies, and they are playing the roles of the mean-fields. Since they are frequency dependent, the name dynamical mean-field comes. Both theories are comprehensive, thermodynamically consistent and conserving in the Kadanoff-Baym sense [14]. Finally, both are exact in the infinite dimensional limit, or equivalently, in systems with infinite number of nearest neighbors on the lattice [15].

The derivation of the DMFT from the high dimensional perspective was discussed in the Jülich lecture series earlier [16–19] and we do not want to repeat it here. Instead, we offer a straightforward presentation how to use the DMFT for lattice systems with inhomogeneous potentials or random impurities.

The main idea hidden behind the DMFT and the CPA approaches is the mapping of a lattice system, homogeneous or inhomogeneous, onto a local impurity (site) problem, where the impurity (site) is coupled to an effective bath. This bath, like a mean-field, mimics the properties of the rest of the lattice on average.

We consider the Anderson-Hubbard model (3) now. There are various formulations, but the most canonical one and useful for our lecture is the approach where the zero-dimensional single site problem, representing the site i-th, is given by a **single-impurity Anderson model** (SIAM) with the Hamiltonian

$$\hat{H}^{(i)}_{\mathrm{SIAM}} = \varepsilon_i \sum_{\sigma} \hat{c}^{\dagger}_{i\sigma}\hat{c}_{i\sigma} + U\,\hat{c}^{\dagger}_{i\uparrow}\hat{c}_{i\uparrow}\,\hat{c}^{\dagger}_{i\downarrow}\hat{c}_{i\downarrow} + \sum_{\mathbf{k}\sigma}\left(V_{\mathbf{k}i\sigma}\,\hat{c}^{\dagger}_{i\sigma}\hat{c}_{\mathbf{k}\sigma} + V^{*}_{i\mathbf{k}\sigma}\,\hat{c}^{\dagger}_{\mathbf{k}\sigma}\hat{c}_{i\sigma}\right) + \sum_{\mathbf{k}\sigma}\varepsilon^{(i)}_{\mathbf{k}\sigma}\,\hat{c}^{\dagger}_{\mathbf{k}\sigma}\hat{c}_{\mathbf{k}\sigma}. \quad (10)$$

The first two terms, those with the ε_i and U parameters, are the same as the local terms within the Anderson-Hubbard model (3). The third term represents a hybridization, i.e., a possibility of hopping the electron from the effective bath onto the site i-th with the amplitude (hybridization matrix element) $V_{\mathbf{k}i\sigma}$ and the reversed process. The last term describes a property of a single particle bath with a dispersion relation $\varepsilon^{(i)}_{\mathbf{k}\sigma}$. All creation and annihilation operators are fermionic for spin $1/2$ particles and $\mathbf{k}$ is a momentum corresponding to a referenced homogeneous lattice. We note that the SIAM Hamiltonian (10) is defined for each site i of the lattice, where the energies ε_i are different in principle. The hybridization $V_{\mathbf{k}i\sigma}$ and the dispersion relation $\varepsilon^{(i)}_{\mathbf{k}\sigma}$ are

not yet known and need to be derived self-consistently. Note that they are spin σ dependent when the magnetic systems are considered.
The common quantity that can be derived for the lattice problem (3) and for the SIAM Hamiltonian (10) are the diagonal and local Green functions, respectively,

$$G^{\rm latt}_{ij\sigma}(\omega) = -i\int d\omega\, e^{i\omega t}\big\langle T\hat{a}_{i\sigma}(t)\hat{a}^{\dagger}_{j\sigma}(0)\big\rangle \tag{11}$$

and

$$G^{\rm imp}_{ii\sigma}(\omega) = -i\int d\omega\, e^{i\omega t}\big\langle T\hat{c}_{i\sigma}(t)\hat{c}^{\dagger}_{i\sigma}(0)\big\rangle, \tag{12}$$

where t is a time and ω is a real frequency [20]. The self-consistency condition requires that both are the same, i.e.

$$G^{\rm latt}_{ii\sigma}(\omega) \stackrel{!}{=} G^{\rm imp}_{ii\sigma}(\omega) \equiv G_{i\sigma}(\omega). \tag{13}$$

The local Green function for the SIAM is given by

$$G^{\rm imp}_{ii\sigma}(\omega) = \frac{1}{\omega+\mu-\varepsilon_i-\Delta_{i\sigma}(\omega)-\Sigma^{\rm imp}_{i\sigma}(\omega)}, \tag{14}$$

where

$$\Delta_{i\sigma}(\omega) = \sum_{\mathbf{k}}\frac{|V_{\mathbf{k}i\sigma}|^2}{\omega-\varepsilon^{(i)}_{\mathbf{k}\sigma}} \tag{15}$$

is the so called hybridization function and $\Sigma_{i\sigma}(\omega)$ is the self-energy. When $U{=}0$ the self-energy vanishes. Similarly, the diagonal Green function for the lattice problem is given from the real-space Dyson equation

$$\big[G^{\rm latt}_{ij\sigma}(\omega)\big] = \Big[\big[G^{\rm latt,0}_{ij\sigma}(\omega)\big]^{-1} - \Sigma_{ij\sigma}(\omega)\Big]^{-1}, \tag{16}$$

where $G^{\rm latt,0}_{ij\sigma}(\omega)$ is the Green function for fermions on the lattice in the absence of interactions, i.e., $U{=}0$, and $\Sigma_{ij\sigma}(\omega)$ is the self-energy. Within the DMFT it is assumed, and shown to be exact in the infinite coordination number limit, that $\Sigma_{ij\sigma}(\omega) = \delta_{ij}\Sigma^{\rm latt}_{i\sigma}(\omega)$ is diagonal. For homogeneous systems, when the Fourier transform is applied, this condition is equivalent to the statement that the self-energy is momentum independent. The self-consistency condition (13) now takes the form

$$\Sigma^{\rm latt}_{i\sigma}(\omega) \stackrel{!}{=} \Sigma^{\rm imp}_{i\sigma}(\omega) \equiv \Sigma_{i\sigma}(\omega). \tag{17}$$

The set of equations (10)–(17) forms the **real-space dynamical mean-field theory** (R-DMFT) [21]. Determining self-consistently $\Sigma_{i\sigma}(\omega)$ together with $V_{\mathbf{k}i}$ and $\varepsilon^i_{\mathbf{k}}$ for each lattice site i allows us to determine all diagonal Green functions $G^{\rm latt}_{ii\sigma}(\omega)$ and other single-particle properties for a many-body lattice system.
The R-DMFT equations, though very general and applicable for homogeneous and for inhomogeneous lattices of any type, are difficult to use, in particular if the system size N_L is large. Indeed, if we deal with random inhomogeneities, the R-DMFT equations must be iterated for many realization of the disorder. It requires that the most difficult and time consuming part, the

SIAM problem (10) needs to be solved $N_L \times N_{\rm it} \times N_{\rm dis}$ times, where $N_{\rm it}$ is the number of iterations to get a self-consistency for a given realization of the disorder and $N_{\rm dis}$ is the number of disorder realizations. This obstacle motivates to search for an average description of the system, reintroducing back homogeneity and utilizing again the Fourier transformation between the real $\mathbf{R}_i$ and the reciprocal $\mathbf{k}$ spaces.

4 Averaged DMFT

In averaged descriptions of the system we need to take a statistical average of a physical observable on various realization of the quenched disorder. This will lead to the **averaged dynamical mean-field theory** (A-DMFT). On a one-particle level the spectral functions or the **density of states** (DOS) are such useful observables. The **local density of states** (LDOS) is defined as [20]

$$A_{i\sigma}(\omega) = -\frac{1}{\pi}\mathrm{Im}\, G_{i\sigma}(\omega+i0^+), \tag{18}$$

where now the Green function $G_{i\sigma}(\omega)$ is determined from the simplified SIAM, where the hybridization matrix and the bath dispersion relations are site independent, i.e.

$$\hat{H}_{\rm SIAM} = \varepsilon_i \sum_\sigma \hat{c}^\dagger_{i\sigma}\hat{c}_{i\sigma} + U\,\hat{c}^\dagger_{i\uparrow}\hat{c}_{i\uparrow}\,\hat{c}^\dagger_{i\downarrow}\hat{c}_{i\downarrow} + \sum_{\mathbf{k}\sigma}\left(V_{\mathbf{k}\sigma}\,\hat{c}^\dagger_{i\sigma}\hat{c}_{\mathbf{k}\sigma} + V^*_{\mathbf{k}\sigma}\,\hat{c}^\dagger_{\mathbf{k}\sigma}\hat{c}_{i\sigma}\right) + \sum_{\mathbf{k}\sigma}\varepsilon_{\mathbf{k}\sigma}\,\hat{c}^\dagger_{\mathbf{k}\sigma}\hat{c}_{\mathbf{k}\sigma}. \tag{19}$$

Taking one of the generalized averages, the p-mean, we obtain the average density of states

$$A_\sigma(\omega) \equiv \big\langle A_{i\sigma}(\omega)\big\rangle_p = \left[\int d\varepsilon_i\, A_{i\sigma}(\omega)^p\, p(\varepsilon_i)\right]^{\frac{1}{p}}. \tag{20}$$

To recover the average Green function, needed to complete the self-consistency DMFT loop, we use the spectral representation theorem [20] and get

$$G_\sigma(\omega) \equiv \big\langle G_{i\sigma}(\omega)\big\rangle_p = \int d\omega' \frac{\langle A_{i\sigma}(\omega')\rangle_p}{\omega-\omega'}. \tag{21}$$

We note that for p=1-mean, i.e., arithmetic averaging, the Hilbert transform leads directly to

$$G^{\rm arith}_\sigma(\omega) = \big\langle G_{i\sigma}(\omega)\big\rangle_{p=1} = \int d\varepsilon_i\, G_{i\sigma}(\omega)\, p(\varepsilon_i), \tag{22}$$

and the real and imaginary parts of the Green function can be averaged independently. For other p-means this linear property does not hold and one must explicitly use the Hilbert transform (21) as a step between.

We will be particularly interested in the geometric averaging when describing the Anderson localization. Then the averaging of the spectral function takes explicitly the form

$$A^{\rm geom}_\sigma(\omega) \equiv \big\langle A_{i\sigma}(\omega)\big\rangle_{p=0} = e^{\int d\varepsilon_i \ln A_{i\sigma}(\omega)\, p(\varepsilon_i)}. \tag{23}$$

Now, since the average Green function is site independent, i.e., homogeneous, and the self-energy is uniform, i.e., site and $\mathbf{k}$ independent, we can use the Fourier transform and write the

self-consistency condition that the average Green function $G_\sigma(\omega)$ and the one of the homogeneous system with the self-energy are equal, i.e.

$$G_\sigma(\omega) \stackrel{!}{=} \sum_{\mathbf{k}} \frac{1}{\omega - E_{\mathbf{k}} - \Sigma_\sigma(\omega)} = \frac{1}{\omega + \mu - \Delta_\sigma(\omega) - \Sigma_\sigma(\omega)}, \tag{24}$$

where $E_{\mathbf{k}}$ is the dispersion relation for the non-interacting particles in the reference homogeneous lattice, and the homogeneous hybridization function is

$$\Delta_\sigma(\omega) = \sum_{\mathbf{k}} \frac{|V_{\mathbf{k}\sigma}|^2}{\omega - \varepsilon_{\mathbf{k}\sigma}}. \tag{25}$$

Indeed, the equations (18)–(25) constitute a close set of the A-DMFT equations that can be solved iteratively until the self-consistency is reached. For systems without disorder this set of equations is exactly the same as in the standard DMFT.

5 DMFT and CPA

5.1 CPA for non-interacting systems

It is instructive to recover the standard CPA equation from the A-DMFT equations. When the system is non-interacting ($U=0$) the Hamiltonian (19) can be solved exactly, e.g., by means of the equations of motion, and we find that the local Green function is

$$G_{i\sigma}(\omega) = \frac{1}{\omega + \mu - \Delta_\sigma(\omega) - \varepsilon_i}\,. \tag{26}$$

The self-consistency equation (24) reads

$$G_\sigma(\omega) = \sum_{\mathbf{k}} \frac{1}{\omega - E_{\mathbf{k}} - \Sigma_\sigma(\omega)} = \int d\varepsilon_i \, \frac{1}{\omega + \mu - \Delta_\sigma(\omega) - \varepsilon_i}\, p(\varepsilon_i) \tag{27}$$

or

$$G_\sigma(\omega) = G^{(0)}_\sigma\big(\omega - \Sigma_\sigma(\omega)\big) = \int d\varepsilon_i \, \frac{1}{\omega + \mu - \Delta_\sigma(\omega) - \varepsilon_i}\, p(\varepsilon_i), \tag{28}$$

where

$$G^{(0)}_\sigma(\omega) = \sum_{\mathbf{k}} \frac{1}{\omega + \mu - E_{\mathbf{k}}} \tag{29}$$

is the Green function for non-interacting and homogeneous system. Using the RHS of the Eq. (24) we see that

$$G^{(0)}_\sigma\big(\omega - \Sigma_\sigma(\omega)\big) = \int d\varepsilon_i \, \frac{1}{\frac{1}{G^{(0)}_\sigma(\omega - \Sigma_\sigma(\omega))} - \big(\varepsilon_i - \Sigma_\sigma(\omega)\big)}\, p(\varepsilon_i), \tag{30}$$

and by arranging terms we finally get

$$\int d\varepsilon_i \, \frac{\varepsilon_i - \Sigma_\sigma(\omega)}{1 - \big(\varepsilon_i - \Sigma_\sigma(\omega)\big) G^{(0)}_\sigma\big(\omega - \Sigma_\sigma(\omega)\big)}\, p(\varepsilon_i) \equiv \int d\varepsilon_i T_{ii\sigma}(\omega)\, p(\varepsilon_i) = 0, \tag{31}$$

where the T-matrix

$$T_{ii\sigma}(\omega) = \frac{\varepsilon_i - \Sigma_\sigma(\omega)}{1 - \big(\varepsilon_i - \Sigma_\sigma(\omega)\big) G^{(0)}_\sigma\big(\omega - \Sigma_\sigma(\omega)\big)} \tag{32}$$

describes multiple-scattering processes on the i-th impurity site with an effective potential $\varepsilon_i - \Sigma_\sigma(\omega)$. This is exactly the CPA self-consistency equation on vanishing of the average T-matrix defined with respect to the mean environment. Thus we see that the A-DMFT with p=1-mean, arithmetic averaging, reduces to the coherent potential approximation in the noninteracting limit.

5.2 Binary alloys and alloy band splitting

In a binary alloy, two different atoms are distributed randomly on lattice sites. It is modeled by assuming that one of the atom has an atomic energy $\varepsilon_A = -\Delta/2$ and the other $\varepsilon_B = \Delta/2$, $\Delta \geq 0$. Since they are distributed randomly the probability distribution function takes the form

$$p(\varepsilon) = x_A \delta(\varepsilon - \varepsilon_A) + x_B \delta(\varepsilon - \varepsilon_B), \tag{33}$$

where $x_A = N_A/N_L$ and $x_B = N_B/N_L$ are the concentrations of the A and B atoms, respectively. Note, $x_A + x_B = 1$. This binary alloy distribution is very special: only two energies are allowed. It leads to the alloy-band splitting. Namely, from the localization theorem (the Hadamard-Gerschgorin theorem in matrix algebra) it is known that if the Hamiltonian (3), with the binary alloy distribution for ε_i, is bounded, then there is a gap in the single particle spectrum for sufficiently large $\Delta \gg \max\big(|t|, U\big)$ [4]. Hence, at $\Delta = \Delta_c$ the DOS splits into two parts corresponding to the lower and the upper alloy subbands with centers of masses at the ionic energies ε_A and ε_B, respectively. The width of the alloy gap is of the order Δ. The lower and the upper alloy subband contains $2x_A N_L$ and $2x_B N_L$ states, respectively. For convenience, we note $x_A = x$ and $x_B = 1 - x$, where $0 \leq x \leq 1$. A simplified proof of that fact is given in Appendix A and actually does not rely on an averaging approximation, like the CPA.

5.3 Mott-Hubbard transition at fractional filling in the binary alloy disordered Hubbard model

The Mott-Hubbard metal-insulator transition occurs upon increasing the interaction strength U in the simple Hubbard models (3) if the number of electrons N_e is commensurate with the number of lattice sites N_L or, more precisely, if the ratio N_e/N_L is an odd integer. At zero temperature it is a continuous transition whereas at finite temperatures the transition is of the first order [13]. The transition happens by a dynamical redistribution of the spectral weight such that two Hubbard subbands are formed and a central, quasiparticle peak in between, which vanishes at the critical interaction $U = U_c$ where the system becomes a Mott insulator.
Surprisingly, in the presence of binary alloy disorder the MIT occurs at fractional filling [22]. We describe this situation by using the Anderson-Hubbard model (3) with the distribution (33), which corresponds to a binary-alloy system composed of two different atoms A and B. As

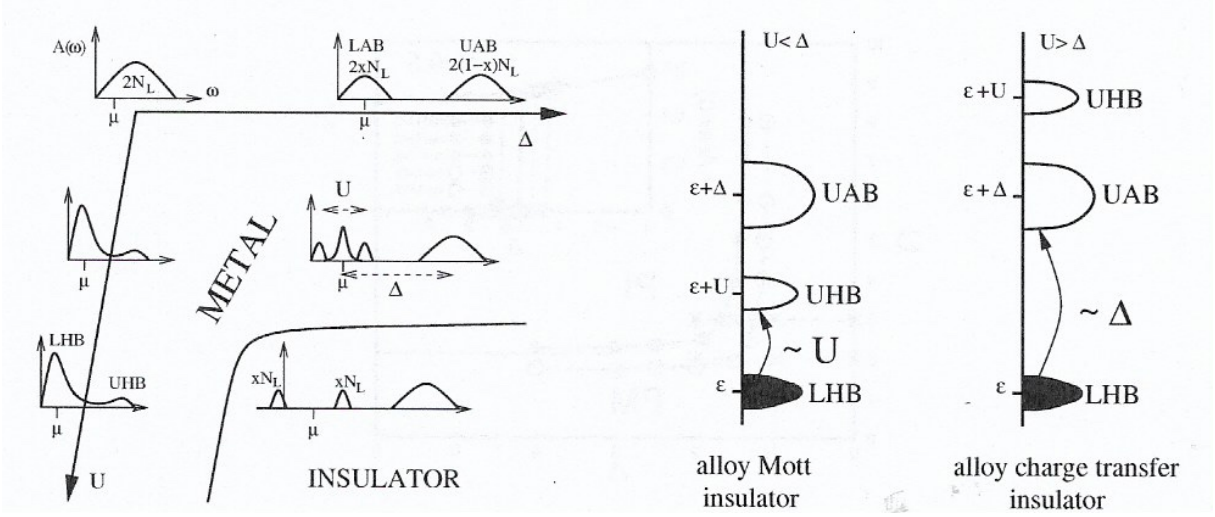


Fig. 1: *Left: Schematic plot representing the Mott-Hubbard metal-insulator transition in a correlated electron system with binary alloy disorder. The shapes of DOS are shown for different interactions U and disorder strengths Δ. Increasing Δ at $U=0$ leads to splitting of the spectral function into the lower (LAB) and the upper (UAB) alloy subbands, which contains $2xN_L$ and $2(1-x)N_L$ states, respectively. Increasing U at $\Delta = 0$ leads to the occurrence of lower (LHB) and upper (UHB) Hubbard subbands. The Fermi energy for filling $n = x$ is indicated by μ. At $n = x$ (or $n = 1+x$, not shown in the plot) the LAB (UAB) is half-filled. In this case an increase in U and Δ leads to the opening of a correlation gap at the Fermi level and the system becomes a Mott insulator. Right: Two possible insulating states in the correlated electron system with binary-alloy disorder. When $U < \Delta$ the insulating state is an alloy Mott insulator with an excitation gap in the spectrum of the order of U. When $U > \Delta$ the insulating state is an alloy charge transfer insulator with an excitation gap of the order of Δ; after Ref. [22].*

discussed there is a binary alloy band splitting expected for large Δ. New possibilities appear in systems with correlated electrons and binary alloy disorder [22]. The Mott-Hubbard metal-insulator transition can occur at any filling $n = N_e/N_L = x$ or $1+x$, corresponding to a half-filled lower or to a half-filled upper alloy subband, respectively, as shown schematically for $n = x$ in Fig. 1.

The Mott insulator can then be approached either by increasing U when $\Delta \geq \Delta_c$ (alloy band splitting limit), or by increasing Δ when $U \geq U_c$ (Hubbard band splitting limit). The nature of the Mott insulator in the binary alloy system can be understood physically as follows. Due to the high energy cost of the order of U the randomly distributed ions with lower (higher) local energies ε_i are singly occupied at $n = x$ ($n = 1+x$), i.e., the double occupancy is suppressed. In the Mott insulator with $n = x$ the ions with higher local energies are empty and do not contribute to the low-energy processes in the system. Likewise, in the Mott insulator with $n = 1+x$ the ions with lower local energies are double occupied implying that the lower alloy subband is blocked and does not play any role.

For $U > Uc(\Delta)$ in the Mott insulating state with binary alloy disorder one may use the lowest excitation energies to distinguish two different types of insulators. Namely, for $U < \Delta$ an excitation must overcome the energy gap between the lower and the upper Hubbard subbands,

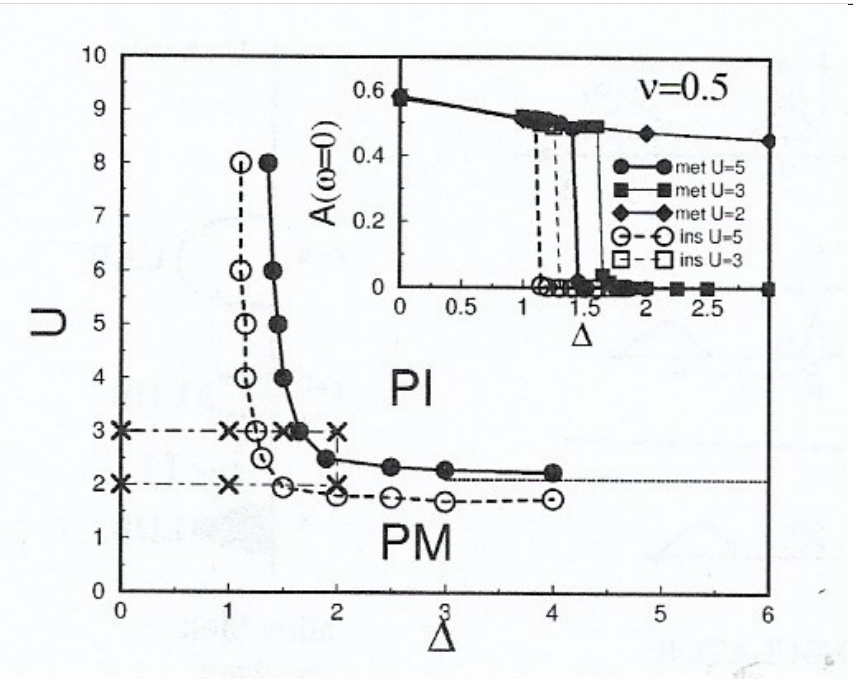


Fig. 2: *Ground state phase diagram of the Hubbard model with binary-alloy disorder at filling n=x=0.5. The filled (open) dots represent the boundary between paramagnetic metallic (PM) and paramagnetic insulating (PI) phases as determined by DMFT with the initial input given by the metallic (insulating) hybridization function. The horizontal dotted line represents U_c obtained analytically from an asymptotic theory in the limit $\Delta \to \infty$. Inset: hysteresis in the spectral functions at the Fermi level obtained from DMFT with an initial metallic (insulating) host represented by filled (open) symbols and solid (dashed) lines; after Ref. [22].*

as indicated in Fig. 1. We call this insulating state an *alloy Mott insulator*. On the other hand, for $\Delta < U$ an excitation must overcome the energy gap between the lower Hubbard subband and the upper alloy-subband, as shown in Fig. 1. We call this insulating state an *alloy charge transfer insulator*.

In Fig. 2 we present a particular phase diagram for the Anderson-Hubbard model at filling $n = 0.5$ showing a Mott-Hubbard type of MIT with a typical hysteresis.

5.4 Ferromagnetism in the binary alloy disordered Hubbard model; disorder-induced enhancement of the Curie temperature

Itinerant ferromagnetism in the pure Hubbard model occurs only away from half-filling and if the DOS is asymmetric and peaked at the lower edge [23, 24]. While the Curie temperature T_c increases with the strength of the electron interaction one would expect it to be lowered by disorder. However, our investigations show that in some cases the Curie temperature can actually be increased by binary alloy disorder [25, 26].

Indeed, the Curie temperature as a function of alloy concentration exhibits a very rich and interesting behavior as is shown in Fig. 3. At some concentrations and certain values of U, Δ, and n, the Curie temperature is enhanced above the corresponding value for the non-disordered case (x= 0 or 1). This is shown in the upper part of Fig. 3 for $0 < x < 0.2$. The relative increase in T_c can be as large as 25%, as is found for $x \approx 0.1$ at $n = 0.7$, $U = 2$ and $\Delta = 4$.

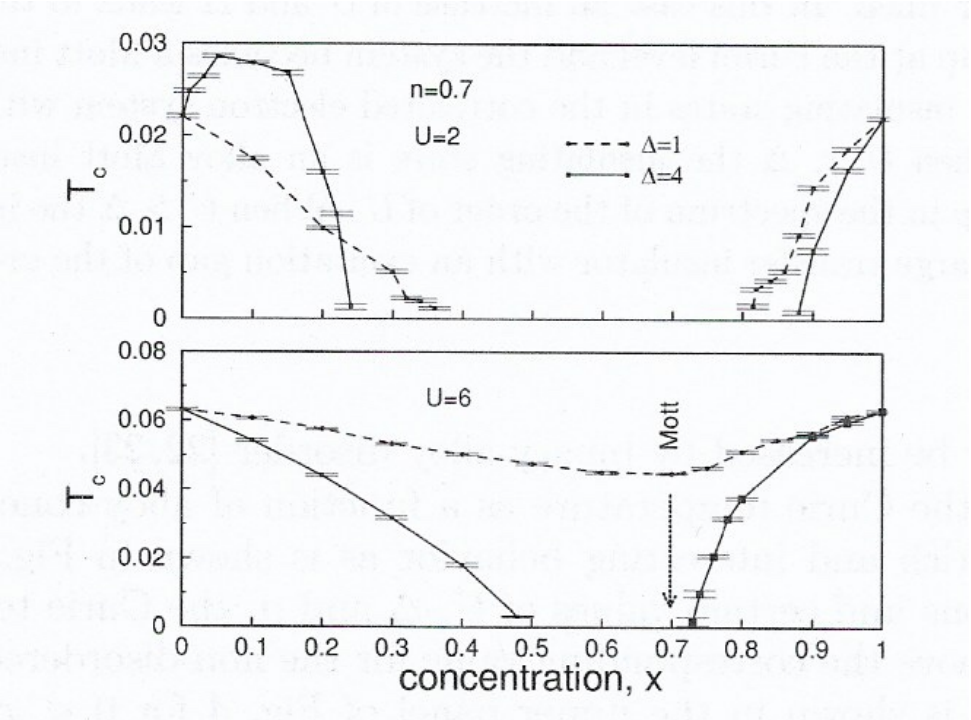


Fig. 3: *Curie temperature as a function of alloy concentration x at $U = 2$ (upper part) and 6 (lower part) for $n = 0.7$ and disorder $\Delta = 1$ (dashed lines) and 4 (solid lines); after Refs. [25, 26]. Temperatures are in the energy units.*

This unusual enhancement of T_c is caused by three distinct features of interacting electrons in the presence of binary alloy disorder:

i) The Curie temperature in the non-disordered case $T_c^p \equiv T_c(\Delta{=}0)$, depends non-monotonically on band filling n [24]. Namely, $T_c^p(n)$ has a maximum at some filling $n = n^*(U)$, which increases as U is increased; see also our schematic plots in Fig. 4.

ii) As described above, in the alloy-disordered system the band is split when $\Delta \gg \max(|t|, U)$. As a consequence, for $n < 2x$ and $T \ll \Delta$ electrons occupy only the lower alloy subband and for $n > 2x$ both the lower and upper alloy subbands are filled. In the former case the upper subband is empty while in the latter case the lower subband is completely full. Effectively, one can therefore describe this system by a Hubbard model mapped onto either the lower or the upper alloy subband, respectively. The second subband plays a passive role. Hence, the situation corresponds to a single band with the effective filling $n_{\text{eff}} = n/x$ for $n < 2x$ and $n_{\text{eff}} = (n{-}2x)/(1{-}x)$ for $n > 2x$. It is then possible to determine T_c from the phase diagram of the Hubbard model without disorder.

iii) The disorder leads to a reduction of $T_c^p(n_{\text{eff}})$ by a factor $\alpha = x$ if the Fermi level is in the lower alloy subband or $\alpha = 1{-}x$ if it is in the upper alloy subband, i.e., we find

$$T_c(n) \approx \alpha T_c^p(n_{\text{eff}}), \tag{34}$$

when $\Delta \gg \max(|t|, U)$. Hence, as illustrated in Fig. 4, T_c can be determined by $T_c^p(n_{\text{eff}})$. Surprisingly, then, it follows that for suitable U and n the Curie temperature of a disordered system can be higher than that of the corresponding non-disordered system.

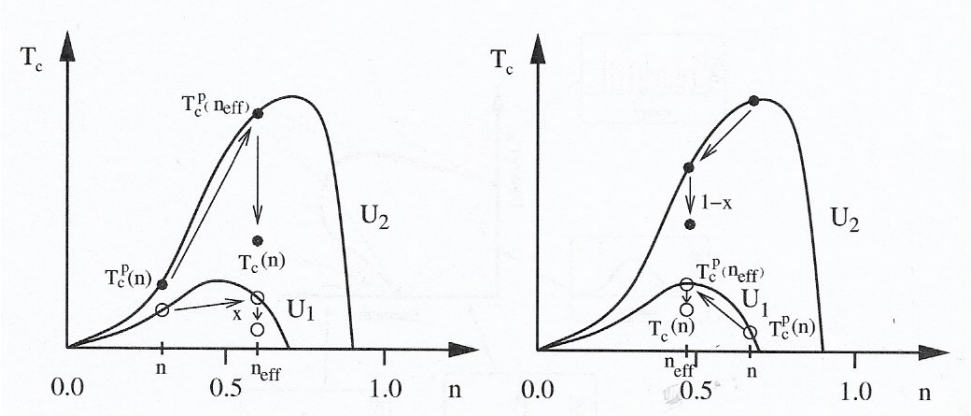


Fig. 4: *Schematic plots explaining the filling dependence of T_c for interacting electrons with strong binary alloy disorder. Curves represent T_c^p, the Curie temperature for the pure system, as a function of filling n at two different interactions $U_1 \ll U_2$. Left: For $n < x$, T_c of the disordered system can be obtained by transforming the open (for U_1) and the filled (for U_2) point from n to $n_{eff} = n/x$, and then multiplying $T_c^p(n/x)$ by x as indicated by arrows. One finds $T_c(n) < T_c^p(n)$ for U_1, but $T_c(n) > T_c^p(n)$ for U_2. Right: For $n > x$, T_c of the disordered system can be obtained by transforming $T_c^p(n)$ from n to $n_{eff} = (n-2x)/(1-x)$, and then multiplying $T_c^p[(n-2x)/(1-x)]$ by $1-x$ as indicated by arrows. One finds $T_c(n) > T_c^p(n)$ for U_1, but $T_c(n) < T_c^p(n)$ for U_2; after Refs. [25, 26].*

6 DMFT and TMT

6.1 Typical medium theory for Anderson localization

The Mott-Hubbard MIT is caused by the Coulomb correlations in the pure system. By contrast, the Anderson MIT, also referred to as the Anderson localization, is due to coherent backscattering from randomly distributed impurities in a system without interaction [5]. It is therefore a challenge to investigate the effect of the simultaneously presence of interactions and disorder on electronic systems [27, 28]. In particular, the question arises whether it will suppress or enlarge a metallic phase. And what about the Mott and Anderson insulating phases: will they be separated by a metallic phase? Possible scenarios are schematically plotted in Fig. 5.

The Mott-Hubbard MIT is characterized by the opening of a gap in the density of states at the Fermi level. At the Anderson localization transition the character of the spectrum at the Fermi level changes from a continuous spectrum to a dense, pure point spectrum. It is plausible to assume that both MITs can be characterized by a single quantity, namely, the local density of states. Although the LDOS is not an order parameter associated with a symmetry breaking phase transition, it discriminates between a metal and an insulator, which is driven by correlations and disorder, cf. insets to Fig. 5.

In a disordered system the LDOS depends on a particular realization of the disorder in the system. To obtain a full understanding of the effects of disorder it would therefore in principle be necessary to determine the entire probability distribution function of the LDOS, which is almost never possible. Instead one might try to calculate moments of the LDOS. This, however, is insufficient because the arithmetically averaged LDOS (first moment) stays finite at the Anderson MIT [29]. It was already pointed out by Anderson [5] that the *typical* values of random quanti-

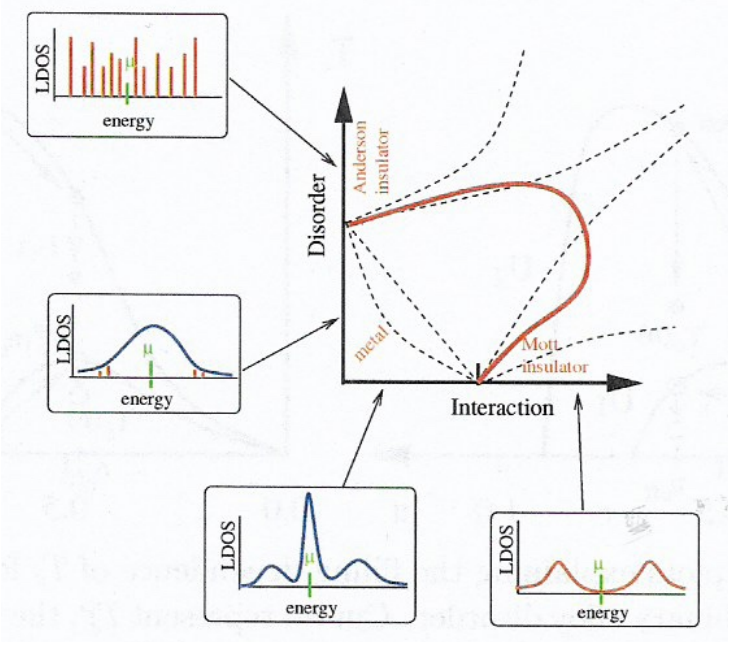


Fig. 5: *Possible phases and phase transitions triggered by interaction and disorder in the same system. According to DMFT investigations the simultaneous presence of correlations and disorder enhances the metallic regime (thick line); the two insulating phases are connected continuously. Insets show the local density of states when disorder or interaction is switched off.*

ties, which are mathematically given by the most probable values of the probability distribution functions, should be used to describe localization. The geometrical mean gives an approximation of the most probable (*typical*) value of the LDOS and vanishes at a critical strength of the disorder, hence providing an explicit criterion for the Anderson localization [5, 30, 31].
In the following we will use the simple box probability distribution function of the on-site random energies ε_i, i.e.

$$p(\varepsilon_i) = \begin{cases} \frac{1}{\Delta} & \text{for } |\varepsilon_i| \leq \Delta \\ 0 & \text{otherwise.} \end{cases} \tag{35}$$

Other types of the continuous probability distribution functions would lead to the same generic results although detailed numbers might be different. The reason is that this probability distribution does not yield any alloy band splitting.

6.2 Anderson localization in disordered Hubbard and Falicov-Kimball models

A non-perturbative framework for investigations of the Mott-Hubbard MIT in lattice electrons with a local interaction and disorder is provided by the DMFT [13]. If in this approach the effect of local disorder is taken into account through the arithmetic mean of the LDOS [32, 33] one obtains, in the absence of interactions, the well-known coherent potential approximation (CPA) [36], which does not describe the physics of Anderson localization. To overcome this deficiency Dobrosavljević *et al.* [31] incorporated the geometrically averaged LDOS into the self-consistency cycle and thereby derived a mean-field theory of Anderson localization which

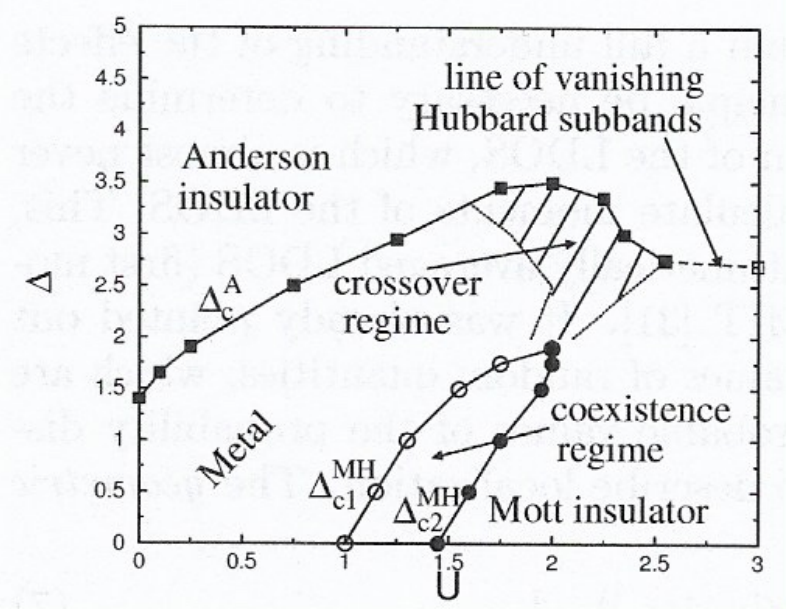


Fig. 6: *Non-magnetic ground state phase diagram of the Anderson-Hubbard model at half-filling as calculated by DMFT with the typical local density of states; after Refs. [27].*

reproduces many of the expected features of the disorder-driven MIT for non-interacting electrons. This scheme uses only one-particle quantities and is therefore easily incorporated into the DMFT for disordered electrons in the presence of phonons [34], or Coulomb correlations [27, 28]. In particular, the DMFT with geometrical averaging allows to compute phase diagrams for the Anderson-Hubbard model (3) and the Anderson-Falicov-Kimball model (4) with the continuous probability distribution function at half-filling [27, 28]. In this way we found that, although in both models the metallic phase is enhanced for small and intermediate values of the interaction and disorder, metallicity is finally destroyed. Surprisingly, the Mott and Anderson insulators are found to be continuously connected. Phase diagrams for the non-magnetic ground state are shown in Fig. 6 for the Anderson-Hubbard model and in Fig. 7 for the Anderson-Falicov-Kimball model.

7 Outlook

In these lecture notes we have seen that a combination between the correlations of interacting electrons and disorder leads to novel and unexpected possibilities. And the combination of the DMFT with statistical methods to treat randomness has turned out to be very successful in describing the correlated electrons with disordered potentials. Continuation of this research turns in many directions.

The influence of non-uniform or random external potentials on the existence and stability of the antiferromagnetic phases in the Hubbard model was investigated in Ref. [21, 35]. The study of the Anderson transition in the presence of binary-alloy disorder was performed in [36]. The same type of disorder was used to study ferromagnetism in the periodic Anderson model in [37]. A spin-selective disorder and the localization MITs were investigated in [38, 39]. More

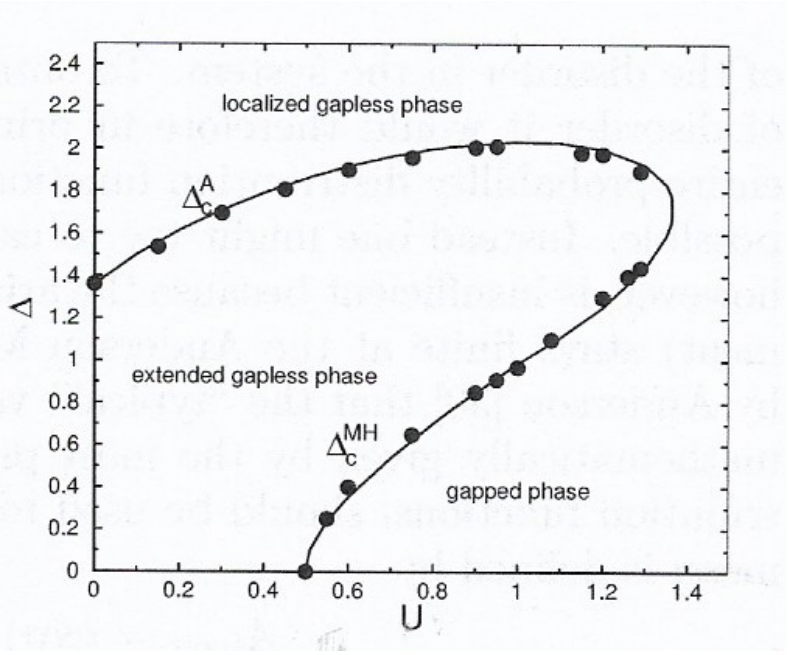


Fig. 7: *Non-magnetic ground state phase diagram of the Anderson-Falicov-Kimball model at half-filling as calculated by DMFT with the typical local density of states; after Refs. [28].*

recently, the typical medium theory was extended to treat systems with off-diagonal, hopping disorder [40].

In conclusion, the dynamical mean-field theory for correlated electrons with disorder is a well established method to comprehensively describe interacting electrons on crystal lattices or even fermionic atoms on optical lattices.

Acknowledgment

The author thanks Dieter Vollhardt for the fruitful quarter-century collaboration on correlated lattice systems with disorder. He also thanks Walter Hofstetter for a long collaboration on this subject. He also acknowledges Liviu Chioncel, Denis Semmler, Jan Skolimowski, Martin Ulmke, and Unjong Yu for various collaborations. The Appendix A is based on the notes from Bedrich Velicky, received in 2001.

A Proof of the alloy band splitting theorem

In order to prove the alloy band splitting theorem we need to show firstly the so called localization theorem. For that we assume that the unperturbed Hamiltonian $\hat{H}_0$ has a point like spectrum, i.e.

$$\hat{H}_0 = \sum_i \varepsilon_i |i\rangle\langle i|, \tag{36}$$

where ε_i are real discrete eigenvalues of the Hamiltonian $\hat{H}_0$ in the $\{|i\rangle\}$ base. Any normalized vector can be expanded in this basis

$$|\alpha\rangle = \sum_i c_i |i\rangle, \tag{37}$$

with $\|\alpha\|^2 \equiv |\langle\alpha|\alpha\rangle|^2 = \sum_i |c_i|^2 = 1$. Now we add a perturbation $\hat{T}$ to our Hamiltonian

$$\hat{H} = \hat{H}_0 + \hat{T}, \tag{38}$$

such that the perturbation part $\hat{T}$ is bounded, i.e., for any normalized vector $|\alpha\rangle$ we have that

$$\|\hat{T}\| \equiv \langle\alpha|\hat{T}|\alpha\rangle < \infty. \tag{39}$$

We also define a *distance* of the complex number λ from the spectrum of $\hat{H}_0$ Hamiltonian as

$$d(\lambda) = \inf\{|\lambda - \varepsilon_i|\}. \tag{40}$$

We can easily show that $d(E) \leq \|\hat{T}\|$ where $\hat{H}|\alpha\rangle = E|\alpha\rangle$, i.e., the distance between the spectra points of the full Hamiltonian $\hat{H}$ and the unperturbed Hamiltonian $\hat{H}_0$ is bounded: Indeed, from $(E - \hat{H}_0)|\alpha\rangle = \hat{T}|\alpha\rangle$ we get that $\langle\alpha|(E - \hat{H}_0)^2|\alpha\rangle = \langle\alpha|\hat{T}^2|\alpha\rangle$ or, equivalently, $\sum_i |c_i|^2 (E - \varepsilon_i)^2 = \|\hat{T}\|^2$. Estimating the left hand side by $\sum_i |c_i|^2 (E - \varepsilon_i)^2 \geq d(E)^2 \sum_i |c_i|^2 = d(E)^2$ we obtain the inequality $d(E) \leq \|\hat{T}\|$. This results is known as a *localization theorem*. In particular, it follows that the spectrum of $\hat{H}$ is covered by the union of spectra sets

$$\mathcal{A} = \bigcup_i \big\langle \varepsilon_i - \|\hat{T}\|, \varepsilon_i + \|\hat{T}\| \big\rangle. \tag{41}$$

If the perturbation Hamiltonian $\hat{T} = \sum_{ij} t_{ij}\, \hat{a}_i^\dagger \hat{a}_j$ is a tight-binding Hamiltonian on a uniform lattice, diagonalized by the Fourier transform to the form $\hat{T} = \sum_{\mathbf{k}} E_{\mathbf{k}}\, \hat{a}_{\mathbf{k}}^\dagger \hat{a}_{\mathbf{k}}$, with the dispersion $E_{\mathbf{k}}$, the spectrum of $\hat{T}$ is bounded between $t_{\text{min}} = \min(E_{\mathbf{k}})$ and $t_{\text{max}} = \max(E_{\mathbf{k}})$. Therefore, we get the estimate for the spectrum of $\hat{H}$

$$\mathcal{A} = \bigcup_i \big\langle \varepsilon_i - t_{\text{min}}, \varepsilon_i + t_{\text{max}} \big\rangle. \tag{42}$$

As a consequence, for a binary alloy systems ($i = A$ or B)

$$\mathcal{A} = \big\langle \varepsilon_A - t_{\text{min}}, \varepsilon_A + t_{\text{max}} \big\rangle \cup \big\langle \varepsilon_B - t_{\text{min}}, \varepsilon_B + t_{\text{max}} \big\rangle, \tag{43}$$

or in our binary alloy model

$$\mathcal{A} = \Big\langle -\frac{\Delta}{2} - t_{\text{min}}, -\frac{\Delta}{2} + t_{\text{max}} \Big\rangle \cup \Big\langle \frac{\Delta}{2} - t_{\text{min}}, \frac{\Delta}{2} + t_{\text{max}} \Big\rangle. \tag{44}$$

If $|t_{\text{max}} - t_{\text{min}}| < \Delta$ the band is split and two separated alloy subbands are formed [4].

References

[1] H. Weyl, *Symmetries* (Princeton University Press, 1952)

[2] Lao Tzu, *Tao teh ching* (St. John's University Press, New York 1961)

[3] R. Zallen, *The physics of amorphous solids* (Wiley, 1983)

[4] J.M. Ziman, *Models of disorders* (Cambridge University Press, 1979)

[5] P.W. Anderson, Phys. Rev. **109**, 1492 (1958)

[6] `https://en.wikipedia.org/wiki/Central_limit_theorem`

[7] R. Brout: *Statistical Mechanical Theory of a Random Ferromagnetic System*, Phys. Rev. **115**, 824, (1959)

[8] G. Schubert, J. Schleede, K. Byczuk, H. Fehske, and D. Vollhardt, Phys. Rev. B **81**, 155106 (2010)

[9] M. de Carvalho: *Mean, What do You Mean?*, Am. Stat. **70**, 270 (2016)

[10] E.L. Crow and K. Shimizu (eds.): *Log-normal distribution - theory and applications* (Dekker, 1988)

[11] E.W Montroll and M.F. Schlesinger, J. Stat. Phys. **32**, 209 (1983)

[12] R.J. Elliot, J.A. Krumhansl, and P.L. Leath, Rev. Mod. Phys. **46**, 465 (1974)

[13] D. Vollhardt, in V.J. Emery (ed.): *Correlated Electron Systems* (World Scientific, 1993), p. 57; Th. Pruschke, M. Jarrell, J.K. Freericks, Adv. Phys. **44**, 187 (1995); A. Georges, G. Kotliar, W. Krauth, and M.J. Rozenberg, Rev. Mod. Phys. **68**, 13 (1996)

[14] G. Baym and L. Kadanoff, Phys. Rev. **124**, 287 (1961); G. Baym, Phys. Rev. **127**, 836 (1962)

[15] W. Metzner and D. Vollhardt, Phys. Rev. Lett. **62**, 1066 (1989)

[16] D. Vollhardt, in E. Pavarini, E. Koch, D. Vollhardt, and A. Lichtenstein (eds.): *The LDA+DMFT approach to strongly correlated electrons*, Modeling and Simulations, Vol. 1 (Forschungszentrum Jülich, 2011)

[17] M. Kollar, in E. Pavarini, E. Koch, D. Vollhardt, and A. Lichtenstein (eds.): *The LDA+DMFT approach to strongly correlated electrons*, Modeling and Simulations, Vol. 1 (Forschungszentrum Jülich, 2011)

[18] D. Vollhardt: in E. Pavarini, E. Koch, A. Lichtenstein, and D. Vollhardt (eds.): *DMFT: From Infinite Dimensions to Real Materials*, Modeling and Simulations, Vol. 8 (Forschungszentrum Jülich, 2018)

[19] M. Kollar: in E. Pavarini, E. Koch, A. Lichtenstein, and D. Vollhardt (eds.):
DMFT: From Infinite Dimensions to Real Materials,
Modeling and Simulations, Vol. 8 (Forschungszentrum Jülich, 2018)

[20] J.W. Negele and H. Orland, *Quantum many-particle systems*, (Perseus, 1988)

[21] M. Snoek, I. Titvinidze, C. Toke, K. Byczuk, and W. Hofstetter,
New J. Phys. **10**, 093008 (2008)

[22] K. Byczuk, W. Hofstetter, and D. Vollhardt, Phys. Rev. B **69**, 045112 (2004)

[23] M. Ulmke, Eur. Phys. J. B **1**, 301 (1998)

[24] J. Wahle, N. Blümer, J. Schlipf, K. Held, D. Vollhardt, Phys. Rev. B **58**, 12749 (1998)

[25] K. Byczuk, M. Ulmke, D. Vollhardt, Phys. Rev. Lett. **90**, 196403 (2003)

[26] K. Byczuk, M. Ulmke, Eur. Phys. J. B **45**, 449 (2005)

[27] K. Byczuk, W. Hofstetter, D. Vollhardt, Phys. Rev. Lett. **94**, 056404 (2005)

[28] K. Byczuk, Phys. Rev. B **71**, 205105 (2005)

[29] D. Lloyd, J. Phys. C **2**, 1717 (1969); D. Thouless, Phys. Rep. **13**, 93 (1974);
F. Wegner, Z. Phys. B **44**, 9 (1981)

[30] V. Dobrosavljević, G. Kotliar, Phys. Rev. Lett. **78**, 3943 (1997)

[31] V. Dobrosavljević, A.A. Pastor, B.K. Nikolić, Europhys. Lett. **62**, 76 (2003)

[32] V. Janiš, D. Vollhardt, Phys. Rev. B **46**, 15712 (1992);
M. Ulmke, V. Janiš, D. Vollhardt, Phys. Rev. B **51**, 10411 (1995)

[33] R. Vlaming, D. Vollhardt, Phys. Rev. B **45**, 4637 (1992)

[34] F.X. Bronold, A. Alvermann, H. Fehske, Philos. Mag. **84**, 637 (2004)

[35] K. Byczuk, W. Hofstetter, and D. Vollhardt, Phys. Rev. Lett. **102**, 146403 (2009)

[36] D. Semmler, K. Byczuk, and W. Hofstetter, Phys. Rev. B **81**, 115111 (2010)

[37] U. Yu, K. Byczuk, and D. Vollhardt, Phys. Rev. Lett. 100, 246401 (2008)

[38] K. Makuch, J. Skolimowski, P.B. Chakraborty, K. Byczuk, and D. Vollhardt,
New J. Phys. **15**, 045031 (2013)

[39] J. Skolimowski, K. Byczuk, and D. Vollhardt, Phys. Rev. B **92**, 094202 (2015);
J. Phys. Commun. **2**, 025031 (2018)

[40] A. Weh, Y. Zhang, A. Östlin, H. Terletska, D. Bauernfeind, K. -M. Tam, H.G. Evertz,
K. Byczuk, D. Vollhardt, and L. Chioncel, Phys. Rev. B **104**, 045127 (2021)

9 Learning Feynman Diagrams with Tensor Trains

Xavier Waintal
PHELIQS
Université Grenoble Alpes, CEA, Grenoble INP, IRIG
Grenoble 38000, France

Contents

1 Introduction **2**

2 Problem formulation **3**
2.1 General model 3
2.2 Summary of the overall approach 4
2.3 The SIAM model 6

3 Interaction expansion (problem A) **7**
3.1 A short reminder of Keldysh formalism 7
3.2 Non-interacting Green functions 8
3.3 The expansion itself 9

4 Tensor cross interpolation for integration (problem B) **11**
4.1 Compressing low rank matrices 12
4.2 TCI: Extension of CI to n-dimensional tensors 15

5 Summing up the series (problem C) and results **20**
5.1 Cross extrapolation 20
5.2 Main results in the stationary limit 22
5.3 What is to take away? 23

E. Pavarini, E. Koch, A. Lichtenstein, and D. Vollhardt (eds.)
Understanding Correlated Materials with DMFT
Modeling and Simulation Vol. 15
Forschungszentrum Jülich, 2025, ISBN 978-3-95806-813-1
http://www.cond-mat.de/events/correl25

1 Introduction

Feynman diagrams form an exact formal solution of quantum field theories and quantum many-body problems in terms of a (huge) sum of (multi-dimensional) integrals of products of free propagators (which are known). For a long time these diagrams were mostly used and studied analytically. Countless articles are devoted to, e.g., analyze their structure or find subsequences of diagrams that could be summed exactly and form an appropriate approximate solution of the many-body problem in this or that regime. The idea to teach a computer how to calculate these diagrams is of course very appealing. A particular route in this direction is known as "diagrammatic Monte Carlo" and can be traced down to, e.g., [1, 2] for equilibrium and [3] in the out-of-equilibrium context. Diagrammatic Monte Carlo combines two ideas: First, since calculating a Feynman diagram amounts to calculating a multi-dimensional integral, and since Monte Carlo (e.g. the Metropolis algorithm) is the primary method for that, one aims at sampling these integrals through a Markov process. Second, since there are a very large number of Feynman diagrams (typically $O(n!)$ for a calculation at order n), it is not possible to calculate them all so one might as well use the Markov process for both integration *and* summing the diagrams. In other words, in diagrammatic Monte Carlo, a configuration is a diagram with its set of vertices (times and positions where an interaction event occurs) and the Markov process introduces a random walk between different diagrams and different sets of vertices. The original version of diagrammatic Monte Carlo had some successes but suffered from three difficulties:

- Problem A: The number of diagrams grows too fast with n, making it difficult to obtain converged results beyond $n = 6$–7.
- Problem B: The integrands may oscillate (depending on the regime) and become intractable through Monte Carlo. This is known as the "sign problem"
- Problem C: The expansion itself may not converge even if large values of n can be obtained. This depends on the nature of the series (asymptotic, finite radius of convergence...).

We will discuss these three aspects, in turn, in details. The present notes describe a set of works [4–10] my collaborators and I did to address these problems in the context of quantum nanoelectronics. There are no new results here, merely this is a high level view of what we did, designed to be much less formal and more accessible than the original research articles. Among the different authors, these notes owe much to my old partner Olivier Parcollet who has been my constant collaborator on this topic. Most of the actual work, as often, has been carried out by young researchers including (using time-ordering as is fit for a diagrammatic paper) Elio Profumo, Corentin Bertrand, Marjan Macek, Philipp Dumitrescu, Matthieu Jeannin, Thomas Kloss and Yuriel Nunez Fernandez.

The most urgent problem was Pb. A and it was also how we got started on the topic. In [4], we found a way to group the $n!$ diagrams into a much smaller sets of 2^n determinants of $n \times n$ matrices, dramatically reducing the complexity. This was done in the context of the Keldysh

formalism suitable to treat out-of-equilibrium problems. A similar reduction in the context of imaginary-time diagrams was found two years later in [11]. These developments made calculations possible up to $n \sim 15$ or so in the absence of a sign problem (Pb. B).

To calculate the resulting integrals (Pb. B) we took a somewhat circumvoluted path. We started with Monte Carlo sampling as was done in diagrammatic Monte Carlo [4,5]. It became quickly obvious that this was inefficient: the integrand was called typically 10^9 times in a practical calculation (each call having a cost of up to $O(2^{15})$ floating-point operations for the largest $n = 15$ that we could reach) but we did not take any advantage of the associated accumulated information. An initial idea was that an approximation of the integrand could be learned along the way (machine learning is the fashion). In turn, this approximation could be used to either speed-up the Markov process (decrease its correlation time through smarter proposed moves) or, as it turned out, obtain better convergence using low discrepancy sequences (better known as quasi-Monte Carlo) [7]. We shall not follow this line of thought here because it was eventually supplanted by a much better technique. Indeed, we found that the integrand could be learned directly using tensor network techniques and that the resulting tensor network could be integrated exactly without any need for Monte Carlo [8]. Hence, the technique in its current form does not use diagrams anymore and does not use Monte Carlo either. It is a sort of "Non-diagrammatic Non-Monte Carlo" technique.

For the last problem (Pb. C), we took two different routes. The first was to consider the resummation as an analytical continuation problem [4, 6] which was effective in some situations but difficult to turn into an automatic technique (i.e. that works without human supervision). Here, I will focus on our latest approach that uses "cross extrapolation" [9] and that is routed in the same mathematics as our tensor network learning technique.

In the remaining of these notes, I will walk the reader through what I just described, i.e., describing the problem, then our technique to try and solve problem A, then problem B and ultimately problem C. I will end by showing some actual data in the context of the out-of-equilibrium Anderson model (SIAM), the main model for which we have had results at the time of this writing [10]. Our main success there was to be able to compute the differential conductance versus bias and gate voltages "exactly" including its most prominent features, the "Kondo ridge" and the "Coulomb diamonds". By "exactly" here, we mean that the technique is controlled: it has error bars that (*i*) are known and (*ii*) can be systematically improved by increasing the computing time (in contrast to, e.g., mean field techniques).

2 Problem formulation

2.1 General model

The type of models we want to study correspond to a finite interacting quantum nanoelectronic system connected to infinite (metallic) electrodes, following the approach of Ref. [12]. The Hamiltonian consists of a quadratic term and an electron-electron interaction term,

$$\hat{\mathbf{H}}(t) = \hat{\mathbf{H}}_0(t) + U\hat{\mathbf{H}}_{\rm int}(t) \tag{1}$$

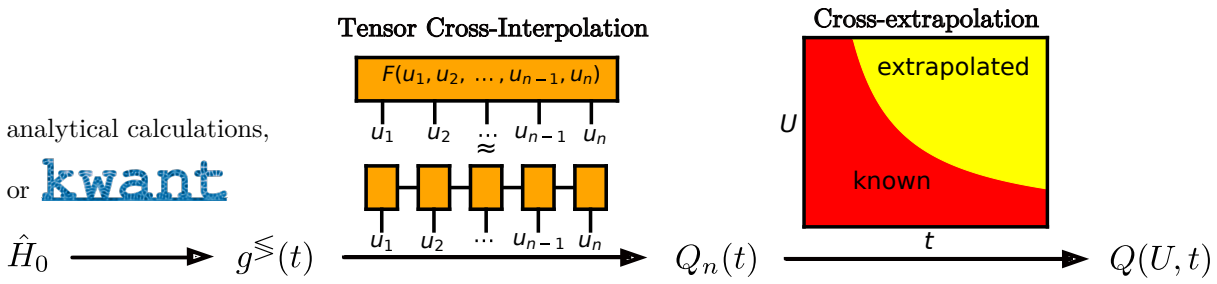


Fig. 1: *Schematic of the overall approach. Starting from non-interacting Green functions, a decomposition of the multidimensional integral is obtained using Tensor Cross-Interpolation to compute the perturbative expansion, from which the physical observables $Q(U,t)$ are reconstructed as a function of interaction U and time t using cross-extrapolation. (Adapted from [10])*

where the parameter U controls the magnitude of the interaction. The non-interacting Hamiltonian takes the form

$$\hat{\mathbf{H}}_0(t) = \sum_{i,j} H^0_{ij}(t)\, \hat{\mathbf{c}}^\dagger_i \hat{\mathbf{c}}_j \tag{2}$$

where $\hat{\mathbf{c}}^\dagger_i$ ($\hat{\mathbf{c}}_j$) are the usual fermionic creation (annihilation) operators of a one-particle state on the site i.

$$\{\hat{\mathbf{c}}^\dagger_i, \hat{\mathbf{c}}_j\} = \delta_{ij}\,. \tag{3}$$

The site index i is general and can include different kinds of degrees of freedom: space, spin, orbitals. A crucial aspect is that the number of "sites" is *infinite* so that the non-interacting system has a well-defined density of states (as opposed to a sum of delta functions for a finite system) while interactions only take place in a finite region. This will ensure the infrared convergence of the various terms of the perturbation expansion while using a discretized system provides ultraviolet convergence. So in contrast to quantum field theory where some diagrams may diverge, here each diagram taken separately will be finite. The interaction Hamiltonian takes the form

$$\hat{\mathbf{H}}_{\rm int}(t) = \sum_{ijkl} V_{ijkl}(t)\, \hat{\mathbf{c}}^\dagger_i \hat{\mathbf{c}}^\dagger_j \hat{\mathbf{c}}_k \hat{\mathbf{c}}_l \tag{4}$$

In contrast to the non-interacting part, it is confined to a *finite* region. We also suppos that the interaction vanishes for negative time and is slowly or abruptly switched on at $t = 0$.

2.2 Summary of the overall approach

Our goal is to perform a systematic expansion of some observable in power of U. For instance, if we are interested in the occupation $Q(U,t)$ of a given site i_0 at time t, we will write its expansion as,

$$Q(U,t) \equiv \left\langle \hat{\mathbf{c}}^\dagger_{i_0} \hat{\mathbf{c}}_{i_0} \right\rangle = \sum_{n=0}^{+\infty} Q_n(t)\, U^n. \tag{5}$$

Our goal will be to first compute the coefficients $Q_n(t)$ for as large a n as possible and then sum up the series. A schematic of the method is shown in Fig. 1. It consists of three main steps:

(*i*) solve the non-interacting model to obtain the corresponding non-interacting Green functions (such as the lesser $g^<_{ij}(t)$ or upper $g^>_{ij}(t)$ Green functions that will be introduced below). (*ii*) Calculating the coefficients $Q_n(t)$ with high precision and (*iii*) resumming this perturbative expansion.

The first step is carried out either analytically in simple models or numerically for more complex geometries using, e.g., the Kwant [13] or Tkwant [14] software. Note that the non-interacting Green function may already be out-of-equilibrium in presence of a bias voltage V_b.

The second step is to perform the actual expansion in powers of U. We shall see that this expansion gives an n-dimensional integral that contains 2^n terms constructed out of products of the non-interacting Green functions [4, 6]. We compute this integral using the Tensor Cross-Interpolation (TCI) algorithm which vastly outperforms previous quantum Monte Carlo and quasi Monte Carlo approaches for this problem [8]. A large fraction of these notes will be devoted to an introduction to TCI which has applications far beyond the present problem. See [15] for an in-depth description of TCI. An associated open source library may also be found at `https://tensor4all.org`. With this we will be able to calculate all Feynman diagrams up to $n = N$ with typically $N = 20$–25 for our example problem.

The last step of the method consist in reconstructing the function $Q(U, t)$, if possible for both short and long times t and interaction strength U from the knowledge of only N coefficients $Q_n(t)$. The analytical structure of $Q(U, t)$ is quite interesting: At any fine time t, it has an infinite radius of convergence [5] since

$$Q_n \sim \frac{t^n}{n!} \to Q_n U^n \sim \left(\frac{eUt}{n}\right)^n. \tag{6}$$

which implies that $N \sim O(Ut)$ terms are required to converge the sum using the finite sum

$$Q(U, t) \approx \sum_{n=0}^{N} Q_n(t)\, U^n. \tag{7}$$

On the other hand, in the steady state $t \to \infty$, it has a finite radius of convergence R and $Q_n \sim 1/R^n$ and the above naive summation fails for $U > R$. In other words, the two limits $t \to \infty$ and $N \to \infty$ do not commute. Here, we will focus on one approach to perform the reconstruction, the *cross-extrapolation* [9]. It is based on two ideas,

- First, using the naive sum we can obtain $Q(U, t)$ in two different regimes
  - Arbitrary times and small interactions $U < R$.
  - Large interactions but small times ($U \sim N/t$).

  To calculate $Q(U, t)$ at both large t *and* U, it is therefore tempting to perform a *double* extrapolation from these two limits simultaneously.
- Second, we will use the fact that $Q(U, t)$ *almost* factorizes, i.e., seen as a matrix where U are the rows and t the columns, it is of low rank.

As we shall see, cross-extrapolation is a general idea that could be used in many other situations.

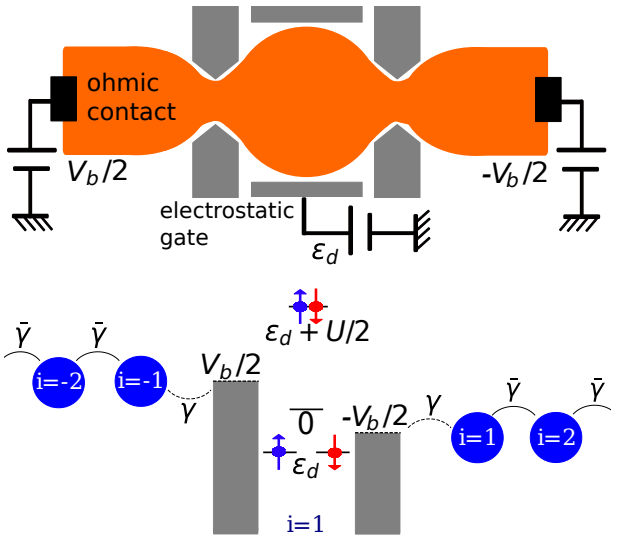


Fig. 2: *Top: electrical diagram of a quantum dot coupled to two electrodes. Bottom: schematic of the SIAM. (Adapted from [10])*

2.3 The SIAM model

Although the approach is in principle general, in practice we will demonstrate it for a concrete model, the out-of-equilibrium SIAM. The model corresponds to a quantum dot, typically constructed by confining electrons with electrostatic gates inside a semiconductor or a semiconductor heterostructure. The quantum dot is modeled by a single interacting level (site $i = 0$) weakly connected to two semi-infinite one dimensional electrodes ($i < 0$ and $i > 0$, respectively) at chemical potential $\mu_{l/r} = \pm V_b/2$, as depicted in Fig. 2. Its Hamiltonian reads

$$\hat{\mathbf{H}} = \sum_{i=-\infty}^{+\infty} \sum_{\sigma\in\{\uparrow,\downarrow\}} \left(\gamma_i \hat{\mathbf{c}}^\dagger_{i,\sigma}\hat{\mathbf{c}}_{i+1,\sigma} + \text{h.c.}\right) + \varepsilon_d\big(\hat{\mathbf{n}}_\uparrow + \hat{\mathbf{n}}_\downarrow\big) + U\,\Theta(t)\,\hat{\mathbf{n}}_\uparrow\hat{\mathbf{n}}_\downarrow \tag{8}$$

where the former sites i are now extended to include the spin $\sigma =\uparrow,\downarrow$ degree of freedom. ε_d is the on-site energy on the dot controlled by an electrostatic gate and $\hat{\mathbf{n}}_\sigma = \hat{\mathbf{c}}^\dagger_{0,\sigma}\hat{\mathbf{c}}_{0,\sigma}$. We work directly in the thermodynamic limit with an infinite number of bath sites. $\Theta(t)$ is the Heaviside function. The hopping between two neighboring sites is denoted by $\gamma_i = \bar{\gamma}$, except for the coupling to the dot $\gamma_0 = \gamma_{-1} = \gamma$. Energies are expressed in units of the tunneling rates to the dot $\Gamma = 2\gamma^2/\bar{\gamma}$. For concreteness, all calculations are performed at zero temperature.

Our goal will be to calculate the charge Q on the dot and the current I flowing from the dot to the right electrode after an interaction quench at $t = 0$.

$$Q(U,t) = \sum_{\sigma\in\{\uparrow,\downarrow\}} \left\langle \hat{\mathbf{c}}^\dagger_{0,\sigma}\hat{\mathbf{c}}_{0,\sigma}\right\rangle \tag{9}$$

$$I(U,t) = -i\gamma \sum_{\sigma\in\{\uparrow,\downarrow\}} \left[\left\langle \hat{\mathbf{c}}^\dagger_{1,\sigma}\hat{\mathbf{c}}_{0,\sigma}\right\rangle - \left\langle \hat{\mathbf{c}}^\dagger_{0,\sigma}\hat{\mathbf{c}}_{1,\sigma}\right\rangle\right]. \tag{10}$$

3 Interaction expansion (problem A)

This section explains the first step of the approach: how to reduce the calculation of $Q_n(t)$ to a multidimensional integral in terms of known objects.

3.1 A short reminder of Keldysh formalism

Our starting point for this work is a formal expansion of the out-of-equilibrium (Keldysh) Green function in powers of electron-electron interactions. This is a standard step [16] which we briefly sketch to introduce our notation. We would also like to demystify Keldysh formalism which is much simpler than often thought to be. In our opinion it is actually conceptually simpler than the imaginary-time or zero temperature formalism at the price of the actual calculations being a bit more cumbersome. Since these calculations will be performed by the computer, this is not necessarily an issue.

One starts by the standard step of "integrating out" the (supposedly known) dynamics of $\hat{\mathbf{H}}_0$, i.e., work in the interaction representation. Using the interaction representation, one defines $\hat{\mathbf{c}}_i(t) = \hat{\mathbf{U}}_0(0,t)\hat{\mathbf{c}}_i\hat{\mathbf{U}}_0(t,0)$ where $\hat{\mathbf{U}}_0(t',t)$ is the evolution operator from t to t' associated with $\hat{\mathbf{H}}_0$. For a time-independent $\hat{\mathbf{H}}_0$, it is simply $\hat{\mathbf{U}}_0(t',t) = e^{-i\hat{\mathbf{H}}_0(t'-t)}$. In this representation, one defines $\tilde{\mathbf{H}}_{\rm int}(\bar{u})$, which is equal to $\hat{\mathbf{H}}_{\rm int}(u)$ with the operators $\hat{\mathbf{c}}_i, \hat{\mathbf{c}}_j^\dagger$ replaced by $\hat{\mathbf{c}}_i(\bar{u}), \hat{\mathbf{c}}_j^\dagger(\bar{u})$. Starting from a non-interacting density matrix ρ_0 at $t = 0$, the average of an observable $\hat{\mathbf{O}}$ at time t is given by

$$\langle\hat{\mathbf{O}}\rangle = \mathrm{Tr}\left[Te^{+i\int d\bar{u}\, U\tilde{\mathbf{H}}_{\rm int}(\bar{u})}\,\tilde{\mathbf{O}}\,Te^{-i\int d\bar{u}\, U\tilde{\mathbf{H}}_{\rm int}(\bar{u})}\,\rho_0\right], \tag{11}$$

where T is the usual time-ordering operator (now necessary because in the interaction representation the interacting Hamiltonian *is* time-dependent even if the original Hamiltonian is not). The above equation is very natural; for instance if $\rho_0 = |\Psi_0\rangle\langle\Psi_0|$ then it corresponds to $\langle\hat{\mathbf{O}}\rangle = \langle\Psi(t)|\hat{\mathbf{O}}|\Psi(t)\rangle$ with $|\Psi(t)\rangle = Te^{-i\int d\bar{u}\, U\tilde{\mathbf{H}}_{\rm int}(\bar{u})}|\Psi_0\rangle$ the state of the system at time t. Looking at Eq. (11), we see that when we perform the expansion in powers of U, there will be two kinds of terms: the ones coming before the operator $\hat{\mathbf{O}}$ and the ones coming after it. To remember if a terms originates from one or the other (before of after), one introduces an index $a = 0$ (before) or $a = 1$ (after). This is the "Keldysh index" and that is all there is to it: the Keldysh formalism is merely a technique for book-keeping the position of the different terms in the expansion.

A bit more formally, one defines the contour ordering for pairs $\bar{t} = (t,a)$: $(t,0) < (t',1)$ for all t,t', $(t,0) < (t',0)$ if $t<t'$ and $(t,1) < (t',1)$ if $t>t'$. The contour ordering operator T_c acts on products of fermionic operators $A, B, C\ldots$ labeled by various "contour times" $\bar{t}_A = (t_A, a_A), \bar{t}_B, \bar{t}_C\ldots$ and reorder them according to the contour ordering: $T_c\, A(\bar{t}_A)B(\bar{t}_B) = AB$ if $\bar{t}_A>\bar{t}_B$ and $T_c\, A(\bar{t}_A)B(\bar{t}_B) = -BA$ if $\bar{t}_A<\bar{t}_B$. The non-interacting contour Green function is defined as

$$g^c_{ij}(\bar{t},\bar{t}') = -i\big\langle T_c\,\hat{\mathbf{c}}_i(\bar{t})\hat{\mathbf{c}}_j^\dagger(\bar{t}')\big\rangle, \tag{12}$$

where $\hat{\mathbf{c}}_i(\bar{t})$ is just $\hat{\mathbf{c}}_i(t)$, the Keldysh index serving only to define the position of the operator after contour ordering. The contour Green function has a matrix structure in a, a' which reads

$$g^c_{ij}(t,t') = \begin{pmatrix} g^T_{ij}(t,t') & g^<_{ij}(t,t') \\ g^>_{ij}(t,t') & g^{\bar{T}}_{ij}(t,t') \end{pmatrix} \tag{13}$$

where $g^T_{ij}(t,t')$, $g^<_{ij}(t,t')$, $g^>_{ij}(t,t')$ and $g^{\bar{T}}_{ij}(t,t')$ are respectively the time-ordered, lesser, greater, and anti-time-ordered Green functions. These non-interacting Green functions will form the actual input of our approach, we will briefly discuss how they are obtained in the next section. Finally, one defines the full Green function $G^c_{ij}(\bar{t},\bar{t}')$ with definitions identical to the above except that $\hat{\mathbf{U}}_0$ is replaced by $\hat{\mathbf{U}}$, the evolution operator associated to the full Hamiltonian $\hat{\mathbf{H}}$. The fundamental expression for $G^c_{ij}(\bar{t},\bar{t}')$ reads

$$G^c_{ij}(\bar{t},\bar{t}') = -i\big\langle T_c\, e^{-i\int d\bar{u}\, U\tilde{\mathbf{H}}_{\rm int}(\bar{u})}\, \hat{\mathbf{c}}_i(\bar{t})\hat{\mathbf{c}}^\dagger_j(\bar{t}')\big\rangle, \tag{14}$$

where the integral over $\bar{u}$ is taken along the Keldysh contour, i.e., increasing u for $a=0$ and decreasing for $a=1$. We are almost ready to perform the expansion.

3.2 Non-interacting Green functions

The dynamics of the non-interacting problem is, in principle, "trivial" in the sense that one simply needs to solve the one-body problem and "fill up" the states up to the Fermi energy. In practice it may not be entirely straightforward but there are well known and mature techniques to calculate both the stationary [17] and time-dependent properties [18]. There are also associated open source software such as Kwant [13] for the stationary problem and TKwant [14] for the time-dependent one. The latter explicitly supports the calculation of $g^T_{ij}(t,t')$, $g^<_{ij}(t,t')$, $g^>_{ij}(t,t')$ and $g^{\bar{T}}_{ij}(t,t')$.

One approach is to relate the non-interacting Green functions to the (Scattering) wave functions in the system [18]

$$g^<_{ij}(t,t') = i\sum_\alpha \int \frac{dE}{2\pi}\, f_\alpha(E)\, \Psi_{\alpha E}(t,i)\Psi^*_{\alpha E}(t',j). \tag{15}$$

Here, α labels the various propagating channels of the leads, $\Psi_{\alpha E}(t,i)$ the scattering state at energy E (in the electrode) and $f_\alpha(E)$ the corresponding Fermi distribution function. The greater Green function $g^>_{ij}(t,t')$ is obtained by replacing the Fermi functions $f(E)$ with $f(E)-1$. The actual calculations performed in this article are restricted to a stationary non-interacting system, where the above expression further simplifies to

$$g^<_{ij}(t-t') = i\sum_\alpha \int \frac{dE}{2\pi}\, f_\alpha(E)\, \Psi_{\alpha E}(i)\Psi^*_{\alpha E}(j)\, e^{-iE(t-t')}. \tag{16}$$

Here again, the stationary scattering wave functions $\Psi_{\alpha E}(i)$ are standard objects [17]. They are the eigenvectors of $\hat{\mathbf{H}}_0$ with one caveat: they need to be classified into states incoming from the

left and states incoming from the right. These objects are in fact direct outputs of the Kwant software [13]. Once the lesser and greater Green functions are known, one completes the 2×2 Keldysh matrix with the standard relations

$$g^T_{ij}(t,t') = \Theta(t-t')\, g^>_{ij}(t,t') + \Theta(t'-t)\, g^<_{ij}(t,t') \tag{17}$$
$$g^{\bar{T}}_{ij}(t,t') = \Theta(t'-t)\, g^>_{ij}(t,t') + \Theta(t-t')\, g^<_{ij}(t,t')\,. \tag{18}$$

3.3 The expansion itself

We continue to follow the literature and perform the expansion in powers of U. We obtain

$$G^c_{ij}(\bar{t},\bar{t}')=-i\sum_{n=0}^{+\infty}\frac{(-i)^n}{n!}U^n\sum_{\{a_i\}}(-1)^{\sum_i a_i}\int du_1\cdots du_n\left\langle T_c\tilde{\mathbf{H}}_{\text{int}}(\bar{u}_1)\tilde{\mathbf{H}}_{\text{int}}(\bar{u}_2)\cdots\tilde{\mathbf{H}}_{\text{int}}(\bar{u}_n)\hat{\mathbf{c}}_i(\bar{t})\hat{\mathbf{c}}^\dagger_j(\bar{t}')\right\rangle \tag{19}$$

and we are left to calculate the non-interacting average of a (possibly large) product of creation and destruction operators. This is done, as usual, using Wick's theorem. Wick's theorem states that an average over a non-interacting density matrix of a product of fermionic operators takes the form

$$\left\langle\hat{\mathbf{c}}^\dagger_1\hat{\mathbf{c}}_1\hat{\mathbf{c}}^\dagger_2\hat{\mathbf{c}}_2\cdots\hat{\mathbf{c}}^\dagger_M\hat{\mathbf{c}}_M\right\rangle = \sum_P(-1)^{|P|}\left\langle\hat{\mathbf{c}}^\dagger_1\hat{\mathbf{c}}_{P(1)}\right\rangle\left\langle\hat{\mathbf{c}}^\dagger_2\hat{\mathbf{c}}_{P(2)}\right\rangle\cdots\left\langle\hat{\mathbf{c}}^\dagger_M\hat{\mathbf{c}}_{P(M)}\right\rangle \tag{20}$$

where the sum runs over all the permutation P of M elements, $|P| = \pm1$ is its signature and $P(a)$ the image of a through the corresponding permutation. The numbers $1, 2, \ldots M$ are just shorthands for all the parameters of the fermionic operators: sites i (including spin), times u and Keldysh index a.

This is where the numerical route starts to differ from the analytical one. Usually, one would identify each permutation with a Feynman diagram and start do derive the corresponding Feynman rules. But as already discussed, the problem is that we would have far too many diagrams (there are $M!$ permutations in the above expression). For numerical purposes, we will make a simple remark: that the right-hand-side of Eq. (20) is actually the definition of the determinant of a $M\times M$ matrix:

$$\left\langle\hat{\mathbf{c}}^\dagger_1\hat{\mathbf{c}}_1\hat{\mathbf{c}}^\dagger_2\hat{\mathbf{c}}_2\cdots\hat{\mathbf{c}}^\dagger_M\hat{\mathbf{c}}_M\right\rangle = \det\left\langle\hat{\mathbf{c}}^\dagger_a\hat{\mathbf{c}}_b\right\rangle. \tag{21}$$

Since the calculation of the determinant of a $M\times M$ matrix takes only $M^3 \ll M!$ operations, this sounds very appealing. Now putting things together, we arrive at a formula that is conceptually very simple: the left-hand-side is what we want and the right-hand-side is a set of multi-dimensional integrals of matrices whose entries are known. The problem is therefore "reduced to quadrature"

$$G^c_{ij}(\bar{t},\bar{t}') =\sum_{n=0}^{+\infty}\frac{i^n}{n!}U^n\sum_{\{a_i\}}(-1)^{\sum_i a_i}\int du_1\cdots du_n\sum_{i_1j_1k_1l_1}V_{i_1j_1k_1l_1}(u_1)\cdots\sum_{i_nj_nk_nl_n}V_{i_nj_nk_nl_n}(u_n)\det\mathbf{M}_n \tag{22}$$

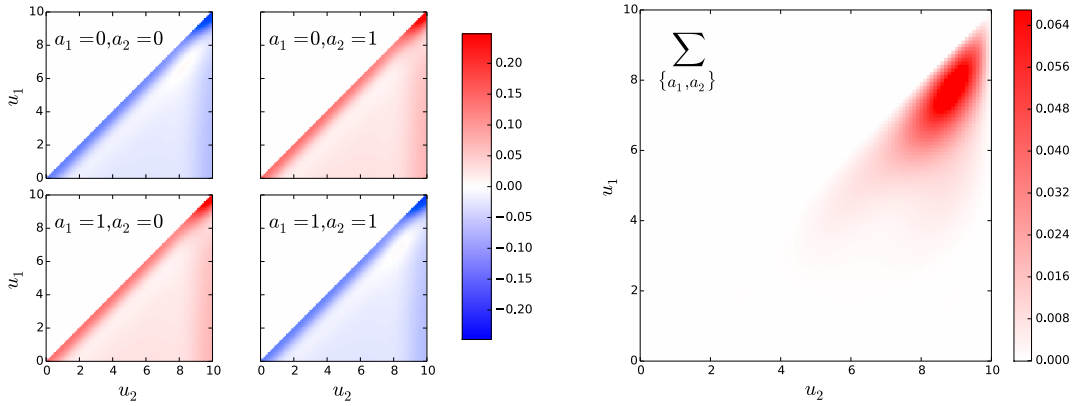


Fig. 3: *Left: Colorplot of the integrand of Q_2 as a function of the two times u_1 and u_2 for SIAM with μ_L=μ_R=0, ε_d=0, T=0 and t=10. The four panels correspond to the four possible values of the two Keldysh indices a_1 and a_2. The explicit form of the integrand is $f(u_1,u_2,a_1,a_2) = -\mathrm{Im}(-1)^{\sum_i a_i} \det \boldsymbol{M}_2(u_1,u_2,a_1,a_2)$. Right: Same parameters as on the left but the integrand has now been summed over Keldysh indices. The colorplot represents $f(u_1,u_2) = i\sum_{a_1,a_2}(-1)^{\sum_i a_i} \det \boldsymbol{M}_2(u_1,u_2,a_1,a_2)$ (f is real). Note that the integrand is now real, positive and concentrated around u_1=u_2=t. (Adapted from [4])*

where the $(2n+1)\times(2n+1)$ matrix $\mathbf{M}_n$ is given by

$$\mathbf{M}_n = \begin{pmatrix} g^<_{k_1 i_1}(\bar{u}_1,\bar{u}_1) & g^>_{k_1 j_1}(\bar{u}_1,\bar{u}_1) & g^c_{k_1 i_2}(\bar{u}_1,\bar{u}_2) & \cdots & g^c_{k_1 j}(\bar{u}_1,\bar{t}') \\ g^<_{l_1 i_1}(\bar{u}_1,\bar{u}_1) & g^<_{l_1 j_1}(\bar{u}_1,\bar{u}_1) & g^c_{l_1 i_2}(\bar{u}_1,\bar{u}_2) & \cdots & g^c_{l_1 j}(\bar{u}_1,\bar{t}') \\ g^c_{k_2 i_1}(\bar{u}_2,\bar{u}_1) & g^c_{k_2 j_1}(\bar{u}_2,\bar{u}_1) & g^<_{k_2 i_2}(\bar{u}_2,\bar{u}_2) & \cdots & g^c_{k_2 j}(\bar{u}_2,\bar{t}') \\ \vdots & \vdots & \vdots & \ddots & \vdots \\ g^c_{k_n i_1}(\bar{u}_n,\bar{u}_1) & g^c_{k_n j_1}(\bar{u}_n,\bar{u}_1) & g^c_{k_n i_2}(\bar{u}_n,\bar{u}_2) & \cdots & g^c_{k_n j}(\bar{u}_n,\bar{t}') \\ g^c_{l_n i_1}(\bar{u}_n,\bar{u}_1) & g^c_{l_n j_1}(\bar{u}_n,\bar{u}_1) & g^c_{l_n i_2}(\bar{u}_n,\bar{u}_2) & \cdots & g^c_{l_n j}(\bar{u}_n,\bar{t}') \\ g^c_{i i_1}(\bar{t},\bar{u}_1) & g^c_{i j_1}(\bar{t},\bar{u}_1) & g^c_{i i_2}(\bar{t},\bar{u}_2) & \cdots & g^c_{i j}(\bar{t},\bar{t}') \end{pmatrix} \tag{23}$$

and the zeroth order term is $g^c_{ij}(\bar{t},\bar{t}')$. [Note that there was a typo in the above expression in [4], see [5] for the correction]. To calculate an actual observable, we just recognize that it corresponds to the lesser Green function at equal times, i.e.,

$$\left\langle \hat{\mathbf{U}}(0,t)\, \hat{\mathbf{c}}^\dagger_i \hat{\mathbf{c}}_j\, \hat{\mathbf{U}}(t,0) \right\rangle = -iG^<_{ji}(t,t). \tag{24}$$

We are just left with a simple problem: to obtain $Q_n(t)$ we must integrate over n times and sum over n Keldysh indices (in general we also need to sum over the n different vertices V_{ijkl} but in the case of SIAM, this sum reduces to a single term). There is a caveat however. To see it, let us look at the integrand of Q_2 in the 4-sectors defined by the two Keldysh indices, as shown in the left panel of Fig. 3. We immediately see that the corresponding integrals are not going to behave well: the integrand does not seem to decay when the time gets away from the time where the measurement is made (reminder: we switch on the interaction at $t = 0$ and measure, here, at $t = 10$). This is to be expected and is why the determinant form of the Wick theorem was not super successful before: the expansion includes all Feynman diagrams, *including* the disconnected diagrams. It is well known that these disconnected diagrams do not contribute to

the final result. Yet, in this expansion they are present and a priori only cancel at the end of the calculation after integration and summation over Keldysh indices.
The magic occurs when one performs the summation over the Keldysh indices, as shown in the right panel of Fig. 3: we find that the cancellation of the disconnected diagrams occurs *before* the integration over times. The proof is a bit technical and is shown in the appendix of [4]. The consequence of this property is that, one is left with a well behaved integral to calculate. The cost of each call to the integrand is $O(2^n)$ which is still exponential but very mild compared to the initial $n!$ cost we started with. To calculate these integrals we will use Tensor Cross Interpolation, which we now explain.

4 Tensor cross interpolation for integration (problem B)

We will now discuss a very important algorithm – Tensor Cross Interpolation (TCI) – that has a very special place in the zoo of tensor network algorithms. This algorithm takes as an input a "virtual" tensor $F_{\sigma_1,\sigma_2,\ldots,\sigma_N}$ where each index σ_i takes d_i different values (for simplicity we assume that $d_i \equiv d$ is constant). It returns as an output a Matrix Product State (MPS) that approximates $F_{\vec{\sigma}}$ in the best possible way. For an introduction to MPS, see [19]. For the purpose of this article, the MPS is merely the following expression

$$F_{\sigma_1,\sigma_2,\ldots,\sigma_N} \approx \sum_{\{\alpha_i\}} M^1_{\alpha_1}(\sigma_1) M^2_{\alpha_1\alpha_2}(\sigma_2) \cdots M^N_{\alpha_{N-1}}(\sigma_N), \tag{25}$$

where the matrices $M_a(\sigma)$ have a maximum size χ, known as the bond dimension. $F_{\vec{\sigma}}$ is virtual in the sense that the input of the algorithm is *not* the actual tensor (which would be an exponentially large object with d^N elements). Rather it is a function that takes $\vec{\sigma} = (\sigma_1, \sigma_2, \ldots, \sigma_N)$ as an input and returns the corresponding value $F_{\vec{\sigma}}$. TCI is very different from many other tensor network algorithms (e.g. DMRG [19]): here $F_{\vec{\sigma}}$ is actually known by the user, what is not known is its MPS representation. Once one has this MPS, one can use it for calculating, e.g., integrals or plenty of other applications that we shall not discuss, see [15]. TCI is really a "gateway" that allows one to take a problem that is *not* formulated in terms of tensor network and transform it into this framework.
Another peculiarity of TCI is that it is a *learning* algorithm akin to what is done in machine learning. More precisely it is an active learning algorithm since TCI decides on the data $(\vec{\sigma}, F_{\vec{\sigma}})$ that will be requested. As in machine learning, only a very tiny fraction of the possible configurations $\vec{\sigma}$ will be explored, and as in machine learning the fact that the resulting model interpolates correctly between the configurations can be spectacular. On the other hand there are strong differences with deep neural networks: the optimization has nothing to do with gradient descent (and is way more effective) and the resulting function much more structured (for instance we can easily calculate, e.g., integrals, we cannot do that with a neural network). The cost for these added features is a more restrictive set of applications: TCI is only effective for problems where the level of "entanglement" is limited (small χ).

The presentation below is mostly based on section III of [8] with a few more advanced aspects borrowed from [15] to which we also refer for the references to the original literature. The readers can also have a look at the tensor4all open source library that implements these algorithms https://tensor4all.org.

4.1 Compressing low rank matrices

Before we can get into TCI, we need a matrix factorization formula for low rank (or approximately low rank) matrices that is based on Gaussian elimination and the concept of the Schur complement [20]. This formula (the "cross interpolation") will be almost as good as the Singular Value Decomposition (SVD, which is optimum) but with a key advantage: it can be performed without the need to access the full matrix A: only a set of χ rows and columns will be needed.

4.1.1 Revisiting Gaussian elimination

We consider an arbitrary matrix A that we put in a 2×2 block form,

$$A = \begin{pmatrix} A_{11} & A_{12} \\ A_{21} & A_{22} \end{pmatrix} \tag{26}$$

Following the strategy of Gaussian elimination, we can put this matrix in triangular form as (provided the A_{11} block is invertible)

$$\begin{pmatrix} 1 & 0 \\ -A_{21}A_{11}^{-1} & 1 \end{pmatrix} \begin{pmatrix} A_{11} & A_{12} \\ A_{21} & A_{22} \end{pmatrix} = \begin{pmatrix} A_{11} & A_{12} \\ 0 & A_{22}-A_{21}A_{11}^{-1}A_{12} \end{pmatrix}. \tag{27}$$

We can proceed on the columns to eliminate the A_{12} block and finally obtain

$$\begin{pmatrix} 1 & 0 \\ -A_{21}A_{11}^{-1} & 1 \end{pmatrix} \begin{pmatrix} A_{11} & A_{12} \\ A_{21} & A_{22} \end{pmatrix} \begin{pmatrix} 1 & -A_{11}^{-1}A_{12} \\ 0 & 1 \end{pmatrix} = \begin{pmatrix} A_{11} & 0 \\ 0 & A_{22}-A_{21}A_{11}^{-1}A_{12} \end{pmatrix}. \tag{28}$$

This equation will play a key role in multiple places. The quantity $A_{22}-A_{21}A_{11}^{-1}A_{12} \equiv [A/A_{11}]$ will also appear over and over and we shall therefore give it its name: it is called the Schur complement $[A/A_{11}]$ of A with respect to the 11 block. The block triangular matrices can be trivially inverted and we arrive at a "block LDU" decomposition $A = LDU$ in terms of a block lower triangular L, block diagonal D and block upper triangular matrix U

$$\begin{pmatrix} A_{11} & A_{12} \\ A_{21} & A_{22} \end{pmatrix} = \begin{pmatrix} 1 & 0 \\ A_{21}A_{11}^{-1} & 1 \end{pmatrix} \begin{pmatrix} A_{11} & 0 \\ 0 & [A/A_{11}] \end{pmatrix} \begin{pmatrix} 1 & A_{11}^{-1}A_{12} \\ 0 & 1 \end{pmatrix}. \tag{29}$$

Among the various corollaries of this equation, it provides a close form for the determinant:

$$\det A = \det[A_{11}]\ \det[A/A_{11}] \tag{30}$$

The Schur complement has many other nice properties, see [15] for a discussion. For instance one does not need to take the Schur complement directly with respect to en entire block A_{11}, one may do it sub-block after sub-block and if one does so, the order in which one takes the Schur complements does not matter.

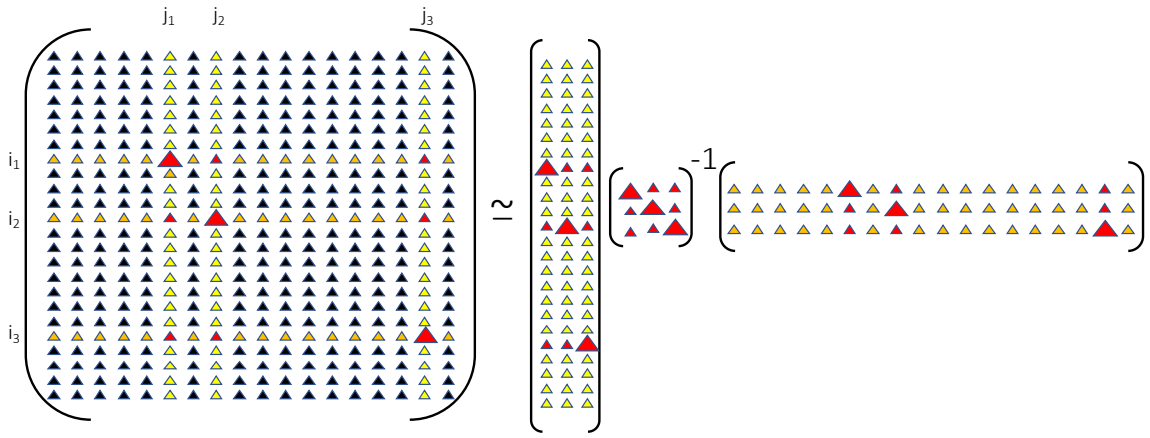


Fig. 4: *Illustration of the cross interpolation (CI) of a matrix. The large red triangles indicate real pivots and the smaller red triangles indicate automatically generated pivots. The right-hand side only contains small subparts of the matrix. (Adapted from [8])*

4.1.2 Cross Interpolation

The cross interpolation formula approximates $A \approx A_{\text{CI}}$, where A_{CI} is defined as

$$A_{\text{CI}} = \begin{pmatrix} A_{11} \\ A_{21} \end{pmatrix} (A_{11})^{-1} \begin{pmatrix} A_{11} & A_{12} \end{pmatrix}. \tag{31}$$

In other words, the Schur complement is the *error* of the cross interpolation,

$$A = A_{\text{CI}} + \begin{pmatrix} 0 & 0 \\ 0 & [A/A_{11}] \end{pmatrix}. \tag{32}$$

An important remark is that to construct A_{CI}, one does not need to know anything about A_{22}. Indeed, when a matrix is of (low) rank χ, we only need χ independent vectors (the first matrix in the definition of A_{CI}) and χ rows (which tells us how the other vectors decompose in terms of the independent ones). The cross interpolation formula has two important properties: (*i*) first it is exact when evaluated on the blocks that have been used to construct it (A_{11}, A_{12} and A_{12}) as evident in the above equation. We refer to this as the interpolation property. (*ii*) Second it is exact if A_{11} is a $\chi \times \chi$ matrix and A is exactly of rank χ. To prove this second assertion, we construct the sub-matrix of A that contains the 11 block plus a single extra row i_0 and a single extra column j_0. Using the Schur complement, we have:

$$\left| \det \begin{pmatrix} A_{11} & A_{1j_0} \\ A_{i_0 1} & A_{i_0 j_0} \end{pmatrix} \right| = \left| \det A_{11} \right| \times \left| A_{i_0 j_0} - A_{i_0 1} A_{11}^{-1} A_{1 j_0} \right|. \tag{33}$$

(with a slight abuse of notations that mixes indexing with block indexing). The left hand side is zero by definition of A being of rank χ (it is a $(\chi{+}1){\times}(\chi{+}1)$ matrix) hence $A_{i_0 j_0} - A_{i_0 1} A_{11}^{-1} A_{1 j_0} = 0$, i.e., the cross interpolation is exact.

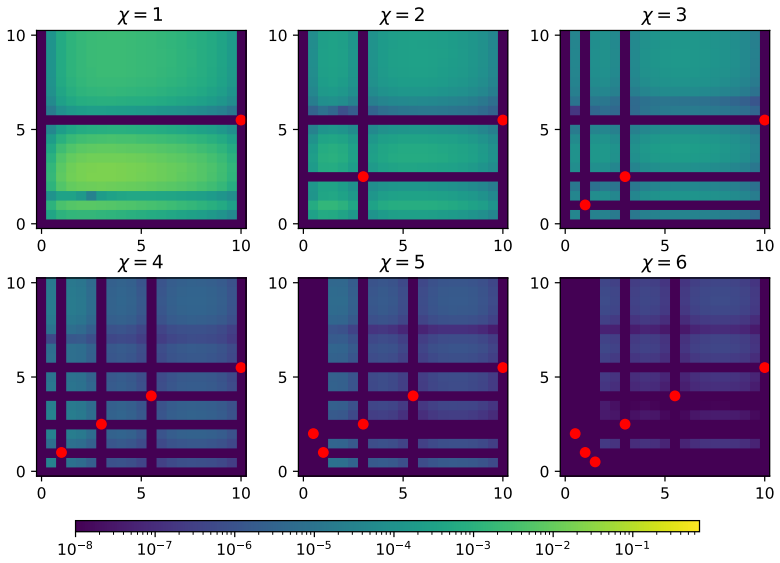


Fig. 5: *Error* $\left|A_{ij}-[A_{\rm CI}]_{ij}\right|$ *versus* i *and* j *at different stages of the Cross-Interpolation for an* $M\times M$ *matrix with* $M=20$. *In this toy example,* $A_{ij} = \left(\frac{i/M}{i/M+1}\right)^4 \left(1+e^{-(j/M)^2}\right)\left[1+(j/M)\cos(j/M)e^{-(j/M)\frac{i/M}{(i/M)+1}}\right]$. *The red dots indicate the pivots. The* x *and* y *axis have been rescaled to be in* $[0,10]$. *(Adapted from Jeannin et al. [10])*

4.1.3 Practical cross interpolation

In practice to build up $A_{\rm CI}$ we need to choose the A_{11} block properly. Let us introduce the notation that we will use to design the chosen rows and columns. Let $\mathcal{I} = \{i_1, i_2, \ldots, i_\chi\}$ (respectively $\mathcal{J} = \{j_1, j_2, \ldots, j_\chi\}$) denote a list of the rows (columns) of A (that will form the A_{11} block). Indexing these sets gives the corresponding index: $\mathcal{I}_a \equiv i_a$ is its a$^{\rm th}$ element. The list of the indices of all rows (columns) is denoted $\mathbb{I} = \{1, 2, \ldots, M\}$ ($\mathbb{J} = \{1, 2, \ldots, N\}$). Following usual programming convention (as in Python/MATLAB/Julia), we denote by $A(\mathcal{I}, \mathcal{J})$ the submatrix of A comprised of the rows $\mathcal{I}$ and columns $\mathcal{J}$; $A(\mathcal{I}, \mathcal{J})_{ab} \equiv A_{\mathcal{I}_a, \mathcal{J}_b}$. We have

$$A = A(\mathbb{I}, \mathbb{J}) \tag{34}$$

$$A_{\rm CI} = A(\mathbb{I}, \mathcal{J})A(\mathcal{I}, \mathcal{J})^{-1}A(\mathcal{I}, \mathbb{J}) \tag{35}$$

Equation (35) is illustrated graphically in Fig. 4. The rows and columns of $A(\mathcal{I}, \mathcal{J})$ are called the *pivots* and $A(\mathcal{I}, \mathcal{J})$ is the *pivot matrix*. The pivots are chosen one by one iteratively in such a way as to maximize the determinant of the matrix $A(\mathcal{I}, \mathcal{J}) = A_{11}$ in order to guarantee that the chosen vectors are truly independent. This is known as the maximum volume (maxvol) principle. Another way to look at the maxvol principle is that each new pivot is chosen to be the one where the current error of $A_{\rm CI}$ is maximum (maxerror) so that adding this pivot brings the largest amount of new information into the approximation. The proof of the equivalence between maxvol and maxerror is in Eq. (33). A practical example of how the error decreases for the cross extrapolation of a (toy) matrix is shown in Fig. 5.

The important thing to remember about cross interpolation is that it is given in terms of slices of the matrix A: it is entirely defined in terms of the two lists $\mathcal{I}$ and $\mathcal{J}$ of the rows and columns of the pivot matrices.

4.1.4 Stable evaluation of the cross interpolation

We need a last ingredient to be able to use cross interpolation in practice. Indeed, as one adds more pivots, the A_{11} matrix becomes increasingly singular so we do not want to calculate A_{11}^{-1} explicitly as it becomes numerically unstable (even for moderate values of χ). There are several ways to stabilize the evaluation of

$$\begin{pmatrix} A_{11} \\ A_{21} \end{pmatrix} (A_{11})^{-1}. \tag{36}$$

The first is to perform a QR factorization of the first matrix, writing

$$\begin{pmatrix} A_{11} \\ A_{21} \end{pmatrix} = \begin{pmatrix} Q_{11} \\ Q_{21} \end{pmatrix} R\,. \tag{37}$$

The Q matrix being an isometry, it is well conditioned. All the (possibly very small) singular values of A_{11} are in the triangular matrix R which disappears from the calculation. Indeed, we have

$$\begin{pmatrix} A_{11} \\ A_{21} \end{pmatrix} (A_{11})^{-1} = \begin{pmatrix} 1 \\ Q_{21}Q_{11}^{-1} \end{pmatrix}. \tag{38}$$

The second way to stabilize this calculation (now our preferred way) is to realize that Eq. (29) can be rewritten as

$$\begin{pmatrix} A_{11} & A_{12} \\ A_{21} & A_{22} \end{pmatrix} = \begin{pmatrix} A_{11} & A_{12} \\ A_{21} & A_{21}A_{11}^{-1}A_{12} \end{pmatrix} + \begin{pmatrix} 0 & 0 \\ 0 & [A/A_{11}] \end{pmatrix} \tag{39}$$

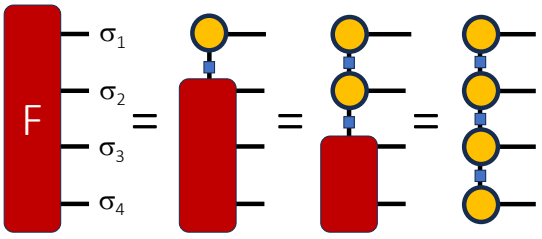
in other words, if one ignores the Schur complement one is left with the cross interpolation, Eq. (32). We can use Eq. (29) iteratively, performing the decomposition pivot after pivot (as stated above, this is legit, the proof can be found in [15]) building a decomposition in the form $A_{\mathrm{CI}} = LDU$ where L is lower triangular, D diagonal and U upper triangular. This is nothing but the celebrated LU decomposition used for, e.g., inverting matrices. The only caveat is that it is partial (we stop it after getting the χ pivots, we do not go all the way through) and it is rank revealing (we use the maxvol criteria to select the pivots). It is the prrLU (partial rank revealing LU) decomposition. But again, this is just a neat way to obtain the cross interpolation in a stable way.

4.2 TCI: Extension of CI to n-dimensional tensors

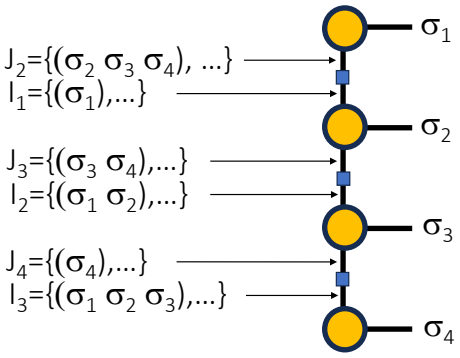
We now have everything we need to factorize matrices, we need to extend cross interpolation to tensors. This is what TCI does.

4.2.1 TCI: naive approach

We can decompose any tensor using cross interpolation iteratively. We first group together all indices except σ_1, apply cross interpolation on the resulting matrix and repeat the procedure until the tensor has been entirely factorized. Graphically this (very naive) algorithm has the following form:



where the small blue squares stand for the inverse of the pivot matrices. This algorithm is not practical since applying cross interpolation on an exponentially large matrix requires an exponentially large amount of memory and computing time. However, it has the merit of showing that such a decomposition exists. More interestingly, it shows the structure of the "pivots" of a TCI representation. Indeed, the cross interpolation is defined in terms of the lists $\mathcal{I}$ and $\mathcal{J}$. Now we have one of such list on each side of the pivot matrices (the blue squares above). Each element of this list is now a list itself that contains the value of the corresponding indices. We call such a list a *multi-index*. More explicitly, we have for our example,



The most tricky thing about writing a TCI code is to correctly do the book keeping of these lists of lists.

4.2.2 TCI: formal form

Let us introduce our notations a bit more formally. A TCI representation is essentially a MPS but we keep the pivot matrices explicit so that the TCI is entirely made of "slices" of the original tensor. For any α such that $1 \leq \alpha \leq N$, we consider "row" multi-indices $(\sigma_1, \sigma_2, \ldots, \sigma_\alpha)$ and "column" multi-indices $(\sigma_\alpha, \sigma_{\alpha+1}, \ldots, \sigma_N)$. The pivot lists are defined as $\mathcal{I}_\alpha = \{i_1, i_2, \ldots, i_\chi\}$ for the "rows" (the multi-indices have size α) and $\mathcal{J}_\alpha = \{j_1, j_2, \ldots, j_\chi\}$ for the "columns" (the multi-indices have size $N-\alpha+1$). For notational convenience, we define $\mathcal{I}_0$ and $\mathcal{J}_{N+1}$ as

singleton sets each comprised of an empty multi-index. Last, we use the symbol $\oplus$ to denote the concatenation of multi-indices

$$(\sigma_1, \sigma_2, \ldots, \sigma_{\alpha-1}) \oplus (\sigma_\alpha) \oplus (\sigma_{\alpha+1}, \ldots, \sigma_N) \equiv (\sigma_1, \ldots, \sigma_N). \tag{40}$$

We are now ready to define the TCI representation formally. The definitions are a bit scary looking but they are nothing else than what we obtained above using the naive algorithm. The blue squares are the pivot matrices P_α defined as,

$$[P_\alpha]_{ij} \equiv F_{[\mathcal{I}_\alpha]_i \oplus [\mathcal{J}_{\alpha+1}]_j} \tag{41}$$

(with $P_N = 1$ for notation convenience). Likewise the orange three leg tensors T_α are defined as,

$$[T_\alpha]_{i\sigma j} \equiv F_{[\mathcal{I}_{\alpha-1}]_i \oplus \sigma \oplus [\mathcal{J}_{\alpha+1}]_j}. \tag{42}$$

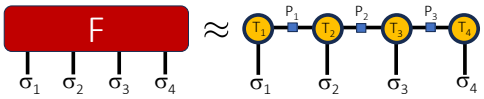
We also introduce the matrix $T_\alpha(\sigma)$ defined as

$$T_\alpha(\sigma)_{ij} \equiv [T_\alpha]_{i\sigma j} \tag{43}$$

to make contact with the standard MPS form. Using these notations, we have,

$$F_{\vec{\sigma}} \approx [F_{\text{TCI}}]_{\vec{\sigma}} \equiv \prod_{\alpha=1}^{N} T_\alpha(\sigma_\alpha) P_\alpha^{-1}. \tag{44}$$

or graphically



The TCI representation is defined entirely by the selected sets of "rows" and "columns" $\mathcal{I}_\alpha$ and $\mathcal{J}_\alpha$, so that constructing an accurate representation of $F_{\vec{\sigma}}$ amounts to optimizing the selection of $\mathcal{I}_\alpha$ and $\mathcal{J}_\alpha$ for $1 \leq \alpha \leq N$. Only $O(Nd\chi^2) \ll d^N$ entries of $F_{\vec{\sigma}}$ are used in the approximation.

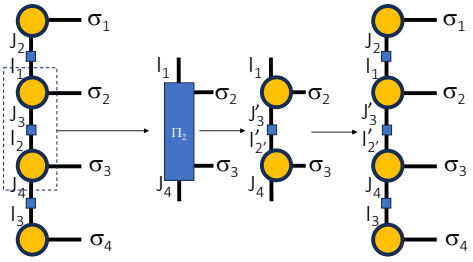
4.2.3 Practical TCI algorithm

We start with an initial point $(\sigma_1, \ldots, \sigma_n)$ which we split in $N-1$ different ways $(\sigma_1, \ldots, \sigma_N) = (\sigma_1, \ldots, \sigma_\alpha) \oplus (\sigma_{\alpha+1}, \ldots, \sigma_N)$ to obtain one element for each of the sets $\mathcal{I}_\alpha$ and $\mathcal{J}_\alpha$. This yields the initial $\chi = 1$ TCI, which is exact if the tensor $F_{\vec{\sigma}}$ factorizes as a product of tensors of one variable.

To improve on this TCI, we are going to sweep over pairs of tensors $(T_\alpha, T_{\alpha+1})$ as is done in two-site DMRG. The sweeping is performed until convergence. For each pair, we use the following procedure: First, we introduce yet another tensor, $\mathit{\Pi}_\alpha$ as

$$[\mathit{\Pi}_\alpha]_{i\sigma\sigma' j} \equiv F_{[\mathcal{I}_{\alpha-1}]_i \oplus \sigma \oplus \sigma' \oplus [\mathcal{J}_{\alpha+2}]_j}. \tag{45}$$

Second, we replace $\left[T_\alpha(\sigma_\alpha) P_\alpha^{-1} T_{\alpha+1}(\sigma_{\alpha+1})\right]_{ij}$ inside the TCI by $[\mathit{\Pi}_\alpha]_{i\sigma_\alpha\sigma_{\alpha+1}j}$ because the former is a cross interpolation of the latter, hence we might as well use the more precise form. Next, we continue the cross interpolation of $\mathit{\Pi}_\alpha$ (seen as a matrix $[\mathit{\Pi}_\alpha]_{i\otimes\sigma,\sigma'\otimes j}$) by adding a new pivot, i.e., one new entry to the list $\mathcal{I}_\alpha$ and $\mathcal{J}_{\alpha+1}$. Graphically, we have



and that is it; this is a fully functional TCI algorithm (although there are versions that are more suitable for certain purposes). During the sweeping, we monitor the so-called pivot error between the $\mathit{\Pi}_\alpha$ tensor and its cross interpolation. We stop the iteration when this error is below a certain threshold during an entire sweep

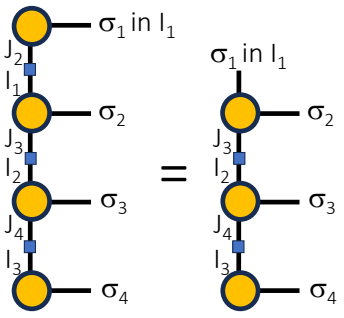
$$\epsilon_{\mathit{\Pi}} = \max_{i\sigma\sigma' j} \left| [\mathit{\Pi}_\alpha]_{i\sigma\sigma' j} - \left[T_\alpha(\sigma) P_\alpha^{-1} T_{\alpha+1}(\sigma')\right]_{ij} \right| . \tag{46}$$

Now, there is a subtle point that we have swept under the rug: the fact that the error $\epsilon_{\mathit{\Pi}}$ is *actually* the error of the TCI approximation for the corresponding pivots,

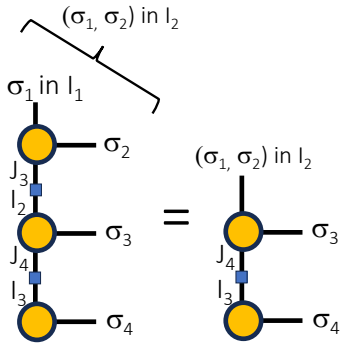
$$\epsilon_{\mathit{\Pi}} = \max_{i\sigma\sigma' j} \left| F_{[\mathcal{I}_{\alpha-1}]_i \oplus \sigma \oplus \sigma' \oplus [\mathcal{J}_{\alpha+2}]_j} - [F_{\mathrm{TCI}}]_{[\mathcal{I}_{\alpha-1}]_i \oplus \sigma \oplus \sigma' \oplus [\mathcal{J}_{\alpha+2}]_j} \right| . \tag{47}$$

Therefore improving the cross interpolation of $\mathit{\Pi}_\alpha$ does indeed improve the TCI approximation itself (at least for these pivots). To prove this point, we need to remember that the cross interpolation is exact on the pivots. We also need to realize that there is a form of "nesting condition" that connects the different pivot lists: a pivot $i_\alpha \in \mathcal{I}_\alpha$ takes the form $i_\alpha = i_{\alpha-1} \oplus \sigma_\alpha$ with $i_{\alpha-1} \in \mathcal{I}_{\alpha-1}$ (and a similar condition for the $\mathcal{J}_\alpha$). Using these two ingredients, one easily sees that there is a telescopic condition for the restriction of the TCI on these pivots.

Let us see how this works concretely. We start by restricting σ_1 to values that belong to $\mathcal{I}_1$. For these values, T_1 and P_1 cancel due to the interpolation property. Schematically, it reads



We continue by requesting that $\sigma_1 \oplus \sigma_2 \in \mathcal{I}_2$ which we can do because of the nested condition. The interpolation property implies that



and we can continue like that down the TCI representation. Since the same thing can be done with the $\mathcal{J}_\alpha$, we can also go up from the bottom of the TCI. See [8] or [15] for a more formal proof of the statement.

4.2.4 Application to integrals

There are many things that one may do with a TCI representation. As stated, it is an entry point to be able to use the many algorithms that have been developed for many-body physics. For the purpose of these notes, we are interested in multi-dimensional integration. It is an alternative to the Monte Carlo approach. When it works (the convergence with χ will depend on the integrand), it compares very favorably to Monte Carlo in two aspects: (*i*) the convergence is much faster than what is allowed by the law of large numbers; (*ii*) it is immune to the sign problem that plagues Monte Carlo whenever the integrand has an oscillatory behavior.
In its plainest version, multi-dimensional integration is quite straightforward. Let us consider a function $f(u_1, \ldots, u_n)$ (our integrand). We discretize it using a plain quadrature rule with d points per dimension $a_1, \ldots, a_d$ and the corresponding weight $w_1, \ldots, w_d$. For instance, we could use the Gauss-Kronrod-21 rule (with $d = 21$) or even the trapezoidal rule. We write

$$\int du_1 \cdots du_n f(u_1, \ldots, u_n) \approx \sum_{\sigma_1 \cdots \sigma_n} F_{\vec{\sigma}}\, w_{\sigma_1} \cdots w_{\sigma_N} \tag{48}$$

with

$$F_{\vec{\sigma}} \equiv f(a_{\sigma_1}, \ldots, a_{\sigma_n}). \tag{49}$$

The problem, of course, is that the sum runs over d^n different configurations which is impractical. This is known as the curse of dimensionality. If, however, we can factorize $F_{\vec{\sigma}}$ using TCI, then calculating this sum reduces to n matrix-vector multiplication. It becomes essentially trivial

$$\sum_{\sigma_1 \cdots \sigma_n} F_{\vec{\sigma}}\, w_{\sigma_1} \cdots w_{\sigma_n} \approx \prod_{\alpha=1}^{n} \sum_{\sigma} T_\alpha(\sigma) P_\alpha^{-1}. \tag{50}$$

This is essentially what we do to calculate our coefficients Q_n. There is a small difficulty that we will not discuss in details though: we do not perform TCI $f(u_1, \ldots, u_n)$ (whose rank is very high) but rather $f(u_1, u_2{-}u_1, u_3{-}u_2, \ldots, u_n{-}u_{n-1})$ (whose rank is much smaller). The reason is that the later function automatically enforces time-ordering – or, more precisely, works in a single sector of the ordering (see the corresponding discussion in [8]).

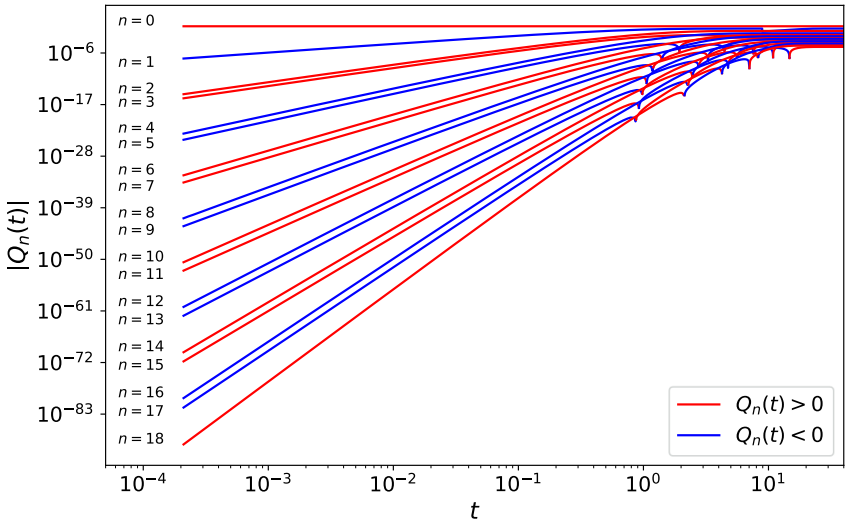


Fig. 6: *Coefficients of the expansion. Absolute value of the coefficients Q_n as a function of time for the charge ($\varepsilon_d = 0$). Red (blue) portion of curve corresponds to positive (negative) values of Q_n. At large time $Q_n(t)$ reaches its known exact value (calculated with Bethe ansatz) with high precision. (Adapted from [10])*

5 Summing up the series (problem C) and results

We are now in position to actually calculate these coefficients $Q_n(t)$. An example of the typical raw data coming out of such a calculation is shown in Fig. 6 up to order eighteen. Please note the span of the x and y axis: times span four orders of magnitude while the coefficients themselves span almost ninety orders of magnitude. The final result (at infinite time) is correct in this instance with close to eight digits precision. These results are orders of magnitude more precise and faster than what was obtained with previous techniques. We have a last problem to solve (problem C) before we can turn to do a little physics.

5.1 Cross extrapolation

Due to the convergence properties of the series of $Q(U,t)$ we can only calculate it accurately in two regimes: small times (but up to large U) and small U (but any t). We would like to extrapolate our results up to the interesting regime where both t and U are large. Let us first discretize U and t to get a matrix $Q_{ij} = Q(U_i, t_j)$. Only a few first rows and columns of this matrix are known.

The cross-extrapolation algorithm [9] is a deceptively simple idea: one merely applies the cross-interpolation formula to the matrix Q_{ij} taking advantage of the fact that the formula *does not use* the entire matrix. The only difference with what was done in the context of TCI is that one restricts the choices of the pivots to the known sector of the matrix (the A_{11} block). This is illustrated in Fig. 7 for a toy example. This is the same matrix as in Fig. 5, the only difference is that we supposed that the data inside the white square was inaccessible, hence we had to restrict the choice of the pivots to inside the red square. The convergence is not as fast or as stable as in a regular cross interpolation, this is to be expected, but in many instance the method works well

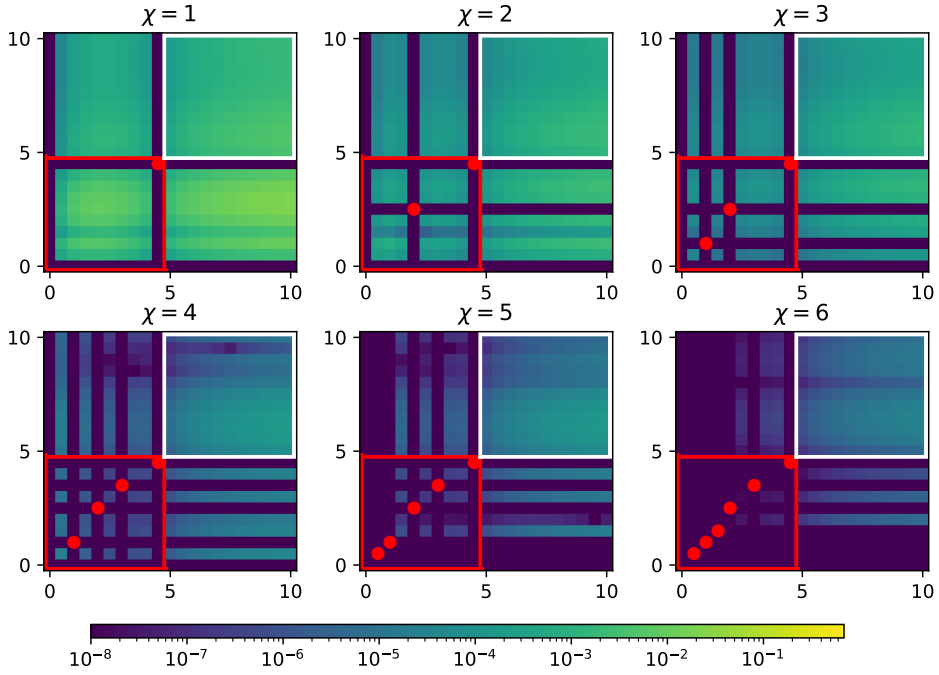


Fig. 7: *Relative error of the cross-extrapolation versus i and j for a toy matrix and different number of pivots $\chi = 1 - 6$. The pivots can only be placed inside the red square in order to extrapolate the results inside the white square. (Adapted from [9])*

and allows one to extrapolate the data further than the initial calculation provides. The error is controlled by varying the rank χ of the extrapolation and the size of the red square region. As in all extrapolation, there is an underlying assumption that must be checked: the fact that $Q(U,t)$ is approximately low rank or in other words that for an error level ϵ, there exist a set of χ one dimensional functions g_k and h_k such that

$$\left|Q(U,t) - \sum_{k=1}^{\chi} g_k(U)h_k(t)\right| < \epsilon. \tag{51}$$

The approach is very general and could in principle be used in many different situations. For instance in Fig. 8, we use it to extrapolate an image whose upper right corner is missing.

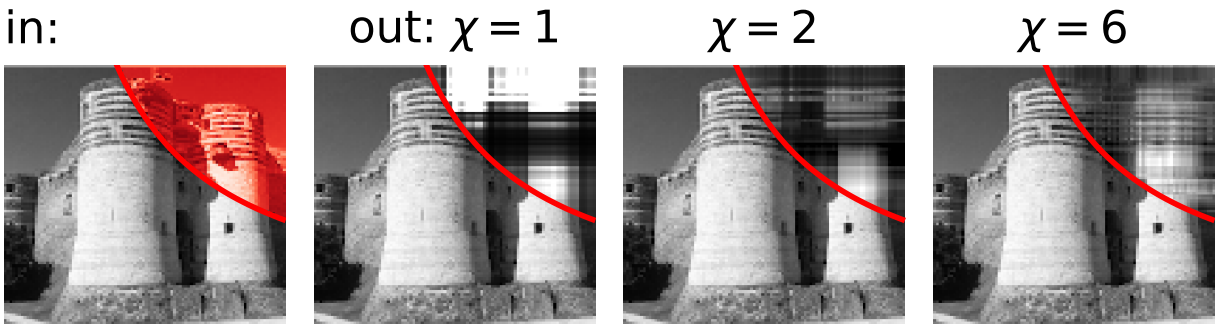


Fig. 8: *Example of cross extrapolation for an image (left) whose upper right corner is missing (reddish zone). In this instance, it does not work so well. (Adapted from [9])*

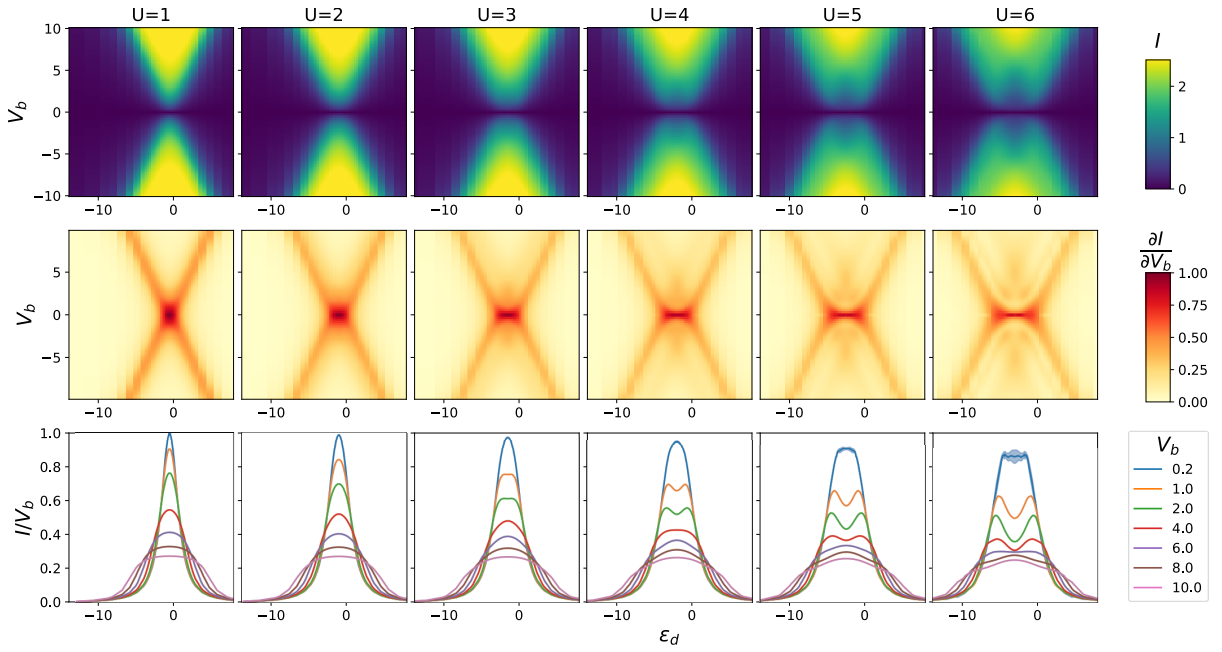


Fig. 9: *Final result of the calculation after cross extrapolation. Upper panels: color plots of the current versus bias voltage V_b and gate voltage ε_d for the SIAM. The diamond like shape shown is known as the "Coulomb diamond" Middle panels: same data but the differential conductance is shown. the horizontal red line around $V_b = 0$ is known as the "Kondo ridge" and its width is the Kondo energy. Bottom panels: a few horizontal cuts of the same data. (Adapted from [10])*

5.2 Main results in the stationary limit

We are now done with the technique itself, it is time to see what it can do in practice and discuss a little the physics of the SIAM. We cannot do justice to the SIAM here. The model is very well understood at equilibrium. It is one of the very few correlated models that is both non-trivial (among other things it features the Kondo effect, hence an emerging energy scale) and very well understood (through Bethe ansatz, the numerical renormalization group, and more). Calculating its properties out-of-equilibrium though is harder and results in this direction are more recent. On the other hand almost all experiments measure current-voltage characteristics, hence take place out-of-equilibrium (see the introduction of [10] for references). So for a long time we were in a semi-comfortable situation where we understood the underlying physics but could not actually calculate the observables that were measured. The present technique contributed to bridge this gap. Fig. 9 shows a snapshot of the results of the calculation featuring both the "Coulomb diamonds" (upper panels) and the "Kondo ridge" (middle panels), two features that have been observed over and over experimentally. Actually, calculating the Coulomb diamond does not require such a sophisticated technique, it can be perfectly well understood at the semi-classical level. Yet, it is nice to obtain the entire colormap observed experimentally with a single technique and in a controlled way.

Let us finish by pushing the technique to its (current) limits which is to calculate $I(V_b)$ in the middle of the Kondo ridge at $U = 12$. We are going to span three orders of magnitude in bias

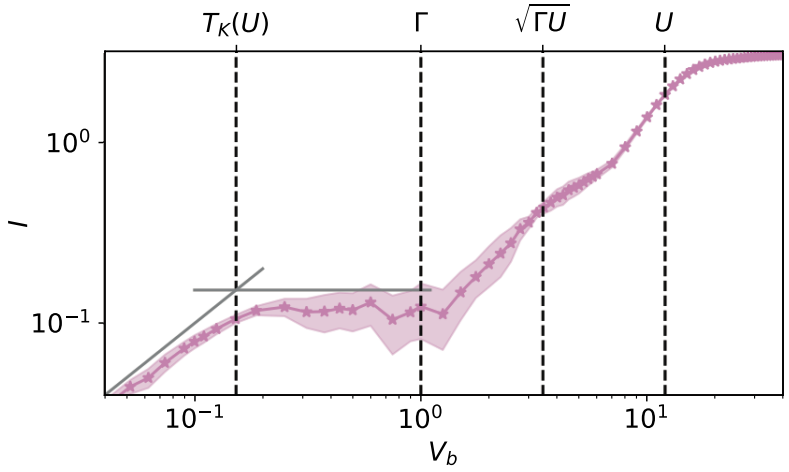


Fig. 10: *Current I as a function of V_b at $U = 12$. The dashed lines indicate the position of the energy scales discussed in the text. The grey lines correspond to perfect transmission $I = V_b$ and a plateau at $I = T_K(U)$. $N = 23$ coefficients were used. The Kondo temperature was extracted from Bethe Ansatz. (Adapted from [10])*

voltage and cross four different energy scales:

- The largest one is the charging energy U. For $V_b > U$ the current must saturate.
- The scale $\sqrt{\Gamma U}$ is associated to the fluctuations of the charge. For energies smaller than this scale, the charge can be considered as "frozen" and the problem reduces to its spin sector (i.e. essentially to the so-called Kondo model).
- The width Γ of the non-interacting resonance.
- The Kondo temperature T_K. This scale is what makes the whole problem interesting. T_K decreases exponentially with U. For $V_b < T_K$ one expects perfect transmission $I = V_b$ (in units where $e^2/h = 1$).

The results are shown in Fig. 10. We find the expected regimes at small and large bias voltages. For $T_K < V_b < \Gamma$, we observe a sort of plateau, that still needs to be confirmed given that the error bars are fairly high in this regime.

5.3 What is to take away?

I would like to end with a few comments as to where this is going. We have seen a technique that consists of several subtechniques (non-interacting Green functions, Wick determinants, tensor cross interpolation, series reconstruction) which put together allow to solve a quite challenging problem. None of these techniques are very difficult once someone has taken the trouble to write a proper open source code that properly isolates the corresponding functionality. This is perhaps my first comment: open source code and proper API are key to being able to assemble complex solutions. We need to be able to program at a level of abstraction that is close to the one we use to think about the problem. My second comment refers to TCI. Finding an underlying structure of the problem to be able to solve it has always be central to how physicists work.

What I find amazing with TCI is that this algorithm is able to discover this structure for us. This is generally true of learning algorithms including with deep neural networks and it is a major paradigm shift in the way we think about algorithms. My last comment is about the overall idea of teaching the computer to calculate Feynman diagrams. At the time of this writing it is not clear how far we will be able to go in this direction but I am quite awed by the number of radical speedups and paradigm shifts that we have seen since our first paper on this subject ten years ago. More generally, it seems that the field of computational many-body physics as a whole is moving very quickly these days and I would not be surprised if some of our central problems (say calculating the properties of the 2D Hubbard model) would soon switch from "about to be solved" to "solved actually".

References

[1] N. Prokof'ev, B. Svistunov, and I. Tupitsyn, Pis'ma v Zh.Eks. Teor. Fiz. **64**, 853 (1996) [English translation: cond-mat/9612091]

[2] K. Van Houcke, E. Kozik, N. Prokof'ev, and B. Svistunov: In D. Landau, S. Lewis, and H. Schuttler (Eds.): *Computer Simulation Studies in Condensed Matter Physics XXI* (Springer, Heidelberg, 2008)

[3] P. Werner, T. Oka, and A.J. Millis, Phys. Rev. B **79**, 035320 (2009)

[4] R.E.V. Profumo, C. Groth, L. Messio, O. Parcollet, and X. Waintal, Phys. Rev. B **91**, 245154 (2015)

[5] C. Bertrand, O. Parcollet, A. Maillard, and X. Waintal, Phys. Rev. B **100**, 125129 (2019)

[6] C. Bertrand, O. Parcollet, A. Maillard, and X. Waintal, Phys. Rev. B **100**, 125129 (2019)

[7] M. Maček, P.T. Dumitrescu, C. Bertrand, B. Triggs, O. Parcollet, and X. Waintal, Phys. Rev. Lett. **125**, 047702 (2020)

[8] Y. Núñez Fernández, M. Jeannin, P.T. Dumitrescu, T. Kloss, J. Kaye, O. Parcollet, and X. Waintal, Phys. Rev. X **12** (2022)

[9] M. Jeannin, Y. Núñez Fernández, T. Kloss, O. Parcollet, and X. Waintal, Phys. Rev. B **110**, 035124 (2024)

[10] M. Jeannin, Y. Núñez-Fernández, T. Kloss, O. Parcollet, and X. Waintal: *A comprehensive study of out-of-equilibrium Kondo effect and Coulomb blockade*, arXiv:2502.16306

[11] R. Rossi, Phys. Rev. Lett. **119**, 045701 (2017)

[12] Y. Meir and N.S. Wingreen, Phys. Rev. Lett. **68**, 2512 (1992)

[13] C.W. Groth, M. Wimmer, A.R. Akhmerov, and X. Waintal, New J. Phys. **16**, 063065 (2014)

[14] T. Kloss, J. Weston, B. Gaury, B. Rossignol, C. Groth, and X. Waintal, New J. Phys. **23**, 023025 (2021)

[15] Y.N. Fernández, M.K. Ritter, M. Jeannin, J.-W. Li, T. Kloss, T. Louvet, S. Terasaki, O. Parcollet, J. von Delft, H. Shinaoka, and X. Waintal, SciPost Phys. **18**, 104 (2025)

[16] J. Rammer and H. Smith, Rev. Mod. Phys. **58**, 323 (1986)

[17] X. Waintal, M. Wimmer, A. Akhmerov, C. Groth, B.K. Nikolic, M. Istas, T. Örn Rosdahl, and D. Varjas: *Computational quantum transport* arXiv:2407.16257

[18] B. Gaury, J. Weston, M. Santin, M. Houzet, C. Groth, and X. Waintal, Phys. Rep. **534**, 1 (2014)

[19] U. Schollwöck, Ann. Phys. **326**, 96 (2011)

[20] G.H. Golub and C.F. Van Loan: *Matrix Computations* (Johns Hopkins Univ. Press, 1996), 3rd ed.

10 QMC for Nonequilibrium Systems

Philipp Werner
Department of Physics
University of Fribourg

Contents

1 Introduction **2**

2 General formalism and model **3**
2.1 Weak- and strong-coupling approach 3
2.2 Model 4

3 Weak-coupling algorithm **5**
3.1 Auxiliary-field formalism 5
3.2 Detailed balance and fast updates 7
3.3 Measurement of the Green function, density and double occupancy 8
3.4 Current measurement 8
3.5 Improved sampling and estimators 9

4 Hybridization expansion algorithm **10**
4.1 Formalism 10
4.2 Measurement of the Green function, density and double occupancy 13
4.3 Current measurement 13

5 Perturbation order and average sign **14**

6 Results: Interaction quench calculations **15**
6.1 Convergence to the long-time limit: large bias voltage 16
6.2 Convergence to the long-time limit: small bias voltage 17
6.3 Temperature dependence 18
6.4 Current-voltage characteristics 19

7 Sampling of connected diagrams **20**
7.1 Weak-coupling approach 20
7.2 Strong-coupling approach 21

8 Beyond Monte Carlo **23**
8.1 Tensor cross interpolation 23
8.2 Weak-coupling expansion with TCI 23
8.3 Strong-coupling expansion with TCI 24

9 Conclusions **24**

E. Pavarini, E. Koch, A. Lichtenstein, and D. Vollhardt (eds.)
Understanding Correlated Materials with DMFT
Modeling and Simulation Vol. 15
Forschungszentrum Jülich, 2025, ISBN 978-3-95806-813-1
http://www.cond-mat.de/events/correl25

1 Introduction

Quantum impurity models play an important role in nanoscience as representations of quantum dots, and in condensed matter physics as auxiliary systems, whose self-consistent solution provides the dynamical mean field theory (DMFT) [1] description of lattice models. A quantum impurity model describes a system with a finite-dimensional Hilbert space ("dot"), which is coupled to one or several infinite but noninteracting systems ("baths"). The equilibrium properties of quantum impurity models are by now reasonably well understood theoretically, and in many cases the properties of interest can be computed numerically to high accuracy.

The nonequilibrium properties of quantum impurity models are much less understood, but they are relevant in connection with transport studies on quantum dots [2] and the DMFT description of pump-probe experiments on solids [3]. Different protocols can be considered to drive a quantum impurity model out of equilibrium. If a system is coupled to more than one reservoir, a chemical potential or temperature difference between the reservoirs can generate a nonequilibrium steady state in which current flows from one reservoir to another across the dot. One can also consider the relaxation to a steady state from an atypical initial condition ("quench"). In the DMFT context, the nonequilibrium reservoirs are selfconsistently computed and represent the lattice environment during the transient evolution of a perturbed system [4], or in a nonequilibrium steady-state situation [5]. While the basic formalism for dealing with these problems was established by Schwinger [6] and Keldysh [7] in the early 1960s, the calculation of unbiased results for generic nonequilibrium situations remains a challenge.

Several numerical techniques have been applied to time-dependent problems in interacting quantum dots. Numerical renormalization group methods [8] provide accurate results for the relaxation dynamics in dots with equilibrium baths. Path integral sampling techniques introduced in the quantum chemistry context [9] have been extended to the quantum dot problem [10] and recent powerful implementations make use of a tensor-train representation of the influence functional of the bath [11, 12]. The time-dependent non-crossing approximation [13] and its higher-order generalizations [14] allows an efficient treatment of the strong-correlation regime, but the correct description of Kondo resonances or weakly correlated states remains a challenge. The time-dependent density matrix renormalization group has also been used to study the transport properties of quantum dots coupled to one-dimensional reservoirs [15, 16].

In this chapter, we discuss quantum Monte Carlo (QMC) methods based on the unbiased sampling of diagrammatic expansions [17]. For equilibrium properties, these so-called continuous-time QMC methods enabled numerically efficient studies of a wide range of impurity problems, and their adaptation to the real-time contour yields potentially useful solvers for quantum dot studies and nonequilibrium DMFT. We provide a systematic analysis of the real-time diagrammatic approach, including a discussion of the strengths and weaknesses of these methods, and the regimes in which accurate results can be obtained. We also briefly discuss alternative schemes which avoid the sampling of disconnected diagrams, as well as recent developments which replace the Monte Carlo sampling of diagrams by an efficient explicit calculation of the integrals over diagram weights. The QMC part is taken from Refs. [18] and [19].

2 General formalism and model

2.1 Weak- and strong-coupling approach

A quantum impurity model is described by a Hamiltonian of the form

$$H_{QI} = H_{\text{dot}} + H_{\text{bath}} + H_{\text{mix}}. \tag{1}$$

Here H_{dot} describes a system with a finite-dimensional Hilbert space, which we refer to as the "impurity", or "dot", H_{bath} describes one or more infinite reservoirs characterized by a continuum of levels, and H_{mix} the coupling between the impurity and the reservoirs. We assume that at time $t = 0$ the state of the system is described by the density matrix ρ_0.
The theoretical task is to evaluate the expectation value $\langle \mathcal{O}(t) \rangle$ of an operator $\mathcal{O}$ at time t, i.e. to compute

$$\langle \mathcal{O}(t) \rangle = \text{Tr}\left[\rho_0\, e^{i\int_0^t dt' H_{QI}(t')} \mathcal{O}\, e^{-i\int_0^t dt'' H_{QI}(t'')}\right] \tag{2}$$

(the generalization to operators with multiple time dependences is straightforward and will not be written explicitly). A nonequilibrium situation can arise through a time dependence of the parameters in H_{QI} ("irradiation"), through the correlators of the operators in H_{bath} ("nonequilibrium reservoirs") or through an initial density matrix ρ_0 which is different from the long-time limit ("quench").
One can view the expectation value in Eq. (2) as an evolution on the Schwinger-Keldysh contour illustrated in Fig. 1 from time $t = 0$ (when the system is described by the density matrix ρ_0) to time t (at which the operator is measured), and then back to time 0 [6]. Our general strategy for evaluating Eq. (2) is to write H_{QI} as a sum of two terms: one, H_0 for which the time evolution can be treated exactly and another, H_I, which is treated by a perturbative expansion. The expansion in H_I generates a series of diagrams, which are sampled stochastically, using an importance sampling which accepts or rejects proposed diagrams on the basis of their contributions to $\langle \tilde{\mathcal{O}} \rangle$ (in the discussed implementations we use $\tilde{\mathcal{O}} = 1$).
Two types of expansion are considered: One is a "weak coupling" method, in which H_{dot} is partitioned into a quadratic part H^0_{dot} and an interacting part H_U, the combination $H^0_{\text{dot}} + H_{\text{mix}} + H_{\text{bath}}$ is treated exactly, ρ_0 is taken to be the corresponding density matrix, and the expansion is constructed in terms of H_U. The other is a "strong coupling" (more properly, "hybridization") expansion in which H_{dot} and H_{bath} are treated exactly, ρ_0 is the density matrix corresponding

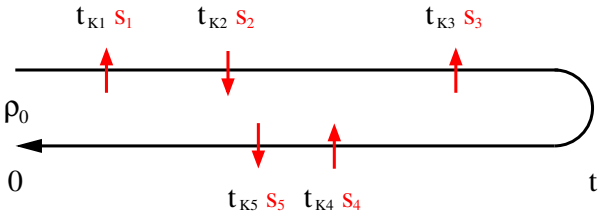


Fig. 1: *Illustration of the Schwinger-Keldysh contour and example of a Monte Carlo configuration corresponding to perturbation order $n = 5$ and $n_+ = 3$, $n_- = 2$. (From Ref. [18])*

to the direct product of a lead density matrix and a density matrix describing the dot decoupled from the leads, and $H_{\rm mix}$ is treated as a perturbation. The hybridization expansion for nonequilibrium problems was originally introduced by Mühlbacher and Rabani [20] in the context of noninteracting electrons coupled to phonons, and has been applied to interacting dots in Ref. [21]. An essentially identical formalism has also been discussed in Ref. [22]. The real-time version of the weak-coupling approach was introduced in Ref. [18].
Methods based on stochastically sampled diagrammatic expansions [23–26] have had considerable success in treating equilibrium quantum impurity problems at temperature $T > 0$ and they have become the main workhorse for DMFT [17]. In equilibrium calculations, the expansion can be formulated on the imaginary time axis $0 \le \tau < 1/T$ (only one contour is needed) and the expansion parameter is $-H_I(\tau) = e^{\tau H_0}(-H_I)\, e^{-\tau H_0}$. The fermionic sign problem can be avoided in many relevant situations, so that average perturbation orders of $\mathcal{O}(100)$ can be easily treated. Three related sources of difficulty arise in nonequilibrium setups. First, the expansion must be done for real times, so the time evolution introduces complex phases and the diagrams come with factors of i to powers relating to the perturbation order. Second, two contour branches rather than one are required (Fig. 1), doubling the perturbation order required to reach a given time. Third, in nonequilibrium situations it may be essential to build up the correct entanglement between the impurity and the bath before observables can be measured. All of these factors limit the range over which accurate results can be obtained, but the crucial constraint is the dynamical sign problem resulting from the oscillatory convergence.

2.2 Model

In the following discussions, we consider a dot consisting of a single spin-degenerate level with a Hubbard interaction U, coupled by hybridization V to two reservoirs ("leads") labeled by $\alpha = L, R$, which can have different chemical potentials μ_α.
The different terms of the Hamiltonian are

$$H_{\rm bath} = \sum_{\alpha=L,R} \sum_{p,\sigma} \big(\varepsilon^\alpha_{p,\sigma} - \mu_\alpha\big) a^{\alpha\dagger}_{p,\sigma} a^\alpha_{p,\sigma}, \tag{3}$$

$$H_{\rm mix} = \sum_{\alpha=L,R} \sum_{p,\sigma} \big(V^\alpha_p a^{\alpha\dagger}_{p,\sigma} d_\sigma + \text{h.c.}\big), \tag{4}$$

$$H^0_{\rm dot} = \big(\varepsilon_d + U/2\big) \sum_\sigma n_{d,\sigma}, \tag{5}$$

$$H_U = U\big(n_{d,\uparrow} n_{d,\downarrow} - (n_{d,\uparrow} + n_{d,\downarrow})/2\big). \tag{6}$$

Here, d_σ ($a^\alpha_{p,\sigma}$) annihilates the spin-σ electron on the dot (spin-σ and lead-α bath electron with index p), $n_{d,\sigma} = d^\dagger_\sigma d_\sigma$ is the spin-density on the dot, and ε_d ($\varepsilon^\alpha_{p,\sigma}$) denotes the dot (bath level) energy. For convenience, we also define

$$H_{\rm dot} = H^0_{\rm dot} + H_U. \tag{7}$$

The initial density matrix is such that the correlators of lead operators are

$$\big\langle a^{\alpha\dagger}_{p,\sigma} a^\beta_{p',\sigma'} \big\rangle = \delta_{\alpha,\beta}\delta_{p,p'}\delta_{\sigma,\sigma'} f_{T_\alpha}(\varepsilon^\alpha_{p,\sigma} - \mu_\alpha), \tag{8}$$

where $f_T(x) = 1/(e^{x/T}+1)$ is the Fermi distribution function for temperature T. The statement that H_{bath} describes infinite reservoirs implies that Eq. (8) holds at all times.
The model has three important energy scales: ε_d which controls the steady state dot occupancy, the interaction scale U, and the level broadening

$$\Gamma^\alpha(\omega) = \pi \sum_p \left|V_p^\alpha\right|^2 \delta(\omega - \varepsilon_p^\alpha) \tag{9}$$

associated with lead α. The total level broadening is

$$\Gamma = \Gamma^L + \Gamma^R \tag{10}$$

and the dimensionless measure of interaction strength is U/Γ. Very roughly, strong coupling physics appears for $U \gtrsim \pi\Gamma$ while the opposite limit is reasonably well described by perturbation theory in U.

3 Weak-coupling algorithm

3.1 Auxiliary-field formalism

In the weak coupling expansion we treat $H_0 \equiv H_{\text{dot}}^0 + H_{\text{mix}} + H_{\text{bath}}$ exactly and H_U as a perturbation. H_0 is a noninteracting problem for which the density matrix and all correlators of the dot-lead system can be determined exactly. We take the initial density matrix to be the steady-state density matrix corresponding to H_0,

$$\rho_0 = \frac{e^{-\beta H_0}}{\operatorname{Tr} e^{-\beta H_0}}, \tag{11}$$

and we turn on the interaction at time $t = 0_+$. Here we assume that the temperatures of the two leads are identical; the generalization to unequal temperatures is straightforward.
We formulate the perturbation theory in U as a real-time adaptation of the continuous-time auxiliary field method of Ref. [26], but the real-time version of the weak-coupling approach by Rubtsov *et al.* [23] works analogously. Considering $\tilde{\mathcal{O}} = 1$, the starting point for the real-time auxiliary field method is the following expression for the identity

$$1 = \operatorname{Tr} \rho_0 \, e^{it(H_0+H_U-K/t)} \, e^{-it(H_0+H_U-K/t)}, \tag{12}$$

with K a constant which is in principle arbitrary and may be chosen to optimize the simulation. Using an interaction representation in which the time evolution of the operators is given by $O(s) = e^{isH_0} \, O \, e^{-isH_0}$ we can rewrite Eq. (12) as

$$1 = \operatorname{Tr} \rho_0 \Big(\tilde{\mathcal{T}} e^{i\int_0^t ds(H_U(s)-K/t)}\Big) \, e^{itH_0} \, e^{-itH_0} \Big(\mathcal{T} e^{-i\int_0^t ds(H_U(s)-K/t)}\Big), \tag{13}$$

with $\mathcal{T}$ the time ordering and $\tilde{\mathcal{T}}$ the anti-time ordering operator, and expand the time-ordered exponentials into a power series. This leads to the expression

$$1=\mathrm{Tr}\,\rho_0\sum_m(-iK/t)^m\int_0^t d\tilde{t}_1\cdots\int_{\tilde{t}_{m-1}}^t d\tilde{t}_m e^{i\tilde{t}_1H_0}(1-tH_U/K)\cdots e^{i(\tilde{t}_m-\tilde{t}_{m-1})H_0}(1-tH_U/K)e^{i(t-\tilde{t}_m)H_0}$$
$$\times\sum_n(iK/t)^n\int_0^t dt_1\cdots\int_{t_{n-1}}^t dt_n e^{-i(t-t_n)H_0}(1-tH_U/K)\cdots e^{-i(t_2-t_1)H_0}(1-tH_U/K)e^{-it_1H_0}. \tag{14}$$

Using the explicit form for H_U (Eq. (6)) and the auxiliary field decomposition of Ref. [27] we can rewrite the interaction term as

$$1-(tU/K)\big(n_{d,\uparrow}n_{d,\downarrow}-(n_{d,\uparrow}+n_{d,\downarrow})/2\big)=1/2\sum_{s=-1,1}e^{\gamma s(n_{d,\uparrow}-n_{d,\downarrow})}, \tag{15}$$

$$\cosh(\gamma)=1+(tU)/(2K). \tag{16}$$

Note that the constant K has been introduced to enable this decomposition. The trace is now a product of exponentials of one-body operators,

$$1=\sum_m\sum_n(-i)^m i^n(K/2t)^{m+n}\sum_{\tilde{s}_1,\ldots,\tilde{s}_n}\sum_{s_1,\ldots,s_m}\int_0^t d\tilde{t}_1\cdots\int_{\tilde{t}_{m-1}}^t d\tilde{t}_m\int_0^t dt_1\cdots\int_{t_{n-1}}^t dt_n\prod_\sigma\frac{1}{\mathrm{Tr}\,e^{-\beta H_{0,\sigma}}}\mathrm{Tr}\,e^{-\beta H_{0,\sigma}}\times$$
$$e^{i\tilde{t}_1H_{0,\sigma}}e^{\gamma\tilde{s}_1\sigma n_{d,\sigma}}\cdots e^{i(\tilde{t}_m-\tilde{t}_{m-1})H_{0,\sigma}}e^{\gamma\tilde{s}_m\sigma n_{d,\sigma}}e^{-i(\tilde{t}_m-t_n)H_{0,\sigma}}e^{\gamma s_n\sigma n_{d,\sigma}}\cdots e^{-i(t_2-t_1)H_{0,\sigma}}e^{\gamma s_1\sigma n_{d,\sigma}}e^{-it_1H_{0,\sigma}}$$

and can be expressed [26] in terms of determinants of two $(n+m)\times(n+m)$ matrices

$$N_\sigma^{-1}=e^{S_\sigma}-iG_{0,\sigma}\big(e^{S_\sigma}-I\big) \tag{17}$$

as

$$1=\sum_m\sum_n(-i)^m i^n(K/2t)^{m+n}\sum_{\tilde{s}_1,\ldots,\tilde{s}_n}\sum_{s_1,\ldots,s_m}\int_0^t d\tilde{t}_1\cdots\int_{\tilde{t}_{m-1}}^t d\tilde{t}_m\int_0^t dt_1\cdots\int_{t_{n-1}}^t dt_n\prod_\sigma\det N_\sigma^{-1}. \tag{18}$$

Here, $e^{S_\sigma}=\mathrm{diag}(e^{\gamma\tilde{s}_1\sigma},\ldots,e^{\gamma\tilde{s}_m\sigma},e^{\gamma s_n\sigma},\ldots,e^{\gamma s_1\sigma})$ and $G_{0,\sigma}$ is given by

$$G_{0,\sigma}(t'_K,t''_K)=\begin{cases}G^<_{0,\sigma}(t',t''), & t'_K<t''_K\\ G^>_{0,\sigma}(t',t''), & t'_K\geq t''_K\end{cases}. \tag{19}$$

In the above expression, $G_0^<(t,t')=i\langle d^\dagger(t')d(t)\rangle_0$, $G_0^>(t,t')=-i\langle d(t)d^\dagger(t')\rangle_0$, t_K is the "Keldysh time" coordinate along the unfolded Keldysh contour (Fig. 1) and t the physical time corresponding to t_K. In quantum dot systems, these Green functions can usually be calculated analytically [28], while in nonequilibrium DMFT simulations, they are the output of the self-consistency procedure [4]. In our quantum dot applications, we will use the infinite bandwidth limit in which the level broadening is independent of ω, so that

$$G_0^{</>}(t',t'')=\pm i\sum_{\alpha=L,R}\Gamma^\alpha\int\frac{d\omega}{2\pi}e^{-i\omega(t'-t'')}\frac{1\mp\tanh\left(\frac{\omega-\mu_\alpha}{2T}\right)}{(\omega-\varepsilon_d-U/2)^2+\Gamma^2}, \tag{20}$$

with the upper sign pertaining to $G_0^<$ and the lower sign to $G_0^>$.

3.2 Detailed balance and fast updates

The algorithm samples auxiliary Ising spin configurations $\{(t_{K,1}, s_1), (t_{K,2}, s_2), \ldots (t_{K,n}, s_n)\}$ time ordered along the Keldysh contour $0 \to t \to 0$ (see Fig. 1) by random insertions and removals of spins. The complex "weight" of a spin configuration is given by

$$w(\{(t_{K,1}, s_1), (t_{K,2}, s_2), \ldots (t_{K,n}, s_n)\}) = (-i^{n_-})(i^{n_+})(Kdt/2t)^{n_- + n_+} \prod_\sigma \det N_\sigma^{-1}, \quad (21)$$

where n_+ denotes the number of spins on the forward contour and n_- the number of spins on the backward contour ($n = n_+ + n_-$).
The detailed balance condition for insertion/removal of a spin is similar to the imaginary time formulation of Ref. [26]. Assuming that we pick a random time on the unfolded contour of length $2t$ and a random direction for this new spin, $p^{\text{prop}}(n-1 \to n) = (1/2)(dt/(2t))$, and propose to remove this spin with probability $p^{\text{prop}}(n \to n-1) = 1/n$ we get

$$\frac{p(n-1 \to n)}{p(n \to n-1)} = \pm i \frac{2K}{n} \prod_\sigma \frac{\det(N_n^{-1})_\sigma}{\det(N_{n-1}^{-1})_\sigma}, \quad (22)$$

with the factor $+i$ corresponding to a spin which is inserted on the forward contour and $-i$ to a spin which is inserted on the backward contour.
For the fast updates, let us consider the most complicated case, which is the insertion of a spin. This update adds one row and one column to the $(n-1)\times(n-1)$ matrix N, resulting in the $n\times n$ matrix N' (we assume here that this new row/column is the last one, n, and drop the spin index). The determinant ratio is

$$r = \frac{\det(N'^{-1})}{\det(N^{-1})} = \left(e^S - iG_0(e^S - I)\right)_{n,n} - \sum_{i=1}^{n-1} R_i \left(e^S - iG_0(e^S - I)\right)_{i,n}, \quad (23)$$

with $R_i = \sum_{j=1}^{n-1} \left(e^S - iG_0(e^S - I)\right)_{n,j} N_{j,i}$. The calculation of this quantity requires $O(n^2)$ operations. The new matrix elements are given by

$$N'_{i,j} = N_{i,j} + \frac{1}{r} L_i R_j, \quad (24)$$

$$N'_{i,n} = -\frac{1}{r} L_i, \quad (25)$$

$$N'_{n,j} = -\frac{1}{r} R_j, \quad (26)$$

$$N'_{n,n} = \frac{1}{r}, \quad (27)$$

with $i = 1, \ldots, n-1$ and $L_i = \sum_{j=1}^{n-1} N_{i,j} \left(e^S - iG_0(e^S - I)\right)_{j,n}$.
From Eq. (27) it follows that computing the determinant ratio for removing a spin is $O(1)$. The elements of the reduced matrix are obtained as

$$N_{i,j} = N'_{i,j} - \frac{N'_{i,n} N'_{n,j}}{N'_{n,n}}. \quad (28)$$

3.3 Measurement of the Green function, density and double occupancy

To measure the Green function $G_\sigma(t'_K, t''_K)$ we have to insert an operator d_σ at time t'_K and an operator $d^\dagger_\sigma$ at time t''_K. The weights of these configurations $w(\{(t_{K,1}, s_1), \dots (t_{K,n}, s_n)\}; d_\sigma(t'_K)d^\dagger_\sigma(t''_K))$ are related to those defined in Eq. (21) by

$$\frac{w(\{(t_{K,1}, s_1), \dots (t_{K,n}, s_n)\}; d(t')d^\dagger(t''))}{w(\{(t_{K,1}, s_1), \dots (t_{K,n}, s_n)\})} = \frac{1}{\det N_\sigma^{-1}} \det \left(\begin{array}{c|c} N_\sigma^{-1}(i,j) & iG_{0,\sigma}(t_{K,i}, t''_K) \\ \hline -iG_{0,\sigma}(t'_K, t_{K,j})(e^{\gamma\sigma s_j} - 1) & iG_{0,\sigma}(t'_K, t''_K) \end{array} \right). \quad (29)$$

Hence, the Green function can be obtained as the Monte Carlo average of the quantity [26]

$$\tilde{G}_\sigma(t'_K, t''_K) = G_{0,\sigma}(t'_K, t''_K) + i \sum_{i,j=1}^{n} G_{0,\sigma}(t'_K, t_{K,i}) \big((e^{S_\sigma} - 1)N_\sigma\big)_{i,j} G_{0,\sigma}(t_{K,j}, t''_K), \quad (30)$$

which yields the measurement formulas

$$G_\sigma(t'_K, t''_K) = \big\langle \tilde{G}_\sigma(t'_K, t''_K) \big\rangle, \quad (31)$$

$$n_\sigma(t_K) = 1 - i\big\langle \tilde{G}_\sigma(t_K, t_K) \big\rangle, \quad (32)$$

$$n_\uparrow n_\downarrow(t_K) = \big\langle (1 - i\tilde{G}_\uparrow(t_K, t_K))(1 - i\tilde{G}_\downarrow(t_K, t_K)) \big\rangle. \quad (33)$$

3.4 Current measurement

The current from the dot to the left lead is

$$I_L = \sum_\sigma I_{L\sigma} = -2 \,\mathrm{Im} \sum_\sigma \sum_{p \in L} V^L_{p,\sigma} \big\langle a^{L\dagger}_{p,\sigma} d_\sigma \big\rangle. \quad (34)$$

Thus, in terms of the composite lead operator $\tilde{a}^\dagger_{L,\sigma} \equiv \sum_{p\in L} V^L_{p,\sigma} a^{L\dagger}_{p,\sigma}$, we find

$$\begin{aligned} I_{L\sigma}(t) =& -2 \,\mathrm{Im}\, \mathrm{Tr}\, \rho_0 \Big(\tilde{\mathcal{T}} e^{i\int_0^t ds (H_I(s) - K/t)} \Big) e^{itH_0}\, \tilde{a}^\dagger_{L,\sigma}\, d_\sigma\, e^{-itH_0} \Big(\mathcal{T} e^{-i\int_0^t ds (H_I(s) - K/t)} \Big) \\ =& -2 \,\mathrm{Im} \sum_m \sum_n (-i)^m i^n (K/2t)^{m+n} \sum_{\tilde{s}_1, \dots, \tilde{s}_n} \sum_{s_1, \dots, s_m} \int_0^t d\tilde{t}_1 \cdots \int_{\tilde{t}_{m-1}}^t d\tilde{t}_m \int_0^t dt_1 \cdots \int_{t_{n-1}}^t dt_n \times \\ & \frac{\det N_{\bar{\sigma}}^{-1}}{\mathrm{Tr}\, e^{-\beta H_{0,\sigma}}} \mathrm{Tr} \Big[e^{-\beta H_0} e^{i\tilde{t}_1 H_{0,\sigma}} e^{\gamma \tilde{s}_1 \sigma n_{d,\sigma}} \cdots \\ & \cdots e^{\gamma \tilde{s}_m \sigma n_{d,\sigma}} e^{i(t - \tilde{t}_m) H_{0,\sigma}}\, \tilde{a}^\dagger_{L,\sigma}\, d_\sigma\, e^{-i(t - t_n) H_{0,\sigma}} e^{\gamma \sigma s_n \sigma n_{d,\sigma}} \cdots e^{\gamma s_1 \sigma n_{d,\sigma}} e^{-it_1 H_{0,\sigma}} \Big], \end{aligned} \quad (35)$$

with $\bar{\sigma}$ the spin which is opposite to σ (this spin component has no operator $\tilde{a}$ and thus simply gives the usual factor $\det N_{\bar{\sigma}}^{-1}$). The measurement of the current is thus very similar to the measurement of the Green functions, but one factor in the Wick decomposition is now

$$A(t_K, t'_K) = \begin{cases} A^<(t,t') \equiv \quad \big\langle \tilde{a}^{L\dagger}_\sigma(t') d_\sigma(t) \big\rangle_0, & t_K \le t'_K \\ A^>(t,t') \equiv -\big\langle d_\sigma(t) \tilde{a}^{L\dagger}_\sigma(t') \big\rangle_0, & t_K > t'_K \end{cases}. \quad (36)$$

In the infinite bandwidth limit we have [18]

$$\left.\begin{matrix} A^<(t,t') \\ A^>(t,t') \end{matrix}\right\} = -2i \int \frac{d\omega}{2\pi} e^{-i\omega(t-t')} \frac{\Gamma_L\Gamma_R\big(f(\omega-\mu_L)-f(\omega-\mu_R)\big)}{(\omega-\varepsilon_d-U/2)^2+\Gamma^2}$$
$$+ 2\Gamma_L \int \frac{d\omega}{2\pi} e^{-i\omega(t-t')} \frac{(\omega-\varepsilon_d-U/2)}{(\omega-\varepsilon_d-U/2)^2+\Gamma^2} \times \begin{cases} f(\omega-\mu_L) \\ \big(f(\omega-\mu_L)-1\big) \end{cases} . \quad (37)$$

The trace factor in Eq. (35) for an n-th order diagram corresponding to the $n\times n$ matrix N_σ^{-1} is the determinant of the $(n+1)\times(n+1)$ matrix

$$M_\sigma^{-1} = \left(\begin{array}{c|c} N_\sigma^{-1}(i,j) & A(t_{K,i},t) \\ \hline -iG_{0,\sigma}(t,t_{K,j})(e^{\gamma\sigma s_j}-1) & A(t,t) \end{array}\right). \quad (38)$$

The current can thus be expressed as follows:

$$I_L = -2\,\mathrm{Im}\sum_\sigma \sum_c w_c^{I_\sigma} = -2\,\mathrm{Im}\sum_\sigma \frac{\sum_c |w_c|(w_c^{I_\sigma}/|w_c|)}{\sum_c |w_c|\phi_c} = -2\,\mathrm{Im}\sum_\sigma \Big\langle \frac{w_c^{I_\sigma}}{|w_c|}\Big\rangle_{|w_c|} \frac{1}{\langle\phi_c\rangle_{|w_c|}}, \quad (39)$$

with ϕ_c the phase of the weight w_c (Eq. (21)) and

$$\frac{w_c^{I_\sigma}}{w_c} = \frac{\det N_{\bar\sigma}^{-1}\det M_\sigma^{-1}}{\det N_{\bar\sigma}^{-1}\det N_\sigma^{-1}} = A(t,t) + \sum_{n,m} iG_{0,\sigma}(t,t_{K,n})\big((e^{S_\sigma}-1)N_\sigma\big)_{n,m} A(t_{K,m},t). \quad (40)$$

Combining Eqs. (39) and (40), the current measurement formula becomes

$$I_L = -2\,\mathrm{Im}\sum_\sigma \Big(A(t,t) + \Big\langle \sum_{n,m} iG_{0,\sigma}(t,t_{K,n})\big((e^{S_\sigma}-1)N_\sigma\big)_{n,m} A(t_{K,m},t)\phi_c\Big\rangle_{|w_c|} \frac{1}{\langle\phi_c\rangle_{|w_c|}}\Big). \quad (41)$$

The first term in this expression is the steady-state current for the non-interacting system

$$I_0 = -2\,\mathrm{Im}\,\big(2A(t,t)\big) = 8\int \frac{d\omega}{2\pi} \frac{\Gamma_L\Gamma_R\big(f(\omega-\mu_L)-f(\omega-\mu_R)\big)}{(\omega-\varepsilon_d U/2)^2+\Gamma^2}. \quad (42)$$

3.5 Improved sampling and estimators

In the particle-hole symmetric case, the parameters K of the algorithm can be chosen such that only even perturbation orders appear in the expansion. In fact, for

$$K = -\frac{tU}{4} \quad (43)$$

the spin degree of freedom effectively disappears ($e^{\gamma s\sigma} = -1$) and the algorithm becomes the real-time version of Rubtsov's weak-coupling method [23] for the particle-hole symmetric interaction term $H_U - K/t = U(n_{d,\uparrow}-\frac{1}{2})(n_{d,\downarrow}-\frac{1}{2})$ [29]. The odd perturbation orders are continuously suppressed as K approaches $-tU/4$. In order to sample only even order diagrams, it is however necessary to implement modified updates, which insert or remove two spins at the same time.

We next discuss some tricks to improve the efficiency of the current measurement [19]. First, we rewrite the expectation value of Eq. (40) as

$$A(t,t)+\int ds_1 \int ds_2\, G_{0,\sigma}(t,s_1)\left\langle i\sum_{n,m}\delta_{\mathcal{C}}(s_1,t_{K,n})\big((e^{S_\sigma}-I)N_\sigma\big)_{n,m}\delta_{\mathcal{C}}(s_2,t_{K,m})\right\rangle A(s_2,t), \quad (44)$$

where the variables s_1 and s_2 run over the entire contour and the contour delta function is defined by $\int ds\, \delta_{\mathcal{C}}(t_K,s)f(s)=f(t_K)$. It is therefore sufficient to accumulate the quantity

$$X_\sigma(s_1,s_2)=\left\langle i\sum_{n,m}\delta_{\mathcal{C}}(s_1,t_{K,n})\big((e^{S_\sigma}-1)N_\sigma\big)_{n,m}\delta_{\mathcal{C}}(s_2,t_{K,m})\right\rangle. \quad (45)$$

Furthermore, it follows from Eq. (21) that the weight of a Monte Carlo configuration changes sign if the last spin (corresponding to the largest time argument) is shifted from the forward contour to the backward contour or vice versa. Since the absolute value of the weight does not change, these two configurations will be generated with equal probability. As a result, all the terms in Eq. (44) which do not involve the last operator on the contour will cancel. It is therefore more efficient and accurate to accumulate

$$X_\sigma(s_1,s_2)=\left\langle i\sum_{l\ \text{not last}}\big(x(s_1,\text{last};s_2,l)+x(s_1,l;s_2,\text{last})\big)\right\rangle, \quad (46)$$

with $x(s_1,n;s_2,m)\equiv\delta_{\mathcal{C}}(s_1,t_{K,n})\left((e^{\Gamma_\sigma}-1)N_\sigma\right)_{n,m}\delta_{\mathcal{C}}(s_2,t_{K,m})$.
Also, by comparing the contributions to the current of the original configuration and the one with the last operator shifted from the upper to the lower contour (or vice versa), one finds that they almost (but not completely) cancel. The error bars on the current can thus be substantially reduced by appropriate symmetrizations of $X(s_1,s_2)$.

4 Hybridization expansion algorithm

4.1 Formalism

A complementary diagrammatic Monte Carlo algorithm to the one described in Sec. 3 can be obtained by performing an expansion in powers of the dot-lead hybridizations V. This simulation approach has been introduced for equilibrium systems (imaginary-time formalism) in Refs. [24, 25] and was discussed for a nonequilibrium quantum dot with phonons (but without electron-electron interactions) in Refs. [20, 22]. It has been applied to interacting dots in Refs. [18,21]. We will present here the derivation for the impurity model defined in Eqs. (3)-(6), but the method can easily be extended to general classes of impurity models by using the matrix formulation of Ref. [25].
In the hybridization expansion approach one adopts an interaction representation with respect to the dot-lead mixing, so the time evolution of the operators is given by the local part of the Hamiltonian, $H_{\rm loc}=H_{\rm dot}+H_{\rm bath}$. Considering $\tilde{\mathcal{O}}=1$, the starting point of the derivation is the identity

$$1=\mathrm{Tr}\,\rho_0\Big(\tilde{\mathcal{T}}e^{i\int_0^t ds H_{\rm mix}(s)}\Big)\,e^{itH_{\rm loc}}\,e^{-itH_{\rm loc}}\,\Big(\mathcal{T}e^{-i\int_0^t ds H_{\rm mix}(s)}\Big). \quad (47)$$

The initial state of the system is specified by the density matrix $\rho_0 = \rho_{\text{dot}} \otimes \rho_{\text{bath}}$, with ρ_{bath} a function of inverse temperature β and the chemical potentials $\mu_{L,R}$. In the calculations presented here we assume that the dot is initially empty, $\rho_{\text{imp}} = |0\rangle\langle 0|$.
Expanding the time-ordered exponentials into a power series yields

$$1 = \operatorname{Tr} \rho_0 \sum_m i^m \int_0^t d\tilde{t}_1 \cdots \int_{\tilde{t}_{m-1}}^t d\tilde{t}_m \, H_{\text{mix}}(\tilde{t}_1) \cdots H_{\text{mix}}(\tilde{t}_m) \sum_n (-i)^n \int_0^t dt_1 \cdots \int_{t_{n-1}}^t dt_n \, H_{\text{mix}}(t_n) \cdots H_{\text{mix}}(t_1). \tag{48}$$

Because $H_{\text{mix}} = \sum_\sigma \left(H_{\text{mix}}^{d_\sigma} + H_{\text{mix}}^{d_\sigma^\dagger} \right)$ with $H_{\text{mix}}^{d_\sigma} = \sum_{\alpha=L,R} \sum_p V_p^\alpha a_{p,\sigma}^{\alpha\dagger} d_\sigma$, $H_{\text{mix}}^{d_\sigma^\dagger} = \left(H_{\text{mix}}^{d_\sigma} \right)^\dagger$ and the time evolution conserves the spin, we need for each σ separately an equal number of creation and annihilation operators on the Keldysh contour $0 \to t \to 0$:

$$1 = \sum_{m_\sigma + n_\sigma = m'_\sigma + n'_\sigma} \prod_\sigma i^{m_\sigma + m'_\sigma} (-i)^{n_\sigma + n'_\sigma} \int_0^t d\tilde{t}_1^\sigma \cdots \int_{\tilde{t}_{m_\sigma - 1}^\sigma}^t d\tilde{t}_{m_\sigma}^\sigma \int_0^t d\tilde{t}_1'^\sigma \cdots \int_{\tilde{t}_{m'_\sigma - 1}^\sigma}^t d\tilde{t}_{m'_\sigma}'^\sigma \int_0^t dt_1^\sigma \cdots \int_{t_{n_\sigma - 1}^\sigma}^t dt_{n_\sigma}^\sigma \int_0^t dt_1'^\sigma \cdots \int_{t'^\sigma_{n'_\sigma - 1}}^t dt_{n'_\sigma}'^\sigma$$

$$\operatorname{Tr} \rho_0 \tilde{\mathcal{T}} \mathcal{T} \prod_\sigma H_{\text{mix}}^{d_\sigma}(\tilde{t}_1^\sigma) H_{\text{mix}}^{d_\sigma^\dagger}(\tilde{t}_1'^\sigma) H_{\text{mix}}^{d_\sigma}(\tilde{t}_2^\sigma) H_{\text{mix}}^{d_\sigma^\dagger}(\tilde{t}_2'^\sigma) \cdot\cdot e^{iH_{\text{loc}}t} e^{-iH_{\text{loc}}t} \cdot\cdot H_{\text{mix}}^{d_\sigma}(t_2^\sigma) H_{\text{mix}}^{d_\sigma^\dagger}(t_2'^\sigma) H_{\text{mix}}^{d_\sigma}(t_1^\sigma) H_{\text{mix}}^{d_\sigma^\dagger}(t_1'^\sigma), \tag{49}$$

where $\tilde{\mathcal{T}}$ is the anti-time ordering operator for the $\tilde{t}$s and $\mathcal{T}$ the time ordering operator for the ts. At this stage we can separate the bath operators $a_{p,\sigma}^\alpha$ from the dot operators d_σ and write

$$\begin{aligned}
\operatorname{Tr} = \operatorname{Tr}_d \Big[\rho_{\text{dot}} \tilde{\mathcal{T}} \mathcal{T} \prod_\sigma d_\sigma(\tilde{t}_1^\sigma) d_\sigma^\dagger(\tilde{t}_1'^\sigma) d_\sigma(\tilde{t}_2^\sigma) d_\sigma^\dagger(\tilde{t}_2'^\sigma) \cdots e^{iH_{\text{dot}}t} e^{-iH_{\text{dot}}t} \cdots d_\sigma(t_2^\sigma) d_\sigma^\dagger(t_2'^\sigma) d_\sigma(t_1^\sigma) d_\sigma^\dagger(t_1'^\sigma) \Big] \\
\times \operatorname{Tr}_{\text{bath}} \Big[\rho_{\text{bath}} \tilde{\mathcal{T}} \mathcal{T} \prod_\sigma \sum_{\tilde{p}_1 \tilde{\alpha}_1; \ldots; \tilde{p}_{m_\sigma} \tilde{\alpha}_{m_\sigma}} \sum_{\tilde{p}'_1 \tilde{\alpha}'_1; \ldots; \tilde{p}'_{m'_\sigma} \tilde{\alpha}'_{m'_\sigma}} \sum_{p_1 \alpha_1; \ldots; p_{n_\sigma} \alpha_{n_\sigma}} \sum_{p'_1 \alpha'_1; \ldots; p'_{n'_\sigma} \alpha'_{n'_\sigma}} V_{\tilde{p}_1}^{\tilde{\alpha}_1} V_{\tilde{p}'_1}^{\tilde{\alpha}'_1 *} \cdots V_{p_1}^{\alpha_1} V_{p'_1}^{\alpha'_1 *} \\
\times a_\sigma^\dagger(\tilde{t}_1^\sigma) a_\sigma(\tilde{t}_1'^\sigma) a_\sigma^\dagger(\tilde{t}_2^\sigma) a_\sigma(\tilde{t}_2'^\sigma) \cdots e^{iH_{\text{bath}}t} e^{-iH_{\text{bath}}t} \cdots a_\sigma^\dagger(t_2^\sigma) a_\sigma(t_2'^\sigma) a_\sigma^\dagger(t_1^\sigma) a_\sigma(t_1'^\sigma) \Big],
\end{aligned} \tag{50}$$

with $\alpha_i \in \{L, R\}$. Since the leads are non-interacting we can evaluate the factor $\operatorname{Tr}_{\text{bath}}[\cdots]$ exactly. Due to Wick's theorem one obtains a product of two determinants $\prod_\sigma \det M_\sigma^{-1}$, with the size of M_σ^{-1} given by the number of operators d_σ on the Keldysh contour ($m_\sigma + n_\sigma$). The matrix elements are given by [20, 25]

$$M_\sigma^{-1}(i,j) = i\Delta(t_{K,i}^\sigma, t_{K,j}'^\sigma), \tag{51}$$

where $t_{K,i}^\sigma$ denotes the position of the ith annihilation operator and $t_{K,j}'^\sigma$ the position of the jth creation operator for spin σ on the unfolded Keldysh contour. The hybridization function Δ is given by

$$\Delta(t_K, t'_K) = \begin{cases} \Delta^<(t'-t) \equiv \Delta_L^<(t'-t) + \Delta_R^<(t'-t) & t_K \geq t'_K, \\ \Delta^>(t'-t) \equiv \Delta_L^>(t'-t) + \Delta_R^>(t'-t) & t_K < t'_K \end{cases}, \tag{52}$$

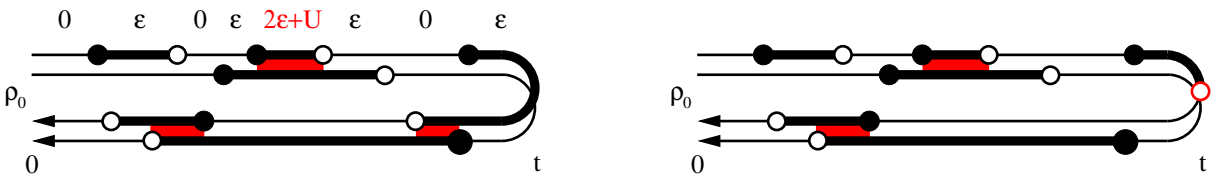


Fig. 2: *Left panel: Segment configuration corresponding to perturbation order 4 for spin up (upper contour) and 2 for spin down (lower contour). Dot creation operators are shown as full circles and annihilation operators as open circles. The segments represent the time intervals in which an electron of the corresponding spin resides on the dot. Right panel: Segment configuration corresponding to the expansion of the current (Eq. (61)) in powers of the dot-lead hybridization. There is a fixed operator d_σ (red open circle) at time t and the hybridization functions connecting to this operator have only a left (L) component. (From Ref. [18])*

with

$$\Delta_\alpha^<(t) = -2i\int_{-\infty}^{\infty}\frac{d\omega}{2\pi}\, e^{-i\omega t}\Gamma^\alpha(\omega)\; f(\omega-\mu_\alpha), \tag{53}$$

$$\Delta_\alpha^>(t) = 2i\int_{-\infty}^{\infty}\frac{d\omega}{2\pi}\, e^{-i\omega t}\Gamma^\alpha(\omega)\big(1-f(\omega-\mu_\alpha)\big). \tag{54}$$

If the bath density of states is flat and centered at zero with a Fermi-function like cutoff at $\omega=\pm\omega_c$,

$$\Gamma^\alpha_{\text{flat}}(\omega) = \frac{\Gamma^\alpha}{\big(1+e^{\nu(\omega-\omega_c)}\big)\big(1+e^{-\nu(\omega+\omega_c)}\big)}, \tag{55}$$

one obtains in the limit $T\ll\omega_c$ the expression [18]

$$\Delta^{</>}_{\text{flat}}(t) \simeq \Gamma\left(\frac{\cos(\frac{V}{2}t)}{\beta\sinh(\frac{\pi}{\beta}t)} - \frac{e^{\pm i\omega_c t}}{\nu\sinh(\frac{\pi}{\nu}t)}\right). \tag{56}$$

To evaluate the trace over the impurity states in Eq. (50), $\mathrm{Tr}_d[\cdots]$, it is useful to employ the segment representation introduced for impurity models with density-density interactions in Ref. [24]. The sequence of dot creation and annihilation operators uniquely determines the occupation of the dot at each time, and we can represent the time evolution using collections of segments for spin up and down electrons as shown in Fig. 2. Each segment depicts a time interval for which an electron with corresponding spin resides on the dot. The trace over the impurity states can then simply be expressed as

$$\mathrm{Tr}_d\left[\cdots\right] = \rho_{\text{imp}}(c)\exp\left[-i\varepsilon_d\sum_\sigma\left(l^\sigma_{\text{forward}}-l^\sigma_{\text{backward}}\right) - iU\left(l^{\text{overlap}}_{\text{forward}}-l^{\text{overlap}}_{\text{backward}}\right)\right]. \tag{57}$$

Here, $\rho_{\text{imp}}(c)$ is the element of the impurity density matrix which is compatible with the operator sequence $c=\{t^\sigma_{K,1},\ldots,t^\sigma_{K,m_\sigma+n_\sigma};t'^\sigma_{K,1},\ldots,t'^\sigma_{K,m'_\sigma+n'_\sigma}\}$ (assumed here to be 1 for configurations which start and end with an empty dot and zero otherwise), l^σ the length of the segments for spin σ and l^{overlap} the length of the overlap between spin up and down segments.

Hence, the Monte Carlo simulation samples collections c of segments on the doubled Keldysh contour (one for each spin) according to their weight

$$w(c) = \prod_\sigma i^{m_\sigma + m'_\sigma} (-i)^{n_\sigma + n'_\sigma} \det M_\sigma^{-1} \, dt^{m_\sigma + m'_\sigma + n_\sigma + n'_\sigma} \, \mathrm{Tr}_d \left[\cdots \right] \tag{58}$$

As in the equilibrium simulations [24], these segment configurations can be sampled using local updates: i) insertion/removal of a segment, ii) insertion/removal of an anti-segment (empty space between segments) and iii) shifts of segment end-points. In order to use fast update formulas similar to those discussed in Sec. 3 one should store and manipulate the matrices M_σ, that is, the inverse of the matrices defined in Eq. (51).

4.2 Measurement of the Green function, density and double occupancy

The Green functions can be obtained from the matrix M in a procedure analogous to the one proposed for imaginary-time simulations in Ref. [24]. Particularly simple is the calculation of the density and double occupancy. From the segment representation it immediately follows that $n_\sigma(t)$ is the probability to have a segment of spin σ present at time t, while $n_\uparrow n_\downarrow(t)$ is the probability to find overlapping segments at time t (taking into account the phases ϕ_c of the Monte Carlo configurations):

$$n_\sigma(t) = \frac{\big\langle \phi_c \, \delta(\text{segment of type } \sigma \text{ at } t) \big\rangle_{|w_c|}}{\langle \phi_c \rangle_{|w_c|}}, \tag{59}$$

$$n_\uparrow n_\downarrow(t) = \frac{\big\langle \phi_c \, \delta(\text{segments of type } \uparrow \text{ and } \downarrow \text{ at } t) \big\rangle_{|w_c|}}{\langle \phi_c \rangle_{|w_c|}}. \tag{60}$$

4.3 Current measurement

The current $I_{L\sigma} = -2 \, \mathrm{Im} \sum_{p \in L} V^L_{p,\sigma} \langle a^{L\dagger}_{p,\sigma} d_\sigma \rangle = -2 \, \mathrm{Im} \left\langle \tilde{a}^\dagger_{L,\sigma} d \right\rangle$ can be measured as explained in Ref. [20]. We expand the quantity

$$I_{L\sigma}(t) = -2 \, \mathrm{Im} \, \mathrm{Tr} \, \rho_0 \Big(\tilde{\mathcal{T}} e^{i \int_0^t ds H_{\mathrm{mix}}(s)} \Big) e^{itH_{\mathrm{loc}}} \, \tilde{a}^\dagger_{L,\sigma} \, d_\sigma \, e^{-itH_{\mathrm{loc}}} \Big(\mathcal{T} e^{-i \int_0^t ds H_{\mathrm{mix}}(s)} \Big) \tag{61}$$

in powers of H_{mix}, which leads to the same collection of diagrams as discussed above, except that there is now an operator d_σ fixed at time t and that the hybridization functions Δ connecting to this operator have only an L-component

$$M^{-1}_\sigma(i,j) = i\Delta_L(t^\sigma_{K,i}, t'^\sigma_{K,j}) + i\Delta_R(t^\sigma_{K,i}, t'^\sigma_{K,j}) \big(1 - \delta_{t, t^\sigma_{K,i}} \big). \tag{62}$$

Having identified the Monte Carlo configurations c (illustrated in the right panel of Fig. 2) and their weights w_c we can implement a random walk based on $|w_c|$ and measure the current as

$$I_{L\sigma} = \sum_c w_c = \langle \phi_c \rangle_{|w_c|} \sum_c |w_c|. \tag{63}$$

In contrast to the density measurement (which was based on an expansion of the identity so that $\sum_c |w_c| = 1/\langle \phi_c \rangle_{|w_c|}$) we cannot directly measure the normalization factor $\sum_c |w_c|$. One

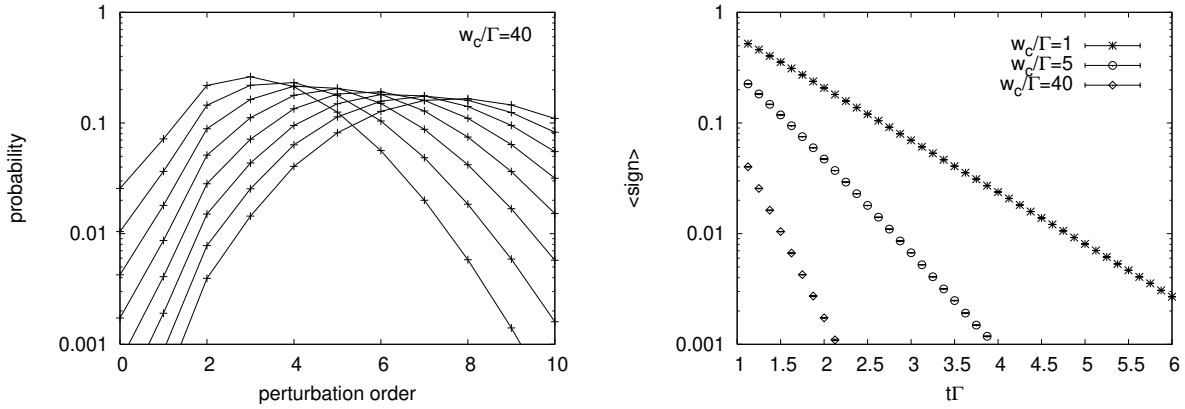


Fig. 3: *Distribution of perturbation orders and average sign obtained using the hybridization expansion algorithm for a non-interacting dot with soft cutoff,* $T = 0$*,* $V = 0$*,* $\varepsilon_d/\Gamma = -0.5$ *and a single fermion species. Left panel: distribution of perturbation orders for different lengths of the contour (*$t\Gamma = 1.25, 1.50, \ldots, 3$ *from left to right) and cutoff* $\omega_c/\Gamma = 40$*. The average perturbation order grows* $\sim t$*. Right panel: average sign as a function of time for the indicated values of the cutoff. (From Ref. [18])*

possibility to get rid of this unknown factor is to consider the ratio $I/I^{(1)}$ between the current and the lowest order contribution $I^{(1)}$ which can be calculated analytically. Since

$$I^{(1)}_{L\sigma} = \left\langle \phi_c \, \delta(c \text{ 1st order}) \right\rangle_{|w_c|} \sum_c |w_c| \tag{64}$$

we can measure the current as

$$I_{L\sigma} = I^{(1)}_{L\sigma} \frac{\left\langle \phi_c \right\rangle_{|w_c|}}{\left\langle \phi_c \delta(c \text{ 1st order}) \right\rangle_{|w_c|}}. \tag{65}$$

5 Perturbation order and average sign

If we switch on the interaction (weak-coupling approach) or hybridization (strong-coupling approach) at time $t = 0_+$, the average perturbation order increases approximately linearly with the time interval to be simulated. This results in a dynamical sign problem: the factors of $(\pm i)$ associated with each order of the expansion and the complex determinants mean that the average sign of the diagrams contributing to any quantity decays exponentially as the perturbation order is increased. Figure 3 presents results obtained using the hybridization expansion algorithm on a model of spinless fermions. The same qualitative behavior is found in interacting models and in the weak coupling algorithm. The left panel shows the distribution of perturbation orders for simulations over different time intervals. The mean perturbation order can be estimated from the positions of the maxima in these curves. The right pannel shows the average sign, which decays exponentially with perturbation order or length of the time interval to be simulated.
In practice, accurate measurements of physical quantities can be obtained for $\langle \text{sign} \rangle \gtrsim 0.001$, and whether a steady state can be reached depends on the method, the parameters, and the observable. Non-zero temperature and voltage bias tend to reduce the sign problem, but not

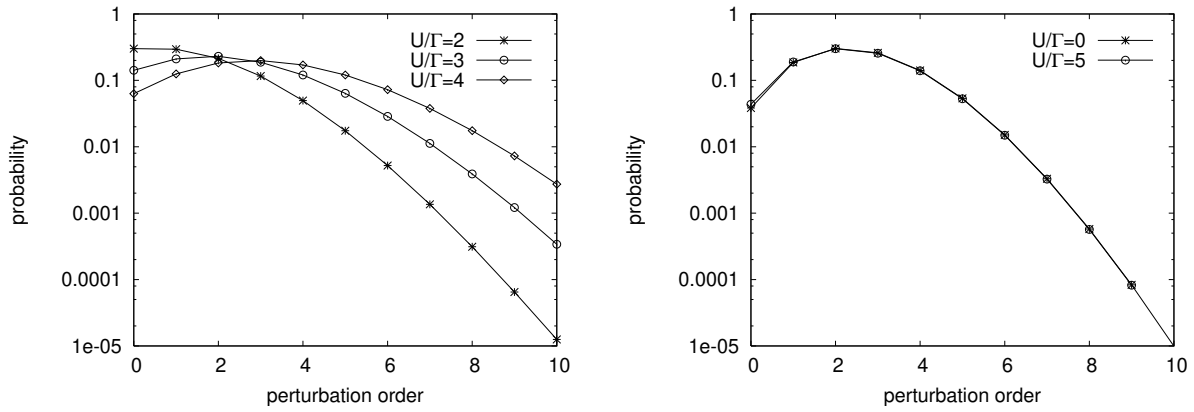


Fig. 4: *Distribution of perturbation orders for different values of the interaction U, for $T = 0$, $V = 0$, ε_d+$U/2 = 0$. The left panel shows the distribution of perturbation orders for the weak-coupling algorithm ($t\Gamma = 1$, infinite bandwidth), where the average perturbation order grows $\sim U$. Right panel: distribution of perturbation orders for the hybridization expansion algorithm ($t\Gamma = 1.5$, $\omega_c/\Gamma = 10$). Here there is almost no dependence on the interaction strength. (From Ref. [18])*

enough to enable simulations on significantly longer contours. The important effect of a non-vanishing voltage bias is to accelerate the relaxation into the steady state, at least in the weak-coupling approach.

The left panel of Fig. 4 shows that in the weak-coupling approach, the average perturbation order (at fixed t) depends on the interaction strength. As in the imaginary-time version of this algorithm [26], the perturbation order grows roughly linearly with increasing U.

In the hybridization expansion algorithm (right panel of Fig. 4), the average perturbation order is essentially independent of interaction strength. This is in contrast to the imaginary-time version of this algorithm [24], where the perturbation order decreases with increasing interaction strength. From Eq. (58) it follows that the interaction term merely adds a phase to the Monte Carlo weight and therefore does not affect $|w(c)|$. While the algorithm can treat strong interactions, it is limited to finite bandwidth, since the average perturbation order diverges as the bandwidth goes to infinity (see cutoff dependence in the right hand panel of Fig. 3).

6 Results: Interaction quench calculations

For practical real-time calculations, the weak-coupling QMC approach turned out to be more useful than the hybridization-expansion QMC method. In particular, this method allowed to obtain accurate current-voltage data for quantum dots (except in the low-voltage regime), and it enabled pioneering nonequilibrium DMFT studies [30–33]. We will illustrate it in this section with interaction quench data for quantum dots, taken from Ref. [19]. Since we consider non-interacting initial states in these simulations, only the real-time branches of the contour need to be considered, and we can use the formalism presented in Sec. 3. Temperature enters only as a parameter in the lead correlators, so that arbitrary temperatures, including $T = 0$, can be treated.

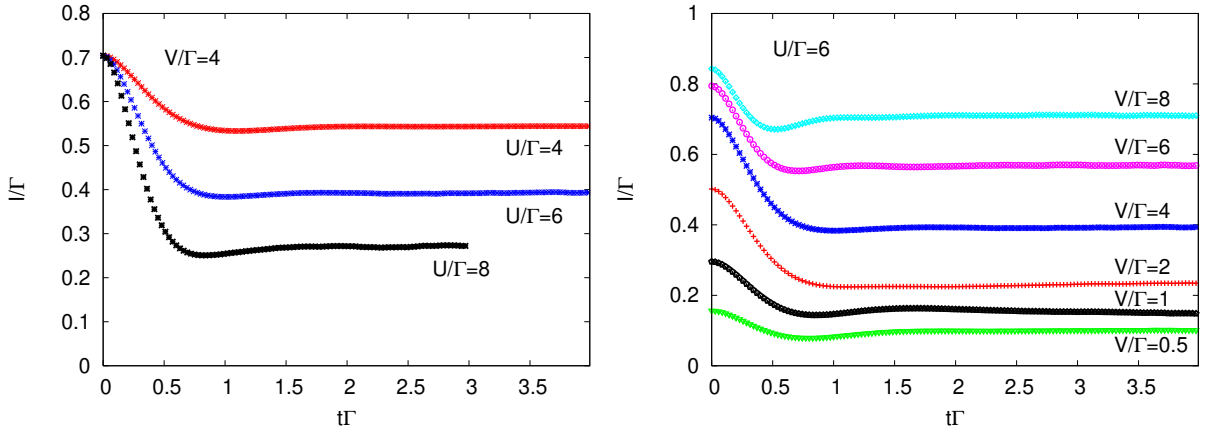


Fig. 5: *Left panel: Time evolution of the current for $V/\Gamma = 4$ and different interaction strengths (bath temperature $T = 0$). In the initial state, the current is given by the steady state current through the non-interacting dot. At time $t = 0_+$, the interaction is turned on. After a time of a few inverse Γ, the current saturates at the value corresponding to the steady state current in the interacting dot. Right panel: Analogous data for different voltage biases and fixed interaction strength $U/\Gamma = 6$. (From Ref. [19])*

6.1 Convergence to the long-time limit: large bias voltage

At time $t = 0$, the system is noninteracting but subject to an applied voltage bias V, so a current $I_0(V)$ corresponding to the noninteracting model is flowing through the dot. At $t = 0_+$ the interaction is turned on and the system relaxes into the steady-state configuration appropriate to the interacting model. The left panel of Fig. 5 shows the time dependence of the current calculated for the large bias voltage $V/\Gamma = 4$ and several interaction strengths. The current initially decreases sharply, overshoots and eventually relaxes back up to the new steady-state value. The interaction-dependence of the steady-state current is a consequence of the Coulomb blockade physics, apparent even at the large voltages studied here.

For intermediate and large voltage bias ($V/\Gamma \gtrsim 2$) and not too large interaction ($U/\Gamma \lesssim 8$) the time required for convergence to the steady state is $t\Gamma \approx 2$, essentially independent of interaction strength. Given the scaling of the perturbation order (and hence the sign problem) with U and t, interactions up to $U/\Gamma \lesssim 10$ are accessible with moderate computational effort.

In the right panel of Fig. 5 we plot the time evolution of the current for fixed $U/\Gamma = 6$ and several voltage biases. For voltages $V/\Gamma \gtrsim 2$, even though the transient behavior is clearly voltage-dependent, the current settles into the new steady state after a time $t\Gamma \approx 2$. However, as the voltage is decreased below $V/\Gamma \approx 2$ the transient time increases. At $V = \Gamma$ the long time limit is attained only for $t\Gamma \gtrsim 3$ and as V is further decreased the approach to the asymptotic behavior becomes even slower.

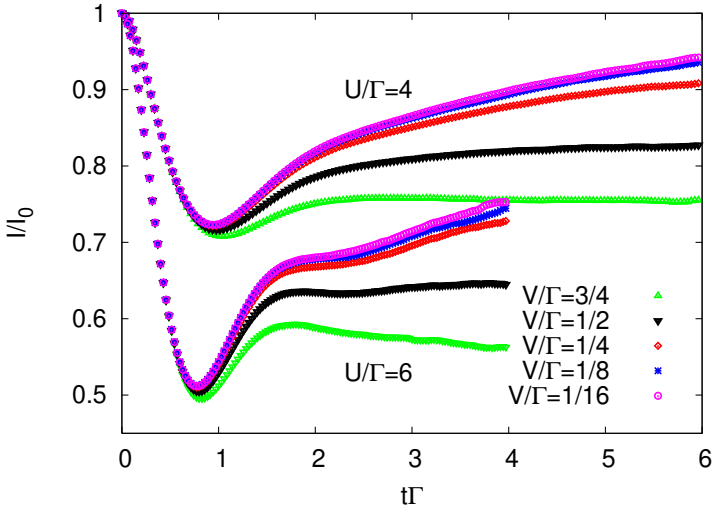


Fig. 6: *Interaction quench in the small-voltage regime ($T = 0$): Ratio of interacting to non-interacting current for $U/\Gamma = 4$ and $U/\Gamma = 6$ and indicated voltage biases. For $V/\Gamma \lesssim 0.5$ the time needed to reach the steady state grows much beyond the largest time accessible in the Monte Carlo simulation. (From Ref. [19])*

6.2 Convergence to the long-time limit: small bias voltage

To better analyze the approach to the steady state at small voltages we present in Fig. 6 the time dependence of the current for several smaller voltages and two interaction strengths. For better comparison, we plot here the ratio I/I_0 of the interacting current I to the noninteracting current I_0. One sees that as V is decreased or U is increased the evolution of the current from the post-quench minimum to the long-time steady state value takes an increasingly long time. Since the longest accessible time is $t\Gamma \approx 6$ for $U/\Gamma = 4$ and $t\Gamma \approx 4$ for $U/\Gamma = 6$, the accurate measurement of I becomes impossible in the small-voltage regime. However the short-time transient behavior is accessible at all voltages. While the ratio $(I/I_0)(t)$ is clearly voltage dependent at higher biases, the data seem to converge as V is reduced to a non-trivial curve with a pronounced minimum near an only weakly U-dependent time $t\Gamma \approx 1$.

It is plausible that the increasingly slow convergence as $V \to 0$ is a signature of the Kondo effect, which is characterized by an energy scale which becomes exponentially small as U increases. After the interaction quench, the Kondo resonance has to be built up as time progresses, and in the limit $V \to 0, T \to 0$ this requires an increasingly large number of interaction vertices and hence an increasingly long simulation time. One expects that the time needed to evolve into the steady state is proportional to the inverse of the associated energy scale.

The slow relaxation becomes an issue in the linear response regime, where the noninteracting and interacting currents are very similar. For $V/\Gamma \gtrsim 0.5$, where the interacting current is substantially smaller than I_0, a useful estimate of I seems possible, even though in the voltage window up to $V/\Gamma \approx 2$ a small drift in the current may remain up to the longest accessible times. This drift makes it difficult to define reliable error bars on I. For $V/\Gamma \lesssim 0.25$, an accurate estimate is not possible from the interaction quench procedure, but the current is very close to the linear response value.

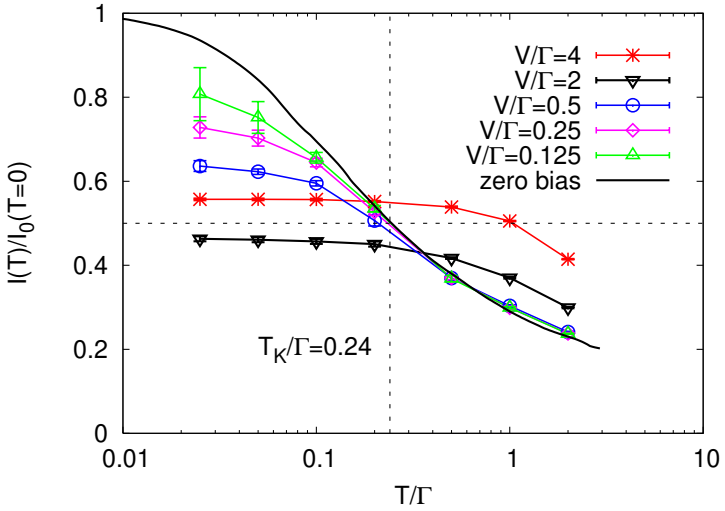


Fig. 7: *Temperature dependence of the ratio of the interacting current at temperature T to the noninteracting current at $T = 0$ for the indicated values of the voltage bias. The interaction strength is $U/\Gamma = 6$. The symbols show Monte Carlo results, the black line the analytical curve for $V \to 0$ extracted from Ref. [34] and plotted for $T_K/\Gamma = 0.24$. (From Ref. [19])*

6.3 Temperature dependence

It is also of interest to examine the temperature dependence of the current. The interplay between voltage and temperature as the Kondo regime is approached presents an interesting problem. One expects that as the temperature is increased, the Kondo effect gets washed out and the simulations would therefore more readily converge even at small bias voltages. The temperature dependence of the current calculated from the interaction quench for $U/\Gamma = 6$ and several values of the voltage bias is plotted in Fig. 7. In the linear response regime ($V/\Gamma = 0.125$, 0.25) the ratio of the interacting current $I(T)$ to the noninteracting current $I_0(T{=}0)$ exhibits a strong temperature dependence, even at $T/V \ll 1$. The temperature dependence arises because lowering the temperature strengthens the Kondo resonance and leads to an increase in the interacting current. The temperature dependence for small voltage bias ($V/\Gamma = 0.125$) approaches the analytical result for the temperature dependent zero-bias conductance in Ref. [34] and thus allows us to estimate (from the temperature at which $I(V{\to}0) = I_0/2$) the Kondo temperature as $T_K/\Gamma \approx 0.24$, in good agreement with the estimate from the formula [35]

$$T_K \approx U\Big(\frac{\Gamma}{2U}\Big)^{1/2} e^{-\pi U/8\Gamma + \pi\Gamma/2U}, \tag{66}$$

which is valid in the strong correlation regime and for $U/\Gamma = 6$ yields $T_K/\Gamma = 0.21$.

As V is increased the temperature dependence is weakened. At intermediate values of V, in the Coulomb blockade regime ($V/\Gamma = 2$), the current has little temperature dependence at low T. At large voltage bias ($V/\Gamma = 4$), correlation effects are significantly weakened due to the voltage, as is evident from the increase in I/I_0. The current in this regime remains insensitive to temperature at low T.

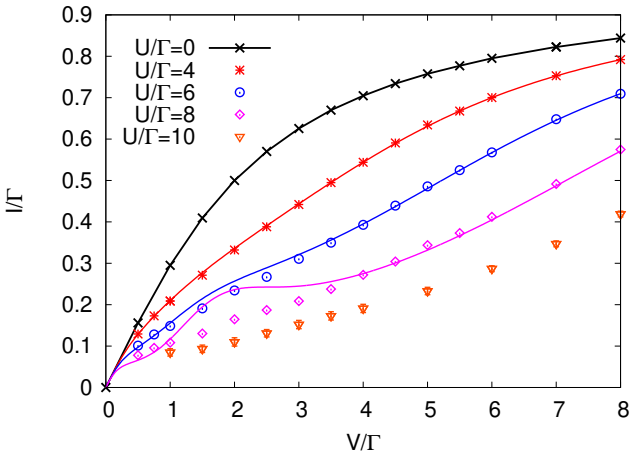


Fig. 8: *Current-voltage characteristics of the single-orbital Anderson impurity model. The symbols show Monte Carlo data for U/Γ=4, 6, 8, 10, while the lines correspond to the fourth order perturbation calculation of Ref. [36]. The Monte Carlo results have been obtained by means of U-quenches at T=0. Error bars are on the order of the symbol size. (From Ref. [19])*

6.4 Current-voltage characteristics

We now apply the weak-coupling QMC approach to compute the current-voltage characteristics of the Anderson impurity model at half-filling.

Figure 8 shows the $T = 0$ result obtained using interaction quenches ($\omega_c/\Gamma = \nu\Gamma = 10$, essentially the wide-band limit). The black curve shows the monotonic increase of the non-interacting current with increasing applied bias voltage. The red, blue and pink lines show the interacting current for $U/\Gamma = 4$, 6, and 8 predicted by fourth order perturbation theory [36]. Consistent with analytical arguments [37, 38], the interacting current initially rises with the same slope as the non-interacting current, and reaches the non-interacting value also in the large-voltage limit. At intermediate values of V, interaction effects suppress the current (Coulomb blockade). In fourth order perturbation theory, a hump appears in the I-V curve around $V/\Gamma = 2$ for $U/\Gamma = 6$ and 8. At even larger U (clearly outside the range of applicability) fourth order perturbation theory will presumably lead to a negative differential conductance at intermediate V. The Monte Carlo data for $U/\Gamma = 4$, 6, 8, and 10 are shown by the red stars, blue circles, pink diamonds, and orange triangles, respectively. Since these are U-quench results for $T = 0$, only $V/\Gamma \gtrsim 0.5$ data are shown. In the large voltage regime ($V/\Gamma \gtrsim 4$), the numerical results agree with the prediction from fourth order perturbation theory. Apparently, the fast decay of the Green functions for large voltage bias simplifies the diagram structure such that fourth order in Σ is sufficient at $V/\Gamma \gtrsim 4$. At intermediate voltages, $1 \lesssim V/\Gamma \lesssim 3$, differences between the Monte Carlo data and fourth order perturbation theory appear. The essentially exact numerical data show no prominent hump feature near $V/\Gamma = 2$, and hence no negative differential conductance in the intermediate to strong correlation regime. The data in Fig. 8 however indicate that fourth order perturbation theory yields correct results over the entire voltage range for $U/\Gamma < 4$. For larger interactions, and in particular around $V/\Gamma \approx 2$ more complicated self energy diagrams become important.

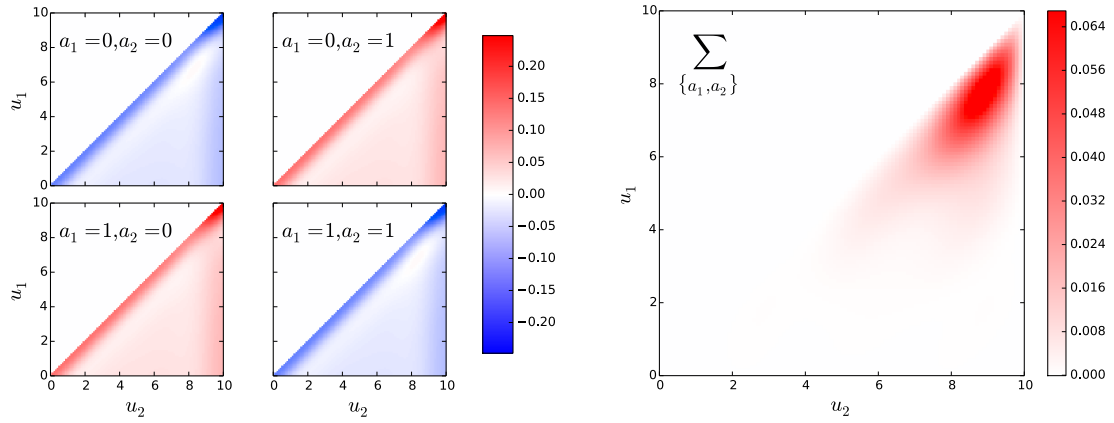


Fig. 9: *Left panels: Color map of the real part of the integrand of Q_2 as a function of the two times u_1 and u_2 (impurity model with $\mu_L = \mu_R = 0$, $T = 0$ and $t = 10$). The four panels correspond to the four possible values of the two Keldysh indices a_1 and a_2. Right panel: Integrand after summation over the Keldysh indices. (From Ref. [39])*

7 Sampling of connected diagrams

The Monte Carlo algorithms described in Sec. 3 and 4 sample both connected and disconnected weak- or strong-coupling diagrams. This is the main reason why the perturbation order grows approximately proportional to the maximum simulation time t and the average sign drops exponentially with t. Since the formulation of these algorithms, alternative QMC approaches have been developed [39, 40], which eliminate the disconnected diagrams. In this section, we briefly discuss the main aspects of these algorithms.

7.1 Weak-coupling approach

Instead of sampling the "partition function" $\tilde{\mathcal{O}} = 1$ (Eq. (12)) and accumulating appropriate estimators for different observables, one can directly implement a weak-coupling diagrammatic expansion for some given observable Q [39],

$$Q(U) = \sum_{n=0}^{\infty} Q_n U^n, \quad Q_n = \sum_{C_n} w_Q(C_n). \tag{67}$$

In this short-hand notation, C_n denotes a configuration of order n and $\sum_{C_n}$ contains the integrations of the vertex positions over the Keldysh contour. The weight $w_Q(C_n)$ includes the $\pm i$ factors from the expansion and a determinant of a matrix whose elements are bath Green functions, analogous to that discussed in Sec. 3.

Instead of parametrizing time on the Keldysh contour by the Keldysh time t_K, one can introduce the pair (t, a), where t is the physical time and the Keldysh index a=0, 1 determines the forward or backward branch of the contour. The important observation in Ref. [39] was that the explicit summation over Keldysh indices eliminates the contribution of the disconnected diagrams from Q_n and allows to absorb significant cancellations between individual diagrams. This leads to a decay of the integrand away from the time t for which the observable is computed, as is

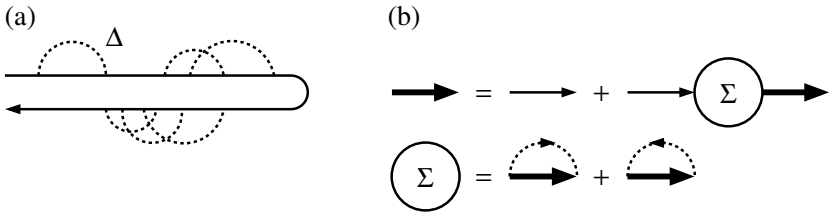


Fig. 10: *Panel (a): Example of a hybridization expansion diagram with a backbone formed by atomic propagators (thin solid lines) and "self-energy" insertions with one, two and three connected hybridization lines (directions left unspecified). Panel (b): NCA pseudo-particle Green function (thick arrow) defined in terms of the atomic propagator (thin arrow) and the NCA self-energy (circle) via the pseudo-particle Dyson equation.*

illustrated in Fig. 9 for the n=2 contribution to the local charge of an impurity model at $t = 10$. The four panels on the left show the real parts of the integrands of Q_2 as a function of the two real-time variables u_1 and u_2 for the indicated combinations of the Keldysh indices a_1 and a_2. The right panel plots the integrand after summation over Keldysh indices. The result is now real and the function is indeed peaked near the measurement time t=10, which suggests that with this approach, large t become more easily accessible. (In quantum dot problems, where the long-time limit is determined entirely by the bath, even $t\to\infty$ can be accessed.)

Implementing a Monte Carlo sampling similar to the one described in Sec. 3 one can measure the ratios Q_n/Q_0 and hence (using an exact evaluation of Q_0) the different terms in the expansion (67). It should be noted though that the summation over the Keldysh indices requires the evaluation of 2^n determinants at order n, so as long as the required orders increase with the measurement time t, the computational effort grows as in a simulation with an exponentially scaling sign problem. At long times, the elimination of the disconnected diagrams should however lead to a slower increase in the relevant orders with t and thus a computational advantage over the method presented in Sec. 3. A downside of the approach is that each observable has to be sampled separately, while the "partition function" sampling allows to measure any observable in one go, including the two-time Green functions which are essential for nonequilibrium DMFT.

7.2 Strong-coupling approach

In the strong-coupling formalism, diagrams with disconnected insertions of hybridization lines (Fig. 10(a)) can be eliminated by defining pseudo-particle propagators for the different atomic states, which resum certain subclasses of diagrams. For example, in the noncrossing approximation (NCA) [41], one sums up all hybridization-expansion diagrams with no crossing hybridization lines by defining a pseudo-particle self-energy as the product of a single hybridization line and a pseudo-particle Green function, and solving a pseudo-particle Dyson equation, in which the bare pseudo-particle propagator is given by the atomic Green function (Fig. 10(b)). At the second oder (one-crossing approximation) [42], one considers pseudo-particle self-energy diagrams with two connected hybridization lines, at third order those with three connected hybridization lines, etc.

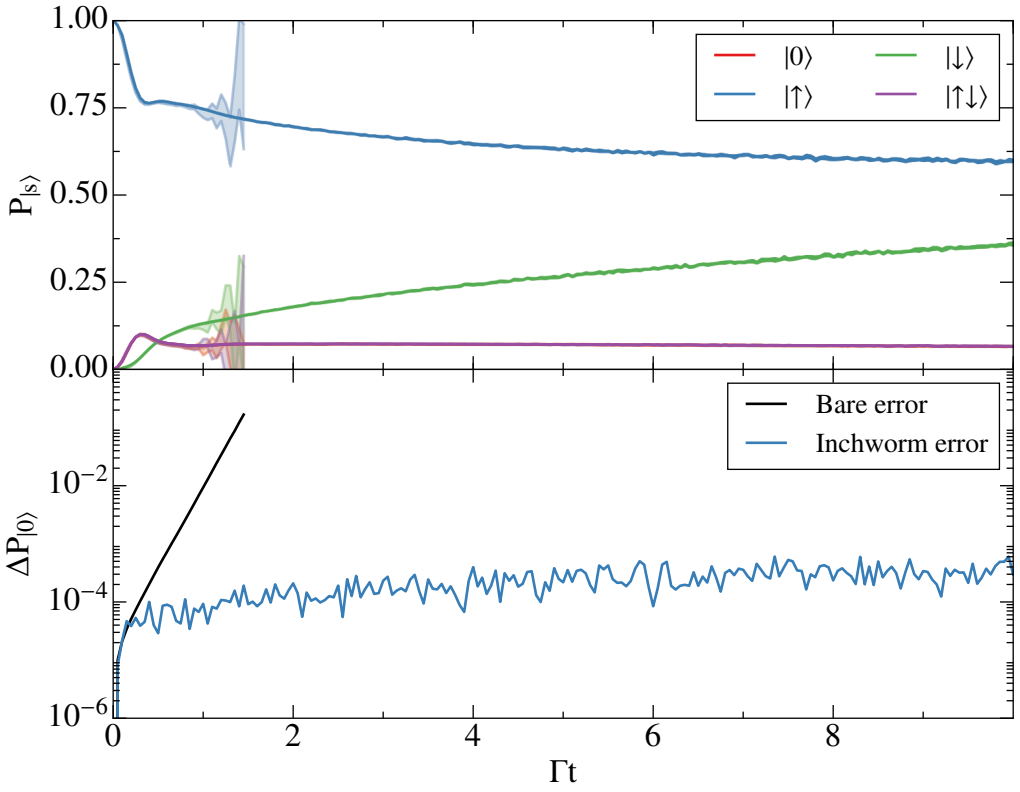


Fig. 11: *Upper panel: Evolution of the local state population for the initial state* $|\uparrow\rangle$ *(*$U = -2\varepsilon = 8\Gamma$ *and* $\beta\Gamma = 50$*). Faint colors show the bare hybridization expansion result for times* $\Gamma t < 1.5$*, while the solid lines plot the inchworm result. Lower panel: Error estimate for the data in the upper panel. (From Ref. [40])*

The implementation of this scheme on the Keldysh contour has been discussed in detail in Ref. [14]. The computational effort for the evaluation of the pseudo-particle self-energy however grows rapidly with increasing order, since each additional hybridization line implies two internal time integrals, each hybridization line has two possible directions (forward or backward) and in a spinful model two spin flavors. Also the number of distinct diagram topologies rapidly increases. Practical calculations have thus been mainly limited to NCA and OCA. A significant step forward occurred with the development of the inchworm approach [40], which uses a Monte Carlo sampling approach to evaluate the internal time integrals. With this method, self-energy diagrams up to fourth or even higher orders can be evaluated.

Thanks to the elimination of disconnected diagrams, longer maximum times t than in the standard hybridization expansion of Sec. 4 can be accessed. This is relevant for example in situations where a slow initial relaxation hampers the measurement of a steady state property. Figure 11 shows the evolution of the probabilities for the four different impurity states after the sudden switch-on of the coupling to the bath at time $t = 0_+$, for a system which is initially in the state $|\uparrow\rangle$. In contrast to the conventional bare hybridization expansion (faint colors), which only allows to calculate the dynamics up to $t\Gamma \approx 1$, the inchworm simulation can track the relaxation almost to the steady state, which has equal probabilities for the states $|\uparrow\rangle$ and $|\downarrow\rangle$.

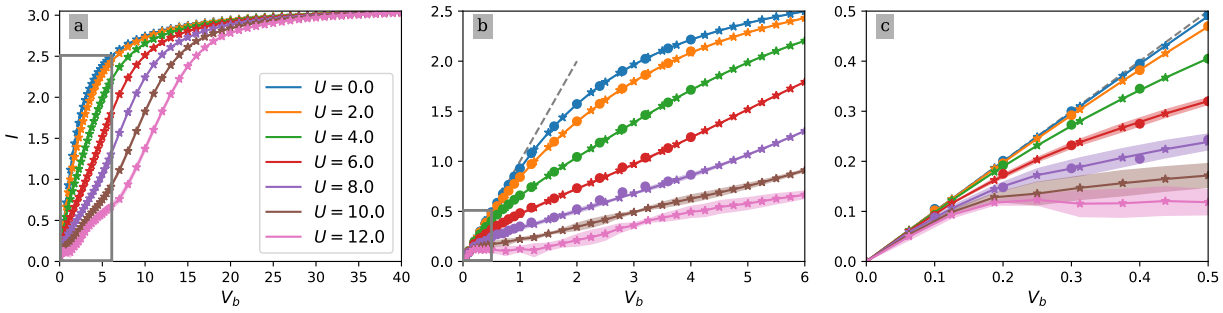


Fig. 12: *Current-voltage characteristic $I(V_b)$ of the Anderson impurity model. Panel (a) shows the full voltage range and panels (b,c) the intermediate and low-V_b behavior. The stars show the results obtained by TCI, while the circles are benchmark data calculated with QMC [45]. (From Ref. [46])*

8 Beyond Monte Carlo

8.1 Tensor cross interpolation

A recent innovation, which may eliminate the need for Monte Carlo sampling in situations which can be handled with perturbation orders $\lesssim 30$, is the tensor cross interpolation (TCI) of multivariable functions [43, 44]. In our case, the multivariable functions of interest are the diagram weights, which depend on a certain number of Keldysh time variables. On a discretized time grid, an n-dimensional function $f(t_{K,1}, t_{K,2}, \ldots, t_{K,n})$ becomes an n-way tensor, which can be factorized by TCI into a tensor train (or matrix-product state),

$$f(t_{K,1}, t_{K,2}, \ldots, t_{K,n}) \approx T_1(t_{K,1}) \cdot T_2(t_{K,2}) \cdot \ldots \cdot T_n(t_{K,n}). \tag{68}$$

where the T_i are matrices whose dimension depends on the properties of the function f and the desired accuracy of the interpolation. The important point is that this factorization reduces an n-dimensional integral to products of one-dimensional integrals, which can be efficiently computed if the matrix dimensions are sufficiently low [44].

Recent studies have applied the TCI approach to both the weak-coupling and strong-coupling diagrammatic schemes discussed in Sec. 7 and obtained promising results.

8.2 Weak-coupling expansion with TCI

The general idea of evaluating Feynman diagrams with the help of TCI has been introduced in Ref. [44], which also demonstrated some applications to real-time impurity problems within the general framework described in Sec. 7.1. Highly accurate results with perturbation orders up to ≈ 25 have recently been published in Ref. [46]. As an illustration, Fig. 12 shows the current-voltage characteristics of the Anderson impurity model, and demonstrates the approach to the linear-response behavior in the numerically challenging low-V regime, even for strong interactions.

8.3 Strong-coupling expansion with TCI

The evaluation of the self-consistently resummed hybridization expansion diagrams (Sec. 7.2) with the help of TCI is a promising strategy, since this expansion converges rapidly with the diagram order in the strongly-correlated regime [14]. Two related but at the technical level distinct implementations for nonequilibrium steady-state problems have recently been presented in Refs. [47] and [48]. One of them uses a standard TCI decomposition of the hybridization part of the pseudo-particle self-energy integrand [47], and the other a so-called quantics-TCI decomposition [49] of the full pseudo-particle self-energy integrand. In the quantics approach [48], the time variables are expressed in a binary representation, and separate tensors are associated with each bit. Pushing these methods to sufficiently high orders and assessing their efficiency is the subject of ongoing research, but the strong-coupling TCI approach is likely to replace QMC approaches for strongly correlated nonequilibrium impurity problems.

9 Conclusions

The basic idea of the QMC approach for nonequilibrium systems is to evaluate a diagrammatic expansion on the two-leg Keldysh or three-leg Kadanoff-Baym contour using Monte Carlo sampling. We detailed the original weak-coupling and strong-coupling formulations of this approach, which are direct generalizations of the widely used continuous-time QMC methods [17] from the Matsubara axis to two-leg or three-leg contours. We discussed these methods for quantum dot problems, where the bath is given and the main goal is the calculation of some steady-state property (typically the current through the dot). The same machinery can however also be used within nonequilibrium DMFT, where the bath Green functions or hybridization functions are self-consistently computed in the DMFT loop [4]. In this context, the main challenge becomes the calculation of the impurity Green function $G(t, t')$.

Especially the weak-coupling approach has allowed to obtain useful results, both for the current-voltage characteristics of quantum dots [19], and for quenched or electric field driven Hubbard models [4]. In the DMFT context, this method has enabled pioneering studies on dynamical phase transitions [30] and dynamical band flipping [31], which even after more than a decade remain exceptional examples of numerically exact nonequilibrium DMFT results. However, in contrast to equilibrium, where the continuous-time QMC approach is powerful enough for a wide range of typical applications, the real-time incarnation of this method is limited by a dynamical sign problem. Since the average perturbation order grows approximately linearly with the maximum time t, the time evolution is complex, and each operator comes with a prefactor $\pm i$, the average sign in the Monte Carlo sampling drops exponentially with increasing t. This limits the simulations to short times.

A promising strategy to tame the sign problem is to suppress disconnected diagrams, which contribute significantly to the sign cancellations, but not to the measured observables. In the weak-coupling approach, this can be achieved by summing all diagrams with the same real-time positions of operators, but different Keldysh indices [39]. While this summation also comes at

an exponential cost, the available results suggest that the suppression of phase cancellations more than compensates this cost. In the strong-coupling approach, one can switch to a pseudo-particle formalism, and work with propagators which resum all the disconnected hybridization-expansion diagrams with self-energy insertions up to a given order. The inchworm algorithm [40] stochastically evaluates the pseudo-particle self-energies within this formalism.
The most recent development is the explicit evaluation of the integrals over diagram weights via TCI [44]. This approach avoids Monte Carlo sampling and looks promising in situations where the required perturbation order is $\lesssim 30$. The basic idea is to factorize the diagram weights into a tensor-train form. Since this factorization reduces the evaluation of a high-dimensional integral to the numerically much more simple evaluation of products of one-dimensional integrals, it allows to treat high-dimensional functions which would be too expensive to integrate with standard quadrature rules. Different flavors of TCI based impurity solvers are currently being developed and tested and they are likely to outperform the real-time QMC solvers in most applications.

References

[1] A. Georges, G. Kotliar, W. Krauth, and M.J. Rozenberg, Rev. Mod. Phys. **68**, 13 (1996)

[2] D. Goldhaber-Gordon, H. Shtrikman, D. Mahalu, D. Abusch-Magder, U. Meirav and M.A. Kastner, Nature **391**, 156 (1998)

[3] C. Giannetti, M. Capone, D. Fausti, M. Fabrizio, F. Parmigiani, and D. Mihailovic, Adv. Phys. **65**, 58 (2016)

[4] H. Aoki, N. Tsuji, M. Eckstein, M. Kollar, T. Oka, and P. Werner, Rev. Mod. Phys. **86**, 779 (2014)

[5] J. Li and M. Eckstein, Phys. Rev. B **103**, 045133 (2021)

[6] L. Kadanoff and G. Baym, *Quantum Statistical Mechanics* (Benjamin, New York, 1962)

[7] L.V. Keldysh, Zh. Eksp. Teor. Fix. **47**, 1515 (1964) [Sov. Phys. JETP **20**, 1018 (1965)]

[8] F.B. Anders and A. Schiller, Phys. Rev. **B** 74, 245113 (2006)

[9] N. Makri, J. Chem. Phys. **111**, 6164 (1999)

[10] S. Weiss, J. Eckel, M. Thorwart, and R. Egger, Phys. Rev. B **77**, 195316 (2008)

[11] J. Thoenniss, M. Sonner, A. Lerose, and D.A. Abanin, Phys. Rev. B **107**, L201115 (2023)

[12] M. Nayak, J. Thoenniss, M. Sonner, D.A. Abanin, P. Werner, arXiv:2503.02848 (2025)

[13] A. Goker, B.A. Friedman, and P. Nordlander, J. Phys.: Condens. Matter **19**, 376206 (2007)

[14] M. Eckstein and P. Werner, Phys. Rev. B **82**, 115115 (2010)

[15] K.A. Al-Hassanieh, A.E. Feiguin, J.A. Riera, C.A. Busser and E. Dagotto, Phys. Rev. B **73**, 195304 (2006)

[16] S. Kirino, T. Fujii, J. Zhao and K. Ueda, J. Phys. Soc. Jpn. **77**, 084704 (2008)

[17] E. Gull, A.J. Millis, A.I. Lichtenstein, A.N. Rubtsov, M. Troyer, and P. Werner, Rev. Mod. Phys. **83**, 349 (2011)

[18] P. Werner, T. Oka, and A.J. Millis, Phys. Rev. B **79**, 035320 (2009)

[19] P. Werner, T. Oka, M. Eckstein and A.J. Millis, Phys. Rev. B **81**, 035108 (2010)

[20] L. Mühlbacher and E. Rabani, Phys. Rev. Lett. **100**, 176403 (2008)

[21] T. Schmidt, P. Werner, L. Mühlbacher, and A. Komnik, Phys. Rev. B **78**, 235110 (2008)

[22] M. Schiro and M. Fabrizio, Phys. Rev. B **79**, 153302 (2009)

[23] A.N. Rubtsov, V.V. Savkin and A.I. Lichtenstein, Phys. Rev. B **72**, 035122 (2005)

[24] P. Werner, A. Comanac, L. de' Medici, M. Troyer and A.J. Millis, Phys. Rev. Lett. **97**, 076405 (2006)

[25] P. Werner and A.J. Millis, Phys. Rev. B **74**, 155107 (2006)

[26] E. Gull, P. Werner, O. Parcollet, and M. Troyer, Europhys. Lett. **82**, 57003 (2008)

[27] S.M.A. Rombouts, K. Heyde, and N. Jachowicz, Phys. Rev. Lett. **82**, 4155 (1999)

[28] J. Rammer and H. Smith, Rev. Mod. Phys. **58**, 323 (1986)

[29] K. Mikelsons, A. Macridin, and M. Jarrell, Phys. Rev. E **79**, 057701 (2009)

[30] M. Eckstein, M. Kollar, and P. Werner, Phys. Rev. Lett. **103**, 056403 (2009)

[31] N. Tsuji, T. Oka, P. Werner and Hideo Aoki, Phys. Rev. Lett. **106**, 236401 (2011)

[32] M. Eckstein and P. Werner, Phys. Rev. Lett. **107**, 186406 (2011)

[33] E. Canovi, P. Werner and M. Eckstein, Phys. Rev. Lett. **113**, 265702 (2014)

[34] R.M. Konik, H. Saleur, and A.W.W. Ludwig, Phys. Rev. Lett. **87**, 236801 (2001)

[35] A.C. Hewson, *The Kondo Problem to Heavy Fermions*, (Cambridge Univ. Press, 1993)

[36] T. Fujii and K. Ueda, Phys. Rev. B **68**, 155310 (2003)

[37] T.K. Ng and P.A. Lee, Phys. Rev. Lett. **61** 1768, (1988)

[38] L.I. Glazman and M.E. Raikh, Zh. Eksp. Teor. Fiz. **47**, 378 (1988) [JETP Lett. **47**, 452]

[39] R.E.V. Profumo, C. Groth, L. Messio, O. Parcollet, and X. Waintal, Phys. Rev. B **91**, 245154 (2015)

[40] G. Cohen, E. Gull, D.R. Reichman, and A.J. Millis, Phys. Rev. Lett. **115**, 266802 (2015)

[41] H. Keiter and J.C. Kimball, J. Appl. Phys. **42**, 1460 (1971)

[42] T. Pruschke and N. Grewe, Z. Phys. B **74**, 439 (1989)

[43] I. Oseledets and E. Tyrtyshnikov, Linear Algebra and its Applications **432**, 70 (2010)

[44] Y. Nunez Fernandez, M. Jeannin, P.T. Dumitrescu, T. Kloss, J. Kaye, O. Parcollet and X. Waintal, Phys. Rev. X **12**, 041018 (2022)

[45] C. Bertrand, S. Florens, O. Parcollet, and X. Waintal, Phys. Rev. X **9**, 041008 (2019)

[46] M. Jeannin, Y. Nunez-Fernandez, T. Kloss, O. Parcollet, and X. Waintal, arXiv:2502.16306 (2025)

[47] M. Eckstein, arXiv:2410.19707 (2024)

[48] A. Kim and P. Werner, Phys. Rev. B **111**, 125120 (2025)

[49] M.K. Ritter, Y. Nunez Fernandez, M. Wallerberger, J. von Delft, H. Shinaoka, and X. Waintal, Phys. Rev. Lett. **132**, 056501 (2024)

11 Analytic Continuation of Quantum Monte Carlo Data

Erik Koch
Jülich Supercomputing Centre
Forschungszentrum Jülich

Contents

1 Setting the stage **3**
1.1 Analytic continuation . . . 3
1.2 Analytic properties of the integral equations . . . 6
1.3 Preparing the data . . . 8

2 Optimization methods **9**
2.1 Least squares and singular values . . . 9
2.2 Non-negative least-squares . . . 12
2.3 Linear regularization . . . 13
2.4 Maximum entropy . . . 17

3 Average spectrum method **19**
3.1 Blocked modes sampling . . . 20
3.2 Rényi entropies from averaging spectra . . . 21

4 Conclusions **26**

A Technical appendices **28**
A.1 Blocking method for correlated data . . . 28
A.2 Non-negative least-squares algorithm (NNLS) . . . 30
A.3 Shannon entropy . . . 32
A.4 Sampling from a truncated normal distribution . . . 35

E. Pavarini, E. Koch, A. Lichtenstein, and D. Vollhardt (eds.)
Understanding Correlated Materials with DMFT
Modeling and Simulation Vol. 15
Forschungszentrum Jülich, 2025, ISBN 978-3-95806-813-1
http://www.cond-mat.de/events/correl25

The analytic continuation of Monte Carlo data may appear as an exercise in achieving the unachievable. To understand why, let us consider the example of a fermionic finite-temperature Matsubara Green function $G(\tau)$. For imaginary times $\tau \in [0,\beta]$ it is related to the spectral function $\rho(\omega)$ by the integral equation

$$G(\tau) = -\frac{1}{2\pi}\int_{-\infty}^{\infty} \frac{\mathrm{e}^{-\omega\tau}}{1+\mathrm{e}^{-\beta\omega}}\,\rho(\omega)\,d\omega\,.$$

While calculating $G(\tau)$ from $\rho(\omega)$ is a straightforward integral, the inverse problem is hard. This is not because we have to solve a Fredholm equation of the first kind, the difficulty rather arises from the remarkable insensitivity of the imaginary-time data on changes in the spectral function. To illustrate this, we write the spectral function as a sum of delta-peaks $w_i\,\delta(\omega-\varepsilon_i)$, for which the imaginary-time Green function becomes a linear combination of exponentials

$$G(\tau) = -\frac{1}{2\pi}\sum_i w_i\big(1-n_{\mathrm{FD}}(\varepsilon_i)\big)\,\mathrm{e}^{-\varepsilon_i\tau} = -\frac{1}{2\pi}\sum_i w_i\,n_{\mathrm{FD}}(\varepsilon_i)\,\mathrm{e}^{+\varepsilon_i(\beta-\tau)},$$

where we have introduced the Fermi-Dirac distribution $n_{\mathrm{FD}}(\varepsilon) = 1/\big(\mathrm{e}^{+\beta\varepsilon}+1\big)$. While a peak at zero energy simply contributes a constant to $G(\tau)$, the contribution of peaks at large frequencies, $|\varepsilon| \gg 0$, is only noticeable close to $\tau = 0$ or β, while inside the interval $(0,\beta)$ it becomes exponentially small. To reconstruct the spectral function reliably over the entire ω-range, we thus need to know $G(\tau)$ with high accuracy very close to the boundaries of the interval $(0,\beta)$. Numerical simulations can give, however, only a finite number of data points, $G(\tau_j)$. Obviously, this does not provide enough information to reconstruct a continuous spectral function: we expect that there are many different spectral functions $\rho(\omega)$ that reproduce a given set of data points $\{G(\tau_j)\}$. Such a problem without a well-defined solution is called ill posed [1]. If we insist on obtaining a unique result, we need to add constraints, e.g., by including additional information about what kind of solution we consider reasonable. In addition, Monte Carlo data are noisy. When reconstructing the spectral function, we thus need to take the accuracy of the data into account and quantify how reliable the result is, given the noise in the input. Both types of information, the estimate of the reliability of the data and our expectations about a reasonable solution of the inverse problem, can be handled using Bayesian reasoning [2].

In the following we will introduce the analytic properties that allow the continuation of Green and correlation functions. We then describe how to quantify the statistical errors in the numerical data and to set up the inverse problem. In the main part we use this to give an overview of methods to solve the inverse problem. The most straightforward approach simply performs a least-squares fit to the data points. We explain why this approach fails spectacularly. We then discuss the idea of regularization by introducing assumptions about a reasonable solution. This makes the problem well posed, but dependent on prior information. The effect of the prior information included in the regularizer can be quantified using Bayesian techniques. We discuss how they are used to argue for the different flavors of the Maximum Entropy method. Finally we introduce the average spectrum method which tries to avoid introducing prior information by calculating $\rho(\omega)$ as a functional integral over the space of all possible spectral functions.

1 Setting the stage

1.1 Analytic continuation

A system at finite temperature with time-independent Hamiltonian H is described as an ensemble of eigenstates, $H|n\rangle = E_n|n\rangle$, weighted by their Boltzmann factor. The expectation value of an operator A is thus given by

$$\langle A\rangle = \frac{\sum_n e^{-\beta E_n}\langle n|A|n\rangle}{\sum_n e^{-\beta E_n}} = \frac{1}{Z}\operatorname{Tr}\left(e^{-\beta H}A\right). \tag{1}$$

For a canonical ensemble the trace is over the N-electron Hilbert space. For a grand-canonical ensemble we get the same expression when measuring energies relative to the chemical potential, i.e., choosing $\mu = 0$, and taking the trace over the entire Fock space.
Time correlation functions can be calculated using the Heisenberg picture

$$\big\langle A(t_0{+}t)B(t_0)\big\rangle = \frac{1}{Z}\operatorname{Tr} e^{-\beta H}\, e^{\mathrm{i}H(t_0+t)}Ae^{-\mathrm{i}H(t_0+t)}\, e^{\mathrm{i}Ht_0}Be^{-\mathrm{i}Ht_0} = \big\langle A(t)B\big\rangle = \big\langle AB(-t)\big\rangle, \tag{2}$$

where the independence on t_0 follows from the cyclic property of the trace $\operatorname{Tr} ABC = \operatorname{Tr} CAB$. Monte Carlo techniques are ideal to evaluate the high-dimensional sums needed to calculate such traces [3]. But since the time-evolution leads to complex coefficients, Monte Carlo sampling will have to fight with a serious phase-problem. This can be avoided using a Wick rotation, i.e., working in imaginary time. For this we need to analytically continue (2). This is straightforward: simply replace t in the analytic expression by the complex variable $\zeta = t{-}i\tau$ and determine for what values of ζ the result is well defined. This is most easily done using the spectral representation, i.e., evaluating the trace in the basis of eigenfunctions

$$\big\langle A(\zeta)B\big\rangle = \frac{1}{Z}\operatorname{Tr}\mathrm{e}^{(\mathrm{i}\zeta-\beta)H}A\,\mathrm{e}^{-\mathrm{i}\zeta H}B = \frac{1}{Z}\sum_{n,m}\mathrm{e}^{(\mathrm{i}t+\tau-\beta)E_n}\,\mathrm{e}^{-(\mathrm{i}t+\tau)E_m}\langle n|A|m\rangle\langle m|B|n\rangle. \tag{3}$$

For systems with a finite number of states the sum is always analytic, while for systems whose spectrum is not bounded from above, we need $\beta \geq \tau \geq 0$ to maintain absolute convergence. Thus (2) can be analytically continued to a stripe below the real axis $\big\{\zeta \in \mathbb{C}\,\big|{-}\beta \leq \operatorname{Im}\zeta \leq 0\big\}$. We can then use quantum Monte Carlo to sample the function $C_{AB}(\tau) := \big\langle A(-\mathrm{i}\tau)B\big\rangle$ for $\tau \in [0,\beta]$. The analytic continuation back to the real axis is a bit less obvious, since QMC only gives us the function values, i.e., the left hand side of (3) for $t = 0$, but not the explicit functional form on the right hand side, for which we would have to know all eigenenergies and matrix elements. We can, however, define a spectral function that neatly contains all the required information by taking the Fourier transform

$$\int_{-\infty}^{\infty} dt\,\mathrm{e}^{\mathrm{i}\omega t}\big\langle A(t)B\big\rangle = \frac{2\pi}{Z}\sum_{n,m}\mathrm{e}^{-\beta E_n}\langle n|A|m\rangle\langle m|B|n\rangle\,\delta\big(\omega-(E_m{-}E_n)\big) =: \rho_{AB}(\omega) \tag{4}$$

in terms of which we can write (3) for any $\zeta \in [-\beta, 0]$ as

$$\big\langle A(t{-}\mathrm{i}\tau)B\big\rangle = \frac{1}{2\pi}\int_{-\infty}^{\infty} d\omega\,\mathrm{e}^{-(\mathrm{i}t+\tau)\omega}\rho_{AB}(\omega). \tag{5}$$

For the special case $t = 0$ this gives us an integral equation directly relating $\rho_{AB}(\omega)$ to $C_{AB}(\tau)$

$$C_{AB}(\tau) = \big\langle A(-\mathrm{i}\tau)B\big\rangle = \frac{1}{2\pi}\int_{-\infty}^{\infty} d\omega\, \mathrm{e}^{-\omega\tau}\rho_{AB}(\omega)\,, \tag{6}$$

which is, however, not suited for practical calculations since the integral kernel, $\exp(-\omega\tau)$, diverges for $\omega \to -\infty$. We can get around this problem by modifying the kernel, dividing it by a function that makes it finite, and correspondingly multiplying the spectral function to leave the integral unchanged

$$C(\tau) = \frac{1}{2\pi}\int_{-\infty}^{\infty} d\omega\, \frac{\mathrm{e}^{-\omega\tau}}{\mu(\omega)}\, \underbrace{\mu(\omega)\rho_{AB}(\omega)}_{=:\tilde\rho(\omega)}\,. \tag{7}$$

A suitable kernel modification would be $\mu(\omega) = 1 \pm \mathrm{e}^{-\beta\omega}$, which makes the kernel finite for $\omega \to -\infty$ as long as $\tau \leq \beta$, while keeping it finite for $\omega \to +\infty$. To analytically continue $C_{AB}(\tau) = \big\langle A(-\mathrm{i}\tau)B\big\rangle$ to the real axis we then solve the integral equation (with finite kernel)

$$C_{AB}(\tau) = \frac{1}{2\pi}\int_{-\infty}^{\infty} d\omega\, \frac{\mathrm{e}^{-\omega\tau}}{1 \pm \mathrm{e}^{-\beta\omega}}\, \tilde\rho^{\pm}_{AB}(\omega) \tag{8}$$

for $\tilde\rho^{\pm}_{AB}(\omega)$ and use $\rho_{AB}(\omega) = \tilde\rho^{\pm}_{AB}(\omega)/(1 \pm \mathrm{e}^{-\beta\omega})$ in (5) to calculate the analytical continuation on the real axis. For the plus sign $1/(1{\pm}\mathrm{e}^{-\beta\omega})$ is related to the Fermi-Dirac function $n_{\mathrm{FD}}(-\omega) = 1{-}n_{\mathrm{FD}}(\omega)$, while for minus to the Bose-Einstein function $-n_{\mathrm{BE}}(-\omega) = n_{\mathrm{BE}}(\omega){-}1$.
In fact, $\tilde\rho^{\pm}_{AB}(\omega)$ is a spectral function in its own right: Reordering the spectral representation (4), we can write it as

$$\begin{aligned}
\tilde\rho^{\pm}_{AB}(\omega) &= \rho_{AB}(\omega) \pm \rho_{AB}(\omega)\,\mathrm{e}^{-\beta\omega} \\
&= \rho_{AB}(\omega) \pm \frac{2\pi}{Z}\sum_{n,m} \mathrm{e}^{-\beta E_n}\langle n|A|m\rangle\langle m|B|n\rangle\, \delta\big(\omega - (E_m{-}E_n)\big)\, \mathrm{e}^{-\beta(E_m-E_n)} \\
&= \rho_{AB}(\omega) \pm \rho_{BA}(-\omega)\,.
\end{aligned} \tag{9}$$

Comparing with (3) and (4) we see that $\tilde\rho^{\pm}_{AB}(\omega)$ is the spectral function of

$$\mathrm{i}G^{\pm}_{AB}(t) := \big\langle A(t)B\big\rangle \pm \big\langle B(-t)A\big\rangle = \big\langle A(t)B\big\rangle \pm \big\langle BA(t)\big\rangle = \big\langle [A(t),\, B]_{\pm}\big\rangle, \tag{10}$$

which, for $t > 0$, is the retarded correlation function $G^{R\pm}_{AB}(t) = \Theta(t)\, G^{\pm}_{AB}(t)$, with Θ the step function, $\Theta(t{>}0) = 1$ and $\Theta(t{<}0) = 0$. As discussed above, the first term can be analytically continued to $\big\{\zeta \in \mathbb{C}\,\big|{-}\beta \leq \operatorname{Im}\zeta \leq 0\big\}$, while the second term can be continued to the stripe of width β above the real axis. It is thus natural to define the Matsubara function

$$-\,G^{M\pm}_{AB}(\tau) := \big\langle \mathcal{T}^{\pm}_{\tau}\, A(-\mathrm{i}\tau)B(0)\big\rangle \tag{11}$$

with the imaginary-time ordering $\mathcal{T}^{\pm}_{\tau}\, A(-\mathrm{i}\tau)B(0) = \Theta(\tau)A(-\mathrm{i}\tau)B(0) \mp \Theta(-\tau)B(0)A(-\mathrm{i}\tau)$ taking care of selecting the appropriate analytic term for the given τ. This introduces a discontinuity at $\tau = 0$

$$-\,G^{M\pm}_{AB}(0^+) + G^{M\pm}_{AB}(0^-) = \big\langle A(0)B\big\rangle \pm \big\langle BA(0)\big\rangle = \big\langle [A,\, B]_{\pm}\big\rangle. \tag{12}$$

From the cyclic property of the trace in (3), it follows that the Matsubara functions for positive and negative τ are related (anti)symmetrically, i.e. for $\tau \in (0, \beta)$

$$G^{M\pm}_{AB}(\beta-\tau) = -\big\langle A(-\mathrm{i}(\beta-\tau))B\big\rangle = -\big\langle B(-\mathrm{i}\tau)A\big\rangle = -\big\langle BA(\,\mathrm{i}\tau)\big\rangle = \mp G^{M\pm}_{AB}(-\tau). \quad (13)$$

For $\tau \in (0, \beta]$ we obviously have (remember the sign introduced in (11)) $G^{M\pm}_{AB}(\tau) = -C_{AB}(\tau)$, so that from (8) we obtain

$$G^{M\pm}_{AB}(\tau) = -\frac{1}{2\pi}\int_{-\infty}^{\infty} d\omega\, \frac{\mathrm{e}^{-\omega\tau}}{1 \pm \mathrm{e}^{-\beta\omega}}\, \tilde{\rho}^{\pm}_{AB}(\omega) \quad \text{for } \tau \in (0, \beta]. \quad (14)$$

It is convenient to choose the sign in the kernel modification to obtain a simple relation for the sum rule, which directly follows from the spectral representation, using $\sum_n |n\rangle\langle n| = \mathbb{1}$

$$\frac{1}{2\pi}\int_{-\infty}^{\infty} d\omega\, \tilde{\rho}^{\pm}_{AB}(\omega) = \big\langle [A,\, B]_{\pm}\big\rangle\,. \quad (15)$$

For observables and bosonic operators we thus choose the commutator, while for fermionic Green functions it is more convenient to choose the anticommutator.
For the special case $B = A^\dagger$ we find

$$\tilde{\rho}^{\pm}_{AA^\dagger}(\omega) = \frac{2\pi}{Z}\sum_{n,m}\big(\mathrm{e}^{-\beta E_n} \pm \mathrm{e}^{-\beta E_m}\big)\,\big|\langle n|A|m\rangle\big|^2\,\delta\big(\omega - (E_m - E_n)\big), \quad (16)$$

which is obviously non-negative for the fermionic case, for the bosonic sign choice it is non-negative for $\omega = (E_m - E_n) > 0$, non-positive for $\omega < 0$, and vanishes at least linearly at $\omega = 0$. We can thus define a non-negative function $\tilde{\rho}^{-}_{AB}(\omega)/\omega$ which is regular at $\omega = 0$

$$\lim_{\omega\to 0}\frac{\tilde{\rho}^{-}_{AB}(\omega)}{\omega} = \frac{2\pi\beta}{Z}\sum_{n,m}\mathrm{e}^{-\beta E_n}\,\big|\langle n|A|m\rangle\big|^2\,\delta(E_n - E_m) \quad (17)$$

so that we can rewrite (14) with non-negative functions as

$$G^{M+}_{AA^\dagger}(\tau) = -\frac{1}{2\pi}\int_{-\infty}^{\infty} d\omega\, \frac{\mathrm{e}^{-\omega\tau}}{1 + \mathrm{e}^{-\beta\omega}}\, \tilde{\rho}^{+}_{AA^\dagger}(\omega) \quad (18)$$

$$G^{M-}_{AA^\dagger}(\tau) = -\frac{1}{2\pi}\int_{-\infty}^{\infty} d\omega\, \frac{\omega\,\mathrm{e}^{-\omega\tau}}{1 - \mathrm{e}^{-\beta\omega}}\, \frac{\tilde{\rho}^{-}_{AA^\dagger}(\omega)}{\omega}\,, \quad (19)$$

which, when A is an annihilator, applies to the diagonal elements of Green functions.
When A is an observable ($A^\dagger = A$), we see from (9) that $\tilde{\rho}^{-}_{AA}(\omega) = -\tilde{\rho}^{-}_{AA}(-\omega)$, so that we can restrict the integral to $\omega > 0$

$$G^{M-}_{AA}(\tau) = -\frac{1}{2\pi}\int_{0}^{\infty} d\omega\, \frac{\omega\big(\mathrm{e}^{-\omega\tau} + \mathrm{e}^{-\omega(\beta-\tau)}\big)}{1 - \mathrm{e}^{-\beta\omega}}\, \frac{\tilde{\rho}^{-}_{AA}(\omega)}{\omega} \quad \text{when } A \text{ hermitian.} \quad (20)$$

We could actually cancel the factor ω in the integrand since $\tilde{\rho}^{-}_{AA}(\omega \geq 0)$ is non-negative by itself, but when calculating susceptibilities it is common to keep it, since it shows the behavior for $\omega \to 0$, (17), more clearly.

1.2 Analytic properties of the integral equations

We can gain some insight into the integral equations (18) and (19) by realizing that they are intimately related to the Euler and Bernoulli polynomials [4]. Introducing the reduced variables $x = \beta\omega$ and $y = \tau/\beta \in [0,1]$ and the functions $f(x) = \tilde{\rho}^{\pm}(x/\beta)/\beta$ (scaled to conserve the sum rule) and $g(y) = G^{M\pm}(\beta y)$ we obtain, for the fermionic case

$$g(y) = -\frac{1}{2\pi}\int_{-\infty}^{\infty} dx\, \frac{\mathrm{e}^{-xy}}{1+\mathrm{e}^{-x}}\, f(x)\,, \tag{21}$$

from which we see that, for fixed kernel, the spectral function is spread out over an ever wider range as we go to lower temperatures. The scaled kernel of this equation is essentially the generating function of the Euler polynomials $E_n(s)$ on $s \in [0,1]$, which are defined by

$$\frac{2\mathrm{e}^{st}}{\mathrm{e}^{t}+1} = \sum_{n=0}^{\infty} E_n(s)\,\frac{t^n}{n!}\,. \tag{22}$$

With $s = \tau/\beta$ and $t = -\beta\omega$ we find from (18)

$$G^{M+}(\tau) = -\frac{1}{4\pi}\sum_{n=0}^{\infty} E_n(\tau/\beta)\;\frac{(-\beta)^n}{n!}\int_{-\infty}^{\infty} d\omega\,\omega^n\,\tilde{\rho}^{+}(\omega) \tag{23}$$

that the fermionic Matsubara function is a linear combination of Euler polynomials, where the expansion coefficients of $E_n(\tau/\beta)$ is proportional to the n-th moment of the spectral function. Since the Euler polynomials are not orthogonal, to determine the moments of $\tilde{\rho}$ from $G^{M+}(\tau)$, we first have to find the dual functions $E^n(s)$ with $\int_0^1 ds\, E^n(s)\, E_m(s) = \delta_{n,m}$. Integrating them with the generating function (22) we obtain

$$\int_0^1 ds\, E^n(s)\,\mathrm{e}^{st} = \frac{t^n}{n!}\,\frac{e^t+1}{2}\,, \tag{24}$$

which is solved by

$$E^n(s) = \frac{(-1)^n}{2\,n!}\Big(\delta^{(n)}(s{-}1) + \delta^{(n)}(s)\Big)\,, \tag{25}$$

where $\delta^{(n)}(s{-}a)$ is the n-th derivative of the delta function at $s = a$ (to make the evaluation for $a = 0$ and 1 unique, we consider the limit from inside the interval of integration). Integration by parts then produces $(-1)^n$ times the n-th derivative of the rest of the integrand at a. Using this in (23) and rewriting the Matsubara function at β as that at 0^-, eq. (13), we find that the discontinuity in the n-th derivative of the Matsubara function is proportional to the n-th moment of the spectral function

$$\frac{d^n G^{M+}(\beta)}{d\,\tau^n} + \frac{d^n G^{M+}(0)}{d\,\tau^n} = \frac{d^n G^{M+}(0^+)}{d\,\tau^n} - \frac{d^n G^{M+}(0^-)}{d\,\tau^n} = -\frac{(-1)^n}{2\pi}\int_{-\infty}^{\infty} d\omega\;\omega^n\,\tilde{\rho}^{+}(\omega)\,. \tag{26}$$

The higher moments contain the information about the spectral function at large frequencies. Extracting the derivatives from Monte Carlo data for $G(\tau)$ is difficult. Instead, they can be sampled directly: For $\tau > 0$ we have, (11),

$$-\,G^{M+}(\tau) = \big\langle A(-\mathrm{i}\tau)B\big\rangle = \frac{1}{Z}\,\mathrm{Tr}\,\mathrm{e}^{-\beta H}\mathrm{e}^{\tau H}A\mathrm{e}^{-\tau H}B\,. \tag{27}$$

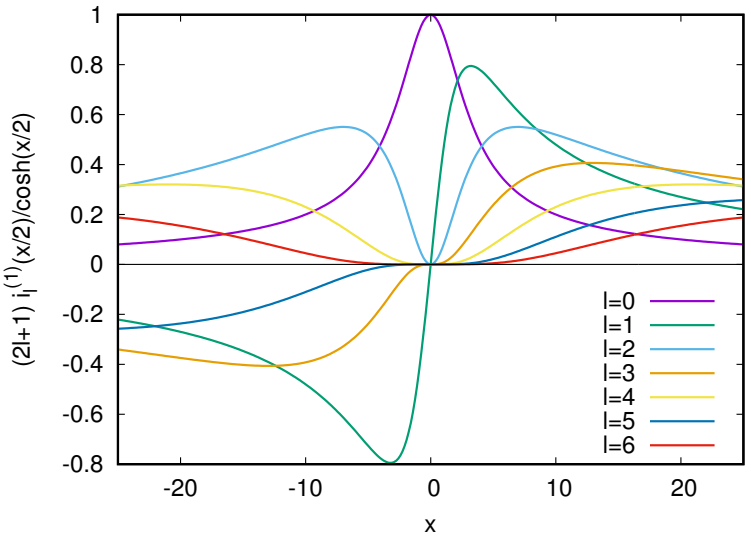


Fig. 1: *Dependence of the scaled Legendre kernel* $(2l{+}1)\, i_l^{(1)}(x/2)/\cosh(x/2)$ *on the order* l*. For* $l = 0$*,* G_l *contains information about the spectral function close to the Fermi level, while for increasing* l *it probes ever larger frequencies. As the Legendre polynomials themselves, the kernel is even/odd for even/odd* l*.*

Taking the derivative with respect to τ brings down the Hamiltonian to the left and the right of A, producing $\langle [H,\, A(-\mathrm{i}\tau)]\, B\rangle$. Repeated derivatives produce repeated commutators defined by $[H;\, A]_n := \big[H,\, [H;\, A]_{n-1}\big]$ and $[H;\, A]_0 := A$ as in the Baker-Campbell-Hausdorff formula. The moments can then be determined directly by sampling the expectation values

$$\Big\langle \big[[H;\, A]_n,\, B\big] \Big\rangle = -\frac{(-1)^n}{2\pi} \int_{-\infty}^{\infty} d\omega\; \omega^n\, \tilde{\rho}^+(\omega) = (-1)^n \Big\langle \big[A, [H;\, B]_n\big] \Big\rangle \,. \tag{28}$$

Working with the Euler polynomials can become cumbersome due to their lack of orthogonality. This inconvenience can be overcome by expressing them in terms of orthogonal polynomials, e.g., shifted Legendre polynomials $P_l(2y-1)$. When the Matsubara function is expanded as [5]

$$G^{M+}(\tau) = \sum_{l=0}^{\infty} \frac{\sqrt{2l{+}1}}{\beta}\, G_l\, P_l(2\tau/\beta - 1) \quad \text{with} \quad G_l = \sqrt{2l{+}1} \int_0^{\beta} d\tau\, P_l(2\tau/\beta - 1)\, G^{M+}(\tau)$$

the expansion coefficients are related to the spectral function via (18) by

$$G_l = (-1)^{l+1} \sqrt{2l{+}1}\, \frac{\beta}{4\pi} \int_{-\infty}^{\infty} d\omega\, \frac{\mathrm{i}_l^{(1)}(\beta\omega/2)}{\cosh(\beta\omega/2)}\, \tilde{\rho}(\omega)\,, \tag{29}$$

where $\mathrm{i}_l^{(1)}(x)$ are the modified spherical Bessel functions of first kind. As shown in Fig. 1, for increasing l the integral kernel probes spectral features at higher and higher frequencies. From the derivatives of the recursion relation $(2l{+}1)P_l(x) = P'_{l+1}(x) - P'_{l-1}(x)$ and (26) we find that the n-th moment of the spectral function is given by a sum over all even or odd Legendre coefficients, starting at $l = n$

$$(-1)^{n+1}\, \frac{2}{n!} \sum_{k=0}^{\infty} \frac{\sqrt{4k+2n+1}}{\beta^{2k+n+1}}\, \frac{\big(2(k{+}n)\big)!}{\big(2(k{-}n)\big)!}\, G_{2k+n} = \frac{1}{2\pi} \int_{-\infty}^{\infty} d\omega\; \omega^n\, \tilde{\rho}^+(\omega)\,. \tag{30}$$

For bosonic Matsubara functions we can obtain similar results using the Bernoulli polynomials $B_n(s)$ whose generating function is directly related to the bosonic kernel.

1.3 Preparing the data

Certainly the most important aspect of preparing Monte Carlo data for analytic continuation is the decision what data to sample. As we have seen, the information about spectral features further away from the chemical potential is concentrated in the Matsubara function close to $\tau = 0$ and β. Reconstructing the spectral function from data given on a uniform τ-grid, we can therefore only expect to get reasonable results close to the chemical potential. Using, on the other hand, the derivatives of the Matsubara function at $\tau = 0$ and β gives us the moments of the spectral function, which, as we know, e.g., form the Lanczos method [6], accurately characterize the spectral function over the entire frequency range using just a few tens of the lowest moments.

The second concern is to properly characterize the statistical errors in the Monte Carlo data. Considering the integral equation

$$g(y) = \int K(y,x)\, f(x)\, dx\,, \tag{31}$$

the actual numerical data is not given as the function $g(y)$ but as vectors of M discrete data points $\boldsymbol{g} = (g_1, \dots, g_M)^\dagger$ representing $g(y)$. The mean over K independent samples is then

$$\bar{\boldsymbol{g}} = \frac{1}{K} \sum_{k=1}^{K} \boldsymbol{g}_k \tag{32}$$

with its statistical uncertainty being characterized by the $M \times M$ covariance matrix

$$\boldsymbol{C} = \frac{1}{K(K-1)} \sum_{k=1}^{K} \big(\boldsymbol{g}_k - \bar{\boldsymbol{g}}\big)\big(\boldsymbol{g}_k - \bar{\boldsymbol{g}}\big)^\dagger. \tag{33}$$

By the central limit theorem the probability density of measuring $\bar{\boldsymbol{g}}$ given the covariance matrix $\boldsymbol{C}$ and the exact result $\boldsymbol{g}_{\text{exact}}$ is then

$$p(\bar{\boldsymbol{g}}|\, \boldsymbol{g}_{\text{exact}}, \boldsymbol{C}) = \frac{1}{(2\pi)^{M/2} \det \boldsymbol{C}} \mathrm{e}^{-(\bar{\boldsymbol{g}}-\boldsymbol{g}_{\text{exact}})^\dagger \boldsymbol{C}^{-1} (\bar{\boldsymbol{g}}-\boldsymbol{g}_{\text{exact}})/2}. \tag{34}$$

This probability will play a central role in the reconstruction of the spectral function representing $\boldsymbol{g}_{\text{exact}}$. It is, therefore, crucial to have an accurate estimate of $\boldsymbol{C}$. Rewriting it as

$$\boldsymbol{C} = \frac{1}{K(K-1)} \sum_k (\boldsymbol{g}_k - \bar{\boldsymbol{g}})(\boldsymbol{g}_k - \bar{\boldsymbol{g}})^\dagger = \frac{1}{K(K-1)} \sum_k \boldsymbol{g}_k\, \boldsymbol{g}_k^\dagger - \frac{1}{K-1}\, \bar{\boldsymbol{g}}\, \bar{\boldsymbol{g}}^\dagger$$

and realizing that $\boldsymbol{g}\, \boldsymbol{g}^\dagger$ is the (scaled) projector onto $\boldsymbol{g}$, we see that the covariance matrix is a linear combination of K projectors to one-dimensional subspaces. We therefore need $K > M$ independent samples $\boldsymbol{g}_k$ in (33) to have a chance of obtaining a non-singular covariance matrix. Thus, reducing the discretization error requires taking more samples. The easiest way for obtaining independent samples are independent Monte Carlo runs, e.g., on a parallel computer. If we do not have enough CPUs available, we need to construct independent samples from a sequential run. This can be done, e.g., using the blocking technique described in appendix, A.1.

For the numerical solution of the integral equation (31) we also have to discretize $f(x)$ into a vector $\boldsymbol{f} = (f_1, \ldots, f_N)^\dagger$, e.g., by representing it as a piecewise constant function of value f_n on interval n. The integral equation then becomes a simple linear equation $\boldsymbol{g} = \boldsymbol{K}\boldsymbol{f}$, where the kernel matrix is obtained, e.g., from the Riemann sum [7]

$$g(y_m) = \sum_n K(y_m, x_n)\, w_n\, f(x_n)\,, \tag{35}$$

with w_n the width of interval n or, when the functions are expanded in an orthonormal set of functions $|\psi_m\rangle$ like in the Legendre expansion of the Green function, it is given by

$$g_m = \sum_n \int dy \int dx\, \overline{\psi_m(y)}\, K(y,x)\, \varphi_n(x)\; f_n = \sum_n \langle \psi_m | K | \varphi_n \rangle\, f_n\,. \tag{36}$$

Assuming $\boldsymbol{f}$ is the exact model, i.e., it gives the exact data, $\boldsymbol{K}\boldsymbol{f} = \boldsymbol{g}_{\text{exact}}$, it follows from (34)

$$p(\bar{\boldsymbol{g}}|\, \boldsymbol{f}, \boldsymbol{C}) \propto e^{-(\bar{\boldsymbol{g}}-\boldsymbol{K}\boldsymbol{f})^\dagger \boldsymbol{C}^{-1} (\bar{\boldsymbol{g}}-\boldsymbol{K}\boldsymbol{f})/2} =: e^{-\chi^2(\boldsymbol{f})/2}. \tag{37}$$

Factorizing the inverse covariance matrix, $\boldsymbol{C}^{-1} = \boldsymbol{T}^\dagger \boldsymbol{T}$, e.g., by Cholesky decomposition, we can absorb the explicit dependence on $\boldsymbol{C}$ by introducing $\tilde{\boldsymbol{g}} := \boldsymbol{T}\bar{\boldsymbol{g}}$ and $\tilde{\boldsymbol{K}} := \boldsymbol{T}\boldsymbol{K}$

$$\big(\bar{\boldsymbol{g}}-\boldsymbol{K}\boldsymbol{f}\big)^\dagger \boldsymbol{C}^{-1} \big(\bar{\boldsymbol{g}}-\boldsymbol{K}\boldsymbol{f}\big) = \big(\tilde{\boldsymbol{g}}-\tilde{\boldsymbol{T}}\boldsymbol{f}\big)^\dagger \big(\tilde{\boldsymbol{g}}-\tilde{\boldsymbol{T}}\boldsymbol{f}\big) = \big\|\tilde{\boldsymbol{g}}-\tilde{\boldsymbol{T}}\boldsymbol{f}\big\|^2. \tag{38}$$

The covariance of the transformed data $\tilde{\boldsymbol{g}}$ is then the unit matrix, i.e. the transformation produces uncorrelated data points $\tilde{g}_n$ that all have the same (unit) errorbar.

2 Optimization methods

After discretization of model $\boldsymbol{f}$ and data $\boldsymbol{g}$ and transformation to $\tilde{\boldsymbol{g}}$, analytic continuation is reduced to solving the linear system

$$\tilde{\boldsymbol{g}} = \tilde{\boldsymbol{K}}\boldsymbol{f}\,. \tag{39}$$

Nothing could be easier than that! When the number of data points M we are given equals the number of points N at which we want to know the model, the solution is unique, $\boldsymbol{f} = \tilde{\boldsymbol{K}}^{-1}\tilde{\boldsymbol{g}}$, as long as the kernel is not singular. When $M > N$ the model is overdetermined so that in general there will be no solution. Normally, however, we want to know the model at many more positions than we are given data points, $M < N$ so that the solution is underdetermined. A natural choice is then the $\boldsymbol{f}$ that gives the best fit to the data.

2.1 Least squares and singular values

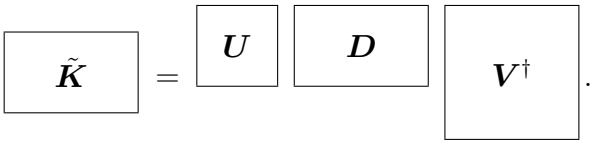
When we ask for a best-fit, we first have to define what we mean by that. Least-squares methods define "best" in terms of the Euclidean norm: minimize $\chi^2(\boldsymbol{f}) := \|\tilde{\boldsymbol{g}} - \tilde{\boldsymbol{T}}\boldsymbol{f}\|^2$. We can justify this choice using Bayesian reasoning: As we have noted in (37), the probability of measuring $\tilde{\boldsymbol{g}}$ when the true model is $\boldsymbol{f}$ is given by $p(\tilde{\boldsymbol{g}}|\, \boldsymbol{f}) = (2\pi)^{-M/2} \exp(-\chi^2(\boldsymbol{f})/2)$. We can invert

this relation using Bayes' theorem [2], $p(B|\,A)\,p(A) = p(A,B) = p(A|\,B)\,p(B)$, stating that the probability of outcome A and B can be written as the probability of B given A times the probability of A, or, equivalently, as the probability of A given B times that of B. For the relation between model and data this implies

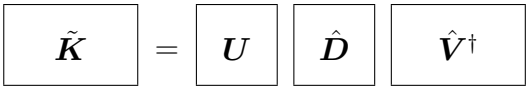
$$p(\boldsymbol{f}|\,\tilde{\boldsymbol{g}}) = \frac{p(\tilde{\boldsymbol{g}}|\,\boldsymbol{f})\,p(\boldsymbol{f})}{p(\tilde{\boldsymbol{g}})}\,. \tag{40}$$

The most probable model $\boldsymbol{f}$ given $\tilde{\boldsymbol{g}}$ thus maximizes $p(\tilde{\boldsymbol{g}}|\,\boldsymbol{f})\,p(\boldsymbol{f})$. In the absence of any further information about possible models it is reasonable to assume that $p(\boldsymbol{f})$ is the same for all $\boldsymbol{f}$, i.e., to use an "uninformative prior". A model that maximizes $p(\boldsymbol{f}|\,\tilde{\boldsymbol{g}})$ is then one that maximizes $\exp\big(-\chi^2(\boldsymbol{f})/2\big)$. It is called a "maximum likelihood estimator" and gives the best fit in the least-squares sense. Since the rank of the kernel matrix, $\operatorname{rank}\boldsymbol{K} \leq \min(N,M)$, for $M < N$ the least-squares solution will not be unique: We can add any vector that is mapped by $\boldsymbol{K}$ into zero, without changing the fit. The least-squares problem is thus ill-posed. The usual way of making the solution unique is to ask in addition that $\boldsymbol{f}_{\mathrm{LS}}$ has vanishing overlap with any vector that is mapped to zero, i.e., $\boldsymbol{f}_{\mathrm{LS}}$ is orthogonal to the null space of $\tilde{\boldsymbol{K}}$.

A convenient tool for the theoretical analysis of least-squares problems is the singular value decomposition (SVD) of the matrix $\tilde{\boldsymbol{K}} = \boldsymbol{U}\boldsymbol{D}\boldsymbol{V}^\dagger$, where $\boldsymbol{U}$ is a unitary $M\times M$ matrix whose column vectors $|\boldsymbol{u}_m\rangle$ define an orthonormal basis in data space and $\boldsymbol{V}$ likewise is a unitary $N\times N$ matrix with columns $|\boldsymbol{v}_n\rangle$ spanning the space of models, while $\boldsymbol{D}$ is a diagonal $M\times N$ matrix with diagonal elements $d_1 \geq d_2 \geq \ldots \geq d_{\min(N,M)} \geq 0$. For the underdetermined case, $M < N$, the singular value decomposition can be pictured as



For the least-squares solution it is convenient to define the reduced singular value decomposition, where the null space of $\tilde{\boldsymbol{K}}$ is dropped in $\boldsymbol{V}$, pictorially,



The singular value decomposition provides a spectral representation of the kernel

$$\tilde{\boldsymbol{K}} = \sum_{i=1}^{\min(M,N)} |\boldsymbol{u}_i\rangle\, d_i\, \langle \boldsymbol{v}_i| \tag{41}$$

which allows us to write the residue vector for $M < N$ as

$$|\tilde{\boldsymbol{g}}\rangle - \tilde{\boldsymbol{K}}|\boldsymbol{f}\rangle = |\tilde{\boldsymbol{g}}\rangle - \sum_i |\boldsymbol{u}_i\rangle\, d_i\, \langle \boldsymbol{v}_i|\boldsymbol{f}\rangle = \sum_i |\boldsymbol{u}_i\rangle \Big(\langle \boldsymbol{u}_i|\tilde{\boldsymbol{g}}\rangle - d_i \langle \boldsymbol{v}_i|\boldsymbol{f}\rangle \Big) \tag{42}$$

so that the least-squares solution (for which the residue vanishes when $d_M > 0$) is

$$|\boldsymbol{f}_{\mathrm{LS}}\rangle = \sum_i \frac{\langle u_i|\tilde{\boldsymbol{g}}\rangle}{d_i}\, |\boldsymbol{v}_i\rangle \quad \text{or, equivalently,} \quad \boldsymbol{f}_{\mathrm{LS}} = \hat{\boldsymbol{V}}\hat{\boldsymbol{D}}^{-1}\boldsymbol{U}^\dagger\tilde{\boldsymbol{g}}\,. \tag{43}$$

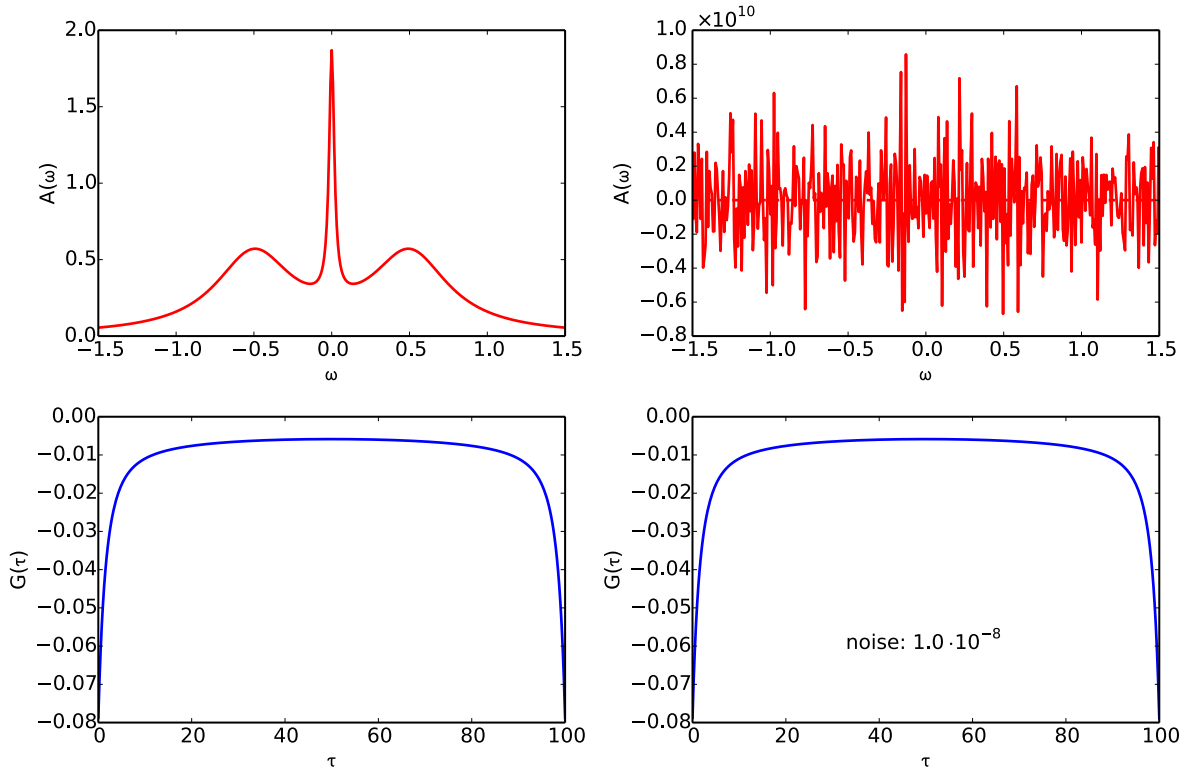


Fig. 2: *Least-squares solution for the analytical continuation of a fermionic imaginary-time Green function. The exact data (bottom left) is constructed from a simple model spectral function consisting of three Lorenz peaks (top left). We add noise of amplitude* 10^{-8} *to the data (bottom right). The least-squares solution given the noisy data is shown in the top right panel. It varies over ten orders of magnitude showing no resemblance at all to the original model.*

As simple and elegantly the least-squares solution can be constructed, as useless it is for the analytic continuation problem. This is illustrated in Fig. 2, showing that $\boldsymbol{f}_{\mathrm{LS}}$, despite giving a perfect fit to the data and, in particular, fulfilling the sum rule for $\sum_n f_n$, is completely dominated by numerical noise. What is the reason for this catastrophic failure? Making the noise in the data explicit, $\tilde{\boldsymbol{g}} = \tilde{\boldsymbol{g}}_{\mathrm{exact}} + \Delta\tilde{\boldsymbol{g}}$ we see that

$$|\boldsymbol{f}_{\mathrm{LS}}\rangle = |\boldsymbol{f}_{\mathrm{exact}}\rangle + \sum \frac{\langle \boldsymbol{u}_i | \Delta\tilde{\boldsymbol{g}}\rangle}{d_i} \, |\boldsymbol{v}_i\rangle \, . \tag{44}$$

When the kernel has close to vanishing singular values, the noise component is divided by a number close to numerical accuracy. This is, in fact, what we are seeing in Fig. 2: dividing noise of order 10^{-8} by the numerical epsilon of double precision numbers (of order 10^{-16}), we would expect the least-squares solution to vary over about eight orders of magnitude. We can verify this picture more quantitatively by looking at the singular values of the kernel matrix, shown in Fig. 3. The exponential decay of the singular values seen in this example actually is the hallmark of an ill-conditioned problem. It is a consequence of the orthogonality of the modes $|\boldsymbol{v}_i\rangle$: With increasing i they develop more and more nodes. Integrating over these oscillating modes with the positive fermionic Green function kernel means that the integral will decrease with the number of nodes. Once the singular value reaches machine precision, the singular modes become numerically degenerate. These modes contribute negligibly to the fit of the data, but cause the catastrophic numerical instability of the least-squares result.

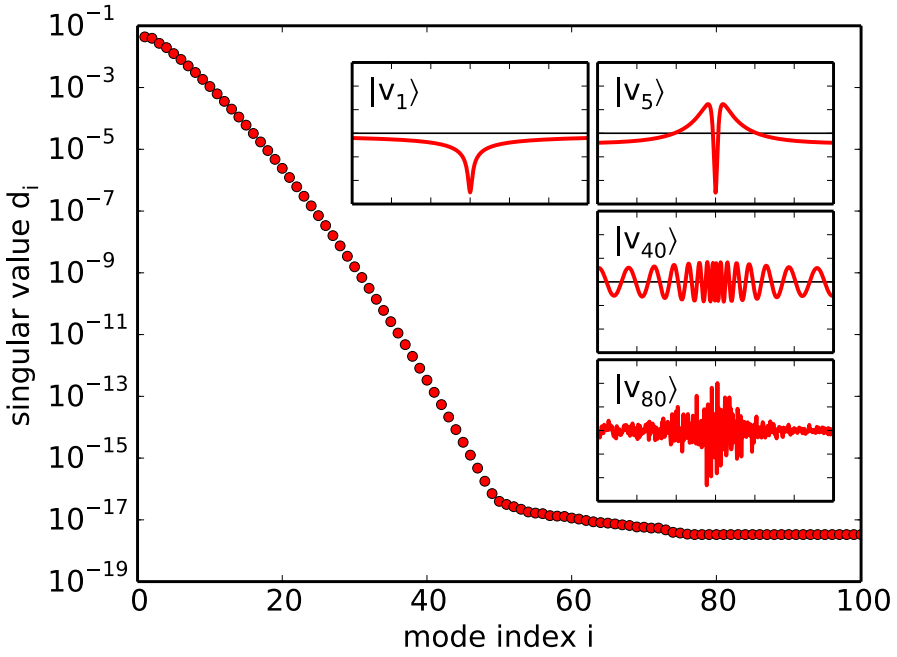


Fig. 3: *Singular values of the kernel matrix used in Fig. 2 on a logarithmic scale. The singular values decay exponentially until leveling off at a value determined by the numerical accuracy of the calculation. The insets show some of the singular modes $|\boldsymbol{v}_i\rangle$. With increasing mode index i, i.e., decreasing singular value, they have an increasing number of nodes. Once the singular value reaches the numerical accuracy, the singular modes become numerically degenerate so that the SVD routine returns arbitrary linear combinations as exemplified here for $|\boldsymbol{v}_{80}\rangle$.*

2.2 Non-negative least-squares

When motivating the least-squares approach using Bayesian reasoning, (40), one assumption was that we have no knowledge whatsoever about the possible models. When we are interested, e.g., in a diagonal spectral function, this is not quite true: We actually do know that $\boldsymbol{f}$ cannot be negative, cf. (18). To incorporate this information, the prior probability $p(\boldsymbol{f})$ should, in fact, vanish when $\boldsymbol{f}$ has a component $f_n < 0$. In other words, we really should maximize the likelihood over non-negative models only: $\max_{\boldsymbol{f}\geq 0} \exp(-\chi^2(\boldsymbol{f}))$. This approach is called non-negative least squares fitting (NNLS). A practical algorithm is discussed in A.2. It will, in general, not give a perfect fit, $\chi^2(\boldsymbol{f}_{\text{NNLS}}) > 0$, but what is not fitted is the part of the data that is incompatible with a non-negative model, i.e., pure noise.

As shown in Fig. 4, using non-negative least squares gives a dramatic improvement over the least-squares solution. Just incorporating the information about the non-negativity of the model reduces the oscillations in the result by nine orders of magnitude, bringing it into a reasonable range. This is because the amplitude of oscillating modes is now strongly limited by non-negativity. In fact, the constraints give the modes with small singular value or in the null space an important role: All modes except the first have nodes, so they can often not be included in the solution with their optimal value (43) without violating the constraint. Since the contribution of the modes with tiny singular value to the fit is tiny, they are free to arrange such that the modes with larger d_i can move closer to their optimum. Thus in NNLS the behavior of all modes is coupled, making the fit much more robust. Moreover, the non-negativity constraint makes the

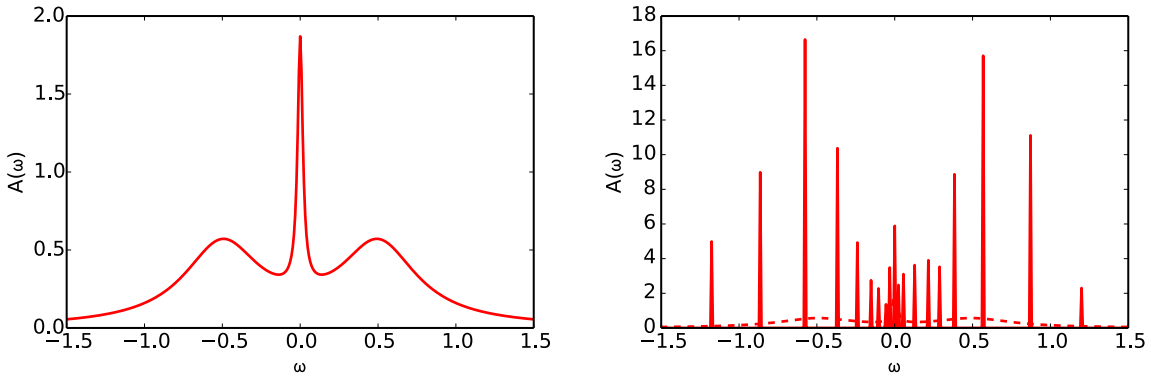


Fig. 4: *Non-negative least-squares solution of the same problem as in Fig. 2. Using our knowledge about the non-negativity of the spectral function gives a dramatic improvement, bringing the solution form a scale of the order of* $\pm 10^{10}$ *to a positive function with peaks of the order of* 10^2 *so that the original model shown on the left can actually also be seen in the plot on the right (dashed line). While the NNLS solution does show some resemblance to the original function it is far to spiky, even in the present case of exceedingly small noise (*$\sim 10^{-8}$*) in the data.*

problem well posed, i.e., giving a unique solution. Still, the spiky NNLS solutions indicate that we are still overfitting the noise in the data and this problem becomes stronger when considering data with noise levels larger than the $\sim 10^{-8}$ used for the example.

While the least-squares approaches do take information about the covariance of the data into account, via the modification of the kernel from $\boldsymbol{K}$ to $\tilde{\boldsymbol{K}}$, so that the data points that are given with higher accuracy have more weight, the results are completely independent of the absolute scale of $\boldsymbol{C}$: Multiplying it by a scalar σ^2 simply rescales all singular values of $\tilde{\boldsymbol{K}}$ by $1/\sigma$, which is compensated by the same rescaling of $\tilde{\boldsymbol{g}}$, leaving the solution unchanged. Thus the least-squares type solutions completely neglect the information about the overall noise in the data. This problem can be addressed when we include our intuition that the "true" solution should show some degree of smoothness. We then have to introduce a measure of smoothness, which puts an absolute scale in the fitting problem. This is the idea behind regularization approaches.

2.3 Linear regularization

To understand the failure of the least-squares methods better, we expand the noisy data and the fit in their respective singular modes $|\boldsymbol{u}_m\rangle$ and $|\boldsymbol{v}_n\rangle$. For the example of Fig. 2 this is shown in Fig. 5. It reveals that, initially, the expansion parameters of $\boldsymbol{g}$ decrease somewhat faster with the mode index i than the singular values. Consequently the expansion of the least-squares solution also decrease with i. But once the $\langle \boldsymbol{u}_i|\boldsymbol{g}\rangle$ reach the level of the noise in the data, here $\sigma = 10^{-8}$, at $i \approx 30$, the expansion coefficients of the data remain constant while the singular values decrease further, leading to exponentially increasing contributions of the highly oscillating modes with large i that render the least-squares solution useless. The situation is quite similar for the non-negative least squares solution. The main difference being that the contributions of the modes with small or vanishing singular value are bounded $|\langle \boldsymbol{v}_n|\boldsymbol{f}_{\mathrm{NNLS}}\rangle| \lesssim 1$ by the non-negativity combined with the sum-rule for the model.

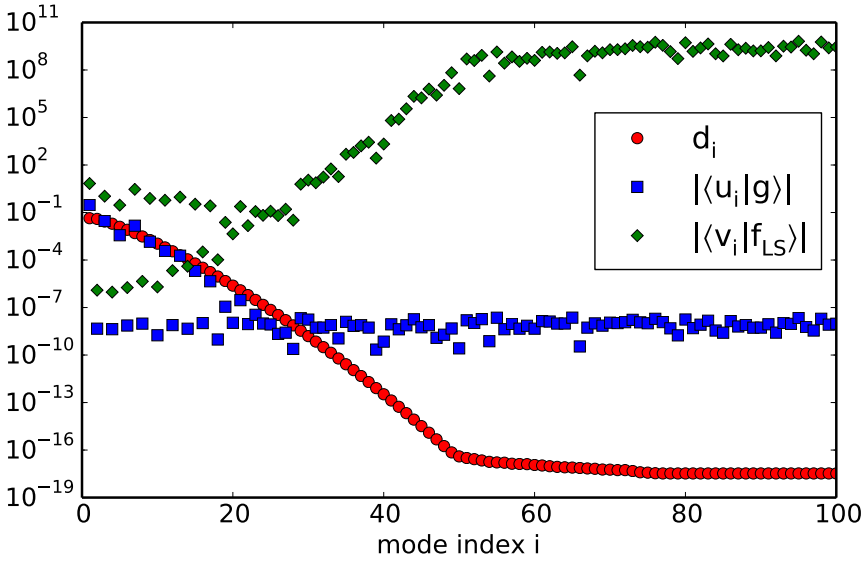


Fig. 5: *Picard plot for the example of Fig. 2. Since the model is symmetric, the expansion coefficients for the odd modes should vanish. For noisy data, instead of vanishing, the coefficients of odd modes are at the noise level. The even coefficients initially decay somewhat faster than the singular values so that the corresponding coefficients of the least-squares solution decrease with i. Once the $\langle \boldsymbol{u}_i|\boldsymbol{g}\rangle$ have decreased to the noise level, here 10^{-8}, they remain at that level while the singular values decrease further. This leads to exponentially increasing contributions of the corresponding modes to the least-squares solution.*

By maximizing the likelihood $\mathrm{e}^{-\chi^2(\boldsymbol{f})/2}$, with or without non-negativity constraint, we apparently overfit the noise that becomes most visible in the modes for which the singular value is below their contribution to the (noisy) data. The assumption behind this is that the exact solution cannot be dominated by the highly oscillating modes with vanishing singular value, i.e., that $\langle \boldsymbol{u}_i|\boldsymbol{g}_{\text{exact}}\rangle/d_i$, for large i decreases with the mode index. This is called the Picard condition. When it is not fulfilled, the reconstruction of the exact model is hopeless, since the relevant information is contained in vanishingly small coefficients $\langle \boldsymbol{u}_i|\boldsymbol{g}_{\text{exact}}\rangle$ that will be completely masked by the noise, cf. (44). When the exact model is not highly oscillating, the Picard condition holds and we have a chance of reconstructing the model from noisy data.

When the Picard condition is fulfilled we can get rid of a large part of the noise by suppressing the contribution of modes with singular value below the noise level in the data. This amounts to a least-squares fit with a truncated singular value decomposition, where the singular values beyond a limiting index are set to zero, $d_{i>i_{\text{trunc}}} := 0$.

A somewhat more refined method is to continuously switch off the small singular modes. This is called Tikhonov regularization. Introducing a regularization parameter α, the Tikhonov solution is given by

$$\boldsymbol{f}_{\text{T}}(\alpha) = \sum_{i=1}^{M} \frac{d_i}{d_i^2+\alpha^2} \langle \boldsymbol{u}_i|\tilde{\boldsymbol{g}}\rangle\, |v_i\rangle, \tag{45}$$

which in the limit $\alpha \to 0$ becomes the least-squares solution (43), while for $\alpha \to \infty$ the solution vanishes. For finite regularization parameter, modes with large singular value $d_i \gg \alpha$ are hardly affected, while the contribution of small singular values to $\boldsymbol{f}_{\text{T}}(\alpha)$ vanishes. To employ

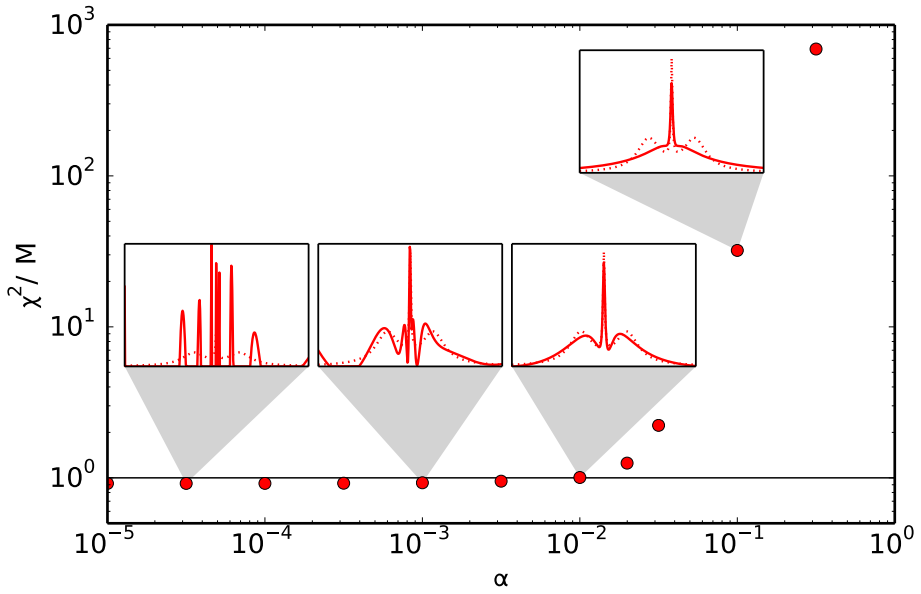


Fig. 6: *Non-negative Tikhonov regularization for the example of Fig. 2, but with noise level increased from* 10^{-8} *to* 10^{-4}*. The insets show the solutions* $\boldsymbol{f}_{\mathrm{T}}(\alpha)$ *at selected values of* α*. The dotted line shows the exact model for comparison. For small* α *the method overfits the noise, leading to strongly oscillating solutions, while the quality of the fit changes little. For large* α *the method underfits the data, leading to a rapid increase in* $\chi^2(\boldsymbol{f}_{\mathrm{T}}(\alpha)$ *and a loss of structure in the reconstructed models. The solid line indicates the expected noise in the data,* $\chi^2 = M$*, relevant for the discrepancy principle.*

Tikhonov regularization for non-negative models we need to formulate it as an optimization problem. Expanding in singular modes and completing the square, it can be written as

$$\begin{aligned} \|\tilde{\boldsymbol{K}}\boldsymbol{f}-\tilde{\boldsymbol{g}}\|^2+\alpha^2\|\boldsymbol{f}\|^2 &= \sum_{i=1}^{M}\left(\langle\boldsymbol{u}_i|\tilde{\boldsymbol{g}}\rangle - d_i\langle\boldsymbol{v}_i|\boldsymbol{f}\rangle\right)^2 + \alpha^2\sum_{n=1}^{N}\langle\boldsymbol{v}_i|\boldsymbol{f}\rangle^2 \\ &= \sum_{i=1}^{M}\left(\frac{\alpha^2\langle\boldsymbol{u}_i|\tilde{\boldsymbol{g}}\rangle}{d_i^2+\alpha^2} + \left(\frac{d_i\langle\boldsymbol{u}_i|\tilde{\boldsymbol{g}}\rangle}{\sqrt{d_i^2+\alpha^2}} + \sqrt{d_i^2+\alpha^2}\langle\boldsymbol{v}_i|\boldsymbol{f}\rangle\right)^2\right) + \alpha^2\sum_{i=M+1}^{N}\langle\boldsymbol{v}_i|\boldsymbol{f}\rangle^2 \end{aligned} \tag{46}$$

which attains its minimum $\sum_i \alpha^2\langle\boldsymbol{u}_i|\tilde{\boldsymbol{g}}\rangle/(d_i^2+\alpha^2)$ for the unique solution (45). In Bayesian terms, (40), Tikhonov regularization chooses $p(\boldsymbol{f}) \propto \mathrm{e}^{-\alpha^2\|\boldsymbol{f}\|^2/2}$ as prior probability.
Alternatively, we can express Tikhonov regularization as a least-squares problem with an expanded kernel and data as

$$\min_{\boldsymbol{f}}\left(\|\tilde{\boldsymbol{K}}\boldsymbol{f}-\tilde{\boldsymbol{g}}\|^2+\alpha^2\|\boldsymbol{f}\|^2\right) = \min_{\boldsymbol{f}}\left\|\begin{pmatrix}\tilde{\boldsymbol{K}}\\ \alpha\mathbb{1}_N\end{pmatrix}\boldsymbol{f}-\begin{pmatrix}\tilde{\boldsymbol{g}}\\ 0_N\end{pmatrix}\right\|^2. \tag{47}$$

Performing the minimization over all models gives Tikhonov regularization, restricting the optimization to $\boldsymbol{f} \geq 0$ defines the non-negative Tikhonov regularization method [8].
The crucial question is how to choose the regularization parameter α. Fig. 6 shows the results of non-negative Tikhonov regularization for the example of Fig. 2 increasing, however, the noise level from 10^{-8} to 10^{-4} to make the problem not too easy. For small α the solutions show

strong oscillations, while the mean-square misfit, χ^2, increases only little with α. For larger α the solution becomes featureless except for the peak at the Fermi level, which is already present in the leading singular mode, cf. Fig. 3, while $\chi^2(\boldsymbol{f}_\mathrm{T}(\alpha))$ rapidly gets worse. The role of the regularization parameter α is thus to strike a balance between (over)fitting the noisy data and keeping the solution smooth. While it is clear that with increasingly accurate data the chosen α should get smaller, there is no unique procedure for determining its value. So there is a wide variety of different recipes for picking α, see [9] for a first overview. An intuitive approach is the discrepancy principle. It assumes that a compromise between overfitting of the noise in the data and smoothness of the model should be reached when α is chosen such that the deviation from the optimum fit $\chi^2(\boldsymbol{f}_\mathrm{T}(\alpha)) = \|\tilde{\boldsymbol{g}} - \tilde{\boldsymbol{K}}\boldsymbol{f}_\mathrm{T}(\alpha)\|^2$ equals the noise expected in M data points $\tilde{g}_m$ (scaled according to (38)) with unit covariance: $\chi^2 = M$. The discrepancy principle thus corresponds to minimizing the regularizer $\|\boldsymbol{f}\|^2$ over the set of models with $\chi^2(\boldsymbol{f}) = M$.

We might wonder why the simple Tikhonov regularizer $\|\boldsymbol{f}\|$ actually has the effect of smoothing the solution. After all, $\|\boldsymbol{f}\|^2 = \sum_n |f_n|^2$ is local, i.e., does not depend on the change in neighboring values. So if we permuted the coordinate values $\{1,\dots,N\}$ in an arbitrary way, the value of $\|\boldsymbol{f}\|^2$ would remain unchanged. We might therefore be tempted to replace $\|\boldsymbol{f}\|^2$ by a regularizer $\langle \boldsymbol{f}|\boldsymbol{M}|\boldsymbol{f}\rangle$ that relates the value on neighboring sites, e.g., $\boldsymbol{M}$ being a finite-difference kernel for the first or higher derivatives. This would, however, be counterproductive: The main reason why the $\|\boldsymbol{f}\|^2$ regularizer leads to smooth models is, of course, that it reduces the effect of modes with small singular value, eq. (45). As we have seen in Fig. 3 these modes are highly oscillatory, while the modes that are least affected are the ones with few nodes that are relatively smooth. Still, even the leading mode is not entirely featureless. While a finite-differences regularizer would reduce the contribution of such a mode, that is usually strongly supported by the data, Tikhonov will leave it largely unaffected. In that sense, Tikhonov regularization respects the variations in the important modes. To emulate this with a finite-difference regularizer would require to laboriously tailor an $\boldsymbol{M}$ suitable for every specific kernel $\tilde{\boldsymbol{K}}$.

There is, however, a clear drawback of the simple Tikhonov regularizer: The result vanishes when $\alpha\to\infty$. For models that fulfill a sum-rule, we have to impose it explicitly, e.g., using a constraint $\sum f_n - 1$. For $\alpha\to\infty$ Tikhonov regularization then gives a flat solution, $f_n = 1/N$. This is the default model of the Tikhonov regularizer with sum-rule constraint. Its form does not change when the grid is transformed, so the default model of the simple Tikhonov regularizer does not transform under coordinate changes as it should: $f(x)\,dx = f(z)\,dz$. We can make Tikhonov regularization independent of the discretization grid by choosing the regularizer $\int dx \left|f(x) - \rho(x)\right|^2/\rho(x)$ which makes the default model $\rho(x)$ explicit and also fulfills the sum-rule. The resulting regularization is still a least-squares problem of the type (47)

$$\min_{\boldsymbol{f}} \left\| \begin{pmatrix} \tilde{\boldsymbol{K}} \\ \alpha\,\mathrm{diag}(1/\sqrt{\rho_n}) \end{pmatrix} \boldsymbol{f} - \begin{pmatrix} \tilde{\boldsymbol{g}} \\ \alpha(\sqrt{\rho_n}) \end{pmatrix} \right\|^2 \tag{48}$$

which can be solved analytically [8] or numerically under the constraint $\boldsymbol{f} \geq 0$ (NNLS).

We are, of course, not limited to bilinear regularizers. Using the entropy as a regularizer is the basis of the maximum entropy approach.

2.4 Maximum entropy

Maximum entropy methods differ from Tikhonov-type regularization in the assumptions they make about the solutions. While Tikhonov is based on the Picard condition giving preference to the modes with large singular value, maximum entropy favors models that contain as little information as possible relative to our expectations (default model). This is measured by the information entropy, see A.3 for details. Using the generalized entropy (111)

$$H(\boldsymbol{f};\boldsymbol{\rho}) = -\sum_n \left(f_n \ln \frac{f_n}{\rho_n} - f_n + \rho_n \right) \tag{49}$$

as regularizer that should be maximized, we have to solve the non-linear optimization problem

$$\min_{\boldsymbol{f}} \Big(\chi^2(\boldsymbol{f})/2 - \alpha H(\boldsymbol{f};\boldsymbol{\rho}) \Big), \tag{50}$$

where we use α instead of α^2 as in (46) to conform with the conventions used, e.g., in [10]. A convenient property of the non-linear entropy regularizer is that it automatically ensures the positivity of the solution since the gradient

$$-\frac{\partial H(\boldsymbol{f};\boldsymbol{\rho})}{\partial f_n} = \ln \frac{f_n}{\rho_n} \tag{51}$$

diverges for $f_n \to 0$ while the gradient of the fit function

$$\frac{\partial \frac{1}{2}\chi^2(\boldsymbol{f})}{\partial f_n} = \frac{\partial}{\partial f_n} \frac{1}{2} \sum_m \Big(\tilde{g}_m - \sum_{n'} \tilde{K}_{mn'} f_{n'} \Big)^2 = -\sum_m \tilde{K}^\dagger_{nm} \Big(\tilde{g}_m - \sum_{n'} \tilde{K}_{mn'} f_{n'} \Big) \tag{52}$$

is always finite, so that any solution of the variational equations f_n has the same sign as ρ_n. Since it is easy to also calculate the Hessians

$$\frac{\partial^2 \frac{1}{2}\chi^2(\boldsymbol{f})}{\partial f_{n'} \partial f_n} = \sum_m \tilde{K}^\dagger_{nm} \tilde{K}_{mn'} \quad \text{and} \quad -\frac{\partial^2 H(\boldsymbol{f};\boldsymbol{\rho})}{\partial f_{n'} \partial f_n} = \frac{1}{f_n}\, \delta_{nn'} \tag{53}$$

it is straightforward to solve the non-linear minimization problem using, e.g., the Levenberg-Marquardt method. The only slight complication being that finite steps in the iteration might change the sign of some component f_n.

In the absence of data, minimizing (50), i.e, setting (51) to zero, we find $\boldsymbol{f} = \boldsymbol{\rho}$. Thus $\boldsymbol{\rho}$ is the default model which, as discussed for Tikhonov regularization above or for (110), it can be related to the choice of the grid. Even when we have decided on a default model, we still have to determine the value of the regularization parameter. Choosing it according to the discrepancy principle is called historic MaxEnt [10]. Remember that, as for Tikhonov regularization, this assumes that we have scaled the data with its covariance matrix according to (38).

Other flavors of the maximum entropy method try to determine the regularization parameter using Bayesian methods. For this we write the entropy regularizer as a prior probability

$$p(\boldsymbol{f}\,|\boldsymbol{\rho},\alpha) \propto \mathrm{e}^{+\alpha H(\boldsymbol{f};\boldsymbol{\rho})} \tag{54}$$

so that the minimization (50) becomes equal to maximizing the posterior probability, cf. (40),

$$p(\boldsymbol{f}\,|\tilde{\boldsymbol{g}},\boldsymbol{\rho},\alpha) = \frac{p(\tilde{\boldsymbol{g}}\,|\boldsymbol{f},\boldsymbol{\rho},\alpha)\,p(\boldsymbol{f}\,|\boldsymbol{\rho},\alpha)}{p(\tilde{\boldsymbol{g}})} \propto \mathrm{e}^{-\chi^2(\boldsymbol{f})/2+\alpha H(\boldsymbol{f};\boldsymbol{\rho})}\,, \tag{55}$$

where we have used that the QMC data $\tilde{\boldsymbol{g}}$ is actually independent of our choice of regularization parameter and default model. The Bayesian approach to determining the regularization parameter uses the posterior probability of α

$$p(\alpha\,|\tilde{\boldsymbol{g}},\boldsymbol{\rho}) = \int\prod_n \frac{df_n}{\sqrt{f_n}}\;\; p(\boldsymbol{f},\alpha\,|\tilde{\boldsymbol{g}},\boldsymbol{\rho}) = \int\prod_n 2d\sqrt{f_n}\;\; \frac{p(\boldsymbol{f}\,|\tilde{\boldsymbol{g}},\boldsymbol{\rho},\alpha)\,p(\tilde{\boldsymbol{g}},\boldsymbol{\rho},\alpha)}{p(\tilde{\boldsymbol{g}},\boldsymbol{\rho})} \tag{56}$$

obtained from marginalizing out $\boldsymbol{f}$, i.e., integrating over the space of models $\boldsymbol{f}$. The peculiar choice of the integration measure, $2d\sqrt{f_n}$, is discussed in [10]. It naturally appears in the expression for the entropy when using Stirling's approximation to one order higher than in the derivation given in A.3, which rather suggests that the factor $1/\sqrt{f_n}$ should be considered part of the entropic prior and not the integration measure.

For historic MaxEnt it was not necessary to know the normalized probabilities (54) and (55). When, however, we want to compare the probabilities of different regularization parameters, we need to determine the normalization of the distributions that depend on α by, again, integrating over $\boldsymbol{f}$

$$Z_{\chi^2}(\tilde{\boldsymbol{g}}) = \int_{-\infty}^{\infty}\prod_n df_n\,\mathrm{e}^{-\chi^2(\boldsymbol{f})} = (2\pi)^{M/2} \tag{57}$$

$$Z_H(\boldsymbol{\rho},\alpha) := \int\prod_n df_n\,\frac{\mathrm{e}^{+\alpha H(\boldsymbol{f},\boldsymbol{\rho})}}{\prod_{n'}\sqrt{f_{n'}}} \tag{58}$$

Since the likelihood is a Gaussian, the integral is straightforward, cf. (34). The normalization of the entropic prior is more difficult. In MaxEnt such functional integrals are approximated by Gaussian integrals obtained from expanding the exponent to second order about its maximum. As already discussed above, the entropy term is maximized when the model equals the default model. The second-order expansion (53) is thus given by the diagonal matrix $-\delta_{nn'}/\rho_n$, i.e., the entropy expanded about the default model becomes just the Tikhonov regularizer of (48):

$$f(x)\ln\frac{f(x)}{\rho(x)} - (f(x)-\rho(x)) = \big(\rho(x)+\delta f(x)\big)\ln\left(1+\frac{\delta f(x)}{\rho(x)}\right) - \delta f(x) = \frac{\big(\delta f(x)\big)^2}{2\rho(x)} + \mathcal{O}^3 \tag{59}$$

Also expanding $1/\sqrt{f_n} \approx \big(1-(f_n-\rho_n)/2\rho_n\big)/\sqrt{\rho_n}$, the normalization of the entropy prior thus is approximated by that of the Tikhonov prior without non-negativity constraint [10]

$$Z_H(\boldsymbol{\rho},\alpha) \approx \prod_n \int_{-\infty}^{\infty} df_n\,\frac{\mathrm{e}^{-\frac{\alpha(f_n-\rho_n)^2}{2\rho_n}}}{\sqrt{\rho_n}}\left(1-\frac{f_n-\rho_n}{2\rho_n}\right) = \left(\frac{2\pi}{\alpha}\right)^{N/2}. \tag{60}$$

To calculate $p(\alpha\,|\tilde{\boldsymbol{g}},\boldsymbol{\rho})$, (56), we still have to choose a prior probability $p(\tilde{\boldsymbol{g}},\boldsymbol{\rho},\alpha)$. From the discrepancy principle it seems reasonable that it should be independent of the data normalized

to have a unit covariance matrix. If we also assume that α is independent of the default model, we only have to choose $p(\alpha)$. Assuming that the prior is scale invariant

$$p(\alpha)\, d\alpha \stackrel{!}{=} p(s\alpha)\, d(s\alpha) \tag{61}$$

one obtains the Jeffreys prior $p(\alpha) \propto 1/\alpha$ [2], which might not be the most appropriate choice, since the scale of the regularization parameter is fixed by the noise in the data, which we know. Using all this for calculating the posterior probability of the regularization parameter, there are two different flavors of how α enters the analytical continuation: Classic MaxEnt chooses the α that maximizes $p(\alpha\,|\tilde{\boldsymbol{g}}, \boldsymbol{\rho})$ to determine $\boldsymbol{f}_{\text{classic}} = \boldsymbol{f}(\alpha_{\text{max}})$. Bryan's method no longer insists on picking a specific value of α. The approach rather determines the model as the average over all regularization parameters, weighted with their posterior probability

$$\boldsymbol{f}_{\text{Bryan}} = \int_0^\infty d\alpha\, \boldsymbol{f}(\alpha)\, p(\alpha\,|\tilde{\boldsymbol{g}}, \rho)\,. \tag{62}$$

It might seem that the MaxEnt approaches could be improved by actually performing the integrals over model space exactly rather than using simple Gaussian approximations that even violate the non-negativity of the models, which is one of the precious priors that we are sure of. But doing these integrals is hard. A second drawback of MaxEnt, or rather of all regularization approaches, is the need to deal with a regularization parameter, introducing the need for making assumptions about its behavior, its prior probability and the like, for which there is no apparent solution. If only we could efficiently integrate over model space there might be a way of eliminating all these complications arising from the need to regularize. Instead of looking for a solution that maximizes some posterior probability, we could ask for the average over all possible models, weighted with their likelihood. This approach which apparently is free of explicit regularization parameters is the average spectrum method.

3 Average spectrum method

The average spectrum methods is an appealing alternative to the optimization approaches. It was probably first proposed by White [11] and reinvented several times after. The basic idea is of striking elegance: The spectral function is obtained as the average over all physically admissible functions, weighted by how well they fit the data

$$f_{\text{ASM}}(x) := (2\pi)^{-M/2} \int_{f(x)\geq 0} \mathcal{D}f\; f(x)\, \mathrm{e}^{-\chi^2[f]/2}. \tag{63}$$

Due to the ill-conditioning of the inverse problem there are very many functions that differ drastically but essentially fit the data equally well. Taking the average, we can thus expect that the spectral features not supported by the data will be smoothed out, providing a regularization without the need for explicit parameters. Unfortunately, the practical application of this conceptually appealing approach has been hampered by the difficulty of numerically implementing the functional integration.

It is worth emphasizing that the non-negativity constraint is essential. An unconstrained integration over the Gaussian in (63) actually produces a least-squares solution. Since the width of the likelihood increases with the inverse of the singular value this would, of course, be numerically very inefficient, and since the width diverges for the modes in the null space of the kernel, their contribution will never converge to a definite value, reflecting that the problem is underdetermined.

3.1 Blocked modes sampling

When we discretize the model function $f(x)$ into a piece-wise constant function as discussed in Sec. 1.3, the functional integral becomes

$$\boldsymbol{f}_{\mathrm{ASM}} \propto \prod_{n=1}^{N} \int_0^\infty df_n \, \boldsymbol{f} \, \mathrm{e}^{-\chi^2(\boldsymbol{f})/2}, \tag{64}$$

where the N-dimensional integral can be evaluated by Monte Carlo techniques. The most straightforward approach is to perform a random walk in the space of non-negative vectors $\boldsymbol{f}$, updating a single component, $f_n \to f'_n$, at a time. Detailed balance is fulfilled when we sample the new component f'_n for the conditional distribution $\propto \mathrm{e}^{-\chi^2(\boldsymbol{f};f'_n)/2}$ with

$$\chi^2(\boldsymbol{f}; f'_n) := \big\| \underbrace{\tilde{\boldsymbol{g}} - \tilde{\boldsymbol{K}}\boldsymbol{f} + \tilde{\boldsymbol{K}}_n f_n}_{=:\tilde{\boldsymbol{g}}_n} - \tilde{\boldsymbol{K}}_n f'_n \big\|^2 = \tilde{\boldsymbol{K}}_n^\dagger \tilde{\boldsymbol{K}}_n \left(f'_n - \tilde{\boldsymbol{K}}_n^\dagger \tilde{\boldsymbol{g}}_n / \tilde{\boldsymbol{K}}_n^\dagger \tilde{\boldsymbol{K}}_n \right)^2, \tag{65}$$

where $\tilde{\boldsymbol{K}}_n$ is the n-th column of $\tilde{\boldsymbol{K}}$. We thus have to sample f'_n from a univariate Gaussian of width $\sigma = 1/\|\tilde{\boldsymbol{K}}_n\|$ centered at $\mu = \tilde{\boldsymbol{K}}_n^\dagger \tilde{\boldsymbol{g}}_n / \|\tilde{\boldsymbol{K}}_n\|^2$ and truncated to the non-negative values $f'_n \in [0, \infty)$. This can be done very efficiently, e.g., as described in A.4.

Still, sampling components can be very slow because the width of the Gaussian (65) is, in general, set by the inverse of the largest singular value, i.e., the random walk performs only exceedingly small steps. This is even more evident when sampling spectral functions, where we cannot change just a single f_n without violating the sum-rule (15). A way around is to introduce global moves along the principal axes of χ^2, i.e., along the singular modes.

Transforming to the new bases $\boldsymbol{h} := \boldsymbol{U}^\dagger \tilde{\boldsymbol{g}}$ in data and $\boldsymbol{e} := \boldsymbol{V}^\dagger \boldsymbol{f}$ in model space diagonalizes

$$\chi^2(\boldsymbol{f}) = \big\| \boldsymbol{U}^\dagger \tilde{\boldsymbol{g}} - \boldsymbol{D}\boldsymbol{V}^\dagger \boldsymbol{f} \big\|^2 = \sum_{i=1}^{M} \big(h_i - d_i e_i \big)^2 \tag{66}$$

so that in the new basis the integral (64) factorizes into Gaussian integrals

$$e_i^{\mathrm{ASM}} \propto \int_{\boldsymbol{f} \geq 0} de_i \, e_i \, \mathrm{e}^{-(h_i - d_i e_i)^2/2}. \tag{67}$$

Without non-negativity constraint the integrals would be independent and result in a least-squares solution. With the constraint they are coupled via their range of integration. Updating modes $e_i \to e'_i$ is restricted by the condition $\boldsymbol{f}' = \boldsymbol{f} + (e'_i - e_i)\boldsymbol{V}_i \geq 0$, where $\boldsymbol{V}_i$ is the i-th

column vector of $\boldsymbol{V}$. This is equivalent to $e_i' \geq e_i - f_n/V_{ni}$ for $V_{ni} > 0$ and correspondingly for $V_{ni} < 0$ so that e_i' is constrained to

$$\max\left\{\frac{f_n}{V_{ni}}\middle| V_{ni} < 0\right\} \leq e_i - e_i' \leq \min\left\{\frac{f_n}{V_{ni}}\middle| V_{ni} > 0\right\}. \tag{68}$$

Sampling modes is usually much more efficient than sampling components: For modes with large singular value the Gaussian is narrow so that the random walk quickly jumps close to the optimal value h_i/d_i and then takes small steps around there. For modes with small or zero singular value the distribution is very broad so that the random walk can take large steps, allowing for an efficient sampling. Still, sampling may become inefficient when non-negativity restricts a mode to a very narrow interval. This will happen when $\boldsymbol{f}$ has regions where it becomes very small, e.g., in the tail of the spectral function. Then the scale for the step size is not given by the singular value but rather by the width of the interval (68). This problem can be overcome by using a real space renormalization group technique, introducing blocks of varying size in which modes are sampled. This way the method can interpolate efficiently between sampling components, i.e., blocks of size 1, and sampling modes, i.e., blocks of size N. Details of the blocked modes sampling method and its performance are given in [12].

Using blocked modes sampling for exploring the average spectrum method, we find that the results depend on the choice of the discretization in (64). In fact, the choice of coordinates for the discretization grid plays the role of a default model, while the number of grid points N acts as a regularization parameter and in the limit $N \to \infty$ the average spectrum method corresponds to a regularization with the entropy of the default model relative to the model [12], i.e., with the Shannon entropy with the role of model and default model exchanged. So, contrary to our expectations, averaging non-negative spectra (63) is not free of regularization parameters. This is not a problem of the particular method, but a general feature when integrating over a constrained functional space. Interestingly it also affects the MaxEnt method were it to perform the normalization and marginalization integrals exactly, see, e.g., Sec. 6.2 of [2].

3.2 Rényi entropies from averaging spectra

To explore the relation between the averaging spectra (63) and regularization with an entropy more systematically, we represent the spectral function as a sum of delta functions

$$f(x) = \sum_{k=1}^{K} a_k\, \delta(x - x_k)\,, \tag{69}$$

and sample the positions x_k and amplitudes $a_k \geq 0$. The result is then discretized by binning the δ-functions on a grid with N intervals I_n

$$f_n = \sum_{x_k \in I_n} a_k \approx \int_{I_n} f(x)\, dx\,. \tag{70}$$

The discretized average spectrum from sampling (69) is then given by

$$\boldsymbol{f}_{ASM} \propto \sum_{\boldsymbol{f}} \boldsymbol{f}\, \mathrm{e}^{-\chi^2(\boldsymbol{f})/2}\, p(\boldsymbol{f})\,, \tag{71}$$

where $p(\boldsymbol{f})$ is the probability of obtaining the discretized $\boldsymbol{f}$ from sampling the positions and amplitudes in (69). To calculate this probability we split it as

$$p(\boldsymbol{f}) = \sum_{\boldsymbol{n}} \Big|_{\sum n_n = K} p(\boldsymbol{n})\, p(\boldsymbol{f}|\boldsymbol{n}) \tag{72}$$

where $p(\boldsymbol{n})$ is the probability of having n_n δ-peaks in interval I_n

$$n_n = \big|\{x_k|\ x_k{\in}I_n\}\big| \quad \text{with} \sum_n n_n = K \tag{73}$$

while $p(\boldsymbol{f}|\boldsymbol{n})$ is the probability that adding the amplitudes of the n_n δ-peaks in I_n gives f_n.

Sampling positions: Let us start by calculating $p(\boldsymbol{n})$ when the positions x_k are sampled from a default model $\rho(x)$ with $\int\rho(x)\,dx = 1$, i.e.,

$$p(x_k{\in}I_n) = \int_{I_n} \rho(x)\,dx =: \rho_n\,. \tag{74}$$

The probability that n_1 of the K sampled positions fall in the interval I_1 is then

$$p(n_1) = \binom{K}{n_1} \rho_1^{n_1}\,(1{-}\rho_1)^{K-n_1}$$

and the probability that n_2 of the remaining $K{-}n_1$ positions are in I_2 is

$$p(n_2|n_1) = \binom{K{-}n_1}{n_2} \rho_2^{n_2}\,(1{-}\rho_1{-}\rho_2)^{K-n_1-n_2}/(1{-}\rho_1)^{K-n_1}\,.$$

In general we obtain, defining $K_n := K{-}\sum_{i=1}^{n} n_i$ and $R_n := \sum_{i=1}^{n}\rho_n$,

$$p(n_n|n_1,\ldots,n_{n-1}) = \binom{K_{n-1}}{n_n} \rho_n^{n_n}\,(1{-}R_n)^{K_n}/(1{-}R_{n-1})^{K_{n-1}}\,. \tag{75}$$

You should convince yourself that $p(K_{N-1}|n_1,\ldots,n_{N-1}) = 1$ as required by $\sum_n n_n = K$. The probability for sampling $\boldsymbol{n}$ is then given by

$$p(\boldsymbol{n}) = p(n_1)\,p(n_2|n_1)\cdots p(n_N|n_1,\ldots,n_{N-1}) = \prod_{n=1}^{N}\binom{K_{n-1}}{n_n}\rho_n^{n_n} = K!\prod_{n=1}^{N}\frac{\rho_n^{n_n}}{n_n!} \tag{76}$$

In the limit $K\to\infty$ of sampling many δ-peaks we can expand using the Stirling approximation $\log n! \approx n\log n - n$

$$\log p(\boldsymbol{f}) \approx \big(\log K - K\big) + \sum_{n=1}^{N}\big(n_n\log\rho_n - n_n\log n_n + n_n\big) = \sum_{n=1}^{N} n_n \log\frac{\rho_n}{n_n/K}\,. \tag{77}$$

This is essentially the derivation of the Shannon entropy discussed in A.3.

Sampling positions with fixed amplitudes: If in the sampling we keep the amplitudes fixed at $a_k = 1/K$ to fulfill the sum rule $\sum a_k = \sum f_n = 1$, the conditional probability $p(\boldsymbol{f}|\boldsymbol{n})$ vanishes, unless $f_n = n_n/K$ for all n, so that (77) becomes

$$\frac{\log p(\boldsymbol{f})}{K} = -\sum f_n \log \frac{f_n}{\rho_n} = S(\boldsymbol{f}|\boldsymbol{\rho})\,. \tag{78}$$

Thus, when sampling the positions x_k from a default model $\rho(x)$, keeping the amplitudes a_k fixed, the discretized average spectrum (71) becomes

$$\sum_{\boldsymbol{f}} \boldsymbol{f}\, \mathrm{e}^{-\chi^2(\boldsymbol{f}/2)+K\,S(\boldsymbol{f}|\boldsymbol{\rho})}\,, \tag{79}$$

i.e., the result is regularized by the entropy of the model relative to the default model. Using the discrepancy principle, the regularization parameter K is replaced by some α. Thus, sampling with fixed amplitudes gives results similar to MaxEnt.

Sampling amplitudes: A reasonable way of sampling the amplitudes is from an exponential distribution

$$p(a) = \lambda\, \mathrm{e}^{-\lambda a} \tag{80}$$

with $\lambda = K$ so that the sum rule $\sum a_k = K$ is fulfilled on average. Considering a single bin, we can then determine the probability of sampling a sum f of amplitudes of n δ-functions by induction

$$\begin{aligned}
p(f|1) &= p(f) \\
p(f|2) &= \int_0^f da\, p(a)\, p(f-a|1) = \lambda^2 \int_0^f da\, \mathrm{e}^{-\lambda f} = \lambda^2\, f\, \mathrm{e}^{-\lambda f} \\
&\;\;\vdots \\
p(f|n) &= \int_0^f da\, p(a)\, p(f-a|n-1) = \lambda^n \frac{f^{n-1}}{(n-1)!}\, \mathrm{e}^{-\lambda f}
\end{aligned} \tag{81}$$

Thus, $p(f|n)$ is a Gamma distribution with shape parameter n and scale parameter λ. The induction above still works when we replace n by γn (and λ by $\gamma\lambda$ to maintain the mean) for any $\gamma > 0$, i.e., when we sample the amplitudes from

$$p_\gamma(a) = (\gamma\lambda)^\gamma \frac{a^{\gamma-1}}{\Gamma(\gamma)}\, \mathrm{e}^{-\gamma\lambda a}\,. \tag{82}$$

As shown in Fig. 7, for $\gamma > 1$ this increases the probability close to the mean amplitude, while for $\gamma < 1$ it increases the probability close to 0.
From (81) it is straightforward to obtain

$$p(\boldsymbol{f}|\boldsymbol{n}) = \prod_{n=1}^N p(f_n|n_n) = \lambda^K \left(\prod_{n=1}^N \frac{f_n^{n_n-1}}{\Gamma(n_n)} \right) \mathrm{e}^{-\lambda \sum f_n}\,. \tag{83}$$

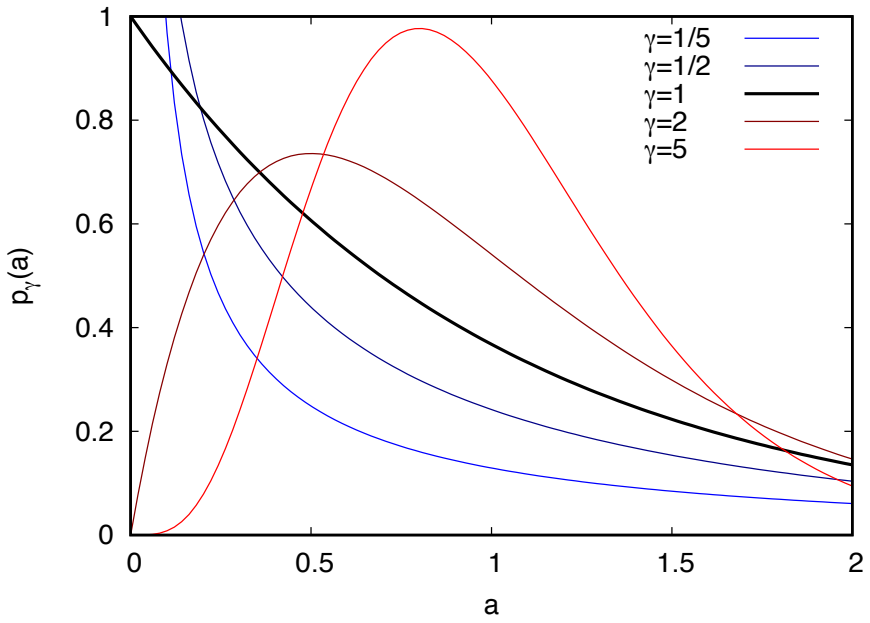


Fig. 7: *Gamma distribution with unit mean for different values of the shape parameter γ. For $\gamma > 1$ the probability increases about the mean value, for $\gamma < 1$ it increases close to 0.*

Restricting to models $\boldsymbol{f}$ that fulfill the sum-rule $\sum f_n = 1$, we have to integrate $p(\boldsymbol{f}|\boldsymbol{n})$ over the space of allowed models to get the normalization of the restricted distribution

$$\int_0^1 df_1 \frac{f_1^{n_1-1}}{\Gamma(n_1)} \int_0^{F_1} df_2 \frac{f_2^{n_2-1}}{\Gamma(n_2)} \cdots \int_0^{F_{N-2}} df_{N-1} \frac{f_{N-1}^{n_{N-1}-1}}{\Gamma(n_{N-1})} \frac{F_{N-1}^{n_N-1}}{\Gamma(n_N)} = \frac{1}{\Gamma(K)}\,, \tag{84}$$

where $F_n := 1 - \sum_{i=1}^{n} f_i = \sum_{i=n+1}^{N} f_i$ and the integrations are successively performed using Euler's Beta integral $\int_0^1 t^{\alpha-1}(1-t)^{\beta-1} = \Gamma(\alpha)\Gamma(\beta)/\Gamma(\alpha+\beta)$.
Including the sum-rule this results in the Dirichlet distribution

$$p(\boldsymbol{f}|\boldsymbol{n})\Big|_{\sum f_n=1} = \Gamma(K) \prod_{n=1}^{N} \frac{f_n^{n_n-1}}{\Gamma(n_n)}\,, \tag{85}$$

where, again, we could multiply all n_n by some $\gamma > 0$. Note the similarity of (85) and (76). For large K we obtain

$$\log p(\boldsymbol{f}|\boldsymbol{n})\Big|_{\sum f_n=1} \approx \sum_{n=1}^{N} n_n \log \frac{f_n}{n_n/K}\,. \tag{86}$$

Sampling amplitudes with fixed positions: If we sample only the amplitudes according to (85), keeping the positions x_k distributed as the default model $\rho(x)$ fixed, i.e., $n_n = K\rho_n$, we obtain

$$\frac{\log p(\boldsymbol{f})}{K} = -\sum_n \rho_n \log \frac{\rho_n}{f_n} = S(\boldsymbol{\rho}|\boldsymbol{f})\,, \tag{87}$$

i.e., this way of sampling corresponds to a regularization with the entropy of the default model relative to the model. This is unusual entropy was found for the blocked modes sampling [12].

Sampling positions and amplitudes: When we sample both positions and amplitudes, we get using (77) and (86)

$$\begin{aligned} p(\boldsymbol{f}) &= \sum_{\boldsymbol{n}} \Big|_{\sum n_n = K} p(\boldsymbol{n})\, p(\boldsymbol{f}|\boldsymbol{n})\Big|_{\sum f_n = 1} \\ &\approx \sum \exp\Big(\sum_n n_n\, 2\log\frac{\sqrt{\rho_n f_n}}{n_n/K}\Big) \\ &= \exp\big(K\, 2\log\sum_n \sqrt{\rho_n f_n}\big)\sum \exp\Big(-2K\sum_n n_n/K\log\frac{n_n/K}{\sqrt{\rho_n f_n}/\sqrt{\sum_i \rho_i f_i}}\Big) \end{aligned}$$

The sum over $\boldsymbol{n}$ is thus over exponentials of the Shannon entropy of $\boldsymbol{n}/K$ relative to a default model given by the square root expression. It is dominated by the term where $\boldsymbol{n}/K$ equals the default model (vanishing relative entropy), while all other terms vanish for large K. Sampling both, positions and amplitudes, thus implies a regularization by

$$\log\frac{p(\boldsymbol{f})}{K} = 2\log\sum_n \sqrt{\rho_n f_n}\,. \tag{88}$$

For the general case of sampling the amplitudes from $p_\gamma(a)$, (82), we obtain instead [17]

$$\log\frac{p(\boldsymbol{f})}{K} = (\gamma{+}1)\log\sum_n f_n\left(\frac{f_n}{\rho_n}\right)^{-1/(1+\gamma)}. \tag{89}$$

These are Rényi entropies, with (88) being the special case $\gamma = 1$, while the Shannon entropy (78) is recovered for $\gamma \to \infty$ (remember that $p_\gamma(a)$ is more concentrated about the mean the larger γ), while (87) is not contained in the expression (89).
Changing the parametrization to $\eta = \gamma/(1{+}\gamma)$ we obtain the standard form of the Rényi entropy [18] (IX, §8, eq. (37b), which actually gives the information gain). Dividing by η, i.e., just scaling the original Rényi entropy by a factor, we obtain

$$S_\eta(\boldsymbol{f}|\boldsymbol{\rho}) = \frac{1}{\eta(1{-}\eta)}\sum_n \frac{f_n^\eta}{\rho_n^{\eta-1}}\,, \tag{90}$$

which makes the symmetry between model and default model explicit

$$S_{1-\eta}(\boldsymbol{f}|\boldsymbol{\rho}) = S_\eta(\boldsymbol{\rho}|\boldsymbol{f})\,. \tag{91}$$

The symmetric entropy (88) is $S_{1/2}(\boldsymbol{f}|\boldsymbol{\rho})$, while Shannon entropy $S(\boldsymbol{f}|\boldsymbol{\rho}) = \lim_{\eta\to 1} S_\eta(\boldsymbol{f}|\boldsymbol{\rho})$ and its symmetric partner $S(\boldsymbol{\rho}|\boldsymbol{f}) = \lim_{\eta\to 0} S_\eta(\boldsymbol{f}|\boldsymbol{\rho})$ are obtained using l'Hôspital's rule.
Instead of eliminating the explicit regularization parameters, the functional integration over non-negative functions introduces a whole family of entropy functions $S_\eta(\boldsymbol{f}|\boldsymbol{\rho})$ to use as regularizers. To get an impression of how results for different choices of η change, we calculate the result of maximizing the Rényi entropy, when the only information about the (normalized) model is its mean and variance (calculated in the coordinates of the default model)

$$\int x\, f(x)\, dx = \mu \quad \text{and} \quad \int (x{-}\mu)^2 f(x)\, dx = \sigma^2\,. \tag{92}$$

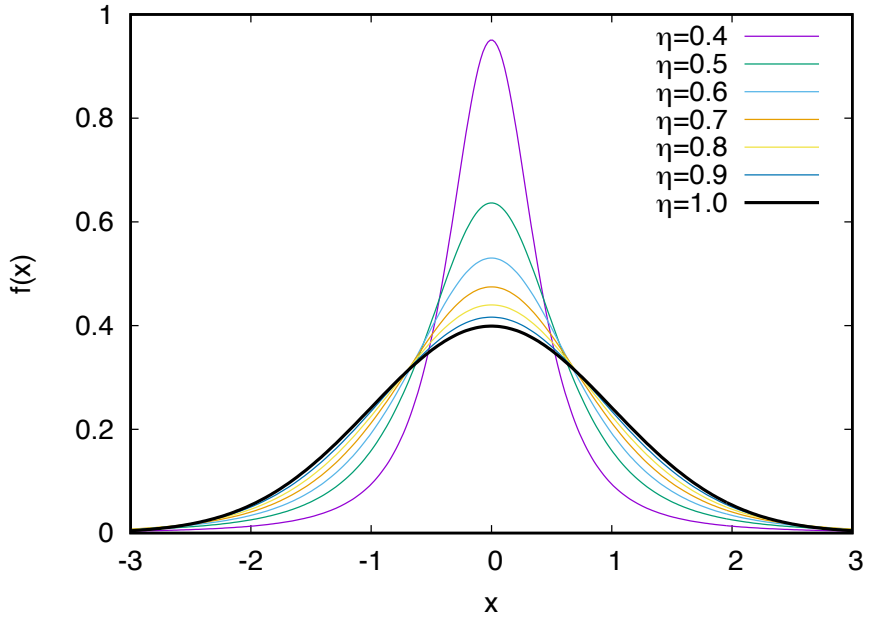


Fig. 8: *Models obtained from maximizing Rényi entropy for a model with mean $\mu = 0$ and variance $\sigma = 1$. For the Shannon entropy $\eta = 1$ the result is a Gaussian.*

for which we obtain [17]

$$f(x) = \frac{\Gamma\left(\frac{1}{1-\eta}\right)\sqrt{\frac{1-\eta}{3\eta-1}}}{\sqrt{\pi}\sigma\Gamma\left(\frac{1+\eta}{2(1-\eta)}\right)}\left(1+\frac{1-\eta}{3\eta-1}\frac{(x-\mu)^2}{\sigma^2}\right)^{\frac{1}{\eta-1}}. \tag{93}$$

For $\eta\to1$ this becomes the familiar Gaussian, while, as shown in Fig. 8, for decreasing η the tails of the peak get fatter, but its full-width-half-maximum (FWHM) decreases (vanishing at $\eta=1/3$)

$$\text{FWHM} = 2\sigma\sqrt{\frac{3\eta-1}{1-\eta}\left(2^{1-\eta}-1\right)}. \tag{94}$$

Hence if we, a priori, expect sharp peaks in the model, it is a good idea to use an entropy regularizer with $\eta < 1$, rather than the Shannon entropy.

4 Conclusions

As for so many problems, there is no magic solution to the problem of analytic continuation. Any method can only reconstruct what is in the data and must substitute missing information, ideally by exact prior knowledge or, otherwise, by mere assumptions about the solution. The most important aspect of analytic continuation is thus encountered already before the solution of the inverse problem is even started: Depending on what features of the model we are interested in, we have to decide where to measure the data. If we want, e.g., to reconstruct the spectral function far from the Fermi level, it does not help to just have highly accurate values for the Green function when they are not close enough to $\tau = 0$ or β to give information about the discontinuity in its derivatives.

Moreover, it is deceiving to just look at the single result returned by a regularization approach. There is not "the" solution, rather every method produces an expected solution with its uncertainty quantified by a non-intuitive $N \times N$ covariance matrix. This is, however, rarely analyzed because it is hard to calculate and difficult to interpret. Still, there are approaches to estimate the error in observables derived by integrating over the spectrum. They are nicely discussed in [10] and should be used wherever possible.

We have presented the approaches to the analytic continuation problem in the order of increasing sophistication and accuracy — and numerical cost. The analysis of QMC data should ideally follow this progression until the desired information about the spectral function has been reliably obtained. A Picard plot will give a first impression of how much information is actually contained in the data and how difficult the reconstruction likely will be. It also gives an important consistency check of the error estimate.

Despite the uncontrolled approximations in the practical flavors of MaxEnt, the approach has developed into the standard approach for analytical continuation. The average spectrum method, has extended that methodology. Instead of the expected parameter-free functional integration using only the noise as a regularizer, it actually works, depending on the way the models are sampled, with the whole family of Rényi entropies, rather than just the Shannon entropy. As the non-Shannon entropies tend to result in narrower peaks with fatter tails, they add welcome flexibility when we, a priori, expect sharp features in the spectral function.

The most important lesson is that results of analytic continuation must not be over-interpreted. When the results depend on the details of the method, they rather reflect the choices made by the approach than the data. Thus before interpreting details of the spectral function, we have to make sure that they are robust under (reasonable) variations in the regularization parameters.

A Technical appendices

A.1 Blocking method for correlated data

Let us assume we have an ergodic Markov chain Monte Carlo method, e.g., using Metropolis sampling, that generates a set of K data points $m_1, \ldots, m_K$ drawn from a probability distribution $p(m)\,dm$ and we are interested in the mean value $\mu = \int dm\, p(m)\, m$. The obvious estimate for μ is the average $\bar{m} = \sum_{k=1}^{K} m_k/K$. It will, of course, vary between Monte Carlo runs but, by the central limit theorem, for large K, the averages $\bar{m}$ of independent runs will tend to be distributed as a Gaussian centered at μ with variance

$$\sigma^2(\bar{m}) = \langle \bar{m}^2 \rangle - \langle \bar{m} \rangle^2 = \frac{1}{K^2} \sum_{k,l=0}^{K} \Big(\langle m_k m_l \rangle - \langle m_k \rangle \langle m_l \rangle \Big), \tag{95}$$

where $\langle \cdot \rangle$ is the average over all possible Monte Carlo runs producing K data points. How can we estimate $\sigma^2(\bar{m})$ from the simulation data of a single run? Splitting the double sum

$$\sigma^2(\bar{m}) = \frac{1}{K} \underbrace{\frac{1}{K} \sum_{k=1}^{K} \Big(\langle m_k^2 \rangle - \mu^2 \Big)}_{= \langle m^2 \rangle - \mu^2 =: s_0} + \frac{1}{K^2} \sum_{k \neq l} \Big(\langle m_k m_l \rangle - \mu^2 \Big) \tag{96}$$

we see that for uncorrelated data, $\langle m_k m_l \rangle = \langle m_k \rangle \langle m_l \rangle$ for $k \neq l$, the variance is given by s_0/K. But in general, samples obtained from Markov chain Monte Carlo will be positively correlated, so that $\sigma^2(\bar{m}) \geq s_0/K$. We can eliminate this correlation using an elegant renormalization group technique [13]. For this we consider the transformation of the original data set $m_1, \ldots, m_K$ of K samples (assuming K is even) into half as many data points, obtained by averaging

$$\hat{m}_{\hat{k}} := \frac{m_{2\hat{k}-1} + m_{2\hat{k}}}{2}\,. \tag{97}$$

Obviously, the average of the new data points $\sum_{\hat{k}=1}^{K/2} \hat{m}_{\hat{k}}/(K/2)$ is still $\bar{m}$ and thus must have the same distribution as the averages of the original data. Consequently, $\sigma^2(\bar{m})$ must remain invariant under the blocking transformation (97). Looking at the uncorrelated part of the variance for the blocked data $\hat{m}_{\hat{k}}$ and remembering that the ensemble average $\langle m_k^2 \rangle$ is independent of k, we see that

$$\hat{s}_0 = \frac{1}{K/2} \sum_{\hat{k}=1}^{K/2} \left(\frac{\big\langle m_{2\hat{k}-1}^2 + 2 m_{2\hat{k}-1} m_{2\hat{k}} + m_{2\hat{k}}^2 \big\rangle}{4} - \mu^2 \right) = \frac{s_0}{2} + \frac{1}{2\,K/2} \sum_{\hat{k}=1}^{K/2} \Big(\big\langle m_{2\hat{k}-1} m_{2\hat{k}} \big\rangle - \mu^2 \Big) \tag{98}$$

contains part of the correlations not contained in s_0. Therefore $\hat{s}_0/(K/2) \geq s_0/K$. Under repeated blocking transformations the uncorrelated part of the variance will thus increase. When it reaches a plateau, i.e., a fixed-point under the blocking transformation, it becomes equal to $\sigma^2(\bar{m})$ and the blocked data has become uncorrelated.

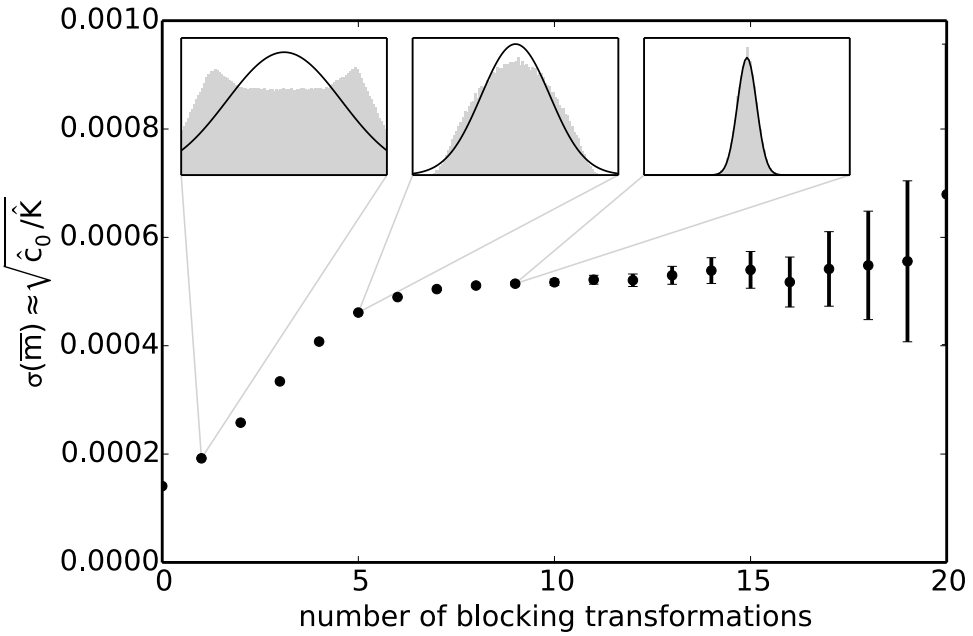


Fig. 9: *Estimate of the standard deviation of the average of correlated data obtained with the blocking method. Initially the variance is severely underestimated but the estimate increases with each blocking step until a plateau is reached, at which point the blocked data has become uncorrelated. By that time the distribution of the $\hat{m}_{\hat{k}}$ has become Gaussian of width $\hat{c}_0$, as shown in the insets. Eventually the number of blocked samples, $\hat{K} = K/2^n$, becomes so small that the estimates become unreliable.*

We can try to estimate the ensemble average s_0 from the data from one specific simulation run as $\sum_{k=1}^{K}(m_k^2 - \bar{m}^2)/K$. Taking the ensemble average and comparing to s_0

$$\frac{1}{K}\sum_{k=1}^{K}\left(\langle m_k^2\rangle - \langle\bar{m}^2\rangle\right) = \frac{1}{K}\sum_{k=1}^{K}\Big(\big(\langle m_k^2\rangle - \langle\bar{m}\rangle^2\big) - \big(\langle\bar{m}^2\rangle - \langle\bar{m}\rangle^2\big)\Big) = s_0\left(1-\frac{1}{K}\right)$$

we find that the unbiased estimator actually is

$$s_0 \approx c_0 := \frac{1}{K-1}\sum_{k=1}^{K}\left(m_k^2 - \bar{m}^2\right) \quad \Rightarrow \quad \sigma^2(\bar{m}) \approx \frac{1}{K(K-1)}\sum_{k=1}^{K}\left(m_k^2 - \bar{m}^2\right). \tag{99}$$

In an actual implementation of the blocking method, we repeatedly block the data and calculate the corresponding estimator of the uncorrelated variance $\hat{s}_0/\hat{K}$. An example is shown in Fig. 9. As expected, $\hat{c}_0/\hat{K}$ increases with each blocking step until it reaches a plateau. There the blocked data $\hat{m}_{\hat{k}}$ are uncorrelated and, by the central limit theorem, approach Gaussian variables of variance $\sigma^2(\hat{m}) = \hat{K}\sigma^2(\bar{m})$. For such variables the variance of the variance $\sigma^2(\bar{m})$ is given by $\langle(\hat{c}_0/\hat{K})^2\rangle - \langle\hat{c}_0/\hat{K}\rangle^2 = 2\sigma^4(\bar{m})/(\hat{K}-1)$, which provides us with the errorbars. Since the number of blocked data points is halved in each step, eventually the blocked sample becomes very small and $\hat{c}_0/\hat{K}$ starts to fluctuate, also indicated by rapidly increasing errorbars. We can then identify the plateau by checking when $\hat{s}_0/\hat{K}$ does not change between blocking steps within its error bar.

A.2 Non-negative least-squares algorithm (NNLS)

The model $\boldsymbol{f}$ fitting a given data vector $\boldsymbol{g}$ best in the least-squares sense minimizes the norm of the residual vector $\chi^2(\boldsymbol{f}) = \|\boldsymbol{K}\boldsymbol{f} - \boldsymbol{g}\|^2$. At the minimum $\boldsymbol{f}_{\rm LS}$ the gradient $\boldsymbol{w}$ vanishes

$$w_n(\boldsymbol{f}_{\rm LS}) := \frac{1}{2}\,\frac{\partial\,\chi^2(\boldsymbol{f})}{\partial f_n}\bigg|_{\rm LS} = \mathrm{Re}\,\big(\boldsymbol{K}^\dagger(\boldsymbol{K}\boldsymbol{f}_{\rm LS}-\boldsymbol{g})\big)_n = 0 \quad \forall n\,. \tag{100}$$

Since χ^2 is a non-negative quadratic form in $\boldsymbol{f}$ stationary points must be minima

$$\chi^2(\boldsymbol{f}_{\rm LS}+\boldsymbol{\delta}) = \chi^2(\boldsymbol{f}_{\rm LS}) + 2\boldsymbol{\delta}^{\mathsf{T}}\boldsymbol{w}(\boldsymbol{f}_{\rm LS}) + \|\boldsymbol{K}\boldsymbol{\delta}\|^2 \geq \chi^2(\boldsymbol{f}_{\rm LS})\,. \tag{101}$$

The least-squares fit can be found from the singular value decomposition (SVD) $\boldsymbol{K}^\dagger = \boldsymbol{V}\boldsymbol{D}\boldsymbol{U}^\dagger$

$$\boldsymbol{f}_{\rm LS} = \boldsymbol{V}\boldsymbol{D}^{-1}\boldsymbol{U}^\dagger\boldsymbol{g}\,, \tag{102}$$

where the diagonal matrix $\boldsymbol{D}$ has dimension $K = \mathrm{rank}(\boldsymbol{K})$ while the matrix $\boldsymbol{U}$ is $M\times K$ and $\boldsymbol{V}$ is $N\times K$-dimensional. In terms of the SVD the gradient (100) is given by

$$\boldsymbol{w}(\boldsymbol{f}) = \mathrm{Re}\,\boldsymbol{V}\boldsymbol{D}(\boldsymbol{D}\boldsymbol{V}^{\mathsf{T}}\boldsymbol{f} - \boldsymbol{U}^\dagger\boldsymbol{g})\,. \tag{103}$$

This way of calculating the gradient is numerically more stable than calculating it directly in terms of $\boldsymbol{K}$. It also immediately shows that the gradient vanishes for $\boldsymbol{f}_{\rm LS}$.
Finding the best fit, $\min\|\boldsymbol{K}\boldsymbol{f} - \boldsymbol{g}\|^2$, under the constraint $\boldsymbol{f} \geq 0$ (non-negative least-squares, NNLS) is more complicated. When all components of the unconstrained solution are non-negative, $(\boldsymbol{f}_{\rm LS})_n \geq 0$, it is obviously also the solution of the constrained problem. When there are components $(\boldsymbol{f}_{\rm LS})_n < 0$ we might expect that the constrained fit assumes its minimum on the boundary, $(\boldsymbol{f}_{\rm NNLS})_n = 0$, where the gradient is positive $w_n > 0$. These are the Karush-Kuhn-Tucker conditions [14]:

$$f_n > 0 \quad \text{and} \quad w_n = 0 \qquad \text{or} \qquad f_n = 0 \quad \text{and} \quad w_n \geq 0\,. \tag{104}$$

We distinguish the two cases by defining the two sets $\mathcal{P} = \{n|\, f_n > 0\}$ and $\mathcal{Z} = \{n|\, f_n = 0\}$ which partition the set of indices, $\mathcal{P}\cup\mathcal{Z} = \{1,\dots,N\}$.
When $\boldsymbol{f}_{\rm KT}$ fulfills the Karush-Kuhn-Tucker conditions, it minimizes $\chi^2(\boldsymbol{f})$ on $\boldsymbol{f} \geq 0$. To see this we consider a vector $\boldsymbol{f}_{\rm KT} + \boldsymbol{\delta}$ with $\delta_z \geq 0$ so that $\boldsymbol{f}_{\rm KT} + \boldsymbol{\delta} \geq 0$. Then

$$\chi^2(\boldsymbol{f}_{\rm KT}+\boldsymbol{\delta}) = \chi^2(\boldsymbol{f}_{\rm KT}) + 2\boldsymbol{\delta}^{\mathsf{T}}\boldsymbol{w}(\boldsymbol{f}_{\rm KT}) + \|\boldsymbol{K}\boldsymbol{\delta}\|^2 \geq \chi^2(\boldsymbol{f}_{\rm KT}) \tag{105}$$

since $\boldsymbol{\delta}^{\mathsf{T}}\boldsymbol{w} = \sum_n \delta_n w_n = \sum_{n\in\mathcal{P}} \delta_n w_n + \sum_{n\in\mathcal{Z}} \delta_n w_n \geq 0$, where the first sum vanishes because of the gradient, while in the second sum both factors in each term are non-negative. Conversely, when $\boldsymbol{f}_{\rm NNLS}$ solves the non-negative least-squares problem it must fulfill the Karush-Kuhn-Tucker condition, otherwise an infinitesimal change (respecting non-negativity) of a component violating it could lower χ^2. Thus, to solve the NNLS problem we just have to find a vector that fulfills the Karush-Kuhn-Tucker conditions. For this we can simply go through all possible partitionings of the indices $\{1,\dots,N\} = \mathcal{P}\cup\mathcal{Z}$. For a given partitioning we determine the

least-squares solution on the indices in $\mathcal{P}$, i.e., we minimize $\|\boldsymbol{K}\boldsymbol{P}_\mathcal{P}\boldsymbol{f}-\boldsymbol{g}\|^2$, where $\boldsymbol{P}_\mathcal{P}$ is the projector to the space spanned by the components in $\mathcal{P}$. This makes sure that the gradients for these components vanish, $w_p=0$, while $f_z=0$. If also $f_p\geq 0$ for all $p\in\mathcal{P}$ and $w_z\geq 0$ for all $z\in\mathcal{Z}$, we have found the NNLS solution, otherwise we try the next partitioning. The only problem is that there are 2^N partitionings of the N indices (each index can be either in $\mathcal{P}$ or $\mathcal{Z}$).

A practical algorithm [14] considers possible partitionings in a much more efficient way. We start from some partition for which $\boldsymbol{f}_\mathcal{P}>0$ and $\boldsymbol{w}_\mathcal{P}=0$, e.g., an empty positive set, $\mathcal{P}=\{\}$ and $\boldsymbol{f}_{\{\}}=0$. Given a set $\mathcal{P}$ and the corresponding $\boldsymbol{f}_\mathcal{P}$ for which the Karush-Kuhn-Tucker condition is not yet fulfilled, we add the component i with the most negative gradient. Least-squares fitting on the expanded set $\mathcal{P}'=\mathcal{P}\cup\{i\}$ will produce an improved fit $\chi^2(\boldsymbol{f}_{\mathcal{P}'})<\chi^2(\boldsymbol{f}_\mathcal{P})$: because of the negative gradient, the new component will not stay at zero but rather take a positive value. In case $\boldsymbol{f}_{\mathcal{P}'}\geq 0$, we calculate the new gradient. If it is non-negative, we have found the Karush-Kuhn-Tucker solution, otherwise we repeat the procedure. Each iteration will produce a non-negative solution with improved fit, so that we will converge to the minimum of $\chi^2(\boldsymbol{f})$ under the constraint $\boldsymbol{f}\geq 0$.

In general, however, the least squares solution $\boldsymbol{f}_{\mathcal{P}'}$ will have negative components. In this case, we can find a mixing with the previous fit $\boldsymbol{f}_\alpha=(1-\alpha)\boldsymbol{f}_\mathcal{P}+\alpha\boldsymbol{f}_{\mathcal{P}'}$ with $\alpha\in(0,1)$, that brings the most negative component of $\boldsymbol{f}_{\mathcal{P}'}$ to zero. Since $\chi^2(\boldsymbol{f}_\alpha)\leq(1-\alpha)\chi^2(\boldsymbol{f}_{\mathcal{P}'})+\alpha\chi^2(\boldsymbol{f}_\mathcal{P})<\chi^2(\boldsymbol{f}_\mathcal{P})$ the fit will still be improved. We remove the components where $\boldsymbol{f}_\alpha$ vanishes from $\mathcal{P}'$ and perform a least-squares fit on the new set, repeating the procedure until we get a non-negative least squares solution. This must happen after a finite number of iterations, since in each step at least one element is removed from the positive set while the resulting $\boldsymbol{f}_\alpha\geq 0$ keeps improving the fit $\chi^2(\boldsymbol{f}_\alpha)<\chi^2(\boldsymbol{f}_\mathcal{P})$. Thus we can continue the outer loop with $\boldsymbol{f}_\alpha$, calculating the new gradient and adding the component where it is most negative to the positive set.

Since each step produces a $\boldsymbol{f}\geq 0$ with improved fit, the algorithm does not visit any partitioning twice and will thus always converge. At worst it may take 2^N steps, but in practice the down-hill search produces a solution after trying less than hundred partitionings. Numerically, the most delicate part is the calculation of the gradient, which should be stabilized using a factorization of the kernel. Obviously, checking the Karush-Kuhn-Tucker condition for the gradient must take the numerical accuracy into account. Moreover, the implementation may not converge, when, after adding the component with the most negative gradient, the least-squares fit gives that component a negative value. This can only happen as a consequence of numerical errors. In this case we rather include the component with the second most negative gradient in $\mathcal{P}$.

Note that the non-negative least squares solution $\boldsymbol{f}_\mathrm{NNLS}$ is unique, unlike the least-squares solution (102), to which we can add any multiple of a vector with zero singular value without changing the fit. While the least-squares problem is thus ill-posed when there are vectors that do not contribute to the fit, these vectors play a crucial role in non-negative least squares fitting: They take values such that the modes that are important for the fit can approach their optimal value as closely as possible without violating the constraint. Thus NNLS is well posed.

function NNLS($\boldsymbol{K}$, $\boldsymbol{g}$)
  $\boldsymbol{f} \leftarrow 0$
  $\mathcal{Z} \leftarrow \{1, \ldots, N\}$ ▷ below we use the abbreviation $\mathcal{P} = \{1, \ldots, N\} \setminus \mathcal{Z}$
  loop
    $\boldsymbol{w} \leftarrow \boldsymbol{K}^\dagger(\boldsymbol{K}\boldsymbol{f} - \boldsymbol{g})$ ▷ for robust calculation use, e.g., SVD
    if $\boldsymbol{w}[\mathcal{Z}] \geq 0$ **then return** $\boldsymbol{f}$
    end if
    $i \leftarrow \mathrm{argmin}(\boldsymbol{w}[\mathcal{Z}])$ ▷ find component with most negative gradient
    $\mathcal{Z} \leftarrow \mathcal{Z} \setminus \{i\}$
    loop
      $\boldsymbol{f}' \leftarrow LS(\boldsymbol{K}\boldsymbol{P}\boldsymbol{f}, \boldsymbol{g})$ ▷ LS solution on components $\mathcal{P}$
        ▷ $\boldsymbol{f}_i > 0$, if not: numerical error in gradient! Do not pick i again this round
      if $\boldsymbol{f}'[\mathcal{P}] > 0$ **then**
        $\boldsymbol{f} \leftarrow \boldsymbol{f}'$
        break
      end if
      $\alpha \leftarrow \min\left\{ \frac{\boldsymbol{f}_i}{\boldsymbol{f}_i - \boldsymbol{f}'_i} \middle| i \in \mathcal{P} \wedge \boldsymbol{f}'_i \geq 0 \right\}$
      $\boldsymbol{f} \leftarrow (1-\alpha)\boldsymbol{f} + \alpha\boldsymbol{f}'$ ▷ now $\boldsymbol{f} \geq 0$ and $\boldsymbol{f}_i = 0$ for $i = \mathrm{argmin}$
      $\mathcal{P} \leftarrow \mathcal{P} \setminus \{i | \boldsymbol{f}_i = 0\}$
    end loop
  end loop
end function

Fig. 10: *Function that returns the non-negative least-squares solution $\boldsymbol{f} \geq 0$ of $\boldsymbol{g} = \boldsymbol{K}\boldsymbol{f}$.*

A.3 Shannon entropy

When developing *The Mathematical Theory of Communication*, Claude Shannon introduced the bit as the amount of information needed to decide between two equally probable events [15]. Receiving an unlikely (surprising) message should convey more information than receiving a likely one, and the information contained in two independent messages should be the sum of the information carried by each individually. These axioms lead to $-\log_2 p_i$ as the information contained in receiving a message of probability p_i. Summing over a set of M possible messages of probabilities p_i and weighting the information contained in them by their probability defines the average information or entropy of an information source

$$H(\{p_i\}) = -\sum p_i \log_2 p_i \,. \tag{106}$$

It gives a lower limit to the number of bits needed for encoding the N messages. The maximum number of bits, $\log_2 N$, is needed when we know least about which message to expect, i.e., when all probabilities are the same. In the opposite limit, when one of the messages is certain, we need not encode it at all. Thus the entropy of an information source measures our ignorance before receiving one of the possible messages.

Changing the base of the logarithm, $\log_b(x) = \log_2(x)/\log_2(b)$, for $b > 1$ simply multiplies the entropy by a positive constant, i.e., changes the units in which we measure information. For convenience, we use the natural logarithm, $\ln$, working in natural units, 1 nat $\approx$ 1.44 bits.

An alternative derivation [2] of (106) starts by considering microstates representing the probabilities as $p_i = n_i/M$ by placing N (distinguishable) objects into M bins. Since we can place any of the N objects into any of the M bins, there are M^N such states. The number of different ways of placing the objects into bins and obtaining the same set of $\{n_i\}$, i.e., the same macrostate, is also easily determined: We can pick any n_1 of the N objects and put them into the first bin. Then we can pick any n_2 of the remaining $N - n_1$ objects and put them into the second bin. The probability of realizing a macrostate $\{n_1, \ldots, n_M\}$ is thus

$$\frac{1}{M^N}\binom{N}{n_1}\binom{N-n_1}{n_2}\binom{N-n_1-n_2}{n_3}\cdots\binom{n_M}{n_M} = \frac{1}{M^N}\,\frac{N!}{n_1!\,n_2!\cdots n_M!}\,.$$

Taking the logarithm and using the Stirling approximation $\ln n! \approx n\ln n - n$ we find

$$-N\ln M + N\ln N - N - \sum_{i=1}^{M}\big(n_i\ln n_i - n_i\big) = N\left(\ln\frac{1}{M} - \sum_i p_i \ln p_i\right),$$

which is proportional to the $H(\{p_i\})$ minus the entropy of a flat distribution $\{1/M\}$.
Subtracting the entropy of the flat distribution becomes crucial when taking the limit of a continuous probability distribution: encoding an infinite number of messages will, in general, take an infinite number of bits. Subtracting $-\log 1/M$ keeps the limit $M \to \infty$ finite. To see this, we discretize a continuous distribution $p(x)$ on an equidistant grid of M points, $p_i = p(x_i)\Delta x$ with $\Delta x = (x_{\text{max}} - x_{\text{min}})/M = (\int dx)/M$, and take the limit of the Riemann sum

$$-\sum_{i=1}^{M} p_i \ln\left(\frac{p_i}{1/M}\right) = -\sum_{i=1}^{M}\Delta x\, p(x_i)\ln\left(\frac{p(x_i)\Delta x}{1/M}\right) \to -\int dx\, p(x)\ln\left(\frac{p(x)}{1/\int dx}\right).$$

This defines the entropy of a distribution $p(x)$

$$H[p] = -\int dx\, p(x)\ln\left(\frac{p(x)}{1/\int dx}\right). \tag{107}$$

We can find the $p(x)$ that maximizes this functional from the variational principle. Remembering that the functional derivatives are defined by the expansion

$$H[p+\delta p] = H[p] + \int dx\,\frac{\delta H[p]}{\delta p(x)}\,\delta p(x) + \frac{1}{2}\int dx\,dx'\,\frac{\delta^2 H[p]}{\delta p(x')\delta p(x)}\,\delta p(x')\,\delta p(x) + \mathcal{O}^3(\delta p)$$

we read off the first variation from

$$H[p+\delta p] = -\int dx\,(p+\delta p)\big(\underbrace{\ln(p+\delta p)}_{=\ln p + \ln(1+\frac{\delta p}{p}) = \ln p + \frac{\delta p}{p} + \mathcal{O}^2} + \ln\textstyle\int dx\big) = H[p] - \int dx\,\underbrace{\left(1 + \ln\frac{p(x)}{1/\int dx}\right)}_{=-\frac{\delta H[p]}{\delta p(x)}}\delta p + \mathcal{O}^2,$$

where we have used $\ln(1+x) = x - x^2/2 + \cdots$. In second order we find $\delta^2 H[p]/\delta p(x')\,\delta p(x) = -2\delta(x-x')/p(x) \le 0$ so that the stationary points are maxima. Imposing normalization of the 0-th moment via a Lagrange parameter, the variational equation becomes

$$0 = \frac{\delta}{\delta p(x)}\,H[p] + \lambda_0\big(1 - \textstyle\int dx\, p(x)\big) = -1 - \ln p(x) - \ln\int dx - \lambda_0$$

which is solved by the constant distribution, where $\lambda_0 = -1$ is fixed by normalization

$$p(x) = \frac{1}{\int dx}\, \mathrm{e}^{-(1+\lambda_0)} = \frac{1}{\int dx}\,. \tag{108}$$

Inserting into (107) we find $H[1/\int dx] = 0$, as it must by construction.
Likewise, we can ask which distribution maximizes the entropy, when we know in addition its first moment $\mu = \int dx\, x\, p(x)$. The variational equation then contains two Lagrange parameters

$$0 = \frac{\delta}{\delta p(x)}\, H[p] + \lambda_0\big(1 - \textstyle\int dx\, p(x)\big) + \lambda_1\big(\mu - \textstyle\int dx\, x\, p(x)\big) = -1 - \ln \frac{p(x)}{1\int dx} - \lambda_0 - \lambda_1\, x$$

and we obtain a Boltzmann distribution

$$p_\mu(x) = \frac{1}{\int dx}\, \mathrm{e}^{-(1+\lambda_0+\lambda_1 x)}, \tag{109}$$

where λ_0 and λ_1 are fixed by solving the system $\int dx\, p_\mu(x) = 1$ and $\int dx\, x\, p_\mu(x) = \mu$. Likewise, when we also know the variance of $p(x)$, maximizing the entropy results in a Gaussian.
Given the entropy functional, it is natural to ask what happens under a change of variable. Remembering that density functions transform as $p(x)\,dx = p(z)\,dz$, we find

$$H[p] = -\int \frac{dx}{dz}\,dz\;\; p(z)\frac{dz}{dx}\;\ln\left(\frac{p(z)\frac{dz}{dx}}{1/\int dx}\right) = -\int dz\, p(z) \ln\left(\frac{p(z)}{\rho(z)}\right),$$

where we introduced $\rho(z)\,dz = dx/\int dx$. It reflects how the intervals on x change under the under transformation to z. When we define $\rho(x) = 1/\int dx$, we see that the form of the entropy functional is invariant under coordinate transformations

$$H[p\,|\,\rho] = -\int dx\, p(x) \ln \frac{p(x)}{\rho(x)}\,. \tag{110}$$

This is the relative entropy or Kullback-Leibler divergence. From $\ln x \le x-1$ it follows that $H[p] \le 0$. By construction, the maximum is attained for $p(x) = \rho(x)$. The relative entropy describes the average information contained in the distribution $p(x)$ when what we expected was the distribution $\rho(x)$. The prior $\rho(x)$ plays the role of a density of states: from the functional derivative of the relative entropy $\delta H[p]/\delta p(x) = -1 - \ln(p(x)/\rho(x))$ we see that the solutions of the variational equations for $p(x)$ derived above become proportional to $\rho(x)$.
For convenience we might want to allow non-normalized densities of states $\tilde\rho(x)$ and correspondingly drop the normalization constraint for $\tilde p(x)$. If we write [16]

$$\tilde H[\tilde p\,|\,\tilde\rho] = \int dx \left(\tilde p(x) - \tilde\rho(x) - \tilde p(x) \ln \frac{\tilde p(x)}{\tilde\rho(x)}\right) \tag{111}$$

we obtain from the variational equation $\delta\tilde H/\delta\tilde p = 0$ (without normalization constraint) the solution $\tilde p(x) = \tilde\rho(x)$ with $\tilde H[\tilde\rho\,|\,\tilde\rho] = 0$ as for (110).
We note that a flat prior $\rho(x) = \textit{const.}$ is bound to the choice of variable: Given any $\rho(z)$ we can always transform to $x(z) \propto \int^z \rho(z')\,dz'$ to obtain $\rho(x) = \rho(z)\,dz/dx = \textit{const.}$, where x must be restricted to a finite interval to be normalizable.

A.4 Sampling from a truncated normal distribution

It is straightforward to generate a random variable x with a normal probability distribution

$$p_n(x) = \frac{1}{\sqrt{2\pi}} \, \mathrm{e}^{-x^2/2} \tag{112}$$

using, e.g., the Box-Muller method [19]. When taking a constraint into account, we need, however, variables with a normal distribution restricted to some interval, $x \in [a, b]$.

$\boldsymbol{x \geq a}$: When x is restricted to be larger than some value a, a straightforward approach is to sample normally distributed values x until we find an $x > a$. The probability for finding such an x is, on average, just the integral over the Gaussian

$$\bar{P}_n(a) = \int_a^\infty dx \, p_u(x) = I(a) \, . \tag{113}$$

This is easily written in terms of the complementary error function $\mathrm{erfc}(z) = 2/\sqrt{\pi} \int_z^\infty dt \, \mathrm{e}^{-t^2}$. For $a > 0$

$$I(a \geq 0) = \frac{1}{2} \, \mathrm{erfc}(a/\sqrt{2}) \, , \tag{114}$$

while for $a < 0$

$$I(a \leq 0) = 1 - I(-a) \, . \tag{115}$$

The average acceptance probability (113) is shown in figure 11. For a to the left of the peak of the normal distribution it is very likely that a proposed random variable x is larger than a and thus is accepted. For $a > 0$ this probability is, however, rapidly decreasing to zero, meaning that we would have to propose very many normally distributed variables x until we find one that is larger than a. This is very inefficient, so for $a > 0$ we need a better approach. Following [20], we generate random variables $x \geq a$ with an exponential probability distribution

$$p_{\mathrm{exp}}(x) = \alpha \, \mathrm{e}^{-\alpha(x-a)} \, . \tag{116}$$

These are easily obtained as $x = a - \ln(u/\alpha)/\alpha$ from uniformly distributed random numbers $u \in [0, 1)$. To transform these exponentially distributed random numbers $x \geq a$ into the desired normally distributed random numbers we use the rejection method [19], accepting x with probability proportional to the ratio $p_n(x)/p_{\mathrm{exp}}(x)$ of the desired and the proposed probability distribution functions. To obtain a probability, we introduce a prefactor to make sure that for no $x \geq a$ the ratio exceed one. Completing the square in the exponential we find

$$p_{\mathrm{acc}}(x; A) = \frac{1}{A} \frac{\mathrm{e}^{-x^2/2}}{\mathrm{e}^{-\alpha(x-a)}} = \frac{1}{A} \underbrace{\mathrm{e}^{-(x-\alpha)^2/2}}_{\leq 1} \mathrm{e}^{\alpha^2/2 - \alpha a} \overset{!}{\leq} 1 \, . \tag{117}$$

For $x \geq a$ the choice $A = \mathrm{e}^{\alpha^2/2 - \alpha a}$ maximizes the acceptance probability, which becomes

$$p_{\mathrm{acc}}(x) = \mathrm{e}^{-(x-\alpha)^2/2} \, . \tag{118}$$

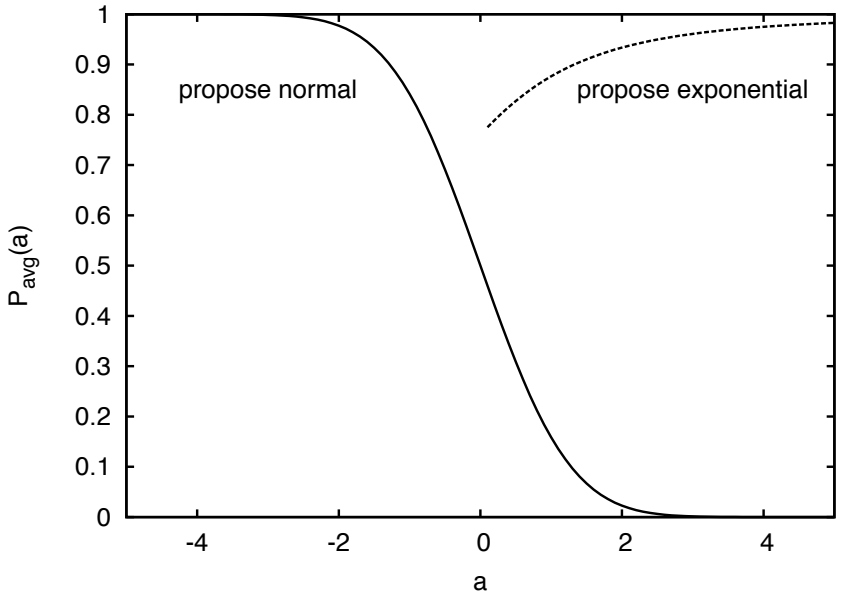


Fig. 11: *Efficiency of the methods for sampling from a normally distributed variable x restricted to the interval $[a,\infty)$: For $a<0$ the average acceptance probability for an unrestricted normally distributed random variable ($\bar{P}_n(a)$, full line) is larger than $1/2$, while for $a>0$ it rapidly approaches zero. For positive a we therefore propose exponentially distributed random numbers ($\bar{P}_{\rm exp}(a\geq 0)$, dotted line), for which the average acceptance probability is at least $\sqrt{\pi/2{\rm e}}\approx 0.76$.*

The corresponding average acceptance probability is then the integral of the product of the probability for proposing a value x times the probability for accepting it

$$\bar{P}_{\rm exp}(a\geq 0)=\int_a^\infty dx\; p_{\rm exp}(x)\,p_{\rm acc}(x)=\sqrt{2\pi}\,\alpha\,{\rm e}^{-\alpha^2/2+\alpha a}\,I(a) \tag{119}$$

In this expression α is still a free parameter, which we choose to maximize the average acceptance. Solving the variational equation we obtain

$$\alpha=\frac{a+\sqrt{a^2+4}}{2}\,. \tag{120}$$

We note that for $a\geq 0$, $\bar{P}_{\rm exp}(a)$ has the same form as (113), differing, however, by a prefactor $\gamma_{\rm exp}=\sqrt{2\pi}\,\alpha\,{\rm e}^{-\alpha^2/2+\alpha a}$ which grows faster than the complementary error function decays. Therefore, as can be seen from Fig. 11, for $a>0$ this method is dramatically more efficient than sampling from an unbounded uniform distribution. Thus for $a<0$ we choose the method with $\gamma_n=1$, while for $a\geq 0$ we choose $\gamma_{\rm exp}$, obtaining an average acceptance probability $\bar{P}_\gamma(a)=\gamma(a)\,I(a)$.

$\boldsymbol{x\geq b}$: When we need to sample a normal variable constrained from above we can use the same methods as above, sampling $-x\geq -b$, with average acceptance probability $\bar{P}_\gamma(-b)$.

$\boldsymbol{a\leq x\leq b}$: When the random variable is constrained to a finite interval, an obvious approach is to first sample an $x\in[a,\infty)$ and to accept it if $x\leq b$. The average acceptance probability is then $\bar{P}_\gamma(a)$ for proposing an $x\in[a,\infty)$, times $\int_a^b dx\,p_n(x)/\int_a^\infty dx\,p_n(x)$ for accepting it, i.e.,

$$\bar{P}_\gamma(a,b)=\gamma\big(I(a)-I(b)\big)\,. \tag{121}$$

For large intervals this will be an efficient approach, while for narrow intervals the acceptance will go to zero. In this case it becomes more efficient to propose x uniformly distributed on $[a, b]$ and accept them with probability

$$p_{\text{acc}} = \mathrm{e}^{-(x^2-m^2)/2}\,, \tag{122}$$

where m is the coordinate at which the normal distribution assumes its maximum value on $[a, b]$, ensuring that $p_{\text{acc}} \le 1$. When $0 \in [a, b]$ then $m = 0$, otherwise $m = \min(|a|, |b|)$. The average acceptance probability for this approach is

$$\bar{P}_u(a, b) = \int_a^b dx\, \frac{1}{b-a}\, \mathrm{e}^{-(x^2-m^2)/2} = \frac{\mathrm{e}^{m^2/2}}{b-a}\, \sqrt{2\pi}\big(I(a)-I(b)\big). \tag{123}$$

Again, (123) differs from (121) only by its prefactor γ_u, which increases as the width of the interval $b - a$ becomes smaller.
For a given interval $[a, b]$ we then choose the most efficient method:

- $a < 0 < b$: Since $a < 0$ we have to choose between normal sampling with $\gamma_n = 1$ and uniform sampling with $\gamma_u = \sqrt{2\pi}/(b-a)$. For $\gamma_n = \gamma_u$ both methods have the same average acceptance probability. Solving this gives us the critical width $w_0 = \sqrt{2\pi}$. For intervals $b - a < w_0$ we thus use uniform sampling with γ_u, otherwise γ_n. The worst case is $\bar{P}_{\gamma=1}(0, w_0) = I(0) - I(w_0) = \mathrm{erf}(\sqrt{\pi})/2 \approx 0.49$.

- $0 < a < b$: Since $a > 0$ we choose between exponential sampling with $\gamma_{\text{exp}} = \sqrt{2\pi}\,\alpha\,\mathrm{e}^{-\alpha^2/2+\alpha a}$ and $\gamma_u = \sqrt{2\pi}\,\mathrm{e}^{a^2/2}/(b-a)$. Solving $\gamma_{\text{exp}} = \gamma_u$ gives the critical width $w_>(a) = e^{(\alpha-a)^2/2}/\alpha$. For intervals $b-a < w_>(a)$ we use uniform sampling with γ_u, otherwise γ_{exp}. The worst case is $\bar{P}_\gamma(0, w_>(0)) = \gamma_{\text{exp}}\big(I(0) - I(\sqrt{e})\big) = \sqrt{\pi/2e}\,\mathrm{erf}(\sqrt{\mathrm{e}/2}) \approx 0.68$.

- $a < b < 0$: We sample $-x$ in the interval from $-b$ to $-a$ as described above.

Overall, we can thus sample from a truncated normal distribution with an average acceptance larger than $\mathrm{erf}(\sqrt{\pi})/2 \approx 0.49$.
The generalization to sampling from a Gaussian distribution $\exp(-(x-\mu)^2/2\sigma^2)/\sqrt{2\pi}\sigma$ of variance σ centered at μ restricted to $x \in [a, b]$ is then straightforward: use $x{=}\sigma\tilde{x}{+}\mu$, where $\tilde{x}$ is sampled, as described above, from a normal distribution (112) on the interval $[(a-\mu)/\sigma, (b-\mu)/\sigma]$.

References

[1] J. Hadamard, Princeton Univ. Bull. **13**, 49–52 (1902): ...ces problèmes se présentait comme parfaitement bien posé, je veux dire comme *possible* et *déterminé*.

[2] D.S. Sivia and J. Skilling: *Data Analysis: A Bayesian Tutorial* (Oxford Univ. Press, 2006)

[3] A. Flesch, E. Gorelov, E. Koch, and E. Pavarini, Phys. Rev. B **87**, 195141 (2013)

[4] A. Erdélyi (ed.): *Higher Transcendental Functions* (McGraw-Hill, New York, 1953)

[5] L. Boehnke, H. Hafermann, M. Ferrero, F. Lechermann, and O. Parcollet, Phys. Rev. B **84**, 075145 (2011)

[6] E. Koch: *The Lanczos Method* in E. Pavarini, E. Koch, D. Vollhardt, A. Lichtenstein (eds.): *The LDA+DMFT approach to strongly correlated materials* Modeling and Simulation Vol. 1 (Forschungszentrum Jülich, 2011)

[7] J. Waldvogel in: W. Gautschi, G. Mastroianni, T. Rassias (eds): *Approximation and Computation*, Springer Optimization and Its Applications, Vol. 42 (Springer, New York, 2010) p. 267

[8] K. Ghanem and E. Koch, Phys. Rev. B **107**, 085129 (2023)

[9] P.C. Hansen: *Discrete Inverse Problems* (SIAM, Philadelphia, 2010)

[10] M. Jarrell: *The Maximum Entropy Method: Analytic Continuation of QMC Data* in E. Pavarini, E. Koch, F. Anders, and M. Jarrell (eds.): *Correlated Electrons: From Models to Materials* Modeling and Simulation Vol. 2 (Forschungszentrum Jülich, 2012)

[11] S.R. White in D.P. Landau, K.K. Mon, and B.B. Schüttler: *Computer Simulation Studies in Condensed Matter Physics III* (Springer, 1991) p. 145–153

[12] K. Ghanem and E. Koch, Phys. Rev. B **101**, 085111 (2020); *ibid.* **102**, 035114 (2020)

[13] H. Flyvbjerg and H.G. Petersen, J. Chem. Phys. **91**, 461(1989)

[14] C.L. Lawson and R.J. Hanson: *Solving Least Squares Problems* (SIAM, 1995)

[15] C. Shannon, Bell Syst. Tech. J. **27**, 379 and 623 (1948)

[16] J. Skilling (ed.): *Maximum Entropy and Bayesian Methods* (Kluwer, 1989) p. 45–52

[17] K. Ghanem and E. Koch, Phys. Rev. B **108**, L201107 (2023)

[18] A. Rényi: *Probability Theory* (North Holland, 1970)

[19] W.H. Press, S.A. Teukolsky, W.T. Vetterling, and B.P. Flannery: *Numerical Recipes* (Cambridge University Press, 2007)

[20] C.P. Robert Statistics and Computing **5**, 121 (1995)

12 Functional Renormalization of Strongly Correlated Electrons: DMFT as a Booster Rocket

Walter Metzner
Max Planck Institute for Solid State Research
Heisenbergstr. 1, D-70569 Stuttgart

Contents

1 Introduction **2**

2 Functional RG for Fermi systems **3**
2.1 Generating functionals 4
2.2 Exact flow equation 6
2.3 Expansion in the fields 8

3 Two-dimensional Hubbard model **10**
3.1 Stability analysis at weak coupling 12
3.2 Spontaneous symmetry breaking 17

4 Leap to strong coupling: DMFT as a booster rocket **19**
4.1 Dynamical mean-field theory 19
4.2 From infinite to finite dimensions 20
4.3 Application to the 2D Hubbard model 21

5 Summary **24**

A Derivation of functional flow equation **25**

E. Pavarini, E. Koch, A. Lichtenstein, and D. Vollhardt (eds.)
Understanding Correlated Materials with DMFT
Modeling and Simulation Vol. 15
Forschungszentrum Jülich, 2025, ISBN 978-3-95806-813-1
http://www.cond-mat.de/events/correl25

1 Introduction

Correlated electron compounds exhibit very distinct behavior on different energy and length scales. Collective phenomena emerge at scales far below the bare energy scales of the microscopic Hamiltonian. For example, in high-temperature superconductors one bridges three orders of magnitude from the highest scale, the bare Coulomb interaction, via the intermediate scale of short-range magnetic correlations, down to the lowest scale of d-wave superconductivity and other ordering phenomena (see Fig. 1). This diversity of scales is a major obstacle to a direct numerical solution of microscopic models, since the most interesting phenomena emerge only in large systems at low temperatures. It is also hard to tackle by conventional many-body methods, if one tries to treat all scales at once and within the same approximation, for example by summing a subclass of Feynman diagrams. Perturbative approaches which do not separate different scales are plagued by infrared divergences, and are therefore often inapplicable even at weak coupling.

It is thus natural to treat degrees of freedom with different energy or length scales step by step. This is the main idea behind all *renormalization group* (RG) schemes. Using a functional integral representation this strategy can be implemented by integrating out degrees of freedom (bosonic or fermionic fields) successively, following a suitable order of scales. One thus generates a one-parameter family of effective actions which interpolates smoothly between the bare action of the system, as given by the microscopic Hamiltonian, and the final effective action from which all physical properties can be extracted. The Green or vertex functions corresponding to the effective action at scale Λ obey a hierarchy of differential flow equations. This hierarchy is exact and involves the flow of functions of generally continuous variables. For these reasons this approach is frequently referred to as *"exact"* or *"functional"* RG [1–4].

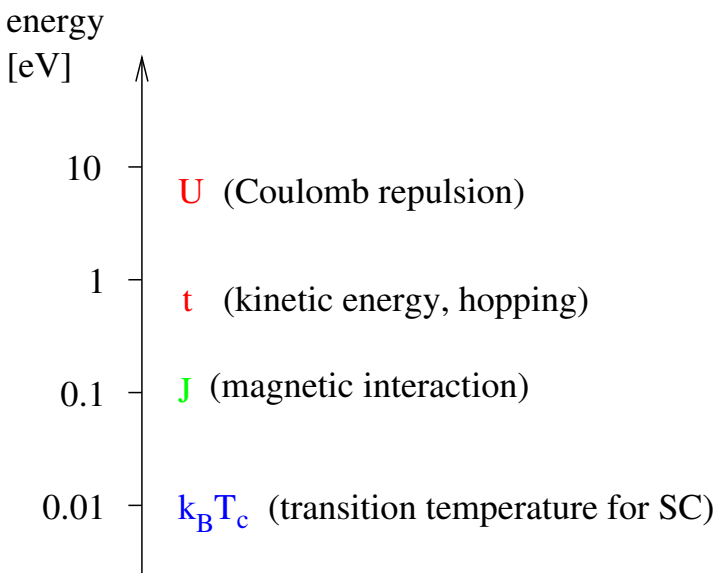


Fig. 1: *Energy scales in cuprate high-temperature superconductors. Magnetic interactions and superconductivity are generated from the kinetic energy and the Coulomb repulsion. Figure taken from Ref. [3].*

The exact hierarchy can be solved exactly only in special cases, where the underlying model can also be solved exactly (and more easily) by other means. However, the functional RG is a valuable source for devising powerful new approximation schemes, which can be obtained by truncating the hierarchy and/or by a simplified parametrization of the Green or vertex functions. These approximations have several distinctive advantages: i) they have a renormalization group structure built in, that is, scales are handled successively and infrared singularities are thus treated properly; ii) they can be applied directly to microscopic models, not only to effective field theories which capture only some asymptotic behavior; iii) they are physically transparent, for example one can see directly how and why new correlations form upon lowering the scale; iv) one can use different approximations at different scales. Small steps from a scale Λ to a slightly smaller scale Λ' are much easier to control than an integration over all degrees of freedom in one shot.

These lectures provide a concise introduction to the functional RG in the context of interacting Fermi systems. To illustrate the method at work, I review applications of the functional RG to the two-dimensional Hubbard model. A more detailed presentation and many other applications can be found in the comprehensive review articles Refs. [3] and [4]. Originally, the unavoidable truncations of the flow equation hierarchy limited the applications of the functional RG to relatively weakly interacting systems. In the final part I will explain how to use the DMFT solution of an interacting Fermi system as a non-perturbative starting point for a functional RG flow. With the DMFT as a "booster rocket", the functional RG can also be applied to *strongly* interacting fermion systems.

2 Functional RG for Fermi systems

Already in the 1970s, various RG methods have been used to deal with infrared singularities arising in one-dimensional Fermi systems [5]. Renormalization group approaches dealing with interacting fermions in higher dimensions have been developed much later. Due to the extended (not point-like) geometry of the Fermi surface singularity in dimensions $d > 1$, the renormalization group flow cannot be reduced to a small number of running couplings, even if irrelevant interactions are discarded. Aiming at a mathematical control of interacting Fermi systems, Feldman and Trubowitz [6], and independently Benfatto and Gallavotti [7], have formulated a *rigorous* fermionic version of Wilson's momentum-shell RG [8] for interacting fermions in dimensions $d > 1$. Important rigorous results for two-dimensional systems have indeed been obtained [9, 10]. An essential message from these results is that no hitherto unknown instabilities or non-perturbative effects occur in Fermi systems with sufficiently weak interactions, at least in the absence of special features such as van Hove singularities at the Fermi level. The Wilsonian RG for interacting Fermi systems was popularized among physicists by Shankar [11] and Polchinski [12], who presented some of the main ideas in a pedagogical style. In particular, they discussed an intuitive RG perspective of Fermi liquid theory.

The Wilsonian RG is not only useful for a rigorous understanding of interacting fermion systems. A specific variant of Wilson's RG known as *exact* or *functional* RG turned out to provide

a valuable framework for computational purposes. Approximations derived from exact functional flow equations play an increasingly important role in the theory of interacting Fermi systems [3, 4]. Exact flow equations describe the evolution of a generating functional for all many-particle correlation or vertex functions as a function of a flow parameter Λ, usually an infrared cutoff. They can be easily derived from a functional integral representation.

For computational purposes the exact flow equation for the effective action Γ^Λ, first derived in the context of bosonic field theories by Wetterich [13], turned out to be most convenient. The effective action is the generating functional for one-particle irreducible vertex functions. The latter are obtained by taking derivatives with respect to the source fields. The flow parameter Λ describes a regularization of the bare action, which regularizes infrared divergencies in perturbation theory. The regularization is removed at the end of the flow, say for $\Lambda \to 0$. The initial regulator (for $\Lambda = \Lambda_0$) can be chosen such that Γ^{Λ_0} is given by the bare action. The flow of Γ^Λ then provides a smooth interpolation between the bare action of the system and the final effective action Γ, from which any desired information can be extracted. This flow is determined by an exact functional differential equation [3, 4]. Expanding in the fields one obtains a hierarchy of flow equations for the one-particle irreducible vertex functions.

The expression *functional* RG stems from the feature that the exact flow equations describe the flow of a functional or (equivalently) of a hierarchy of functions. An important difference compared to Wilson's original formulation is that a complete set of source fields is kept in the flowing generating functionals, not only those corresponding to scales below Λ. Hence, the full information on the properties of the system remains accessible, not only the low energy or long wavelength behavior.

In the remainder of this section I present the exact flow equations and their expansion in the source fields. The first subsection summarizes the standard functional integral formalism as described, for example, in the excellent textbook by Negele and Orland [14].

2.1 Generating functionals

A system of interacting fermions can be represented by Grassmann fields ψ, $\bar\psi$, and an action of the form

$$\mathcal{S}[\psi,\bar\psi] = -(\bar\psi, G_0^{-1}\psi) + V[\psi,\bar\psi]\ , \tag{1}$$

where $V[\psi,\bar\psi]$ is an arbitrary many-body interaction, and G_0 is the propagator of the non-interacting system. The bracket $(.,.)$ is a shorthand notation for the sum $\sum_K \bar\psi_K\,(G_0^{-1}\psi)_K$, where $(G_0^{-1}\psi)_K = \sum_{K'} G_0^{-1}(K,K')\,\psi_{K'}$. The Grassmann field index K collects the quantum numbers of a suitable single-particle basis set and the Matsubara frequency. The K-sums include integrals over continuous variables, and normalization factors such as temperature and volume. In particular, for spin-$\frac{1}{2}$ fermions with a single-particle basis labeled by momentum $\mathbf{k}$ and spin orientation σ, one has $K = (k_0, \mathbf{k}, \sigma)$, where k_0 is the fermionic Matsubara frequency. If the bare part of the action is translation and spin-rotation invariant, the bare propagator has

the diagonal and spin-independent form $G_0(K,K') = \delta_{KK'}\, G_0(K)$ with

$$G_0(K) = \frac{1}{ik_0 - \xi_{\mathbf{k}}} \;, \tag{2}$$

where $\xi_{\mathbf{k}} = \epsilon_{\mathbf{k}} - \mu$ is the single-particle energy relative to the chemical potential. A two-particle interaction has the general form

$$V[\psi,\bar\psi] = \frac{1}{4} \sum_{K_1,K_2,K_1',K_2'} V(K_1',K_2';K_1,K_2)\, \bar\psi_{K_1'} \bar\psi_{K_2'} \psi_{K_2} \psi_{K_1} \;. \tag{3}$$

The generating functional

$$\mathcal{G}[\eta,\bar\eta] = -\log \int \prod_K d\psi_K d\bar\psi_K \, e^{-\mathcal{S}[\psi,\bar\psi]}\, e^{(\bar\eta,\psi)+(\bar\psi,\eta)} \;, \tag{4}$$

yields connected m-particle *Green functions* via derivatives with respect to the source fields, that is

$$\begin{aligned} G^{(2m)}(K_1,\cdots,K_m;K_1',\cdots,K_m') &= -\left\langle \psi_{K_1}\cdots\psi_{K_m}\bar\psi_{K_m'}\cdots\bar\psi_{K_1'}\right\rangle_c \\ &= (-1)^m \frac{\partial^m}{\partial\bar\eta_{K_1}\ldots\partial\bar\eta_{K_m}} \frac{\partial^m}{\partial\eta_{K_m'}\ldots\partial\eta_{K_1'}} \mathcal{G}[\eta,\bar\eta]\Big|_{\eta=\bar\eta=0} , \end{aligned} \tag{5}$$

where $\langle\cdots\rangle_c$ is the connected average of the product of Grassmann variables between the brackets. The one-particle Green function $G^{(2)}$ is the propagator of the interacting system, which is usually denoted without the superscript as G.
Legendre transforming $\mathcal{G}[\eta,\bar\eta]$ yields the *effective action*

$$\Gamma[\psi,\bar\psi] = (\bar\eta,\psi) + (\bar\psi,\eta) + \mathcal{G}[\eta,\bar\eta] \;, \tag{6}$$

where $\psi = -\partial\mathcal{G}/\partial\bar\eta$ and $\bar\psi = \partial\mathcal{G}/\partial\eta$. The effective action is the generating functional for one-particle irreducible *vertex functions*

$$\Gamma^{(2m)}(K_1',\ldots,K_m';K_1,\ldots,K_m) = \frac{\partial^{2m}\Gamma[\psi,\bar\psi]}{\partial\bar\psi_{K_1'}\ldots\partial\bar\psi_{K_m'}\partial\psi_{K_m}\ldots\partial\psi_{K_1}}\bigg|_{\psi,\bar\psi=0} . \tag{7}$$

The Legendre correspondence between the functionals $\mathcal{G}$ and Γ yields relations between the Green functions $G^{(2m)}$ and the vertex functions $\Gamma^{(2m)}$. In particular,

$$\Gamma^{(2)} = G^{-1} = G_0^{-1} - \Sigma \;, \tag{8}$$

where Σ is the self-energy. The two-particle Green function is related to the two-particle vertex by

$$G^{(4)}(K_1,K_2;K_1',K_2') = \sum_{P_1,P_2,P_1',P_2'} G(K_1,P_1')\, G(K_2,P_2')\, \Gamma^{(4)}(P_1',P_2';P_1,P_2)\, G(P_1,K_1')\, G(P_2,K_2'). \tag{9}$$

The effective action obeys the reciprocity relations

$$\frac{\partial \Gamma}{\partial \psi} = -\bar{\eta} \,, \quad \frac{\partial \Gamma}{\partial \bar{\psi}} = \eta \,. \tag{10}$$

The second functional derivatives of $\mathcal{G}$ and Γ with respect to the fields are also reciprocal. We define the matrices of second derivatives at *finite* source fields

$$\mathbf{G}^{(2)}[\eta,\bar{\eta}] = \begin{pmatrix} -\dfrac{\partial^2 \mathcal{G}}{\partial \bar{\eta}_K \, \partial \eta_{K'}} & \dfrac{\partial^2 \mathcal{G}}{\partial \bar{\eta}_K \, \partial \bar{\eta}_{K'}} \\ \dfrac{\partial^2 \mathcal{G}}{\partial \eta_K \, \partial \eta_{K'}} & -\dfrac{\partial^2 \mathcal{G}}{\partial \eta_K \, \partial \bar{\eta}_{K'}} \end{pmatrix} = - \begin{pmatrix} \langle \psi_K \bar{\psi}_{K'} \rangle & \langle \psi_K \psi_{K'} \rangle \\ \langle \bar{\psi}_K \bar{\psi}_{K'} \rangle & \langle \bar{\psi}_K \psi_{K'} \rangle \end{pmatrix}, \tag{11}$$

and

$$\mathbf{\Gamma}^{(2)}[\psi,\bar{\psi}] = \begin{pmatrix} \dfrac{\partial^2 \Gamma}{\partial \bar{\psi}_{K'} \, \partial \psi_K} & \dfrac{\partial^2 \Gamma}{\partial \bar{\psi}_{K'} \, \partial \bar{\psi}_K} \\ \dfrac{\partial^2 \Gamma}{\partial \psi_{K'} \, \partial \psi_K} & \dfrac{\partial^2 \Gamma}{\partial \psi_{K'} \, \partial \bar{\psi}_K} \end{pmatrix}. \tag{12}$$

The reciprocity relation for the second derivatives reads

$$\mathbf{\Gamma}^{(2)}[\psi,\bar{\psi}] = \big(\mathbf{G}^{(2)}[\eta,\bar{\eta}]\big)^{-1} . \tag{13}$$

Note that *anomalous* (off-diagonal) components are involved as long as the source fields are finite. Only at $\eta = \bar{\eta} = 0$ and $\psi = \bar{\psi} = 0$, and in the absence of $U(1)$ charge symmetry breaking one has the simple relation $\Gamma^{(2)} = G^{-1}$.

2.2 Exact flow equation

We now endow the bare propagator G_0 with a dependence on a *flow parameter* Λ. Usually Λ is a cutoff suppressing contributions from fields with a single-particle energy or a Matsubara frequency below the scale Λ in the functional integral. For example, in a translation invariant system this may be done by modifying $G_0(K)$ to

$$G_0^\Lambda(K) = \frac{\Theta^\Lambda(\mathbf{k})}{ik_0 - \xi_\mathbf{k}} \,, \tag{14}$$

where $\Theta^\Lambda(\mathbf{k})$ is a function that vanishes for $|\xi_\mathbf{k}| \ll \Lambda$ and tends to one for $|\xi_\mathbf{k}| \gg \Lambda$. In this way the infrared singularity of the propagator at $k_0 = 0$ and $\xi_\mathbf{k} = 0$ is cut off at the scale Λ. The simplest choice for Θ^Λ is a step function, $\Theta^\Lambda(\mathbf{k}) = \Theta\big(|\xi_\mathbf{k}| - \Lambda\big)$, such that momenta in a shell around the Fermi surface are strictly excluded (see Fig. 2).

In the first applications of the functional RG to interacting Fermi systems a momentum cutoff was used, but later a frequency cutoff became more popular, since the latter does not interfere with Fermi surface shifts, and particle-hole excitations with a small momentum transfer are captured smoothly by the flow [15]. Moreover, a frequency cutoff can also be used in systems without translation invariance, such as systems with impurities [16].

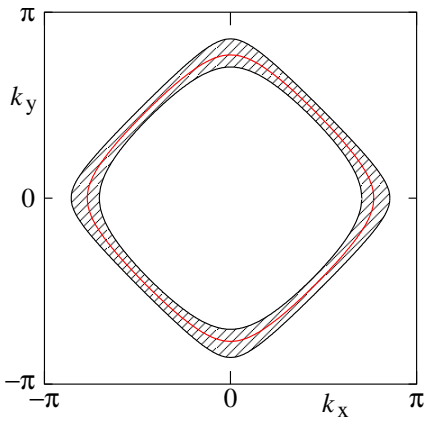


Fig. 2: *Momentum space region around the Fermi surface excluded by a sharp momentum cutoff in a two-dimensional lattice fermion system. Figure taken from Ref. [3].*

The generating functionals constructed with G_0^Λ instead of G_0 depend on the flow parameter and will be denoted by $\mathcal{G}^\Lambda[\eta,\bar\eta]$ and $\Gamma^\Lambda[\psi,\bar\psi]$. The original functionals $\mathcal{G}$ and Γ are recovered in the limit $\Lambda \to 0$. The evolution of $\Gamma^\Lambda[\psi,\bar\psi]$ as a function of Λ is described by an *exact functional flow equation* [3]

$$\frac{d}{d\Lambda}\Gamma^\Lambda[\psi,\bar\psi] = -\big(\bar\psi, \partial_\Lambda Q_0^\Lambda \psi\big) - \frac{1}{2}\,\mathrm{tr}\left[\big(\partial_\Lambda \mathbf{Q}_0^\Lambda\big)\,\big(\mathbf{\Gamma}^{(2)\Lambda}[\psi,\bar\psi]\big)^{-1}\right], \tag{15}$$

where

$$\mathbf{Q}_0^\Lambda = \begin{pmatrix} Q_0^\Lambda(K,K') & 0 \\ 0 & -Q_0^\Lambda(K',K) \end{pmatrix} \tag{16}$$

with $Q_0^\Lambda = (G_0^\Lambda)^{-1}$, and $\mathbf{\Gamma}^{(2)\Lambda}[\psi,\bar\psi]$ is the matrix of second derivatives of Γ^Λ at finite fields,

$$\mathbf{\Gamma}^{(2)\Lambda}[\psi,\bar\psi] = \begin{pmatrix} \dfrac{\partial^2\Gamma^\Lambda}{\partial\bar\psi_K\,\partial\psi_{K'}} & \dfrac{\partial^2\Gamma^\Lambda}{\partial\bar\psi_K\,\partial\bar\psi_{K'}} \\ \dfrac{\partial^2\Gamma^\Lambda}{\partial\psi_K\,\partial\psi_{K'}} & \dfrac{\partial^2\Gamma^\Lambda}{\partial\psi_K\,\partial\bar\psi_{K'}} \end{pmatrix}. \tag{17}$$

The trace on the right hand side of the flow equations includes a sum over the Grassmann field index K. Note that the inversion of $\mathbf{\Gamma}^{(2)\Lambda}[\psi,\bar\psi]$ in Eq. (15) is not merely an inversion of a 2×2 matrix, since it involves also the additional matrix structure coming from the dependence on the Grassmann field indices K and K'. A derivation of the functional flow equation (15) is presented in Appendix A.

Alternative definitions of the effective action Γ^Λ, differing by interaction-independent terms, have also been used. A frequently used variant is [1,4]

$$\Gamma_R^\Lambda[\psi,\bar\psi] = \Gamma^\Lambda[\psi,\bar\psi] + (\bar\psi, R^\Lambda\psi)\,, \tag{18}$$

where $R^\Lambda = Q_0^\Lambda - Q_0$. The additional quadratic term cancels the first term in the flow equation (15) for Γ^Λ, and one obtains the equivalent flow equation

$$\frac{d}{d\Lambda}\Gamma_R^\Lambda[\psi,\bar\psi] = -\frac{1}{2}\,\mathrm{tr}\left[\big(\partial_\Lambda \mathbf{R}^\Lambda\big)\,\Big(\mathbf{\Gamma}_R^{(2)\Lambda}[\psi,\bar\psi] + \mathbf{R}^\Lambda\Big)^{-1}\right], \tag{19}$$

where $\mathbf{R}^\Lambda = \mathrm{diag}\left(R^\Lambda(K,K'), -R^\Lambda(K',K)\right)$. The functional Γ_R^Λ and its analogue for bosonic fields is known as *effective average action* in the literature [1]. Both Γ_R^Λ and Γ^Λ tend to the same effective action Γ in the limit $\Lambda \to 0$, where R^Λ vanishes.
Choosing the initial cutoff Λ_0 such that $G_0^{\Lambda_0}$ is identically zero, all contributions to the functional integral are suppressed. For a sharp momentum cutoff this is achieved by choosing Λ_0 larger than $\max_{\mathbf{k}} |\xi_{\mathbf{k}}|$, while for a frequency cutoff one has to start with $\Lambda_0 = \infty$ to eliminate all modes. At the initial scale Λ_0, one then has the simple initial condition $\Gamma_R^{\Lambda_0}[\psi,\bar\psi] = \mathcal{S}[\psi,\bar\psi]$, while

$$\Gamma^{\Lambda_0}[\psi,\bar\psi] = -(\bar\psi, Q_0^{\Lambda_0}\psi) + V[\psi,\bar\psi] = \mathcal{S}^{\Lambda_0}[\psi,\bar\psi] = \mathcal{S}[\psi,\bar\psi] - (\bar\psi, R^{\Lambda_0}\psi)\ . \tag{20}$$

Hence, Γ_R^Λ interpolates smoothly between the (unregularized) bare action $\mathcal{S}$ and the final effective action Γ, while Γ^Λ interpolates between the *regularized* bare action $\mathcal{S}^{\Lambda_0}$ and Γ. The initial "regularization" with $Q_0^{\Lambda_0} = \infty$ amounts to a complete suppression of all contributions to the functional integral, not just a regularization of divergent contributions.

2.3 Expansion in the fields

Expanding the functional flow equation (15) for the effective action in powers of the fields yields a hierarchy of flow equations for the m-particle vertex functions. To expand the inverse of $\mathbf{\Gamma}^{(2)\Lambda}[\psi,\bar\psi]$, we split

$$\mathbf{\Gamma}^{(2)\Lambda}[\psi,\bar\psi] = (\mathbf{G}^\Lambda)^{-1} - \tilde{\mathbf{\Sigma}}^\Lambda[\psi,\bar\psi]\ , \tag{21}$$

where

$$\mathbf{G}^\Lambda = \left(\mathbf{\Gamma}^{(2)\Lambda}[\psi,\bar\psi]\big|_{\psi=\bar\psi=0}\right)^{-1} = \begin{pmatrix} G^\Lambda(K,K') & 0 \\ 0 & -G^\Lambda(K',K) \end{pmatrix}, \tag{22}$$

and $\tilde{\mathbf{\Sigma}}^\Lambda[\psi,\bar\psi]$ contains all contributions which are at least quadratic in the fields. Now the inverse of $\mathbf{\Gamma}^{(2)\Lambda}[\psi,\bar\psi]$ can be expanded in a geometric series,

$$\begin{aligned}\left(\mathbf{\Gamma}^{(2)\Lambda}[\psi,\bar\psi]\right)^{-1} &= \left(1 - \mathbf{G}^\Lambda\tilde{\mathbf{\Sigma}}^\Lambda[\psi,\bar\psi]\right)^{-1}\mathbf{G}^\Lambda \\ &= \left[1 + \mathbf{G}^\Lambda\tilde{\mathbf{\Sigma}}^\Lambda[\psi,\bar\psi] + (\mathbf{G}^\Lambda\tilde{\mathbf{\Sigma}}^\Lambda[\psi,\bar\psi])^2 + \dots\right]\mathbf{G}^\Lambda.\end{aligned} \tag{23}$$

Inserting this into the functional flow equation yields

$$\begin{aligned}\frac{d}{d\Lambda}\Gamma^\Lambda[\psi,\bar\psi] = &-\mathrm{tr}\left[(\partial_\Lambda Q_0^\Lambda)G^\Lambda\right] - \left(\bar\psi, \partial_\Lambda Q_0^\Lambda\psi\right) \\ &+ \frac{1}{2}\,\mathrm{tr}\left(\mathbf{S}^\Lambda(\tilde{\mathbf{\Sigma}}^\Lambda[\psi,\bar\psi] + \tilde{\mathbf{\Sigma}}^\Lambda[\psi,\bar\psi]\mathbf{G}^\Lambda\tilde{\mathbf{\Sigma}}^\Lambda[\psi,\bar\psi] + \dots)\right),\end{aligned} \tag{24}$$

with the so-called *single scale propagator*

$$\mathbf{S}^\Lambda = -\mathbf{G}^\Lambda\left(\partial_\Lambda \mathbf{Q}_0^\Lambda\right)\mathbf{G}^\Lambda = \frac{d}{d\Lambda}\mathbf{G}^\Lambda\Big|_{\mathbf{\Sigma}^\Lambda\ \mathrm{fixed}}\ . \tag{25}$$

The latter usually has its main support *at* the scale Λ. For example, for a sharp momentum cutoff acting on $\xi_{\mathbf{k}}$ as in Eq. (14), $\mathbf{S}^\Lambda$ has a delta-peak at $|\xi_{\mathbf{k}}| = \Lambda$ and vanishes elsewhere.

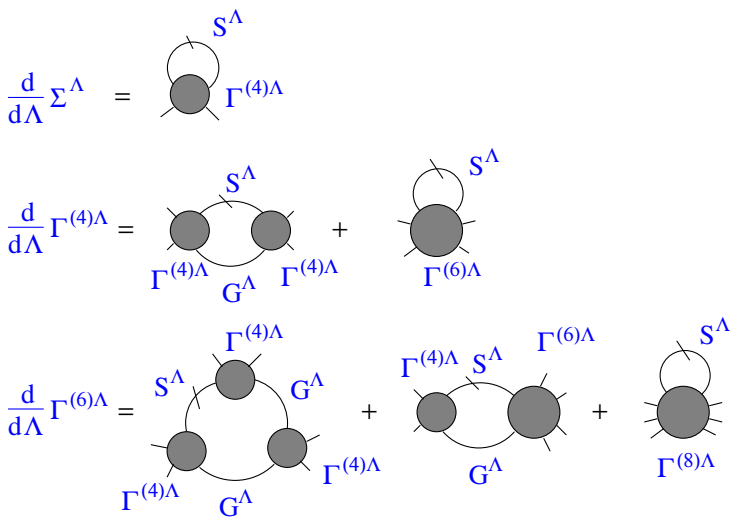


Fig. 3: *Diagrammatic representation of the flow equations for the self-energy, the two-particle vertex, and the three-particle vertex. Lines with a dash correspond to the single-scale propagator S^Λ, and the other lines to the full propagator G^Λ. Figure taken from Ref. [3].*

Expanding $\Gamma^\Lambda[\psi,\bar\psi]$ and $\tilde{\mathbf{\Sigma}}^\Lambda[\psi,\bar\psi]$ in powers of ψ and $\bar\psi$, and comparing coefficients in Eq. (24), one obtains the flow equations for the self-energy $\Sigma^\Lambda = Q_0^\Lambda - \Gamma^{(2)\Lambda}$, the two-particle vertex $\Gamma^{(4)\Lambda}$, and all other m-particle vertices. The first three equations of this hierarchy are represented diagrammatically in Fig. 3. Note that only one-particle irreducible one-loop diagrams contribute, and internal lines are dressed by the self-energy. Contributions with several loops are generated only indirectly upon inserting the flow of higher order vertices into lower order flow equations. The flow equation for the self-energy has the simple form [3]

$$\frac{d}{d\Lambda}\Sigma^\Lambda(K',K) = \sum_{P,P'} S^\Lambda(P,P')\,\Gamma^{(4)\Lambda}(K',P';K,P). \tag{26}$$

The flow equation for the two-particle vertex reads [3]

$$\begin{aligned}\frac{d}{d\Lambda}\Gamma^{(4)\Lambda}(K_1',K_2';K_1,K_2) = &-\sum_{P_1,P_1'}\sum_{P_2,P_2'} G^\Lambda(P_1,P_1')\,S^\Lambda(P_2,P_2')\\
&\times\Big\{\Gamma^{(4)\Lambda}(K_1',K_2';P_1,P_2)\Gamma^{(4)\Lambda}(P_1',P_2';K_1,K_2)\\
&-\Big[\Gamma^{(4)\Lambda}(K_1',P_2';K_1,P_1)\Gamma^{(4)\Lambda}(P_1',K_2';P_2,K_2)+(P_1\leftrightarrow P_2,P_1'\leftrightarrow P_2')\Big]\\
&+\Big[\Gamma^{(4)\Lambda}(K_2',P_2';K_1,P_1)\Gamma^{(4)\Lambda}(P_1',K_1';P_2,K_2)+(P_1\leftrightarrow P_2,P_1'\leftrightarrow P_2')\Big]\Big\}\\
&-\sum_{P,P'} S^\Lambda(P,P')\,\Gamma^{(6)\Lambda}(K_1',K_2',P';K_1,K_2,P)\,.\end{aligned} \tag{27}$$

There are several contributions which are quadratic in $\Gamma^{(4)\Lambda}$, corresponding to the particle-particle, direct particle-hole, and crossed particle-hole channel, respectively.

The one-particle irreducibility is a convenient feature of flow equations derived from the effective action $\Gamma^\Lambda[\psi,\bar\psi]$. Flow equations derived from other functionals, such as the Polchinski equations [17] and their Wick ordered variant [9], contain also one-particle reducible contributions.

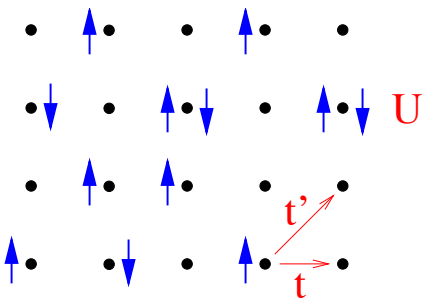


Fig. 4: *Hubbard model with nearest and next-to-nearest neighbor hopping on a square lattice.*

The full hierarchy of flow equations does not close at any finite order, since the flow of each $\Gamma^{(2m)\Lambda}$ receives a contribution from a tadpole diagram with $\Gamma^{(2m+2)\Lambda}$. Exact solutions of the flow equation hierarchy are possible only for relatively simple models, such as the Luttinger model [18], the reduced BCS model [19], or other mean-field models [20, 21], which can also be solved more directly by other methods. Usually the hierarchy of flow equations has to be truncated by neglecting effective interactions of higher order, and by using a simplified parametrization of the functional dependence of the remaining interactions on momenta, frequencies, et cetera. Truncations of the hierarchy at some finite order can be justified in case of sufficiently weak interactions, or if higher order terms are suppressed due to small phase space volumina [22]. Geometrical phase space restrictions are typically stronger in multi-loop integrals. A simplified parametrization of effective interactions can be obtained by neglecting dependences which become irrelevant in the low-energy limit.

3 Two-dimensional Hubbard model

Shortly after the discovery of high-temperature superconductivity in several cuprate compounds, Anderson [23] pointed out that the essential physics of the electrons in the copper-oxide planes of these materials can be described by the two-dimensional Hubbard model. The Hubbard model describes tight-binding electrons with inter-site hopping amplitudes $t_{\mathbf{ij}}$ and a local repulsion $U > 0$, as specified by the Hamiltonian (see also Fig. 4)

$$H = \sum_{\mathbf{i},\mathbf{j}} \sum_{\sigma} t_{\mathbf{ij}}\, c^{\dagger}_{\mathbf{i}\sigma} c_{\mathbf{j}\sigma} + U \sum_{\mathbf{j}} n_{\mathbf{j}\uparrow} n_{\mathbf{j}\downarrow} \,. \tag{28}$$

Here $c^{\dagger}_{\mathbf{i}\sigma}$ and $c_{\mathbf{i}\sigma}$ are creation and annihilation operators for spin-$\frac{1}{2}$ fermions with spin orientation σ on a lattice site $\mathbf{i}$, and $n_{\mathbf{j}\sigma} = c^{\dagger}_{\mathbf{j}\sigma} c_{\mathbf{j}\sigma}$. The number of lattice sites will be denoted by L. A hopping amplitude $-t$ between nearest neighbors and an amplitude $-t'$ between next-nearest neighbors on a square lattice leads to the dispersion relation

$$\epsilon_{\mathbf{k}} = -2t\big(\cos k_x + \cos k_y\big) - 4t'\big(\cos k_x \, \cos k_y\big) \tag{29}$$

for single-particle states. This dispersion relation has saddle points at $\mathbf{k} = (0,\pi)$ and $(\pi,0)$, which entail logarithmic van Hove singularities in the non-interacting density of states at the

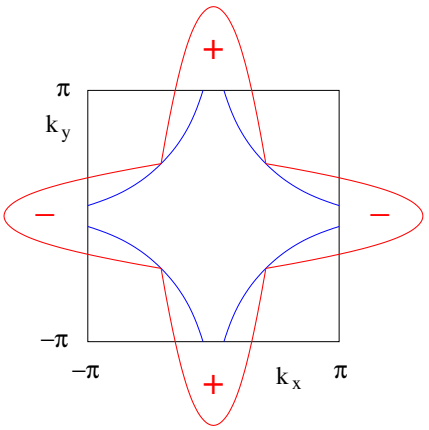


Fig. 5: *Schematic shape of the gap function $\Delta_{\mathbf{k}}$ with $d_{x^2-y^2}$-wave symmetry, for $\mathbf{k}$ tracing the Fermi surface.*

energy $\epsilon_{\mathrm{vH}} = 4t'$. For recent reviews on the two-dimensional Hubbard model, see Refs. [24] and [25].

In agreement with the generic phase diagram of the cuprates, the Hubbard model exhibits antiferromagnetic order at half-filling, and is expected to become a d-wave superconductor away from half-filling in two dimensions already for quite some time [26]. The exchange of antiferromagnetic spin fluctuations has been proposed as a plausible mechanism leading to d-wave pairing [27–29]. In this picture the BCS effective interaction $V_{\mathbf{k}\mathbf{k}'}$ is roughly proportional to the spin correlation function $\chi_s(\mathbf{q})$ at $\mathbf{q} = \mathbf{k}-\mathbf{k}'$. Close to half-filling, $\chi_s(\mathbf{q})$ has a pronounced maximum at or near the antiferromagnetic wave vector (π, π). As a consequence, the BCS gap equation

$$\Delta_{\mathbf{k}} = -\int \frac{d^2\mathbf{k}'}{(2\pi)^2}\, V_{\mathbf{k}\mathbf{k}'}\, \frac{\Delta_{\mathbf{k}'}}{2E_{\mathbf{k}'}} \tag{30}$$

with $E_{\mathbf{k}} = \left(\xi_{\mathbf{k}}^2 + |\Delta_{\mathbf{k}}|^2\right)^{1/2}$ has a solution with $d_{x^2-y^2}$-wave symmetry, such that the gap $\Delta_{\mathbf{k}}$ has maximal modulus but opposite sign near the points $(\pi, 0)$ and $(0, \pi)$ in the Brillouin zone, respectively [26], as illustrated in Fig. 5. This qualitative argument has been corroborated by a self-consistent perturbative solution of the two-dimensional Hubbard model within the so-called fluctuation-exchange approximation [30, 31].

The spin-fluctuation mechanism for pairing might be spoiled by other contributions to the BCS interactions, and also by spin density wave instabilities. It turned out to be very hard to detect superconductivity in the Hubbard model by exact numerical computation [25], as a consequence of finite size and/or temperature limitations. Fortunately, the tendency toward antiferromagnetism and d-wave pairing is already captured by the two-dimensional Hubbard model at *weak* coupling. Conventional perturbation theory breaks down for densities close to half-filling, since competing infrared divergences appear as a consequence of Fermi surface nesting and van Hove singularities. A controlled and unbiased treatment of these divergences is achieved by a renormalization group analysis, which takes into account the particle-particle and particle-hole channels on equal footing.

Early RG studies of the two-dimensional Hubbard model started with simple scaling approaches, very shortly after the discovery of high-T_c superconductivity [32–34]. These studies focussed on dominant scattering processes between the van Hove points in $\mathbf{k}$-space, for which a small number of running couplings could be defined and computed on one-loop level. Spin-density and superconducting instabilities were identified from divergences of the corresponding correlation functions.

A complete treatment of all scattering processes in the Brillouin zone is more complicated since the effective interactions cannot be parametrized accurately by a small number of variables, even if irrelevant momentum and energy dependences are neglected. The *tangential* momentum dependence of effective interactions along the Fermi surface is strong and important in the low-energy limit. Hence, one has to deal with the renormalization of *functions*. This problem is treated most naturally by the functional RG.

3.1 Stability analysis at weak coupling

To detect instabilities in the weak-coupling limit, one can truncate the infinite hierarchy of flow equations at second order in the effective two-particle interaction and discard all vertices of higher order, and also self-energy corrections. The flow of the two-particle vertex is then fully determined by the first contribution in the second line of Fig. 3. In the absence of self-energy corrections, the internal lines are given by the bare propagator G_0^Λ and its scale derivative $S_0^\Lambda = \frac{d}{d\Lambda} G_0^\Lambda$.

Due to translation invariance on the lattice, G_0^Λ is diagonal in momentum representation, that is, $G_0^\Lambda(K,K') = \delta_{KK'}\, G_0^\Lambda(K)$, where $K = (k,\sigma)$ with $k = (k_0, \mathbf{k})$. Hence, the truncated (without $\Gamma^{(6)\Lambda}$) flow equation (27) for the two-particle vertex can be written as

$$\begin{aligned}\frac{d}{d\Lambda}\Gamma^\Lambda(K_1',K_2';K_1,K_2) = &-\frac{1}{\beta L}\sum_{P,P'}\frac{d}{d\Lambda}\left[G_0^\Lambda(P)\,G_0^\Lambda(P')\right]\\ &\times\Big[\frac{1}{2}\Gamma^\Lambda(K_1',K_2';P,P')\Gamma^\Lambda(P,P';K_1,K_2)\\ &\quad -\Gamma^\Lambda(K_1',P';K_1,P)\Gamma^\Lambda(P,K_2';P',K_2)\\ &\quad +\Gamma^\Lambda(K_2',P';K_1,P)\Gamma^\Lambda(P,K_1';P',K_2)\Big]. \qquad (31)\end{aligned}$$

Here and in the following we denote the two-particle vertex as Γ^Λ, and we now write temperature ($\beta = 1/T$) and volume factors explicitly. The three terms on the right hand side correspond to the particle-particle (PP), the direct particle-hole (PH) and the crossed particle-hole (PH') channel, respectively, see Fig. 6.

Due to spin rotation invariance, the spin structure of the two-particle vertex is relatively simple. One can express the vertex by a single function V^Λ depending only on momenta and Matsubara frequencies [22]

$$\Gamma^\Lambda(K_1',K_2';K_1,K_2) = V^\Lambda(k_1',k_2';k_1,k_2)\,\delta_{\sigma_1\sigma_{1'}}\,\delta_{\sigma_2\sigma_{2'}} - V^\Lambda(k_2',k_1';k_1,k_2)\,\delta_{\sigma_1\sigma_{2'}}\,\delta_{\sigma_2\sigma_{1'}}. \quad (32)$$

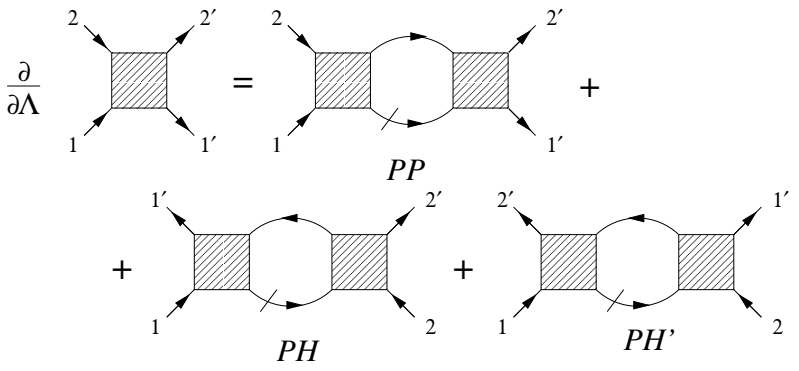


Fig. 6: *One-loop flow equation for the two-particle vertex Γ^Λ with the particle-particle channel (PP) and the two particle-hole channels (PH and PH') written explicitly.*

Alternatively, one may decompose the vertex in singlet and triplet components [35],

$$\Gamma^\Lambda(K_1', K_2'; K_1, K_2) = \Gamma_s^\Lambda(k_1', k_2'; k_1, k_2)\, S_{\sigma_1',\sigma_2';\sigma_1,\sigma_2} + \Gamma_t^\Lambda(k_1', k_2'; k_1, k_2)\, T_{\sigma_1',\sigma_2';\sigma_1,\sigma_2}\,, \quad (33)$$

where

$$\begin{aligned} S_{\sigma_1',\sigma_2';\sigma_1,\sigma_2} &= \tfrac{1}{2}\left(\delta_{\sigma_1\sigma_1'}\,\delta_{\sigma_2\sigma_2'} - \delta_{\sigma_1\sigma_2'}\,\delta_{\sigma_2\sigma_1'}\right)\,, \\ T_{\sigma_1',\sigma_2';\sigma_1,\sigma_2} &= \tfrac{1}{2}\left(\delta_{\sigma_1\sigma_1'}\,\delta_{\sigma_2\sigma_2'} + \delta_{\sigma_1\sigma_2'}\,\delta_{\sigma_2\sigma_1'}\right)\,. \end{aligned} \quad (34)$$

Of course one can easily compute Γ_s^Λ and Γ_t^Λ from V^Λ and vice versa [21]. The singlet vertex is symmetric and the triplet vertex is antisymmetric under exchanges $k_1 \leftrightarrow k_2$ or $k_1' \leftrightarrow k_2'$.
We now outline the steps made to cast the one-loop flow equations in a form amenable to a numerical solution. To be specific, we use the singlet-triplet decomposition of the vertex and a momentum cutoff. Carrying out the spin sum in the flow equation one obtains

$$\begin{aligned} \partial_\Lambda \Gamma_\alpha^\Lambda(k_1', k_2'; k_1, k_2) = -\sum_{i=s,t}\sum_{j=s,t} \big[& C_{\alpha ij}^{\mathrm{PP}} \beta_{ij}^{\mathrm{PP}}(k_1', k_2'; k_1, k_2) \\ & + C_{\alpha ij}^{\mathrm{PH}} \beta_{ij}^{\mathrm{PH}}(k_1', k_2'; k_1, k_2) + C_{\alpha ij}^{\mathrm{PH}'} \beta_{ij}^{\mathrm{PH}'}(k_1', k_2'; k_1, k_2)\big] \end{aligned} \quad (35)$$

for $\alpha = s, t$, where $C_{\alpha ij}^{\mathrm{PP}}$ etc. are simple numerical coefficients [35] and

$$\begin{aligned} \beta_{ij}^{\mathrm{PP}}(k_1', k_2'; k_1, k_2) &= \frac{1}{2\beta L}\sum_{k,k'} \partial_\Lambda \left[G_0^\Lambda(k)\, G_0^\Lambda(k')\right] \Gamma_i^\Lambda(k_1', k_2'; k, k')\, \Gamma_j^\Lambda(k, k'; k_1, k_2), \\ \beta_{ij}^{\mathrm{PH}}(k_1', k_2'; k_1, k_2) &= -\frac{1}{\beta L}\sum_{k,k'} \partial_\Lambda \left[G_0^\Lambda(k)\, G_0^\Lambda(k')\right] \Gamma_i^\Lambda(k_1', k; k_1, k')\, \Gamma_j^\Lambda(k', k_2'; k, k_2), \\ \beta_{ij}^{\mathrm{PH}'}(k_1', k_2'; k_1, k_2) &= -\beta_{ij}^{\mathrm{PH}}(k_2', k_1'; k_1, k_2). \end{aligned} \quad (36)$$

It is clearly impossible to solve the flow equations with the full energy and momentum dependence of the vertex function, since Γ^Λ has three independent energy and momentum variables. However, the flow equations can be simplified considerably by ignoring dependences which are irrelevant (in the RG sense) in the low-energy limit, that is, the energy dependence and the momentum dependence normal to the Fermi surface [3, 11].

Neglecting the energy dependence, we approximate

$$\Gamma^{\Lambda}_{\alpha}(k'_1,k'_2;k_1,k_2) \approx \Gamma^{\Lambda}_{\alpha}(\mathbf{k}'_1,\mathbf{k}'_2;\mathbf{k}_1,\mathbf{k}_2). \tag{37}$$

Choosing an energy independent cutoff function $\Theta^{\Lambda}(\mathbf{k})$ as in Eq. (14), the Matsubara sums on the right hand side of the flow equations can be performed analytically, yielding

$$\begin{aligned}\partial_{\Lambda}\Gamma^{\Lambda}_{\alpha}(\mathbf{k}'_1,\mathbf{k}'_2;\mathbf{k}_1,\mathbf{k}_2) = -\sum_{i=s,t}\sum_{j=s,t}\big[&C^{\mathrm{PP}}_{\alpha ij}\beta^{\mathrm{PP}}_{ij}(\mathbf{k}'_1,\mathbf{k}'_2;\mathbf{k}_1,\mathbf{k}_2)\\ &+ C^{\mathrm{PH}}_{\alpha ij}\beta^{\mathrm{PH}}_{ij}(\mathbf{k}'_1,\mathbf{k}'_2;\mathbf{k}_1,\mathbf{k}_2) + C^{\mathrm{PH}'}_{\alpha ij}\beta^{\mathrm{PH}'}_{ij}(\mathbf{k}'_1,\mathbf{k}'_2;\mathbf{k}_1,\mathbf{k}_2)\big]\end{aligned} \tag{38}$$

for $\alpha = s,t$, where the β-functions are now energy independent and read

$$\begin{aligned}\beta^{\mathrm{PP}}_{ij}(\mathbf{k}'_1,\mathbf{k}'_2;\mathbf{k}_1,\mathbf{k}_2) &= \frac{1}{2L}\sum_{\mathbf{k},\mathbf{k}'}\partial_{\Lambda}\left[\Theta^{\Lambda}(\mathbf{k})\,\Theta^{\Lambda}(\mathbf{k}')\right]\\ &\qquad\times\frac{f(-\xi_{\mathbf{k}})-f(\xi_{\mathbf{k}'})}{\xi_{\mathbf{k}}+\xi_{\mathbf{k}'}}\,\Gamma^{\Lambda}_{i}(\mathbf{k}'_1,\mathbf{k}'_2;\mathbf{k},\mathbf{k}')\,\Gamma^{\Lambda}_{j}(\mathbf{k},\mathbf{k}';\mathbf{k}_1,\mathbf{k}_2),\\ \beta^{\mathrm{PH}}_{ij}(\mathbf{k}'_1,\mathbf{k}'_2;\mathbf{k}_1,\mathbf{k}_2) &= -\frac{1}{L}\sum_{\mathbf{k},\mathbf{k}'}\partial_{\Lambda}\left[\Theta^{\Lambda}(\mathbf{k})\,\Theta^{\Lambda}(\mathbf{k}')\right]\\ &\qquad\times\frac{f(\xi_{\mathbf{k}})-f(\xi_{\mathbf{k}'})}{\xi_{\mathbf{k}}-\xi_{\mathbf{k}'}}\,\Gamma^{\Lambda}_{i}(\mathbf{k}'_1,\mathbf{k};\mathbf{k}_1,\mathbf{k}')\,\Gamma^{\Lambda}_{j}(\mathbf{k}',\mathbf{k}'_2;\mathbf{k},\mathbf{k}_2),\\ \beta^{\mathrm{PH}'}_{ij}(\mathbf{k}'_1,\mathbf{k}'_2;\mathbf{k}_1,\mathbf{k}_2) &= -\beta^{\mathrm{PH}}_{ij}(\mathbf{k}'_2,\mathbf{k}'_1;\mathbf{k}_1,\mathbf{k}_2),\end{aligned} \tag{39}$$

with the Fermi function $f(\xi)=1/\big(e^{\beta\xi}+1\big)$. Note that momentum conservation implies that $\mathbf{k}$ and $\mathbf{k}'$ are related by $\mathbf{k}+\mathbf{k}'=\mathbf{k}_1+\mathbf{k}_2$ in the particle-particle channel and by $\mathbf{k}+\mathbf{k}'_1=\mathbf{k}'+\mathbf{k}_1$ in the direct particle-hole channel. Hence, only one independent momentum variable needs to be summed. For a sharp momentum cutoff $\Theta^{\Lambda}(\mathbf{k})=\Theta\big(|\xi_{\mathbf{k}}|-\Lambda\big)$ one has $\partial_{\Lambda}\Theta^{\Lambda}(\mathbf{k})=-\delta\big(|\xi_{\mathbf{k}}|-\Lambda\big)$, so that the two-dimensional momentum integral can be reduced to a one-dimensional integral. The flow equation can be solved only if the momentum dependence of the vertex function is simplified. At least for weak coupling (in practice also for moderate ones), the vertex function acquires strong momentum dependences only for momenta close to the Fermi surface. Note that for the Hubbard model the bare vertex function Γ^{Λ_0} does not depend on momentum at all. Weak coupling instabilities are signalled by divergencies of the vertex function Γ^{Λ} which are driven by momenta close to the Fermi surface. Hence we will focus on the flow of the vertex function with momenta close to the Fermi surface. For arbitrary momenta, we approximate the vertex by

$$\Gamma^{\Lambda}_{\alpha}(\mathbf{k}'_1,\mathbf{k}'_2;\mathbf{k}_1,\mathbf{k}_2) \approx \Gamma^{\Lambda}_{\alpha}(\mathbf{k}'_{F1},\mathbf{k}_{F1}+\mathbf{k}_{F2}-\mathbf{k}'_{F1};\mathbf{k}_{F1},\mathbf{k}_{F2}), \tag{40}$$

where $\mathbf{k}_{F1}$ etc. are projections of $\mathbf{k}_1$ etc. on the Fermi surface (see Fig. 7). Strong momentum dependences of the effective vertex are built up only by contributions with intermediate momenta $\mathbf{k}$ and $\mathbf{k}'$ (on the right hand side of the flow equations) which are close to the Fermi surface, because for such momenta the ratios $\big(f(\mp\xi_{\mathbf{k}})-f(\xi_{\mathbf{k}'})\big)/(\xi_{\mathbf{k}}\pm\xi_{\mathbf{k}'})$ in Eq. (39) can be big. Hence, for the most important momenta, the error made by the projection is relatively

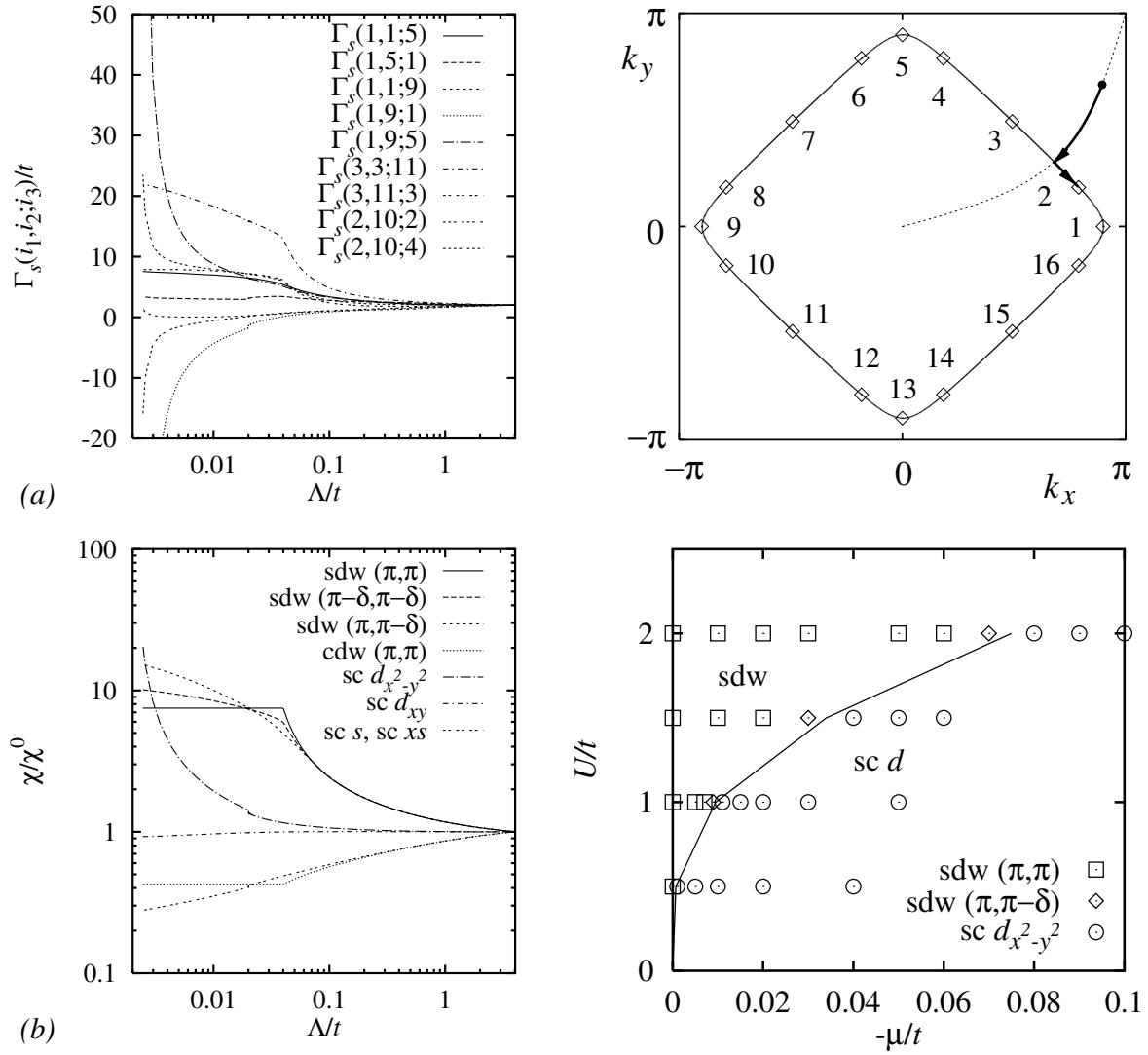


Fig. 7: *(a) Flow of the singlet component of the two-particle vertex Γ_s^Λ as a function of Λ for several choices of the Fermi momenta $\mathbf{k}_{F1}$, $\mathbf{k}_{F2}$ and $\mathbf{k}'_{F1}$, which are labeled according to the projection in the figure on the right. The model parameters are $U = t$ and $t' = 0$, the chemical potential is $\mu = -0.02t$, and the temperature is zero. (b) Left: Flow of the ratio of interacting and non-interacting susceptibilities, $\chi^\Lambda/\chi_0^\Lambda$, for the same parameters as in (a). Right: Ground state phase diagram for $t' = 0$ and $\mu \leq 0$ (at and below half-filling), as obtained from divergent susceptibilities. Figures taken from Ref. [35].*

small (even if Λ is not small), because these momenta are close to their projected counterparts. The projected vertex function can be parameterized by three angles ϕ_1, ϕ_2, ϕ_3 associated with $\mathbf{k}_{F1}$, $\mathbf{k}_{F2}$ and $\mathbf{k}'_{F1}$, respectively, i.e.,

$$\Gamma_\alpha^\Lambda(\mathbf{k}'_{F1}, \mathbf{k}_{F1}+\mathbf{k}_{F2}-\mathbf{k}'_{F1}; \mathbf{k}_{F1}, \mathbf{k}_{F2}) = \Gamma_\alpha^\Lambda(\phi_1, \phi_2, \phi_3). \tag{41}$$

The angular dependence turns out to be strong for small Λ and cannot be neglected. The remaining tangential momentum dependence is discretized (see again Fig. 7). Equivalently one can view this parametrization as a discretization of momentum dependences corresponding to a partition of the Brillouin zone in "patches" or "sectors" [36, 37].

The flow of the two-particle vertex in the ground state of the two-dimensional Hubbard model has been computed for many different model parameters t'/t and U/t (t just sets the absolute energy scale) and densities near half-filling [35–38]. In all cases the vertex develops a strong momentum dependence for small Λ with divergences for several momenta at some critical scale $\Lambda_c > 0$, which vanishes exponentially for $U \to 0$. To see which physical instability is associated with the diverging vertex function, several susceptibilities have been computed, in particular commensurate and incommensurate spin susceptibilities $\chi_S(\mathbf{q})$ with $\mathbf{q} = (\pi, \pi)$, $\mathbf{q} = (\pi - \delta, \pi)$ and $\mathbf{q} = (1-\delta)(\pi, \pi)$, where δ is a function of density [39], the commensurate charge susceptibility $\chi_C\big((\pi, \pi)\big)$, and singlet pair susceptibilities with s-wave and d-wave form factors. Some of these susceptibilities diverge together with the vertex function at the scale Λ_c. Depending on the choice of U, t' and μ, the strongest divergence is found either for the commensurate or incommensurate spin susceptibility, or for the pairing susceptibility with $d_{x^2-y^2}$ symmetry.

Fig. 7 shows a typical result for the flow of the two-particle interactions and susceptibilities in the ground state of the two-dimensional Hubbard model, as obtained from the Wick ordered version of the functional RG [35]. Within the lowest order truncation for the two-particle vertex, the results obtained from different functional RG versions do not deviate significantly from each other. Only the singlet part of the vertex is plotted, for various choices of two incoming momenta and one outgoing momentum on the Fermi surface. The triplet part of the vertex flows generally more weakly than the singlet part. Note the threshold at $\Lambda = 2|\mu|$ below which the amplitudes for various scattering processes, especially umklapp scattering, renormalize only very slowly. The flow of the antiferromagnetic spin susceptibility is cut off at the same scale. The infinite slope singularity in some of the flows at scale $\Lambda = |\mu|$ is due to the van Hove singularity being crossed at that scale. The *pairing* susceptibility with $d_{x^2-y^2}$-symmetry diverges at the scale Λ_c, at which also the two-particle interaction diverges in the Cooper channel.

Following the flow of the vertex function and susceptibilities, one can see that those interaction processes which enhance the antiferromagnetic spin susceptibility (especially umklapp scattering) also build up an attractive interaction in the $d_{x^2-y^2}$ pairing channel. This confirms the spin-fluctuation route to d-wave superconductivity. Running the flow for various choices of μ/t and U/t one obtains an educated guess for the ground state phase diagram from the dominant divergences of the vertex and susceptibilities.

The static approximation of the vertex with a discretized momentum dependence as described above is sufficient for a weak coupling stability analysis. However, near the scale Λ_c, where the vertex diverges, this crude parametrization does not capture the momentum and energy dependence of the emerging singularities, and the power-counting argument invoked for its justification breaks down. An improved parametrization of the two-particle vertex based on a decomposition in charge, magnetic, and pairing channels has been established [15, 40, 41]. In this channel decomposition, singular momentum and energy dependences are isolated in a single bosonic momentum and energy variable, corresponding to a sum or difference of fermionic variables, which can then be parametrized much more accurately.

3.2 Spontaneous symmetry breaking

Within the one-loop truncation the effective two-particle interaction Γ^Λ always diverges in some momentum channels at a finite energy scale Λ_c, even for a small bare interaction U. Hence one is always running into a strong coupling problem in the low-energy limit. The one-loop truncation breaks down, and also the simplified parametrization of the two-particle vertex described above cannot be justified in the presence of singular momentum and energy dependences.

If the vertex function diverges only in the Cooper channel, driven by the particle-particle contribution to the flow, the strong coupling problem emerging in the low-energy region can be controlled by exploiting Λ_c as a small parameter [42]. The formation of a superconducting ground state can then be described essentially by a BCS theory with renormalized input parameters. In the Hubbard model the pure Cooper channel instability is always realized for $\mu \neq \epsilon_{\rm vH}$ at sufficiently small U. In that regime one can safely infer superconductivity with a d-wave order parameter from the divergence of the one-loop pairing susceptibility. At finite temperature the off-diagonal long-range order will of course turn into the quasi long-range order of a Kosterlitz-Thouless phase.

In general, the one-loop calculation can produce divergences of the vertex function in various momentum channels, with large contributions from both particle-particle and particle-hole diagrams. This can happen even in the weak coupling limit $U \to 0$, namely when the chemical potential approaches the van Hove singularity. In that case different possible instabilities can compete in a complicated way. Besides spin density wave and pairing instabilities one has to deal with ferromagnetism (at moderate $|t'/t|$ in the Hubbard model) [43–45] and a d-wave Pomeranchuk instability of the Fermi surface [46] as alternative or coexisting candidates.

A complete theory of the effective strong coupling problem emerging from strong particle-particle and particle-hole fluctuations has not yet been achieved. For weak bare coupling, one may again try to exploit the smallness of the scale Λ_c where strong fluctuations appear to construct a tractable effective low-energy theory. Spontaneous symmetry breaking can be handled within the functional RG framework by adding an infinitesimal symmetry breaking term at the beginning of the flow, which is then promoted to a finite order parameter at the scale Λ_c [19,20]. The calculations are complicated by the appearance of anomalous interaction vertices, and, in case of continuous symmetries, by singularities associated with Goldstone modes. Nevertheless, fermionic functional RG flows with spontaneous symmetry breaking were computed for the superconducting ground state of the attractive [47,48] and repulsive [49] Hubbard model. In systems with a metastable phase, e.g., near a first order transition, a shift of the initial conditions by a counter term is needed to drive the flow into the stable symmetry broken phase [50]. Order parameter fluctuations are most conveniently treated by introducing appropriate bosonic fields, as first discussed for antiferromagnetic order in the half-filled Hubbard model [51].

In case of competing order parameters, such as antiferromagnetism and d-wave superconductivity near half-filling, a full RG treatment of spontaneous symmetry-breaking and order parameter fluctuations is a rather complicated [52]. As a simpler alternative one may neglect low-energy fluctuations and combine the RG with a mean-field (MF) theory of symmetry-breaking [53,54].

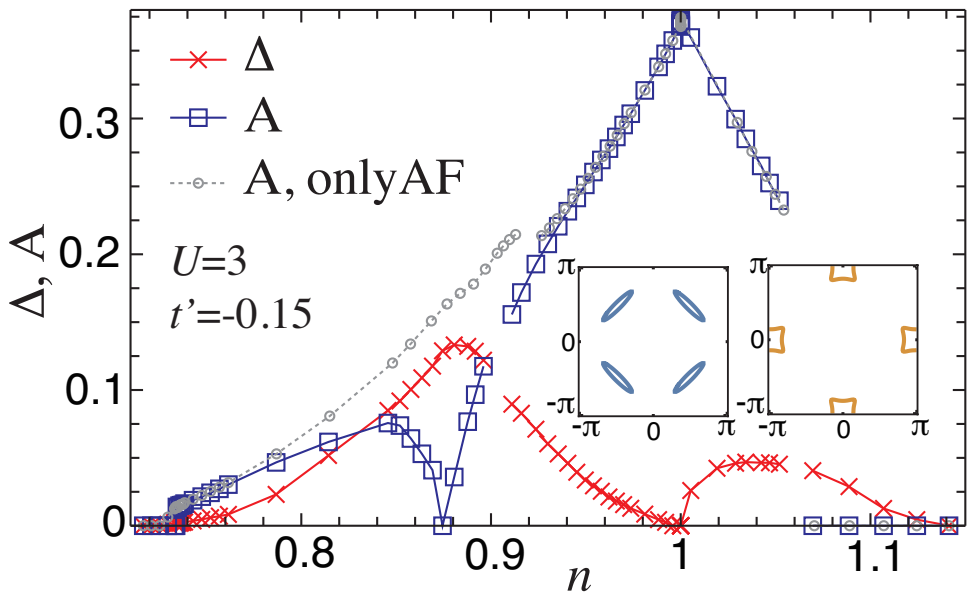


Fig. 8: *Amplitudes of magnetic and superconducting gap functions in the ground state of the two-dimensional Hubbard model as a function of the electron density n, for $U/t = 3$ and $t'/t = -0.15$. Results from a coupled solution of magnetic and superconducting gap equations with possible coexistence of orders are compared to a purely magnetic solution. Corresponding hole and electron pockets at $n = 0.96$ and $n = 1.05$ are shown in the left and right insets, respectively. First order transitions (see broken lines near $n = 0.9$ and $n = 1.06$) lead to small density intervals where no homogeneous solution exists. Figure taken from Ref. [55].*

In such a *renormalized mean-field* (RG+MF) approach the one-loop flow is stopped at a scale $\Lambda_{\rm MF}$ that is small compared to the band width but still above the scale Λ_c where the two-particle vertex diverges. At this point the vertex has developed already a pronounced momentum dependence, reflecting in particular magnetic and superconducting correlations. The integration over the remaining modes, below $\Lambda_{\rm MF}$, is treated in a mean-field approximation allowing, in particular, antiferromagnetic and superconducting order, where the effective interactions entering the mean-field equations are extracted from $\Gamma^{\Lambda_{\rm MF}}$. At zero temperature, this approach should yield a decent approximation for the order parameters, since order parameter fluctuations usually do not play a crucial role for the gross features of the ground state.

Results obtained for the amplitudes of the antiferromagnetic and superconducting gap amplitudes in the ground state of the 2D Hubbard model, as obtained from a functional RG + MF calculation [55], are shown in Fig. 8. The amplitudes are defined as the maxima $\Delta^{\rm AF} = \max_{\mathbf{k}} \Delta^{\rm AF}_{\mathbf{k}}$ and $\Delta^{\rm SC} = \max_{\mathbf{k}} \Delta^{\rm SC}_{\mathbf{k}}$ of the gap functions. There is an extended region of *coexistence* of magnetic and superconducting order, which occurs naturally due to pairing of electrons near the reconstructed Fermi surface (pockets) in the antiferromagnetic state. The superconducting gap function has the expected d-wave symmetry. The magnetic order is purely antiferromagnetic (Néel) for $n > 0.9$, and incommensurate with a wave vector near to but distinct from (π, π) for $n < 0.9$.

4 Leap to strong coupling: DMFT as a booster rocket

A truncation of the functional RG hierarchy of flow equations can be justified only for weak interactions, with the exception of mean-field models where phase space restrictions suppress higher order contributions [19]. Although bare interactions are usually two-particle interactions, m-particle effective interactions with $m > 2$ are generated by the flow and affect the effective two-particle interaction and the self-energy. For example, an effective three-particle interaction $\Gamma^{(6)\Lambda}$ is generated by a contribution of third order in the two-particle vertex $\Gamma^{(4)\Lambda}$, which then feeds back into the flow of $\Gamma^{(4)\Lambda}$, as can be seen in Fig. 3. For strong bare interactions, these contributions from effective interactions beyond the two-particle level become important already at relatively high energy scales, that is, at scales well above the critical scales for instabilities.

For systems with short-range interactions such as the Hubbard model, the correlations at high and intermediate energy scales are well described by the dynamical mean-field theory (DMFT) [56] and its quantum cluster extensions [57], since long-range correlations emerge only at low energy scales. In particular, the DMFT captures non-perturbative phenomena such as the Mott-Hubbard metal-insulator transition, which is a consequence of strong local correlations.

The DMFT is based on a local approximation for the fermionic self-energy, which is exact in the limit of infinite lattice dimensionality [58]. In that limit, irreducible m-particle vertices are local, too. It is thus natural to use the DMFT solution as a starting point, and include non-local correlations subsequently by expanding around the DMFT vertices and self-energy [59]. Several such extensions of the DMFT, involving various types of resummed perturbation expansions for non-local corrections, have already been proposed [60–63].

The DMFT can also be used as a non-perturbative starting point for the functional RG flow [64]. The DMFT vertices and self-energy set the initial condition of the flow. In the remainder of this section, I will describe the fusion of DMFT and functional RG to the non-perturbative $\mathrm{DMF^2RG}$, and discuss results for the two-dimensional Hubbard model at strong coupling [65].

4.1 Dynamical mean-field theory

The DMFT was developed in two steps. First, it was shown that models of interacting lattice fermions have a non-trivial infinite dimensionality ($d \to \infty$) limit [58], where local correlations survive, while non-local contributions to one-particle irreducible quantities such as the self-energy vanish [58, 66]. Second, it was shown that a lattice fermion system with a local self-energy can be mapped to a quantum impurity problem with a self-consistency condition [67, 68]. The resulting equations are a dynamical variant of the static Weiss mean-field theory for magnets—hence the name "dynamical mean-field theory" commonly used since 1995.

For the Hubbard model, the DMFT equations can be derived on the back of an envelope as follows. The propagator G is related to the bare propagator G_0 and the self-energy Σ by Dyson's equation, $G^{-1}(k_0, \mathbf{k}) = G_0^{-1}(k_0, \mathbf{k}) - \Sigma(k_0)$. Non-local (in real space) contributions to the self-energy are discarded in the DMFT, so that $\Sigma(k)$ depends only on frequency. This approximation becomes exact in the limit $d \to \infty$ [58, 66]. In a one-particle irreducible skeleton expansion,

the local part of the self-energy is a functional of the local propagator

$$G_{\rm loc}(k_0) = \int_{\mathbf{k}} G(k_0, \mathbf{k}) \ , \tag{42}$$

where $\int_{\mathbf{k}} = \int \frac{d^d\mathbf{k}}{(2\pi)^d}$. The same skeleton expansion yields the self-energy of the purely local action

$$\mathcal{S}_{\rm loc}[\psi, \bar\psi] = -\sum_{k_0,\sigma} \bar\psi_{k_0,\sigma} \mathcal{G}_0^{-1}(k_0) \psi_{k_0,\sigma} + U \int_0^\beta d\tau \, \bar\psi_\uparrow(\tau)\psi_\uparrow(\tau)\bar\psi_\downarrow(\tau)\psi_\downarrow(\tau) \ , \tag{43}$$

where τ denotes imaginary time and $\psi_\sigma(\tau)$ and $\bar\psi_\sigma(\tau)$ are the Fourier transforms of $\psi_{k_0,\sigma}$ and $\bar\psi_{k_0,\sigma}$, respectively. The dynamical *Weiss field* $\mathcal{G}_0^{-1}$ is determined by the self-consistency condition requiring that the local propagator and the self-energy of the lattice electrons coincide with the propagator and the self-energy of $\mathcal{S}_{\rm loc}$, that is,

$$G_{\rm loc}^{-1}(k_0) = \mathcal{G}_0^{-1}(k_0) - \Sigma(k_0) \ . \tag{44}$$

The main difficulty is to compute the self-energy as a functional of $\mathcal{G}_0$ from the action $\mathcal{S}_{\rm loc}$. Introducing an auxiliary bath of non-interacting conduction electrons, this problem can be mapped to a well-known quantum impurity problem, the single-impurity Anderson model [67, 68], for which efficient non-perturbative numerical algorithms exist. Once a self-consistent $\mathcal{G}_0$ has been determined, one can also compute DMFT vertices from $\mathcal{S}_{\rm loc}$ [69].

4.2 From infinite to finite dimensions

We now set up a flow which starts from the local self-energy and local vertices as given by the DMFT, and builds up non-local correlations successively [64]. Without truncations, the exact non-local quantities would be obtained at the end of the flow. There is no double-counting of contributions. One way of defining such a flow, which is associated with an intuitive picture, is to flow from infinite dimensions, where the DMFT is exact, to the actual dimensionality of the system.

To be specific, let us consider a d-dimensional hypercubic lattice with nearest neighbor hopping, supplemented by $\bar d$ additional auxiliary dimensions with $\bar d \to \infty$. The flow equations derived in Sec. 2 are valid for an arbitrary scale dependence of the bare propagator. To flow from infinite to d dimensions, we introduce scale dependent hopping amplitudes in the physical and auxiliary directions, denoted by t^Λ and $\bar t^\Lambda$, respectively. The initial hopping amplitudes are $t^{\Lambda_0} = 0$ and $\bar t^{\Lambda_0} = (d/\bar d)^{1/2}\, t$. The scaling with $\bar d^{-1/2}$ is required for a proper limit $\bar d \to \infty$ [58]. At the end of the flow, for $\Lambda \to 0$, the hopping amplitude in the auxiliary dimensions are switched off, $\bar t^{\Lambda\to 0} = 0$, while the real hopping amplitude is turned on, $t^{\Lambda\to 0} = t$.

The corresponding scale dependent bare propagator has the form

$$G_0^\Lambda(k_0, \mathbf{k}, \bar{\mathbf{k}}) = \frac{1}{ik_0 + \mu - \epsilon_{\mathbf{k}}^\Lambda - \bar\epsilon_{\bar{\mathbf{k}}}^\Lambda} \ , \tag{45}$$

with the scale dependent dispersion relations

$$\epsilon_{\mathbf{k}}^\Lambda = -2t^\Lambda \left(\cos k_1 + \cdots + \cos k_d\right) \quad \text{and} \quad \bar\epsilon_{\bar{\mathbf{k}}}^\Lambda = -2\bar t^\Lambda \left(\cos \bar k_1 + \cdots + \cos \bar k_{\bar d}\right) . \tag{46}$$

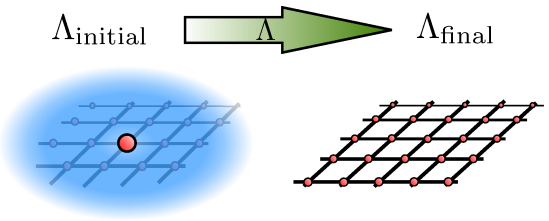


Fig. 9: *Illustration of the flow from a DMFT solution to the solution of the d-dimensional (here $d=2$) lattice system. Figure taken from Ref. [64].*

For $\bar{d} \to \infty$, only the part of the propagator which is local in the auxiliary dimensions contributes to the self-energy and vertices. This local part is given by a $\bar{\mathbf{k}}$-integration,

$$G_0^\Lambda(k_0, \mathbf{k}) = \int_{\bar{\mathbf{k}}} G_0^\Lambda(k_0, \mathbf{k}, \bar{\mathbf{k}}) = \int d\bar{\epsilon}\, \frac{\bar{\rho}^\Lambda(\bar{\epsilon})}{ik_0 + \mu - \epsilon_{\mathbf{k}}^\Lambda - \bar{\epsilon}} \,, \tag{47}$$

where $\bar{\rho}^\Lambda(\bar{\epsilon})$ is the density of states for $\bar{\epsilon}_{\mathbf{k}}^\Lambda$. The latter is a normalized Gaussian distribution with a width that shrinks to zero for $\Lambda \to 0$, so that $G_0^{\Lambda\to 0}(k_0, \mathbf{k}) = \big(ik_0 + \mu - \epsilon_{\mathbf{k}}\big)^{-1}$.
G_0^Λ defines a flow that interpolates smoothly between the DMFT solution for the infinite dimensional model at Λ_0 and the solution of the d-dimensional system for $\Lambda \to 0$, as illustrated schematically in Fig. 9. The flow equations derived in Sec. 2 apply without any modification. However, the initial condition for the flow is not given by bare quantities, but by the self-energy and vertices as obtained from the DMFT, that is, $\Sigma^{\Lambda_0} = \Sigma_{\text{DMFT}}$ and $\Gamma^{(2m)\Lambda_0} = \Gamma^{(2m)}_{\text{DMFT}}$. Hence, non-perturbative local correlations effects, such as the Mott-Hubbard transition, are built in already at the starting point. The DMFT thus becomes a "booster rocket" for the flow.
The infinite dimensionality limit served as a guide to develop the idea of setting up a flow that starts with the DMFT. However, the DMFT is usually applied as an approximation for a finite dimensional system, without introducing extra dimensions. In the same spirit, one can also define a flow with the DMFT as a starting point, while staying entirely in the d-dimensional physical space. A particularly simple choice for the scale dependence of the bare propagator is given by [64]

$$\big[G_0^\Lambda(k_0, \mathbf{k})\big]^{-1} = \Lambda\, \mathcal{G}_0^{-1}(k_0) + (1-\Lambda)\, G_0^{-1}(k_0, \mathbf{k}) \,, \tag{48}$$

with $\Lambda_0 = 1$. This choice is very simple but certainly not optimal. In particular, it does not regularize infrared singularities. Better choices obeying additional requirements besides the correct boundary conditions can be constructed on demand.

4.3 Application to the 2D Hubbard model

Let us now see how the DMF^{2}RG can be applied to the two-dimensional Hubbard model at strong coupling [65]. The hierarchy of flow equations (see Fig. 3) needs to be truncated to be manageable. Once again, we discard the three-particle vertex, leading to the closed system of flow equations represented diagrammatically in Fig. 10, which involves only the self-energy Σ^Λ and the two-particle vertex Γ^Λ. In contrast to the weak coupling stability analysis discussed above, it is now crucial to keep the self-energy feedback on the right hand side of the flow

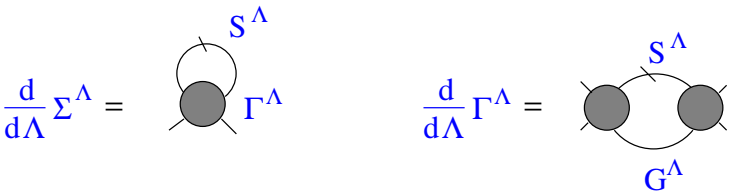


Fig. 10: *Truncation of flow equations in* $\mathrm{DMF^2RG}$ *applied to the 2D Hubbard model.*

equations. The initial condition at $\Lambda = \Lambda_0$ is given by the DMFT self-energy and vertex. For reasons explained below, we improve on the simple choice (48) for G_0^Λ, and define the flow such that

$$G^\Lambda_{\mathrm{loc}}(k_0)\Big|_{\Sigma^\Lambda=\Sigma_{\mathrm{DMFT}}} = G^{\Lambda_0}_{\mathrm{loc}}(k_0) \tag{49}$$

for all Λ. This can be achieved by the ansatz [65]

$$\big[G_0^\Lambda(k_0,\mathbf{k})\big]^{-1} = ik_0 + \mu - (1-\Lambda)\epsilon_{\mathbf{k}} - g^\Lambda(k_0)\Delta(k_0)\,, \tag{50}$$

with $\Delta(k_0) = ik_0+\mu-\mathcal{G}_0^{-1}(k_0)$. The function $g^\Lambda(k_0)$ is equal to one at $\Lambda_0{=}1$, and it vanishes for $\Lambda{\to}0$. For $0{<}\Lambda{<}1$ it is determined by the condition (49). The condition (49) implies that the local single-scale propagator S^Λ_{loc} with $\Sigma^\Lambda = \Sigma_{\mathrm{DMFT}}$ vanishes. Hence, for $\Sigma^\Lambda = \Sigma_{\mathrm{DMFT}}$, there are no local contributions to the flow, and thus no corrections to the DMFT solution. The flow is thus exclusively generated by *non-local* contributions. This improves the accuracy of the truncation. In particular, the three-particle contributions to the flow of the two-particle vertex, which are neglected in our truncation, contribute only after non-local correlations have been generated. At the initial stage of the flow, where the three-particle vertex is local and the self-energy is given by Σ_{DMFT}, the three-particle tadpole contribution to the flow of Γ^Λ vanishes. In the course of the flow it starts contributing due to non-local corrections to the DMFT three-particle vertex and due to deviations of the self-energy from the DMFT solution.

Another critical issue is the parametrization of the two-particle vertex Γ^Λ. At the beginning of the flow it is given by the DMFT vertex, which depends only on Matsubara frequencies [69]. In the course of the flow momentum dependences are generated, too. At strong coupling the full dependence on all three Matsubara frequencies must be taken into account to accurately parametrize the vertex [65]. To parametrize the momentum dependence, the corrections to the DMFT vertex are decomposed in charge, magnetic, and pairing channels [15], which are closely related to the three channels contributing to the one-loop flow of the vertex in Fig. 10. In each of these channels only the momentum transfer or the total momentum of the two interacting particles is particularly important and must be discretized accurately, while the remaining momentum dependences can be treated more grossly by s-wave and d-wave form factors. Hence, as a compromise between accuracy and feasibility, one is dealing with several functions of one momentum and three independent frequency variables.

The numerical solution of the flow equations is quite challenging, due to the large number of variables and due to the very strong frequency dependence of the vertex at strong coupling. At sufficiently high temperatures, the flow can be fully carried out until $\Lambda \to 0$, while sizable non-local correlations already become visible. Fig. 11 shows the real part of the self-energy along a

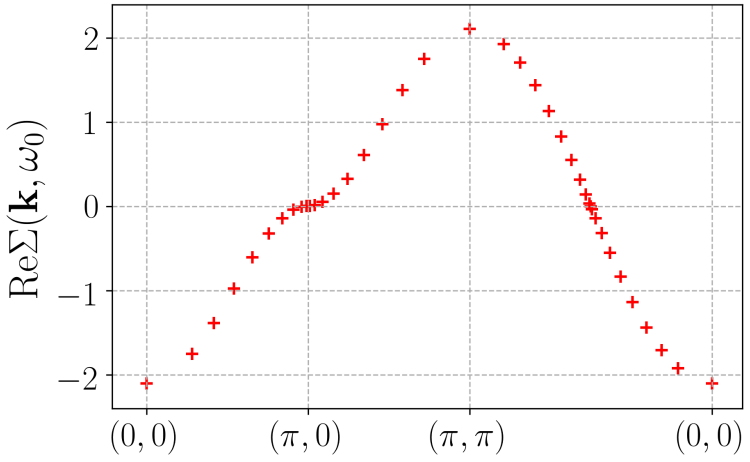


Fig. 11: *Real part of the self-energy as a function of momentum at the lowest Matsubara frequency $\omega_0 = \pi T$ as obtained from the* $\mathrm{DMF}^2\mathrm{RG}$ *for the 2D Hubbard model at half-filling. Parameters: $t' = 0$, $U = 8t$, and temperature $T = 0.5t$. Figure taken from Ref. [65].*

momentum path in the Brillouin zone at the lowest Matsubara frequency for a set of parameters that was previously used for benchmarking various numerical methods [70]. This result agrees with those obtained from the dynamical cluster approximation, diagrammatic Monte Carlo, and the dual-fermion approach as reported in Fig. 16 of Ref. [70].

At low temperatures the flowing two-particle vertex diverges at some critical value $\Lambda_c > 0$ of the flow parameter, and the truncation in Fig. 10 breaks down. Similarly to the situation in the weak-coupling stability analysis discussed above, this divergence signals an instability toward spontaneous symmetry breaking. The order parameter fluctuations preventing such a symmetry breaking at finite temperatures in two dimensions are not captured by the truncation in Fig. 10. For a complete theory such fluctuations would need to be included, for example by introducing order parameter fields via a Hubbard Stratonovich transformation. However, even the simple truncation in Fig. 10 contains already the information in which channel and at which temperature scale strong non-local correlations develop.

Close to half-filling, the two-particle vertex diverges in the magnetic channel, indicating a magnetic instability. A sizable d-wave pairing interaction is also generated, but it remains subleading in this regime. Further away from half-filling, the interaction in the d-wave pairing becomes leading, indicating an instability toward d-wave superconductivity. The flow of the d-wave pairing interaction $\mathcal{D}^\Lambda$ is shown for two choices of the density and the temperature in Fig. 12. One can see that a pairing instability develops at a temperature scale of order $T \approx 0.05t$, which, for typical values of the hopping amplitude t in cuprates, corresponds to roughly 150 Kelvin. Hence, the $\mathrm{DMF}^2\mathrm{RG}$ provides evidence for d-wave pairing at reasonable temperature scales in the two-dimensional Hubbard at strong coupling. Note that the truncation in Fig. 10 yields only an estimate for the temperature scale for the formation of Cooper pairs. The critical temperature for superconductivity is a Kosterlitz-Thouless temperature, related to the superfluid stiffness, which will be somewhat lower.

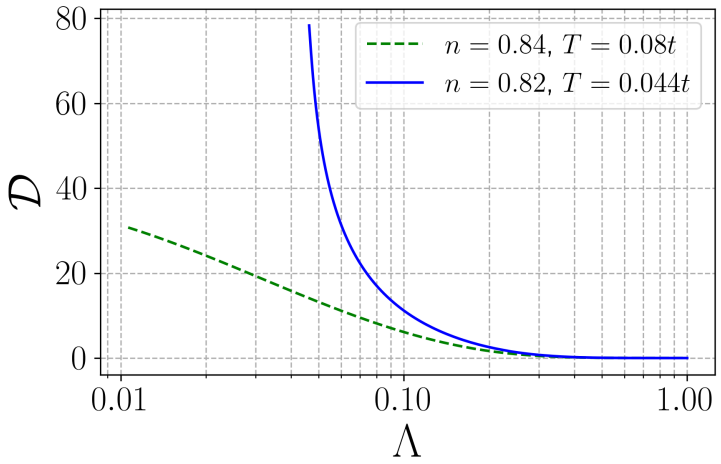


Fig. 12: *Flow of the d-wave pairing interaction as obtained from the* $\mathrm{DMF^2RG}$ *for the 2D Hubbard model with $t' = -0.2t$ and $U = 8t$. Figure taken from Ref. [65].*

5 Summary

The functional renormalization group is a valuable source of new approximation schemes for interacting Fermi systems [3, 4]. The method is based on an exact flow equation, which describes the flow of the effective action as a function of a suitable flow parameter. From the final effective action, at the end of the flow, any desired information about the system can be obtained. Approximations are constructed by truncating the effective action. In many cases, rather simple truncations turned out to capture rather complex many-body phenomena. Compared to the traditional resummations of perturbation theory these approximations have the advantage that infrared singularities are treated properly due to the built-in RG structure. Unlike other RG methods, approximations derived in the functional RG framework can be applied directly to microscopic models, not only to renormalizable effective field theories. Remarkably, the functional RG reviewed here as a computational tool is very similar to RG approaches used by mathematicians to derive general rigorous results for interacting Fermi systems.

Applications of the functional RG to the two-dimensional Hubbard model have improved our understanding of its instabilities. In particular, the existence of d-wave superconductivity in that model was conclusively established.

With the fusion of DMFT and functional RG [64, 65], where the DMFT is used as a non-perturbative starting point for the functional RG flow, a promising route has been opened to capture all aspects of strongly interacting Fermi systems, such as the 2D Hubbard model at large U, over all energy scales in one framework.

Acknowledgment

I would like to thank my coworkers S. Andergassen, A. Eberlein, C. Halboth, K. Held, C. Honerkamp, A. Katanin, J. Reiss, D. Rohe, M. Salmhofer, C. Taranto, A. Toschi, D. Vilardi, D. Vollhardt, J. Wang, and H. Yamase for their enjoyable collaboration on the work presented in this lecture.

Appendix

A Derivation of functional flow equation

Here we describe the derivation of the functional flow equation (15) for the effective action Γ^Λ. Introducing a scale dependent bare propagator $G_0^\Lambda = (Q_0^\Lambda)^{-1}$ in the functional integral representation (4) of the generating functional for connected Green functions, one can write

$$e^{-\mathcal{G}^\Lambda[\eta,\bar\eta]} = \int \prod_K d\psi_K d\bar\psi_K \, e^{(\bar\psi, Q_0^\Lambda \psi)} \, e^{-V[\psi,\bar\psi]} \, e^{(\bar\eta,\psi)+(\bar\psi,\eta)}. \tag{51}$$

Taking a Λ-derivative on both sides yields

$$\begin{aligned} -(\partial_\Lambda \mathcal{G}^\Lambda[\eta,\bar\eta])\, e^{-\mathcal{G}^\Lambda[\eta,\bar\eta]} &= \int \prod_K d\psi_K d\bar\psi_K \, (\bar\psi, \partial_\Lambda Q_0^\Lambda \psi)\, e^{(\bar\psi, Q_0^\Lambda\psi)} \, e^{-V[\psi,\bar\psi]} \, e^{(\bar\eta,\psi)+(\bar\psi,\eta)} \\ &= -(\partial_\eta,\, \partial_\Lambda Q_0^\Lambda \partial_{\bar\eta})\, e^{-\mathcal{G}^\Lambda[\eta,\bar\eta]}, \end{aligned} \tag{52}$$

which leads directly to a flow equation for $\mathcal{G}^\Lambda$,

$$\frac{d}{d\Lambda}\mathcal{G}^\Lambda[\eta,\bar\eta] = \left(\frac{\partial \mathcal{G}^\Lambda}{\partial\eta},\, \frac{dQ_0^\Lambda}{d\Lambda}\,\frac{\partial \mathcal{G}^\Lambda}{\partial\bar\eta}\right) + \mathrm{tr}\left(\frac{dQ_0^\Lambda}{d\Lambda}\,\frac{\partial^2 \mathcal{G}^\Lambda}{\partial\bar\eta\partial\eta}\right). \tag{53}$$

The effective action is the Legendre transform

$$\Gamma^\Lambda[\psi,\bar\psi] = \mathcal{G}^\Lambda[\eta^\Lambda,\bar\eta^\Lambda] + (\bar\psi,\eta^\Lambda) + (\bar\eta^\Lambda,\psi). \tag{54}$$

Note that η^Λ and $\bar\eta^\Lambda$ are Λ-dependent functions of ψ and $\bar\psi$, so that

$$\frac{d}{d\Lambda}\Gamma^\Lambda[\psi,\bar\psi] = \frac{d}{d\Lambda}\,\mathcal{G}^\Lambda[\eta^\Lambda,\bar\eta^\Lambda] + (\bar\psi,\partial_\Lambda\eta^\Lambda) + (\partial_\Lambda\bar\eta^\Lambda,\, \psi). \tag{55}$$

The total derivative acts also on the Λ-dependence of η^Λ and $\bar\eta^\Lambda$. Using the relations $\partial\mathcal{G}^\Lambda/\partial\bar\eta = -\psi$, and $\partial\mathcal{G}^\Lambda/\partial\eta = \bar\psi$, all terms arising from the Λ-dependence of η^Λ and $\bar\eta^\Lambda$ cancel, yielding

$$\frac{d}{d\Lambda}\Gamma^\Lambda[\psi,\bar\psi] = \left.\frac{d}{d\Lambda}\mathcal{G}^\Lambda[\eta^\Lambda,\bar\eta^\Lambda]\right|_{\eta^\Lambda,\bar\eta^\Lambda \text{ fixed}}. \tag{56}$$

The flow equation (15) for Γ^Λ now follows directly from Eq. (53) and the reciprocity relation $\mathbf{\Gamma}^{(2)\Lambda}[\psi,\bar\psi] = \left(\mathbf{G}^{(2)\Lambda}[\eta^\Lambda,\bar\eta^\Lambda]\right)^{-1}$.

References

[1] J. Berges, N. Tetradis, and C. Wetterich, Phys. Rep. **363**, 223 (2002)

[2] P. Kopietz, L. Bartosch, and F. Schütz: *Introduction to the Functional Renormalization Group* (Springer, Berlin, 2010)

[3] W. Metzner, M. Salmhofer, C. Honerkamp, V. Meden, and K. Schönhammer, Rev. Mod. Phys. **84**, 299 (2012)

[4] N. Dupuis, L. Canet, A. Eichhorn, W. Metzner, J.M. Pawlowki, M. Tissier, and N. Wschebor, Phys. Rep. **910**, 1 (2021)

[5] J. Solyom, Adv. Phys. **28**, 201 (1979)

[6] J. Feldman and E. Trubowitz, Helv. Phys. Acta **63**, 156 (1990); *ibid* **64**, 214 (1991)

[7] G. Benfatto and G. Gallavotti, J. Stat. Phys. **59**, 541 (1990)

[8] K.G. Wilson and J. Kogut, Phys. Rep. C **12**, 75 (1974)

[9] M. Salmhofer: *Renormalization: An Introduction* (Springer, Heidelberg, 1999)

[10] J. Feldman, H. Knörrer, and E. Trubowitz, Rev. Math. Phys. **15**, 949-1169 (2003); Commun. Math. Phys. **247**, 1-320 (2004)

[11] R. Shankar, Rev. Mod. Phys. **66**, 129 (1994)

[12] J. Polchinski, in J. Harvey and J. Polchinski (eds.): *Proceedings of 1993 Theoretical Advanced Studies Institute in Elementary Particle Physics*, (World Scientific, 1993)

[13] C. Wetterich, Phys. Lett. B **301**, 90 (1993)

[14] J.W. Negele and H. Orland: *Quantum Many-Particle Systems* (Addison-Wesley, 1987)

[15] C. Husemann and M. Salmhofer, Phys. Rev. B **79**, 195125 (2009)

[16] S. Andergassen, T. Enss, V. Meden, W. Metzner, U. Schollwöck, and K. Schönhammer, Phys. Rev. B **70**, 075102 (2004)

[17] J. Polchinski, Nucl. Phys. **B231**, 269 (1984)

[18] F. Schütz, L. Bartosch, and P. Kopietz, Phys. Rev. B **72**, 035107 (2005)

[19] M. Salmhofer, C. Honerkamp, W. Metzner, and O. Lauscher, Prog. Theor. Phys. **112**, 943 (2004)

[20] R. Gersch, C. Honerkamp, D. Rohe, and W. Metzner, Eur. Phys. J. B **48**, 349 (2005)

[21] A. Eberlein and W. Metzner, Prog. Theor. Phys. **124**, 471 (2010)

[22] M. Salmhofer and C. Honerkamp, Prog. Theor. Phys. **105**, 1 (2001)

[23] P.W. Anderson, Science **235**, 1196 (1987)

[24] D.P. Arovas, E. Berg, S.A. Kivelson, and S. Raghu,
Annu. Rev. Condens. Matter Phys. **13**, 239 (2022)

[25] M. Qin, T. Schäfer, S. Andergassen, P. Corboz, and E. Gull,
Annu. Rev. Condens. Matter Phys. **13**, 275 (2022)

[26] D.J. Scalapino, Rev. Mod. Phys. **84**, 1383 (2012)

[27] K. Miyake, S. Schmitt-Rink, and C.M. Varma, Phys. Rev. B **34**, 6554 (1986)

[28] D.J. Scalapino, E. Loh, and J.E. Hirsch, Phys. Rev. B **34**, 8190 (1986)

[29] N.E. Bickers, D.J. Scalapino, and R.T. Scalettar, Int. J. Mod. Phys. B **1**, 687 (1987)

[30] N.E. Bickers, D.J. Scalapino, and S.R. White, Phys. Rev. Lett. **62**, 961 (1989)

[31] D. Manske, *Theory of Unconventional Superconductors*,
Springer Tracts in Modern Physics, Vol. 202 (Springer, Berlin, 2004)

[32] H.J. Schulz, Europhys. Lett. **4**, 609 (1987)

[33] I. Dzyaloshinskii, Sov. Phys. JETP **66**, 848 (1987)

[34] P. Lederer, G. Montambaux, and D. Poilblanc, J. Phys. (Paris) **48**, 1613 (1987)

[35] C.J. Halboth and W. Metzner, Phys. Rev. B **61**, 7364 (2000)

[36] D. Zanchi and H.J. Schulz, Europhys. Lett. **44**, 235 (1998); Phys. Rev. B **61**, 13609 (2000)

[37] C. Honerkamp, M. Salmhofer, N. Furukawa, and T.M. Rice,
Phys. Rev. B **63**, 035109 (2001)

[38] A.P. Kampf and A.A. Katanin, Phys. Rev. B **67**, 125104 (2003)

[39] See, for example, H.J. Schulz, Phys. Rev. Lett. **64**, 1445 (1990), where also the choice of δ as a function of doping is discussed.

[40] C. Husemann, K.-U. Giering, and M. Salmhofer, Phys. Rev. B **85**, 075121 (2012)

[41] A similar channel decomposition was derived and applied also for the single-impurity Anderson model by C. Karrasch, R. Hedden, R. Peters, T. Pruschke, K. Schönhammer, and V. Meden, J. Phys. Condens. Matter **20**, 345205 (2008)

[42] J. Feldman, J. Magnen, V. Rivasseau, and E. Trubowitz, Europhys. Lett. **24**, 437 (1993)

[43] R. Hlubina, S. Sorella, and F. Guinea, Phys. Rev. Lett. **78**, 1343 (1997)

[44] C. Honerkamp and M. Salmhofer, Phys. Rev. Lett. **87**, 187004 (2001)

[45] A.A. Katanin and A.P. Kampf, Phys. Rev. B **68**, 195101 (2003)

[46] C.J. Halboth and W. Metzner, Phys. Rev. Lett. **85**, 5162 (2000)

[47] R. Gersch, C. Honerkamp, and W. Metzner, New J. Phys. **10**, 045003 (2008)

[48] A. Eberlein and W. Metzner, Phys. Rev. B **87**, 174523 (2013)

[49] A. Eberlein and W. Metzner, Phys. Rev. B **89**, 035126 (2014)

[50] R. Gersch, J. Reiss, and C. Honerkamp, New J. Phys. **8**, 320 (2006)

[51] T. Baier, E. Bick, and C. Wetterich, Phys. Rev. B **70**, 125111 (2004)

[52] S. Friederich, H.C. Krahl, and C. Wetterich, Phys. Rev. B **81**, 235108 (2010); ibid. **83**, 155125 (2011)

[53] J. Reiss, D. Rohe, and W. Metzner, Phys. Rev. B **75**, 075110 (2007)

[54] J. Wang, A. Eberlein, and W. Metzner, Phys. Rev. B **89**, 121116(R) (2014)

[55] H. Yamase, A. Eberlein, and W. Metzner, Phys. Rev. Lett. **116**, 096402 (2016)

[56] A. Georges, G. Kotliar, W. Krauth, and M. Rozenberg, Rev. Mod. Phys. **68**, 13 (1996)

[57] T.A. Maier, M. Jarrell, T. Pruschke, and M.H. Hettler, Rev. Mod. Phys. **77**, 1027 (2005)

[58] W. Metzner and D. Vollhardt, Phys. Rev. Lett. **62**, 324 (1989)

[59] Within the Gutzwiller variational ansatz, a perturbative expansion for non-local corrections around the local $d = \infty$ solution was shown to be very promising already long ago, see W. Metzner, Z. Phys. **77**, 253 (1989)

[60] J.P. Hague, M. Jarrell, and T.C. Schulthess, Phys. Rev. B **69**, 165113 (2004)

[61] A. Toschi, A.A. Katanin, and K. Held, Phys. Rev. B **75**, 045118 (2007); A. Valli, G. Sangiovanni, O. Gunnarsson, A. Toschi, and K. Held, Phys. Rev. Lett. **104**, 246402 (2010); G. Rohringer, A. Toschi, A.A. Katanin, and K. Held, Phys. Rev. Lett. **107**, 256402 (2011)

[62] A.N. Rubtsov, M.I. Katsnelson, and A.I. Lichtenstein, Phys. Rev. B **77**, 033101 (2008); H. Hafermann, G. Li, A.N. Rubtsov, M.I. Katsnelson, A.I. Lichtenstein, and H. Monien, Phys. Rev. Lett. **102**, 206401 (2009)

[63] G. Rohringer, H. Hafermann, A. Toschi, A.A. Katanin, A.E. Antipov, M.I. Katsnelson, A.I. Lichtenstein, A.N. Rubtsov, and K. Held, Rev. Mod. Phys. **90**, 025003 (2018)

[64] C. Taranto, S. Andergassen, J. Bauer, K. Held, A.A. Katanin, W. Metzner, G. Rohringer, and A. Toschi, Phys. Rev. Lett. **112**, 196402 (2014)

[65] D. Vilardi, C. Taranto, and W. Metzner, Phys. Rev. B **99**, 104501 (2019)

[66] E. Müller-Hartmann, Z. Phys. B **74**, 507 (1989); *ibid.* **76**, 211 (1989)

[67] A. Georges and G. Kotliar, Phys. Rev. B **45**, 6479 (1992)

[68] M. Jarrell, Phys. Rev. Lett. **69**, 168 (1992)

[69] For a comprehensive analysis of the two-particle vertex obtained by DMFT, see G. Rohringer, A. Valli, and A. Toschi, Phys. Rev. B **86**, 125114 (2012)

[70] J.P.F. LeBlanc, A.E. Antipov, F. Becca, *et al.*, Phys. Rev. X **5**, 041041 (2015)

13 Path Integrals and Reference Systems

Alexander Lichtenstein
I. Institut für Theoretische Physik
Universität Hamburg, 22607 Hamburg, Germany

Contents

1 Idea of reference systems **2**

2 Path integral for correlated lattice model **3**

3 Expansion around reference system **8**

4 Dual fermions in spinor space **16**

5 Discussion **19**

A Path integral for fermions **20**

E. Pavarini, E. Koch, A. Lichtenstein, and D. Vollhardt (eds.)
Understanding Correlated Materials with DMFT
Modeling and Simulation Vol. 15
Forschungszentrum Jülich, 2025, ISBN 978-3-95806-813-1
http://www.cond-mat.de/events/correl25

1 Idea of reference systems

In this lecture we give an introduction to the theoretical description of correlated electron systems within a path integral approach. First, numerically exact calculations of interacting path integrals via continuous-time Quantum Monte Carlo methods (QMC) [1] are revisited. Next, the strong-coupling path-integral Dual-Fermion (DF) expansion around optimally chosen reference system is presented. Finally, the response of the single-band, hole doped t-t' Hubbard model to an external superconducting d-wave field is discussed.

The most well known reference system scheme in quantum material science is related to the celebrated Density Functional Theory (DFT) and their Local Density Approximation (LDA). In this case a homogeneous electron gas with constant external potential and the same Coulomb electron-electron interactions have been solved (see Fig. 1), and this results served as the reference for inhomogeneous electron crystals via a simple LDA ansatz. Such a reference system is exactly solvable via a diffusion quantum Monte Carlo scheme for the ground state energy as a function of the electron density [2]. On other hand, the Dynamical Mean-Field Theory (DMFT) [3] for strongly interacting fermionic systems is based on the self-consistent solutions of an effective impurity reference system (Fig. 1). For realistic multi-orbital systems such a scheme uses a fermionic impurity bath with frequency dependent hybridization function Δ_ω for the correlated part of electrons described by the family of DFT+DMFT approaches [4]. The DMFT scheme becomes exact in the limit of infinite lattice dimension [5].

At finite lattice dimension one can start from the DMFT reference system and use different perturbation schemes for non-local correlation effects [3]. The frequency dependent effective impurity DMFT problem nowadays can be efficiently solved within the continuous time quantum Monte Carlo (CT-QMC) scheme [1]. Therefore the perturbation theory needs to be formulated within the action path integral formalism. We discuss here a general way to include correlations beyond the interacting reference system [6] which are based on the strong coupling dual-fermion path-integral formalism [7]. In the case of additional non-local interactions, the so-called GW+DMFT scheme and impurity reference systems with fermionic and bosonic bathes can be used and so-called dual-boson approach for non-local correlations [6].

For DMFT an effective impurity model, designed to the problem of correlated materials, serves as the reference system, see Fig. 1. Since the zeroth order of such a non-local perturbative expansion coincides with the DMFT problem, we already have an interacting system from the beginning. Moreover, the perturbation is momentum and frequency dependent, so we are forced to replace the Hamiltonian approach by an actions path-integral formalism. Note that the fermion path integral can be used also to formulate the DMFT problem [3, 7]. The dual-fermion approach is not necessarily bound to a specific starting point and can also be used for correlated lattice reference system.

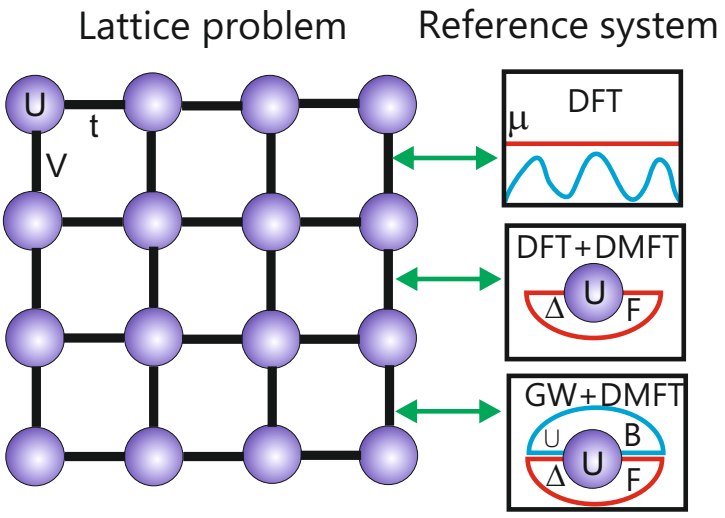


Fig. 1: *Schematic representation of reference systems in many-body approaches to lattice-fermion models: (i) Density-functional theory (DFT) with the interacting homogeneous electron gas as a reference system, defined by a constant external potential μ. (ii) Dynamical mean-field theory (DMFT) with an effective impurity problem as a reference system, defined by a fermionic bath with hybridization function Δ. (iii) GW+DMFT with a correlated atom in a fermionic (Δ) and bosonic (Λ) bathes describes effects of frequency-dependent screened long-range Coulomb (V) interactions.*

2 Path integral for correlated lattice model

Let us consider a general interacting lattice fermion model in d-dimensions described by following Hamiltonian $\hat{H} = \hat{H}_0 + \hat{V}_{\text{int}}$ in second quantization form

$$\hat{H} = \sum_{12} t_{12}\, \hat{c}_1^\dagger \hat{c}_2 + \frac{1}{2} \sum_{1234} V_{1234}\, \hat{c}_1^\dagger \hat{c}_2^\dagger \hat{c}_4 \hat{c}_3 \,. \tag{1}$$

In order to keep the notation simple, it is useful to introduce a combined index for the orthonormal Wannier basis set: $|1\rangle \equiv |r, m, \sigma\rangle$ with site r, orbital m and spin σ. The one electron hopping matrix elements reads $t_{12} = \langle 1|\hat{H}_0|2\rangle$ and general interaction tensor is $V_{1234} = \langle 12|\hat{V}_{\text{int}}|34\rangle$. For multiorbital systems it is useful to introduce the fully antisymmetric interactions vertex: $U_{1234} = V_{1234} - V_{1243}$ with an additional factor $\frac{1}{2}$ in the last sum of Eq. (1). We use atomic units with $\{m, e, \hbar, k_B\} = 1$. In the path-integral formalism (see Appendix A), the equilibrium partition function of a general fermionic lattice system with Hamiltonian Eq. (1) and inverse temperature $\beta = 1/T$ can be written in the form of a functional integral in d+1 dimensions over Grassmann variables $[c^*, c]$ (corresponding to the original operators $[\hat{c}^\dagger, \hat{c}]$)

$$Z = \int \mathcal{D}[c^*, c]\, e^{-S[c^*, c]} \tag{2}$$

with Euclidean action for imaginary time $\tau = it$

$$S[c^*, c] = -\sum_{1,2} c_1^*\, \mathcal{G}_{12}^{-1}\, c_2 + \frac{1}{4} \sum_{1234} U_{1234}\, c_1^* c_2^* c_4 c_3 \,, \tag{3}$$

with inverse bare Green function matrix

$$\mathcal{G}_{12}^{-1} = -\partial_\tau - t_{12}\,, \tag{4}$$

where the Grassmann variable index means $|1\rangle \equiv |r, m, \sigma, \tau\rangle$ and following the definition of "summation" over continuous imaginary time τ in the $[0, \beta]$ interval

$$\sum_1 \{\cdots\} \equiv \sum_{i,m,\sigma} \int_0^\beta d\tau\, \{\cdots\}\,. \tag{5}$$

All single-particle effects in solids can be described with the help of the one-electron Green function for interacting fermion systems with Hamiltonian in Eq. (1), which may be represented as the following path-integral over action in Eq. (3)

$$G_{12} = -\langle c_1 c_2^* \rangle_S = -\frac{1}{Z}\int \mathcal{D}[c^*, c]\, c_1 c_2^*\, e^{-S[c^*,c]}\,. \tag{6}$$

Note, that in the functional integral of Eq. (6) the anti-commuting Grassmann variables are automatically "ordering" in the imaginary times and one does not need to introduce the "time-ordering" operator in the definition of Green function.

We will discuss in this chapter different methods for numerical "path-integrations" of Eq. (6) which are all related to different flavors of the continuous time (CT) quantum Monte Carlo (QMC) scheme. The first approach, namely Diagrammatic Monte Carlo (DiagMC) was developed for bosonic systems [8] and is related to a QMC-summation of Feynman diagrams with an important sampling strategy. For fermionic systems two successful versions of CT-QMC exist and are related with the interaction expansion (CT-INT) [9] and the hybridization expansion (CT-HYB) family of impurity solvers [1]. Finally, the lattice version of the CT-INT scheme for the one-particle irreducible self-energy with only connected Feynman diagrams, the so called CDet approach was developed recently [10].

The main problem with calculations of the path integral in Eq. (6) is related with the fact that the only known answers refer to non-interacting system (see Appendix A). The interaction expansion (CT-INT) continuous-time quantum Monte Carlo algorithm for fermions is based on a formal series expansion for the partition function (3) in the U-terms of the action in Eq. (3) [9]. In a schematic form we have

$$Z = \int \mathcal{D}[c^*, c]\, e^{-S_0[c^*,c]} \sum_{k=0}^{\infty} \sum_{1234} \frac{(-1)^k}{4^k k!} \int_0^\beta d\tau_1 \cdots d\tau_k \big(U_{1234}\, c_1^* c_2^* c_4 c_3\big)^k \tag{7}$$

where S_0 is the Gaussian part of the action (3) related with the bare Green function $\mathcal{G}_{12}$. In this case we can integrate out the fermionic path integral in Eq. (7) for each k-th terms and get a $k\times k$ determinant of bare Green functions of two spin-projections of $\mathcal{G}^\sigma$ in the paramagnetic state (the factor $k!$ is cancelled for new time integration area)

$$Z = Z_0 \sum_{k=0}^{\infty} \sum_{1234} \big(-\frac{1}{2} U_{1234}\big)^k \int_0^\beta d\tau_1 \cdots \int_{\tau_{k-1}}^\beta d\tau_k\, \det \mathcal{G}^\uparrow_{k(31)} * \det \mathcal{G}^\downarrow_{k(42)} \equiv \sum_{\mathcal{C}} s(\mathcal{C}) W(\mathcal{C}), \tag{8}$$

where the $k\times k$ matrix of bare Green function is defined as

$$\hat{\mathcal{G}}_k = \begin{pmatrix} \mathcal{G}_{11} & \mathcal{G}_{12} & \cdots & \mathcal{G}_{1k} \\ \mathcal{G}_{21} & \mathcal{G}_{22} & \cdots & \mathcal{G}_{2k} \\ \vdots & \vdots & \ddots & \vdots \\ \mathcal{G}_{k1} & \mathcal{G}_{k2} & \cdots & \mathcal{G}_{kk} \end{pmatrix}, \tag{9}$$

and the indices (31) and (42) in Eq. (8) just indicates how pairs of space-orbital-time indices are connected to the corresponding indices of the interaction vertex U_{1234} and is "repeated" k-times to couple $\hat{\mathcal{G}}_k^{\uparrow}$ and $\hat{\mathcal{G}}_k^{\downarrow}$ matrices to all k-vertices: $(U_{1234})^k$. In order to overcome a trivial sign problem related with the factor $(-U)^k$ one uses a particle-hole transformation related with so-called α-shift [9]. The CT-INT scheme is performed by Monte Carlo importance sampling in the space $\mathcal{C}$ of $k\times k$ fermionic determinants with the probability defined by absolute value of the full expression in Eq. (7) under sum and integral. We also introduce the "sign" $s(\mathcal{C})$ of the product of two determinants which is not always positive. This is the reason for the so-called QMC fermionic sign problem which plays an important role in all quantum Monte Carlo simulations. One can rewrite Eq. (7) as $Z = \big\langle s(\mathcal{C})\big\rangle_{MC}$ with the average over Monte Carlo runs with corresponding probabilities. Note, that for a half-filled particle-hole symmetric Hubbard-like model the product of two fermionic determinants is always positive and there is no sign problem. The probability to change from k-th to $k{+}1$-th order in the Metropolis algorithm is related with ratio of the fermionic determinants [9]

$$P(k \to k{+}1) = \min\left(1, \frac{\beta U}{k{+}1} \prod_{\sigma} \frac{\det \mathcal{G}_{k+1}^{\sigma}}{\det \mathcal{G}_{k}^{\sigma}}\right). \tag{10}$$

The optimal order of k-perturbation, which corresponds to the maximum of the distribution function of the fermionic determinants size for a cluster of N-sites is of the order $k_{\text{opt}} \sim \beta N U$ [9]. We can see that for finite fermionic system at non-zero temperature ($\beta \neq \infty$) the CT-INT "perturbation" k-series is convergent (Fig. 2).

The simplest way to find the expressions for the Green function and other correlation functions uses functional derivatives of the action Eq. (3) in an external Grassmann fields (J^*, J)

$$S[J^*, J] = S[c^*, c] + \sum_i (c_i^* J_i + J_i^* c_i)\,. \tag{11}$$

In this case we have:

$$G_{ij} = -\langle c_i c_j^* \rangle_S = \frac{1}{Z} \frac{\delta^2 S[J^*, J]}{\delta J_i^* \delta J_j} \bigg|_{J^*=J=0}. \tag{12}$$

Using Eq. (8) we can write the Green function schematically as

$$G_{ij}^{\sigma} = \frac{1}{Z} \big\langle s(\mathcal{C}) \det \mathcal{G}_{k+(ij)}^{\sigma} / \det \mathcal{G}_{k}^{\sigma} \big\rangle_{kMC}\,, \tag{13}$$

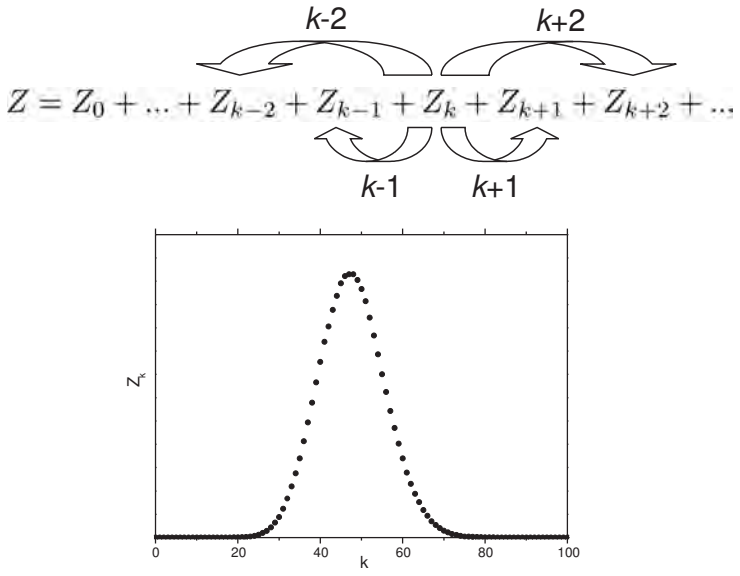


Fig. 2: *A random walk in the space of fermionic determinants Z_k according to the perturbation series expansion Eq.(8) and an example of the histogram for the perturbation order Z_k in Eq.(10). For single-particle properties it is enough to use only $k \mapsto k\pm1$ moves. For two-particle properties it is useful to include also $k \mapsto k\pm2$ moves.*

where $\hat{\mathcal{G}}_{k+(ij)}$ is the $(k+1)\times(k+1)$ matrix

$$\hat{\mathcal{G}}_{k+(ij)} = \begin{pmatrix} \mathcal{G}_{11} & \mathcal{G}_{12} & \cdots & \mathcal{G}_{1k} & \mathcal{G}_{1j} \\ \mathcal{G}_{21} & \mathcal{G}_{22} & \cdots & \mathcal{G}_{2k} & \mathcal{G}_{2j} \\ \vdots & \vdots & \ddots & \vdots & \vdots \\ \mathcal{G}_{k1} & \mathcal{G}_{k2} & \cdots & \mathcal{G}_{kk} & \mathcal{G}_{kj} \\ \mathcal{G}_{i1} & \mathcal{G}_{i2} & \cdots & \mathcal{G}_{ik} & \mathcal{G}_{ij} \end{pmatrix}, \tag{14}$$

and Monte Carlo just averages over the k-space of fermionic determinants. The ratio of the two determinants in Eq. (13) we can calculate exactly [9] and the final CT-INT expression reads (skip the same index σ)

$$G_{ij} = \mathcal{G}_{ij} - \frac{1}{Z}\,\mathcal{G}_{ii'} * \left\langle s(\mathcal{C})\,\left[\mathcal{G}_k^{-1}\right]_{i'j'} \right\rangle_{kMC} * \mathcal{G}_{j'j}\,, \tag{15}$$

The CT-INT scheme gives a very stable and accurate results for the Green function for small clusters, but for bigger systems the average size of the determinants in Eq. (13) becomes prohibitively large. Note that $\det \mathcal{G}_k^\sigma$ together with the interaction vertices U^k represents $k!$ Feynman diagrams both connected and disconnected. It is known from the "linked cluster theorem" [11] that the disconnected diagrams are exactly cancelled with the denominator Z. Therefore, the most efficient way to obtain the Green function is related with a lattice diagrammatic Monte Carlo scheme within the connected determinants (CDet) approach [10]. The main idea of the CDet method is related with the fact that one can iteratively subtract all non-connected diagrams during the Monte Carlo move in the space of fermionic determinants. These disconnected Feynman diagrams can be represented as subset $\mathcal{S}\subsetneq\mathcal{C}$ of connected diagrams of the lower order times all remaining diagrams. We can represent schematically the Green function

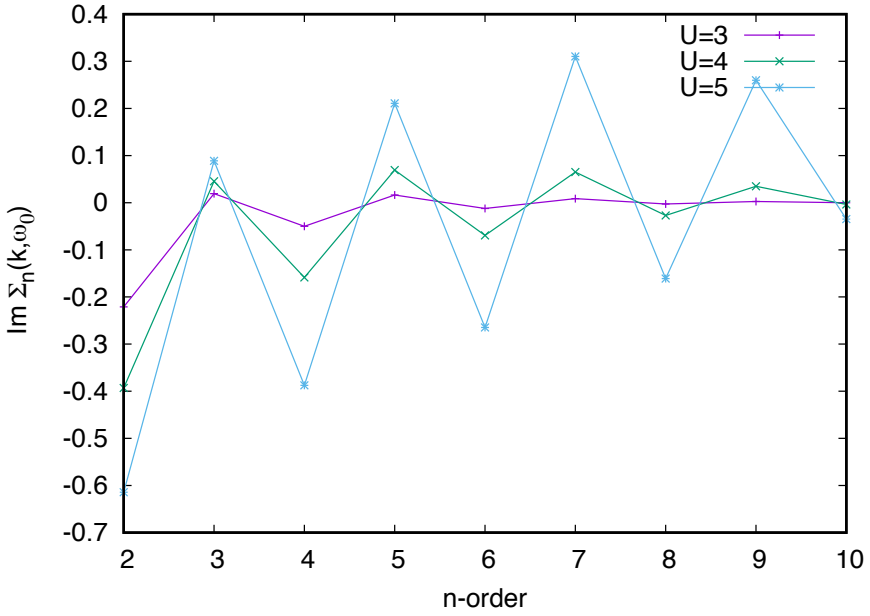


Fig. 3: *Contribution of different perturbation orders to the imaginary part of the self-energy* $\Sigma(\mathbf{k},\omega_0) = \sum_n \Sigma_n(\mathbf{k},\omega_0)$ *for* $\mathbf{k} = (\pi, 0)$, $\beta = 5$, $t'/t = -0.3$, $N = 0.85$ *with increasing interaction strength* U *in the* 64×64 *Hubbard lattice within the CDet scheme [12].*

calculations within a CDet Monte Carlo step in the space of $\mathcal{C}$ configuration as

$$G(\mathcal{C}) = \det \mathcal{G}(\mathcal{C}) - \sum_{\mathcal{S}\subsetneq\mathcal{C}} G(\mathcal{S}) \det \mathcal{G}\big(\mathcal{C}\backslash\mathcal{S}\big) \,. \tag{16}$$

This is the most "time-consuming" procedure to get rid of all disconnected diagrams for the given k-order of determinants using all smaller rank determinants on the right-hand side of Eq. (16). The great progress of the CDet approach compared with DiagMC allowed to calculate up to 12-th order in the U^k perturbation series in Eq. (8) for the Hubbard model for very large systems in the thermodynamic limit. It is also possible to formulate iterative series of connected Feynman diagram directly for a self-energy similar to Eq. (16), which reduces the computational cost for such one-particle irreducible schemes. Moreover, the sign-problem in lattice QMC turns to a "sign-blessing" which can help in averaging to zero all higher diagrammatic contributions that are not calculated in the CDet scheme [10]. Investigations of pseudogap phase for a one-band Hubbard model of doped cuprates [12] show the high accuracy of such path-integral scheme. For young researchers there is the very useful possibility to test the CDet code included in the Supplementary Materials of [12].

The main problem of the CDet scheme is the poor convergence of series $\Sigma = \sum_k U^k \Sigma_k$ which for large $U{>}5t$ start to diverge (see Fig. 3) and one needs to use a resummation scheme from conformal field theory. Nevertheless, for the part of phase space (U, β, n) where the CDet scheme is converged (e.g. for large temperature, $\beta{=}5$), this method can be considerd as numerically exact solution of correlated lattice problem. As example of CDet results [12] we show in Fig. 4 the spectral function of Hubbard model for a large system of of 64×64 sites with strong interactions. One can see the complicated electronic structure of interacting fermions with the pseudogap feature at the $X{=}(\pi, 0)$ point and the antiferromagnetic shadow bands.

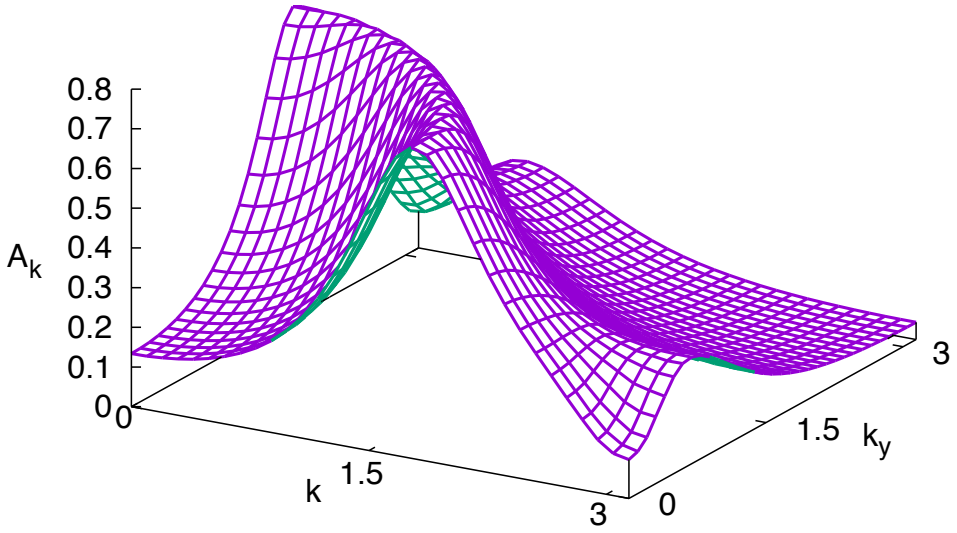


Fig. 4: *Spectral function* $A_k{=}-\operatorname{Im} G(\mathbf{k},\omega_0)$ *at the lowest Matsubara frequency* $\omega_0{=}\pi/\beta$ *for* $\beta{=}5$, $N{=}0.85$, $t'/t{=}-0.3$, $U{=}5$ *in the* $64{\times}64$ *Hubbard lattice within the CDet scheme [12].*

We now turn to a different route to tackle the "sign problem" in the determinant lattice QMC scheme and design a strong-coupling perturbative solution for a general Hubbard model. The starting point is related to the "reference system" idea [13]. The choice of a single-site approximation like dynamical mean-field theory [3] as the reference system leads to the dual fermion technique [7].

3 Expansion around reference system

We discuss a general path-integral method for expansions around arbitrary reference systems. In fact, the CT-INT scheme (see Eq. (8)) can be considered as a special case of the reference system approach which is just the free fermion case, described by the Gaussian quadratic part $\mathcal{G}_{12}$ of the action in Eq. (3). In this case the path-integral expansion is particularly simple and coincides with the weak coupling perturbation which is described by the series of fermionic determinants built from the bare propagators $\mathcal{G}_{12}$. Now we considered a more general case, where the reference system consists of interacting fermions. We start with the simple case of a Hubbard-like model, where the interaction strength U is fixed to be the same for the reference and target systems, and only small changes in the one-electron part will be considered in lowest orders of the path-integral expansion. In fact this approach has many commons details with the Dual-Fermion (DF) lattice expansion around the local DMFT starting point [7]. In a more general case, when the interactions strength is different in reference and system, one should use a so-called Dual-Boson theory [6].

We consider the simple case of interacting fermions on a lattice within the single band Hubbard model, defined by the Hamiltonian

$$\hat{H}_\alpha = -\sum_{i,j,\sigma} t_{ij}^{\alpha}\, \hat{c}^{\dagger}_{i\sigma}\hat{c}_{j\sigma} + \sum_i U\left(\hat{n}_{i\uparrow}-\frac{1}{2}\right)\left(\hat{n}_{i\downarrow}-\frac{1}{2}\right) \tag{17}$$

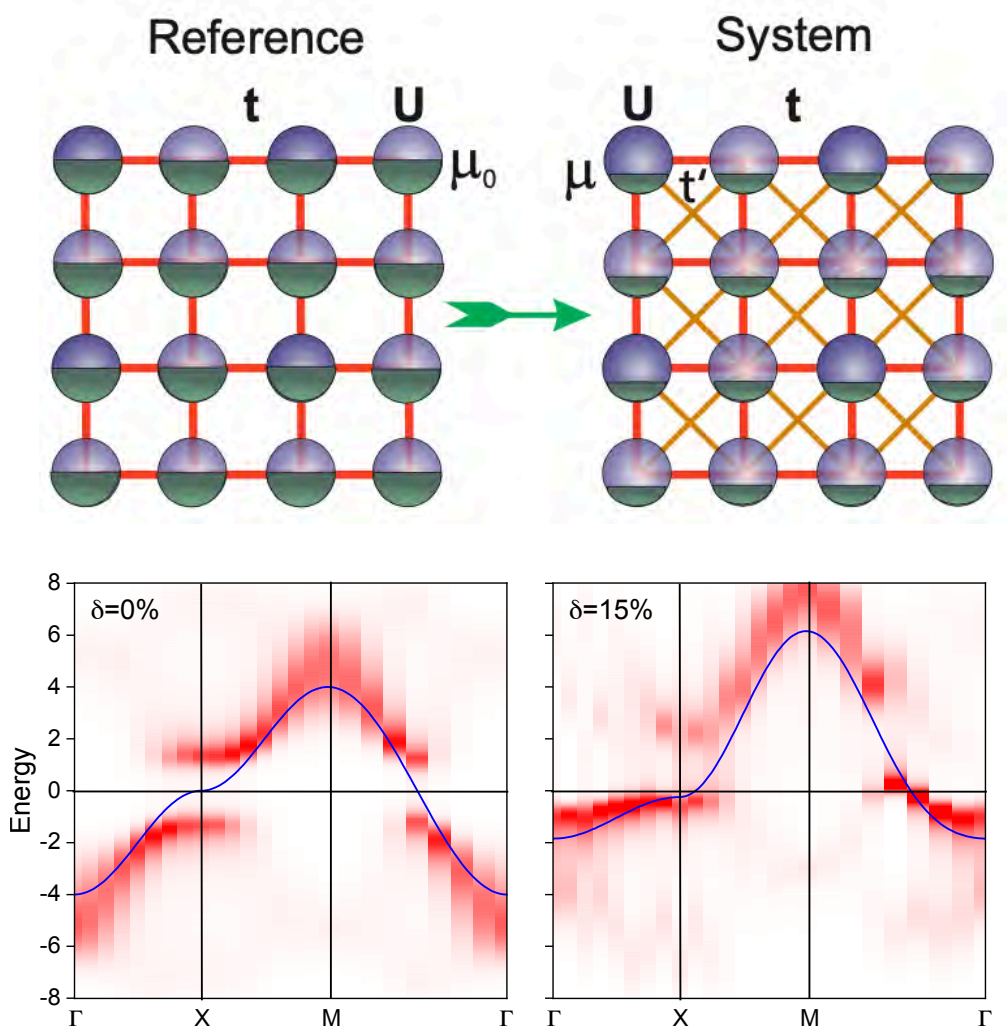


Fig. 5: *Schematic representation of a half-filled reference system (left) for the doped* $(t$-t'-$U)$ *square lattice (right). Bottom: Electronic spectral function of the* t-t' *Hubbard model calculated for* U=5.6 *at* β=5 *relative to the chemical potential together with the non-interacting dispersions (blue line). The reference results are obtained for the half-filled particle-hole symmetric case* t'=0*, (left panel), the DF-QMC results for* δ=15% *hole doping with* t'=−0.3 *(right).*

where t_{ij} are the hopping matrix elements including the chemical potential μ in the diagonal

$$t_{ij}^{\alpha} = \begin{cases} t & \text{if } i \text{ and } j \text{ are nearest neighbors,} \\ \alpha t' & \text{if } i \text{ and } j \text{ are next nearest neighbors,} \\ \alpha\mu & \text{if } i = j, \\ 0 & \text{otherwise,} \end{cases} \tag{18}$$

where $\hat{n}_{i\sigma} = \hat{c}_{i\sigma}^{\dagger}\hat{c}_{i\sigma}$. We use a "scaling" parameter α, which distinguishes the reference system H_0 for α=0 corresponding to the half-filled Hubbard model (μ_0=0) with only nearest neighbors hopping (t_0'=0) from the final system H_1 for α=1 with given μ and t'. Note that longer-range hoping parameters can be trivially included in the present formalism similarly to t'.
The reference system now corresponds to the half-filled (μ_0=0) particle-hole symmetric (t_0'=0) case (Fig. 5) where lattice Monte Carlo has no sign problem and the numerically exact solution

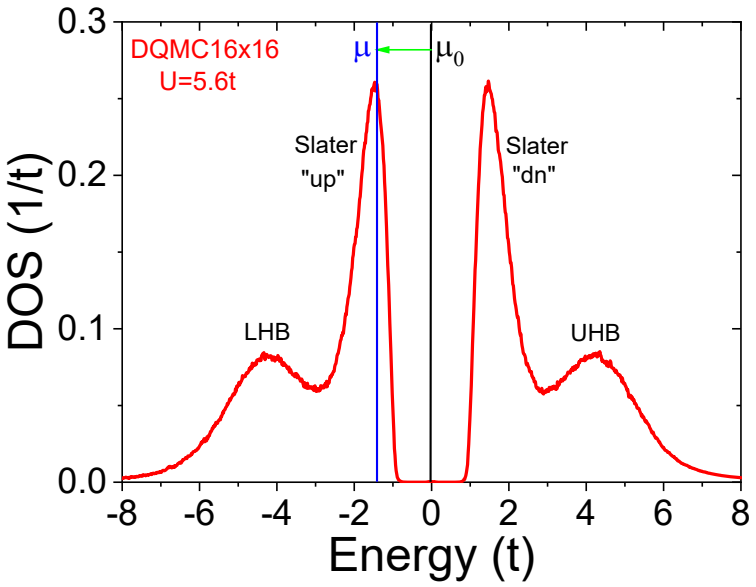


Fig. 6: *The DOS of the normal state at* β=10 *for the reference system corresponding to a* 16×16 *lattice with* t=1, U=5.6, t'=0, *and* μ=0 *using the DQMC scheme and the MaxEnt analytical continuation to real energy.*

for any practical value of U is possible within a broad range of temperatures [14]. Then we apply the lattice dual fermion QMC perturbation theory [7, 13, 15] to find the first-order perturbative corrections in μ and t'. To this aim, it is sufficient to calculate the two-particle Green function or, equivalently, the four-leg vertex, which can be done accurately enough with continuous time quantum Monte Carlo. Our reference system already has the main correlation effects in the lattice and shows the characteristic "four-peak" structure [16] with the high-energy "lower" and "upper" Hubbard bands at $E \simeq \pm 5t$ as well as the two "Slater" peaks close to the Mott gap at $E \simeq \pm 2t$ related to the "band-like" antiferromagnetic splitting of "spin-up" and "spin-down" electrons for a particular local site, which can be seen in Fig. 6. This is an ideal reference point to investigate the effects of doping and breaking of partial-hole symmetry by a particular sign of t'. After the dual-fermion perturbation approach, which we will discuss, the correlated metallic states appeared on Fig. 5 (right panel). The results for the strong-coupling case (U=5.6t) with practically interesting values of the chemical potential and next-nearest-neighbor hopping corresponding to cuprate superconductors indicate the formation of a pseudogap and the nodal-antinodal dichotomy (that is, well-defined quasiparticles in the nodal part of the Fermi surface and strong quasiparticle damping for the antinodal part) which gives this approximation a perspective for practical applications.

We start with a most general definition of a perturbation matrix related to the difference of one-electron part of action

$$\tilde{t} = \mathcal{G}_0^{-1} - \mathcal{G}_1^{-1} \,. \tag{19}$$

This can apply to a general case of a system in an external fermionic bath and therefore defines our perturbation $\tilde{t}$ in terms of the one-electron part of reference-system action. In case of a pure Hamiltonian systems, our perturbation is related with the difference of the effective hopping

matrix t_{ij}^{α} and in $\mathbf{k}$-space is equal to

$$\tilde{t}_{\mathbf{k}} = -4t' \cos k_x \cos k_y - \mu \,. \tag{20}$$

In order to formulate an expansion around reference action S_0 we express the connection to the final action $S \equiv S_1$ with the same local interaction in the following form

$$S[c^*, c] = S_0[c^*, c] + \sum_{12} c_1^* \, \tilde{t}_{12} \, c_2 \,. \tag{21}$$

The main idea of the dual fermion transformation is the change of variables (similar to the Fourier transform) from the strongly correlated fermions (c^*, c) in Eq. (3) to the weakly correlated "dual" Grassmann fields (d^*, d) in the path integral representation for the partition function in Eq. (21), followed by a simple perturbation treatment. The new variables were introduced through the following Hubbard-Stratonovich transformation with the perturbation matrix $\tilde{t}_{12}$ in real-space (the Einstein summation convention over repeated indices is assumed)

$$e^{-c_1^* \, \tilde{t}_{12} \, c_2} = Z_t \int \mathcal{D}\,[d^*, d] \, e^{d_1^* \, \tilde{t}_{12}^{-1} \, d_2 + d_1^* c_1 + c_1^* d_1} \tag{22}$$

with $Z_t = \det(-\tilde{t})$ and we always assume the matrix inversion: $\tilde{t}_{12}^{-1} \equiv (\tilde{t}^{-1})_{12}$. Using this transformation, the lattice partition function becomes

$$Z = Z_0 Z_t \int \mathcal{D}[d^*, d] \, e^{d_1^* \, \tilde{t}_{12}^{-1} \, d_2} \, \left\langle e^{d_1^* c_1 + c_1^* d_1} \right\rangle_0 \tag{23}$$

with the standard definition of average over S_0

$$\langle \cdots \rangle_0 = \frac{1}{Z_0} \int \mathcal{D}[c^*, c] \cdots e^{-S_0[c^*, c]}. \tag{24}$$

Now we can integrated out the c^*, c fermions and show that the average over S_0 can be rewritten in the form of a "cumulant expansion" [17] or connected correlators $\langle \cdots \rangle_{0c}$

$$\left\langle e^{d_1^* c_1 + c_1^* d_1} \right\rangle_0 = \exp \left[\sum_{n=1}^{\infty} \frac{(-1)^n}{(n!)^2} \gamma^{(2n)}_{1 \cdots n, n' \cdots 1'} d_1^* \cdots d_n^* d_{n'} \cdots d_{1'} \right] \tag{25}$$

with cumulants or connected correlators for the reference system which can be calculated within the QMC

$$\gamma^{(2n)}_{1 \cdots n, n' \cdots 1'} = (-1)^n \left\langle c_1 \cdots c_n c^*_{n'} \cdots c^*_{1'} \right\rangle_{0c}. \tag{26}$$

We can write the effective action for the "dual fermions" $\tilde{S}[d^*, d]$ in the lowest order approximation for the dual interaction [15]. The first term in the cumulant expansion in Eq. (25) with $n = 1$ or $\gamma^{(2)}_{11'}$ which is bilinear over $[d_1^* \, , d_2]$ the Grassmann variables, corresponds to the exact Green function of reference system

$$\gamma^{(2)}_{11'} \equiv g_{11'} = -\langle c_1 c^*_{1'} \rangle_0 = -\frac{1}{Z_0} \int \mathcal{D}[c^*, c] \, c_1 c_2^* \, e^{-S_0[c^*, c]}. \tag{27}$$

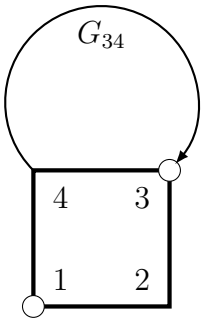


Fig. 7: *Feynman diagram for the first order dual fermion perturbation for the self-energy $\tilde{\Sigma}_{12}$: the line represents the non-local dual Green function $\tilde{G}_{43}$, the box the two-particle vertex γ_{1234}.*

Note, that all correlators of the "reference system" will be written with the small letters. Together with the term $\tilde{t}^{-1}_{12}$ in Eq. (23) this gives a bare Green function for the dual fermions

$$\tilde{G}^0_{12} = \left[\, \tilde{t}^{-1} - \hat{g} \,\right]^{-1}_{12} . \tag{28}$$

The second term in the cumulant expansion in Eq. (25) with $n{=}2$ corresponds to $\gamma^{(4)}_{122'1'}$ which is biquadratic over the $[d^*_1\,, d_2]$ Grassmann variables, and gives an effective two-particle interaction among the dual-fermions.The corresponding connected four-point vertex has the following form (we skip the "(4)" abbreviation)

$$\gamma_{122'1'} = \langle c_1 c_2 c^*_{2'} c^*_{1'} \rangle_0 - \langle c_1 c^*_{1'} \rangle_0 \langle c_2 c^*_{2'} \rangle_0 + \langle c_1 c^*_{2'} \rangle_0 \langle c_2 c^*_{1'} \rangle_0 \tag{29}$$

with four points correlator or two-particle Green function for the reference system

$$\langle c_1 c_2 c^*_3 c^*_4 \rangle_0 = \frac{1}{Z_0} \int \mathcal{D}[c^*, c]\; c_1 c_2 c^*_3 c^*_4 \; e^{-S_0[c^*,c]}. \tag{30}$$

Finally the dual-fermion action in the two-particle approximation has the following form

$$\tilde{S}[d^*, d] = -\sum_{12} d^*_1 \; (\tilde{G}^0)^{-1}_{12} \; d_2 + \frac{1}{4} \sum_{1234} \gamma_{1234} \, d^*_1 d^*_2 d_4 d_3. \tag{31}$$

Note, the effective interaction term for anti-commuting Grassmann variables has the same form as for the standard antisymmetric Coulomb interactions (Eq. (3)). We have shown, that the dual "Fourier" trick transforms strongly correlated fermions with large U_{1234} interactions to weakly correlated dual fermions with effective interactions γ_{1234} which are defined by the screened fully connected two-particle vertex of the reference system. The first order correction to the dual self-energy is given by the diagram shown in Fig. 7 and can be calculated for a large system using the QMC-scheme

$$\tilde{\Sigma}^{(1)}_{12} = \sum_{s-QMC} \sum_{3,4} \gamma^d_{1324}(s) \, \tilde{G}^0_{43} \,, \tag{32}$$

where the density vertex reads

$$\gamma^d_{1234} = \gamma^{\uparrow\uparrow\uparrow\uparrow}_{1234} + \gamma^{\uparrow\uparrow\downarrow\downarrow}_{1234} \,. \tag{33}$$

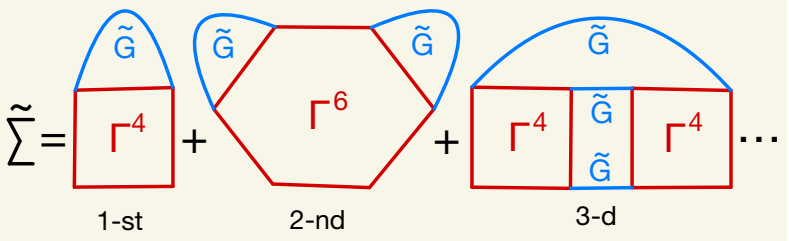


Fig. 8: *Diagrammatic series for the dual self-energy up to the 3-rd order in $\tilde{G}$.*

The main trick for practical computations of large systems is related with the possibility to "factorize" the complicated vertex γ_{1234} inside the stochastic DQMC process with $\{s\}$-auxiliary fields or the CT-INT scheme with stochastic sampling of interaction order expansion $\{s\}$, using the Wick-theorem

$$\gamma_{1234}(s) \equiv \langle c_1 c_2 c_3^* c_4^* \rangle_s = \langle c_1 c_4^* \rangle_s \langle c_2 c_3^* \rangle_s - \langle c_1 c_3^* \rangle_s \langle c_2 c_4^* \rangle_s \,. \tag{34}$$

Finally, one needs to find an exact relationship between the dual and real Green functions [7]. We make variation of $\ln Z$ in Eq.(23) and Eqs.(2, 21) with respect to $\tilde{t}$

$$G_{12} = \frac{\delta \ln Z}{\delta \tilde{t}_{21}} = -\tilde{t}^{-1}_{12} + \tilde{t}^{-1}_{13} \tilde{G}_{34} \tilde{t}^{-1}_{42} \,. \tag{35}$$

Using the definition of the exact dual Green function $\tilde{G}^{-1} = \tilde{G}_0^{-1} - \tilde{\Sigma}$ we can get the expression for the real Green function

$$G_{12} = \left(\left(g + \tilde{\Sigma} \right)^{-1} - \tilde{t} \right)^{-1}_{12} , \tag{36}$$

which means that the dual self-energy has meaning of effective T-matrix term.

The Dual Fermion transformation allowed us to use arbitrary reference systems and transform the strongly correlated lattice fermion problem to an effective action of weakly coupled dual quasi-particles. In this case even the lowest order approximation can give already reasonable results. The exact diagrammatic series for the dual self-energy is presented in Fig. 8. The second order diagram in $\tilde{G}$ which includes $\gamma^{(6)}$ is local within the cluster and can be calculated with a similar QMC scheme. The 3-rd order correction contains two $\gamma^{(4)}$ vertices and it is not easy to sample inside a QMC run. One may compare second order contributions to $\tilde{\Sigma}$ with the fist one and conclude on the convergence of the DF-series.

We can establish also a connection of the DF-formalism with the DMFT approximation: in this case we choose the reference system as an impurity system defined by a frequency dependent hybridization function Δ_ω so that $\tilde{t} = t - \Delta_\omega$. Moreover, all vertices for such a DF-theory will be local and the first non-local contribution to $\tilde{\Sigma}$ will be the 3-rd order diagram in Fig. 8. We can eliminate all local contributions (e.g. fist two diagrams in Fig. 8) if we chose Δ_ω such that $\tilde{G}^0_{loc} = 0$ or using the $\mathbf{k}$-space: $\sum_{\mathbf{k}} \left[\tilde{t}^{-1}_{\mathbf{k}} - g_\omega \right]^{-1} = 0$. Since the impurity Matsubara Green function $g_\omega \neq 0$, we can rewrite this condition as

$$g_\omega = \sum_{\mathbf{k}} \left[g^{-1}_\omega + \Delta_\omega - t_{\mathbf{k}} \right]^{-1} , \tag{37}$$

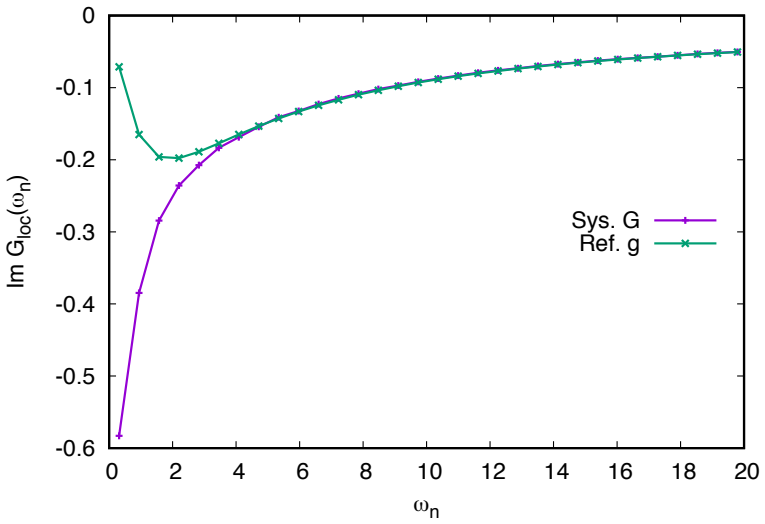


Fig. 9: *Imaginary part of the normal local Green function obtained for a* 16×16 *lattice at* β=10, t=1, *and* U=5.6 *using DF-QMC. The results are obtained for the half-filled reference* g *(green) and lattice* G *(magenta) problems, and plotted as a function of Matsubara frequency* ω_n=$(2n+1)\pi/\beta$. *The lattice problem is calculated for* t'=-0.3 *and* μ=-1.8 *(*δ=13.3% *of hole doping).*

which is nothing else but the celebrated DMFT self-consistent condition for the optimal hybridization function Δ_ω and the right hand side corresponds to the $\mathbf{k}$-sum of a lattice DMFT Green function.

As a "raw" output from this DF-QMC scheme we can present the Matsubara Green functions in Eq. (36). The result is obtained for a 16×16 periodic lattice with 64 time slices. We normally measure a DF-self energy using 10^4–10^5 QMC sweeps. In Fig. 9 we show the imaginary part of the starting Green function g, obtained for the half-filled particle-hole-symmetric ($\mu = 0$, $t' = 0$) reference problem using DQMC. The full local lattice Green function G of the final system is calculated within the DF-QMC scheme. One can see that in the high-frequency limit $\omega_n \geq 10$ the dual perturbation is very small and G almost coincides with g. However, at low-frequency the lattice Green function G shows a metallic character, while the reference Green function g extrapolates to zero at $\omega \to 0$, which corresponds to the Mott-Hubbard-Slater gap. In Fig. 5 (bottom) we show the transformation of the electronic spectral function from the half-filled (reference) case with $\mu_0 = 0$ and $t' = 0$ (left panel) to the doped system with $\mu = -1.45$ and $t' = -0.3$ (right panel). The results are calculated at the inverse temperature $\beta = 5$ using stochastic analytical continuation from Matsubara space to real energy [18]. In the Mott insulator phase, corresponding to $\delta = 0\%$ doping, one can see the formation of broad Hubbard bands around the energy $E = \pm5t$, an antiferromagnetic gap $E = \pm2t$ in the antinodal point $\mathrm{X} = (\pi, 0)$ and a shadow antiferromagnetic bands at $E \simeq -3t$ in the vicinity of the $\mathrm{M} = (\pi, \pi)$ point. Upon $\delta = 15\%$ hole doping, the spectral function changes dramatically. One can clearly see a strong effect of t' on the van Hove singularity that results in the formation of a narrow, almost flat band in the Γ-X direction and the appearance of a pseudogap near the X point, which signals the quasi-localized behavior of electrons related to the formation of fluctuating local moments. On the other hand, the spectrum remains metallic near the nodal point $(\pi/2, \pi/2)$.

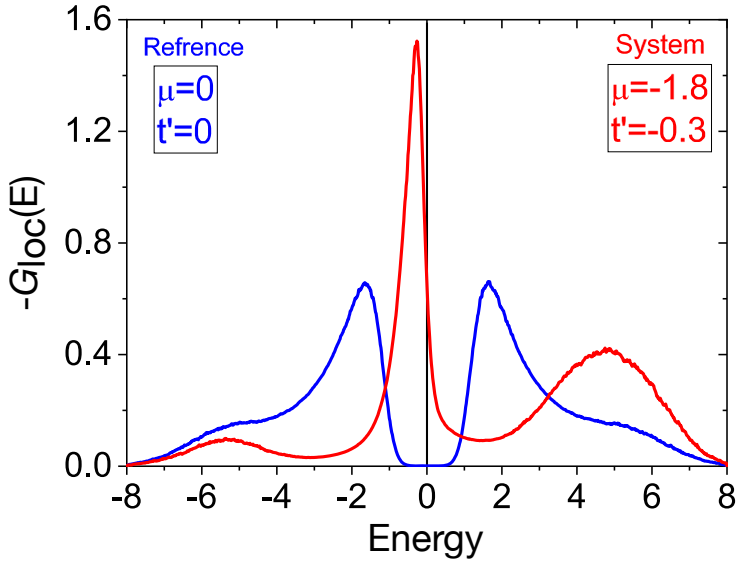


Fig. 10: *Imaginary part of the local Green function (proportional to the density of states) obtained for* $\beta = 10$ *and* $U = 5.6$ *for the half-field reference system (blue line) and the lattice problem with* $t' = -0.3$ *and* $\mu = -1.8$ *(red line), which corresponds to 13% hole doping.*

An example of the calculated the density of states or local Green function for real energies is presented in the Fig. 10 with standard t' and the μ for cuprates in comparison with the reference case. We can clearly see the formation of a narrow quasiparticle peak from the "low Slater band", while the Hubbard bands stay approximately at the same position due to the local nature of Mott-correlations. The intensity of the metallic upper Hubbard bands increases due to the "merging" with the upper Slater band.

In order to prove the convergence properties of the DF-QMC scheme we calculate the second-order contribution to the dual self-energy or the second Feynman diagram in Fig. 8. The results for lattice Green functions of the first order theory with the second order approach for a small periodic 4×4 system with relatively weak perturbations together with the exact CT-INT solution for a hole doped lattice with t' is shown in Fig. 11. There are 6 non-equivalent $\mathbf{k}$-points in the

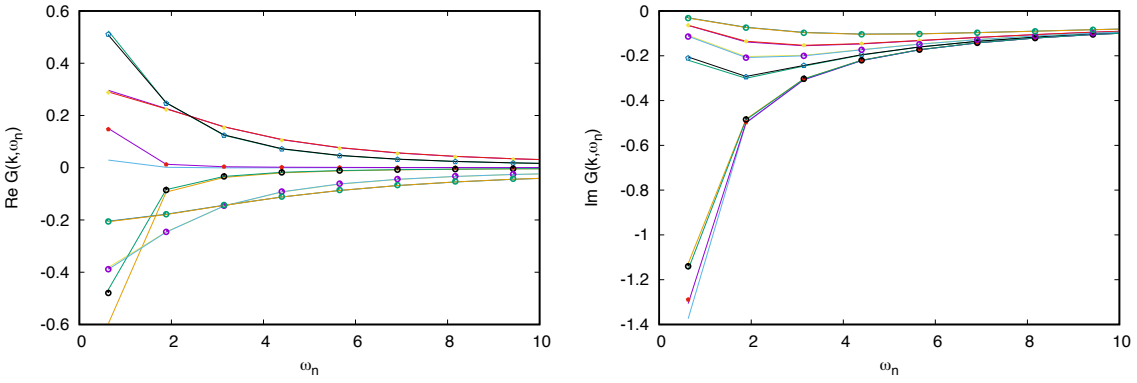


Fig. 11: *Comparison of real (left) and imaginary (right) part of the Matsubara Green functions for 6 non-equivalent* $\mathbf{k}$*-points for first and second order DF-QMC approximations (different color lines) together with exact CT-INT solution (dots) of* 4×4 *periodic system for* $U = 2$*,* $t'/t = -0.1$*,* $\mu = -0.5$ *and* $\beta = 5$*.*

Brillouin zone of the 4×4 lattice. Note that the CT-INT exact results (the dots in the Fig. 11) almost coincide with the second order DF-QMC theory and the first order scheme has small deviations (better seen for the $\mathrm{Re}\, G(\mathbf{k},\omega_0)$ part) and only for two $\mathbf{k}$-points close to the Fermi-surface: the antinodal point at $(\pi,0)$ around 0.2 and the nodal point $(\pi/2,\pi/2)$ around -0.5 on the left panel of the Fig. 11. Corresponding deviations for $\mathrm{Im}\, G(\mathbf{k},\omega_0)$ with the same color code are much smaller and the main deviation can be seen only for the antinode point (red dot in Fig. 11). All other $\mathbf{k}$-points are already converged with the first order theory. This example shows the strength and fast convergence of lattice DF-QMC expansions around the suitable reference system.

4 Dual fermions in spinor space

We can generalize the path integral DF-QMC scheme to include external magnetic or superconducting fields and investigate response of the correlated lattice model [19]. In case of an antiferromagnetic (AFM) external field in k-space $h_Q = h\,\sigma_x\delta_{k,Q}$ with $\mathrm{Q} = (\pi,\pi)$ we have a general spinor form of the perturbation

$$\tilde{t}_k(h_Q) = \begin{pmatrix} \tilde{t}_k & h_Q \\ h_Q^* & \tilde{t}_{k+Q} \end{pmatrix}. \tag{38}$$

For a d-wave superconducting field (Q=0) $\Delta_k = 2h_{dw}(\cos k_x - \cos k_y)$ the quasi-spinor perturbation in Nambu-Gor'kov space reads

$$\tilde{t}_k(h_{dw}) = \begin{pmatrix} \tilde{t}_k & \Delta_k \\ \Delta_k^* & -\tilde{t}_k^* \end{pmatrix}. \tag{39}$$

In the both case we can use the spinor form of the bare dual Green matrix in Nambu space

$$\hat{\tilde{G}} = \begin{pmatrix} \tilde{\mathcal{G}}^{\uparrow\uparrow} & \tilde{\mathcal{G}}^{\uparrow\downarrow} \\ \tilde{\mathcal{G}}^{\downarrow\uparrow} & \tilde{\mathcal{G}}^{\downarrow\downarrow} \end{pmatrix}. \tag{40}$$

The correlation effects beyond the reference problem are taken into account by the first-order contribution to the self-energy (Fig. 7) in the dual space [19]

$$\begin{aligned} \tilde{\Sigma}_{12}^{\uparrow\uparrow} &= -\sum_{3,4}\Big[\langle c_{1\uparrow}c_{2\uparrow}^*c_{3\uparrow}c_{4\uparrow}^*\rangle\,\tilde{\mathcal{G}}_{43}^{\uparrow\uparrow} + \langle c_{1\uparrow}c_{2\uparrow}^*c_{3\downarrow}c_{4\downarrow}^*\rangle\,\tilde{\mathcal{G}}_{43}^{\downarrow\downarrow}\Big], \\ \tilde{\Sigma}_{12}^{\uparrow\downarrow} &= -\sum_{3,4}\langle c_{1\uparrow}c_{2\downarrow}^*c_{3\downarrow}c_{4\uparrow}^*\rangle\tilde{\mathcal{G}}_{43}^{\uparrow\downarrow}, \end{aligned} \tag{41}$$

and similarly for the remaining two spin components. The final expression for the lattice Green function of real fermions in a superconducting external field has the following matrix form

$$\hat{G}_k = \left[\begin{pmatrix} g_k + \tilde{\Sigma}_k^{\uparrow\uparrow} & \tilde{\Sigma}_k^{\uparrow\downarrow} \\ \tilde{\Sigma}_k^{\downarrow\uparrow} & -g_k^* + \tilde{\Sigma}_k^{\downarrow\downarrow} \end{pmatrix}^{-1} - \begin{pmatrix} \tilde{t}_k & \Delta_k \\ \Delta_k^* & -\tilde{t}_k^* \end{pmatrix}\right]^{-1} \equiv \begin{pmatrix} G_k & F_k \\ F_k^* & -G_k^* \end{pmatrix}, \tag{42}$$

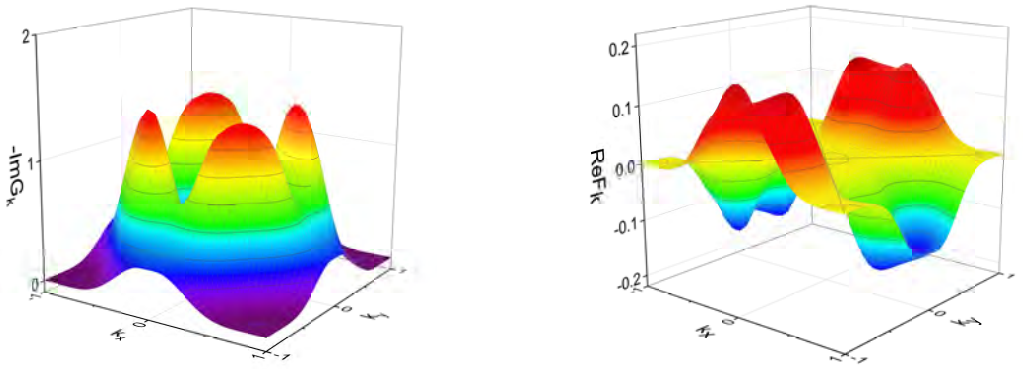


Fig. 12: *The imaginary part of the normal Green function G (left panel) and the real part of the anomalous Green function F (right panel) calculated by DF-QMC with a d-wave external field of $h_{dw} = 0.05$ at the lowest Matsubara frequency $\omega_0 = \pi/\beta$ for 12% hole doping and $\beta = 8$ for periodic 16×16 lattice [19].*

where we introduced a shortened notations for the normal $G = G^{\uparrow\uparrow}$ and anomalous $F = G^{\uparrow\downarrow}$ Green function in Nambu space. Similar spinor expressions hold for the AFM Green function.

In the Fig. 12 we plot the imaginary part of the normal Green function $G(\mathbf{k})$ (left panel), as well as the real part of the anomalous Green function $F(\mathbf{k})$ (right panel). The results are obtained at the lowest Matsubara frequency $\omega_0 = \pi T$ for the first Brillouin zone in the presence of a small external superconducting d-wave field with the amplitude $h_{dw} = 0.05$. These calculations clearly capture the formation of a large pseudogap in the electronic spectral function $-\frac{1}{\pi}\,\mathrm{Im}\,G(\mathbf{k})$ at the antinodal $\mathrm{X} = (\pi, 0)$ point, which exists already at relatively high temperatures $\beta = 5$ corresponding to $T \simeq 700\,\mathrm{K}$ for the realistic hopping amplitude $t = 0.3\,\mathrm{eV}$. Additionally, we found that the anomalous Green function $F(\mathbf{k})$ is relatively large and has a very unusual shape. Indeed, $\mathrm{Re}\,F(\mathbf{k})$ features a suppressed spectral weight at the X points, related to a pseudogap formation in the spectral function, which shifts its extrema in the direction of the nodal point.

In order to investigate connection of the pseudogap effects with the coherence properties of fermions at the antinodal X-point with $\mathbf{k} = (0, \pi)$ we calculate the imaginary part of the normal Matsubara Green function ($\mathrm{Im}\,G_k$) within DF-QMC at the anti-nodal point for a relatively high temperature $\beta = 5$ and different chemical potentials, which correspond to an underdoped system with $\delta = 2 - 9\%$, optimal doping $\delta = 10 - 18\%$, and overdoping with $\delta = 20 - 25\%$ (the left panel of the Fig. 13). It is useful to take the normalized trace of the Gor'kov Green function $(G_k - G_{-k})/2$ which just means the particle-hole symmetry with the same ($\mathrm{Im}\,G_k$) and ($\mathrm{Re}\,G_k$=0). Using this Green function, we perform a stochastic analytical continuation to real energy (right panel of the Fig. 13). We can clearly seen the complicated transformation of the pseudogap spectral function for fermions at the X-point in the underdoped system to more coherent fermions in the optimally doped case with a DMFT-like three peak structure, and finally to almost normal sharp correlated quasiparticles in the overdoped case.

We would also like to discuss the dependence of the superconducting enhancement on hole doping. For these calculations we consider a 8×8 periodic lattice with a "bare" fermionic bath,

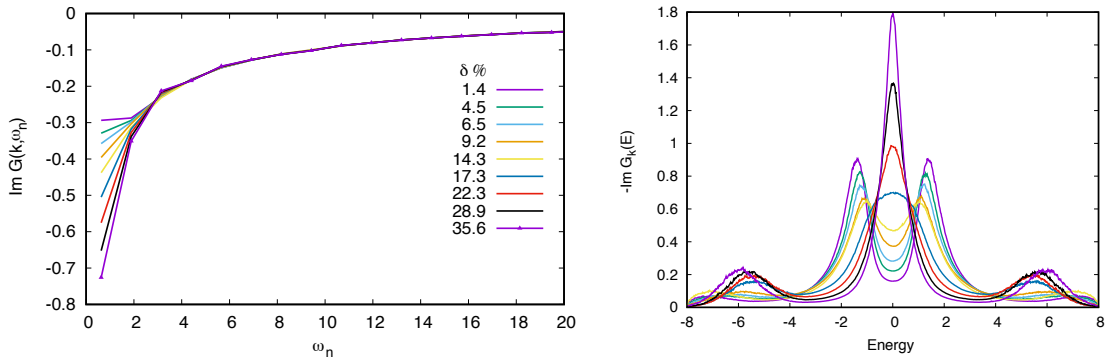


Fig. 13: *The imaginary part of the normal Green function for periodic a* 16×16 *lattice on the Matsubara axis* $\nu_n = (2n+1)\pi/\beta$ *(left panel) obtained in DF-QMC for* $\beta = 5$, $t = 1$, $t' = -0.3$ *and* $U = 5.6$ *and different chemical potentials* $-\omega = (0.8, 1.1, 1.2, 1.3, 1.45, 1.5, 1.6, 1.7, 1.8)$ *which correspond to the hole dopings shows with different colors. Corresponding analytical continuations using a SOM-scheme to the real axis* $-\operatorname{Im} G_k(E)$ *with the same color-scheme (right panel) for the* $\mathbf{k} = \mathrm{X} = (0, \pi)$.

which is introduced to reduce effects of the finite spectrum of small a system. In Fig. 14 we plot the d-wave enhancement of the anomalous Green function (F) normalized by the external superconducting field (h_{dw}) calculated at the X point, as a function of hole doping for the two values of the NNN hopping ($t' = -0.3$ and $t' = 0$). Remarkably, the dome-like superconducting behavior is found only for $t' \neq 0$. Moreover, the maximal superconducting enhancement around $\delta = 15\%$ corresponds to $\mu = -1.4$, which is very close to the position of the van Hove singularity $4t' = -1.2$ in the non-interacting spectrum. The increase of the superconducting enhancement at $\delta = 15\%$ for the optimal second-neighbor hopping $t' = -0.3$ compared to $t' = 0$ is about a factor of two. Note that in the electron doped case with $t'/t = -0.3$ the superconducting response is always smaller compare to the hole one, in agreement with the general experimental knowledge.

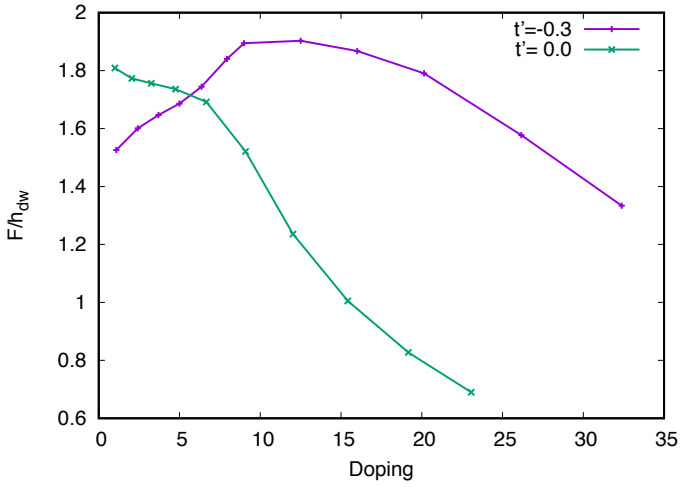


Fig. 14: *The enhancement of the anomalous Green function at the lowest Matsubara frequency* $\nu_0 = \pi/\beta$, *with respect to the external* d*-wave field* $h_{dw} = 0.05$. *The ratio of* F/h_{dw} *is calculated at the* $\mathbf{k} = \mathrm{X} = (0, \pi)$ *point for the* 8×8 *lattice at* $\beta = 10$ *using DF-QMC for the NNN hoppings* $t' = -0.3$ *(magenta) and* $t' = 0$ *(green) [19].*

5 Discussion

We developed the first-order strong-coupling dual fermion expansion for Hubbard-like correlated lattice models in the shift of the chemical potential (doping) and in the second-neighbor hopping (t'). The starting reference point corresponds to the half-filled particle-hole symmetric system which can be calculated numerically exactly, without fermionic sign problem. For the physically interesting parameter range of cuprate like systems (around 10% doping and $t'/t = -0.3$ we can obtain a reasonable Green function for a periodic 16×16 lattice for a temperature $T = 0.1t$. The formation of a pseudogap around the antinodal X-point and the nodal-antinodal dichotomy are clearly seen in the present approach.

We would like to point out a few main reasons why such a "super-perturbation" scheme works: first of all, the reference system already contains the main correlation effects which result in the four-peak structure of the density of states for the half-filled lattice Monte Carlo calculations [16]; second, the first-order strong-coupling perturbation relies on the lattice four-point vertex γ_{1234} (Eq. (30)) which is obtained numerically exactly and has all the information about the spin and charge susceptibilities of the lattice; and third, in case the perturbation or dual Green function $\tilde{G}^0_{12}$ (Eq. (28)) is relatively small, results will be reasonable. We discuss also the complicated question of convergence for such a dual-fermion perturbations and checked numerically the second-order contribution in $\tilde{\Sigma}_{12}$. For this term one needs to calculate, in lattice QMC, a six-point vertex $\gamma^{(6)}$ which is a time consuming problem. Finally, we also discuss an instability towards d-wave superconductivity, introducing symmetry-breaking fields and show the complicated structure of the anomalous Green functions.

It is worthwhile to mention that for the starting reference system we can choose not only the half-filled case, but any doped case where the sign problem is mild, so we can use the DF theory to expand this numerically exact solution to regions where the sign problem in the CT-INT or convergence of the CDet is unacceptable for direct QMC calculations.

Acknowledgements

The author acknowledges support from the European Research Council via Synergy Grant No. 854843 (the FASTCORR project) and valuable communications with Mikhail Katsnelson, Alexei Rubtsov, Sergei Iskakov, Evgeny Stepanov, Igor Krivenko, Fedor Šimkovic IV, Michel Ferrero and Riccardo Rossi.

Appendices

A Path integral for fermions

We first introduce a formalism of the path integral over fermionic fields [20]. Let us consider a simple case of a single quantum state $|i\rangle$ occupied by fermionic particles [21]. Due to the Pauli principle the many-body Hilbert space is spanned by only two orthonormal states $|0\rangle$ and $|1\rangle$. In the second quantization scheme for fermions with annihilation $\hat{c}_i$ and creation $\hat{c}_i^\dagger$ operators with anticommutation relations $\{\hat{c}_i, \hat{c}_j^\dagger\} = \delta_{ij}$ we have the following simple rules

$$\hat{c}_i\,|1\rangle = |0\rangle \quad \hat{c}_i\,|0\rangle = 0 \quad \text{and} \quad \hat{c}_i^\dagger\,|0\rangle = |1\rangle \quad \hat{c}_i^\dagger\,|1\rangle = 0\,. \tag{43}$$

Moreover, the density operator and the Pauli principle have the form

$$\hat{c}_i^\dagger \hat{c}_i\,|n\rangle = n_i\,|n\rangle \quad \text{and} \quad \hat{c}_i^2 = (\hat{c}_i^\dagger)^2 = 0\,.$$

The central object here are the so-called fermionic coherent states $|c\rangle$, which are eigenstates of annihilation operator $\hat{c}_i$ with eigenvalue c_i

$$\hat{c}_i\,|c\rangle = c_i\,|c\rangle\,. \tag{44}$$

It is worthwhile to note that such a left-eigenbasis has only annihilation operators, due to the fact that they are bounded from the below and one can rewrite one of equations from Eq. (43) in the following "eigenvalue" form

$$\hat{c}_i\,|0\rangle = 0\,|0\rangle\,.$$

Due to the anti-commutation relations for the fermionic operators the eigenvalues of coherent states c_i are so-called Grassmann numbers with the multiplication rules

$$c_i c_j = -c_j c_i \quad \text{and} \quad c_i^2 = 0\,. \tag{45}$$

It is convenient to assume that the Grassmann numbers also anti-commute with the fermionic operators

$$\{c, \hat{c}\} = \{c, \hat{c}^\dagger\} = 0\,.$$

An arbitrary function of one Grassmann variable can be represented by only the first two Taylor coefficients

$$f(c) = f_0 + f_1 c\,. \tag{46}$$

One can prove the following general many-body representation of coherent states

$$|c\rangle = e^{-\sum_i c_i \hat{c}_i^\dagger}\,|0\rangle\,. \tag{47}$$

Let us show this for the simple case of one fermionic state

$$\hat{c}\,|c\rangle = \hat{c}\big(1 - c\hat{c}^\dagger\big)\,|0\rangle = \hat{c}\big(\,|0\rangle - c\,|1\rangle\,\big) = -\hat{c}c\,|1\rangle = c\,|0\rangle = c\,|c\rangle\,. \tag{48}$$

One can also define a "left" coherent state $\langle c|$ as the left-eigenstates of creation operators $\hat{c}_i^\dagger$

$$\langle c|\, \hat{c}_i^\dagger = \langle c|\, c_i^* .$$

Note that the new eigenvalue c_i^* is just another Grassmann number, not the complex conjugate of c_i. The left coherent state can be obtained similar to Eq. (47)

$$\langle c| = \langle 0|\, e^{-\sum_i \hat{c}_i c_i^*} .$$

A general function of two Grassmann variables can, analogously to Eq. (46), be represented by only four Taylor coefficients

$$f(c^*, c) = f_{00} + f_{10} c^* + f_{01} c + f_{11} c^* c \,. \tag{49}$$

Using this expansion we can define a derivative of Grassmann variables in the natural way

$$\frac{\partial c_i}{\partial c_j} = \delta_{ij} \,.$$

One needs to be careful with the "right order" of such a derivative and remember the anti-commutation rules, i.e.,

$$\frac{\partial}{\partial c_2} c_1 c_2 = -c_1 \,.$$

For the case of the general two-variable function in Eq. (49) we have

$$\frac{\partial}{\partial c^*}\frac{\partial}{\partial c} f(c^*, c) = \frac{\partial}{\partial c^*}\big(f_{01} - f_{11} c^*\big) = -f_{11} = -\frac{\partial}{\partial c}\frac{\partial}{\partial c^*} f(c^*, c).$$

One also needs a formal definition of the integration over Grassmann variables, and the natural way consists of the following rules [22]

$$\int 1\, dc = 0 \quad \text{and} \quad \int c\, dc = 1 \,,$$

which just shows that the integration over a Grassmann variable is equivalent to differentiation

$$\int \cdots\, dc \to \frac{\partial}{\partial c} \cdots$$

The coherent states are not orthonormal and the overlap of any two such states is equal to

$$\langle c|c\rangle = e^{\sum_i c_i^* c_i}$$

which is easy to see for the case of one particle

$$\langle c|c\rangle = \big(\langle 0| - \langle 1|\, c^*\big)\big(|0\rangle - c\,|1\rangle\big) = 1 + c^* c = e^{c^* c}.$$

An important property of coherent states is the resolution of unity

$$\int dc^* \int dc\, e^{-\sum_i c_i^* c_i}\, |c\rangle\langle c| = \hat{1} = \iint dc^* dc\, \frac{|c\rangle\,\langle c|}{\langle c|c\rangle}.$$

For simplicity we demonstrate this relation only for one fermion state

$$\iint dc^* dc\, e^{-c^* c}\, |c\rangle\langle c| = \iint dc^* dc \left(1 - c^* c\right)\left(|0\rangle - c\,|1\rangle\right)\left(\langle 0| - \langle 1|\, c^*\right)$$
$$= -\iint dc^* dc\; c^* c \left(|0\rangle\langle 0| + |1\rangle\langle 1|\right) = \sum_n |n\rangle\langle n| = \hat{1}\,.$$

Matrix elements of normally ordered operators are very easy to calculate in the coherent basis by operating with $\hat{c}^\dagger$ on the states to the right and $\hat{c}$ to the left:

$$\langle c^*|\, \hat{H}(\hat{c}^\dagger, \hat{c})\, |c\rangle = H(c^*, c)\, \langle c^*|c\rangle\,. = H(c^*, c)\, e^{\sum_i c_i^* c_i} \tag{50}$$

Within the manifold of coherent states we can map the fermionic operators to the Grassmann variables $(\hat{c}_i^\dagger, \hat{c}_i) \to (c_i^*, c_i)$.
Finally, we prove the so-called "trace-formula" for arbitrary fermionic operators in normal order (in one-fermion notation)

$$\mathrm{Tr}\ \hat{O} = \sum_{n=0,1} \langle n|\, \hat{O}\, |n\rangle = \sum_{n=0,1} \iint dc^* dc\, e^{-c^* c}\, \langle n|\, c\rangle\langle c|\, \hat{O}\, |n\rangle =$$
$$= \iint dc^* dc\, e^{-c^* c} \sum_{n=0,1} \langle -c|\, \hat{O}\, |n\rangle\langle n|\, c\rangle = \iint dc^* dc\, e^{-c^* c}\, \langle -c|\, \hat{O}\, |c\rangle\,.$$

The fermionic "minus" sign in the left coherent states come from the commutation of the (c^*) and (c) coherent state in such a transformation: $\langle n|c\rangle\, \langle c|n\rangle = \langle -c|n\rangle\, \langle n|c\rangle$. One has to use the standard Grassmann rules: $c_i^* c_j = -c_j c_i^*$ and $|-c\rangle = |0\rangle + c\,|1\rangle$.
We are ready now to write the partition function for the grand-canonical quantum ensemble with $H = \hat{H} - \mu\hat{N}$ and inverse temperature β. One has to use the N-slices Trotter decomposition for the partition function in $[0, \beta)$ with imaginary time $\tau_n = n\Delta\tau = n\beta/N$ $(n = 1, \ldots, N)$, and insert N times the resolution of unity as follows

$$Z = \mathrm{Tr}\, e^{-\beta H} = \iint dc^* dc\, e^{-c^* c} \big\langle -c \big| e^{-\beta H} \big| c \big\rangle$$
$$= \int \Pi_{n=1}^N dc_n^* dc_n\, e^{-\sum_n c_n^* c_n}\, \langle c_N|\, e^{-\Delta\tau H}\, |c_{N-1}\rangle\, \langle c_{N-1}|\, e^{-\Delta\tau H}\, |c_{N-2}\rangle\, ...\, \langle c_1|\, e^{-\Delta\tau H}\, |c_0\rangle$$
$$= \int \Pi_{n=1}^N dc_n^* dc_n\, e^{-\Delta\tau \sum_{n=1}^N \left(c_n^*(c_n - c_{n-1})/\Delta\tau + H(c_n^*, c_{n-1})\right)}$$

In the continuum limit $(N \to \infty)$

$$\Delta\tau \sum_{n=1}^N \cdots \to \int_0^\beta d\tau \cdots, \qquad \frac{c_n - c_{n-1}}{\Delta\tau} \to \partial_\tau \quad \text{and} \quad \Pi_{n=0}^{N-1} dc_n^* dc_n \to \mathcal{D}\,[c^*, c]$$

with antiperiodic boundary conditions for fermionic Grassmann variables in imaginary time $c(\tau)$ and $c^*(\tau)$

$$c(\beta) = -c(0), \qquad c^*(\beta) = -c^*(0)$$

we end up in the standard path-integral formulation of the partition function

$$Z = \int \mathcal{D}\left[c^*, c\right] e^{-\int_0^\beta d\tau \left(c^*(\tau)\partial_\tau c(\tau) + H(c^*(\tau), c(\tau))\right)} \; . \tag{51}$$

It is useful to mention the general form of the Gaussian path-integral for a non-interacting "quadratic" fermionic action, which is equivalent to the Hubbard-Stratonovich transformation used in the dual-fermion derivation Eq. (22). For an arbitrary matrix M_{ij} and Grassmann vectors J_i^* and J_i one can calculate analytically the following integral

$$Z_0\left[J^*, J\right] = \int \mathcal{D}\left[c^* c\right] e^{-\sum_{i,j=1}^N c_i^* M_{ij} c_j - \sum_{i=1}^N \left(c_i^* J_i + J_i^* c_i\right)} = \det M \; e^{\sum_{i,j=1}^N J_i^* (M^{-1})_{ij} J_j} \; . \tag{52}$$

To prove this relation one needs to first change variables in order to eliminate J_i^* and J_i and expand the exponential function (only the N-th oder is non-zero)

$$e^{-\sum_{i,j=1}^N c_i^* M_{ij} c_j} = \frac{1}{N!}\left(-\sum_{i,j=1}^N c_i^* M_{ij} c_j\right)^N .$$

Finally, different permutations of c_i^* and c_j and integration over Grassmann variables will give $\det M$. As a small exercise we will check such integrals for the first two many-particle dimensions. For N=1 it is trivial

$$\int \mathcal{D}\left[c^* c\right] e^{-c_1^* M_{11} c_1} = \int \mathcal{D}\left[c^* c\right] \left(-c_1^* M_{11} c_1\right) = M_{11} = \det M$$

and for N=2 we have

$$\int \mathcal{D}\left[c^* c\right] e^{-c_1^* M_{11} c_1 - c_1^* M_{12} c_1 - c_2^* M_{21} c_1 - c_2^* M_{22} c_2} =$$

$$= \frac{1}{2!}\int \mathcal{D}\left[c^* c\right] \left(-c_1^* M_{11} c_1 - c_1^* M_{12} c_1 - c_2^* M_{21} c_1 - c_2^* M_{22} c_2\right)^2 = M_{11} M_{22} - M_{12} M_{21} = \det M.$$

For a change of variables in the path integral one uses the following transformation with unit Jacobian: $c \to c + M^{-1} J$ and

$$c^* M c + c^* J + J^* c = \left(c^* + J^* M^{-1}\right) M \left(c + M^{-1} J\right) - J^* M^{-1} J \, ,$$

which proves Eq. (52). Using the Gaussian path-integral it is very easy to calculate any correlation function for a non-interaction action (Wick-theorem)

$$\left\langle c_i c_j^* \right\rangle_0 = -\frac{1}{Z_0} \frac{\delta^2 Z_0\left[J^*, J\right]}{\delta J_i^* \, \delta J_j}\bigg|_{J=0} = M_{ij}^{-1}$$

$$\left\langle c_i c_j c_k^* c_l^* \right\rangle_0 = \frac{1}{Z_0} \frac{\delta^4 Z_0\left[J^*, J\right]}{\delta J_i^* \delta J_j^* \delta J_l \delta J_k}\bigg|_{J=0} = M_{il}^{-1} M_{jk}^{-1} - M_{ik}^{-1} M_{jl}^{-1}.$$

Corresponding bosonic path-integrals can be formulated in a similar way with complex variables and periodic boundary conditions on imaginary time. The Gaussian path-integral over bosonic fields is equal to inverse of the M-matrix determinant [20].

References

[1] E. Gull, A.J. Millis, A.I. Lichtenstein, A.N. Rubtsov, M. Troyer, and P. Werner, Rev. Mod. Phys. **83**, 349 (2011)

[2] D.M. Ceperley and B.J. Alder, Phys. Rev. Lett. **45**, 566 (1980)

[3] A. Georges, G. Kotliar, W. Krauth, and M.J. Rozenberg, Rev. Mod. Phys. **68**, 13 (1996)

[4] H. Hafermann, F. Lechermann, A. Rubtsov, M. Katsnelson, A. Georges, and A. Lichtenstein, in D.C. Cabra, A. Honecker, and P. Pujol (eds.): *Modern theories of many-particle systems in condensed matter physics* (Springer, 2012), Vol. 843, chap. 4

[5] W. Metzner and D. Vollhardt, Phys. Rev. Lett. **62**, 324 (1989)

[6] G. Rohringer, H. Hafermann, A. Toschi, A.A. Katanin, A.E. Antipov, M.I. Katsnelson, A.I. Lichtenstein, A.N. Rubtsov, and K. Held, Rev. Mod. Phys. **90**, 025003 (2018)

[7] A.N. Rubtsov, M.I. Katsnelson, and A.I. Lichtenstein, Phys. Rev. B **77**, 033101 (2008)

[8] N.V. Prokof'ev and B.V. Svistunov, Phys. Rev. Lett. **81**, 2514 (1998)

[9] A.N. Rubtsov, V.V. Savkin, and A.I. Lichtenstein, Phys. Rev. B **72**, 035122 (2005)

[10] R. Rossi, Phys. Rev. Lett. **119**, 045701 (2017)

[11] A.A. Abrikosov, L.P. Gorkov, and I.E. Dzyaloshinski: *Methods of quantum field theory in statistical physics* (Dover, New York, 1975)

[12] F. Šimkovic, R. Rossi, A. Georges, and M. Ferrero, Science **385**, eade9194 (2024)

[13] S. Brener, E.A. Stepanov, A.N. Rubtsov, M.I. Katsnelson, and A.I. Lichtenstein, Ann. Phys. **422**, 168310 (2020)

[14] R. Scalettar, R. Noack, and R. Singh, Phys. Rev. B **44**, 10502 (1991)

[15] S. Iskakov, M.I. Katsnelson, and A.I. Lichtenstein, npj Comput. Mater. **10**, 36 (2024)

[16] D. Rost, E.V. Gorelik, F. Assaad, and N. Blümer, Phys. Rev. B **86**, 155109 (2012)

[17] Pairault, S., Sénéchal, D., and A.-M.S. Tremblay, Eur. Phys. J. B **16**, 85 (2000)

[18] I. Krivenko and A.S. Mishchenko, Comput. Phys. Commun. **280**, 108491 (2022)

[19] E. Stepanov, S. Iskakov, M. Katsnelson, and A. Lichtenstein: *Superconductivity of Bad Fermions: Origin of Two Gaps in HTSC Cuprates*, arXiv:2502.08635

[20] J.W. Negele and H. Orland: *Quantum Many-particle Systems* (Westview Press, 1998)

[21] A. Kamenev: *Field Theory of Non-Equilibrium Systems* (Cambridge Univ. Press, 2011)

[22] F.A. Berezin *Method of Second Quantization* (Academic Press , New York, 1966)

14 Unconventional Superconductivity in the Dynamical Vertex Approximation

Karsten Held
Institute for Solid State Physics, TU Wien
1040 Wien, Austria

Contents

1 Introduction **2**

2 Dynamical vertex approximation **5**

3 Ladder dynamical vertex approximation **10**

4 Hubbard model, cuprates and nickelates **11**

5 Spin fluctuations **15**

6 Superconductivity **20**

7 Conclusion and outlook **23**

E. Pavarini, E. Koch, A. Lichtenstein, and D. Vollhardt (eds.)
Understanding Correlated Materials with DMFT
Modeling and Simulation Vol. 15
Forschungszentrum Jülich, 2025, ISBN 978-3-95806-813-1
http://www.cond-mat.de/events/correl25

1 Introduction

With the success of dynamical mean-field theory (DMFT) [1–4] in calculating strongly correlated electron systems, there have been attempts from the very beginning [5] to systematically extend DMFT. The aim of such extensions is to keep the good description of DMFT for local electronic correlations, but at the same time also to capture non-local correlations beyond.

Indeed, the local DMFT correlations are doing an excellent job in describing a quasiparticle renormalization with a weight Z that is uniform in momentum space—a surprisingly good approximation for many transition metal-oxides and heavy fermion systems; as well as the Mott-Hubbard metal-insulator transition that emerges for $Z \to 0$ [2]. Furthermore, all kinds of orders (magnetic, orbital, charge density wave...) are quite well captured in three-dimensional systems up to the vicinity of the phase transition. Here, close to the phase transition, the mean-field nature of DMFT surfaces, among others, in the form of mean-field critical exponents. Non-local correlations are here essential for describing the proper critical behavior. With a diverging correlation length, long-range correlations feed back to the self-energy which thus becomes non-local.

The DMFT approach has been covered already in various other chapters of this Autumn School [3], and the present chapter will thus focus instead on non-local electronic correlations beyond DMFT. When are such non-local correlations important?

A lot of our insight into physical phenomena stems from weak coupling perturbation theory. Even though such an approach is certainly not applicable to strongly correlated electron systems, it often nonetheless provides for some qualitative understanding. One example, where non-local correlations enter the self-energy are spin-fluctuations. These can be calculated at weak coupling in the random phase approximation (RPA) which is discussed in quantum field theory textbooks. The RPA is the geometric series of all ladder diagrams with no, one, two etc. Coulomb interaction lines, as illustrated in Fig. 1 (top). The figure just shows one term of the sum, where "$\cdots$" indicates that all orders in U are included. The RPA can be used to calculate the magnetic susceptibility Fig. 1 (top, without dashed line). As we will see later, the poles of this susceptibility constitute bosonic quasiparticle excitations coined magnons or, in the paramagnetic phase, paramagnons.

Now, when we add the dashed black line in Fig. 1 (top), we obtain a self-energy Feynman diagram. It describes the coupling of the electron to the spin-fluctuations. We can also call it the electron-(para)magnon interaction. As spin-fluctuations are very non-local we get—whenever spin-fluctuations become important—contributions from diagrams with lattice sites $i \neq j \neq k$ in Fig. 1 (top). Such self-energy diagrams are certainly not contained in DMFT, which sums up all *local* contributions of Feynman diagrams for the self-energy. Hence, whenever spin-fluctuations become large, we must expect important corrections to the DMFT self-energy. Indeed this is not restricted to spin-fluctuations, but depending on what kind of spin combination the particle and the hole in the RPA ladder have, one can also obtain the coupling of electrons to charge, orbital etc. fluctuations.

The present chapter is an updated version of the author's lecture note at the Jülich Autumn School 2022 [4].

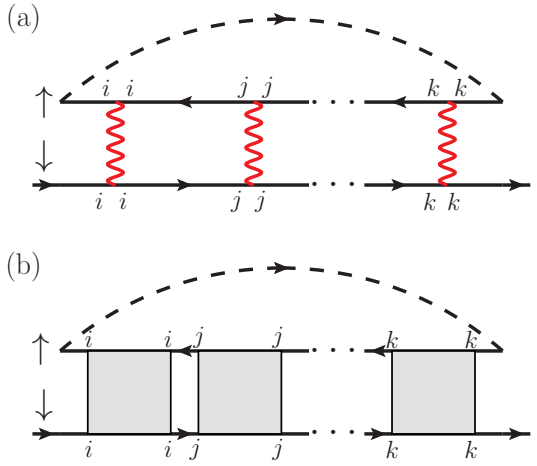


Fig. 1: *Top: Feedback of spin fluctuations (paramagnons) calculated in RPA to the self-energy. Bottom: In diagrammatic extensions of DMFT such physics is taken into account but with the bare interaction U (red wiggled line) replaced by a local vertex calculated from an impurity model (light gray box). Depending on the flavor of the diagrammatic extension of DMFT different local vertices are employed. Reproduced from [6].*

That means non-local correlations are certainly relevant whenever spin, charge etc. fluctuations are important. An obvious regime where this is the case is the vicinity of a second-order phase transition as already mentioned. Here the magnetic, charge etc. susceptibility diverges and significant changes to the DMFT solution are thus to be expected. For low dimensional systems we will get corrections also further away from the phase transition. The Mermin-Wagner theorem prohibits long-range order with a continuous symmetry breaking in two-dimensions at finite temperature. Hence, antiferromagnetic order is restricted to zero temperature. However, above this zero-temperature antiferromagnetic phase, we have now strong antiferromagnetic fluctuations in a wide temperature range, even with exponentially large correlation lengths. DMFT has been developed with the limit of dimension $d = \infty$ in mind, see [1] and Chapter "Understanding Correlated Materials with Lattice Fermions in Infinite Dimensions" by D. Vollhardt [3]. Hence, also from this perspective it is not surprising that we need to expect larger corrections to DMFT for low dimensional systems.

On the other hand, we would like to keep the success of DMFT in describing a major part of electronic correlations rather well: the local correlations. Two major routes to do so have been developed to this end. These are illustrated in Fig. 2: (i) Cluster extensions of DMFT [7] put the DMFT concept of locality onto a cluster (instead of a single site). This cluster is then embedded in a DMFT bath. For a single site cluster this is just DMFT. Illustrated in Fig. 2 is a two-site cluster where thus non-local correlations between the two red sites of the cluster are captured. Such two site clusters can, e.g., describe the formation of a spin singlet between two electrons on the two sites. For a four site cluster also d-wave superconductivity can be described. However such small clusters tend, in practice, to largely overestimate the physics that is compatible with the cluster such as the spin singlet formation and d-wave superconductivity for a two and four site cluster, respectively. While one can go to clusters of size 10×10, a proper finite size scaling remains challenging. This is even more true for realistic multi-orbital calculations that are restricted to a handful of sites.

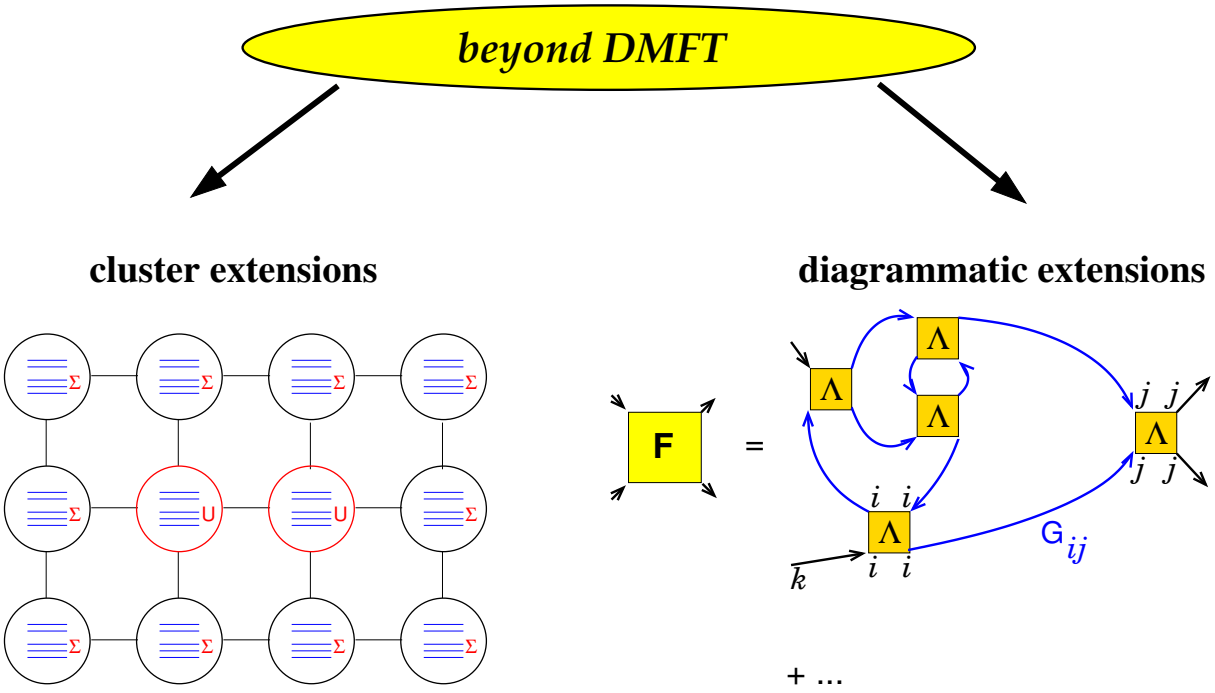


Fig. 2: *Left: In cluster extensions, a couple of sites (here two marked in red) are embedded in a dynamical mean field which can be formulated through the self energy Σ. Restricted to a single site, DMFT is obtained; extended to the full lattice the exact solution is recovered. Right: In diagrammatic extensions, the locality of DMFT is put to the next level, the two-particle level. Local two-particle building blocks Λ are connected by non-local Green function lines G_{ij}, resulting in a non-local full vertex F or susceptibility χ. When restricting G_{ij} to its local contribution G_{ii}, DMFT is recovered. Adapted from [8].*

The other route extends DMFT [6] Feynman diagrammatically. Here, the concept of locality is not extended to a cluster but instead to the n-particle vertex. For $n = 1$ we have the one-particle vertex which is nothing but the self-energy. And a local self-energy is just the DMFT approximation. For $n = 2$, i.e., the two-particle level, we start instead with a local two-particle vertex and construct from it the non-local full vertex F, see Fig. 2 (right), as well as the non-local self-energy and Green function. This is the level most commonly applied nowadays. Similarly as for the cluster extensions there are different flavors depending on which local vertex and which connecting Green functions are taken. At the end of the day, most of these different flavors are very similar, at least as long as they take the two-particle, four-point vertex as a starting point. Other approaches start from a three-point local vertex which is a more severe approximation. For an overview and comparison, see the review [6].

The originary method, called dynamical vertex approximation (DΓA) [9], considers the vertex in terms of real fermions as local. A second widely applied approach is the dual fermion (DF) approach [10] which is covered in the Chapter "Path Integrals and Dual Particles" by A. Lichtenstein [3]. Also within DΓA different flavors are used. In its most complete form, the fully irreducible vertex Λ is approximated to be local. Then the parquet equations are needed to construct F and the self-energy Σ. A local Λ is an excellent approximation, even for the two-dimensional Hubbard model in the superconducting doping regime [11]. In the ladder DΓA

variant, the irreducible vertex Γ_ℓ in a certain channel ℓ such as the particle-hole (ph) channel is considered to be local. In this case, the Bethe-Salpeter equation is sufficient to calculate F along the same lines as in the RPA, only now with Γ_ℓ instead of U as a building block, i.e the light gray box in Fig. 1 (bottom) is Γ_ℓ in this case. The ladder variant is numerically much less expensive. It is sufficient if a certain channel dominates, but does not capture the coupling of different channels into each other.

One can also extend the concept of locality to higher n-particle vertices. The n=3-particle vertex level, for example, has been employed for estimating the error of the n=2-particle calculations [12]. Correlation functions for n=3 or more particles are also relevant for non-linear response functions, and are thus naturally connected to n=3-particle vertices [13]. For $n\to\infty$ the exact solution is recovered.

Turning back to Fig. 1, we see that such diagrammatic extensions are well suited to describe spin-fluctuations and their feedback to the fermionic self-energy. The same physics as is qualitatively described in RPA, is now captured for strongly correlated electrons since the local Λ already encodes non-perturbatively all DMFT correlations. The Bethe-Salpeter ladder of Fig. 1 is precisely the same as is also used to calculate the DMFT susceptibility, cf. the Chapter "DMFT for response functions" by E. Pavarini in 2022 [4]. What is not covered in DMFT is how these spin-fluctuations impact the self-energy as well as self-consistency effects, i.e., how the changed Σ modifies G or that the local Γ_ℓ itself becomes different from DMFT. These self-consistency effects lead to a dampening of the spin-fluctuations compared to the mean-field DMFT solution, up to the point of fulfilling the Mermin-Wagner theorem in two-dimensions.

Diagrammatic extensions of DMFT have been highly successful: (i) The critical behavior in the vicinity of (quantum) phase transition could be described for the first time in electronic models, a topic which was covered already excessively in the Autumn School 2018 [14], see also the review [6]. (ii) It was realized that the two-dimensional square lattice Hubbard model with perfect nesting is insulating all the way down to zero interaction [15], correcting earlier cluster DMFT results. (iii) The pseudogap and d-wave superconductivity can be described in the two-dimensional Hubbard model, a topic which we will cover in the following chapters. (iv) A new polariton, the π-ton has been discovered in model calculations [16]. (v) Realistic materials calculations are possible and have been pursued, e.g., for $SrVO_3$ [17].

In the following, we will first introduce one of the diagrammatic extensions of DMFT, the DΓA, in Sec. 2. Simplifications when using the ladder variant of DΓA are outlined in Sec. 3. The Hubbard model is introduced in Sec. 4 and its justification for cuprates and nickelates is discussed. Physical results regarding spin-fluctuations and superconductivity are discussed in Sec. 5 and 6, respectively. Finally, Sec. 7 provides a conclusion and outlook.

2 Dynamical vertex approximation

The aim of the present section is to provide the reader with the basic idea of the dynamical vertex approximation. It builds upon a similar chapter of a preceding Jülich Autumn School [14]. A more detailed description for a second reading can be found in the review [6]. Further

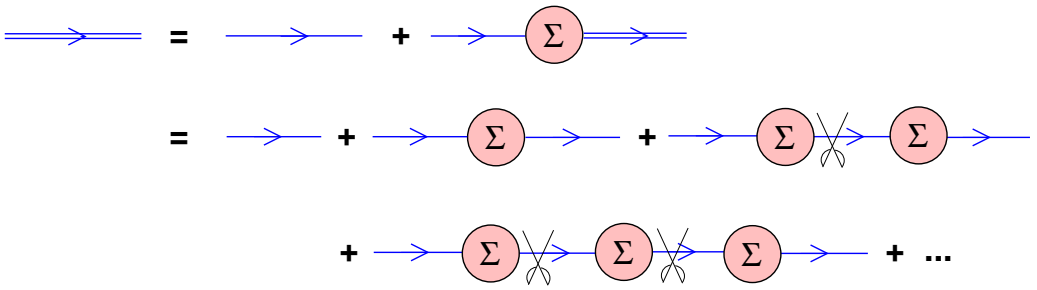


Fig. 3: *Dyson equation connecting the Green function and self energy Σ (single blue line: non-interacting G_0; double blue line: interacting G). The pair of scissors indicates that these diagrams are one-particle reducible (i.e., cutting one G_0 line separates the Feynman diagram into two parts). From [14].*

information on how to calculate the superconducting critical temperature T_c and how to include the asymptotic form of the vertex, can be found in [18].

The basic idea of the dynamical vertex approximation (DΓA) is a resummation of Feynman diagrams, not order by order of the Coulomb interaction as in conventional perturbation theory, but in terms of their locality. That is, we assume the fully irreducible n-particle vertex to be local and from this building block we construct further diagrams and non-local correlations.

The first level ($n = 1$) is then just the DMFT which corresponds to all local Feynman diagrams for the self-energy Σ. Note that Σ is nothing but the fully irreducible n=1-particle vertex. One particle-irreducibility here means that cutting one Green function line does not separate the Feynman diagram into two pieces. Indeed such reducible diagrams must not be included in the self-energy since it is exactly these diagrams that are generated from the Dyson equation (Fig. 3) which resolved for G reads

$$G_{\mathbf{k}\nu} = \left(1/G^0_{\mathbf{k}\nu} - \Sigma_{\mathbf{k}\nu}\right)^{-1} \tag{1}$$

for momentum $\mathbf{k}$, Matsubara frequency ν and non-interacting Green function $G^0_{\mathbf{k}\nu}$. In Fig. 3 and in the following, single blue lines denote non-interacting Green functions G_0 and double blue lines indicate interacting Green functions G. Fig. 3 further shows how one-particle reducible diagrams are generated through the Dyson equation. Hence these must not be contained in the Feynman diagrams that constitute Σ, to avoid a double counting. That means, Σ must be one-particle reducible in terms of G^0.[1]

On the next level, for $n = 2$, we assume the locality of the two-particle fully irreducible vertex Λ. For the two-particle vertex, fully irreducible means that cutting two Green function lines does not separate the diagram into two pieces. There are three different kinds (channels) ℓ of reducible vertices Φ_ℓ and a fourth, Λ, that is fully irreducible. Most importantly each diagram falls in one and only one of those four subgroups. Thus the full vertex F, containing all diagrams, can be written as the sum those. This decomposition of the vertex is called *parquet decomposition* and is graphically displayed in Fig. 4.

[1] In terms of G the skeleton diagrams for Σ are also two-particle reducible. But that is another story that is connected with the way how Σ enters G.

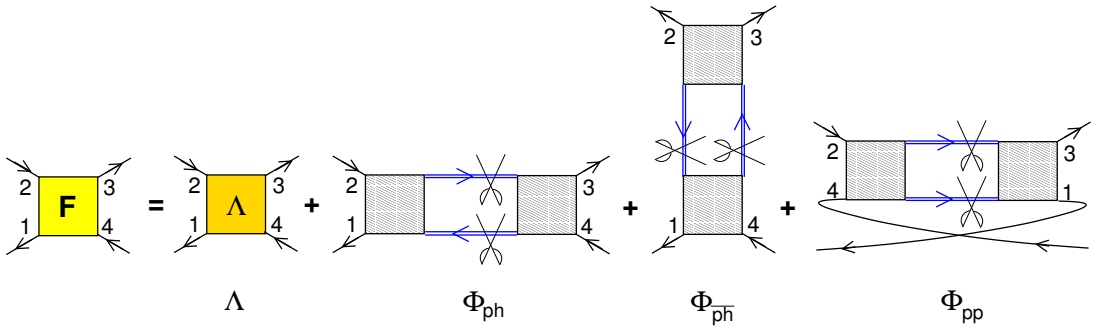


Fig. 4: *Parquet decomposition of the full (reducible) vertex F into the fully irreducible vertex Λ and two-particle reducible diagrams Φ_ℓ in the three channels. The two pairs of scissors indicate the reducibility of the three Φ_ℓ's. Each two-fermion Feynman diagram belongs to one and only one of the three Φ_ℓ's or to Λ.*

The reason why there are three distinct reducible parts Φ_ℓ is that, say, leg 1 may stay connected with leg 2, 3, or 4 when cutting two Green function lines as indicated in Fig. 4. These three possible channels ℓ are denoted as particle-hole (ph), transversal particle-hole ($\overline{ph}$) and particle-particle (pp). The irreducible vertex of each channel is just the complement: $\Gamma_\ell = F - \Phi_\ell$. It is important to note that each reducible diagram is contained in one and only one of these channels. One can show this by contradiction: otherwise cutting lines in two channels would result in a diagram with one incoming and two outgoing lines, which is not possible because of the conservation of (fermionic) particles.

There is further a set of six exact equations, which is also called the "parquet equations" [19, 6] to the confusion of the common student. These six equations allow us to calculate from a given Λ the six quantities: full vertex F, self-energy Σ, Green function G and the three reducible vertices Φ_ℓ.

(1) The first equation is the actual parquet equation [Fig. 4, Eq. (2)]

$$F^{\nu\nu'\omega}_{r,\mathbf{k}\mathbf{k}'\mathbf{q}} = \Lambda^{\nu\nu'\omega}_{r,\mathbf{k}\mathbf{k}'\mathbf{q}} + \Phi^{\nu\nu'\omega}_{ph,r,\mathbf{k}\mathbf{k}'\mathbf{q}} + \Phi^{\nu\nu'\omega}_{\overline{ph},r,\mathbf{k}\mathbf{k}'\mathbf{q}} + \Phi^{\nu\nu'\omega}_{pp,r,\mathbf{k}\mathbf{k}'\mathbf{q}} \tag{2}$$

where $r \in \{c, s\}$ is the symmetric/antisymmetric spin combination, i.e., $F_{c/s} = F_{\uparrow\uparrow} \pm F_{\uparrow\downarrow}$ and similarly for other vertices.[2] The name indicates that F_c and F_s give rise to the charge and spin-fluctuations, respectively.

(2-4) Three of the six "parquet" equations are the Bethe-Salpeter equation in the three channels ℓ. In [Fig. 5, Eq. (3)] we here only reproduce the $\ell = ph$ channel; again with $r \in \{c, s\}$ for a symmetric/antisymmetric spin combination[3]

$$F^{\nu\nu'\omega}_{r,\mathbf{k}\mathbf{k}'\mathbf{q}} = \Gamma^{\nu\nu'\omega}_{r,ph,\mathbf{k}\mathbf{k}'\mathbf{q}} + \sum_{\mathbf{k_1}\nu_1} F^{\nu\nu_1\omega}_{r,\mathbf{k}\mathbf{k_1}\mathbf{q}}\, G_{\mathbf{k_1}\nu_1}\, G_{(\mathbf{k_1}+\mathbf{q})(\nu_1+\omega)}\, \Gamma^{\nu_1\nu'\omega}_{ph,r,\mathbf{k_1}\mathbf{k}'\mathbf{q}}\,. \tag{3}$$

[2] This assumes SU(2) symmetry, if this is broken altogether four spin combinations need to be taken into account.

[3] We implicitly assume a proper normalization of the momentum and Matsubara frequency sums, i.e., $\sum_{\mathbf{k}} \widehat{=} \frac{1}{N_K} \sum_{\mathbf{k}}$ and $\sum_{\nu} \widehat{=} \frac{1}{\beta} \sum_{\nu}$, where N_k is the number of momentum points and $\beta = 1/T$ the inverse temperature.

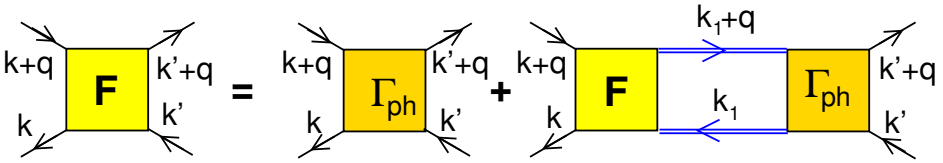


Fig. 5: *Bethe-Salpeter equation in the particle-hole channel, $\ell = ph$, allowing us to calculate F from the irreducible vertex in Γ_{ph} in this channel. The rightmost term produces the particle-hole reducible diagrams denoted as Φ_{ph} in Fig. 4; $\Gamma_{ph} = \Lambda + \Phi_{\overline{ph}} + \Phi_{pp}$.*

One often combines frequency ν and momentum $\mathbf{k}$ to a four vector $k = (\mathbf{k}, \nu)$. We do not do so in this chapter for the equations, but in the figures k represents $(\mathbf{k}, \nu)$. Further it is important to choose a momentum-frequency convention for the vertices and stick to it. Because of energy and momentum conservation we only need three momenta and frequencies for the four points $1, 2, 3, 4$ of the two-particle vertices in Fig. 4. Unless noted otherwise, we use the ph convention which is the natural one for the ph channel and already used in Fig. 5. That is, the $1, 2, 3, 4$ frequency-momenta of Fig. 4 are related to Fig. 5 as follows: $k_1 = k$, $k_4 = k'$, $k_2 = k+q$, and—because of energy-momentum conservation— $k_3 = k'+q$. The Bethe-Salpeter equations in the other channels have the same structure just with another Γ_ℓ, $\ell = \overline{ph}$ or pp, and with another way to connect the building blocks (see Fig. 4). For these channels, there is another natural (diagonal) frequency-momentum q.

(5) The fifth equation is the Dyson equation that we already introduced [Fig. 3, Eq. (1)].

(6) Finally, the sixth equation is the Schwinger-Dyson equation [Fig. 6, Eq. (4)] which reads

$$\Sigma_{\mathbf{k}\nu} = \frac{Un}{2} - \frac{U}{2} \sum_{k',q} \sum_{\nu',\omega} \left[F^{\nu\nu'\omega}_{c,\mathbf{k}\mathbf{k}'\mathbf{q}} - F^{\nu\nu'\omega}_{s,\mathbf{k}\mathbf{k}'\mathbf{q}} \right] G_{(\mathbf{k}+\mathbf{q})(\nu+\omega)}\, G_{\mathbf{k}'\nu'}\, G_{(\mathbf{k}'+\mathbf{q})(\nu'+\omega)} \tag{4}$$

and connects Σ and F. Here we consider a single-orbital and local interaction U that connects opposite spins. For this reason only $F_{\uparrow\downarrow} = (F_c - F_s)/2$ enters. The first term is simply the Hartree(-Fock) term, which is not included in Fig. 6 and where n is the average number of electrons per site in the paramagnetic phase.

This set of six exact parquet equations allows us to determine the six quantities F, Φ_ℓ, Σ, and G, as well as $\Gamma_\ell = F - \Phi_\ell$. If we knew the exact Λ, we could determine all of these quantities exactly, as well as associated one- and two-particle physics. Unfortunately, we do not know the exact Λ. Hence we need some approximation. If we approximate Λ by the bare Coulomb interaction U, we obtain the parquet approximation [19]. We can do better than this, and in DΓA we approximate Λ by all local Feynman diagrams. Quantum Monte Carlo simulations show that this is an excellent approximation [11]. Indeed Λ is very compact. All two-particle reducible diagrams are generated from it and the first irreducible diagram that enters Λ besides the bare Coulomb interaction is of fourth order, see Fig. 7. So to speak the irreducible diagrams Λ form a skeleton from which many more diagrams are generated. Because of this, it is more local than Γ_ℓ and, in particular, much more local than F, Σ or G.

This local irreducible Λ is "summed up" in practice by solving an Anderson impurity model, similar as in DMFT but now we calculate the two-particle Green function of the impurity model and from this Λ. For example, we can use continuous-time quantum Monte Carlo simulations

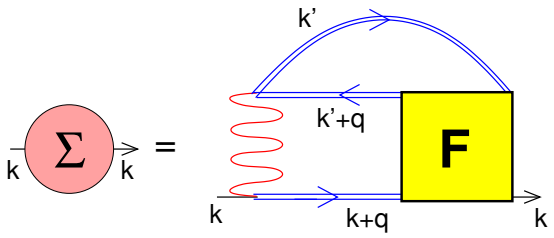


Fig. 6: *Schwinger-Dyson equation connecting the full vertex F and the self-energy Σ.*

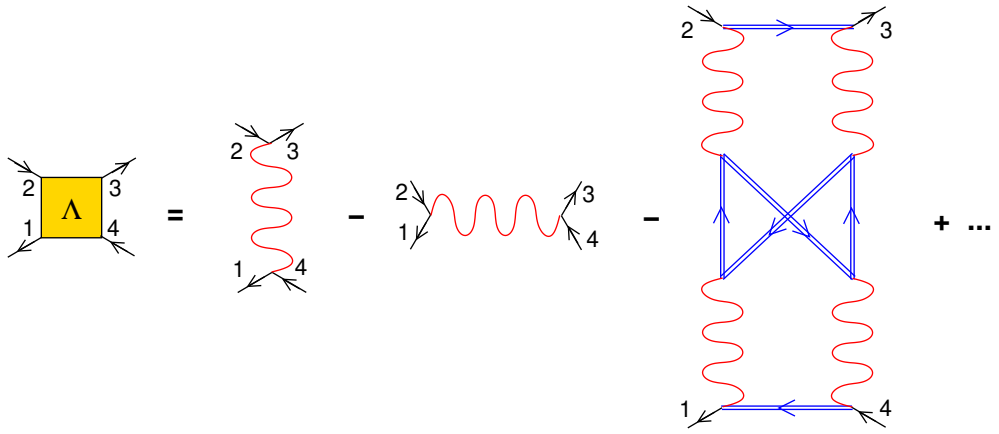


Fig. 7: *Lowest order Feynman diagrams that contribute to the fully irreducible vertex Λ.*

in the hybridization expansion see "QMC as a solver for DMFT" by P. Werner in 2022 [4], e.g., using the `w2dynamics` package [20] which allows us to calculate all two-particle responses using worm sampling [21].

In principle, one can then further turn to the n=3-particle level etc.; and, for the $n\to\infty$-particle fully irreducible local vertex DΓA one recovers the exact solution. As a matter of course determining the n=3-particle vertex becomes already cumbersome. But it may serve at least as an error estimate [12] if one is truncating the scheme at the two-particle vertex level. Also completely new physics, that is hitherto not understood, may be hiding behind diagrams generated from the n=3-particle irreducible vertex. Some physical processes such as Raman scattering and non-linear response naturally require three-particle vertex functions [13].

In the present section we have learned about the full-fledged parquet DΓA. It is unbiased with respect to all three channels ℓ and thus treats antiferromagnetic or charge fluctuations in the ph-channel on a par with e.g., superconducting fluctuations or weak localization corrections in the pp channel. It also mixes the different channels. For two channels this mixing generates, with some fantasy, a traditional parquet floor like pattern with ladder rungs in one direction intermixed by ladder rungs in the orthogonal direction etc., hence the name. Being unbiased definitely is a great advantage. For example, in [16] we were looking for weak localization corrections to the optical conductivity in the pp channel and excitons that live in the ph channel. Instead we found that for strongly correlated systems that host strong alternating spin or charge fluctuations, the $\overline{ph}$ channel is actually dominant for the optical conductivity, against all expectations.

The drawback of the full parquet solution is that we deal with three momenta and three frequencies. Even on a rather coarse discretization grid, we thus easily end up with terabytes of data. In the Bethe-Salpeter equation (3) the bosonic momentum $\mathbf{q}$ and frequency ω decouple, so that it can be well distributed on several computer cores without the need to communicate. However, this natural $\mathbf{q}$ and ω is channel-dependent (see [6]), i.e., different for the three channels of Fig. 4. Hence, when we add the three channels in the parquet equation (2), we mix different momenta, requiring a lot of communication between different computer cores, which, say, have previously solved the Bathe-Salpeter equation in different channels. Network traffic thus becomes the computational bottleneck on a supercomputer for parquet DΓA. Efforts to mitigate this problem are the truncated unity basis for momentum space [22], the intermediate representation (IR) for frequency space [23], the single boson exchange decomposition [24], and quantics tensor trains which are covered in Chapter "Learning Feynman Diagrams with Tensor Trains" by X. Waintal [3].

3 Ladder dynamical vertex approximation

If we know that a certain channel is dominating, we can restrict ourselves to this particular channel and neglect the others and the mixing of different channels through the parquet equation. Since Φ_{ph} and $\Phi_{\overline{ph}}$ are related by crossing symmetry (invariance of exchanging the two incoming lines [6]) both of these channels contribute to F in the same way, albeit with a crossing-symmetry exchanged frequency and momentum combination. Hence, both channels must be included in general.[4] In this case, we hence only need to solve the Bethe-Salpeter equation (3) and can consider a local Γ_{ph} as input. For a bare interaction U, the Bethe-Salpeter equation (3) yields diagrams as in Fig. 8(a). If we improve on this and use a local Γ_{ph} we get the ladder DΓA approach and the diagrams of Fig. 8(b). From these diagrams (plus the contribution from the crossing-symmetrically related $\overline{ph}$ channel) we get F, and from F in turn through the Schwinger-Dyson equation (4) the self-energy.

If we want to calculate superconducting fluctuations in ladder DΓA we can plug the antiferromagnetic spin-fluctuations as a superconducting pairing glue (which is nothing but Γ_{pp}) into the pp channel. This is so-to-speak a poor man's one-step parquet calculation. It mixes the ph and $\overline{ph}$ channel into the pp (or Cooper) channel. That is, spin (and charge) fluctuations from the ph and $\overline{ph}$ channels can induce superconductivity, but we do not feed back the pp fluctuations to the ph and $\overline{ph}$ channel. For details on the superconducting calculations and also regarding the treatment of high frequencies, see [18].

A self-consistency with respect to the recalculation of the Green function entering the Bethe-Salpeter equation (3) is possible [25]. Different schemes have been proposed as well for a self-consistency with respect to Γ (or Λ) starting with [26], for an overview see [6]. A simpler

[4] When we eventually connect F with altogether four Green functions to a susceptibility with a single bosonic momentum and frequency [see Eq. (6) and Fig. 12 below)], the $\mathbf{q} = (\pi, \pi, \ldots)$ susceptibility is dominated in case of antiferromagnetic spin fluctuations by the ph channel, whereas the $\mathbf{q} = (0, 0, \ldots)$ optical susceptibility (conductivity) is dominated by the transversal particle-hole channel (π-tons [16]).

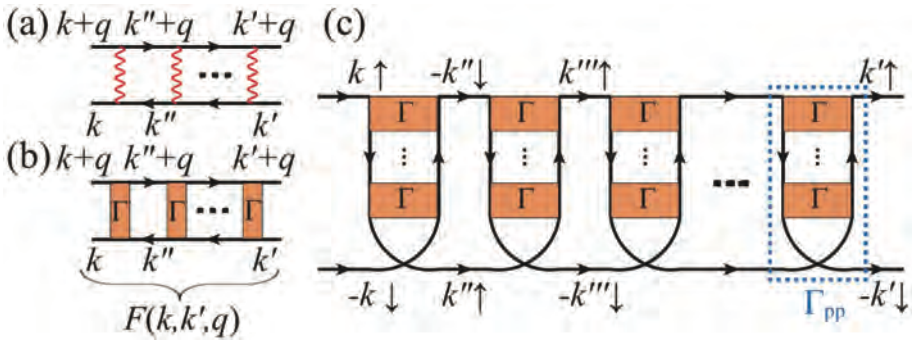


Fig. 8: *(a) Spin-fluctuations as calculated from the Bethe-Salpeter ladder diagrams in terms of the bare Coulomb interaction U in RPA. (b) Same as (a) but now calculated in ladder DΓA from the local irreducible vertex in the ph channel: $\Gamma \equiv \Gamma_{ph}$. (c) These antiferromagnetic spin-fluctuations enter as Γ_{pp} (via the parquet equation) in the particle-particle channel. This leads to the binding of two electrons into a Cooper pair, and if this bosonic Cooper pair Bose-Einstein condensates to superconductivity. From [27].*

and widely used approach is to do, instead, a so-called Moriyaesque λ-correction [6]. It essentially adds a mass to the paramagnons (dampens the antiferromagnetic spin fluctuations). This mass is fixed by a sum-rule for the susceptibility, and automatically ensures the correct high-frequency asymptotics of the self-energy. This λ-correction has been introduced to mimic the self-consistency and represents a considerable simplification of the calculations. For a further-going discussion see [6, 27].

The advantage of the ladder DΓA is that—as long as we do not couple the ladders through the parquet equations—the ladder only depends on a single frequency-momentum q instead of three (q,k,k'). Hence numerically much lower temperatures, larger frequency grids and finer momentum grids are feasible. Also realistic multi-orbital *ab initio* DΓA calculations are possible with the ladder DΓA version [17]. The results presented in the following have been obtained by ladder DΓA with a Moriyaesque λ-correction.

4 Hubbard model, cuprates and nickelates

In this chapter, we consider the one-band Hubbard model in two or three-dimensions

$$\mathcal{H} = -\sum_{ij,\sigma} t_{ij}\, c^\dagger_{i\sigma} c_{j\sigma} + U \sum_i n_{i\uparrow} n_{i\downarrow}. \tag{5}$$

It consists of two terms: (i) a hopping term t_{ij} between sites i and j, which we restrict in the following to a nearest neighbor t, next-nearest neighbor t' and next-next-nearest neighbor t''; and (ii) a local Coulomb repulsion U. Here $c^\dagger_{i\sigma}$ ($c_{i\sigma}$) creates (annihilates) an electron on site i with spin σ in second quantization and $n_{i\sigma} = c^\dagger_{i\sigma} c_{i\sigma}$.

The Hubbard model is the quintessential model for strongly correlated electron systems, similar as the Ising model for statistical physics or the drosophila fly for genetics. For $t_{ij} = 0$, we have just a collection of atoms and a spectra with peaks at $\pm U/2$ for half-filling. For $U = 0$, there is no interaction and we can solve the tight-binding Hamiltonian by Fourier transforming t_{ij} to $\varepsilon_{\mathbf{k}}$ in momentum space. Then, just occupying all single-particle states up to the Fermi

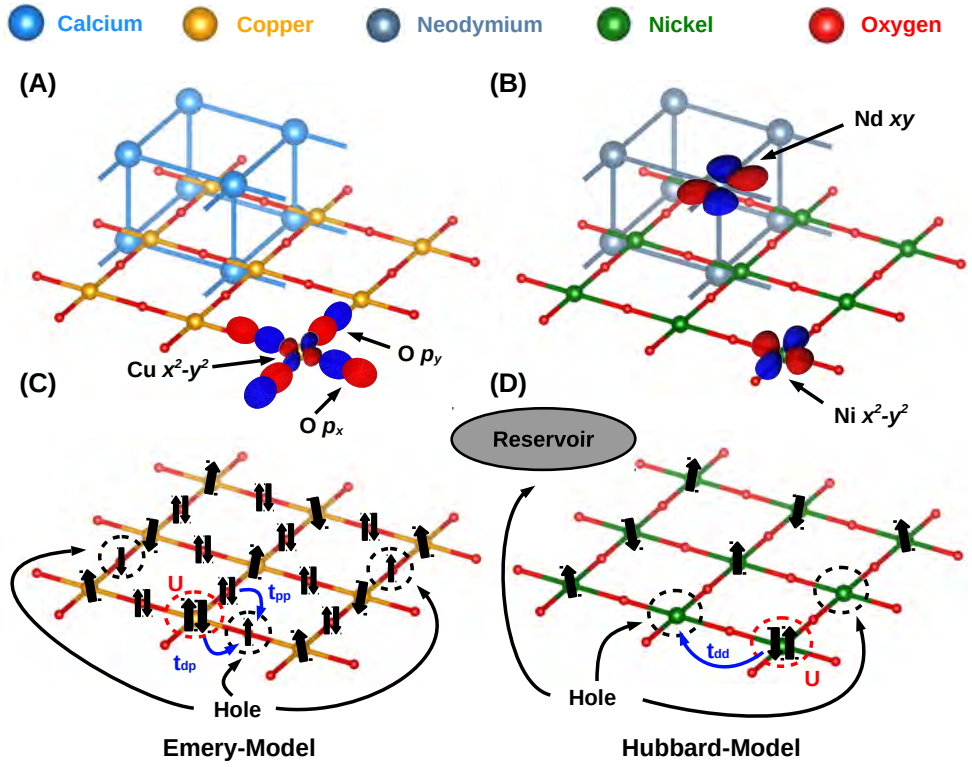


Fig. 9: *Crystal structure of (A) a characteristic cuprate, $CaCuO_2$, and (B) the nickelate $NdNiO_2$. The Cu(Ni)O_2 layers are separated by Ca(Nd) spacing layers in this "infinite-layer" structure. Also shown are the relevant low-energy orbitals in both cases. (C) Cuprates are charge transfer insulators so that the oxygen orbitals need to be included for an accurate microscopic description. The simplest such model is the* **Emery model** *with copper $3d_{x^2-y^2}$, oxygen p_x and p_y orbitals. As indicated there is a hopping t_{pd} between Cu and O sites, and further a hopping t_{pp} between O sites; double occupations are suppressed by the interaction U on the Cu sites just as in the Hubbard model. (D) For nickelates we have a Ni-$3d_{x^2-y^2}$-band and a A-pocket derived from the Nd $5d_{xy}$ band crossing the Fermi energy. Both are largely decoupled but we need to calculate, e.g., by DFT+DMFT, how many holes go into the Ni-$3d_{x^2-y^2}$-band* **Hubbard model** *and how many go into the A-pocket* **reservoir**. *From [28].*

energy gives the ground state. But, if we switch on U the electrons become correlated, the expectation value is correlated: $\langle n_{i\sigma} n_{j\sigma'}\rangle \neq \langle n_{i\sigma}\rangle\langle n_{j\sigma'}\rangle$, i.e., local double occupations $\langle n_{i\uparrow} n_{i\downarrow}\rangle$ are heavily reduced compared to the non-interacting, uncorrelated value on the right-hand-side of the equation.

While a screened interaction can—to a good approximation—often be replaced by the purely local interaction U, materials require typically the consideration of more bands than the single-band Hubbard model. This is even the case when we restrict ourselves to the low-energy orbitals around the Fermi energy. An important exception are cuprate and nickelate[5] superconductors. For the Ruddlesden-Popper $La_3Ni_2O_7$ under pressure, critical temperatures are close to 100 K.

[5]Here, we refer to infinite-layer nickelates. More recently also superconducting Ruddlesden-Popper nickelates have been synthesized [29] which have a very different physics: (i) oxygen orbitals strongly connect a few NiO_2 layers making the system much more three dimensional; (ii) further these Ruddlesden-Popper nicklelates have more than two holes in the Ni $3d$ orbitals so that multi-orbital physics is immanent.

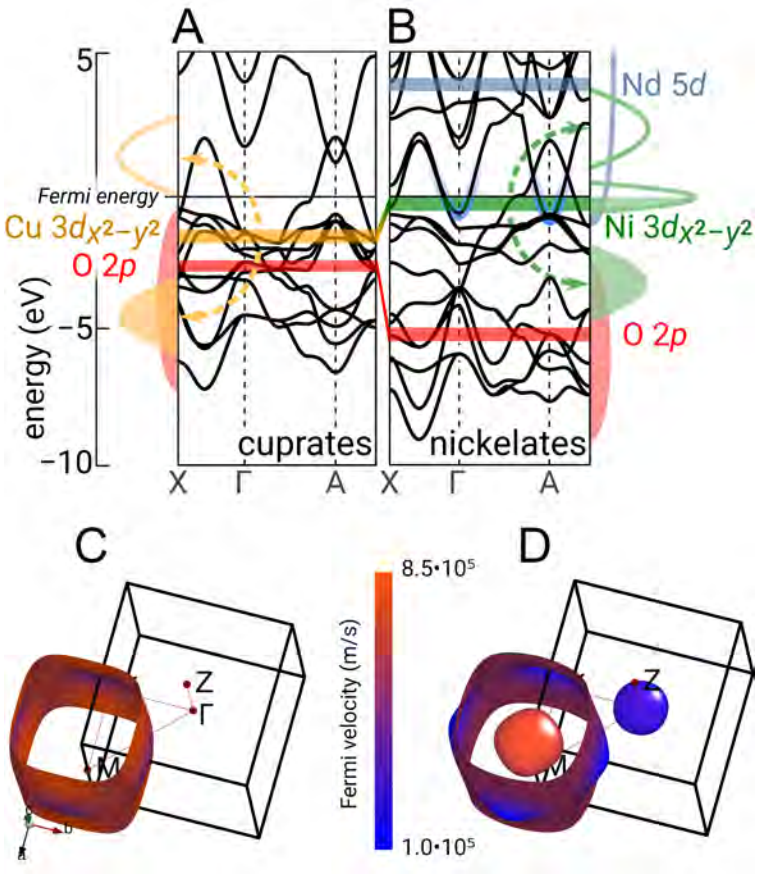


Fig. 10: *(A,B) Electronic structures of (A) $CaCuO_2$ and (B) $LaNiO_2$ as calculated in DFT. The side panels indicate the effect of electronic correlations and the color bars the center of energy of the most important bands. (C) and (D) DFT Fermi surface corresponding to (A) and (B), respectively. From [28].*

The arguably simplest cuprate and nickelate crystal structure is the "infinite-layer"[6] structure displayed in Fig. 9(A) and (B). Since the valence of the spacer cations is Ca^{+2} and $Nd(La)^{+3}$, the formal oxidation state is Cu^{+2} and Ni^{+1}, respectively, so that both cuprates and nickelates are in a formal $3d^9$ configuration. After such basic chemistry considerations, the first step to get an idea of the relevant orbitals is doing a density functional theory (DFT) calculation.

Fig. 10 shows that for the cuprates a single $3d_{x^2-y^2}$-orbital is crossing the Fermi level. It gives rise to the single hole-like Fermi surface sheet displayed in the lower left panel of Fig. 10. This Cu $3d_{x^2-y^2}$-band and Fermi surface can well be described with proper hopping parameters t, t' and t''. But now we need to include the effect of electronic correlations. These are indicated by the dashed arrows and the side panels of Fig. 10(A): the Cu $3d_{x^2-y^2}$-band splits into an upper and lower Hubbard band. Since the oxygen orbitals are just a few eV below the Fermi energy, these oxygen orbitals end up above the lower Hubbard band. As a consequence we have a charge transfer insulator according to the scheme of Zaanen-Sawatzky-Allen and not a Mott insulator, which one might have expected from the splitting into Hubbard bands. That is, if we dope cuprates, and we need to do so to have a superconductor, the holes go into the

[6]The two distinct layers displayed in Fig. 9 are repeated on top of each other ad infinitum.

oxygen bands. Hence, in the case of cuprates, an Emery model description which incorporates the copper $3d_{x^2-y^2}$-band and oxygen p_x and p_y bands as visualized in Fig. 9(C) is the most appropriate low-energy model. Nonetheless, the majority of theoretical papers studying the cuprates use the single-band Hubbard model. This is to some extend justified by the fact that oxygen-hole spin and copper spin form a Zhang-Rice singlet, which can be described effectively by the Hubbard model. Also in experiment, there is a single Fermi surface as in Fig. 10(C) of mixed oxygen and copper character.

In case of the nickelates, these oxygen bands are instead at a considerably lower energy. Hence the lower Hubbard band is now above the oxygen band and we would have a Mott insulator, if it was not for the Nd(La) $4d$-bands.[7] These Nd(La) $4d$ bands are closer to the Ni $3d$-bands than the unoccupied Ca and Cu s bands are to the Cu bands. They even cross the Fermi level around the Γ and A momentum, which leads to the formation of pockets around these momenta in DFT, see Fig. 10(D). The charge transferred to the Nd(La) pockets also leads to a self-doping of the Ni $3d_{x^2-y^2}$-band: even the parent compound Nd(La)NiO_2 has about 0.05 holes per Ni. In such a situation, a quasi-particle peak develops as indicated in the side panel of Fig. 10(B) with a quasiparticle mass enhancement $m^*/m = 1/Z$ calculated to be about five for the undoped parent compound and about three at 20% Sr doping [30]. A further correlation effect is that the Γ-pocket is shifted above the Fermi level, at least for larger Sr-doping and for $LaNiO_2$.

Altogether this leaves us with two relevant bands as displayed in Fig. 9(B): the Ni $3d_{x^2-y^2}$-band and the Nd(La)-derived A-pocket. Both bands do not hybridize and can hence, to a first approximation, be considered as decoupled. The expectation is that the more strongly correlated Ni $3d_{x^2-y^2}$-band is responsible for the superconductivity. Using Occam's razor, i.e., if we try to identify the most simple model, we end up with a one-band Hubbard model for the Ni $3d_{x^2-y^2}$-band and a decoupled reservoir (A-pocket) that must be taken into account for translating the Sr-doping of Nd(La)$_{1-x}$Sr$_x$NiO$_2$ into the actual hole doping of this Hubbard model. Otherwise the A-pocket is merely a passive bystander. This simple model is illustrated in Fig. 9(D).

The hopping parameters of the nickelate Hubbard model can be obtained from a Wannier function projection onto the Ni $3d_{x^2-y^2}$-band: $t = 0.395\,\text{eV}$, $t'/t = -0.25$, $t''/t = 0.12$ [30]. Further, the interaction strength U can be calculated by constrained random phase approximation (cRPA, see Chapter "Screened Coulomb Interactions from cRPA" by J.M. Tomczak [3]). Considering the fact that U is frequency(ω)-dependent in cRPA and—within the relevant energy range—on average slightly larger than $U(\omega{=}0)$, one obtains $U \approx 8t$ from cRPA. For further details see [30].

The translation from Sr-doping to the occupation of the $3d_{x^2-y^2}$-band has been calculated in DFT+DMFT[8] including all five Nd and all five Ni d bands in DMFT. Fig. 11 (blue curve) shows the results: One sees that roughly 50% of the holes (there is one hole per Sr) go into the $3d_{x^2-y^2}$-band and the remaining 50% go into the pockets. For larger Sr-dopings, at around 25%,

[7] We here show $LaNiO_2$ since it is slightly easier to calculate than $NdNiO_2$ in DFT because it has no $4f$-electrons. Experimentally, La$_{1-x}$Sr(Ca)$_x$NiO$_2$ is also a nickelate superconductor with a T_c comparable to $NdNiO_2$.

[8] For the DFT+DMFT method, see the Chapter "LDA+DMFT for strongly correlated materials" by A. Lichtenstein in 2022 [4]

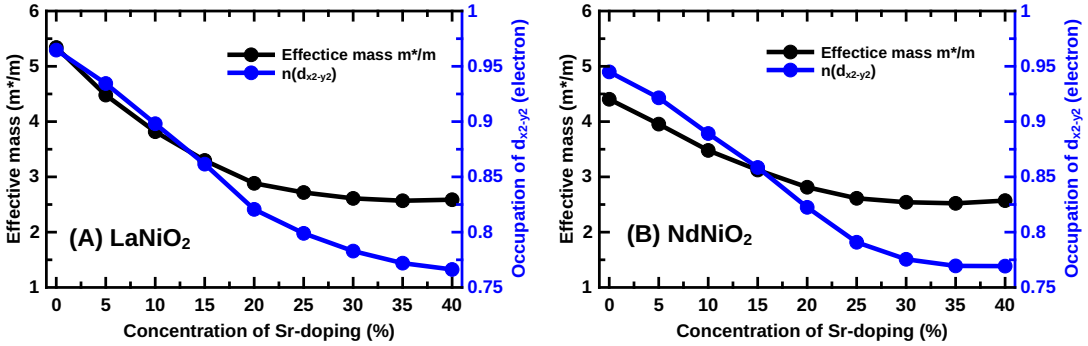


Fig. 11: *Translation of Sr-doping to the occupation of the Ni $3d_{x^2-y^2}$-band (blue line; right y-axis) and corresponding effective mass enhancement m^*/m (black line; left y-axis) as calculated by DFT+DMFT for (A) $La_{1-x}Sr_xNiO_2$ and (B) $Nd_{1-x}Sr_xNiO_2$. From [30] (Supplemental Material).*

the curve flattens because here the Ni $3d_{3z^2-r^2}$ orbital approaches the Fermi level and accommodates holes as well. The one-band Hubbard model DMFT calculation gives a very similar spectrum as the full DFT+DMFT calculations with 5+5 Nd+Ni orbitals. Also the effective mass plotted in Fig. 11 (black curve) agrees [30]. Altogether this hints that the simple Hubbard model is a good approximation for nickelates; experimental results are also consistent with this picture as detailed below.

5 Spin fluctuations

Spin fluctuations as visualized in Fig. 8(a,b) enter the full vertex F but subsequently also the susceptibility which is connected to F as follows (Fig.12)

$$\chi_{r,\mathbf{q}\omega} = \underbrace{\sum_{\mathbf{k}\nu} G_{\mathbf{k}\nu}\, G_{(\mathbf{k}+\mathbf{q})(\nu+\omega)}}_{\equiv \chi^0_{\mathbf{q}\omega}} - \sum_{\mathbf{k}\mathbf{k}'\nu\nu'} G_{\mathbf{k}\nu} G_{(\mathbf{k}+\mathbf{q})(\nu+\omega)}\, F^{\nu\nu'\omega}_{r,\mathbf{k}+\mathbf{k}'\mathbf{q}}\, G_{\mathbf{k}'\nu}\, G_{(\mathbf{k}'+\mathbf{q})(\nu+\omega)} \qquad (6)$$

for $r = c/s$, i.e., the spin and charge susceptibility, respectively. As before, we restrict ourselves to the paramagnetic phase for simplicity. The first term on the right hand side of Eq. (6) is just the bare bubble contribution χ^0, obtained directly from two (interacting) Green function; the second term are vertex corrections calculated form F. The minus sign is a matter of definition of F. When F is calculated in RPA as in Fig. 8(a), we have $\Gamma_r = \pm U$ for $r = c/s$ and obtain a

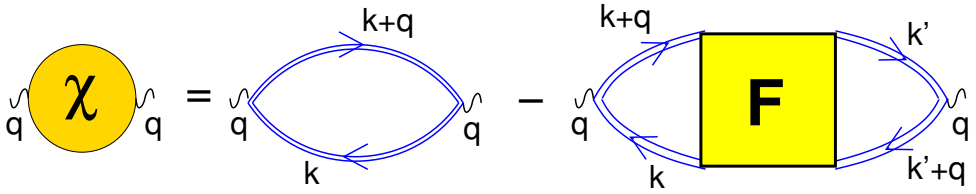


Fig. 12: *The susceptibility χ consists of the bare bubble χ^0 (first term on the right hand side) and vertex corrections that can be calculated from the full vertex F.*

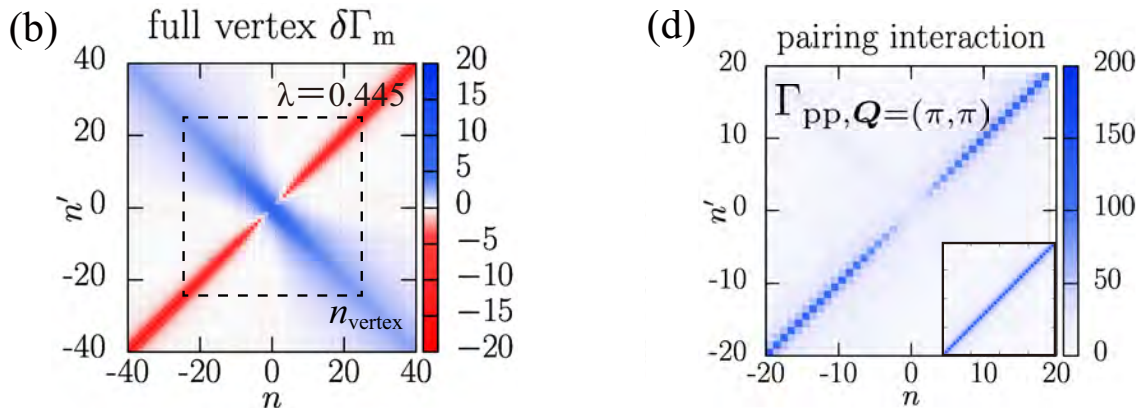


Fig. 13: *Left: Difference of the local ph vertex in the magnetic channel from $-U$, i.e., $\delta\Gamma_m = \Gamma_s - (-U)$ vs. the two fermionic Matsubara frequencies $\nu_n = i(2n+1)\pi T$ and $\nu'_{n'}$ at zero bosonic frequency $\omega = 0$. At small frequencies, $\Gamma_{s,ph}$ and associated spin-fluctuations are suppressed. Right: This suppression also leads to a suppression of the non-local pp vertex Γ_{pp}, i.e., the superconducting pairing glue, at small frequencies. It is obtained from antiferromagnetic spin fluctuations (i.e., from the local Γ_s corresponding to the left panel and the Bethe-Salpeter equation, see Sec. 6). Right inset: Γ_{pp} as calculated in RPA. From [27] where further details and parameters can be found.*

geometric sum, which eventually yields

$$\chi^{RPA}_{r,\mathbf{q}\omega} = \frac{\chi^0_{\mathbf{q}\omega}}{1 \pm U\chi^0_{\mathbf{q}\omega}} \tag{7}$$

where the +/- is for $r = c/s$. For certain ω's and $\mathbf{q}$'s Eq. (7) develops poles. We call these bosonic excitations (para)magnons. The ω-$\mathbf{q}$ energy-momentum dispersion relation of these quasiparticles follows the position of the poles.

The minus sign in Eq. (7) already indicates that spin-fluctuations are generally stronger in a Hubbard model. This can change if additional non-local interactions V are included. These trigger a transition from an antiferromagnetic spin to a charge density wave order for $\mathcal{Z}V > U$ in mean field ($\mathcal{Z}$: number of neighbors; V: nearest neighbor Coulomb repulsion). Which magnetic order dominates in RPA, solely depends on the $\mathbf{q}$ for which $\chi^0_{\mathbf{q}\,\omega=0}$ is strongest. Close to half-filling, we often have Fermi surfaces where for a $\mathbf{k}$ on the Fermi surface (ν=0) also $\mathbf{k}$+$\mathbf{q} = (\pi, \pi, \ldots)$ is at or close to the Fermi surface. Then both $G_{\mathbf{k}\nu=0}$ and $G_{(\mathbf{k}+(\pi,\pi,\ldots))(\nu+\omega)=0}$ are large in Eq. (6), and the antiferromagnetic susceptibility $\chi^0_{\mathbf{q}=(\pi,\pi,\ldots)\omega=0}$ is maximal. Of course, this is just the weak coupling picture. For larger Coulomb interactions we form large magnetic moments and the change of physics is reflected in vertex F corrections beyond RPA. More recently it could be demonstrated [27] that the local vertex $\Gamma_{r=m}$ is suppressed compared to the RPA value $\Gamma_s = -U$. This is shown in Fig. 13 (left). This suppression, in particular that at the relevant small frequencies, leads to reduced spin-fluctuations. Consequently, the superconducting pairing as calculated along the line of Fig. 8(b,c) is suppressed as well, see Fig. 13 (right). The origin of the suppression of Γ_s at small frequencies are local particle-particle excitations that enter Γ_s. These reduce Γ_s along the side diagonal frequencies $\nu = -\nu'$. In the literature such particle-particle screening of the spin vertex is also known as the Kanamori screening.

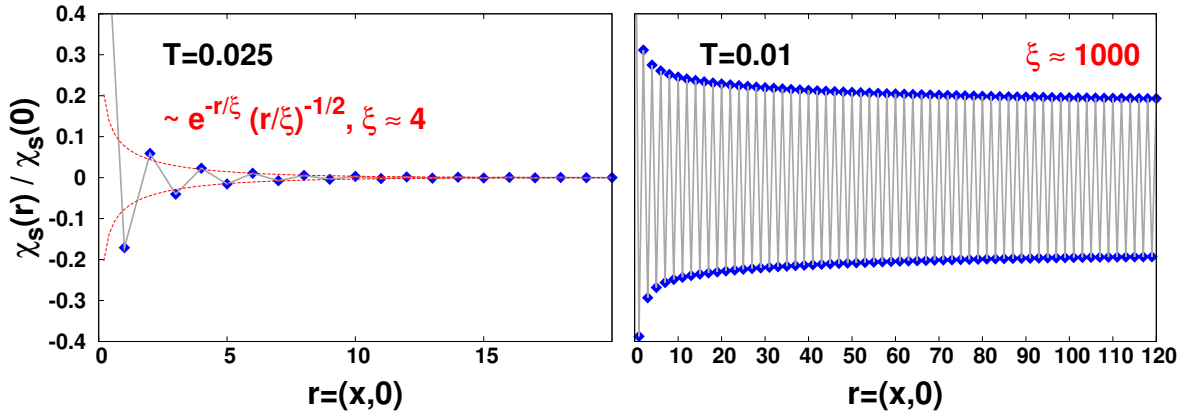


Fig. 14: *Antiferromagnetic correlation function $\chi_{s,\mathbf{r}}$ normalized to its $\mathbf{r} = 0$ value vs. distance $\mathbf{r}$ for the two dimensional Hubbard model along the x-direction ($t' = t'' = 0$, $U = 0.5(4t)$; all energies are here in units of $4t$). The left and right panel show two different temperatures, $T = 0.025(4t)$ (left) and $T = 0.025(4t)$ (right), where largely different correlation lengths (ξ) are observed. From [15].*

This reduction of the DΓA spin susceptibility is key for a good description of antiferromagnetic spin-fluctuations which are hugely overestimated in RPA. In fact, it was shown that qualitatively and quantitatively the DΓA susceptibility excellently agrees with other numerical calculations [31].

From the susceptibility one can obtain the correlation length ξ. Fourier-transformed to real space $\mathbf{r}$ and time, the (equal-time) magnetic susceptibility behaves as

$$\chi_{s\mathbf{r}} = \langle \mathbf{S}(\mathbf{r})\mathbf{S}(\mathbf{0})\rangle \sim \left(\frac{|\mathbf{r}|}{\xi}\right)^{-1/2} e^{-\frac{|\mathbf{r}|}{\xi}} \tag{8}$$

at large distances $\mathbf{r}$. Here, $\mathbf{S}(\mathbf{r})$ denotes the spin operator of the electrons at position (lattice site) $\mathbf{r}$. Fig. 14 shows this spin-spin correlations or susceptibility of the Hubbard model. Clearly, an alternating (antiferromagnetic) correlation is visible. At high temperatures (left panel), the correlation length is short and correlations quickly decay. In two dimensions we get however an exponential increase of the correlation length with $1/T$ in DΓA [15] which is the reason behind the very large correlation length of Fig. 14 (right panel). While a correlation length of $\xi = 4$ lattice sites (left panel) can still be covered in cluster extensions of DMFT and lattice quantum Monte Carlo methods, with the rapidly increasing correlation length at lower temperatures such cluster approaches reach their numerical limits.

At a three dimensional phase transition, the susceptibility diverges with critical exponent ν: $\xi \sim (T-T_c)^{-\nu}$, and similarly $\chi_{r,\mathbf{Q}\omega=0} \sim (T-T_c)^{-\gamma}$ with a critical exponent γ. These critical exponents could be calculated in DΓA and DF for the first time for correlated electronic models, a topic that has been covered in a preceding Jülich Autumn School [14].

In practice, the correlation length is not calculated from fitting $\chi_{s\mathbf{r}}$. Instead one fits it Fourier-transform $\chi_{s,\mathbf{q}\omega=0}$ in momentum space. For large correlation lengths and in the vicinity of its

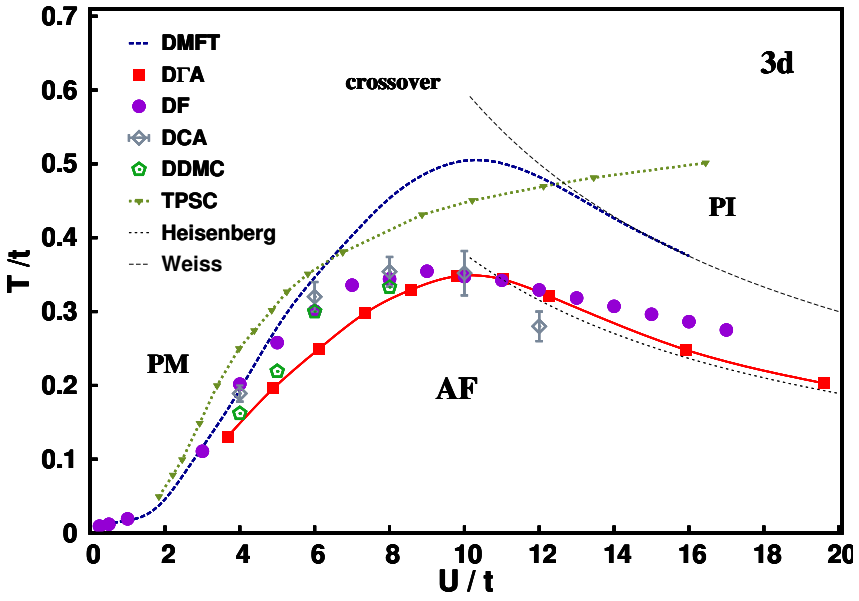


Fig. 15: *Phase diagram of the half-filled three-dimensional Hubbard model on a cubic lattice with nearest-neighbor hopping t comparing various methods for the phase transition from the paramagnetic metallic (PM) and insulating (PI) phase to the antiferromagnetic insulating phase (AF). From [6] where further details and the abbreviation of the various methods can be found.*

maximum at the dominating wave vector $\mathbf{Q}$,[9] the susceptibility is of the Ornstein-Zernike form

$$\chi_{s,\mathbf{q}\,\omega=0} \sim \frac{1}{(\mathbf{q}-\mathbf{Q})^2 + \xi^{-2}} \,. \tag{9}$$

That is, the inverse correlation length ξ^{-1} corresponds to the width of the susceptibility around its peak at $\mathbf{q} = \mathbf{Q}$.

In two dimensions, the Mermin-Wagner theorem is fulfilled and there is no long range antiferromagnetic order for finite temperature in the DΓA and diagrammatic extension of DMFT [6]. In three-dimensions the antiferromagnetic phase transition temperature T_c is reduced compared to DMFT, as shown in Fig. 15. Also the critical behavior in the vicinity of the phase transition is not any longer of mean-field type as in DMFT. Instead the critical exponents well agree[10] with those of the Heisenberg model [6, 14] for half-filling, as to be expected from universality.

Besides the susceptibility, spin-fluctuations also impact the electronic self-energy, as already indicated in Fig. 1. The effect F on the self-energy Σ can be directly calculated via the Schwinger-Dyson Eq. (4) [Fig. 6]. Physically, this corresponds to electron-(para)magnon scattering which can reduce the lifetimes of the quasiparticles.

A hallmark phenomenon of the effect of these spin-fluctuations on the self-energy is the opening of a pseudogap. Here, the self-energy is strongly momentum dependent. At the node, we have a Fermi liquid-like self-energy with a linear decay of self-energy at small frequencies, see Fig. 16. In contrast for the antinode we have an enhanced self-energy at small frequencies, which with decreasing temperatures develops a $1/\nu$ pole.

[9] For example, $\mathbf{Q} = (\pi, \pi)$ for the two-dimensional Hubbard model at half-filling.

[10] within the numerical error bars in the studied critical temperature regime

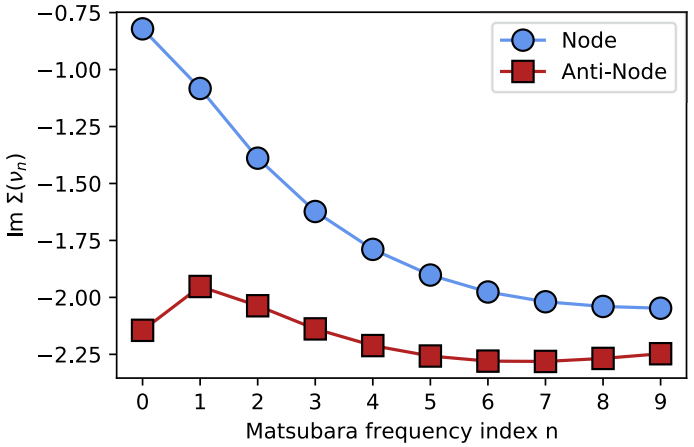


Fig. 16: *Imaginary part of the DΓA self-energy vs. index n of the Matsubara frequency $\nu_n = i(2n+1)\pi T$, in the pseudogap region for a typical Hubbard model. Parameters: $U = 8$, $t' = -0.2$, $t'' = 0.1$, $T = 0.05$ (all in units of t), and 10% hole doping. Clearly the self-energy is very different for the two momenta plotted, i..e, in the nodal direction of the Fermi surface and in the anti-nodal direction. The downturn of the anti-nodal self-energy indicates the development of a pole and thus a splitting of the spectral function away from the Fermi energy. Figure by courtesy of Paul Worm.*

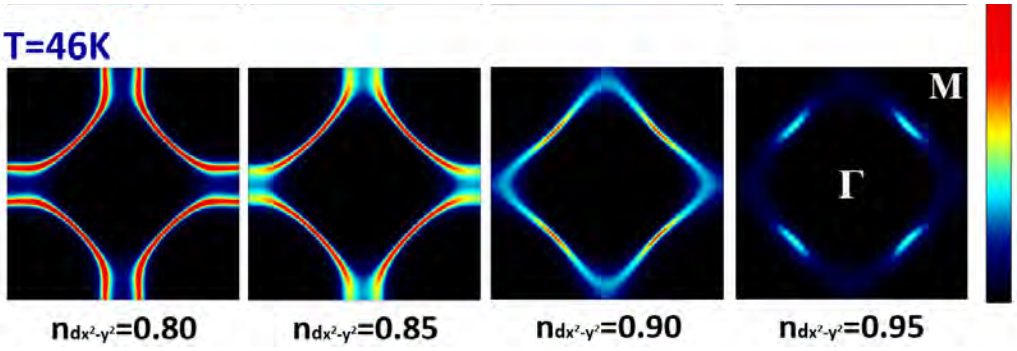


Fig. 17: *DΓA spectrum at the Fermi energy for different dopings of nickelate superconductors throughout the Brillouin zone (i.e, x- and y-axis are the k_x and k_y momentum ranging from $-\pi$ to π, and the false color show the spectral function at the Fermi energy $\nu = 0$). From [30].*

Turning to the infinite-layer nickelates, Fig. 17 shows the DΓA spectrum of the Ni $3d_{x^2-y^2}$ band[11] for nickelates as calculated by DΓA for the effective Hubbard model (see Sec. 4 where also the parameters can be found). The parent compound $NdNiO_2$, corresponding to $n_{3d_{x^2-y^2}} = 0.95$ (rightmost panel) has a pseudogap in the antinodal (PG) region, indicated by missing spectral weight in Fig. 17. This DΓA prediction still awaits an experimental confirmation.
For making nickelates superconducting, one needs to dope this $3d_{x^2-y^2}$ band, e.g., to $n_{3d_{x^2-y^2}} = 0.80$ or 0.85. For these superconducting dopings, we have a clear Fermi surface throughout the Brillouin zone in Fig. 17 and no pseudogap.[12]

[11] There are additional Nd pockets, see Sec. 4.

[12] As a technical remark, the spectrum has been calculated from $A_{\mathbf{k}\nu_0} = -G_{\mathbf{k}\nu_0}/\pi$ at the lowest Matsubara frequency $\nu_0 = i\pi T$, which leads to some additional broadening (smearing) but avoids the error-prone and cumbersome analytical continuation.

6 Superconductivity

Next we turn to the task of calculating the superconducting order and critical temperature T_c from the antiferromagnetic spin-fluctuations. The general procedure has already been indicated in Fig. 8(c). More specifically, the first step is the calculation of the full vertex F from Γ_{ph} (plus the crossing symmetrically related $\overline{ph}$ channel), by summing the Bethe-Salpeter ladder diagrams in this channel(s). This calculation includes spin and charge fluctuations, but in the Hubbard model spin-fluctuations prevail. In the second step, we insert these spin-fluctuations into the pp channel. That is, we calculate $\Gamma_{pp} = \Lambda + \Phi_{ph} + \Phi_{\overline{ph}}$. Since no pp reducible diagrams have yet been included (except for the local ones), we can also rewrite this as $\Gamma_{pp} = F - \Phi_{pp}^{\rm local}$. From this Γ_{pp} we can next recalculate F including superconducting fluctuations via the Bethe-Salpeter equation in the pp channel. This is akin to the Schwinger-Dyson Eq. (3) in the ph channel, except that we have to properly rotate the momenta and to use Γ_{pp} instead of Γ_{ph}.
Similarly as in RPA [Eq. (7)], we get a superconducting (SC) susceptibility of the form

$$\chi_{SC,\mathbf{q}=\mathbf{0}\,\omega=0} = \sum_{kk'\nu\nu'} \underline{\underline{\chi^0}} \Big(1 + \underline{\underline{\Gamma_{pp,\mathbf{q}=\mathbf{0}\omega=0}}}\ \underline{\underline{\chi^0}}\Big)^{-1}. \tag{10}$$

Here, we are interested in the instability at $\omega = 0$ and the coupling of two fermions with momentum $\mathbf{k}$ and $-\mathbf{k}$ into a Cooper pair as in Fig. 8(c), i.e., a total momentum $\mathbf{q} = 0$ in the pp channel.[13] The generalized[14] bare bubble susceptibility at $\omega = 0$ and $\mathbf{q} = 0$ is

$$\chi^0_{\mathbf{k}\mathbf{k}'\nu\nu'} = G_{\mathbf{k}'\nu'} G_{-\mathbf{k}-\nu} \delta(\mathbf{k} - \mathbf{k}') \delta_{\nu,\nu'} \tag{11}$$

and the double underlines denote matrices with respect to $\mathbf{k}\nu$ and $\mathbf{k}'\nu'$.
In order to obtain superconductivity, i.e., a diverging $\chi_{SC,\mathbf{q}=\mathbf{0}\,\omega=0}$ one of the eigenvalues λ of the matrix $-\underline{\underline{\Gamma_{pp,\mathbf{q}=\mathbf{0}\omega=0}}}\ \underline{\underline{\chi^0}}$ has to approach $\lambda = 1$. For electron-phonon mediated superconductivity this is simple since the electron-phonon coupling gives rise to an attractive (negative) Γ_{pp}. For the repulsive Hubbard model, this is much more difficult to achieve since Γ_{pp} also includes the repulsive (positive) Coulomb interaction $+U$. Nonetheless, an attraction can be mediated by antiferromagnetic spin-fluctuations through retardation (ν, ν') and non-locality (k, k'). The k, k' structure of the diverging ($\lambda \to 1$) eigenvector (or the corresponding real space structure) determines the symmetry of the superconducting symmetry breaking and gap (s-wave, d-wave etc.). For phonons with an across the board attraction, one gets s-wave superconductivity. For the spin-fluctuations in the Hubbard model d-wave is more favorable to avoid the large local repulsion $+U$.[15]
In an infinitely-extended strictly two-dimensional system there is no superconductivity at finite temperatures. Instead, a finite temperature topological Berezinskii-Kosterlitz-Thouless (BKT)

[13] This $\mathbf{q}$ is not to be confused with that in the ph channel which is peaked around $\mathbf{Q} = (\pi, \pi)$ and corresponds to another combination of the external legs of the four-point vertex F.

[14] without $kk'\nu\nu'$ summation

[15] For the d-wave, Γ_{pp} mediates between momenta $\mathbf{k}$ and $\mathbf{k}'$ on the Fermi surface, for which the superconducting eigenvalue has opposite sign.

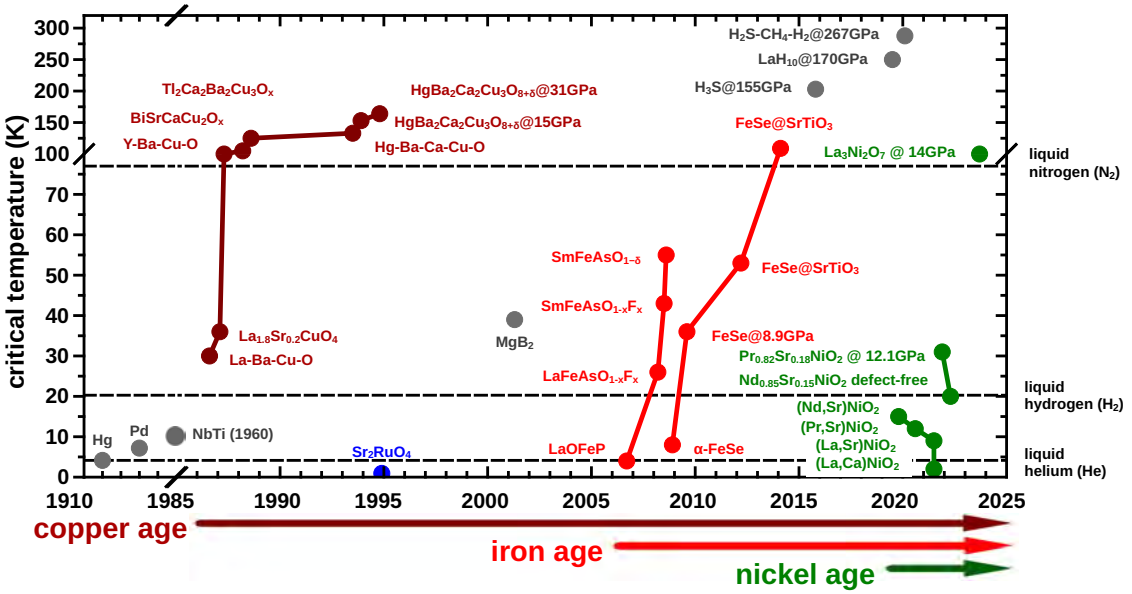


Fig. 18: *Superconducting T_c vs. year of discovery for various important superconductors. After the copper age, there came an iron age, and now we are in the nickel age. From [33] (updated).*

transition is possible. At first glance, this is a contradiction to the observed superconductivity in cuprates and nickelates. However, these materials are not perfectly two-dimensional but layered quasi-two-dimensional materials. In this situation, and with the strongly increasing correlation length around the BKT transition, even a tiny coupling in the inter-layer direction will trigger superconductivity, a little bit below the BKT transition. In the DΓA calculation, a self-consistency is necessary to (possibly) get a BKT transition. Without the self-consistent feedback of the superconducting fluctuations, we eventually get a mean-field kind of superconducting transition and a finite T_c which is closer to experiment than the ideal two-dimensional calculation with a BKT transition.

As for superconducting materials, the nickelate superconductors [32] have led to enormous theoretical and experimental efforts. One therefore also speaks of the nickel age for superconductivity, see Fig. 18.

Also shown are hydrogen-based superconductors that are phonon-mediated and have a T_c close to room temperature, but only under the enormous pressure of a diamond anvil cell. Hence the challenge is to increase T_c for the unconventional (i.e., not phonon-mediated) correlated superconductors or to reduce the pressure for the hydrogen-based superconductors. Here, the nickelates have a T_c that is still quite substantially below that of the cuprates. However, one can expect T_c to further increase somewhat with new and better synthesized nickelate films. For example, T_c above 30 K was demonstrated recently for infinite-layer nickelates [34]. The high hope is that infinite-layer nickelates and cuprates, being very similar but also decisively distinct, put us in the ideal situation to discriminate the essentials from the incidentals for high-temperature superconductivity. The iron pnictides and Ruddlesden-Popper nickelates are instead pretty far away from the cuprate or nickelate physics with their imminent multi-orbital physics.

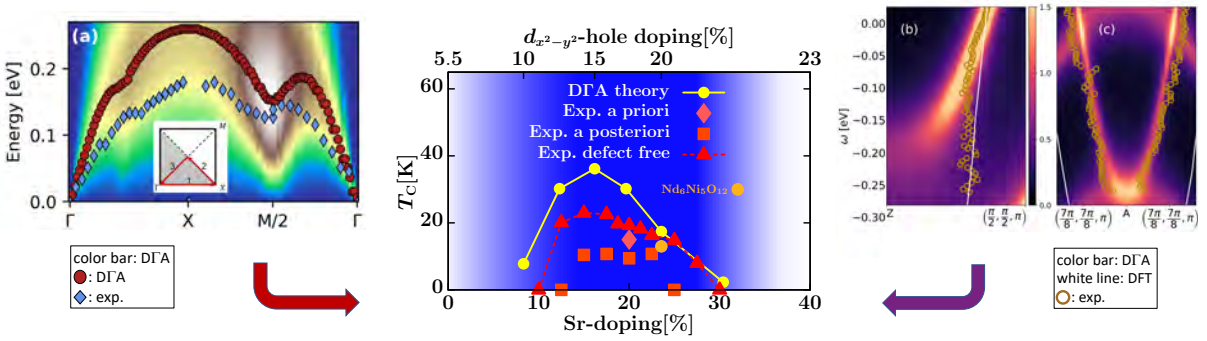


Fig. 19: Center: *Superconducting T_c vs. doping x of $Sr_xNd_{1-x}NiO_2$ as predicted by DΓA [30] and "a posteriori" [35] confirmed experimentally; the agreement further improved after synthesizing "defect free" films [36]. "A priori" [32] a single nickelate superconductor was known. The T_c of $Nd_6Ni_5O_{12}$ aligns as well [37, 38]. More recently, also the underlying spin-fluctuations and one-electron states were found to agree excellently with resonant inelastic x-ray scattering (***RIXS, left***) [39, 40] and angular-resolved photoemission spectroscopy (**ARPES, right**) [41–43]. As these enter the calculation of T_c, indicated by the arrows, this gives us altogether a high level of confidence that the modeling is correct and accurate. (Note, the experimental ARPES dispersion is from the 2nd derivative, which also shows waterfalls in theory [43, 44].) For such a notoriously difficult to determine quantity as the superconducting T_c and without adjustable parameters, the accuracy is indeed astonishing.*

In Sec. 4, we have already pointed out that the nickelates can be described by a one-band Hubbard model with an approximately adjusted doping; and in Fig. 17 we have shown the thus calculated spectrum with a pseudogap for the (non-superconducting) parent compound $NdNiO_2$. For this nickelate Hubbard model, we find [30] (not surprisingly) d-wave superconductivity in ladder DΓA. The superconducting T_c vs. doping is plotted in Fig. 19 as a function of Sr-doping. Actually the theoretical calculation was a prediction here since, when three years ago superconductivity in nickelates has been discovered [32], only a single T_c at 20% doping was available at first because of the difficulties to synthesize $Nd_{1-x}Sr_xNiO_2$ in the low oxidation state Ni^{+1}. With the recent progress to synthesize clean superconducting nickelate films [36], the theoretical predicted phase diagram has been spectacularly confirmed in experiment, see Fig. 19. Also the strength of spin-fluctuations that were found to mediate superconductivity in DΓA and the one-particle electron spectrum were predicted correctly, see Fig. 19 left and right panel, respectively. This provides altogether a high level of confidence that we have achieved an excellent modeling of infinite-layer nickelates, using a novel methodology for the calculation of strongly correlated superconductors.

The physical reason that we see in Fig. 19 a superconducting dome is two-fold: The downturn at large doping is because antiferromagnetic spin-fluctuations get weaker the further we are away from half-filling. The down-turn at small doping, towards half-filling, on the other hand is a consequence of the pseudogap which develops in this doping region, see Fig. 17. Thus, the electron propagators in Fig. 8(c) lose coherence in a larger part of the Fermi surface, and the superconducting susceptibility is suppressed despite considerable spin-fluctuations.

Recently also finite-layer variants of the infinite-layer nickelate superconductor have been synthesized [37]. These have very similar hopping parameters and physics [38,45]. Their T_c agrees with DΓA as well [38, 45] (and with the T_c of the infinite layer nickelates shown in Fig. 19). Here, DMFT indicates that, if we only have a few layers, finite-layer nickelates have no pockets. This is confirmed by a—in contrast to infinite-layer nickelates—positive (hole-like) hall resistivity [37]. The absence of pockets also further corroborates the picture of a decoupled reservoir that is not relevant for superconductivity as advocated in Fig. 9. Altogether the DFT+DMFT and DΓA calculations for nickelates and the experiments for the different nickelates provide for a consistent picture [38]. This gives us some hope that we might finally be able to actually calculate and predict superconducting T_c's, the arguably biggest challenge of solid state theory.

7 Conclusion and outlook

Diagrammatic extensions of DMFT are very appealing in several ways: They combine the good description of DMFT with the, to the best of our knowledge, most important non-local physics. In this chapter we have focused on spin-fluctuations and how they mediate superconductivity, but other fluctuations such as charge fluctuations, weak localization corrections, excitons—you name it—are treated on an equal footing. Also (quantum) criticality can be described, a topic that has been discussed in an earlier Jülich Autumn School [14]. Diagrammatic extensions of DMFT are also very appealing since they merry quantum field theoretical with its qualitative understanding and numerics which is unavoidable for a quantitative description of strongly correlated electrons systems.

Different variants of diagrammatic extensions of DMFT exist, and for the sake of brevity we have concentrated here on the first (and widely employed) variant: the dynamical vertex approximation. All variants have in common that they calculate a local vertex and construct non-local correlations from this vertex diagrammatically. In regions of the phase diagram where non-local correlations are short range, results are similar to those from cluster extensions of DMFT. However, the diagrammatic extensions also offer the opportunity to study long-range correlations, which is key for (quantum) criticality but also important in other situations, as well as to calculate materials with many orbitals [17].

There is still plenty of room for improvement: starting from (i) various self-consistencies, using (ii) a clusters instead of a single site as a starting point [46], (iii) compactifying the vertex with various methods such as the intermediate representation (IR) in frequency space [23], quantics tensor trains (see Chapter "Learning Feynman Diagrams with Tensor Trains" by X. Waintal [3]), the truncated unity in momentum space [22], and the single-boson exchange [24] in Feynman diagram space. The hope is that the reduced memory burden then allows parquet DΓA calculations at lower temperatures or with multi orbitals. Another development has been (iv) the calculation of the underlying two-particle vertices directly for real frequencies, which is possible using the numerical renormalization group (NRG) method, see Chapter "The physics of quantum impurity models" by J. von Delft in 2022 [4].

In this chapter, we have concentrated on antiferromagnetic spin-fluctuations and how they me-

diate superconductivity. The T_c predicted for nickelates well agrees with experiment—actually much better than what we dared to hoped for. This gives us some confidence that we are on the right track to better model and understand superconductivity, that we eventually have the tools to predict T_c for new materials. While many theoreticians in the many-body community consider antiferromagnetic spin-fluctuations to be at the origin of high temperature superconductivity, the mechanism for unconventional superconductivity remains hotly debated. Maybe through a careful analysis and predictions we can now prove that this is indeed the microscopic mechanism for high-temperature superconductivity.
Diagrammatic extensions of DMFT such as the DΓA also offer the opportunity to study many other phenomena and to do material calculations. This leaves plenty of opportunities for the next generation of physicists.

Acknowledgment First of all, I would like to thank my co-workers on the research presented here, Oleg Janson, Andrey Katanin, Anna Kauch, Motoharu Kitatani, Jan M. Tomczak, Liang Si, Alessandro Toschi, and Paul Worm. Without them, the success of diagrammatic extensions of DMFT would not have been possible. Finally, I gratefully acknowledge financially support by the Austrian Science Fund (FWF) through project Grant DOI 10.55776/I5398, 10.55776/36213 and the Research Unit QUAST of German Science Foundation (DFG) (DFG FOR5249; Austrian part financed through FWF project Grant DOI 10.55776/I5868).

References

[1] W. Metzner and D. Vollhardt, Phys. Rev. Lett. **62**, 324 (1989)

[2] A. Georges and G. Kotliar, Phys. Rev. B **45**, 6479 (1992)

[3] E. Pavarini, E. Koch, D. Vollhardt, and A.I. Lichtenstein (eds.):
Understanding Correlated Materials with DMFT,
Modeling and Simulations, Vol. 15 (Forschungszentrum Jülich, 2025)
`http://www.cond-mat.de/events/correl22`

[4] E. Pavarini, E. Koch, D. Vollhardt, and A.I. Lichtenstein (eds.):
Dynamical Mean-Field Theory of Correlated Electrons,
Modeling and Simulations, Vol. 12 (Forschungszentrum Jülich, 2022)
`http://www.cond-mat.de/events/correl22`

[5] A. Schiller and K. Ingersent, Phys. Rev. Lett. **75**, 113 (1995)

[6] G. Rohringer, H. Hafermann, A. Toschi, A.A. Katanin, A.E. Antipov, M.I. Katsnelson, A.I. Lichtenstein, A.N. Rubtsov, and K. Held, Rev. Mod. Phys. **90**, 025003 (2018)

[7] T. Maier, M. Jarrell, T. Pruschke, and M.H. Hettler, Rev. Mod. Phys. **77**, 1027 (2005)

[8] K. Held, A. Katanin, and A. Toschi, Prog. Theor. Phys. (Suppl.) **176**, 117 (2008)

[9] A. Toschi, A.A. Katanin, and K. Held, Phys Rev. B **75**, 045118 (2007)

[10] A.N. Rubtsov, M.I. Katsnelson, and A.I. Lichtenstein, Phys. Rev. B **77**, 033101 (2008)

[11] T.A. Maier, M.S. Jarrell, and D.J. Scalapino, Phys. Rev. Lett. **96**, 047005 (2006)

[12] T. Ribic, P. Gunacker, S. Iskakov, M. Wallerberger, G. Rohringer, A.N. Rubtsov, E. Gull, and K. Held, Phys. Rev. B **96**, 235127 (2017)

[13] P. Kappl, T. Ribic, A. Kauch, and K. Held, arXiv:2412.01848.

[14] K. Held: *Quantum criticality and superconductivity in diagrammatic extensions of DMFT*,
in E. Pavarini and E. Koch and D. Vollhardt and A.I. Lichtenstein (eds.):
DMFT: From Infinite Dimensions to Real Materials,
Modeling and Simulations, Vol. 8 (Forschungszentrum Jülich, 2018)
`http://www.cond-mat.de/events/correl18`

[15] T. Schäfer, F. Geles, D. Rost, G. Rohringer, E. Arrigoni, K. Held, N. Blümer, M. Aichhorn, and A. Toschi, Phys. Rev. B **91**, 125109 (2015)

[16] A. Kauch, P. Pudleiner, K. Astleithner, P. Thunström, T. Ribic, and K. Held,
Phys. Rev. Lett. **124**, 047401 (2020)

[17] A. Galler, P. Thunström, P. Gunacker, J.M. Tomczak, and K. Held, Phys. Rev. B **95**, 115107 (2017)

[18] M. Kitatani, R. Arita, T. Schäfer, and K. Held, arXiv:2203.12844

[19] N.E. Bickers: *Theoretical Methods for Strongly Correlated Electrons* (Springer, Heidelberg, 2004), chap. 6, pp. 237–296

[20] M. Wallerberger, A. Hausoel, P. Gunacker, A. Kowalski, N. Parragh, F. Goth, K. Held, and G. Sangiovanni, Comp. Phys. Commun. **235**, 388 (2019)

[21] P. Gunacker, M. Wallerberger, E. Gull, A. Hausoel, G. Sangiovanni, and K. Held, Phys. Rev. B **92**, 155102 (2015)

[22] C.J. Eckhardt, C. Honerkamp, K. Held, and A. Kauch, Phys. Rev. B **101**, 155104 (2020)

[23] M. Wallerberger, H. Shinaoka, and A. Kauch, Phys. Rev. Res. **3**, 033168 (2021)

[24] F. Krien, A. Valli, and M. Capone, Phys. Rev. B **100**, 155149 (2019)

[25] J. Kaufmann, C. Eckhardt, M. Pickem, M. Kitatani, A. Kauch, and K. Held, Phys. Rev. B **103**, 035120 (2021)

[26] T. Ayral and O. Parcollet, Phys. Rev. B **94**, 075159 (2016)

[27] M. Kitatani, T. Schäfer, H. Aoki, and K. Held, Phys. Rev. B **99**, 041115 (2019)

[28] K. Held, L. Si, P. Worm, O. Janson, R. Arita, Z. Zhong, J.M. Tomczak, and M. Kitatani, Front. Phys. **9** (2022)

[29] H. Sun *et al.*, Nature **621**, 493 (2023)

[30] M. Kitatani, L. Si, O. Janson, R. Arita, Z. Zhong, and K. Held, npj Quantum Mater. **5**, 59 (2020)

[31] T. Schäfer *et al.*, Phys. Rev. X **11**, 011058 (2021)

[32] D. Li, K. Lee, B.Y. Wang, M. Osada, S. Crossley, H.R. Lee, Y. Cui, Y. Hikita, and H.Y. Hwang, Nature **572**, 624 (2019)

[33] L. Si, P. Worm, and K. Held, Crystals **12** (2022)

[34] S. Lin Er Chow, Z. Luo, and A. Ariando, Nature **642**, 58 (2025)

[35] D. Li, B.Y. Wang, K. Lee, S.P. Harvey, M. Osada, B.H. Goodge, L.F. Kourkoutis, and H.Y. Hwang, Phys. Rev. Lett. **125**, 027001 (2020)

[36] K. Lee *et al.*, Nature **619**, 288 (2023)

[37] G.A. Pan *et al.*, Nat. Mater. **21**, 160 (2022)

[38] P. Worm, L. Si, M. Kitatani, R. Arita, J.M. Tomczak, and K. Held, arXiv:2111.12697

[39] H. Lu *et al.*, Science **373**, 213 (2021)

[40] P. Worm *et al.* Phys. Rev. B **109**, 235126 (2024)

[41] W. Sun *et al.*, Sci. Adv. **11**, eadr5116 (2025)

[42] X. Ding *et al.*, Natl. Sci. Rev. **11**, nwae194 (2024

[43] L. Si, E. Jacob, W. Wu, A. Hausoel, J. Krsnik, P. Worm, S.D. Cataldo, O. Janson, K. Held, Phys. Rev. Res. **6**, 043104 (2024)

[44] J. Krsnik and K. Held, Nat. Comm. **16**, 255 (2025)

[45] A. Hausoel, S. Di Cataldo, M. Kitatani, O. Janson, and K. Held, arXiv:2502.12144

[46] D. Kiese, N. Wentzell, I. Krivenko, O. Parcollet, K. Held, and F. Krien, Phys. Rev. Res. **6**, 043159 (2024)

15 Dynamical Mean-Field Theory with Quantum Computing

Thomas Ayral
Eviden Quantum Laboratory
Les Clayes-sous-Bois, France

Contents

1 Introduction: why quantum computers for dynamical mean-field theory? 2
1.1 The difficulties of classical methods... and of quantum computers 2
1.2 A method to reduce the complexity of the problem 3

2 Dynamical mean-field theory and impurity solvers 5
2.1 Self-consistency equations 5
2.2 Classical impurity solvers... and their limitations 7

3 Quantum computing tools for impurity models 12
3.1 Quantum computing in a nutshell 12
3.2 Quantum algorithms for Green functions 21
3.3 The exponential wall of decoherence: noisy quantum states and gates 26
3.4 Near-term algorithms. Variational quantum algorithms for ground states and for time evolution. 28

4 Conclusion: state of the art, challenges and ways ahead 34

E. Pavarini, E. Koch, A. Lichtenstein, and D. Vollhardt (eds.)
Understanding Correlated Materials with DMFT
Modeling and Simulation Vol. 15
Forschungszentrum Jülich, 2025, ISBN 978-3-95806-813-1
http://www.cond-mat.de/events/correl25

1 Introduction: why quantum computers for dynamical mean-field theory?

Quantum computers were originally proposed to solve the challenges met by classical computers to tackle the quantum many-body problem [1]. One famous representative of these problems is the Fermi-Hubbard model [2]

$$H = \sum_{ij,\sigma} t_{ij}\, c^\dagger_{i\sigma} c_{j\sigma} + U \sum_i n_{i\uparrow} n_{i\downarrow} - \mu \sum_i n_i, \tag{1}$$

which describes the competition between a kinetic term with hopping amplitudes t_{ij} that favors delocalized states, and an interaction term with interaction strength U that favors localized states, with extra complexity coming from the possibility to tune the average density using a chemical potential μ. Here, creation (resp. annihilation) operators $c^\dagger_{i\sigma}$ (resp. $c_{i\sigma}$) create electrons of spin $\sigma =\uparrow,\downarrow$ on lattice site i, and $n_{i\sigma} = c^\dagger_{i\sigma} c_{i\sigma}$, $n_i = n_{i\uparrow} + n_{i\downarrow}$. Among other reasons, the purported relation between this model and the physics of high-temperature cuprate superconductors spurred early and prolonged interest into the phase diagram of this model, with phases as diverse as Fermi liquids, Mott insulators, superconductors or charge density insulators.
In particular, one central object to elucidate these phase diagrams is the so-called spectral function $A(\boldsymbol{k}, \omega)$, a quantity that is accessible via, e.g., angle-resolved photoemission experiments: its momentum $\boldsymbol{k}$ and energy ω dependence contains distinctive features of the aforementioned phases. From a computational point of view, the spectral function can be computed from the imaginary part of the retarded Green function $G^{\mathrm{R}}(\boldsymbol{k}, \omega)$ ($A(\boldsymbol{k}, \omega) = -\frac{1}{\pi} \operatorname{Im} G^{\mathrm{R}}(\boldsymbol{k}, \omega)$), itself defined as the space and time Fourier transform of the following sum of correlation functions

$$G^{\mathrm{R}}(i, j; t) = \Theta(t) \left(-i \big\langle c_i(t) c^\dagger_j \big\rangle - i \big\langle c^\dagger_j c_i(t) \big\rangle \right). \tag{2}$$

Here, the average denotes $\langle \cdots \rangle = \frac{1}{Z} \operatorname{Tr} \left(e^{-\beta H} \cdots \right)$, with the partition function $Z = \operatorname{Tr}(e^{-\beta H})$ and the inverse temperature $\beta = 1/T$. Time-dependence is to be understood in the Heisenberg picture, $c_i(t) = e^{iHt} c_i\, e^{-iHt}$. In the zero-temperature limit, the average becomes $\langle \cdots \rangle = \langle \Psi_0 | \cdots | \Psi_0 \rangle$, with $|\Psi_0\rangle$ the ground state of H. The retarded Green function describes how an electron created at site j ($c^\dagger_j$) in the system (described by a Gibbs state at finite temperature or the ground state at zero temperature) propagates to site i for a time t, where it is annihilated (and likewise for a hole, described by the second term). From this definition, one sees that computing $A(\boldsymbol{k}, \omega)$ implies the ability to describe the time evolution of an electron or a hole in a quantum system prepared in its Gibbs or ground state.

1.1 The difficulties of classical methods... and of quantum computers

Due to the many-body nature of the problem, traditional mean-field theories fail to properly describe these states and their subsequent evolution: for instance, the Hartree-Fock method does not capture Mott insulators because they cannot be described with single Slater determinants. In other words, Hubbard physics is generally not described well by single-particle physics:

correlations (essentially entanglement beyond the trivial entanglement required by the Pauli principle) play an important role. This warrants the use of more sophisticated classical methods. These are either exact, but with a cost exponential in some parameter (like the system size in exact diagonalization or some quantum Monte Carlo methods)—or approximate, and therefore limited to certain regimes (think of tensor networks, which are limited to weakly entangled states).

These limitations (some of which were known when quantum computers were first proposed) make processors with quantum properties—commonly called quantum computers or quantum simulators—ideal candidates for computing the spectral function: if these many-body systems can be engineered or programmed to follow similar dynamics to Hubbard dynamics, the time evolution of the processor will require resources than scale, at least at face value, only linearly with the size of the system and evolution time: to reach, say, larger lattice sizes, one just has to add more "particles" (or quantum bits, as we shall call them), and perform longer time evolutions... raising hope for exponential speedups to perform time evolutions. Several quantum algorithms, which we will explain in this lecture, were proposed to exploit this fact.

However, as we shall see, quantum algorithms are subject to strong constraints inherent to their quantum nature. A major constraint, which became obvious with the advent of physical realizations of quantum computers in the last decade, is decoherence, namely unwanted entanglement with the outside environment. Decoherence places hard limitations on the duration (number of operations) of quantum algorithms, which rules out many textbook quantum algorithms if no countermeasures are taken. It can possibly be suppressed with quantum error correction techniques, but these in turn require formidable resources that will remain out of the reach of quantum processors for many years. Worse still, even in the absence of decoherence, the local nature of available operators and measurements, and the projective nature of the latter, also need to be taken into consideration when designing a quantum algorithm, and when comparing it to classical counterparts. Finally, even on a complexity-theoretic level, preparing ground states or low-temperature states of many-body systems is likely hard (that is, exponential) even for perfect quantum computers.

Quantum processors are therefore not to be considered a silver bullet to solve strongly-correlated models like the Hubbard model, but rather as powerful heuristics that could outperform classical heuristics in some difficult regimes whose precise delineations yet need to be determined... One should perhaps even consider quantum processors as coprocessors to be used in combination with classical heuristics to reach regimes hitherto inaccessible to either classical or quantum algorithms: in the same way as graphics processing units (GPUs) are now used routinely to speed up some linear algebra operations, quantum processing units (QPUs) could be used to accelerate some well-defined subroutines of an otherwise classical program.

1.2 A method to reduce the complexity of the problem

One very successful classical heuristic for tackling the Hubbard model is dynamical mean-field theory (DMFT, [3]). It maps the Hubbard model to a simpler, yet still many-body problem

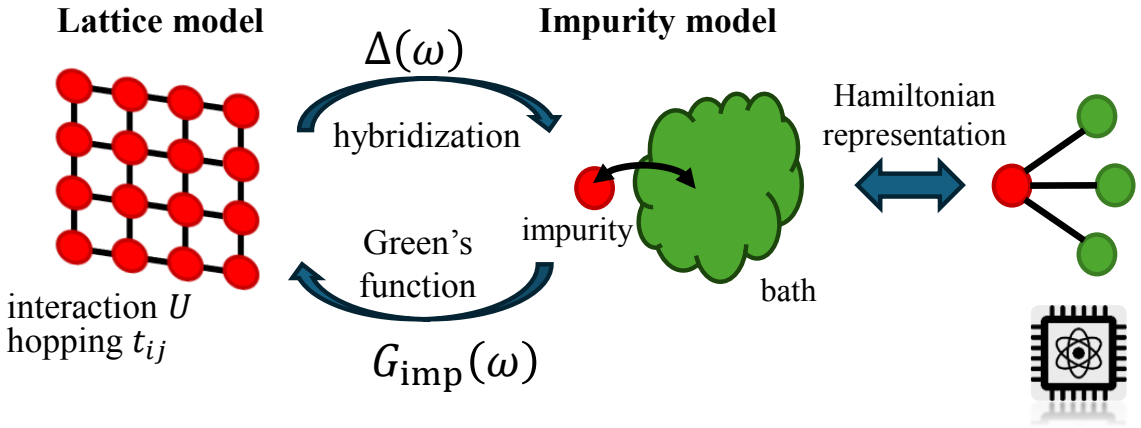


Fig. 1: *DMFT self-consistency cycle: a lattice model (here the Hubbard model) is self-consistently mapped to an impurity model, defined by its hybridization function $\Delta(\omega)$. This impurity model can be represented with an Anderson impurity Hamiltonian describing a correlated impurity site coupled to noninteracting bath sites (right). Quantum processors can be used to solve the impurity model, namely compute its Green function $G_{\mathrm{imp}}(\omega)$.*

called an impurity model. This impurity model describes one (or a few) interacting fermionic sites embedded in a noninteracting environment. The properties of this environment are adjusted to have the Green function of the impurity $G^{\mathrm{R}}_{\mathrm{imp}}(\omega)$ match the local component of the lattice Green function $G^{\mathrm{R}}_{\mathrm{loc}}(\omega) = \sum_{\boldsymbol{k}} G^{\mathrm{R}}(\boldsymbol{k}, \omega)$. This mapping is exact only in the limit of lattices of infinite dimensions thanks to the local nature of the Hubbard interaction, but DMFT is typically used in lower dimensions. Yet, it is able, among other successes, to capture the Fermi-liquid to Mott-insulator transition. Perhaps more importantly, DMFT comes with a control parameter, the number N_c of correlated sites (also called the size of the impurity "cluster") of the impurity model: it becomes exact in the limit of infinite N_c; gradually increasing N_c until convergence of quantitites of interest provides a well-defined way of quantifying errors.

Over the years, very sophisticated methods to solve this correlated, yet simpler impurity model, called "impurity solvers", have been developed. While some of these impurity solvers (think of the numerical renormalization group or segment-picture continuous-time quantum Monte Carlo solvers) yield essentially exact solutions for the $N_c = 1$ case at equilibrium, they face a number of difficulties beyond this regime. For instance, as the number N_c of impurities (or orbitals when going beyond the single-orbital Hubbard model) increases, the exponential wall plaguing classical methods to tackle the Hubbard model makes its comeback. Besides, many of these solvers (like quantum Monte-Carlo methods) work on the imaginary time axis, and thus require uncontrolled analytical continuation techniques to obtain data on the real axis. Conversely, most real-axis techniques (like exact diagonalization) must deal with the large number of bath sites used to represent the noninteracting environment, and the associated exponential complexity. As for tensor network techniques, the time evolution required to obtain Green functions may lead to large entanglement levels and thus make these methods either unreliable or unpractical. All these issues are made worse when turning to out-of-equilibrium regimes, which are beyond the scope of this lecture.

Given these limitations of impurity solvers, quantum computers, now that the problem has been "distilled" down from a large lattice problem to its "quantum quintessence", an impurity model, appear as interesting candidates to reach regimes that are out of the reach of classical impurity solvers: for instance, the regime of large cluster size N_c, or the long-time limit needed to resolve low-energy components of the spectral function. Even though the inherent difficulties of quantum computers are still there, they are made less severe by the reduction to an impurity model.

The goal of this lecture is to explain how the impurity problem of DMFT could be tackled by quantum computers in theory (that is, with perfect or error-corrected quantum computers), but also in practice (taking into account the limitations of current and near-term quantum hardware). To this aim, we will first very briefly recall the DMFT formalism (illustrated in Fig. 1), and then introduce the basic tools of quantum computing. Then, we will describe the textbook quantum algorithms that can be used to solve impurity models, before turning to the practical issues and how other types of algorithms can be used to try and overcome those issues.

2 Dynamical mean-field theory and impurity solvers

In this section, we briefly introduce the main DMFT concepts, and in particular the main computational bottleneck of DMFT, the impurity model. We also explain the main challenges of classical methods.

2.1 Self-consistency equations

The main target of equilibrium DMFT is the lattice retarded Green function, $G^{\mathrm{R}}(\boldsymbol{k},\omega)$ (Eq. (2)). A perturbation expansion of the Hubbard Hamiltonian (Eq. (1)) in powers of the interaction U generates a series expansion around the unperturbed Green function $G_0^{\mathrm{R}}(\boldsymbol{k},\omega)$. This series can in turn be cleverly resummed to yield the following equation, called the Dyson equation

$$G^{\mathrm{R}}(\boldsymbol{k},\omega) = G_0^{\mathrm{R}}(\boldsymbol{k},\omega) + G_0^{\mathrm{R}}(\boldsymbol{k},\omega)\Sigma(\boldsymbol{k},\omega)G^{\mathrm{R}}(\boldsymbol{k},\omega), \tag{3}$$

with a new object, $\Sigma(\boldsymbol{k},\omega)$, called the self-energy, that vanishes when U vanishes. This self-energy captures the effect of interactions on the propagation of electrons. In the limit when the Hubbard model is defined on a lattice with infinite dimensions, the self-energy becomes local, namely independent of $\boldsymbol{k}$. DMFT consists in (i) making the approximation that the self-energy remains local also in finite (and even low) dimensions, and (ii) using a surrogate model, which we will later call impurity model, from which a local self-energy $\Sigma_{\mathrm{imp}}(\omega)$ can be computed as an approximation to the lattice self-energy. This surrogate model also originates from the infinite-dimensional limit of the Hubbard model. It is defined by its action

$$S_{\mathrm{imp}} = \iint_0^\beta \mathrm{d}\tau\mathrm{d}\tau' \sum_\sigma c_\sigma^*(\tau)\big(-\mathcal{G}_0^{-1}(\tau-\tau')\big)c_\sigma(\tau') + \int_0^\beta \mathrm{d}\tau\, U n_\uparrow(\tau)n_\downarrow(\tau)\,. \tag{4}$$

Here, $c_{i\sigma}^*(\tau)$ and $c_{i\sigma}(\tau)$ denote two Grassmann fields. S_{imp} depends entirely on U and on the noninteracting Green function $\mathcal{G}_0$ (here given in imaginary time τ for simplicity; in general,

$f^{\mathrm{R}}(\omega)$ can be recovered, at least formally, from $f(\tau)$ by first Fourier transforming $f(\tau)$ to $\tilde{f}(i\omega_n) = \int_0^\beta \mathrm{d}\tau\, e^{i\tau\omega_n} f(\tau)$ and then performing an analytical continuation $f^{\mathrm{R}}(\omega) = \tilde{f}(z = \omega + i\eta)$). $\mathcal{G}_0^{\mathrm{R}}$, $\Sigma_{\mathrm{imp}}^{\mathrm{R}}$ and the impurity Green function $G_{\mathrm{imp}}^{\mathrm{R}}$ are related by the Dyson equation: $\Sigma_{\mathrm{imp}}^{\mathrm{R}}(\omega) = \mathcal{G}_0^{-1}(\omega) - \left(G_{\mathrm{imp}}^{\mathrm{R}}\right)^{-1}(\omega)$. One often defines the hybridization function $\Delta^{\mathrm{R}}(\omega)$ as $\Delta^{\mathrm{R}}(\omega) = \omega + \mu - \mathcal{G}_0^{-1}(\omega)$. With this, the impurity action reads

$$S_{\mathrm{imp}} = S_{\mathrm{loc}} + S_{\mathrm{hyb}}. \tag{5}$$

Here, $S_{\mathrm{loc}} = \int_0^\beta \mathrm{d}\tau \sum_\sigma c_\sigma^*(\tau)\,(\partial_\tau - \mu)\, c_\sigma(\tau) + \int_0^\beta \mathrm{d}\tau\, U\, n_\uparrow(\tau) n_\downarrow(\tau)$ is easily seen to be the action of a single correlated site, namely a single fermionic site with potential energy $-\mu$ and interaction energy U to penalize double occupancies. The hybridization term in the impurity action, $S_{\mathrm{hyb}} = \int\int_0^\beta \mathrm{d}\tau \mathrm{d}\tau' \sum_\sigma c_\sigma^*(\tau) \Delta(\tau - \tau') c_\sigma(\tau')$, describes how this site is coupled to an environment that is completely characterized by the (dynamical) mean-field $\Delta^{\mathrm{R}}(\omega)$. This dynamical mean-field a priori describes an infinite number of degrees of freedom. Since the spectral function is the central object of interest, one adjusts the surrogate model (and hence $\Delta^{\mathrm{R}}(\omega)$) in such a way that its Green function $G_{\mathrm{imp}}^{\mathrm{R}}(\omega)$ coincides with the local component of $G^{\mathrm{R}}(\boldsymbol{k}, \omega)$

$$G_{\mathrm{imp}}^{\mathrm{R}}(\omega)\left[\Delta^{\mathrm{R}}\right] = \sum_{\boldsymbol{k}} G^{\mathrm{R}}(\boldsymbol{k}, \omega)\left[\Delta^{\mathrm{R}}\right]. \tag{6}$$

In this self-consistency equation, we made explicit the functional dependence on Δ^{R}: (i) as the Green function of S_{imp}, $G_{\mathrm{imp}}^{\mathrm{R}}$ is directly a functional of Δ^{R} (see Eq. (9) below); (ii) the dependence of $G^{\mathrm{R}}(\boldsymbol{k}, \omega)$ comes from the Dyson equation (3), which, when performing the DMFT approximation $\Sigma(\boldsymbol{k}, \omega) \approx \Sigma_{\mathrm{imp}}(\omega)$, explicitly reads

$$G^{\mathrm{R}}(\boldsymbol{k}, \omega) = \frac{1}{\omega - \varepsilon(\boldsymbol{k}) + \mu - \Sigma_{\mathrm{imp}}^{\mathrm{R}}(\omega)[\Delta^{\mathrm{R}}]}, \tag{7}$$

with $\varepsilon(\boldsymbol{k})$ the space Fourier transform of the hopping matrix t_{ij} of the Hubbard model (Eq. (1)). Finally, $\Sigma_{\mathrm{imp}}^{\mathrm{R}}(\omega)[\Delta^{\mathrm{R}}] = \omega + \mu - \Delta^{\mathrm{R}} - G_{\mathrm{imp}}^{\mathrm{R}}(\omega)^{-1}\left[\Delta^{\mathrm{R}}\right]$. Putting everything together, we obtain a fixed-point equation

$$G_{\mathrm{imp}}^{\mathrm{R}}(\omega)\left[\Delta^{\mathrm{R}}\right] = \sum_{\boldsymbol{k}} \frac{1}{\Delta^{\mathrm{R}}(\omega) + G_{\mathrm{imp}}^{\mathrm{R}}(\omega)^{-1}\left[\Delta^{\mathrm{R}}\right] - \varepsilon(\boldsymbol{k})}. \tag{8}$$

Solving DMFT amounts to adjusting $\Delta^{\mathrm{R}}(\omega)$ to fulfill the above equation. It is usually solved iteratively. The process crucially hinges on the ability to find a $G_{\mathrm{imp}}^{\mathrm{R}}(\omega)$ for a given $\Delta^{\mathrm{R}}(\omega)$. We will henceforth refer to this task as "solving the impurity model": it is the bottleneck of DMFT. We note that the derivation above can easily be adapted to the case of several correlated atoms (or "impurities") instead of one (this is then called "cluster DMFT"), and to the nonequilibrium case ("out-of-equilibrium DMFT").

Before turning to solving impurity models, let us emphasize that imposing constraints at the level of the (single-particle) Green function is a choice driven by the physical question at stake (here the study of phase transitions with order parameters related to G). Other choices are possible, leading to a whole spectrum of so-called quantum embedding theories (of which DMFT

is the earliest representative): one may require self-consistency on "simpler" objects (like one-particle reduced density matrices $\langle c_i^\dagger c_j \rangle$ (same as DMFT but with no time dependence), leading to theories like density-matrix embedding theory (DMET, [4]) or rotationally-invariant slave bosons (RISB, [5, 6])), or on more sophisticated objects (like two-particle Green functions, leading to theories like the dynamical vertex approximation, DΓA [7]). In the former case, one can have the intuition that the corresponding surrogate model will be simpler; conversely, in the latter case, the impurity model should be more complicated [8]).

2.2 Classical impurity solvers... and their limitations

In this section, we briefly address the problem of finding the Green function G_{imp} for a given hybridization function Δ. In a Grassmann path integral formalism, it is given, as a function of imaginary time τ, by the expression

$$G_{\text{imp}}(\tau) = -\int \mathcal{D}\left[c, c^*\right] c_\sigma(\tau) c_\sigma^*(0)\, e^{-S_{\text{imp}}[\Delta]}\,. \tag{9}$$

(We dropped the σ dependence in G_{imp} to simplify notation, but phases with spin-symmetry breaking can be studied). Impurity solvers can be classified in two main families, Hamiltonian-based solvers and action-based solvers.

2.2.1 Hamiltonian-based solvers

We start with Hamiltonian-based solvers, whose formalism is more directly translatable to quantum algorithms. In Hamiltonian-based solvers, one introduces a Hamiltonian model, dubbed the "Anderson impurity model" (AIM)

$$H_{\text{AIM}} = U\, n_\uparrow n_\downarrow - \mu \sum_\sigma c_\sigma^\dagger c_\sigma + \sum_{k\sigma} \varepsilon_k\, a_{k\sigma}^\dagger a_{k\sigma} + \sum_{k\sigma} V_k \left(a_{k\sigma}^\dagger c_\sigma + \text{h.c.} \right), \tag{10}$$

which describes a single atom (called the impurity) with potential energy $-\mu$ and interaction energy U coupled via hopping terms V_k to a bath of noninteracting fermions with energies ε_k (and creation (resp. annihilation) operators $a_{k\sigma}^\dagger$ (resp. $a_{k\sigma}$)). This model was originally introduced by Anderson to describe isolated impurities in metals [9], hence its name. It is also central to explain so-called Kondo physics (a Schrieffer-Wolff transformation of this model yields its low-energy simplification, the Kondo model). We are now going to show that the hopping V_k and energy ε_k parameters can be adjusted so that the Green function of this model coincides with the impurity Green function (Eq. (9)).
The Green function of the impurity site in H_{AIM} is given by

$$G_{\text{AIM}}(\tau) = -\int \mathcal{D}\left[c, c^*, a_k, a_k^*\right] c_\sigma(\tau) c_\sigma^*(0)\, e^{-S_{\text{AIM}}}, \tag{11}$$

where S_{AIM} is the action corresponding to H_{AIM}. Since S_{AIM} is quadratic in the bath fields $a_k(\tau)$ and $a_k(\tau)^*$, they can be integrated out

$$\int \mathcal{D}\left[a_k, a_k^*\right]\, e^{-S_{\text{AIM}}} = e^{-S_{\text{loc}} - \int_0^\beta \mathrm{d}\tau \mathrm{d}\tau' \sum_\sigma c_\sigma^*(\tau) \Delta_{\text{AIM}}(\tau - \tau') c_\sigma(\tau')}$$

with $\Delta^{\mathrm{R}}_{\mathrm{AIM}}(\omega) = \sum_k V_k^2/(\omega+i\eta-\varepsilon_k)$. By comparing Eqs (11) and (9), we see that G_{AIM} can be made to coincide with G_{imp} provided $\Delta^{\mathrm{R}}_{\mathrm{AIM}}(\omega) = \Delta^{\mathrm{R}}(\omega)$. In other words, if one can find parameters (V_k, ε_k) such that

$$\Delta^{\mathrm{R}}(\omega) = \sum_k \frac{V_k^2}{\omega + i\eta - \varepsilon_k}, \tag{12}$$

then the AIM's Green function coincides with that of the impurity. This exact correspondence (up to a fit) between our action-based impurity model and a Hamiltonian model makes it possible to tackle the impurity model with a variety of Hamiltonian-based techniques. Before we turn to the main methods and their limitations, let us emphasize that the fitting problem (Eq. (12)) itself is not straightforward: in practice, one needs to perform this fit with a finite number of bath orbitals, possibly leading to fitting errors and finite-size effects. Different choices of metrics to optimize the fitting parameters (V_k, ε_k) will a priori lead to different results.

Hamiltonian-based techniques consist in finding the eigenvectors $|\Psi_\alpha\rangle$ and eigenvalues E_α of H_{AIM} to compute the Green function. Indeed, one can rewrite, in the operator formalism, $G_{\mathrm{AIM}}(\tau) = -\operatorname{Tr}\left[\rho\, c_\sigma(\tau) c^\dagger(0)\right]$, with $\rho = e^{-\beta H_{\mathrm{AIM}}}/Z$ (and $\tau > 0$ here). Inserting completeness relations and expanding the trace, we get $G_{\mathrm{AIM}}(\tau) = -\frac{1}{Z}\sum_{\alpha,\alpha'} e^{-\beta E_\alpha} e^{-\tau(E_{\alpha'}-E_\alpha)} \left|\langle\Psi_\alpha|c|\Psi_{\alpha'}\rangle\right|^2$ that becomes, once Fourier-transformed to Matsubara frequencies $i\omega_n$, the so-called Lehmann representation

$$G_{\mathrm{AIM}}(i\omega_n) = -\frac{1}{Z}\sum_{\alpha,\alpha'} \frac{e^{-\beta E_{\alpha'}} + e^{-\beta E_\alpha}}{i\omega_n - (E_\alpha - E_{\alpha'})} \left|\langle\Psi_\alpha|c|\Psi_{\alpha'}\rangle\right|^2. \tag{13}$$

In the zero-temperature limit ($\beta \to \infty$)

$$G_{\mathrm{AIM}}(i\omega_n) = -\sum_{\alpha\in\mathcal{H}_{N_e+1}} \frac{1}{i\omega_n - (E_0 - E_\alpha)} \left|\langle\Psi_0|c|\Psi_\alpha\rangle\right|^2 - \sum_{\alpha\in\mathcal{H}_{N_e-1}} \frac{1}{i\omega_n - (E_\alpha - E_0)} \left|\langle\Psi_\alpha|c|\Psi_0\rangle\right|^2. \tag{14}$$

where we supposed that the ground state $|\Psi_0\rangle$ contains N_e electrons, and $\mathcal{H}_{N_e\pm1}$ denotes the eigenspace with $N_e \pm 1$ electrons. The spectral function $A_{\mathrm{imp}}(\omega) = -\frac{1}{\pi}\operatorname{Im} G_{\mathrm{AIM}}(z = \omega+i\eta)$ thus has Dirac delta peaks at energies $\omega = E_0 - E_\alpha$ (with $\alpha \in \mathcal{H}_{N_e+1}$, namely minus the electron addition energy) and $\omega = E_\alpha - E_0$ (with $\alpha \in \mathcal{H}_{N_e-1}$, namely the electron removal energy).

The numerical challenge thus consists in finding the eigenvectors $|\Psi_\alpha\rangle$ and eigenvalues E_α of H_{AIM} (at low temperatures, only the low-lying ones). The sheer size of the Hilbert space ($4^{N_{\mathrm{c}}+N_{\mathrm{b}}}$ if we denote by N_{b} the number of bath sites) makes it a difficult problem, but the methods below either try to exploit the sparsity of H_{AIM} and the fact that only the low-lying states are needed, or use a compressed state representation that works well when entanglement is low.

Exact diagonalization: Lanczos method. A first method, called the Lanczos method (see [10]), avoids the $O\left(\left(4^{N_c+N_b}\right)^3\right)$ cost of a direct diagonalization of H_{AIM} by using the sparsity of H_{AIM}: in the Fock basis representation of H_{AIM} (Eq. (10)), the number of nonzero elements per row or column of H_{AIM} is of the order of $s = O(N_c+N_b)$. Thus, matrix-vector multiplications $H_{\mathrm{AIM}}|\Psi\rangle$ take only $O\left(s4^{N_c+N_b}\right)$ time. This property is exploited in the Lanczos method by finding the matrix of H_{AIM} in the so called Krylov basis $\{|\chi_n\rangle\}_{n=1\ldots K}$ of the K-dimensional

vector space spanned by the family $\left\{|\Phi_0\rangle, H_{\rm AIM}|\Phi_0\rangle, H_{\rm AIM}^2|\Phi_0\rangle, \ldots, H_{\rm AIM}^K|\Phi_0\rangle\right\}$, with $|\Phi_0\rangle$ is an initial state that must not be orthogonal to the exact ground state $|\Psi_0\rangle$. $H_{\rm AIM}$ is tridiagonal in this basis, which makes it easy to compute its ground state energy. The error on the ground state energy obtained in this reduced space decreases exponentially with K [10].
Let us now turn to the Green function. Using Eq. (2) in the case of the AIM and at zero temperature, we obtain

$$G^{\rm R}(t) = \Theta(t)\Big(-ie^{iE_0t}\big\langle\Psi_0\big|c_\sigma e^{-iH_{\rm AIM}t}c_\sigma^\dagger\big|\Psi_0\big\rangle - ie^{-iE_0t}\big\langle\Psi_0\big|c_\sigma^\dagger e^{iH_{\rm AIM}t}c_\sigma\big|\Psi_0\big\rangle\Big). \tag{15}$$

Taking the Fourier transform of the first term (the second term, $G^<(\omega)$, can be dealt with in a similar fashion), and inserting resolutions of the identity, we obtain

$$G^>(\omega) = -i\sum_\alpha\int_0^\infty {\rm d}t\, e^{i\omega t}\big\langle\Psi_0\big|e^{iH_{\rm AIM}t}c_\sigma\, e^{-iH_{\rm AIM}t}\big|\Psi_\alpha\big\rangle\big\langle\Psi_\alpha\big|c_\sigma^\dagger\big|\Psi_0\big\rangle \tag{16}$$

$$= -i\sum_\alpha\int_0^\infty {\rm d}t\, e^{i(\omega+E_0-E_\alpha)t}\,\big|\langle\Psi_\alpha|c_\sigma^\dagger|\Psi_0\rangle\big|^2. \tag{17}$$

Performing the integration and adding a $\eta > 0$ factor to ensure convergence, we find the so-called resolvent form of the Green function

$$G^>(\omega{+}i\eta) = \sum_\alpha \frac{\big|\langle\Psi_0|c_\sigma|\Psi_\alpha\rangle\big|^2}{E_0{-}E_\alpha+\omega+i\eta} = \big\langle\Psi_0\big|c_\sigma\,\frac{1}{E_0{-}H+\omega+i\eta}\,c_\sigma^\dagger\big|\Psi_0\big\rangle. \tag{18}$$

Having computed $|\Psi_0\rangle$ and E_0 in the first Lanczos step, one can now perform a second Lanczos step, this time with $|\Phi_0\rangle \propto c_\sigma^\dagger|\Psi_0\rangle$. In the corresponding second Krylov basis, taking advantage of the fact that H is tridiagonal in any Krylov basis, one can easily write a continued fraction expression for $G^>(\omega{+}i\eta)$. One can thus obtain an approximation of the Green function in real frequency with a run time that scales (with a naive estimate) as $O(sK4^{N_c+N_b})$.

Matrix product states: density matrix renormalization group method A second method allows avoiding the exponential cost of storing the wave function by assuming the bipartite entanglement in the system is low. Instead of representing the wavefunction as

$$|\Psi\rangle = \sum_{b_1,\ldots b_N}\psi_{b_1,\ldots b_N}|b_1,\ldots,b_N\rangle, \tag{19}$$

with $N = 2\,(N_c{+}N_{\rm b})$, with associated storage cost 2^N, we assume the wavefunction amplitudes to be representable as

$$\psi_{b_1,\ldots b_N} = \sum_{\alpha_1,\ldots\alpha_{N-1}}\big[A^{(1)}\big]_{\alpha_1}^{b_1}\big[A^{(2)}\big]_{\alpha_1,\alpha_2}^{b_2}\cdots\big[A^{(2)}\big]_{\alpha_{N-2},\alpha_{N-1}}^{b_{N-1}}\big[A^{(1)}\big]_{\alpha_{N-1}}^{b_N}, \tag{20}$$

with N rank-3 tensors $\big[A^{(k)}\big]_{\alpha_{k-1},\alpha_k}^{b_k}$—or matrices if one considers b_k to be fixed, hence the name "matrix product state" (MPS) representation. This is illustrated in Fig. 2(a). Each tensor index has dimension 2, χ, χ for b_k, α_{k-1} and α_k, respectively, with χ called the bond dimension

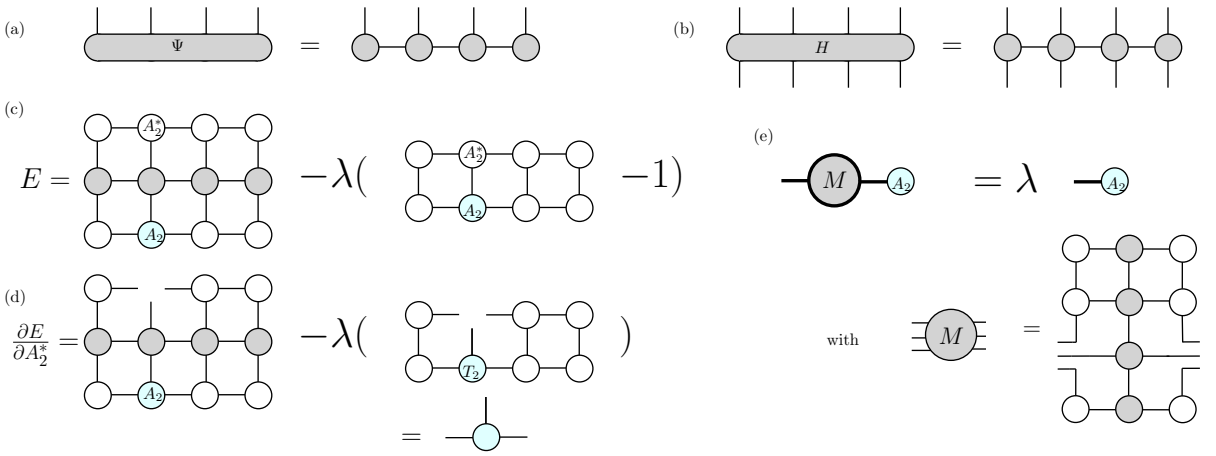


Fig. 2: *Matrix product states and the density matrix renormalization group method. (a) MPS representation of $|\Psi\rangle$. (b) MPO representation of H. (c) Tensor-network representation of the energy functional of DMRG. (d) TN representation of a partial derivative. (e) TN representation of the eigenproblem (thick lines denote groupings of tensor legs).*

of the MPS. The total storage cost thus scales as $O(N\chi^2)$: it is now linear in the number $N \propto N_\mathrm{c}+N_\mathrm{b}$ of sites! However, a fixed bond dimension χ places a limitation on how large the so-called von Neumann entanglement entropy S of the state can be. One can easily show that χ needs to fulfill $\chi \geq 2^S$ ([11]); otherwise, truncation errors appear. It turns out that for Anderson impurity models with $N_\mathrm{c} = 1$, one can always make the problem one-dimensional, in which case known results about the entanglement entropy of ground states of one-dimensional Hamiltonians apply: S follows an "area law", which in 1D means that $S \propto$ const. This allows for a very inexpensive storage of the ground state of the AIM for the $N_\mathrm{c} = 1$ case.

To find the actual MPS form of the ground state, one usually resorts to a variational algorithm known as the density matrix renormalization group algorithm (DMRG), which consists in minimizing $\left\langle \Psi(A^{(1)},\dots,A^{(N)})\middle|H\middle|\Psi(A^{(1)},\dots,A^{(N)})\right\rangle$ while imposing normalization, $\left\langle \Psi(A^{(1)},\dots,A^{(N)})\middle|\Psi(A^{(1)},\dots,A^{(N)})\right\rangle = 1$, (Fig. 2(c)). Writing stationarity conditions for a given tensor $A^{(k)}$ (given a fixed value of the other $N-1$ tensors) leads to an eigenvalue problem $H^{(k)}_\mathrm{eff}\psi^{(k)} = E^{(k)}\psi^{(k)}$ with $\psi^{(k)}$ of size $2\chi^2$ (Fig. 2 (e)): it can be easily solved exactly. The process is then iterated over $k = 1,\dots,N$ several times (sweeps) until convergence of the individual tensors. The computational cost thus scales as $N_\mathrm{s}\,(2\chi^2)^3$ with N_s the number of sweeps, if one uses a direct diagonalization procedure.

With the ground state in hand, one can now in principle compute the Green function: in Eq. (15), we see that to get the first term, we need to start from $|\Psi_0\rangle$, apply a creation operator to get $c^\dagger_\sigma|\Psi_0\rangle$, time evolve ($e^{-iH_\mathrm{AIM}t}$) and then project back onto $c^\dagger_\sigma|\Psi_0\rangle$. The operation $c^\dagger_\sigma|\Psi_0\rangle$ is straightforward to perform with matrix product states. The time evolution can be performed with a number of methods. The most straightforward one is time-evolving block decimation (TEBD), which consists in splitting the time-evolution operator $e^{-iH_\mathrm{AIM}t}$ in a sequence of so-

called Trotter time steps

$$e^{-iH_{\mathrm{AIM}}t} = \left(e^{-iH_{\mathrm{AIM}}t/N_{\mathrm{t}}}\right)^{N_{\mathrm{t}}} \approx \left(1 - iH_{\mathrm{AIM}}\frac{t}{N_{\mathrm{t}}}\right)^{N_{\mathrm{t}}}. \tag{21}$$

Then, the operator $\delta U \equiv 1 - iH_{\mathrm{AIM}}\frac{t}{N_{\mathrm{t}}}$ (represented in so-called matrix product operator, MPO, format) is applied to the current wavevector (represented in MPS format) N_{t} times. This is in principle simple, but the bond dimension χ of the MPS is not conserved upon application of δU: it generically increases, because time evolving the ground state generates excited states that are usually more entangled than the ground state, and thus requires a larger bond dimension to be represented exactly. One faces a dilemma: either ones tries to keep up with the increasing entanglement by increasing χ (but one quickly reaches memory limits), or one truncates the MPS to a fixed maximal bond dimension, thereby incurring truncation errors. More sophisticated methods exists (see [12] for a review), but they generically meet the challenge of an increasing entanglement entropy with evolution time t.

2.2.2 Action-based solvers

The above methods rely on a Hamiltonian representation (Eq. (10)) of the impurity action (5). A major drawback of these methods is that they require a Hamiltonian model with a large bath (large N_{b}) to faithfully represent the hybridization function of DMFT. This large bath, in turn, leads to large numerical costs (unless one chooses a small bath... but then suffers from large finite-size effects).

Action-based solvers avoid this problem by working directly in the action formalism. Starting from Eq. (5), they fall into two main categories, depending on whether they use an expansion in powers of S_{loc} (interaction expansion solvers) or S_{hyb} (hybridization expansion solvers). The resulting infinite sum is sampled using Monte-Carlo methods. The two categories come with distinct properties: intuitively, interaction expansion solvers are better behaved when interactions are weak, while hybridization expansion solvers are better behaved in the strong interaction limit. Both families yield the impurity Green function in imaginary time $G_{\mathrm{imp}}(\tau)$ exactly up to statistical uncertainty. It turns out that this statistical uncertainty (namely the variance of the Monte-Carlo averages used to compute the Green function) generically blows up (exponentially) with decreasing temperature and with increasing cluster size (or number of orbitals) N_{c}, a manifestation of the so-called fermionic sign problem. To curb this variance, one in principle needs very long Markov chains and thus very long run times.

Let us also stress that even in the absence of this sign problem (say in the $N_c{=}\,1$ case), obtaining the real-time frequency Green function $G^{\mathrm{R}}_{\mathrm{imp}}(\omega)$ from noisy (due to Monte-Carlo statistical noise), imaginary-time $G_{\mathrm{imp}}(\tau)$, a problem called the analytical continuation, is notoriously difficult (it amounts to inverting an ill-conditioned matrix), so that it would be highly desirable to work directly in real time. However, in real time, Monte-Carlo methods struggle with another sign problem stemming from the complex imaginary factors of the time evolution operator ("dynamical sign problem"), strongly limiting these methods to short times, and thus not allowing enough low-frequency accuracy in the resulting spectral functions.

3 Quantum computing tools for impurity models

In the previous section, we saw that DMFT can be seen as a classical heuristic that self-consistently reduces strongly correlated lattice models like the Hubbard model to simpler, yet still strongly-correlated models known as impurity models (Fig. 1). To compute the spectral function of the lattice model within the DMFT approximation, one needs to compute the impurity retarded Green function, namely the Green function of a few (N_c) correlated sites exchanging electrons with a large noninteracting fermionic bath. Essentially, as we saw, the computation of this Green function boils down to computing objects of the form

$$G^{>}(t) = -i\big\langle c_\sigma(t) c_\sigma^\dagger \big\rangle \tag{22}$$

which, together with its counterpart $G^{<}(t) = i\langle c_\sigma^\dagger c_\sigma(t)\rangle$, appear in the definition (2) of the retarded Green function (here for simplicity we dropped the σ dependence of G, and assumed $N_\mathrm{c} = 1$; also, because of the $\Theta(t)$ appearing in (2), we can assume $t > 0$).
The goal of this section is to show how quantum computers can be used to compute objects of form of $G^{>}(t)$ for the specific case of impurity models. If we expand its zero-temperature expression, we recall that we obtain

$$G^{>}(t) = -i\big\langle \Psi_0 | e^{iH_\mathrm{AIM}t}\, c_\sigma\, e^{-iH_\mathrm{AIM}t}\, c_\sigma^\dagger | \Psi_0 \big\rangle. \tag{23}$$

This form makes it clear that we can decompose the computation in two parts: the computation of the ground state $|\Psi_0\rangle$, and the time evolution $e^{-iH_\mathrm{AIM}t}$ of the ground state with one added particle. This is similar to the strategy we described above for matrix product states, but as we shall see, using a quantum processor comes, at least in theory, with added benefits.

3.1 Quantum computing in a nutshell

In this section, we introduce the main tools available to a quantum programmer, with a focus on tools that will be useful for solving impurity models. In particular, a goal of this section is to describe a simple way to perform the operation $e^{-iH_\mathrm{AIM}t}$ on a quantum computer.

3.1.1 Definition of a quantum computer

A quantum computer is a system described by a time-dependent Schrödinger equation

$$i\hbar \frac{\mathrm{d}|\Psi(t)\rangle}{\mathrm{d}t} = H(t)\big|\Psi(t)\big\rangle, \tag{24}$$

and whose initial state $|\Psi(t{=}0)\rangle$ and time-dependent Hamiltonian $H(t)$ can be *controlled* to reach a target final state $|\Psi(t_\mathrm{f})\rangle$, on which observables (hermitian operators) $\hat{O}$ of interest can be measured. This can be done either in a one-shot way (giving access to a bit of information λ with a probability given by the overlap of $|\Psi(t_\mathrm{f})\rangle$ with one of the eigenvectors $|\varphi_\lambda\rangle$ of $\hat{O}$), or in an average way (giving access to a statistical estimate of the average value $\langle\hat{O}\rangle = \big\langle\Psi(t_\mathrm{f})\big|\hat{O}\big|\Psi(t_\mathrm{f})\big\rangle$).

What this system is varies from one quantum computer implementation to the other. A distinction is usually made between analog computers (also known as quantum simulators)—whose Hamiltonian is very specific (e.g with a limited control on the individual degrees of freedom), and digital (or gate-based) computers—which are characterized by the possibility to control individually each degree of freedom, with a practical consequence: this individual (or local) control, complemented with an entangling operation between the degrees of freedom, leads to a form of "universality", namely any unitary operation U can be approximated by the unitary operator corresponding to the full time evolution

$$U(t) = T \exp\left(-i \int_0^t H(\tau)\, \mathrm{d}\tau\right). \tag{25}$$

A universal quantum computer can thus be regarded as a machine that implements arbitrary unitary operations. The space on which these operations are performed is, for mainstream quantum computers, the Hilbert space of N two-level systems (aka quantum bits or qubits) $\mathcal{H}_N$. Its size is exponential ($\dim\mathcal{H}_N = 2^N$), and a generic N-qubit state (recall Eq. (19)) a priori requires 2^N complex coefficients to be represented on a classical computer. While simulating such a time evolution on a classical computer would a priori involve resources scaling as $O(2^N)$, letting the quantum computer evolve "naturally" leads to resources linear in the number of degrees of freedom N.

Let us note that quantum computers are not limited to qubit (or spin-1/2) systems. In particular, a natural candidate implementation for dealing with fermionic systems would be a system with fermionic degrees of freedom like ultracold fermionic atoms in optical lattices, whose Hamiltonian is engineered as close as possible to, say, the Hubbard model. These systems are indeed promising platforms for gaining insights, among others, into Hubbard physics, with very recent major improvements in the reachable temperatures. In this lecture, however, we will focus only on qubit-based computers, and within this category, on gate-based quantum computers. As we shall see, using these computers to tackle fermionic systems will require a translation from the world of fermions to the world of qubits; but the exquisite control afforded by this type of computers makes them very convenient to design algorithms.

3.1.2 The circuit model

One usually picks, as a basis of the Hilbert space $\mathcal{H}_n$, the tensor basis of the eigenstates of Pauli z matrix σ_z: it is denoted as $|b_1, \ldots, b_N\rangle$, with $b_k \in \{0, 1\}$ and $\sigma_z^{(k)}|b_k\rangle = (-)^{b_k}|b_k\rangle$. It is usually called the computational basis. In the following, $\sigma_\alpha^{(k)}$ will denote a Pauli matrix ($\alpha = x, y, z$) acting on the k-th qubit.

A quantum computation consists in modifying the state $|\Psi\rangle$ by cleverly designing the time dependence of the Hamiltonian. In gate-based quantum computers, the time evolution $U \equiv U(t)$ (Eq. (25), we drop the t dependence for clarity) is split into a sequence

$$U = \prod_{k=1}^{N_g} U_k \tag{26}$$

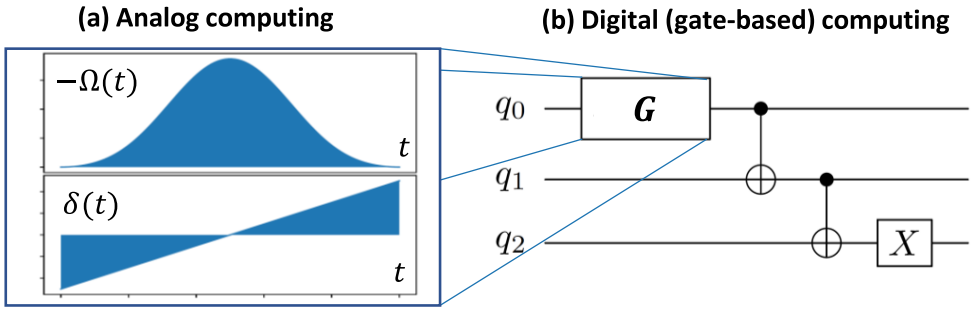


Fig. 3: *Circuit model: a quantum circuit (on the right) describes a sequence of gates, which are individually implemented in an analog fashion with time-dependent terms in the hardware Hamiltonian. Reproduced from [13].*

of N_g elementary unitary operations U_k, referred to as quantum "gates", that correspond to switching-on some terms in the Hamiltonian. For instance, in Fig. 3, the G gate, corresponding to a unitary U_G, may correspond to a Hamiltonian $H_G(t) = \Omega(t)\sigma_x^{(1)}/2 - \delta(t)\,\sigma_z^{(1)}$, with U_G given by the Dyson series $U_G = Te^{-i\int_0^t H_G(\tau)\,d\tau}$. Since H_G acts only on the first qubit, so does U_G. Such a single-qubit gate (depicted by a box acting only on one line, namely one qubit) does not create entanglement (acting with U_G on a factorized state yields a factorized state). A standard single-qubit gate is the Hadamard gate, whose expression in the $\{|0\rangle, |1\rangle\}$ basis reads

$$U_{\mathrm{H}} = \frac{1}{\sqrt{2}}\begin{pmatrix} 1 & 1 \\ 1 & -1 \end{pmatrix}. \tag{27}$$

In other words, $U_{\mathrm{H}}|0\rangle = \big(|0\rangle + |1\rangle\big)/\sqrt{2}$: the Hadamard gate creates superpositions. Other important standard single-qubit gates are single-qubit rotations, defined as

$$R_\alpha(\theta) = e^{-i\frac{\theta}{2}\sigma_\alpha}. \tag{28}$$

They rotate the qubit around the axis α by an angle θ.

Gates depicted as boxes spanning several lines, on the other hand, are many-qubit gates. They require Hamiltonians that couple several qubits (like, say, $H(t) = g(t)\sigma_x^{(1)} \otimes \sigma_x^{(2)}$, which generates a gate $U_{\mathrm{XX}}(t) = \exp\left(-i\int_0^t \mathrm{d}\tau\, g(\tau)\sigma_x^{(1)} \otimes \sigma_x^{(2)}\right)$). The specific two-qubit gate shown in Fig. 3 after gate G is a so-called CNOT gate. Its expression in the $\{|00\rangle, |01\rangle, |10\rangle, |11\rangle\}$ basis reads

$$U_{\mathrm{CNOT}} = \begin{pmatrix} 1 & 0 & 0 & 0 \\ 0 & 1 & 0 & 0 \\ 0 & 0 & 0 & 1 \\ 0 & 0 & 1 & 0 \end{pmatrix}. \tag{29}$$

For instance, $U_{\mathrm{CNOT}}|10\rangle = |11\rangle$: if the first ("control") qubit is in state $|1\rangle$, the second ("target") qubit is flipped. This notion of controlled gate can be generalized: a controlled-U gate U_c is such that $U_c|0\rangle|\psi\rangle = |0\rangle|\psi\rangle$ and $U_c|1\rangle|\psi\rangle = |1\rangle U|\psi\rangle$.

Let us stress that several Hamiltonians $H(t)$ can yield the same unitary evolution (for instance several functions $g(t)$ generate the same U_{XX} gate in the example above, provided the integral

$\int_0^t g(\tau)\,\mathrm{d}\tau$ is the same). Thus, going to a circuit-level description of the time evolution instead of staying at the Hamiltonian level allows one to abstract away the implementation details. Depending on the architecture, we may have different $H(t)$ yielding the same unitary evolution. To benefit from this description, we of course need to be able to switch on and off terms of the Hamiltonian acting on selected qubits, a property we called "local control" above, and that analog computers do not possess. Finally, we call "quantum circuit" the graphical representation of the sequence of gates: it describes the unitary operation that is effected by the quantum computer.

3.1.3 Time evolution

In view of our goal of computing the Green function (Eq. (23)), there is a special unitary operation we would like to realize, namely a time evolution (like $U = e^{-iH_{\text{AIM}}t}$ in Eq. (23)).
Many quantum algorithms have been and are being developed to perform this task, also known as the "Hamiltonian simulation problem". With an analog quantum computer (or quantum simulator) that directly implements the Hamiltonian under study (say $H_{\text{hardware}} = H_{\text{AIM}}$), this just consists in letting the system evolve for a time t. For gate-based quantum computers, we need to find a sequence of gates that at least approximately implements e^{-iHt} (the same method applies to the more time-dependent case $Te^{-i\int_0^t H(\tau)\,d\tau}$). The most straightforward algorithm, known as the Trotterization or product formula method, relies on decomposing H as a weighted sum of, e.g., products of Pauli matrices

$$H = \sum_{i=1}^{M} \lambda_i P_i, \tag{30}$$

with $\lambda_i \in \mathbb{R}$ and $P_i = \bigotimes_{k=1}^{N} \sigma_{\alpha_k}^{(k)}$, where here the index α_k runs over $0, x, y, z$, where $\sigma_0 = I$ by convention. Because the individual Pauli terms P_i do not commute with one another, one then performs a similar time slicing (called Trotterization) as the one we encountered in the TEBD algorithm in a tensor network context (see Eq. (21))

$$e^{-iHt} = \left(e^{-iHt/N_t}\right)^{N_t} = \left(\prod_{i=1}^{M} e^{-i\frac{\lambda_i}{N_t}P_i t} + O\left(\frac{t}{N_t}\right)^2\right)^{N_t} = \prod_{m=1}^{N_t}\prod_{i=1}^{M} e^{-i\frac{\lambda_i}{N_t}P_i t} + O\left(\frac{t^2}{N_t}\right). \tag{31}$$

With this slicing, one obtains a sequence of $N_t \cdot M$ unitary operators with the form of a Pauli rotation $R_{P_i}(\theta_i) = e^{-i\frac{\theta_i}{2}P_i}$, with $\theta_i = 2\lambda_i t/N_t$.
Let us know show that each $R_{P_i}(\theta_i)$ is easy to implement in terms of a simple quantum circuit. Let us start with a simple case $P_i = \sigma_z^{(1)}\sigma_z^{(2)}$. It is easy to check that the circuit shown in Fig. 4 implements $R_{\sigma_z^{(1)}\sigma_z^{(2)}}(\theta)$. One easily shows, by induction, that $R_{\bigotimes_{m=1}^{K}\sigma_z^{(k_m)}}(\theta)$ is implemented by a circuit with CNOTS on pairs (k_1, k_2), (k_2, k_3), ..., (k_{K-1}, k_K), a rotation $R_z(\theta)$ on the K-th qubit, and then the reversed sequence of CNOTs, as illustrated in Fig. 4(c). Finally, to perform a general Pauli rotation (with Paulis on the x and y axis), one performs single-qubit rotations on the requisite qubits to go back to the z axis. For instance, for $P_i = \sigma_x^{(1)}\sigma_z^{(2)}$, noticing that

$$U_{\text{H}}\sigma_z U_{\text{H}}^{(\dagger)} = \sigma_x, \tag{32}$$

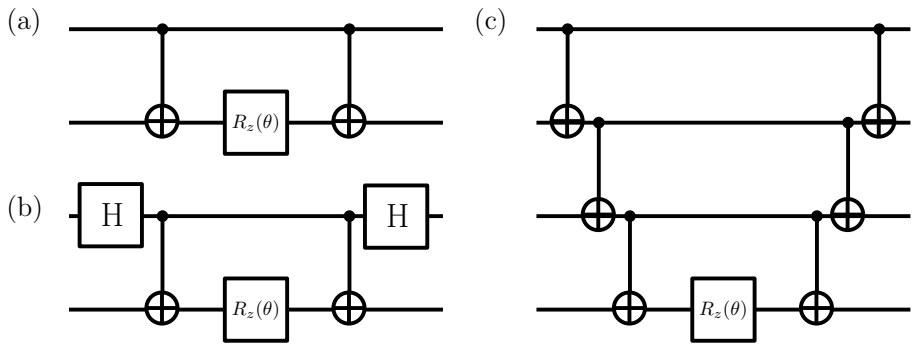


Fig. 4: *Circuits for $R_{P_i}(\theta)$. (a) Circuit for $R_{\sigma_z^{(1)}\sigma_z^{(2)}}(\theta)$. (b) Circuit for $R_{\sigma_x^{(1)}\sigma_z^{(2)}}(\theta)$. (c) Circuit for $R_{\sigma_z^{(1)}\sigma_z^{(2)}\sigma_z^{(3)}\sigma_z^{(4)}}(\theta)$.*

we see that

$$\begin{aligned} U_{\mathrm{H}}^{(1)} R_{\sigma_z^{(1)}\sigma_z^{(2)}}(\theta) U_{\mathrm{H}}^{(1)} &= U_{\mathrm{H}}^{(1)} \big(\cos(\theta) I - i \sin(\theta) \sigma_z^{(1)} \sigma_z^{(2)} \big) U_{\mathrm{H}}^{(1)} \\ &= \cos(\theta) I - i \sin(\theta) \sigma_x^{(1)} \sigma_z^{(2)} \\ &= R_{\sigma_x^{(1)}\sigma_z^{(2)}}(\theta). \end{aligned}$$

This is illustrated in Fig. 4(b).

We thus have a generic, approximate way to perform the time evolution of a Hamiltonian that we have decomposed as a sum of Pauli operators (Eq. (30)). Let us now count the number of operations contained in this circuit: there are N_t Trotter steps, each of which contains M operators of the form $R_{P_i}(\theta)$. The number of gates in each operator depends on the support s_i (number of non-identity Pauli operators) in P_i: we have $O(s_i)$ gates in the corresponding subcircuit. If we call $s = \max_i s_i$, we obtain $N_g = O(N_t M s)$, with a total error $\epsilon = O(t^2/N_t)$. One usually wants to adjust N_t to reach a desired error ϵ: $N_t = O(t^2/\epsilon)$ and thus,

$$N_g = O(M t^2 s/\epsilon). \tag{33}$$

This calls forth several remarks: (i) the number of terms M needs to be "small". A generic Hamiltonian in $\mathcal{H}_N$ will have $M = 2^N$, which is intractable. However, as we shall see, the Hamiltonians we are interested in have a number of terms M that scales polynomially with N (which is considered to be tractable); (ii) the longer the evolution time t, the more gates. Here, the quadratic dependence (instead of the expected linear dependence) comes from the fact we had to slice the time evolution. We can use higher-order Suzuki-Trotter formulas that will lead to a scaling that is closer to linear, but with an overhead in the number of gates per slice (see [14] for a general upper bound on the Trotter error). More advanced methods such as qubitization [15] achieve a linear scaling, but they usually require additional ("ancilla") qubits. They can also achieve a better scaling than $1/\epsilon$; (iii) finally, the support s of the terms in the decomposition of H plays an important role. As we shall see below, the fermionic nature of the Hamiltonian of interest here leads to quite large supports.

3.1.4 Quantum measurements and the variance issue

Before we turn to the specifics of fermionic problems on qubit quantum computers, let us examine one last issue with the quantity we need to compute, Eq. (23). It is expressed as a quantum mechanical average value $\langle\psi|\hat{O}|\psi\rangle$, with operator $\hat{O} = U^\dagger c_\sigma U c_\sigma^\dagger$ and $U = e^{-iH_{\text{AIM}}t}$. We have seen in the previous section how to perform U as a quantum circuit, but what quantum mechanics gives us easy access to is the estimation of $\langle\psi|\hat{A}|\psi\rangle$, where $\hat{A}$ is a Hermitian operator, not any operator like $\hat{O}$.

Before we turn to specific quantum circuits that allow us to get access to $\langle\psi|\hat{O}|\psi\rangle$, let us focus on the Hermitian case. In quantum mechanics, the measurement of an observable $\hat{A}$ with eigenvalues λ and eigenvectors $|\varphi_\lambda\rangle$ results (in the nondegenerate case) in a collapse of $|\psi\rangle$ to one of the eigenvectors $|\varphi_\lambda\rangle$ with a probability given by Born's rule, $p(\lambda) = |\langle\varphi_\lambda|\psi\rangle|^2$, and gives access to the value λ of the corresponding eigenvalue. Repeating the circuit and measurement several (say N_s) times (usually called "shots") allows to compute a statistical estimator $\bar{A}(N_s)$ that converges to the expectation value of $\hat{A}$ in state $|\psi\rangle$ in the large N_s limit

$$\bar{A}(N_s) = \frac{1}{N_s}\sum_{i=1}^{N_s}\lambda_i \xrightarrow[N_s\infty]{} \sum_\lambda p(\lambda)\,\lambda = \big\langle\psi\big|\hat{A}\big|\psi\big\rangle = \langle A\rangle. \tag{34}$$

Quantum computers can either be used in a one-shot way or to compute averages. The one-shot way is particularly useful when the distribution $p(\lambda)$ is peaked around a value λ_0 which one wants to discover: in that case, a single (or a few) shots will yield λ_0. As for the computation of averages, it also works when $p(\lambda)$ is not peaked, but one has to contend with the statistical error (standard error on the mean)

$$\Delta A(N_s) = \sqrt{\big\langle\,\big(\langle A\rangle - \bar{A}(N_s)\big)^2\,\big\rangle} = \sqrt{\frac{\text{Var}(A)}{N_s}}, \tag{35}$$

where the second equality holds because independent experiments (shots) are independent and identically distributed (iid). The variance is, explicitly,

$$\text{Var}(A) = \langle\psi|A^2|\psi\rangle - \big(\langle\psi|A|\psi\rangle\big)^2,$$

so the number of shots needed to attain a fixed accuracy ΔA depends both on the observable A to be measured and the state $|\psi\rangle$ on which it is measured. For instance, if one is trying to generate the ground state $|\Psi_0\rangle$ of some Hamiltonian H, and wants to measure its energy $\langle H\rangle$, then, because $|\Psi_0\rangle$ is an eigenstate of H, the variance will vanish and only one shot will suffice. This property, called variance reduction, is often exploited in (classical) variational Monte-Carlo algorithms: as the algorithm converges to the ground state, a fixed number of samples (shots) gives an increased accuracy.

However, not every observable $\hat{A}$ can be measured on quantum computers. In fact, in most technologies, only Pauli z matrices $\sigma_z^{(k)}$, for $k = 1, \ldots, N$, and tensor products thereof, can be measured. This is represented by a meter symbol in quantum circuits (see the symbols at the end of the first lines of Fig. 5(a) and (b)). Other Pauli expectation values can be computed by

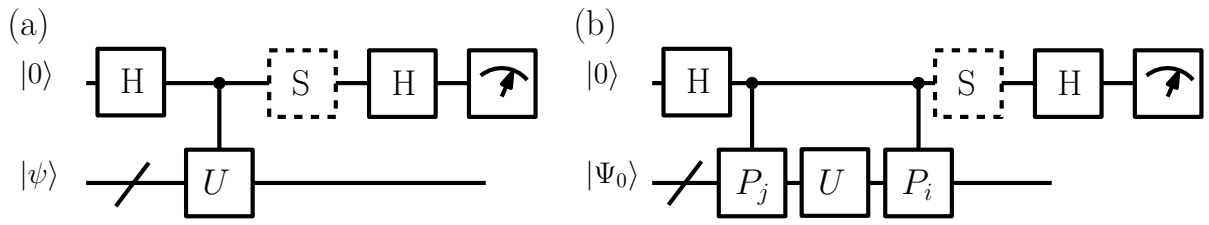


Fig. 5: *Hadamard test: (a) Computation of $\langle\psi|U|\psi\rangle$ by the Hadamard test circuit. The S gate is used only to compute the imaginary part. (b) Application to the computation of $\langle\Psi_0|U^\dagger P_i U P_j|\Psi_0\rangle$ terms.*

rotating the state to the right axis: for instance, to measure $\langle\sigma_x\rangle = \langle\psi|\sigma_x|\psi\rangle$, one can apply a Hadamard gate to get $|\psi'\rangle = U_{\rm H}|\psi\rangle$ and then, using (32), measure $\langle\sigma_x\rangle' = \langle\psi'|\sigma_x|\psi'\rangle$.

As for generic, multi-qubit observables $\hat{A}$, they can, as we saw earlier for the Hamiltonian, always be decomposed as a weighted sum of products of Pauli matrices

$$\hat{A} = \sum_{i=1}^{M} \lambda_i \, P_i. \tag{36}$$

One can thus in principle compute $\langle A\rangle$ by computing separately the M terms $\langle P_i\rangle$. For example, to measure $\left\langle \sigma_x^{(1)}\sigma_z^{(2)}\right\rangle$, one first applies a Hadamard gate on the first qubit, and then measures the operator $\sigma_z^{(1)}\otimes\sigma_z^{(2)}$ repeatedly.

We now turn to the problem at hand, namely computing $\langle\psi|\hat{O}|\psi\rangle$ for a generic operator. A generic strategy is to decompose $\hat{O}$ as a sum of unitaries, $\hat{O} = \sum_i \lambda_i \hat{U}_i$ (with $\lambda_i \in \mathbb{C}$), and compute $\langle\psi|\hat{U}_i|\psi\rangle$ separately. (Note that a Pauli decomposition like Eq. (36) is also a decomposition as a linear combination of unitaries since Pauli matrices are unitary).

The circuit shown in Fig. 5(a), dubbed a Hadamard test, does the job of computing $\langle\psi|\hat{U}|\psi\rangle$ for a given unitary U: starting from a state $|0\rangle\otimes|\psi\rangle$, applying the first Hadamard gate yields $\big(|0\rangle+|1\rangle\big)/\sqrt{2}\otimes|\psi\rangle$. Then, the controlled unitary yields $\big(|0\rangle|\psi\rangle+|1\rangle U|\psi\rangle\big)/\sqrt{2}$, and the final Hadamard yields the final state $|\psi_f\rangle = \big(|0\rangle\,(I+U)\,|\psi\rangle + |1\rangle\,(I-U)\,|\psi\rangle\big)/2$. The meter symbol stands for a $\sigma_z^{(0)}$ measurement. The probability of getting outcome 0 is given by Born's rule $p(0) = \langle\psi_f|\,(|0\rangle\langle 0|\otimes I)\,|\psi_f\rangle = \big\|(I+U)|\psi\rangle\big\|^2/4 = \big(1+\mathrm{Re}\langle\psi|U|\psi\rangle\big)/2$, so that

$$\mathrm{Re}\langle\psi|U|\psi\rangle = 2p(0) - 1. \tag{37}$$

If one adds an S gate to the circuit (dashed box in Fig. 5(a), whose matrix is $U_S = \begin{pmatrix} 1 & 0 \\ 0 & i \end{pmatrix}$), U changes to iU in the above computation, giving $\mathrm{Im}\langle\psi|U|\psi\rangle = 1-2p(0)$. Thus, provided the ability to implement a controlled-U evolution, we can compute terms of the form $\langle\psi|U|\psi\rangle$, and thus arbitrary values $\langle\psi|\hat{O}|\psi\rangle$ via the linear combination of unitaries.

The last step we have to go through is how to express $\hat{O} = U^\dagger c_\sigma U c_\sigma^\dagger$ as a linear combination of unitaries. For this, we need to go from fermionic operators to qubit ones.

3.1.5 Quantum computing for fermions

In the previous sections, we have learned to perform time evolutions of Hamiltonian operators decomposed as a weighted sum of Pauli operators (Eq. (30)), and to measure quantities of the form $\langle\psi|\hat{O}|\psi\rangle$ given a decomposition of $\hat{O}$ as a weighted sum of unitaries. We now explain how to obtain the precise form of these decompositions in the case where H is a fermionic operator like the AIM, and $\hat{O} = U^\dagger c_\sigma U c_\sigma^\dagger$.
The task consists in finding a mapping between a Fock space with N fermionic orbitals, with a Fock basis $\left\{|n_1,\dots,n_N\rangle = \prod_{k=1}^N \left(c_k^\dagger\right)^{n_k}|0,\dots,0\rangle, n_k \in \{0,1\}\right\}$, and a Hilbert space with N qubits, with a basis $\{|b_1\rangle \otimes |b_2\rangle \otimes \cdots \otimes |b_N\rangle, b_k \in \{0,1\}\}$.

The Jordan-Wigner mapping The simplest mapping (also called encoding) between these two bases consists in defining, for all $k = 1,\dots,N$,

$$b_k = n_k. \tag{38}$$

It is called the Jordan-Wigner encoding. Having chosen this correspondence between states, we want to find the qubit operator $\tilde{c}^\dagger$ that acts on the $|b_1,\dots,b_N\rangle$ the same way as $c^\dagger$ acts on the $|n_1,\dots,n_N\rangle$, namely:

$$\begin{aligned} c_k^\dagger|n_1,\dots,0,\dots,n_N\rangle &= (-)^{\sum_{k'=1}^{k-1} n_{k'}}|n_1,\dots,1,\dots,n_N\rangle \\ c_k^\dagger|n_1,\dots,1,\dots,n_N\rangle &= 0 \end{aligned} \tag{39}$$

The operator that turns a two-level system $|0\rangle$ into $|1\rangle$ and vanishes on $|1\rangle$ is $\sigma_+ = \begin{pmatrix} 0 & 0 \\ 1 & 0 \end{pmatrix} = \big(\sigma_x - i\sigma_y\big)/2$. To take into account the $(-)^{\sum_{k'=1}^{k-1} n_{k'}}$ factor, one needs to introduce σ_z operators on qubits $k' < k$, so that

$$\tilde{c}_k^\dagger = \sigma_z^{(1)} \cdots \sigma_z^{(k-1)} \sigma_+^{(k)}. \tag{40}$$

For a spinful fermionic model, we further need to pick an ordering of the (i,σ) index. Two natural choices arise: either $(1,\uparrow),(1,\downarrow),(2,\uparrow),(2,\downarrow),\dots$ or $(1,\uparrow),(2,\uparrow),\dots,(1,\downarrow),(2,\downarrow),\dots$. These choices will yield equivalent, but different quantum circuits. Choosing the second ordering (the one that does not mix different spins), a $c_{i\sigma}^\dagger c_{j\sigma}$ term appearing in the kinetic term of the Hubbard model will transform into

$$\tilde{c}_{i\sigma}^\dagger \tilde{c}_{j\sigma} = \sigma_+^{(i\sigma)} \sigma_z^{(i+1,\sigma)} \cdots \sigma_z^{(j-1,\sigma)} \sigma_-^{(j\sigma)} \tag{41}$$

while Hubbard interaction terms like $n_{i\uparrow}n_{i\downarrow}$ will transform into $\tilde{n}_{i\uparrow}\tilde{n}_{i\downarrow} = \big(I - \sigma_z^{(i\uparrow)}\big)\big(I - \sigma_z^{(i\downarrow)}\big)/4$. In other words, the Anderson Hamiltonian, with terms acting on at most 2 fermionic orbitals at the same time, is turned into a spin Hamiltonian with terms acting on up to $2N_b$ orbitals due to the strings of σ_z operators, called Jordan-Wigner strings, appearing in (41). Explicitly: mapping the impurity orbital ($c_\sigma^\dagger$) to spin index 1 and the k-th bath orbital ($a_{k\sigma}^\dagger$) to spin index $1{+}k$ we

obtain

$$\tilde{H}_{\text{AIM}} = \left(\frac{U}{4} - \frac{\mu}{2} + \sum_{k\sigma}\frac{\varepsilon_k}{2}\right) I - \sum_{k\sigma}\frac{\varepsilon_k}{2}\sigma_z^{(1+k,\sigma)} + \left(\frac{\mu}{2} - \frac{U}{4}\right)\sum_{\sigma}\sigma_z^{(1,\sigma)} + \frac{U}{4}\,\sigma_z^{(1,\uparrow)}\sigma_z^{(1,\downarrow)} + \sum_{k\sigma}\frac{V_k}{4}\Big(\big(\sigma_x^{(1\sigma)} - i\sigma_y^{(1\sigma)}\big)\sigma_z^{(2,\sigma)}\cdots\sigma_z^{(k,\sigma)}\big(\sigma_x^{(1+k,\sigma)} + i\sigma_y^{(1+k,\sigma)}\big) + \text{h.c.}\Big) \tag{42}$$

We now have a Pauli decomposition of $\tilde{H}_{\text{AIM}}$ with a total of $2(N_b{+}1)$ 1-qubit terms (disregarding the identity term), one two-qubit term stemming from the Hubbard interaction, and $8N_b$ terms stemming from the hybridization term, with supports ranging from 2 to $N_b{+}1$.
Using this decomposition, we can apply the Trotterization method introduced above to construct a quantum circuit that approximates $e^{-iH_{\text{AIM}}t}$. One Trotter step will consist in applying $R_z(\theta)$ rotation gates to all qubits (with angles given by the prefactors in the terms of the first line of expression (42)). As for the second line of (42), it gives rise to four subcircuits of the type $R_{P_i}(\theta)$ that we described in subsection 3.1.3, with circuits of length up to $O(N_b)$, and thus a general scaling of $N_g = O(Mt^2s/\epsilon) = O\left(N_{\text{b}}^2t^2/\epsilon\right)$ for the time evolution circuit.
Expression (40) also allows us to express $\hat{O}_\sigma = U^\dagger c_\sigma U c_\sigma^\dagger$ as a linear combination of unitaries: replacing the creation and annihilation operators by (40), we obtain

$$\begin{aligned} 4\hat{O}_\uparrow &= U^\dagger\left(\sigma_x^{(1,\uparrow)} + i\sigma_y^{(1,\uparrow)}\right)U\left(\sigma_x^{(1,\uparrow)} - i\sigma_y^{(1,\uparrow)}\right) \\ &= U^\dagger\sigma_x^{(1,\uparrow)}U\sigma_x^{(1,\uparrow)} - iU^\dagger\sigma_x^{(1,\uparrow)}U\sigma_y^{(1,\uparrow)} + iU^\dagger\sigma_y^{(1,\uparrow)}U\sigma_x^{(1,\uparrow)} + U^\dagger\sigma_y^{(1,\uparrow)}U\sigma_y^{(1,\uparrow)}, \end{aligned} \tag{43}$$

which is in the requisite form.
We thus have achieved our goal. We note that in the single-impurity case that we have picked as an example, we could have "linearized" the bath, namely transformed the current problem, where the impurity is hybridized to every bath site (a so-called "star geometry"), to a problem where the $\uparrow$ impurity site is hybridized only to one bath site (itself hybridized to a single other bath site and so on and so forth), and likewise for the $\downarrow$ impurity site. This would have allowed for a "chain geometry" where the Jordan-Wigner strings disappear, yielding a scaling of $N_{\text{g}} = O\left(N_{\text{b}}t^2/\epsilon\right)$ gates for the time evolution circuit. However, in the $N_c > 1$ case, we can no longer perform this trick.

Other encodings The Jordan-Wigner encoding is not the only possible fermion-to-spin mapping. While the Jordan-Wigner encoding stores all the information about the orbital occupation in the states (see Eq. (38)) and the information about the parity in the operators (see the string of σ_z operators in (40)), a mirror encoding called the parity encoding does the reverse. For instance, in the parity encoding, $b_k = \sum_{k'=1}^{k} n_k \mod 2$, namely the states store the parity information, and likewise a string of Pauli operators in the expression for the operators will store the occupation... yielding, as for the Jordan-Wigner transformation, terms with a support $O(N)$ (with N the number of fermionic orbitals) in the Pauli decomposition of the corresponding qubit Hamiltonian. A more sophisticated encoding called the Bravyi-Kitaev encoding [16, 17] mixes the occupation and parity information in a tree structure that allows one to obtain terms with

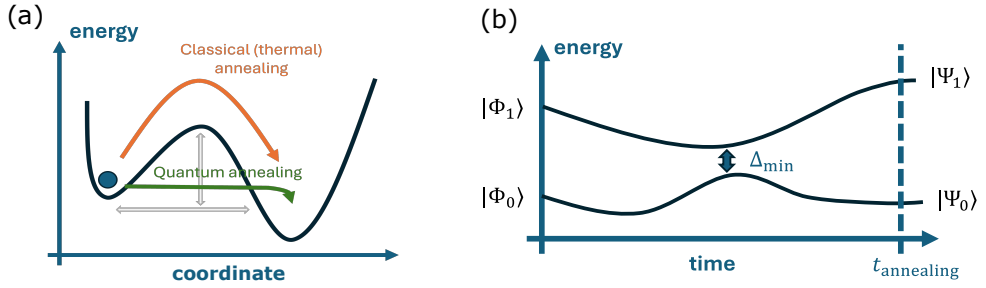


Fig. 6: *Adiabatic quantum annealing method. (a) Quantum tunneling (green) vs. thermal hopping (orange). (b) Time evolution of the instantaneous energy levels and definition of the minimum gap.*

$O(\log(N))$ support. Let us also note that while the aforementioned encodings use a Hilbert space of the same size as the fermionic Fock space, other encodings use larger Hilbert spaces (and thus more qubits than fermionic modes) to obtain local qubit Hamiltonians (at the expense of ancillary qubits) [18–20].

3.2 Quantum algorithms for Green functions

In the previous section, we introduced the main quantum computing building blocks to deal with fermionic models. In this section, we use these building blocks to introduce several methods to compute Green functions with gate-based quantum computers.

3.2.1 Ground state preparation: the example of the adiabatic method

The greater Green function $G^{>}(t)$ (see Eq. (23) for a definition) requires the preparation of the ground state $|\Psi_0\rangle$ (at zero temperature) or the Gibbs state $\rho = e^{-\beta H}/Z$ at finite temperature. In this section we tackle only the zero-temperature case, although quantum algorithms have also been developed for Gibbs state preparation, usually with the help of additional qubits.
A standard method to perform this state preparation is the adiabatic method. It consists of initializing the qubit register in an easy-to-prepare state $|\Phi_0\rangle$ that should also be the ground state of a Hamiltonian H_0. This Hamiltonian, sometimes called the mixer Hamiltonian, must be simple enough that its ground state $|\Phi_0\rangle$ is easy to prepare, and it must be such that it couples the different (usually unknown) eigenstates of the Hamiltonian H whose ground state $|\Psi_0\rangle$ we want to prepare. One then slowly deforms H_0 into H over a period of time $t_{\text{annealing}}$, for instance

$$H(t) = \left(1 - t/t_{\text{annealing}}\right) H_0 + t/t_{\text{annealing}} H \,. \tag{44}$$

In this time evolution, the role of H_0 can be seen as allowing for tunneling events between local minimal of the energy landscape of H, as pictorially represented in Fig. 6 (a). Over time, H_0 is slowly turned off, hence the name "quantum annealing" given to this method, in analogy to the classical (thermal) annealing method, which consists in slowly lowering the temperature. The adiabatic theorem (see [21]) guarantees that for long enough annealing times the system remains in the instantaneous ground state of $H(t)$. More precisely,

$$t_{\text{annealing}} \gg V/\Delta_{\min}^2, \tag{45}$$

with V a matrix element, and Δ_{min} the minimum gap over time between the instantaneous ground state of $H(t)$ and the first excited state, as represented in Fig. 6 (b).
Thus, to prepare the ground state $|\Psi_0\rangle$ using the quantum annealing method, we need to construct a circuit that implements the time evolution $H(t)$ for a long enough $t_{\text{annealing}}$. The construction of the quantum circuit to perform this time evolution uses the methods described in subsection 3.1.3, for instance Trotterization. We note that a longer $t_{\text{annealing}}$ will generically lead to a deeper state preparation circuit: the best Hamiltonian evolution methods (like qubitization) achieve a linear scaling of the number of gates as a function of the evolution time. This scaling is optimal owing to the so-called no-fast-forwarding theorem, which stipulates that time evolutions of sparse Hamiltonians of duration t will require a number of gates at best linear in t [22]. As a consequence, an important practical question is the size Δ_{min}, which itself depends on H_0, H and the shape of the interpolation between both. It is in general hard to compute, but we at least know that $\Delta_{\text{min}} \geq \Delta$, with Δ the gap of H. Therefore, trying to prepare the ground state of a small-gap Hamiltonian (and for that matter a gapless one, like a metal) will take very long circuits.
There exists heuristic alternatives around adiabatic quantum annealing that set out to find shortcuts to adiabaticity (see [23] for a review). Variational methods like the ones we will introduce below (see subsection 3.4) can be regarded as examples of such heuristics.

The complexity of ground state preparation On a more formal level, let us note that the generation of the ground state of a many-body Hamiltonian is generally expected to be hard (that is, exponential) even on quantum computers: it has been proven to be "QMA-complete" for $k \geq 2$-local Hamiltonians [24] (and hence for the Hubbard model [25]). Here, k denotes the maximal support of the terms appearing in, e.g., the Pauli decomposition of H, and QMA—for quantum Merlin-Arthur—is a quantum analog of the NP class. Impurity problems may be less difficult in terms of ground state preparation: they are in the QCMA (for quantum-classical Merlin-Arthur) class [26], a class that stands between NP and QMA in terms of hardness. If they are gapped, they become easy (efficiently solvable) both for classical and quantum computers [26]. If not, recent work claims evidence that their ground state can be efficiently prepared by a quantum computer, while remaining hard for classical computers [27]. This would provide an a posteriori justification of quantum embedding methods like DMFT: using locality properties of the interaction, they would help reduce an exponentially problem (the Hubbard model) to an efficiently solvable problem (the impurity problem).

3.2.2 Time domain: Hadamard test

Once the ground state is prepared, the Hadamard test method to compute the greater Green function $G^{>}(t)$ (Eq. (23)) is a straightforward application (first introduced by [28], and well summarized in [29]) of the few methods we just introduced.
Using the decomposition (43) of $U^\dagger c_\sigma U c_\sigma^\dagger$, we see that computing $G^{>}(t)$ amounts to summing four contributions of the form $\langle\Psi_0|U^\dagger P_i U P_j|\Psi_0\rangle$, with $P_{i,j} \in \left\{\sigma_x^{(1\uparrow)}, \sigma_y^{(1\uparrow)}\right\}$. Since $U^\dagger P_i U P_j$

is itself unitary, we only have to use the Hadamard test depicted in Fig. 5, with a controlled-$U^\dagger P_i U P_j$ operation. A naive implementation of this operation would be a sequence of a controlled P_j, controlled U, controlled P_i and then controlled $U^\dagger$. Yet, the precise structure of the $U^\dagger P_i U$ allows for one simplification: the controls on the time evolution U and its inverse $U^\dagger$ can be removed. Let us show that we get the same outcome with and without controls: with controls, if the ancilla qubit is in state $|0\rangle$ and the state register in state $|\psi\rangle$, we end up with $|0\rangle|\psi\rangle$. If the ancilla is in state $|1\rangle$, we end up with $|1\rangle U^\dagger P_i U|\psi\rangle$. Without controls, if the ancilla qubit is in state $|0\rangle$ and the state register in state $|\psi\rangle$, we end up with $|0\rangle U^\dagger U|\psi\rangle = |0\rangle|\psi\rangle$. If the ancilla is in state $|1\rangle$, we end up with $|1\rangle U^\dagger P_i U|\psi\rangle$. QED.
The corresponding circuit can be further simplified by noticing that the $U^\dagger$ operation has no influence on the final measurement as it commutes with the remaining operations (that act only on the ancilla qubit). It can thus be removed, which yields the circuit shown in Fig. 5(b): this circuit makes it clear that computing the Green function amounts to first generating the ground state $|\Psi_0\rangle$, coupling it to an ancilla qubit (controlled-P_j operation), time evolving the system (operation U), and then coupling again to the ancilla (controlled-P_i operation) and measuring the ancilla.
Let us end this subsection by estimating the scaling of the run time of the Hadamard test method with respect to the precision ϵ achieved on the Green function. Since it requires an estimate of $p(0)$ (Eq. (37)), it is characterized by a $1/\epsilon^2$ scaling: the statistical error on $p(0)$ scales as $\epsilon \sim 1/\sqrt{N_{\text{samples}}}$, with N_{samples} the number of repetitions of the circuit to estimate the probability of getting a 0 outcome. Therefore, the run time scales as $N_{\text{samples}} \sim 1/\epsilon^2$. This is typical of classical Monte-Carlo methods, and is a direct consequence of the central limit theorem. As we shall see in the next subsection, this scaling can be improved by resorting to quantum interferences.

3.2.3 Frequency domain: quantum phase estimation

High-level description Another quantum algorithm allows one to compute the Green function directly in the frequency domain, and with a better accuracy scaling. Starting from Eq. (17), and using $\int_0^\infty \mathrm{d}t\, e^{i\omega t} = \pi\delta(\omega) + i\mathcal{P}\frac{1}{\omega}$ ($\mathcal{P}$ denotes the Cauchy principal value), we obtain

$$G^>(\omega) = \sum_\alpha \left(-i\pi\delta\left(\omega - (E_\alpha - E_0)\right) + \mathcal{P}\left(\frac{1}{\omega - (E_\alpha - E_0)}\right)\right) \left|\langle\Psi_\alpha|c_\sigma^\dagger|\Psi_0\rangle\right|^2. \tag{46}$$

The imaginary part of $G^>(\omega)$ is therefore a distribution of peaks of weight $\left|\langle\Psi_\alpha|c_\sigma^\dagger|\Psi_0\rangle\right|^2$ at locations $E_\alpha - E_0$.
One of the most important quantum algorithms, quantum phase estimation (QPE, [30]), can be applied to this problem, as first pointed out by [29]. Given a unitary operator $U = e^{iHt}$ and one of its eigenvectors $|\Psi_\alpha\rangle$ with eigenvalue $e^{iE_\alpha t}$, it returns, in a single repetition of the QPE circuit, an m-bit estimate $\hat{E}_\alpha$ of E_α (t is adjusted so that $E_\alpha t$ is normalized: resolving smaller energies requires longer times). When starting from any state $|\Psi\rangle$ as an input, it returns a m-bit estimate $\hat{E}_\alpha$ of one of the eigenvalues E_α and projects the input state to $|\Psi_\alpha\rangle$ with probability $|\langle\Psi_\alpha|\Psi\rangle|^2$.

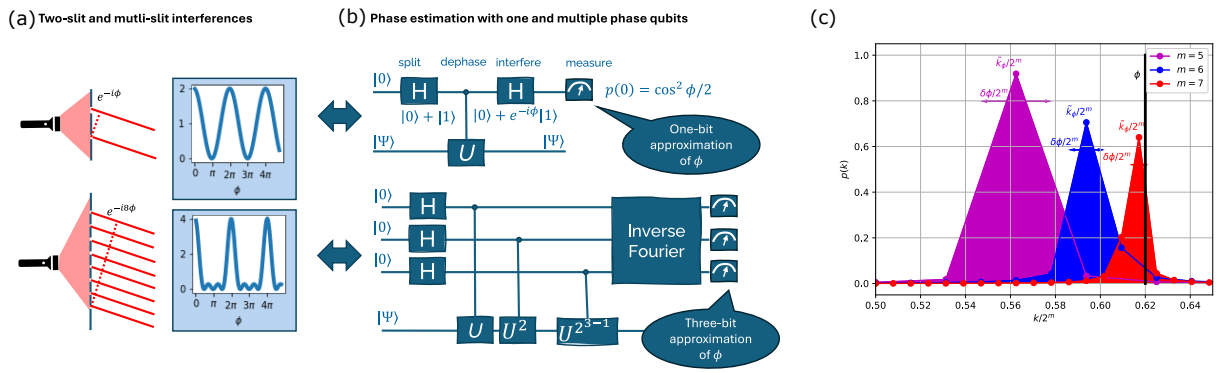


Fig. 7: *Phase estimation. Analogy between interferometry in optics (a) and quantum phase estimation circuits (b), with $m = 1$ ancilla qubit (two slits, top) or $m = 3$ ancilla qubits (8 slits, bottom). Adapted from [31]. (c) Histogram of the bitstring probabilities $p(j) = |\tilde{a}_j|$ for $\phi = E_\alpha t = 0.62$ and a variable number m of ancilla qubits.*

Therefore, several calls to QPE on an input state $|\Psi\rangle$ will return a histogram with peaks of height $|\langle\Psi_\alpha|\Psi\rangle|^2$ at location $\hat{E}_\alpha$. We thus see that applying QPE to the input state $c_\sigma^\dagger|\Psi_0\rangle$ and with $H = H_{\text{AIM}} - E_0$ will directly yield an estimate of $\text{Im}\, G^>(\omega)$ (and hence, via Kramers-Kronig relations, of its real part).
In practice, however, $c_\sigma^\dagger|\Psi_0\rangle$ is not a properly normalized state because $c_\sigma^\dagger$ is not unitary. However, in a Jordan-Wigner encoding, assuming the impurity orbital is the first orbital in the orbital order, $c_\sigma^\dagger + c_\sigma$ maps to $\tilde{c}_\sigma^\dagger + \tilde{c}_\sigma = \sigma_x^{(1)}$, which is a bona fide unitary gate. Since the QPE circuit contains gates that conserve the electron number, an input state $c_\sigma^\dagger|\Psi_0\rangle + c_\sigma|\Psi_0\rangle$ will be projected onto eigenstates $|\Psi_\alpha\rangle$ of H with N_e+1 or N_e-1 electrons (where N_e is the number of electrons in the ground state $|\Psi_0\rangle$). To obtain the histogram of the greater Green function, we need to take into account only those measurements that stem from N_e+1 states. To select them, we just need to measure the number of electrons in the final state.

Circuit implementation We now turn to the implementation of QPE. QPE is essentially a multi-slit Mach-Zehnder interferometry experiment [32]. It can be thought of as a Young slit experiment, with a number of slits exponential in the number m of ancilla bits. Since interference experiments yield an accuracy scaling inversely with the number of slits, this will give a $1/2^m$ accuracy (Fig. 7(a)). Note that the $m{=}1$ circuit reduces to the Hadamard test circuit (or two Young slits).
The construction of the phase estimation circuit is illustrated in Fig. 7(b). It consists in two groups (registers) of qubits: the lower one, called the state register, for preparing a state $|\Psi\rangle$ close to an eigenstate state $|\Psi_\alpha\rangle$, and the upper one for m ancilla qubits ($m = 3$ on Fig. 7(b), lower circuit), that will be used to read a m-bit estimate of E_α.
If $|\Psi\rangle = |\Psi_\alpha\rangle$, the state after the wall of Hadamard gates and the controlled-$U^{2^{k-1}}$ ($k{=}1,\ldots,m$) gates is

$$|\Psi_{\text{tot}}\rangle = \bigotimes_{k=1}^{m} \left(\frac{|0\rangle + e^{iE_\alpha 2^{k-1}t}|1\rangle}{\sqrt{2}} \right) \otimes |\Psi_\alpha\rangle = \frac{1}{2^{m/2}} \sum_{b_1,\ldots b_m} e^{iE_\alpha t \sum_{k=1}^m b_k 2^{k-1}} |b\rangle \otimes |\Psi_\alpha\rangle.$$

Defining $b = \sum_{k=1}^{m} b_k\, 2^{k-1}$ (the integer representation of the binary string $(b_1, \ldots, b_m)$), we see that the state before the inverse Fourier transform is $|\Psi_{\text{tot}}\rangle = \sum_b a_b(E_\alpha)|b\rangle \otimes |\Psi_\alpha\rangle$, with $a_b(E_\alpha) = \frac{1}{2^{m/2}} e^{iE_\alpha t b}$. We further note that $a_{b+2\pi/(E_\alpha t)} = a_b$, if one assumes for the sake of argument that $2\pi/(E_\alpha t)$ is an integer. That is, the first part of the QPE circuit creates a state on the ancilla register whose amplitudes are a periodic function of period $2\pi/(E_\alpha t)$. The role of the Fourier transform is to extract this period by producing the associated spectrum, which we expect to be peaked at a frequency $\sim E_\alpha t$, from which we will extract the sought-after E_α.
Let us check this intuition by doing the math: the inverse quantum Fourier transform performs the (inverse) discrete Fourier transform (DFT) of the amplitudes a_b: it yields ket $\sum_j \tilde{a}_j(E_\alpha)|j\rangle$ on the ancilla register, with

$$\begin{aligned}\tilde{a}_j(E_\alpha) = \text{DFT}^{-1}\left[a_b(E_\alpha)\right] &= \frac{1}{\sqrt{2^m}} \sum_b e^{i2\pi bj/2^m} a_b(E_\alpha) \\ &= \frac{1}{2^m} \sum_{b=0}^{2^m-1} e^{i(2\pi j/2^m + E_\alpha t)b} = \frac{1}{2^m} \frac{\sin\left(\left(j + E_\alpha t \frac{2^m}{2\pi}\right)\pi\right)}{\sin\left(\left(j + E_\alpha t \frac{2^m}{2\pi}\right)\frac{2^m}{2}\pi\right)}.\end{aligned}$$

Defining $\phi = E_\alpha t$, this function is peaked at $j = k_\phi$ with $k_\phi = \lfloor 2^m \phi \rfloor$, as shown in Fig. 7(c). We can thus take as an estimate of the actual phase ϕ (and thus E_α):

$$\hat{\phi} = \frac{k_\phi}{2^m} \tag{47}$$

with an error $\hat{\phi} - \phi = \delta\phi/2^m$: we see that we are making an error $\delta\phi/2^m$ on the actual phase ϕ: QPE does yield an estimate of the phase (and hence E_α) to an m-bit precision, as advertised.

Resource estimation To conclude this subsection, let us evaluate the depth (number of gates) of the QPE circuit, neglecting the state preparation: the dominant contribution is given by the controlled-U^{2^k} operations (k= 0 to $m-1$). Each U^{2^k} operation (neglecting the controls, which will result in an additional overhead) will at least require a depth of 2^k as per the non-fast-forwarding theorem ($U^{2^k} = e^{-iH(2^k t)}$ so the evolution time is $\propto 2^k$), adding up to $O(2^m)$ gates. The quantum Fourier transform requires $O(m^2)$ gates, which is negligible compared to the controlled evolutions. Here, we did not specify the implementation of U itself, but we could use Trotterization, which will introduce a dependence of the gate count on the number of terms M and support of each term s as per Eq. (33), and achieve a t^2 depth (at first order). Qubitization will achieve a linear dependence in t, with additional dependence on the coefficients of the sum-of-unitaries decomposition.
Let us emphasize that the $O(2^m)$ depth is not to be considered an exponential cost: it helps achieve an error $\epsilon = O(1/2^m)$ on the estimate, so that the run time of QPE scales as $O(1/\epsilon)$, a scaling known as "Heisenberg scaling". This scaling can be shown to be optimal. It is quadratically better than the $1/\epsilon^2$ scaling of the Hadamard test method above, at the cost of a longer circuit.
Let us finally point out that in both methods, the circuit depth (excluding state preparation) scales polynomially with the system size, in contrast to the classical methods that all come with

some sort of exponential scaling. As for the state preparation itself, it may require very long circuits as discussed in subsection 3.2.1.
Alternative methods exist. [33] uses the resolvent form of the Green function, Eq. (18). Using this form, we can transform the problem of computing the Green function to the solution of a linear system of equations $Ax = b$ with $b = c_\sigma^\dagger|\Psi_0\rangle$ and $A = E_0 - H + \omega + i\eta$ (typical algorithms for this task use QPE as a subroutine). The overlap with solution $x = \frac{1}{E_0-H+\omega+i\eta}c_\sigma^\dagger|\Psi_0\rangle$ can then be computed with variations of the Hadamard test. Alternatively, [33] advocates the use of other advanced methods to compute the matrix inverse appearing in the resolvent formula.

3.3 The exponential wall of decoherence: noisy quantum states and gates

The algorithms presented above in principle allows for a tractable (polynomial) computation of the (greater) Green function in real time or frequency, provided the ground or Gibbs state can be prepared... and provided we are working with a perfect, that is, decoherence-free, quantum computer. Here, we discuss the impact of decoherence.

Decoherence: density matrix and quantum channels In subsection 3.1, we described perfect quantum computers. The physical implementations of quantum computers that have become available in the recent years differ from this ideal model. Their main constraint is decoherence, a phenomenon that stems from the entanglement of the quantum computer with the outside world, often called the environment. Denoting by $|\psi_i\rangle$ a basis of the quantum computer's Hilbert space and $|\chi_j\rangle$ a basis of said environment, the total wavefunction reads $|\Psi_{\text{tot}}\rangle = \sum_{ij} c_{ij}|\psi_i\rangle \otimes |\chi_j\rangle$. It is however impractical to work with such an object given the size of the environment. All average observables on the quantum computer, of the form $\langle O\rangle = \langle\Psi_{\text{tot}}|\hat{O}\otimes I|\Psi_{\text{tot}}\rangle$, can be computed from the so-called density matrix $\rho = \text{Tr}_{\text{env}}\left(|\Psi_{\text{tot}}\rangle\langle\Psi_{\text{tot}}|\right)$ of the quantum computer (here Tr_{env} denotes the partial trace $\sum_j\langle\chi_j|\cdots|\chi_j\rangle$) through the formula

$$\langle O\rangle = \text{Tr}(\rho\,\hat{O}), \tag{48}$$

where the trace here is to be understood as the trace over the quantum computer's Hilbert space. Therefore, for all practical purposes, quantum states in the presence of decoherence will no longer be described by a wavefunction $|\Psi\rangle$ but by a density matrix ρ, a unit trace and positive definite matrix (as can be checked from its definition). Of course, the density matrix also captures so-called pure states (quantum states described by a single wavefunction $|\Psi\rangle$): in a pure state has density matrix $\rho = |\Psi\rangle\langle\Psi|$. Similarly, the time evolution of quantum states (which we conveniently described with unitary gates) will no longer be described by a unitary operator $|\Psi_{\text{f}}\rangle = U|\Psi_{\text{i}}\rangle$. Instead we will consider linear, completely positive and trace-preserving (CPTP) mappings $\mathcal{E}$ that act on the density matrix as

$$\rho_{\text{f}} = \mathcal{E}(\rho_{\text{i}}) = \sum_{k=1}^{K} E_k\,\rho_{\text{i}}E_k^\dagger, \tag{49}$$

with $\sum_k E_k^\dagger E_k = I$. A noisy gate (also called a quantum channel or CPTP map) is thus completely characterized by K operators $\{E_k\}$ known as Kraus operators. The trace preservation

property ensures that the normalization of the state ($\mathrm{Tr}\,\rho = 1$) is preserved, while complete positivity means that applying the channel $\mathcal{E}$ on any subsystem (i.e applying $\mathcal{E} \otimes \mathcal{I}$ with $\mathcal{I}$ the identity channel) keeps the total density matrix positive definite (applying a gate on, say, a single qubit should keep the many-qubit quantum register physical). Note that when the Kraus rank K is one, we revert to the unitary case as $K_1^\dagger K_1 = I$ and $\rho_\mathrm{f} = K_1 |\Psi_\mathrm{i}\rangle\langle\Psi_\mathrm{i}| K_1^\dagger = |\Psi_\mathrm{f}\rangle\langle\Psi_\mathrm{f}|$.

Standard error models Decoherence in quantum processors is usually described with a few error metrics. An oft-used metric is the T_1 relaxation time and the T_2 dephasing time, which are obtained through Rabi and Ramsey experiments, respectively. From T_1, one can extract a typical relaxation probability $p_\mathrm{AD}(T_1)$ that enters the quantum channel $\mathcal{E}_\mathrm{AD}$, dubbed amplitude damping, that corresponds to this noise process. It is characterized by the Kraus operators

$$K_1 = \begin{pmatrix} 1 & 0 \\ 0 & \sqrt{1-p_\mathrm{AD}} \end{pmatrix}, \quad K_2 = \sqrt{p_\mathrm{AD}}\,\sigma_-. \tag{50}$$

This means that with probability p_AD, the state relaxes from $|1\rangle$ to $|0\rangle$. Similarly, from T_1 and T_2 one can compute a so-called pure-dephasing time $T_\varphi = \left(1/T_2 - 1/(2T_1)\right)^{-1}$, which in turn determines a pure-dephasing probability $p_\mathrm{PD}(T_\varphi)$ that enters the pure-dephasing quantum channel $\mathcal{E}_\mathrm{PD}$. It is characterized by the Kraus operators

$$K_1 = \sqrt{1-p_\mathrm{PD}}\; I, \quad K_2 = \sqrt{p_\mathrm{PD}}\,\sigma_z. \tag{51}$$

This means that with probability p_PD, a superposition state $|0\rangle + |1\rangle$ is dephased to $|0\rangle - |1\rangle$. A similar channel, called the bit-flip channel (with σ_x to replace σ_z in K_2), corresponds to bit-flip errors.

Finally, let us introduce a widely used noise channel called the depolarizing channel that, contrary to the pure-dephasing and bit-flip channels, does not favor errors of one type (e.g. z or x) over others. It is often defined (in the N-qubit case) as

$$\mathcal{E}_\mathrm{D}(\rho_\mathrm{f}) = (1-p_\mathrm{D})\,\rho_\mathrm{f} + p_\mathrm{D} I/2^N. \tag{52}$$

Namely, with probability p_D the state is changed into the so-called completely mixed state $I/2^N$, where all quantum information is erased. (One can easily show that this channel has four Kraus operators proportional to I, σ_x, σ_y and σ_z, respectively, with the same coefficient in front of the Pauli matrices, hence the claim that it does not favor one error type over the others). The depolarizing channel is often used for lack of more precise information as to the type of errors. For instance, when one knows only the error rate of a certain unitary gate $U^{(\mathrm{g})}$, one often models it as the composition $\mathcal{E}^{(g)} = \mathcal{E}_\mathrm{D} \circ \mathcal{E}^{(g)}_\mathrm{perfect}$, with $\mathcal{E}^{(g)}_\mathrm{perfect}(\rho) = U^{(g)} \rho\, U^{(g)\dagger}$.

Let us end this section by examining the overall effect of noise on a quantum circuit with N_g gates that we assume to be plagued by the same depolarizing noise $\mathcal{E}_\mathrm{D}$. The final state can be written as

$$\rho_\mathrm{f} = \mathcal{E}^{(N_\mathrm{g})} \circ \mathcal{E}^{(N_\mathrm{g}-1)} \circ \cdots \circ \mathcal{E}^{(1)}(\rho_\mathrm{i}). \tag{53}$$

Using the simple compositional noise model we just used, we easily get the expression

$$\rho_{\mathrm{f}} = (1-p_{\mathrm{D}})^{N_{\mathrm{g}}}\, U|\Psi_{\mathrm{i}}\rangle\langle\Psi_{\mathrm{i}}|U^{\dagger} + \left(1-(1-p_{\mathrm{D}})^{N_{\mathrm{g}}}\right) I/2^{N},$$

with $U = U^{(N_{\mathrm{g}})} \cdot U^{(N_{\mathrm{g}}-1)} \cdots U^{(1)}$ the perfect circuit. We can readily evaluate the so-called fidelity of the noisy final state with the perfect final state $|\Psi_{\mathrm{f}}\rangle = U|\Psi_{\mathrm{i}}\rangle$

$$\mathcal{F}(\rho_{\mathrm{f}}, |\Psi_{\mathrm{f}}\rangle) = \langle\Psi_{\mathrm{f}}|\rho_{\mathrm{f}}|\Psi_{\mathrm{f}}\rangle = (1-p_{\mathrm{D}})^{N_{\mathrm{g}}} + \left(1-(1-p_{\mathrm{D}})^{N_{\mathrm{g}}}\right) 1/2^{N} \approx (1-p_{\mathrm{D}})^{N_{\mathrm{g}}} \approx e^{-p_{\mathrm{D}}N_{\mathrm{g}}}. \quad (54)$$

The fidelity of the final state of a quantum circuit decays exponentially with the number of gates N_{g} in this circuit. Conversely, this means that for a given error rate p_{D} only circuits of size $N_{\mathrm{g}} \lesssim 1/p_{\mathrm{D}}$ are viable.

Today's error rates are between 1% and 0.01% for the limiting operations (two-qubit gates), meaning only circuits that contain between 100 and 10,000 of these gates are viable. This, in practice, places very severe constraints on the quantum circuits that can actually be run on current and near-term processors. For instance, this rules out the quantum phase estimation circuits we discussed in subsection 3.2.3. Even simple Trotterization is limited to very short times and hence poor energy resolutions. In fact, it already severely limits the preparation of the ground state needed for the Green function. In particular, the use of adiabatic state preparation methods presented in subsection 3.2.1, which require long circuits due to the long annealing times, is prohibited.

To address this issue, new algorithms have been developed in the past decade to reduce the number of requisite gates. This is the topic of the next section.

3.4 Near-term algorithms. Variational quantum algorithms for ground states and for time evolution.

Current and near-term quantum processors come with drastic limitations in terms of the number of gates that can be executed before decoherence sets in. Starting in the mid-2010s, algorithms have been designed for these "noisy, intermediate-scale quantum" (NISQ [34]) devices.

3.4.1 Ground state preparation: the variational quantum eigensolver

The most prominent example is the variational quantum eigensolver (VQE, [35], see [36] for a review), which is used to prepare ground states of Hamiltonians and measure their energy. Like DMRG above (paragraph 2.2.1), VQE is a variational method that sets out to minimize a variational energy $E_{\boldsymbol{\theta}} = \big\langle\Psi(\boldsymbol{\theta})|H|\Psi(\boldsymbol{\theta})\big\rangle$, with $|\Psi(\boldsymbol{\theta})\big\rangle$ a family of variational states (also called "ansatz"). The specificity of VQE is that the variational states are generated on a quantum processor by a unitary operation $U(\boldsymbol{\theta})$

$$|\Psi(\boldsymbol{\theta})\rangle = U(\boldsymbol{\theta})|\Phi_{\text{init}}\rangle,$$

where $|\Phi_{\text{init}}\rangle$ is usually state $|0\rangle \otimes |0\rangle \cdots \otimes |0\rangle$, and $U(\boldsymbol{\theta})$ represents a quantum circuit with parameters $\boldsymbol{\theta}$ (that may be, for instance, the angles of rotation gates $R_{\alpha}(\theta)$). Then, the energy

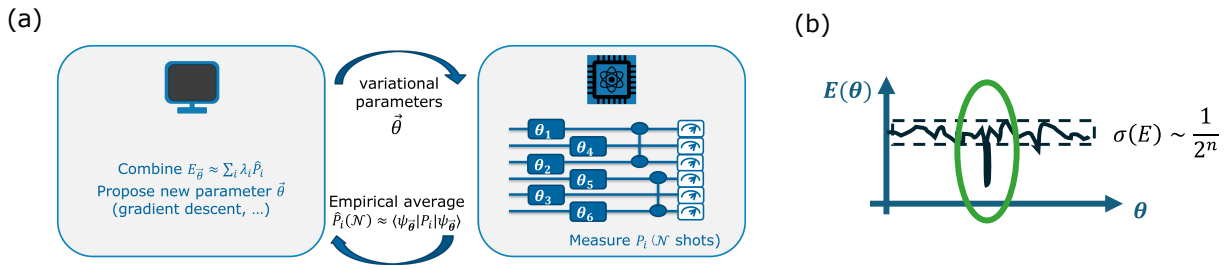


Fig. 8: *(a) Sketch of the variational quantum eigensolver (VQE) algorithm. (b) Illustration of the barren plateau problem: the variance vanishes exponentially on average.*

$E_{\boldsymbol{\theta}}$ of this state is measured on the quantum computer. As explained in subsection 3.1.4, this measurement can be done by achieving a Pauli decomposition of H (see Eq. (30)) and then summing up each contribution:

$$E_{\boldsymbol{\theta}} = \sum_{i=1}^{M} \lambda_i \langle \Psi(\boldsymbol{\theta}) | P_i | \Psi(\boldsymbol{\theta}) \rangle. \tag{55}$$

Each expectation value $\langle \Psi(\boldsymbol{\theta}) | P_i | \Psi(\boldsymbol{\theta}) \rangle$ is then estimated by an empirical average over N_s shots. Based on the computed $E_{\boldsymbol{\theta}}$, a classical optimizer updates the parameters $\boldsymbol{\theta}$. This is summarized in Fig. 8(a). VQE comes with three main challenges: decoherence, the measurement of $E_{\boldsymbol{\theta}}$, and the variational optimization of the parameters.

Decoherence and the design of ansätze Decoherence, as we just saw, limits the size of the circuit $U(\boldsymbol{\theta})$ that can be run in VQE. The main advantage of VQE is its flexibility in terms of the ansatz: given a fixed gate budget, one is free to pick the ansatz that best fits the problem at hand. Ansatz construction strategies fall into two main categories: hardware-efficient ansätze [37] and physics-inspired ones. The former aims at achieving the most expressivity given the gates available on the quantum processor. Typically, hardware-efficient ansätze feature a repetition of the following pattern: a sequence of one qubit rotations applied to each qubit, followed by the hardware's native two-qubit gate (there is usually only one) applied to all qubits pairs compatible with the connectivity of the qubits. The rotations introduce variational parameters, while the two-qubit gates generate entanglement. In fact, this construction guarantees a fast growth of entanglement—an important feature given the limited coherence time. However, it does not take into account the specifics of the Hamiltonian at hand. This is what the latter approach does.

For instance, the Hamiltonian variational ansatz (HVA, [38]) draws inspiration from the adiabatic quantum annealing algorithm (subsection 3.2.1): based on the intuition that one should start with the ground state $|\Phi_0\rangle$ of a simple Hamiltonian H_0 and deform the latter to the Hamiltonian at hand H, it uses a Trotterized form of the time evolution

$$|\Psi(t_\mathrm{annealing})\rangle = U(t_\mathrm{annealing})|\Phi_0\rangle = \prod_{k=1}^{M} e^{-i\left(1-t_k/t_\mathrm{annealing}\right)H_0 t_k} e^{-i t_k/t_\mathrm{annealing} H t_k} |\Phi_0\rangle$$

(for $t_k = kt_{\text{annealing}}/M$) as an inspiration for the following variational form

$$|\Psi(\boldsymbol{\theta})\rangle = \prod_{k=1}^{M} e^{-i\theta_{2k}H_0} e^{-i\theta_{2k+1}H} |\Phi_0\rangle \tag{56}$$

with $2M$ parameters $\boldsymbol{\theta}$. (Then the operators $e^{-i\theta_{2k}H_0}$ and $e^{-i\theta_{2k+1}H}$ can be translated to quantum circuits using the Trotterization tools we introduced in subsection 3.1.3). In the limit of large M, the assignment $\theta_{2k} = (1 - t_k/t_{\text{annealing}})t_k$ and $\theta_{2k+1} = t_k^2/t_{\text{annealing}}$ of the parameters guarantees a convergence to the ground state. However, the premise of HVA is that the variational optimization of $\boldsymbol{\theta}$ can lead to a good enough approximation of the ground state in a much shorter time (that is, compatible with the coherence time)... providing a sort of shortcut to adiabaticity.
Typically, in the context of the AIM (Eq. (10)), a natural choice of the simple Hamiltonian is $H_0 = Un_\uparrow n_\downarrow - \mu \sum_\sigma c_\sigma^\dagger c_\sigma + \sum_{k\sigma} \varepsilon_k a_{k\sigma}^\dagger a_{k\sigma}$ because its ground state, after a Jordan-Wigner encoding, is a computational basis state that can be prepared with σ_x gates only. Then, one can replace H with $H' = \sum_{k\sigma} V_k \left(a_{k\sigma}^\dagger c_\sigma + \text{h.c.}\right)$.
Other approaches are targeted more specifically at fermionic states: for instance, the low-depth circuit ansatz (LDCA, [39]) proposes to intercalate so-called Gaussian gates (which generate only Gaussian states, namely states generated by Hamiltonians quadratic in the c and $c^\dagger$ operators) with non-Gaussian gates (corresponding to quartic terms or beyond).
Once the ansatz is picked, other optimizations to reduce the circuit depth and thus counter decoherence is the choice of the orbital basis in which the states are expressed. For instance, while a Fock state $\prod_{k=1}^{N} \left(c_k^\dagger\right)^{n_k} |0, \ldots, 0\rangle$ expressed in the Fock basis can be generated, upon Jordan-Wigner encoding, simply by applying σ_x gates to the qubits with occupations $n_k = 1$, if the same state is expressed in any other basis, longer circuits (possibly including entangling gates) will be necessary. For a generic state $|\Psi\rangle$, the choice of the natural-orbital basis (that diagonalizes the one-particle reduced density matrix $D_{ij} = \langle\Psi|c_i^\dagger c_j|\Psi\rangle$) is supposed to yield the most compact representation of the state and should therefore require shorter quantum circuits [40–42].
Finally, one can also build the ansatz iteratively instead of starting from a fixed ansatz: this is what the ADAPT-VQE method ([43, 44]) does. At each step, it picks from a pool of gates the gate that maximizes the gradient of the energy with respect to the gate's parameter, therefore ensuring the fastest convergence to the minimum.
A major mostly uncharted territory is the design of ansätze specific to the nature of the AIM (beyond what the HVA does). In particular, the fact that the bath is non-interacting, which allows for drastic simplifications in action-based impurity solvers (subsection 2.2.2), has not been exploited so far.

The measurement problem VQE resorts to a classical summation of individual samples to compute the variational energy $E_{\boldsymbol{\theta}}$ (Eq. (55)). This means that the statistical error will scale as $\epsilon = O(1/\sqrt{N_\text{s}})$, with N_s the number of samples (shots). As explained before, this scaling of $1/\epsilon^2$ of the run time is much less favorable than the $1/\epsilon$ scaling of quantum phase estimation.

The prefactor of this scaling can be mitigated by many methods. One can, for instance, group terms that commute with one another: they can be measured without regenerating the state. One can also allocate the total shot budget based on the importance of each term in the Pauli decomposition: larger coefficients $|\lambda_i|$ in Eq. (55) should receive more shots. The optimal shot allocation can be worked out [45] (and see [46] for an adaptive shot allocation strategy), leading to a standard error on the mean that satisfies the upper bound:

$$\Delta E_{\boldsymbol{\theta}} \leq \frac{\sum_{i=1}^{M} |\lambda_i|}{\sqrt{N_{\mathrm{s}}}}. \tag{57}$$

The numerator of the upper bound is referred to as the one-norm H. Proposals have been made to minimize it by orbital rotations [47].

Another method called classical shadows [48] is based on the realization that measuring $E_{\boldsymbol{\theta}}$ by measuring each P_i (or group thereof) individually on the final state $|\Psi(\boldsymbol{\theta})\rangle$ (or $\rho_{\boldsymbol{\theta}}$ in the general case where it is afflicted by noise) is a poor reuse of the information in $\rho_{\boldsymbol{\theta}}$. Classical shadows thus first produce an estimate (called classical shadow) $\hat{\rho}_{\boldsymbol{\theta}}$ of $\rho_{\boldsymbol{\theta}}$ by appending gates drawn randomly for smartly chosen groups of unitaries to the circuit and then measuring along the σ_z axis…and then return estimates $\langle \hat{P}_i \rangle = \mathrm{Tr}(\hat{\rho}_{\boldsymbol{\theta}} P_i)$ to compute the energy $E_{\boldsymbol{\theta}}$. By so doing, the statistical error is still behaving as $1/\sqrt{N_{\mathrm{s}}}$(as per the central limit theorem), but the numerator can be mitigated (achieving, in some cases, a $\log(M)$ scaling, with M the number of Pauli terms). Adaptations to fermionic settings have appeared recently, albeit not in a VQE context [49].

The optimization problem Supposing the ansatz is short enough to beat decoherence, and the energy $E(\boldsymbol{\theta})$ can be measured to enough statistical accuracy, the VQE practitioner is still facing the problem of finding the minimum of $E_{\boldsymbol{\theta}}$. The difficulty of this optimization task has been a major focus of recent years.

On the practical side, methods have been developed to measure the gradients required in gradient-based minimization methods, like the gradient descent method, which updates parameters through

$$\boldsymbol{\theta}_{i+1} = \boldsymbol{\theta}_i - \alpha \boldsymbol{\nabla}_\theta E(\boldsymbol{\theta}_i), \tag{58}$$

with a learning rate α and $[\boldsymbol{\nabla}_\theta E(\boldsymbol{\theta})]_k = \frac{\partial E(\boldsymbol{\theta})}{\partial \theta_k} = \frac{\partial}{\partial \theta_k} \langle \Psi_\theta | H | \Psi_\theta \rangle$. It turns out that if the parametric gates used in the ansatz are of the form $U_k(\theta_k) = e^{-i\theta_k/2P_k}$, with $P_k^2 = I$, then the following identity (called "parameter shift rule") can be easily derived

$$\frac{\partial E(\boldsymbol{\theta})}{\partial \theta_k} = \frac{1}{2}\big(E(\theta_k{+}\pi/2) - E(\theta_k{-}\pi/2)\big), \tag{59}$$

where $E(\theta_k{+}\alpha)$ is shorthand for $E(\theta_1, \ldots, \theta_k{+}\alpha, \ldots, \theta_L)$. Estimating gradients is therefore relatively straightforward. It however requires a number of evaluations proportional to the number L of parameters, a major overhead compared to the $O(1)$ cost of computing gradients in classical deep neural networks using the backpropagation algorithm [50]. Other machine-learning-inspired methods like natural gradients can also be implemented [51], albeit at a much larger cost since the required quantum geometric tensor necessitates $O(L^2)$ energy evaluations.

On the more formal side, the potential landscape $E(\boldsymbol{\theta})$ (and more specifically its variance) has been studied for some classes of variational circuits $U(\boldsymbol{\theta})$ and observables H. The empirically observed vanishing of gradients in large regions of the variational space, dubbed "barren plateau problem" [52] is now understood as a curse of dimensionality issue [53, 54]: the larger the dimension of the effective space explored by the variational search, the more concentrated $E(\boldsymbol{\theta})$ around its mean and therefore the smaller the gradients (on average, as illustrated in Fig. 8(b)). This issue is particularly pressing for the hardware-efficient parametrized circuits we introduced above: if they are deep enough, the ensemble of unitaries $U(\boldsymbol{\theta})$ is very close to the group of Haar random matrices and the variance $\left\langle \left(E(\boldsymbol{\theta}) - \langle E(\boldsymbol{\theta})\rangle\right)^2 \right\rangle$ over the parameter landscape vanishes exponentially with the number N of qubits. In other words, the more expressive, the less trainable parametrized circuits become. On the other hand, physics-inspired ansätze, which usually come with more structure, could suffer less from this issue. Note also that the existence of barren plateaux is an average phenomenon: on average, energies are (exponentially) close to their mean. However, non-zero gradient portions of the parameter space exist (see circled region in 8(b)). The challenge lies in finding them. In particular, finding a good starting point $\boldsymbol{\theta_0}$ for the optimization appears crucial. There again, physics-informed choices (by, e.g., perturbation theory or classical pretraining of the variational ansatz) could play a crucial role. Adaptive techniques like the aforementioned ADAPT-VQE methods, or other ways of solving the eigenvalue problem (see e.g [55]) could also mitigate this issue.

3.4.2 Time evolution: variational circuits for time evolution.

The Trotter circuits described in a previous section are often too long compared to the available number of gates given the coherence time. Methods, like "variational quantum simulation" [56], have been designed to train variational circuits to perform a given time evolution. They are a simple adaptation of the variational principle used in VQE to the time-dependent case: given a variational state $|\Psi(\boldsymbol{\theta}(t))\rangle = U(\boldsymbol{\theta}(t))|\Psi_{\text{init}}\rangle$ ($|\Psi_{\text{init}}\rangle = c^\dagger|\Psi_0\rangle$ for the greater Green function), one can use the McLachlan variational principle

$$\min \delta \left\| \left(\frac{\mathrm{d}}{\mathrm{dt}} + iH \right) |\Psi(\boldsymbol{\theta}(t))\rangle \right\|$$

to write a differential equation for the parameters $\boldsymbol{\theta}(t)$

$$\sum_j M_{ij}\dot{\theta}_j = V_i$$

with $M_{i,j} = \mathrm{Re}\left(\frac{\partial\langle\Psi(\boldsymbol{\theta}(t))|}{\partial\theta_i}\frac{\partial|\Psi(\boldsymbol{\theta}(t))\rangle}{\partial\theta_j}\right)$ and $V_i = \mathrm{Im}\left(\langle\Psi(\boldsymbol{\theta}(t))|H\frac{\partial|\Psi(\boldsymbol{\theta}(t))\rangle}{\partial\theta_i}\right)$. Both quantities can be evaluated with dedicated quantum circuits similar to the Hadamard test [57, 58]. Interestingly, the aforementioned natural gradient approach can be obtained by invoking the McLachlan principle with imaginary times.

3.4.3 Reducing the effect of imperfections: error mitigation.

All the methods above aim at creating shorter circuits, but still suffer from decoherence. A variety of techniques known as error mitigation has been developed over the years to counter the exponential decay of fidelity (Eq. (54)). They generically trade a systematic bias generated by decoherence for an increased classical cost—that essentially helps recover the lost information. A representative example of this tradeoff is probabilistic error cancellation [59, 60]. To suppress the bias in energy in a noisy VQE, caused by the deviation between the noisy energy $E_{\text{noisy}} = \text{Tr}(\rho_{\text{f}} H)$, with ρ_{f} given by Eq. (53), and the perfect energy $E_{\text{perfect}} = \langle \Psi_{\text{f}} | H | \Psi_{\text{f}} \rangle$, one decomposes the "perfect" channels $\mathcal{E}^{(k)}_{\text{perfect}}(\rho)$ as a linear combination of the actual (noisy) channels $\mathcal{E}^{(k)}(\rho)$ that are realized in the experiment

$$\mathcal{E}^{(k)}_{\text{perfect}} = \sum_l q^{(k)}_l \mathcal{E}_l, \tag{60}$$

with the underlying assumption that these noisy channels form an independent family, and the $\sum_l q^{(k)}_l = 1$ to preserve the trace-preserving character (but the $q^{(k)}_l$ may be negative). The perfect energy can thus be decomposed as a very large sum, which is sampled through Monte-Carlo

$$\begin{aligned} E_{\text{perfect}} &= \sum_{l_1 \dots l_{N_{\text{g}}}} q^{(1)}_{l_1} \cdots q^{(N_{\text{g}})}_{l_{N_{\text{g}}}} \text{Tr}\big(H \mathcal{E}_{l_{N_{\text{g}}}} \circ \mathcal{E}_{l_{N_{\text{g}}-1}} \circ \cdots \mathcal{E}_{l_1}(\rho_{\text{i}})\big) \\ &= \Gamma \sum_{l_1 \dots l_{N_{\text{g}}}} p^{(1)}_{l_1} \cdots p^{(N_{\text{g}})}_{l_{N_{\text{g}}}} \text{s}(l_1, \dots l_{N_{\text{g}}}) \, \text{Tr}\big(H \mathcal{E}_{l_{N_{\text{g}}}} \circ \mathcal{E}_{l_{N_{\text{g}}-1}} \circ \cdots \mathcal{E}_{l_1}(\rho_{\text{i}})\big) \qquad (61) \\ &\approx \frac{\Gamma}{N_s} \sum_{i=1}^{N_s} \text{s}(l^{(i)}_1, \dots l^{(i)}_{N_{\text{g}}}) \, \text{Tr}\big(H \mathcal{E}_{l^{(i)}_{N_{\text{g}}}} \circ \mathcal{E}_{l^{(i)}_{N_{\text{g}}-1}} \circ \cdots \mathcal{E}_{l^{(i)}_1}(\rho_{\text{i}})\big). \qquad (62) \end{aligned}$$

Here, the probabilities $p^{(k)}_l = q^{(k)}_l / \sum_{l'} q^{(k)}_{l'}$ are introduced to deal with the possible negativity of the $q^{(k)}_l$, $\Gamma = \prod_{k=1}^{N_g} \sum_{l'} \left| q^{(k)}_{l'} \right|$ and $\text{s}(l_1, \dots l_{N_{\text{g}}}) = \prod_{k=1}^{N_g} \text{sign}(q^{(k)}_{l_k})$. The advantage of the summand of Eq. (62) is that it can be estimated with the noisy computer at hand by running a circuit with (noisy) gates $\mathcal{E}_{l^{(i)}_1}, \dots, \mathcal{E}_{l^{(i)}_{N_{\text{g}}}}$ and measuring H at the end, resulting in an unbiased estimate of E_{perfect}! The price to pay is, however, twofold: one needs to know precisely the noise models of the hardware to be able to perform the decomposition of Eq. (60), which requires quite expensive process tomography experiments. More fundamentally, the estimator comes with a statistical uncertainty that scales with the Γ factor, which can be rewritten as $\Gamma = \prod_{k=1}^{N_g} (1+2\eta_k)$, with the so-called "negativity" $\eta_k = \sum_{l, q_l<0} q^{(k)}_l$. To get an intuition how it scales, let us suppose that all gates have the same negativity η. Then

$$\Gamma \approx e^{2\eta N_{\text{g}}}. \tag{63}$$

In other words, to get a fixed statistical error bar $\epsilon \propto \Gamma / \sqrt{N_{\text{s}}}$, one needs to scale the number N_{s} of samples as $\Gamma^2 = e^{4\eta N_{\text{g}}}$, namely exponentially with the number of gates! This essentially tells us that to fight against the exponential loss in fidelity (Eq. (54)), we need to pay an exponential price. In practice, this exponential can be manageable provided the negativity is not too large. The better the hardware, the closer η to unity, the lower the sampling overhead.

4 Conclusion: state of the art, challenges and ways ahead

The tools we just introduced have been used in the past 10 years to solve the impurity model of DMFT with the help of quantum processors. Table 1 summarizes the various attempts. After the original proposal by [61] and [62], most works [63–66,68,71,73] focused on the simplest DMFT scheme, namely two-site DMFT [76], which consists in limiting the bath to only one bath site, requiring only 4 qubits. Most works used VQE in combination with the Hadamard test circuit we introduced before, with various ansätze and methods to optimize the time evolution needed in the Hadamard test. The Hadamard test method is replaced by a Lanczos-type algorithm in [69, 75] that builds the Krylov states using a variational ansatz $|\chi_n\rangle = U(\boldsymbol{\theta}_n)|\Phi_{\text{init}}\rangle$.

Driven by the optimization issues of variational methods, quantum subspace expansions are also proposed, in an impurity model context, by [70]: the Krylov bases (whether for the ground state or for the Green function, see paragraph 2.2.1) are constructed not in the full Hilbert space but in a reduced subspace built with states obtained by Trotter iterations: $|\psi_k\rangle = U(\delta t)^k|\Phi_{\text{init}}\rangle$, with $U(\delta t) = e^{-iH_{\text{AIM}}\delta t}$. The conjecture of the method is that Trotter iterates will yield a good enough subspace of the full Hilbert space to perform the Lanczos method in. The first (ground state) Lanczos iteration can also be replaced by a purely classical method, as advocated in [72]: there, DMRG is used to compute the ground state in the matrix product state form. The MPS is converted to a quantum circuit and then Trotter iterates $|\psi_k\rangle$ are generated on top of this state.

The above quantum Krylov variants require the computation of various matrix elements of the Trotter iterates $|\psi_k\rangle$, which incurs the aforementioned $1/\epsilon^2$ overhead. [77] proposes a way to avoid this overhead by simply sampling bitstrings $s_{i,k}$ from the $|\psi_k\rangle$'s and building the classical representation of H in the subspace corresponding to these bitstrings. [77] then classically finds the ground state energy by diagonalizing the restriction of H to this subspace for systems of up to 41 bath sites (but does not compute the Green function).

[63] looks at a nonequilibrium setting, which requires extending the formalism we introduced to Keldysh Green functions.

Alternative embedding techniques—which can be regarded as low-energy approximations of DMFT [6]—have been used, motivated by the fact that these techniques require an impurity problem with fewer bath sites ($N_b = N_c$), and require not the full time-dependent Green function, but only the one-particle reduced density matrix (essentially the $t{=}0$ Green function). This includes rotationally-invariant slave bosons (aka Gutzwiller [67,40]) and density-matrix embedding theory [78–80]. Finally, simpler slave-particle methods like $\mathbb{Z}_2$ slave spins were used to reduce the Hubbard model to even simpler (namely spin-based, as opposed to fermionic) effective models [81].

The current state of affairs is that the small sizes considered in the aforementioned publications are not yet large enough (except perhaps for [72, 77]) that ground state preparation issues with VQE (like barren plateaux) become severe, so that whether a variational preparation of low-energy states of the AIM with quantum methods can succeed is still an open question. As for the time evolution needed to compute the Green function, the decoherence rates of current processors have so far prevented one from reaching numbers of bath sites competitive with

Ref.	N_c	N_b	State preparation	Green function method	Noisy emul.	Physical implem.	Remark
[62]	any	any	Adiabatic state preparation	Hadamard test	No	No	Generic proposal.
[61]	1	10	N-A	Hadamard (Trotter)	Yes	Ions (th)	Nonequilibrium: kinetic ramp
[63]	1	1	Exact	Hadamard with Trotter	Yes	SC (th)	Study of noise in bath.
[64]	1	1	VQE (HEA)	Lehmann (excited-VQE)	No	SC + Ions (exp)	No self-consistency
[65]	1	1	Exact and VQE	Hadamard (Trotter)	Yes	No	Variational compression.
[66]	1	1	VQE (adhoc)	Hadamard (Trotter)	No	SC (exp)	
[67]	1	1	VQE (UCC)	N/A	No	SC (exp)	Periodic Anderson model. Parity mapping
[68]	1	1	VQE (adhoc)	Hadamard (fast-forwarding)	No	SC (exp)	
[40]	2	2	VQE (adhoc)	N/A	Yes	No	RISB.
[69]	1	3	VQE (HEA)	Krylov variational algorithm	No	No	QSGW+DMFT La_2CuO_4
[70]	1	7	Quantum subspace expansion	Quantum subspace expansion	No	No	
[71]	1	1	VQE (symmetric HEA)	Lehmann (excited-VQE)	Yes	SC (exp)	
[72]	3	17	Matrix product states	Quantum subspace expansion	No	No	$SrVO_3$, chain geometry.
[73]	1	1	VQE ([66])	Hadamard (Trotter)	No	No	
[74]	1	6	VQE (HEA, classical optim.)	Lehmann (qEOM)	No	SC (exp)	$Ca_2CuO_2Cl_2$, chain geometry
[75]	1	6	VQE (sym.-preserving ansatz)	Krylov variational algorithm	No	No	

Table 1: *Summary of early implementations of impurity solvers with quantum computers, sorted in chronological order. N_c: number of impurities. N_b: (maximum) number of bath sites. SC stands for superconducting qubits. All DMFT computations except those on materials are done on the Bethe lattice. The encoding is always Jordan-Wigner, unless otherwise stated.*

the best classical methods: larger bath sizes mean that larger evolution times, and thus larger circuits, are needed, at least with the Hamiltonian representation of the impurity model we worked with so far.

The bath size of a Hamiltonian-based representation of the AIM of DMFT will likely remain a major issue. Large bath sizes (many Dirac delta peaks, as in (12)) are needed to represent the spectral features of the hybridization function, and these in turn entail large numbers of qubits, and thus large circuits. From a nonequilibrium perspective, one can also argue that reaching long times requires large baths to avoid finite-size effects. In principle, the fact that the bath is noninteracting could be exploited to simplify circuits or perhaps reduce the number of qubits, but this has not been attempted yet, to the best of our knowledge—other than switching from DMFT to simpler embedding techniques like RISB and DMET, which can be seen as well-defined prescriptions for truncating the bath, albeit with access only to one-particle reduced density matrices (as opposed to frequency-dependent Green functions).

An alternative, promising route is to use another representation of the impurity model. For instance, open-system representations of the impurity model have been proposed [82–84] that use a dissipative bath instead of a noninteracting closed bath: each bath site can exchange electrons with an environment. The rate of dissipation Λ (as well as the usual other hybridization parameters) can be fixed by matching the hybridization function not with a sum of Dirac peaks (Eq. (12)) but of Lorentzians of width Λ

$$\Delta^{\mathrm{R}}(\omega) = \sum_k \frac{V_k^2}{\omega + i\Lambda - \varepsilon_k}. \tag{64}$$

On a classical processor, this allows to use fewer peaks to fit the same hybridization function (with many possible sophistications of the open-system representation [85]), and then, using a master equation-based solver, compute the corresponding Green function. Alternatively, one could use a noisy quantum processor to perform the corresponding dissipative time evolution [86]. This way, the natural decoherence of the processor could, at least partly, be used to mimic the physics of impurity electrons in solids.

This open-system representation may also solve a deeper issue of quantum algorithms for impurity models, namely the preparation of a ground (or low-energy) state. Working with dissipative models changes the perspective to preparing the steady state of an open quantum system... In such a context, more noise could help reach this steady state faster.

References

[1] R.P. Feynman, Int. J. Theor. Phys. **21**, 467 (1982)

[2] J. Hubbard, Proc. Roy. Soc. A **276**, 238 (1963)

[3] A. Georges, G. Kotliar, W. Krauth, and M.J. Rozenberg, Rev. Mod. Phys. **68**, 13 (1996)

[4] G. Knizia and G.K.-L. Chan, Phys. Rev. Lett. **109**, 186404 (2012)

[5] F. Lechermann, A. Georges, G. Kotliar, and O. Parcollet, Phys. Rev. B **76**, 155102 (2007)

[6] T. Ayral, T.-H. Lee, and G. Kotliar, Phys. Rev. B **96**, 235139 (2017)

[7] K. Held: In E. Pavarini, E. Koch, D. Vollhardt, and A.I. Lichtenstein (Eds.): *Autumn School on Correlated Electrons. DMFT at 25: Infinite Dimensions* (Forschungszentrum Julich, 2014), Vol. 4, chap. 10

[8] T. Ayral and O. Parcollet, Phys. Rev. B **94**, 075159 (2016)

[9] P.W. Anderson, Phys. Rev. **124**, 41 (1961)

[10] E. Koch: In E. Pavarini, E. Koch, D. Vollhardt, and A. Lichtenstein (Eds.): *The LDA+DMFT approach to strongly correlated materials* (Forschungszentrum Jülich, 2011), Vol. 1, chap. 8

[11] U. Schollwöck, Ann. Phys. **326**, 96 (2011)

[12] S. Paeckel, T. Köhler, A. Swoboda, S.R. Manmana, U. Schollwöck, and C. Hubig, Ann. Phys. **411**, 167998 (2019)

[13] T. Ayral, P. Besserve, D. Lacroix, and E.A. Ruiz Guzman, Europ. Phys. J. A **59**, 227 (2023)

[14] A.M. Childs, Y. Su, M.C. Tran, N. Wiebe, and S. Zhu, Phys. Rev. X **11**, 011020 (2021)

[15] G.H. Low and I.L. Chuang, Quantum **3**, 163 (2019)

[16] S.B. Bravyi and A.Y. Kitaev, Ann. Phys. **298**, 210 (2002)

[17] V. Havlíček, M. Troyer, and J.D. Whitfield, Phys. Rev. A **95**, 032332 (2017)

[18] F. Verstraete and J.I. Cirac, J. Stat. Mech.: Theory Exp. **2005**, P09012 (2005)

[19] C. Derby and J. Klassen, Phys. Rev. B **104**, 035118 (2020)

[20] M.G. Algaba, P.V. Sriluckshmy, M. Leib, and F. Simkovic, arXiv:2302.01862

[21] T. Albash and D.A. Lidar, Rev. Mod. Phys. **90**, 015002 (2018)

[22] D.W. Berry, G. Ahokas, R. Cleve, and B.C. Sanders, Commun. Comp. Phys. **270** 359 (2007)

[23] D. Guéry-Odelin, S. Mart, and J.G. Muga, Rev. Mod. Phys. **91** 045001 (2019)

[24] J. Kempe, A. Kitaev, and O. Regev in K. Lodaya, M. Mahajan: *FSTTCS 2004: Foundations of Software Technology and Theoretical Computer Science* (Springer, Heidelberg, 2004), pp. 372–383

[25] N. Schuch and F. Verstraete, Nat. Phys. **5**, 732 (2009)

[26] S. Bravyi and D. Gosset, Commun. Math. Phys. **356**, 451 (2017)

[27] M. Erakovic, F. Witteveen, D. Harley, J. Günther, M. Bensberg, O.R. Meitei, M. Cho, T. Van Voorhis, M. Reiher, and M. Christandl, PRX Life **3**, 013003 (2025)

[28] G. Ortiz, J.E. Gubernatis, E. Knill, and R. Laflamme, Phys. Rev. A **64**, 022319 (2001)

[29] D. Wecker, M.B. Hastings, N. Wiebe, B.K. Clark, C. Nayak, and M. Troyer, Phys. Rev. A **92**, 062318 (2015)

[30] A.Y. Kitaev, arXiv:quant-ph/9511026

[31] T. Ayral, Photoniques **131** 66 (2025)

[32] R. Cleve, A. Ekert, C. Macchiavello, and M. Mosca, Proc. Roy. Soc. A **454**, 339 (1998)

[33] Y. Tong, D. An, N. Wiebe, and L. Lin, arXiv:2008.13295

[34] J. Preskill, Quantum **2**, 79 (2018)

[35] A. Peruzzo, J. McClean, P. Shadbolt, M.-H. Yung, X.-Q. Zhou, P.J. Love, A. Aspuru-Guzik, and J.L. O'Brien, Nat. Commun. **5**, 4213 (2013)

[36] J. Tilly, H. Chen, S. Cao, D. Picozzi, K. Setia, Y. Li, E. Grant, L. Wossnig, I. Rungger, G.H. Booth, and J. Tennyson, Phys. Rep. **986**, 1 (2022)

[37] A. Kandala, A. Mezzacapo, K. Temme, M. Takita, M. Brink, J.M. Chow, and J.M. Gambetta, Nature **549**, 242 (2017)

[38] D. Wecker, M.B. Hastings, and M. Troyer, Phys. Rev. A **92**, 042303 (2015)

[39] P.-L. Dallaire-Demers, J. Romero, L. Veis, S. Sim, and A. Aspuru-Guzik, arXiv:1801.01053

[40] P. Besserve and T. Ayral, Phys. Rev. B **105**, 115108 (2022)

[41] P. Besserve, M. Ferrero, and T. Ayral, arXiv:2406.14170

[42] P. Besserve: *Quantum-classical hybrid algorithms for quantum many-body physics* (PhD Thesis, École Poytechnique, 2023)

[43] H.R. Grimsley, S.E. Economou, E. Barnes, N.J. Mayhall, Nat. Commun. **10**, 3007 (2019)

[44] H.L. Tang, V. Shkolnikov, G.S. Barron, H.R. Grimsley, N.J. Mayhall, E. Barnes, and S.E. Economou, PRX Quantum **2**, 020310 (2021)

[45] N.C. Rubin, R. Babbush, and J. McClean, New J. Phys. **20**, 053020 (2018)

[46] A. Arrasmith, L. Cincio, R.D. Somma, and P.J. Coles, arXiv2004.06252

[47] E. Koridon, S. Yalouz, B. Senjean, F. Buda, T.E. O'Brien, and L. Visscher, Phys. Rev. Res. **3**, 033127 (2021)

[48] H.-Y. Huang, R. Kueng, and J. Preskill, Nat. Phys. **16**, 1050 (2020)

[49] K. Wan, W.J. Huggins, J. Lee, and R. Babbush, Commun. Math. Phys. **404**, 629 (2023)

[50] G. Atilim, B.A. Pearlmutter, A.A. Radul, and J.M. Siskind, J. Machine Learning Res. **18**, 1 (2017)

[51] J. Stokes, J. Izaac, N. Killoran, and G. Carleo, Quantum **4**, 269 (2020)

[52] J.R. McClean, S. Boixo, V.N. Smelyanskiy, R. Babbush, and H. Neven, Nat. Commun. **9**, 4812 (2018)

[53] M. Ragone, B.N. Bakalov, F. Sauvage, A.F. Kemper, C. Ortiz Marrero, M. Larocca, and M. Cerezo, Nat. Commun. **15**, 7172 (2024)

[54] M. Larocca, S. Thanasilp, S. Wang, K. Sharma, J. Biamonte, P.J. Coles, L. Cincio, J.R. McClean, Z. Holmes, and M. Cerezo, arXiv:2405.00781

[55] M. Plazanet and T. Ayral, arXiv:2410.15129

[56] S. Endo, I. Kurata, and Y.O. Nakagawa, arXiv:1909.12250

[57] K. Mitarai and K. Fujii, Phys. Rev. Res. **1**, 013006 (2019)

[58] S. McArdle, A. Mayorov, X. Shan, S. Benjamin, and X. Yuan, Chem. Sci. **10**, 5725 (2019)

[59] S. Endo, S.C. Benjamin, and Y. Li, Phys. Rev. X **8**, 031027 (2018)

[60] K. Temme, S. Bravyi, and J.M. Gambetta, Phys. Rev. Lett. **119**, 180509 (2017)

[61] J.M. Kreula, S.R. Clark, and D. Jaksch, Sci. Rep. **6**, 32940 (2016)

[62] B. Bauer, D. Wecker, A.J. Millis, M.B. Hastings, and M. Troyer, Phys. Rev. X **6**, 031045 (2016)

[63] J.M. Kreula, L. García-Álvarez, L. Lamata, S.R. Clark, E. Solano, and D. Jaksch, EPJ Quantum Technol. **3**, 11 (2016)

[64] I. Rungger, N. Fitzpatrick, H. Chen, C.H. Alderete, H. Apel, A. Cowtan, A. Patterson, D.M. Ramo, Y. Zhu, N.H. Nguyen, E. Grant, S. Chretien, L. Wossnig, N.M. Linke, and R. Duncan, arXiv:1910.04735

[65] B. Jaderberg, A. Agarwal, K. Leonhardt, M. Kiffner, and D. Jaksch, Quantum Sci. Technol. **5**, 034015 (2020)

[66] T. Keen, T. Maier, S. Johnston, and P. Lougovski, Quantum Sci. Technol. **5**, 035001 (2020)

[67] Y. Yao, F. Zhang, C.-Z. Wang, K.-M. Ho, and P.P. Orth, Phys. Rev. Res. **3**, 013184 (2021)

[68] T. Steckmann, T. Keen, E. Kökcü, A.F. Kemper, E.F. Dumitrescu, and Y. Wang, arXiv:2112.05688

[69] F. Jamet, A. Agarwal, C. Lupo, D.E. Browne, C. Weber, and I. Rungger, arXiv:2105.13298

[70] F. Jamet, A. Agarwal, and I. Rungger, arXiv:2205.00094

[71] J. Ehrlich, D. Urban, and C. Elsässer, arXiv:2311.10402

[72] F. Jamet, L.P. Lindoy, Y. Rath, C. Lenihan, A. Agarwal, E. Fontana, F. Simkovic, B.A. Martin, and I. Rungger, arXiv:2304.06587

[73] A. Baul, H.F. Fotso, H. Terletska, J. Moreno, and K.-m. Tam, arXiv:2308.01392

[74] J. Selisko, M. Amsler, C. Wever, Y. Kawashima, G. Samsonidze, R.U. Haq, F. Tacchino, I. Tavernelli, and T. Eckl, arXiv:2404.09527

[75] E.B. Jones, C.J. Winkleblack, C. Campbell, C. Rotello, E.D. Dahl, M. Reynolds, P. Graf, and W. Jones, arXiv:2405.15069

[76] M. Potthoff, Phys. Rev. B **64**, 165114 (2001)

[77] J. Yu, J.R. Moreno, J.T. Iosue, L. Bertels, D. Claudino, B. Fuller, P. Groszkowski, T.S. Humble, P. Jurcevic, W. Kirby, T.A. Maier, M. Motta, B. Pokharel, A. Seif, A. Shehata, K.J. Sung, M.C. Tran, V. Tripathi, A. Mezzacapo, and K. Sharma, arXiv:2501.09702

[78] N.C. Rubin, arXiv:1610.06910

[79] H. Ma, M. Govoni, and G. Galli, npj Comp. Mater. **6**, 85 (2020)

[80] C. Cao, J. Sun, X. Yuan, H.-s. Hu, H.Q. Pham, and D. Lv, npj Comp. Mater. **9**, 78 (2023)

[81] A. Michel, L. Henriet, C. Domain, A. Browaeys, and T. Ayral, Phys. Rev. B **109**, 174409 (2024)

[82] E. Arrigoni, M. Knap, W.V.D. Linden, and W. Von Der Linden, Phys. Rev. Lett. **110**, 1 (2012)

[83] A. Dorda, M. Sorantin, W. von der Linden, and E. Arrigoni, New J. Phys. **19**, 063005 (2017)

[84] F. Schwarz, M. Goldstein, A. Dorda, E. Arrigoni, A. Weichselbaum, and J. von Delft, Phys. Rev. B **94**, 155142 (2016)

[85] Z. Huang, G. Park, G.K. Chan, and L. Lin, arXiv:2506.10308

[86] C. Bertrand, P. Besserve, M. Ferrero, and T. Ayral, Phys. Rev. B **111**, 245159 (2024)

Index

A
adiabatic method, 15.21
alloy band splitting, 8.18
analytic continuation, 11.3
Anderson localization, 8.14
Anderson model, 8.3
Anderson molecule, 3.7, 3.45
Anderson-Hubbard model, 8.4
annealed disorder, 8.4
antiferromagnetism, 14.18
atomic-sphere truncation, 3.33
average spectrum method, 11.19
averaged dynamical mean-field theory, 8.8

B
Bayes' theorem, 11.10
Bernoulli polynomials, 11.7
Bethe-Salpeter equation, 7.7, 14.7, 14.8
binary alloy distribution, 8.10
bit, 11.32
Brinkman-Rice transition, 1.14
broken symmetry, 2.20

C
Car-Parrinello method, 2.12
$CaVO_3$, 6.15
central limit theorem, 11.8
charge disproportionation, 6.18
charge self-consistency, 6.7
cluster dynamical mean field theory, 14.3, 14.4
cluster extensions of DMFT, 1.26
coherent potential approximation, 1.24, 8.9
cold atoms in optical lattices, 1.25
competing instabilities, 12.12
connected correlators, 13.11
connected determinants , 13.6
continuous-time quantum Monte Carlo, 3.15, 13.4
corrections to mean-field theory, 1.25
correlated subspace, 6.4
cross extrapolation, 9.20
cross interpolation, 9.13
crystal-field effects, 3.40
cuprates, 14.12

D
d-wave superconductivity, 12.10, 12.12
decoherence, 15.26
default model, 11.16
density functional theory, 2.2, 3.2, 14.13
DF, *see* density functional theory
DFT+DMFT, 1.27, 3.28, 6.6
diagrammatic Monte Carlo, 9.2, 13.6
dielectric environment, 5.12
dielectric function, 7.4, 7.21
Dirac, P.A.M., 2.5
discrepancy principle, 11.16
disorder, 1.24
dispersion (van der Waals) forces, 2.17
DMFT and functional RG, 12.19
doped Mott insulator, 4.12, 4.19
double counting correction, 3.3, 3.30, 3.38, 6.12
downfolding, 3.30, 6.7
dual fermions, 13.8, 14.4
  action, 13.12
dual functions, 11.6
dynamical mean-field theory, 1.20, 3.25, 12.19, 14.2
  impurity solver, 3.15
  multi-site and multi-orbital problems, 3.28
dynamical sign problem, 10.14
dynamical vertex approximation, 1.27, 14.4, 14.5, 14.10
Dyson equation, 3.7, 7.6, 7.7, 14.6

E
effective action, 12.4
Ehrenfest theorem, 2.5
electron density, 2.6
electron gas
  eigenmodes, 7.9
  excitation spectrum, 7.11
  particle-hole excitations, 7.8
electron-electron interaction, 6.11
electronic correlations, 1.3, 1.20, 1.27

electronic spectral function, 13.14
entropy, 11.32
    Rényi, 11.25
Euler polynomials, 11.6
exact flow equations, 12.6
exact renormalization group, 12.2
exchange hole, 2.6
exchange-correlation energy, 2.16
exchange-correlation hole, 2.10
excitations
    particle-hole, 7.11
    plasmon, 7.10

F
Falicov-Kimball model, 1.18, 8.4
Fe-based superconductors, 4.4
Fermi liquid, 1.13, 1.19
fermionic sign problem, 13.5
ferromagnetism, 1.8, 1.24
Feynman diagrams
    screened interaction, 7.6
    self-energy, 7.13
    susceptibility, 7.6, 7.7
four points correlator, 13.12
frontier orbitals, 6.14
functional integral, 11.19
functional renormalization group, 12.2, 12.3

G
Gáspár, R., 2.7
generalized mean (average), 8.5
geometric series, 7.5
Green function, 15.2
    Matsubara, 11.4
    retarded, 11.4
Gutzwiller approximation, 1.12
Gutzwiller wave function, 1.14
GW approximation, 7.12
GW+DMFT, 1.27

H
Hölder or p-mean, 8.5
Hadamard test, 15.18
Hartree approximation, 2.3
Hartree-Fock approximation, 2.4, 3.20, 3.26
Hubbard bands, 13.15
Hubbard dimer, 3.5, 3.43
Hubbard model, 1.3, 1.10, 1.16, 3.25, 12.10, 14.11
Hubbard models for t_{2g} and e_g systems, 3.34
Hubbard-Stratonovich transformation, 13.11
Hund's coupling, 4.9
Hund's metal, 4.2
Hund's rules, 4.2
hybridization function, 3.6

I
ill-conditioned problem, 11.11
ill-posed problem, 11.2
inchworm algorithm, 10.22
infinite dimensions, 1.7, 1.14, 12.19
interaction
    RPA screened, 7.4, 7.5
    RPA, diagrams, 7.6
    Yukawa, 7.10, 7.12, 7.13
Ising model, 1.8

J
Jordan-Wigner encoding, 15.19

K
Kanamori interaction, 4.9, 6.11
Karush-Kuhn-Tucker conditions, 11.30
Keldysh
    contour, 10.3
    formalism, 9.7
    index, 9.7, 10.20
    time, 9.7, 10.6, 10.20
Kohn-Sham theory, 2.8
Kondo ridge, 9.22
Kubo formula, 7.5
Kullback-Leibler divergence, 11.34

L
LDA+DMFT, 3.25, 3.28
LDA+U vs LDA+DMFT, 3.20, 3.24, 3.40
least-squares (LS)
    non-negative (NNLS), 11.12, 11.30
Lehmann representation, 3.47
Lindhard function, 7.8, 7.11
linear response theory, 7.5

liquid bismuth, 2.14
local density approximation, 2.10, 2.17
local Dyson equation, 3.7
local moment, 4.12
localization of the basis, 3.33
LSD approximation, 2.15

M
magnon, 14.16
matrix product states, 9.11, 15.9
maximally localized Wannier functions, 4.8
maximum entropy method, 11.17
  Bryan, 11.19
  classic, 11.19
  historic, 11.17
maximum likelihood estimator, 11.10
mean field, 1.21
mean-field theory, 1.7, 1.10
metal-insulator transition, 1.13, 1.23, 6.16
model building, 3.30
moiré, 5.2
  flat bands, 5.7, 5.13
Mott insulator, 4.13
Mott transition, 1.13, 1.28, 3.25, 8.10
multi-orbital Hubbard models, 3.28

N
Nambu space, 13.17
nickelates, 14.12, 14.19
nodal-antinodal dichotomy, 13.19
non-crossing approximation, 10.21
non-negative least-squares, 11.12
non-spherical Coulomb terms, 3.38
nonequilibrium DMFT, 1.25
normal distribution, truncated, 11.35

O
one-crossing approximation, 10.21
orbital ordering, 3.41
orbital polarization, 6.15
orbital-selective correlations, 4.7

P
parameter shift rule, 15.31
parquet equation, 14.7, 14.8
path integral, 11.19
  formalism, 13.2
Picard plot, 11.14
plasma frequency, 7.10
plasmon, 7.10
pseudo-particle formalism, 10.21
pseudogap, 14.19

Q
quantum circuits, 15.15
quantum impurity model, 10.3, 10.4
  current-voltage characteristics, 10.19
  hybridization function, 10.11
  Kondo temperature, 10.18
  level broadening, 10.5
quantum Monte Carlo, 13.2
  continuous-time, 3.15
quantum phase estimation, 15.24
quenched disorder, 8.4

R
Rényi entropy, 11.25
random phase approximation, 14.2
rare earth elements, 2.2
real materials, 2.3
real-space dynamical mean-field theory, 8.6
reciprocity relations, 12.4
reference system, 13.9
regularization, 11.13
renormalization
  group, 11.28
renormalized mean-field theory, 12.17

S
Schur complement, 9.12
Schwinger-Dyson equation, 14.8, 14.9
screening
  dynamical, 7.14
  Thomas-Fermi, 7.12
self-consistency, 3.25
self-consistent equation, 1.10, 1.20
self-energy, 1.15, 1.19
  GW, 7.13, 7.16
  diagrams, 7.13
  dynamical, 7.16
  exchange, 7.13, 7.14
  Hubbard dimer, 3.6
  local, 3.6, 3.9

self-interaction correction, 2.16
Shannon entropy, 11.32
shear viscosity, 2.14
single-impurity Anderson model, 1.4, 1.20, 8.6, 9.6, 15.7
singular value decomposition (SVD), 11.10
Slater determinant, 2.4
Slater exchange potential, 2.7
slave-boson mean-field theory, 1.14
slave-spin mean-field, 4.10, 4.16
Sommerfeld coefficient of specific heat, 4.2, 4.7
spectral function, 11.3
spin fluctuations, 14.3, 14.15, 14.17
spin-orbit effects, 3.35, 3.40
spin-orbit interaction, 3.35
spontaneous symmetry breaking, 12.17
$SrCrO_3$, 6.19
strong-coupling, 13.2
strong-coupling CTQMC, 10.10
  current measurement, 10.13
  segment representation, 10.12
strongly correlated systems, 2.2, 2.17
super-exchange Hamiltonians, 3.41
superconductivity, 14.20
susceptibility, 14.15
  diagrams, 7.6
  Feynman diagrams, 7.7
  RPA, 7.4, 7.5
    electron gas, 7.9
  RPA diagrams, 7.6
  vertex corrections, 7.7

T
tensor cross interpolation, 9.11, 10.23
  algorithm, 9.17
Thomas-Fermi theory, 2.2, 2.4
Tikhonov regularization, 11.14
topological heavy fermions, 5.16
topological properties, 1.23, 1.24
transition metal oxides, 6.12
Trotterization, 15.15
twisted bilayer graphene, 5.2, 5.4, 5.5, 5.13
typical medium theory, 8.14

U
upfolding, 6.6

V
variational quantum eigensolver, 15.28
vertex, 14.3, 14.9, 14.16
vertex functions, 12.4

W
Wannier functions, 3.31, 5.9, 5.20, 6.5, 7.18
  spread, 7.19
weak-coupling CTQMC, 10.5
  auxiliary-field decomposition, 10.6
  auxiliary-field formalism, 10.5
  current measurement, 10.9
  detailed balance, 10.7
  disconnected diagrams, 10.20
  fast updates, 10.7
  Green function measurement, 10.8
Weiss field, 3.26
Wick rotation, 11.3
Wick's theorem, 7.6, 9.9, 13.13

X
Xα approximation, 2.16

Schriften des Forschungszentrums Jülich
Modeling and Simulation

1. **The LDA+DMFT approach to strongly correlated materials**
   Lecture Notes of the Autumn School 2011 Hands-on LDA+DMFT
   edited by E. Pavarini, E. Koch, D. Vollhardt, A. Lichtenstein (2011), 420 pages
   ISBN 978-3-89336-734-4

2. **Correlated Electrons: From Models to Materials**
   Lecture Notes of the Autumn School on Correlated Electrons 2012
   edited by E. Pavarini, E. Koch, F. Anders, and M. Jarrell (2012), 450 pages
   ISBN 978-3-89336-796-2

3. **Emergent Phenomena in Correlated Matter**
   Lecture Notes of the Autumn School on Correlated Electrons 2013
   edited by E. Pavarini, E. Koch, and U. Schollwöck (2013), 520 pages
   ISBN 978-3-89336-884-6

4. **DMFT at 25: Infinite Dimensions**
   Lecture Notes of the Autumn School on Correlated Electrons 2014
   edited by E. Pavarini, E. Koch, D. Vollhardt, A. Lichtenstein (2014), 450 pages
   ISBN 978-3-89336-953-9

5. **Many-Body Physics: From Kondo to Hubbard**
   Lecture Notes of the Autumn School on Correlated Electrons 2015
   edited by E. Pavarini, E. Koch, and P. Coleman (2015), 500 pages
   ISBN 978-3-95806-074-6

6. **Quantum Materials: Experiments and Theory**
   Lecture Notes of the Autumn School on Correlated Electrons 2016
   edited by E. Pavarini, E. Koch, J. van den Brink, G. Sawatzky (2016), 420 pages
   ISBN 978-3-95806-159-0

7. **The Physics of Correlated Insulators, Metals, and Superconductors**
   Lecture Notes of the Autumn School on Correlated Electrons 2017
   edited by E. Pavarini, E. Koch, R. Scalettar, and R. Martin (2017), 450 pages
   ISBN 978-3-95806-224-5

8. **DMFT: From Infinite Dimensions to Real Materials**
   Lecture Notes of the Autumn School on Correlated Electrons 2018
   edited by E. Pavarini, E. Koch, A. Lichtenstein, D. Vollhardt (2018), 480 pages
   ISBN 978-3-95806-313-6

9. **Many-Body Methods for Real Materials**
   Lecture Notes of the Autumn School on Correlated Electrons 2019
   edited by E. Pavarini, E. Koch, and S. Zhang (2019), 520 pages
   ISBN 978-3-95806-400-3

Schriften des Forschungszentrums Jülich
Modeling and Simulation

10. **Topology, Entanglement, and Strong Correlations**
    Lecture Notes of the Autumn School on Correlated Electrons 2020
    edited by E. Pavarini and E. Koch (2020), 500 pages
    ISBN 978-3-95806-466-9

11. **Simulating Correlations with Computers**
    Lecture Notes of the Autumn School on Correlated Electrons 2021
    edited by E. Pavarini and E. Koch (2021), 420 pages
    ISBN 978-3-95806-529-1

12. **Dynamical Mean-Field Theory of Correlated Electrons**
    Lecture Notes of the Autumn School on Correlated Electrons 2022
    edited by E. Pavarini, E. Koch, A. Lichtenstein, D. Vollhardt (2022), 450 pages
    ISBN 978-3-95806-619-9

13. **Orbital Physics in Correlated Matter**
    Lecture Notes of the Autumn School on Correlated Electrons 2023
    edited by E. Pavarini and E. Koch (2023), 520 pages
    ISBN 978-3-95806-689-2

14. **Correlations and Phase Transitions**
    Lecture Notes of the Autumn School on Correlated Electrons 2024
    edited by E. Pavarini and E. Koch (2024), 480 pages
    ISBN 978-3-95806-751-6

15. **Understanding Correlated Materials with DMFT**
    Lecture Notes of the Autumn School on Correlated Electrons 2025
    edited by E. Pavarini, E. Koch, A. Lichtenstein, D. Vollhardt (2025), 480 pages
    ISBN 978-3-95806-813-1